

1997

The dynamics of liquids in moving containers: Numerical models for viscous unsteady free surface flows

Adonis C. Kassinos
Iowa State University

Follow this and additional works at: <https://lib.dr.iastate.edu/rtd>

 Part of the [Aerospace Engineering Commons](#), and the [Applied Mechanics Commons](#)

Recommended Citation

Kassinos, Adonis C., "The dynamics of liquids in moving containers: Numerical models for viscous unsteady free surface flows " (1997). *Retrospective Theses and Dissertations*. 12261.
<https://lib.dr.iastate.edu/rtd/12261>

This Dissertation is brought to you for free and open access by the Iowa State University Capstones, Theses and Dissertations at Iowa State University Digital Repository. It has been accepted for inclusion in Retrospective Theses and Dissertations by an authorized administrator of Iowa State University Digital Repository. For more information, please contact digirep@iastate.edu.

INFORMATION TO USERS

This manuscript has been reproduced from the microfilm master. UMI films the text directly from the original or copy submitted. Thus, some thesis and dissertation copies are in typewriter face, while others may be from any type of computer printer.

The quality of this reproduction is dependent upon the quality of the copy submitted. Broken or indistinct print, colored or poor quality illustrations and photographs, print bleedthrough, substandard margins, and improper alignment can adversely affect reproduction.

In the unlikely event that the author did not send UMI a complete manuscript and there are missing pages, these will be noted. Also, if unauthorized copyright material had to be removed, a note will indicate the deletion.

Oversize materials (e.g., maps, drawings, charts) are reproduced by sectioning the original, beginning at the upper left-hand corner and continuing from left to right in equal sections with small overlaps. Each original is also photographed in one exposure and is included in reduced form at the back of the book.

Photographs included in the original manuscript have been reproduced xerographically in this copy. Higher quality 6" x 9" black and white photographic prints are available for any photographs or illustrations appearing in this copy for an additional charge. Contact UMI directly to order.

UMI

A Bell & Howell Information Company
300 North Zeeb Road, Ann Arbor MI 48106-1346 USA
313/761-4700 800/521-0600

**The dynamics of liquids in moving containers:
Numerical models for viscous unsteady free surface flows**

by

Adonis C. Kassinos

A dissertation submitted to the graduate faculty
in partial fulfillment of the requirements for the degree of
DOCTOR OF PHILOSOPHY

Major: Mechanical Engineering

Major Professor: Joseph M. Prusa

Iowa State University

Ames, Iowa

1997

Copyright © Adonis C. Kassinos, 1997. All rights reserved.

UMI Number: 9737774

**Copyright 1997 by
Kassinos, Adonis C.**

All rights reserved.

**UMI Microform 9737774
Copyright 1997, by UMI Company. All rights reserved.
This microform edition is protected against unauthorized
copying under Title 17, United States Code.**

UMI
300 North Zeeb Road
Ann Arbor, MI 48103

**Graduate College
Iowa State University**

**This is to certify that the Doctoral dissertation of
Adonis C. Kassinos
has met the dissertation requirements of Iowa State University**

Signature was redacted for privacy.

Committee Member

Signature was redacted for privacy.

Major Professor /

Signature was redacted for privacy.

For the Major Program

Signature was redacted for privacy.

For the Graduate College

DEDICATION

To my heart's twin . . . Mary.

TABLE OF CONTENTS

LIST OF TABLES	viii
LIST OF FIGURES	xi
1. OVERVIEW OF THE SLOSHING PROBLEM	1
1.1 The Theoretical Background	2
1.1.1 The Liquid-Vapor Interface	3
1.1.2 The Linearized Theory of Gravity Waves	8
1.1.3 Aspects of Rotating Flows	11
1.2 The Numerical Approach to Liquid Sloshing	15
1.2.1 Numerical Works on Free Surface Flows	19
1.3 Overview of the Present Study	23
1.4 Outline of the Thesis	24
PART I. SLOSHING IN 2-D MOVING CONTAINERS	
2. LIQUID SLOSHING IN A 2-D TRANSLATING CONTAINER	27
3. MATHEMATICAL FORMULATION	29
3.1 Dimensional Governing Equations	31
3.1.1 Pressure Poisson Equation	32
3.1.2 Free Surface Kinematic Condition	33
3.1.3 Boundary Conditions	34
3.2 Initial Conditions	37
3.2.1 Characteristic Scales	38
3.3 Dimensionless Formulation	42
3.3.1 Dimensionless Governing Equations	44
3.3.2 Dimensionless Boundary Conditions	45
3.4 Dimensionless Initial Conditions	46
3.5 Inviscid Irrotational Model	49

3.6	Streamfunction-Vorticity Formulation	53
3.7	Steady State Condition	55
3.8	First Law Analysis	56
3.9	Coupling of Fluid and Vehicular Dynamics	61
4.	NUMERICAL METHOD	71
4.1	Grid Generation	72
4.2	Transformation of Equations onto (ξ, η) Space	73
4.2.1	Discretization of the Momentum Equations	76
4.2.2	Setup of the Pressure Correction Scheme	80
4.2.3	Discretization of the Pressure Poisson Equation	84
4.2.4	Discretization of the Kinematic Condition	86
4.2.5	Discretization of the Boundary and Initial Conditions	87
4.3	Computational Procedure	88
4.3.1	Relaxation Parameters	89
4.3.2	Convergence Criteria	90
4.3.3	Outline of Solution Algorithm	91
4.4	Evaluation of the Method	95
4.4.1	Spatial Truncation Error Behavior	95
4.4.2	Time Differencing	99
4.4.3	Integration of the Kinematic Equation	103
4.4.4	Free Surface Position at the Contact Point	106
4.4.5	Pressure Solution	109
5.	RESULTS	112
5.1	Kinematic Description of the Liquid Sloshing	114
5.1.1	Case 1: Liquid Flow in an Accelerating Container	115
5.1.2	Case 2: Liquid Flow in an Impulsively Started Container	128
5.1.3	Case 3: Liquid Flow at Higher Galileo Numbers.	141
5.1.4	Case 4: Effects of Surface Tension	153
5.1.5	Case 5: Effects of Liquid Depth	166
5.2	Parametric Effects on Sloshing	170
5.2.1	Effects of Initial Liquid Depth	173
5.2.2	Effects of Forcing Conditions	178
5.2.3	Effects of Liquid Viscosity	182
5.2.4	Effects of Surface Tension	187

5.3	Liquid Interaction with the Moving Container	205
PART II. SLOSHING IN 3-D MOVING CONTAINERS		214
6.	A GENERAL THREE DIMENSIONAL SLOSHING MODEL	215
7.	FORMULATION OF THE 3D MODEL	217
7.1	Mathematical Model	217
7.1.1	Linearly Accelerating Coordinate System	218
7.1.2	Spinning Nutating Coordinate System.	219
7.1.3	Body Centered Coordinate System	222
7.1.4	Body Fixed Coordinate System	223
7.1.5	Self Adjusting Body Fixed Coordinates	225
7.1.6	Poisson Equation for Pressure	227
7.1.7	Free Surface Kinematic Condition	227
7.1.8	Boundary Conditions	228
7.1.9	Initial Conditions	229
7.1.10	Nondimensionalization	231
7.2	Numerical Method	232
7.2.1	Generalized Grid Coordinates	233
7.2.2	Metric Term Evaluation and Singularities	235
7.2.3	Governing Equations	238
7.2.4	Boundary Conditions	239
7.2.5	Finite Difference Method	241
7.3	Computational Procedure	242
7.3.1	Adjustment of Surface Tracking Angles	243
7.3.2	Grid Generation Procedure	244
7.3.3	Pressure Solution Algorithm	249
8.	RESULTS AND DISCUSSION	251
8.1	Liquid Flows in Translating Rectangular Containers	251
8.1.1	Use of the Numerical Model for Rectangular Geometries	252
8.1.2	Liquid Flow in an Impulsively Started Container	253
8.1.3	Parametric Effects of the Container Depth	259
8.2	Axisymmetric Spin-up in a Cylinder	264
8.2.1	Use of the Numerical Model for the Cylindrical Spinup	264

8.2.2	Development of the Flowfield	267
8.2.3	Comparison with Experimental Results	283
8.3	Three Dimensional Flow in a Rotating Spherical Container	286
9.	CONCLUDING REMARKS	303
9.1	Formulation Summary	303
9.2	Numerical Method Summary	305
9.3	Summary of Results	306
	APPENDIX A: FREE SURFACE DYNAMIC CONDITIONS	307
	APPENDIX B: BOUNDARY LAYER SOLUTION	309
	APPENDIX C: TRANSFORMATION METRICS	314
	BIBLIOGRAPHY	315

LIST OF TABLES

Table 5.1:	Representative Values of Ga for Various Fluids	113
Table 5.2:	Cases Considered for Kinematic Analysis	114
Table 5.3:	Average Period of Oscillation, \bar{T} , at Several Ga Values	183
Table 8.1:	Effect of Container Depth, Λ , on the Period of Oscillation, \bar{T} , and Modulus of Decay, τ	259

LIST OF FIGURES

Figure 3.1:	Translating Rectangular Container	30
Figure 3.2:	Free Surface Curvilinear Coordinates	36
Figure 3.3:	Initial Conditions Solution	50
Figure 3.4:	Initial Liquid Kinetic Energy	62
Figure 3.5:	Forces on an Accelerating Vehicle	63
Figure 3.6:	Apparent Liquid Mass at $t = 0^+$	70
Figure 4.1:	Grid Generation	74
Figure 4.2:	Grid Star Definition	78
Figure 4.3:	Iterative Solution Cycle	92
Figure 4.4:	Iterative Convergence History	94
Figure 4.5:	Effect of Grid Stretching	97
Figure 4.6:	Grid Refinement and Spatial Truncation Error	98
Figure 4.7:	Effect of Δt on the Truncation Error	101
Figure 4.8:	Long Term Accuracy of the Solution	102
Figure 4.9:	Required Computation Time vs Δt	104
Figure 4.10:	Integration of the Kinematic Condition	105
Figure 4.11:	Contact Point Movement	108
Figure 4.12:	A Comparison of ACM and PPM Methods	111
Figure 5.1:	Velocity Field for $Q = 0.2$, $F_o = 0.5$, $Ga = 10^6$, and $Bo = \infty$.	116
Figure 5.2:	Pressure Field for $Q = 0.2$, $F_o = 0.5$, $Ga = 10^6$, and $Bo = \infty$.	121
Figure 5.3:	Vorticity Field for $Q = 0.2$, $F_o = 0.5$, $Ga = 10^6$, and $Bo = \infty$.	124
Figure 5.4:	Velocity Field for $U_o = 0.15$, $F_o = 0.3$, $Ga = 10^6$, and $Bo = \infty$.	129
Figure 5.5:	Pressure Field for $U_o = 0.15$, $F_o = 0.3$, $Ga = 10^6$, and $Bo = \infty$.	133
Figure 5.6:	Hydrodynamic Pressure for $U_o = 0.15$, $F_o = 0.3$, $Ga = 10^6$, and $Bo = \infty$	137
Figure 5.7:	Velocity Field for $Q = 0.2$, $F_o = 0.5$, $Ga = 10^{10}$, and $Bo = \infty$.	142

Figure 5.8: Pressure Field for $Q = 0.2$, $F_o = 0.5$, $Ga = 10^{10}$, and $Bo = \infty$. 145

Figure 5.9: Free Surface Evolution for Cases 1 and 3 150

Figure 5.10: Free Surface Elevation Maps for Cases 1 and 3 151

Figure 5.11: First Three Modes of Sloshing for Case 3 152

Figure 5.12: Velocity Field for $Q = 0.2$, $F_o = 0.5$, $Ga = 10^8$, and $Bo = 20$. 155

Figure 5.13: Pressure Field for $Q = 0.2$, $F_o = 0.5$, $Ga = 10^8$, and $Bo = 20$. 158

Figure 5.14: Hydrodynamic Pressure for $Q = 0.2$, $F_o = 0.5$, $Ga = 10^8$, and $Bo = 20$ 161

Figure 5.15: First Three Modes of Sloshing for Case 4 165

Figure 5.16: Free Surface Evolution for Case 4 167

Figure 5.17: Free Surface Elevation Maps for Case 4 168

Figure 5.18: Centerline Velocity Profiles for Case 5 169

Figure 5.19: Effect of Initial Liquid Depth, F_o , on the Period, T 175

Figure 5.20: Effect of Initial Liquid depth, F_o , on the Dissipation Rate, τ . 176

Figure 5.21: Effect of Apparent Acceleration, Q , on the Period, T 179

Figure 5.22: Effect of Apparent Acceleration, Q , on the Viscous Dissipation Rate 181

Figure 5.23: Effect of the Galileo Number, Ga , on the Period of Oscillation, T 185

Figure 5.24: Effect of Galileo Number, Ga , on the Modulus of Decay, τ . . . 186

Figure 5.25: Effect of Bond Number on Surface Elevation 189

Figure 5.26: Energy Balance for $Bo = 20$ and $Ga = 10^8$ 191

Figure 5.27: Energy Balance for $Bo = 20$ and $Ga = \infty$ 194

Figure 5.28: Trajectories of the Liquid System in (E_p, E_k) Space 195

Figure 5.29: Liquid Oscillations in (E_p, E_k) Space at $Bo = 20$ 197

Figure 5.30: Liquid Oscillations in (E_p, E_k) Space at $Bo = 50$ 198

Figure 5.31: Maximum Surface Tension Energy Storage 199

Figure 5.32: Free Surface Profiles at Static Equilibrium 202

Figure 5.33: Residual System Energy at Static Equilibrium 203

Figure 5.34: Effect of Bond Number on Viscous Dissipation 204

Figure 5.35: Effect of Bond Number on Period of Oscillation 206

Figure 5.36: Effects of a Finite Vehicle Mass, M , on the Sloshing Dynamics 210

Figure 5.37: Effect of Vehicle Payload, λ , on the Period of Oscillation, T . . 213

Figure 7.1: Linearly Accelerating Coordinate System, x_0 219

Figure 7.2: Spinning Nutating Coordinate System, x_1 221

Figure 7.3:	Body Centered Coordinate System, x_2	223
Figure 7.4:	Surface Tracking Coordinates, x_4	226
Figure 7.5:	Generalized Grid Coordinates, ξ	234
Figure 7.6:	Local Grid Molecules on the x_{41} Axis	237
Figure 7.7:	Adjustment of the Grid at the Free Surface	246
Figure 7.8:	Algebraic Grid Generation Scheme	248
Figure 8.1:	Problem Geometry for 3D Rectangular Containers	252
Figure 8.2:	Velocity Field for an Impulsively Translated Rectangular Con- tainer	255
Figure 8.3:	Free Surface Position for an Impulsively Translated Rectangu- lar Container	260
Figure 8.4:	Computational Domain for Cylindrical Spin-up	266
Figure 8.5:	Developing Flowfield in a Spinning Cylinder	269
Figure 8.6:	Flowfield in the Corner Region of the Cylinder	280
Figure 8.7:	Angular Momentum of Liquid in a Spinning Cylinder	282
Figure 8.8:	Comparison of Numerical and Experimental Free Surface Position	285
Figure 8.9:	Simplified Geometry for Asymmetric Spherical Spinup.	287
Figure 8.10:	Initial Pressure Impulse, Π , in a Rotating Sphere.	289
Figure 8.11:	Initial Velocity Field, u_3^+ , in a Rotating Sphere.	290
Figure 8.12:	Liquid Motion in a Rotating Spherical Container.	292
Figure 8.13:	Trajectory of the Liquid Center of Gravity for Spherical Spinup.	298
Figure 8.14:	Viscous Decay for Spherical Spinup.	300
Figure 8.15:	Liquid Volume Error for Spherical Spinup.	302

1. OVERVIEW OF THE SLOSHING PROBLEM

The dynamic behavior of liquids in moving containers poses a problem of immense analytical and practical interest. The understanding of this complex dynamic behavior has far reaching implications encompassing a wide field of technologies. Sloshing occurs in moving vehicles with contained liquid masses, such as trucks, railroad cars, oil tankers, aircraft, and spacecraft (see [1], [2], [3], and [4]). The dynamic forcing of the liquid due to the vehicle motion can generate substantial periodic forces capable of threatening the functional as well as the structural integrity of the vehicle. This becomes a factor of primary concern in spacecraft design where long term vehicle control is critical [5]. If the sloshing frequency is sufficiently close to the natural frequency of the vehicle's structure, resonance can result in instabilities with catastrophic consequences. This has been demonstrated by past failures to successfully control the launching of a number of spin-stabilized satellites. The failure of the spacecraft's control system has been attributed to the destabilizing effects caused by sloshing within liquid stores carried aboard the spacecraft.

Applications of the sloshing problem are by no means limited to the design of moving vehicles. Forces generated by the seismic excitation of contained liquid masses in storage tanks and dams must be carefully considered in the design and construction of such facilities (see [6], [7]). Successful designs of Tuned Sloshing Dampers (TSD) have been implemented to counteract the unpredictable forcing of tall structures due to earthquakes as well as to reduce their pitching motions due to everyday wind forcing (see [8], [9], and [10]). Furthermore, valuable knowledge pertaining to the modeling of large amplitude waves along a liquid-gas interface can be gained in this study. The prediction of tides and bores, the reduction of wave induced drag on floating bodies, and the development of interactive ocean-atmosphere models, are all possible applications [4].

The sloshing problem falls into the category of moving boundary problems. Their solution is complicated by the fact that the position of at least some part of the

problem domain, represented here by the free surface, is not known *a priori*, but is instead found as part of the solution. In addition, the shape of the moving boundary is generally irregular which further complicates the problem. The study of liquid sloshing in moving containers suffers from an additional degree of complexity. The easiest and physically most meaningful way to describe the liquid motion is in terms of a coordinate frame that moves along with the container. However, the motion of the container can be quite complex, composed of several superimposed translational and rotational components. Modifying the conservation principles needed to describe the problem, for this noninertial coordinate frame can result in a very complicated set of governing equations.

1.1 The Theoretical Background

Liquid sloshing, in its broader sense, deals with the description of the dynamics of incompressible liquids in moving containers. The differential equations governing the motion of such a liquid suggest that two kinds of natural oscillations are possible [11]. These are, *sloshing waves*, and *inertial waves*. Sloshing waves are characterized by oscillations of the free surface and center of mass of the liquid. They represent a dynamic interaction between the effective gravity forces and inertial forces. Inertial waves are internal liquid oscillations. They can be excited in completely filled, or partially filled containers. If the free surface oscillates, the oscillations are small, thus resulting in negligible center of mass oscillations.

The development of a successful model to describe the motion of a viscous incompressible fluid within a moving container hinges upon the successful modeling of the free surface. The accurate prediction of the free surface position and the use of appropriate dynamic conditions are critical factors that influence the accuracy of the model. Thus some of the underlining theory behind the free surface model will be touched upon here.

The theoretical study of wave dynamics and free surface flows in general is rapidly approaching its two hundred year mark. Numerous analytical works have been accumulated over this period building on a considerable body of knowledge and understanding of the basic liquid wave behavior. The majority of these early studies deal with ideal flow situations. Even present day analytical techniques are still far from being capable to capture the full extent of the underlining physics of wave dynamics. Wave dynamics is a very rich topic, filled with non-linearities, and in its fullest extent can even lead to

possible chaotic behavior [12], [13]. Thus, the scope of these works in terms of present day applications is somewhat limited. However, since they represent the foundation upon which our basic understanding of wave phenomena relies, a brief review of gravity waves is included.

Liquid sloshing problems are generally separated into one of three major categories based on the nature of the container motion. In *lateral sloshing*, the liquid excitation is brought about by the translational or pitching motion of the container in a direction parallel to the equilibrium free surface position. The motion of the container is transmitted into the fluid through immediate changes that occur in the pressure field in response to the container motion. The ensuing dynamic balance, governing the motion of the liquid, is primarily between the pressure and body forces, with the viscous forces playing a secondary role in acting to bring the liquid back to an equilibrium state. The situation is similar for the case of *vertical sloshing*, which occurs in response to the translational motion of the container in a direction normal to the equilibrium free surface position. The only notable difference here, is the possibility of surface spray occurring in response to a very high frequency vertical excitation of the liquid. The third category is that of *rotational sloshing*, which occurs in response to a rotational or rolling motion of the container. The transmission of this motion into the fluid could occur either through pressure or viscous effects. If the container is rotated about its axis of symmetry then viscous diffusion becomes the sole mechanism responsible for initiating the liquid motion. However, this is a slow process, and is easily dominated by pressure effects even for a slightly asymmetric rotation of the container. The resulting flow in the case of axisymmetric rotation, or spinup, is very intricate, with numerous applications in the field of geophysical fluid dynamics. In view of this special attention is paid to the physics underlining this case.

1.1.1 The Liquid-Vapor Interface

Physical scientists have long recognized that when at least two homogeneous phases of a substance come in contact, a region of small but finite thickness forms in between them, called the interfacial region, where matter in this region exhibits a rheological behavior that is distinct from that of either bulk phase. The interfacial region is a dynamic one, where physical properties change continuously either through molecular diffusion of one phase into the other or through the absorption and accumulation of impurities. The interfacial region is very thin, usually only a few molecular

diameters wide, thus we tend to think of and treat interfaces as two dimensional surfaces.

According to [14], the concept that the interfacial viscosity differs from that of the adjoining phases was first suggested by Hagen in 1845, while, Plateau in 1869, was the first to conduct a series of simple experiments aimed at describing the behavior of interfacial viscosity. Boussinesq, in 1913, postulated for the first time that a linear relationship exists between the interfacial stress tensor and the interfacial rate of deformation. This relation involves three parameters, the interfacial surface tension, σ , the interfacial shear viscosity ϵ , and the interfacial dilatational viscosity, κ . Scriven [15], using a tensorial approach, formally formulated the dynamics of the interfacial region in terms of a set of differential equations (see also Aris [16]). These equations represent the analog of the Navier-Stokes equations for the interfacial region, and can be used as boundary or “connecting” conditions to determine the flow in the adjoining bulk phases. Slattery [17], arrived at a similar result following an integro-differential approach.

The description of interfacial dynamics is indeed a complicated subject which continues to receive extensive attention from physical scientists. Recently, several studies ([14], [18], [19], and [20]), reported experimentally measured values of interfacial viscosities, some of them even suggesting the troubling possibility of Newtonian fluids exhibiting non-Newtonian behavior in the interfacial region. However, there are some good news for the fluid dynamicist interested primarily in the description of the flow in the bulk phases. Wasen *et. al.* [21], reported that the interface between two pure liquids, or a pure liquid and its vapor or a gas, exhibits no viscosity other than bulk viscosity. This was also verified by the experiments of Jiang *et. al.* [20]. Thus, for an interface free of any impurities, imposing the conditions that the velocity and stress tensor be continuous across the interface is sufficient for the complete description of the flow.

For a liquid-vapor interface, assuming that knowledge of the flow in the vapor phase is not of primary importance, the stress conditions at the interface can be further simplified. This is done by ignoring the viscous contribution of the vapor phase to the stress balance equation which yields the traditional free surface conditions of zero liquid tangential stress components and a normal stress condition which accounts for a possible pressure jump across the interface due to surface tension. The free surface conditions are valid in the limit as the ratio of the vapor to liquid viscosity approaches

zero.

A vast number of practical applications that involve fluid interfaces occur in bounded domains such as containers. This requires additional knowledge pertaining to the dynamic behavior of contact lines. Here, a contact line is defined as the intersection of the fluid interface with a solid boundary such as the container walls. Unfortunately, the level of knowledge on the physics governing the motion of contact lines can be at best described as minimal. The lack of attention paid to this problem is partly due to the success of ad-hoc procedures that are commonly used to circumvent it, but mainly due to the enormous complexity involved in modeling its underlining physics.

The most common approach used in studying the contact line behavior involves the use of the contact angle, θ , which represents the angle formed between the fluid interface and the solid boundary due to surface tension effects. The origin of surface tension can be traced to differences in the intermolecular structure and the cohesive forces present in each of the bulk phases. As a result of these differences, the fluid interface is endowed with an excess free energy per unit area. Surface tension, σ , is used to represent the cumulative effects of this Helmholtz free energy, and is generally treated as a property of the interface. The value of the surface tension for a particular interface generally decreases with temperature and with increasing concentration of contaminants. The dependence of the surface tension on temperature has been studied, leading to the identification of Maragoni effects, where variations in the surface tension are seen to drive the flow. The effects of surface tension due to variations in the molecular structure of the interface, either due to impurities or variations in the concentrations of the bulk phases, are usually ignored.

The difficulty in understanding the contact line behavior extends even to cases of static equilibrium. A system that involves a fluid interface is said to be in state of thermostatic equilibrium if its is in a configuration of minimal free energy. Under these conditions Young's equation is used to provide a relation between the free energies of each of the components of the system and the contact angle. Assuming a liquid-gas interface, without loss of generality, Young's equation requires:

$$\gamma_{lg} \theta_{ls} = \gamma_{gs} - \gamma_{ls} \quad (1.1)$$

Here, each phase has been modeled as having constant energy per unit area, with the quantities γ_{lg} , γ_{gs} , and γ_{ls} denoting its value on the gas-liquid, gas-solid, and liquid-solid interface respectively. The contact angle is denoted by θ_{lg} and is measured

between the liquid and solid phases. Unfortunately, Young's equation can not be used to predict the value of the contact angle due to the inability to measure or otherwise determine values for γ_{gs} and γ_{ls} . Furthermore, equation (1.1) implies the existence of a unique value of the contact line. This is contradicted by many experimental observations, where the contact angle is seen to exhibit a multivalued behavior, bounded by two angles referred to as the advancing, θ_A , and the receding, θ_R , contact angles. Thus, as long as the value of the static contact angle falls within this range, $\theta_{lg} \in [\theta_R, \theta_A]$, the contact line will not move. This behavior is referred to as the *contact angle hysteresis*, and its origins are not yet very well understood. However, this behavior raises the possibility that contact lines move in a discrete rather than a continuous fashion.

The analytical study of the motion of contact lines is also complicated by the classical boundary conditions used in describing the behavior of real (viscous) fluids. Imposing the no-slip condition at the contact line, in the strict sense of requiring fluid particles to adhere to the wall, will inevitably lead to multivalued velocity fields. This implies the existence of unbounded stresses exerting unbounded forces on the solid surface, as it was demonstrated in a model developed by Huh and Scriven, [22]. Clearly, the no-slip condition can not be used in the strict sense of adherence, as in [22], with the implication that a fluid particle once in contact with a given solid particle will retain this contact indefinitely. This will preclude the existence of a physical mechanism through which two immiscible fluids can displace each another along a solid surface. Based on its historical development, see [23], the no-slip condition provides an excellent approximation on a macroscopic scale, to the molecular kinematic behavior of viscous fluids in the vicinity of a solid surface. However, one should not lose sight of the fact that the no-slip condition is after all just an approximation. Other conditions have been successfully used, such as Navier's slip condition where the slip velocity depends linearly on the local shear.

Models for the qualitative description of the contact line motion usually resort to a mechanism that involves some type of a rolling motion for the fluid interface. The concept of the rolling motion mechanism was formalized by the work of Dussan and Davis [24]. Through a series of qualitative simple experimental observations, they studied the motion of food dye marks placed on honey and glycerin drops as well as on the interface of glycerin with silicon oil in a rectangular container. An interesting observation that they made, pertaining to the above discussion on the no-slip condition, involved dye that was placed near the bottom surface of the container

wall. The glycerin-silicon oil contact line was made to sweep the bottom wall surface by slowly tilting the container. The dyed glycerin appeared to remain adhered to wall until it was reached by the receding contact line, at which time it began to be lifted off the wall, eventually becoming part of the glycerin-silicon oil interface. Based on these observations, in an effort to explain the multivalueness of the velocity at the contact line, Dussan and Davis went on to postulate the existence of material surfaces that are emitted (or injected) from a moving contact line into (or from) the interior of at least one of the bulk fluids. The fluid that constitutes these material surfaces is believed to originate on the solid-fluid boundary of the fluid-fluid interface.

Dussan's and Davis's model is an interesting conception. However it is based solely on kinematic observations of the contact line and does not address any of the dynamic requirements needed in developing a model. Furthermore, it is not yet clear whether the fluid interface in the immediate vicinity of the contact line can be accurately modeled as a two dimensional surface or as a surface of constant free energy. The interface in the vicinity of the contact line can not be modeled as a material surface. Fluid particles of each of the bulk phases get absorbed into or ejected from the interface at the contact line. On a molecular level, this could lead into non equilibrium variations in the concentration of bulk phases within the interfacial region adjacent to the solid surface, with the resulting surface tension gradients giving rise to significant Maragoni type effects. The resulting tangential stresses could act to balance the unbounded stresses encountered in Huh's analytical model [22]. Furthermore, experimental observations pertaining to the appearance of a primary film, or a "foot", ahead of an advancing contact line, seem to suggest that the interface itself could become multivalued at the contact line through some bifurcation mechanism.

The singularity in the velocity field at the common line can be removed by the inclusion of effective or apparent slip on the solid-fluid surface. Any type of a slip model will relieve the force singularity at the contact line. However, in practice generally only two types of models have been used. These are models based on Navier's slip condition, or the so called "fixed interval" models where the velocity at the wall is set equal to the contact line velocity only in a prescribed fixed interval surrounding the contact line. The sensitivity of the velocity field away from the contact line, based on the particular type of slip model used, was studied in [25]. The results of this study seem to suggest that different slip models could not be distinguished through observations based solely upon the dynamics of the fluids away from the contact line.

Most models that involve the use of a slip condition give rise to fluid motions characterized by two length scales. The smaller scale characterizes the size of the region neighboring the contact line within which the velocity of the fluid differs substantially from that of the solid. Within this region, often referred to as the *inner region*, the dynamics of the fluids are very sensitive to the form of the slip boundary condition used. The other length scale characterizes the size of the entire fluid body. In this *outer region*, the dynamics of the fluids are generally insensitive to the type of boundary condition used at the contact angle. The extent to which approximations made in the contact line modelling within the inner region will affect the viscous solution in the outer region can be also be determined in terms of the dimensionless capillary number, Ca . The capillary number is defined as:

$$Ca = \frac{u \mu}{\mathcal{Y}} \quad \left(= \frac{Bo}{\sqrt{Ga}} \right) \quad (1.2)$$

Here, u represents a characteristic velocity scale near the contact line, μ is the fluid viscosity, and \mathcal{Y} is the coefficient of surface tension. The dimensionless capillary number represents the ratio of the viscous to the surface tension effects. For the present study it does not emerge as an independent parameter as it can be represented as the ratio of the Bond number, Bo , to the square root of the Galileo number, Ga , two of the parameters used in this study. For large values of the capillary number, $Ca \gg 1$, viscous deformation dominates. Surface tension and contact line effects are confined to a thin boundary layer near the contact line. As the value of the capillary number decreases the surface tension and contact angle effects become more important, and for small values of Ca , $Ca \ll 1$, the interface behaves nearly like a static meniscus whose shape could be globally affected by the conditions at the contact angle.

1.1.2 The Linearized Theory of Gravity Waves

The theory on gravity waves is based on potential flow to describe the motion of waves in a horizontally unbounded liquid with a free surface. The free surface is assumed to be at a uniform constant pressure. As the free surface is displaced from its equilibrium position by a wave disturbance, gravity causes a higher pressure to build under the crests than under the troughs. The flow that results in response to these pressure variations is assumed to be unsteady, irrotational, and incompressible.

The formulation is carried out in terms of the velocity potential with an unsteady form of the Bernoulli equation serving as the boundary condition at the free surface.

The general kinematic condition, originally proved by Lord Kelvin [4], is used to calculate the free surface position. The kinematic condition requires that the material derivative of the function used to describe the free surface position be equal to zero. Physically, this condition implies that a fluid particle initially lying on the free surface must remain there. The kinematic condition introduces a nonlinearity into the problem even when the shape of the wave disturbance is assumed. At this point, in order to remove this nonlinearity from the problem one of two simplifying assumptions, pertaining to the shape of the wave, is usually made.

In the first and more general approach, introduced by Stokes in 1847 [26], the amplitude of the waves, A , is assumed to be small compared to their wavelength, λ . The equations are linearized based on a Taylor series expansion with Ak serving as the small parameter. Here, k represents the wave number and is defined in terms of the wavelength by $k = 2\pi/\lambda$. This leads to what is known as the *linearized theory of gravity waves*. In the second approach, introduced independently by Boussinesq in 1871, [27], and Lord Rayleigh in 1876, [28], the simplifying assumption is that the wavelength of the disturbance is large compared to the liquid depth, h . This implies that the vertical acceleration of fluid particles is negligible compared to gravity resulting in a pressure field that is purely hydrostatic.

The central result coming out of the linearized theory of gravity waves can be expressed in terms of the following eigenvalue relation that determines the velocity of propagation c , *celerity*, according to:

$$c_k = \sqrt{\frac{g}{k} \tanh(kh)} \quad (1.3)$$

where g is the acceleration due to gravity. Thus, the speed of a gravity wave is fixed by the wave number and the fluid depth. The motion of fluid particles is along elliptical pathlines with the strongest motion occurring along the free surface. Since in general a wave disturbance will be composed of several Fourier components the shape of the wave will continuously change. For this reason equation (1.3) is called the *dispersion relation*. The speed of propagation, or group velocity, of a wave packet is equal to half the dominant phase speed, c_k , [4].

The above dispersion relation for the celerity can be further simplified by examining its limiting behavior. In the limit of $kh \rightarrow \infty$, that is the depth of the liquid is large compared to the wavelength, the expression for the celerity reduces to:

$$c_k = \sqrt{\frac{g}{k}} \quad \text{as } kh \rightarrow \infty \quad (1.4)$$

Note that the velocity of propagation is determined by the wavenumber, k . This limiting case is known as the *deep water wave theory*. In deep water wave theory waves have a speed of propagation that depends only upon the wavelength.

In the opposite limit, under Boussinesq's and Rayleigh's approximation of large wavelength compared to liquid depth, $kh \rightarrow 0$, equation (1.3) reduces to:

$$c = \sqrt{gh} \quad \text{as } kh \rightarrow 0 \quad (1.5)$$

This simplified case is known as the *shallow water wave theory*. The speed of propagation as $kh \rightarrow 0$ is independent of k . In a horizontally unbounded liquid the speed of propagation of any wavelength disturbance depends only on the liquid depth below the free surface. Waves of infinitesimal amplitude propagate without any changes in their shape while waves of finite but small amplitude undergo a change in shape as the crests travel faster than the troughs. The energy of a small amplitude wave train is half potential and half kinetic [4].

Within the framework of either shallow or deep water wave theory, a number of additional aspects of wave motion have been examined. These include the effects of variable depth, forced oscillations, small but finite amplitude waves, waves in circular basins and spherical sheets, rotation, and traveling pressure disturbances, to list a few [4]. More recently, two and three dimensional sloshing in horizontal cylindrical and spherical containers has been investigated, ([29],[30]). An interesting result has been the observation that the dependence of frequency on depth is also mode dependent. For the lowest modes of oscillation, frequency simply increases with the depth of fluid in the container. For higher mode oscillations, however, the frequency first decreases and then increases with depth.

The potential flow theory has also been used to examine some of the nonlinear aspects of waves, such as waves whose amplitude are not small. In the theory developed by Penney and Price [31], a perturbation method is used to examine finite amplitude standing waves in an infinitely deep rectangular container. They worked out the wave shape to the fifth power term in the predominant amplitude. The main conclusion of their work is that the wave frequency decreases with increasing wave amplitude. Furthermore, the angle enclosed by the crest in the limiting wave form for the standing wave is 90° in contrast to 120° for the progressive wave. Another wave which seems to defy the results of the shallow wave theory is the *soliton*. A soliton propagates through a liquid of depth comparable to the wave amplitude without the wave changing its shape. The key requirement for this behavior is that the wavelength of the soliton not

be so great compared to the depth that vertical accelerations are negligible. Thus the basic assumption of shallow wave theory is untenable in this case [4]. With decreasing amplitude, and thus decreasing vertical acceleration, the wavelength of the soliton increases, and it approaches that of a shallow wave of infinitesimal amplitude.

The effects of surface tension and viscosity have been investigated theoretically using deep wave theory. If surface tension dominates gravitational effects, then the celerity increases with surface tension and decreases with disturbance wavelength. With both surface tension and gravitational effects taken into account, the frequency of oscillation is found to increase with increases in gravity, surface tension, and/or disturbance wave number, k . The celerity first decreases, but then it reaches a minimum value and finally increases with k . For a free surface at which the gas (or vapor) density is negligible compared to the liquid density ρ , the critical wavelength corresponding to the minimum value of celerity is given by,

$$\lambda_c = 2\pi \sqrt{\frac{\mathcal{Y}}{\rho}} \quad (1.6)$$

where \mathcal{Y} is the coefficient of surface tension. If $\lambda/\lambda_c > 3$, then gravitational effects dominate the wave dynamics, while for $\lambda/\lambda_c < 1/3$, surface tension effects dominate [4]. A more recent work employing a regular perturbation in terms of wave amplitude shows that surface tension acts to decrease wave amplitude and to increase the potential energy of the wave to values well beyond the level of kinetic energy. These increases in potential energy are due to surface tension [32]. The effect of viscosity is to cause a damping of the wave such that its amplitude decays exponentially in time like $e^{-\nu k^2 t}$ where ν is the kinematic viscosity of the liquid. For the case of infinitesimal deep waves, viscosity has no effect on wavelength, frequency, or wavespeed [4].

1.1.3 Aspects of Rotating Flows

The understanding of the underlining physics which govern flows that involve rotating fluid systems finds numerous practical applications in every day life. These, include among others, the modeling of flows in centrifuges, spin-stabilized projectiles and spacecraft, as well as most geophysical flows. Within the scope of the present study, the use of an inertial coordinate frame to describe liquid sloshing in a moving container does not always represent the most suitable choice. That is, the nature of the forcing (and thus the ensuing container motion) dictates the use of coordinate frames that must remain attached to the container. The use of *body fixed* coordinates

simplifies the application of boundary conditions but it also results in an overall more qualitatively descriptive model. Thus, the inclusion of cases which involve container rotation leads to the use of rotating coordinate frames.

The most profound changes which occur when considering the physics of a rotating fluid system become evident when the Lagrangian acceleration of a fluid particle in the inertial frame, \vec{a}_i , is expressed in terms of its components in the rotating frame. For a coordinate frame that undergoes a pure rotation $\vec{\Omega}$ with respect to the inertial frame, the acceleration of a fluid particle at position \vec{R} is given by:

$$\vec{a}_i = \vec{a}_r + \vec{\Omega} \times (\vec{\Omega} \times \vec{R}) + 2\vec{\Omega} \times \vec{V}_r + \dot{\vec{\Omega}} \times \vec{R} \quad (1.7)$$

In addition to the Lagrangian acceleration component in the rotating frame, \vec{a}_r , three new fictitious acceleration components appear to be present to an observer in the rotating frame. The second term on the right hand side of equation (1.7), $\vec{\Omega} \times (\vec{\Omega} \times \vec{R})$, is the *centripetal* acceleration. It points in a direction radially outwards from the axis of rotation. The next term in equation (1.7), $2\vec{\Omega} \times \vec{V}_r$, represents the *Coriolis* acceleration, while the last term, $\dot{\vec{\Omega}} \times \vec{R}$, represents the *angular* acceleration. The angular acceleration is brought about by changes in the angular velocity of the system and it points in the circumferential direction.

From the three new acceleration terms that appear in the rotating frame, the Coriolis acceleration is the only new term which explicitly involves the fluid velocity, \vec{V} , and it is responsible for the only structural change in the momentum equations for the case of uniform rotation. It is directed at right angles to both the axis of rotation and the velocity vector and as such it acts as a deflecting force which does no work on a fluid particle. The Coriolis force tends to deflect the direction of motion of a fluid element to its right. It is linear in velocity and for uniform rotation it is independent of the position of the axis of rotation.

The net effect of the Coriolis force on the flowfield is to oppose displacements of fluid elements which lead to changes in the angular momentum of the fluid [33]. If a fluid element that moves along an orbit in the lateral plane, a plane that is normal to the direction of rotation, becomes displaced outwards, then the effect of the Coriolis force is to decrease its angular momentum. This leads to a lower centrifugal force and the fluid element tends to move back to its original orbit. The extent to which this restoring effect of the Coriolis force restricts the displacement of fluid elements depends on its magnitude relative to other forces acting on the fluid.

The significance of the Coriolis effects are measured in terms of the Rossby number ϵ , defined as $\epsilon = V/L\Omega$, where L represents a characteristic spatial dimension of the flow. The Rossby number represents the ratio of inertia to Coriolis effects. For *geostrophic flow*, steady inviscid flow with $\epsilon \ll 1$, the Coriolis effects dominate. The ensuing balance in the momentum equations is between the Coriolis force and an augmented pressure gradient to account for the centripetal force. The resulting flow does not vary in the direction of $\vec{\Omega}$. That is all steady slow motions in a rotating inviscid fluid are necessarily two-dimensional. This case and its implications were first pointed out by Proudman [34] and subsequently demonstrated by a series of experiments conducted by Taylor [35] and have come to be known as the Taylor-Proudman theorem.

Another interesting case where the Coriolis effects play a predominant role was demonstrated by Ekman for wind-driven ocean currents (see [36]). For steady flow with negligible pressure gradients and the horizontal velocity components varying only in the vertical direction the momentum equations reduce to a balance between the Coriolis and viscous terms. The resulting analytical solution, which has come to be known as the *Ekman Spiral*, has some fascinating implications. The direction of the ocean current changes with depth with the surface current directed at a 45° angle to the right of the wind (laminar flow result for the Northern Hemisphere) [37].

The resistance offered by the Coriolis force to changes in the angular momentum of the fluid acts as a mechanism which allows the propagation of inertial waves in a rotating fluid. That is, in the presence of forces that are derivable from a potential, the equations of motion governing a viscous incompressible fluid allow periodic solutions representing the propagation of waves. Two types of inertial waves can be sustained in a rotating fluid. These are *plane* and *axisymmetric* waves. Plane waves are transverse, circularly polarized, and for a viscous fluid damped. The solutions representing these waves are not limited to infinitesimal amplitudes. Axisymmetric waves can be either standing or progressive but are generally limited to small amplitudes. The relation describing the natural modes and frequencies of axisymmetric waves in rotating column of liquid was first given by Lord Kelvin in 1880 [38]. More recently, in a series of experiments Fultz [39] has shown how these waves can be excited and maintained. Other investigators performed similar experiments for different container geometries [40].

The problem of the stability of an inviscid rotating column of fluid was first treated by Lord Rayleigh in 1920. Rayleigh's criterion states that: a stratification of angular

momentum about an axis is stable if and only if it increases monotonically outward [41]. Taylor [42] treated the corresponding problem, both theoretically and experimentally, for viscous flow arriving at the general criterion for the stability of Couette flow which is expressed in terms of a critical value of the dimensionless Taylor number (see [41]).

More recently, several studies focused on the analysis of developing rotating flows. The most fundamental of these works is by Greenspan and Howard [43]. They examined the spinup of a homogeneous fluid occurring between two infinite rotating disks for an impulsive and small change to the rotation rate of the disks. The rotation vector, $\tilde{\Omega}$, was taken as normal to the disks. Their work, which was carried out within the context of geophysical fluid dynamics, identified the major contribution to the spinup process by the secondary circulation driven by the Ekman layers at the endwalls. They demonstrated that the fluid attains solid body rotation in a “convective” time scale of order, $T_c \sim H/\sqrt{\nu\Omega}$, rather than a diffusive scale of order, $T_v \sim R^2/\nu$. Here, ν represents the fluid viscosity, and H the depth of fluid between the disks.

The basic analytical model for impulsive spinup in a cylinder is due to Wedemeyer [44]. His solution divides the interior flow into two distinct regions separated by a moving front that propagates from the cylinder sidewall towards the central axis. The fluid ahead of the front remains non-rotating while the fluid behind the front is spun up. The flow in the interior is assumed to be independent of the axial direction, which along with additional approximations leads to the formulation of single partial differential equation for the description of the azimuthal flow in the interior. Approximate compatibility relations are used to connect the interior flow to the flow in the Ekman layers in terms of the secondary circulation. This secondary circulation, also called *Ekman pumping*, is modeled in terms of an *Ekman suction velocity* ahead of the front, and an *Ekman blowing velocity* behind the front. The suction velocity is used to represent fluid from the interior, which is low in angular momentum, that enters the Ekman layers ahead for the front. As this fluid passes through the boundary layer it gains additional angular momentum. Its return to the interior flow behind the front as high angular momentum fluid is represented by the blowing velocity.

Wedemeyer’s model provides a qualitatively correct picture of the spinup process. However, inherent in his model are the assumptions that the boundary layer flow is quasi-steady, the finite geometry of the cylinder does not influence the boundary layer flux, and also that the interior flow can be approximated throughout the spinup by a solid-body rotation. Experimental observations and analysis of spinup identify

significant departures of the flow from these assumptions [36]. The spinup process appears to go through three distinct phases. Immediately after startup it is dominated by viscous diffusion. Then, radial advection takes over, with Coriolis effects dominating the later stages of the process. Furthermore, the flow behind the front shows strong departures from solid body rotation, and in the vicinity of the front significant axial velocity gradients exist.

Several additional contributions have been offered to the original Wedemeyer model. These include better compatibility conditions, [45], as well as attempts to model the moving front as a region of finite thickness, [46]. A very recent analytical study, which focused on the spin-down of axisymmetric vortices, has also yielded some interesting results [47]. A dynamically active surface was found to increase the spin-down time for a vortex by offsetting the compression of vortex columns. Furthermore, this study raised the possibility of the azimuthal velocity profile becoming multivalued and breaking down when the Rossby number is not small.

1.2 The Numerical Approach to Liquid Sloshing

A vast and rich collection of analytical works has been accumulated over the last two hundred years on wave phenomena. Nevertheless, the analytical approach, at least within present day limitations, is only capable of providing glimpses to the full scope of wave phenomena encompassed by the solution to the full nonlinear set of equations. Thus, numerical methods provide the only available alternative for exploring these phenomena. Several questions pertaining to modeling choices will be encountered during the development of a numerical sloshing model. The most fundamental ones are:

- How should the free surface be modeled?
- What type of formulation should be utilized?
- What type of numerical algorithm should be used?
- How should the algebraic equations be solved?

Liquid sloshing problems represent a special case of moving boundary problems. By far the most complicating factor in the solution of these problems is brought about by the lack of prior knowledge of the entire problem domain. For a free surface problem,

the position of the free surface represents a major component of the sought solution. Numerical models for free surface problems generally employ one of two techniques in dealing with the determination of the free surface position. These are, *surface fitting* and *surface capturing* techniques [48].

In surface fitting methods the position of the free surface is described by an auxiliary function in terms of the independent problem variables. A coordinate transformation can then be used to immobilize the position of the free surface in transformed space. The evolution of the free surface can then be determined by the general kinematic condition [4]. This is essentially an Eulerian type method. The major advantage of surface fitting is the accuracy with which boundary conditions at the free surface can be implemented. In addition, the air or vapor phase solution is not coupled to the liquid side and thus can often be omitted. However, the resulting form of the governing equations becomes more complicated by the coordinate transformation. Furthermore, modeling of more complex wave dynamics, such as breaking, becomes more difficult as the problem domain needs to be divided in such a way as to ensure that the transformation used for the free surface remains one-to-one.

In contrast, surface capturing methods rely on Lagrangian techniques to determine the position of the free surface while leaving the problem domain unaltered. The equations are solved in both the liquid and vapor phases and the position of the free surface is determined by either following fictitious tracking particles that move with the fluid or by locating the steep density gradients that occur across the interface. However, neither of these procedures yield the precise position of the surface. The application of boundary conditions becomes somewhat of an ad-hoc procedure, thus limiting the overall accuracy of capturing methods. The major advantage of surface capturing methods is that they can easily handle complex wave dynamics. Since no coordinate transformation is employed, no restrictions on the free surface shape are imposed. The equations for simple problems could be solved on a fixed grid. In most cases grid refinement around the free surface is necessary, thus dictating the need for continuous grid adjustment. In certain cases the physics of the problem will dictate the choice of method used for the free surface. However, if the choice exists then a surface fitting method is preferable.

Another choice confronting the development of the numerical model is whether the formulation should be carried out in terms of primitive or derived variables. The primitive variable approach, in terms of the velocity components and the pressure, can

be extended to three dimensions without any major difficulties. On the other hand, the derived variable approach in terms of the streamfunction and the vorticity requires a minimum of six equations when applied to three dimensional flows. That's two more equations than in the primitive variable formulation. When the streamfunction vorticity method is applied to sloshing problems another difficulty, which is inherent in the very nature of the equations, arises. In the derivation of the equations all forces derivable from a potential drop from the governing equations themselves. But this is precisely the type of forcing most common to sloshing problems. As a result, these terms have to enter into the problem through the boundary conditions, and more specifically through the free surface conditions. The familiar zero-stress conditions associated with free surfaces can not be applied in their traditional forms. New forms of boundary conditions need to be derived to enforce the required conditions at free surface. The derivation and application of these conditions are not trivial. Extensive care must be undertaken as these conditions are easily susceptible to both numerical error and instability. As a result of these shortcomings, and in contrast with the case of primitive variables, literature on the application of the streamfunction vorticity method to sloshing problems is virtually non-existent.

The equations governing liquid sloshing in moving containers are the incompressible Navier-Stokes equations. The final form of these equations could be quite complex due to numerous new terms that appear as a result of coordinate transformations needed to capture the physics of the problem. The solution to these equations in terms of a streamfunction vorticity formulation is necessarily divergence free. However, that is not the case for a primitive variable approach (the likely choice). The set of governing equations in terms of the primitive variables consists of one momentum equation for each of the velocity components and the continuity equation. For the closure of the problem an equation for the remaining depended variable of the problem, namely the pressure, is required. The goal is to determine the pressure field which yields a divergence free velocity field that also satisfies the momentum equations. Most commonly, some variation of the popular SIMPLE algorithm by Patankar and Spalding [49] is used. These methods rely on a Pressure Poisson equation derived from the momentum equations to iteratively obtain corrections to the pressure field until the solution is reached. An alternative scheme is the artificial (or pseudo) compressibility method introduced by Chorin [50]. In this method a fictitious unsteady compressibility term is added to the continuity equation and the equations are marched in pseudo-time until

steady-state is reached. The fictitious terms vanish from the equations at steady state. The artificial compressibility method is not as strongly elliptic as a pressure Poisson method. As a result, quite often smoothing has to be used to avoid pressure oscillations. It should be noted that pending on the details of their actual implementation these two methods can be nearly equivalent.

To obtain a numerical solution the continuous problem is converted into a discrete one. That is, the governing equations are replaced by a set of approximate algebraic equations. The solution of the problem is found by solving this set of algebraic equations. Several methods are available, and more continue to become available, for accomplishing this task. These include both direct and iterative methods. Direct methods involve some type of Gaussian elimination and in general they require a formidable amount of storage when applied to three dimensional flows. Furthermore, for the incompressible equations, some form of iterative procedure to deal with linearization errors is usually needed. Thus, indirect methods appear to be better suited for the solution of the incompressible Navier-Stokes equations. The most simple of the iterative methods is the Gauss-Seidel method. It is extremely easy to implement and requires the minimum resources. However, it converges very slow. A variation of the Gauss-Seidel method is the successive over-relaxation method (SOR). Here, an over-relaxation parameter is used to accelerate convergence. Both of these methods are *point-iterative*. A faster convergence rate can be achieved with *block-iterative* methods. In these methods, a subgroup of the unknowns is singled out, and some form of a direct elimination method is used to obtain the solution of the resulting group of simultaneous algebraic equations. The most simple block-iterative methods are the SLOR method (SOR by lines) and the ADI method (alternative direction implicit). Block-iterative methods are very popular because they usually lead to tridiagonal or block tridiagonal systems of equations. Fast tridiagonal matrix solvers are readily available. *Strongly implicit methods*, such as the SIP (strongly implicit procedure) method by Stone [51] and the MSIP (modified SIP) by Schneider and Zedan [52] have been gaining in popularity as more computer resources become available. These methods provide stronger coupling by treating the unknowns implicitly in a plane (or in a cube for three dimensional flows). These methods result in even faster convergence rates, but they do so at the expense of higher resource requirements. Another method offering the fastest convergence rate theoretically possible is the *multigrid method*. Multigrid methods owe their fast convergence rates to the use of successively coarser grids to address low

wave number errors. However, they are generally more difficult to implement and often require problem specific tuning [53].

The methods for solving the algebraic equations, in the order discussed above, offer increasing rates of convergence, but also increasing requirements in both hardware and time resources needed for their implementation. These are important factors that should be considered in selecting one of these methods. Another factor, equally important, is the type of problem at hand. Solutions to sloshing problems generally exhibit some degree of periodicity. Usually, long term solutions are sought, thus limiting the size of the time step used in marching the equations. This is done to prevent error accumulation. Based on this limitation, the number of iterations required to advance the solution to the next time step are fairly low. Thus, the savings in the required time for the solution of the problem, which will be anticipated with one of the “faster” methods, could fail to be realized as a result of increased overhead. Perhaps for sloshing problems, a method like SOR or SLOR offer the safest starting point.

1.2.1 Numerical Works on Free Surface Flows

Perhaps the first numerical method to deal successfully with arbitrary wave problems was the Particle in Cell (PIC) method [54]. In the PIC method a continuum model was not used. Instead, the motion of a finite number of fluid particles was followed using a Lagrangian description of the dynamics. In certain cases, momentary crowding or depletion of particles occurred in a computational region resulting in high frequency oscillations of fluid properties. First order upwind differencing was also used adding significant numerical viscosity to the method.

A similar idea of using fluid particles to track down the position of the free surface was used in the Marker and Cell (MAC) method [55]. The MAC method, is finite difference method which solves the equations in terms of primitive variable on a staggered mesh. A Poisson equation is used to enforce the continuity. Although the position of the free surface is deduced from the position of the marker particles, unlike the PIC method, these particles are not involved in any other dynamical calculation. The marker particles are used solely for determining the location of the free surface. Some interesting results were obtained with the MAC method. They indicate that for sloshing in moving containers the period of sloshing increases with viscosity. Furthermore they demonstrated the lack of perfect periodicity in the sloshing, and that the free surface is never flat except at the initial and final stages of the problem. Although the

MAC method generally can be used to make successful predictions of wave phenomena it suffers from two major drawbacks. First, the marker particles do not always remain evenly distributed. This in conjunction with the bilinear interpolation on the velocity field, used to determine the marker particle velocities, leads to a free surface and a pressure field which are not smooth. The second difficulty arises in the application of the boundary conditions at the surface. Since in general the free surface will lie in the interior of a computational cell, rather than on the edge, the application of boundary conditions is of ad hoc nature. In the original MAC method [55], zero normal stress at the surface was approximated by setting the pressure in the cell containing the free surface equal to zero. This is only correct in the double limit of vanishing viscosity and surface tension. The tangential stress approximation was even cruder. It was approximated by setting the gradient of the velocity in a direction normal to the surface equal to zero. This approach is only correct in the double limit of vanishing surface curvature and negligible tangential velocity gradient. A more general formulation for the free surface conditions which significantly improved the accuracy of the MAC method was given in [56]. The inclusion of the more general normal stress condition was found to increase the accuracy of the bore calculation by a factor of 2 to 3. Despite these improvements, the lack of knowledge on the precise location of the free surface and the omission of higher order curvature terms from the formulation limits the accuracy of the MAC method.

Another general purpose algorithm for free surface flows, which is a by-product of the MAC method is the SOLA-SURF method [57]. This algorithm relied upon the kinematic condition rather than marker particles in determining the free surface position. As a result, the free surface location was determined much more accurately than in the typical MAC method. The pressure at the free surface was chosen by linear interpolation between the cell containing the free surface and the cell immediately below it such that it would yield zero pressure at the surface. The vertical velocity at the top of the surface cell was set so that the surface cell will be divergence free. This is a limitation of staggered grid formulations for free surface flow and results in a velocity field that is not accurately aligned with the free surface. Like the MAC method, the SOLA-SURF method is fully explicit in time. However, whereas the MAC method uses only centered differences, this method uses a hybrid differencing for the convective terms. Although this differencing helps keep solutions smoother, it does so at the expense of increased artificial viscosity. Solutions for several wave problems were illustrated in [56]. Al-

though these appear qualitatively correct, no definitive information on numerical error is given.

The SOLA-SURF method represents a considerable advance over the MAC method in terms of being able to predict the free surface position more accurately. However, the use of the kinematic condition requires that the surface position has to remain a singly valued function of all but one of the independent variables of the problem. This implies that the surface may not fold over upon itself. Based on the implementation of the SOLA-SURF algorithm this restriction requires that the free surface could not be inclined more than the diagonal of the surface cell. This restriction was not present in the MAC method which is quite capable of handling multiply connected fluid regions separated by free surfaces of arbitrary orientation.

The development of the SOLA-VOF algorithm [58], where VOF stands for Volume of Fluid, represents an attempt to retain the fluid region tracking ability of the MAC method while at the same time improving the accuracy with which the free surface position is determined. The key is to introduce an auxiliary function F , whose average value in a surface cell gives the volume of fluid in that cell. Since F moves with the fluid, the substantial derivative can be used to determine a simple partial differential equation for F . The differencing for F is of an extremely ad hoc nature, and reflects the fact that F is a step function. The free surface is approximated by a straight line segment in the surface cell. Its slope and height can be determined from the volume of fluid function F . Solutions to several interesting problem are given in [58]. They all look qualitatively correct, and show reasonable agreement with analytical results where available.

The main difficulty in the application of any of the *capturing* algorithms in the MAC family to three dimensional sloshing problems was demonstrated in [59]. The goal of this study was to evaluate the applicability of the SOLA-VOF method to sloshing problems. The VOF method, perhaps the most accurate of these methods, was used to model liquid sloshing in a horizontal cylinder. The results of [59] appear qualitatively correct with the exception of fictitious bubbles and droplets that develop in the flowfield in the vicinity of the free surface. The authors of [59] attribute these errors to deficiencies in the method, and more specifically to the fact that the kinematics of boundary surfaces are not defined and computed exactly in the VOF method. They conclude that the VOF method is suited for sloshing problems based on the justification that only global features of the flowfield, such as resulting forces and moments, are

essential in a sloshing problem calculation.

The basic model by Wedemeyer for the qualitative description of the spin-up of a viscous fluid in rotating cylinder, [44], has served as the basis for several numerical works on the subject. The full Navier-Stokes equations for spin-up in a liquid filled cylinder were solved by Kitchens [60] using a streamfunction-vorticity formulation. Grid stretching transformations were used to resolve the boundary layers. His results point to some of the inadequacies of the Wedemeyer model, such as the use of a simple Ekman suction formula to parameterize the entire endwall boundary layer. Inertial oscillations and regions of reversed flow occurred early in the spinup process. Another solution to the same problem was presented by Hyun *et al.* [61]. Their results demonstrate strong departures from solid-body rotation in the azimuthal flow behind the propagating front.

The extension of the Wedemeyer model to a partially filled container was attempted by Goller and Ranov [62]. Their model uses approximate equations in the boundary layers, which are based on Wedemeyer's assumptions, while in the core the equations are simplified by assuming that the tangential velocity component is independent of the axial position. The free surface position is calculated from an approximate equation derived from a force balance at the surface. Based on the assumption that spin-up is a slow process, only the centrifugal and gravitational forces are retained in this equation. Thus, this equation imposes the requirement that the inward unit normal vector at the free surface be aligned with force vector defined by the local gravitational and centrifugal accelerations. The exact position of the free surface is then calculated from a global mass balance based on the above slope requirements. The velocities at the free surface are determined by the displacement of the free surface. The results of this model are in very good agreement with the Wedemeyer model. This is however obvious since it is based on almost the identical assumptions. Reasonable agreement with experimental data for the free surface position is also demonstrated. Unfortunately, the model by Goller and Ranov been adopted by several other studies such as [63] and [64]. Due to the severe restrictions placed on the flowfield by the assumptions made in this model, no useful information can be extracted by its continued use other than a reaffirmation of the qualitative validity of the Wedemeyer result.

A recent study by Dommermuth uses Helmholtz's decomposition to separate the irrotational and solenoidal components of the flowfield into separate nonlinearly coupled equations [65]. This model is applied to the laminar interaction of a pair of vortex

tubes with a free surface. Based on the decomposition of the flow field used in [65], the extension of this model to sloshing problems seems unlikely. The solution of the resulting Poisson equation for the rotational component of the pressure field becomes more complicated by a fourth Neumann boundary condition at the free surface. The results of this paper make for a good reading and the treatment of the free surface conditions is precise and detailed, thus, the reason for this work being cited here.

1.3 Overview of the Present Study

The goal of the present study has been the development of a numerical model for the description of wave dynamics in moving containers. Special attention has been devoted to the description of liquid sloshing under forcing conditions characteristic of those present in spin stabilized spacecraft.

Several numerical codes have been developed in the course of this study. The only design limitation imposed early on their development stems from the decision to focus solely on surface fitting techniques for the free surface model. Capturing methods, when applied to three dimensional flows or complex geometries, are more difficult to implement and are more easily susceptible to errors. For greater accuracy, the position of the free surface is calculated from the kinematic condition. A general formulation for the dynamic conditions at the free surface is developed. The consequences arising from the specific numerical implementation of these conditions are carefully examined.

Both the physics and the numerics of liquid sloshing are examined in detail. This is accomplished by utilizing both two, and, three dimensional finite difference models. Some of these models are based on a primitive variable formulation, whereas others are based on a streamfunction vorticity formulation. For primitive variable formulations, a Poisson equation is used to calculate the pressure. This approach, which preserves the elliptic character of the pressure field, results in velocity fields that satisfy globally the divergence free condition more accurately.

For three dimensional flows in spherical containers, several innovative techniques are developed and implemented which improve the accuracy and extend the range of the model. A transformation is utilized prior to the grid generation, which allows for the continuous interactive transformation of the governing equations to a coordinate system that is best suited for the solution of the equations. Thus, by following the bulk of the moving liquid, a more nearly orthogonal grid can be generated with less effort, using a combination of algebraic and elliptic schemes. But more important, this

allows for the adaptation of the governing equations in a manner that either alleviates or eases the limitations imposed on shape of the free surface by the use of the kinematic condition.

A careful parametric study of the various conditions affecting the dynamics of sloshing in moving containers has been conducted. The effects of the physical properties of the liquid, the type of forcing conditions, and the container geometry are analyzed. Furthermore, sample results from several interesting cases are given. These include,

- Lateral sloshing in accelerating rectangular containers.
- Lateral sloshing in impulsively started rectangular containers.
- Axisymmetric spinup in a cylindrical container.
- Asymmetric spinup in a spherical container.

The evolution of the free surface and the associated velocity and pressure fields are analyzed for each of these cases. The sloshing dynamics are also analyzed in terms of the First Law, and the dynamic interaction of the sloshing liquid with the enclosing solid structure is considered.

1.4 Outline of the Thesis

The motivation behind this work has been the development of a numerical model capable of predicting liquid sloshing flows under a fairly broad range of forcing conditions. Some of the basic physics, as well as analytical and numerical works contributing to the success of this study have been presented in this chapter. In the course of meeting the stated goal of this work several two dimensional models have been developed. These models dealt with sloshing in a rectangular containers. The relative simplicity in geometry and the moderate computational requirements, permitted the use of these models for the exploration and understanding of the various aspects that enter into the development of sloshing models. In an effort to preserve the clarity of this work, and to avoid confusing the reader with continuous references to different models, the main body of the thesis is divided into two parts.

In Part I of the thesis the focus is on the two dimensional rectangular geometry models. A brief outline of Part I is given in Chapter 2. The mathematical formulation for the problem is presented in Chapter 3. It includes the development of the

governing equations, the initial and boundary conditions, as well as the free surface conditions. The numerical method is presented in Chapter 4. It includes all the details pertaining to the discretization and solution of the governing equations. Alternative approaches for the numerical solution of the problem are evaluated, and information on the truncation errors associated with the model is given. In Chapter 5 results from several characteristic cases solved with these models are presented. The solutions are analyzed from a kinematic as well as a First Law point of view. A parametric study on the influence of various nondimensional parameters affecting the dynamics of the problem is presented. Comparisons with analytical and experimental results, where available, are also included here.

In Part II of the thesis, the main focus is on the development of a more general, three dimensional model. A brief outline of Part II is given in Chapter 6. In Chapter 7 the mathematical formulation for the model is laid out. The equations governing the dynamics of the flow are developed through a series of coordinate transformations. Boundary and initial conditions are specified and the free surface model is presented. All the information pertaining to the numerical method adopted for the model is also discussed in Chapter 7. The grid generation scheme along with various techniques that were developed and implemented to improve the accuracy and extend the range of the model are presented here. Results from sample cases used in evaluating the model are discussed in Chapter 8. These include solutions for lateral sloshing in a three dimensional impulsively translated container, axisymmetric spinup in a cylindrical container, and a solution for a fully 3D asymmetric spinup in a spherical container.

A brief overall summary of this study is given in Chapter 9. The strengths and limitations of these models are identified and discussed here. Appendices A, B, and C, provide supplemented information and detailed derivations omitted from the main body of the thesis for clarity.

PART I.

SLOSHING IN 2-D MOVING CONTAINERS

2. LIQUID SLOSHING IN A 2-D TRANSLATING CONTAINER

The goal of this study has been the development of a numerical model capable of predicting the sloshing of a liquid within a moving container under fairly general forcing conditions. Some of the basic fundamentals as well as previous works pertaining to this subject have been reviewed in Chapter 1. Several difficulties encountered in developing a model have been identified. The free surface of the liquid represents a moving boundary of unknown shape and position. Consequently, the problem domain needs to be determined as part of the solution. The forcing of the liquid, which is brought about by the motion of the container, further complicates the problem. The motion of the container will in general be described by the superposition of several translational and rotational components. For three dimensional flows the resulting form of the governing equations is formidable. Their solution can be extremely straining on the available computational resources. Furthermore, it becomes increasingly difficult to isolate and investigate the physical, mathematical, and numerical parameters, which influence the accuracy of the model.

In view of these difficulties, a relatively more simple model is developed here. It deals with the sloshing of an incompressible viscous liquid within a two dimensional rectangular container. The forcing of the liquid is limited to translational (rectilinear) motions of the container. Sudden changes in both the acceleration and the velocity of the container are considered. In the presence of surface tension, the response of the liquid in each of these cases is decisively different.

The mathematical formulation for the 2D problem is presented in Chapter 3. Detailed information on the development of the governing equations, initial, and boundary conditions is given. The focus of the presentation is in terms of a primitive variable formulation. A brief description of a streamfunction vorticity formulation is included, which details the basic differences between the two models. The formulation for the corresponding inviscid problem, based on potential theory, is also presented. The First Law of Thermodynamics is used to analyze the problem in terms of an energy balance.

Finally, some of the difficulties encountered in coupling the dynamics of the fluid with those of the enclosing solid structure are also considered. A computationally efficient method, for the study of the solid-liquid interaction, is developed based on a simple extension of the problem.

The numerical formulation for the 2D model is presented in Chapter 4. The discretization of the governing equations, initial, and boundary conditions is presented in detail. A pressure correction scheme is developed which retains the elliptic character of the pressure field, and yet, allows for the efficient solution of the equations. Alternative approaches are considered, and the truncation error behavior of the method is carefully examined.

The presentation of results in Chapter 5 is separated into three parts. In the first part, the liquid flow is analyzed from a kinematic prospective, with detailed information on the evolution of the velocity, pressure, and vorticity fields being included. The sloshing of the liquid is also examined from the prospective of a second order dynamic system. This is presented in the second part of Chapter 5, in terms of a detailed parametric study of the effects of the various similarity parameters on dynamic behavior of the system. Finally, in the third part, sample results for the interaction of the liquid with the enclosing solid structure are given.

3. MATHEMATICAL FORMULATION

The basic geometry for the model is depicted in Figure 3.1. A viscous incompressible liquid, initially at rest, fills a rectangular container of width L to a depth F_0 . Let (\bar{x}, \bar{y}) represent a coordinate frame attached to the lower left corner of container. The container is free to translate along the horizontal direction of an inertial frame of reference (\bar{x}_o, \bar{y}_o) . The position of the free surface, depicted by \bar{F} , is a function of the horizontal coordinate \bar{x}_o , and time, \bar{t}_o . The gravitational field g , is pointed vertically down along the negative \bar{y} axis.

The container is initially at rest with respect to coordinate frame \bar{x}_o . At time, $\bar{t}=0$, it suddenly begins to translate to the right such that its position is described by,

$$\begin{pmatrix} \bar{x} \\ \bar{y} \end{pmatrix} = \begin{pmatrix} \bar{x}_o - U_o\bar{t} - \frac{1}{2}q\bar{t}^2 \\ \bar{y}_o \end{pmatrix} \quad (3.1)$$

where here, q represents the constant horizontal acceleration experienced by the container for time $\bar{t} > 0$, and U_o the initial horizontal impulsive velocity that the container experiences at time $\bar{t}=0$.

The fluid is initially in a state of hydrostatic equilibrium with respect to the constant gravitational field. The sudden translation of the container to the right, when viewed with respect to the noninertial frame of reference (\bar{x}, \bar{y}) , results in an *apparent uniform body acceleration of magnitude q , directed to the left* (the principle of equivalence).

A primitive variable formulation was initially chosen to model the problem primarily because it was felt that it was more readily generalizable to 3D and because information on the pressure field was one of the major types of information to be obtained from the study. A formulation based on the streamfunction-vorticity approach was later developed and tested. However, it did not fare as well as the primitive variable model. The motion of the liquid is primarily driven by a balance between pressure and body forces. In the streamfunction-vorticity formulation these forces have to enter

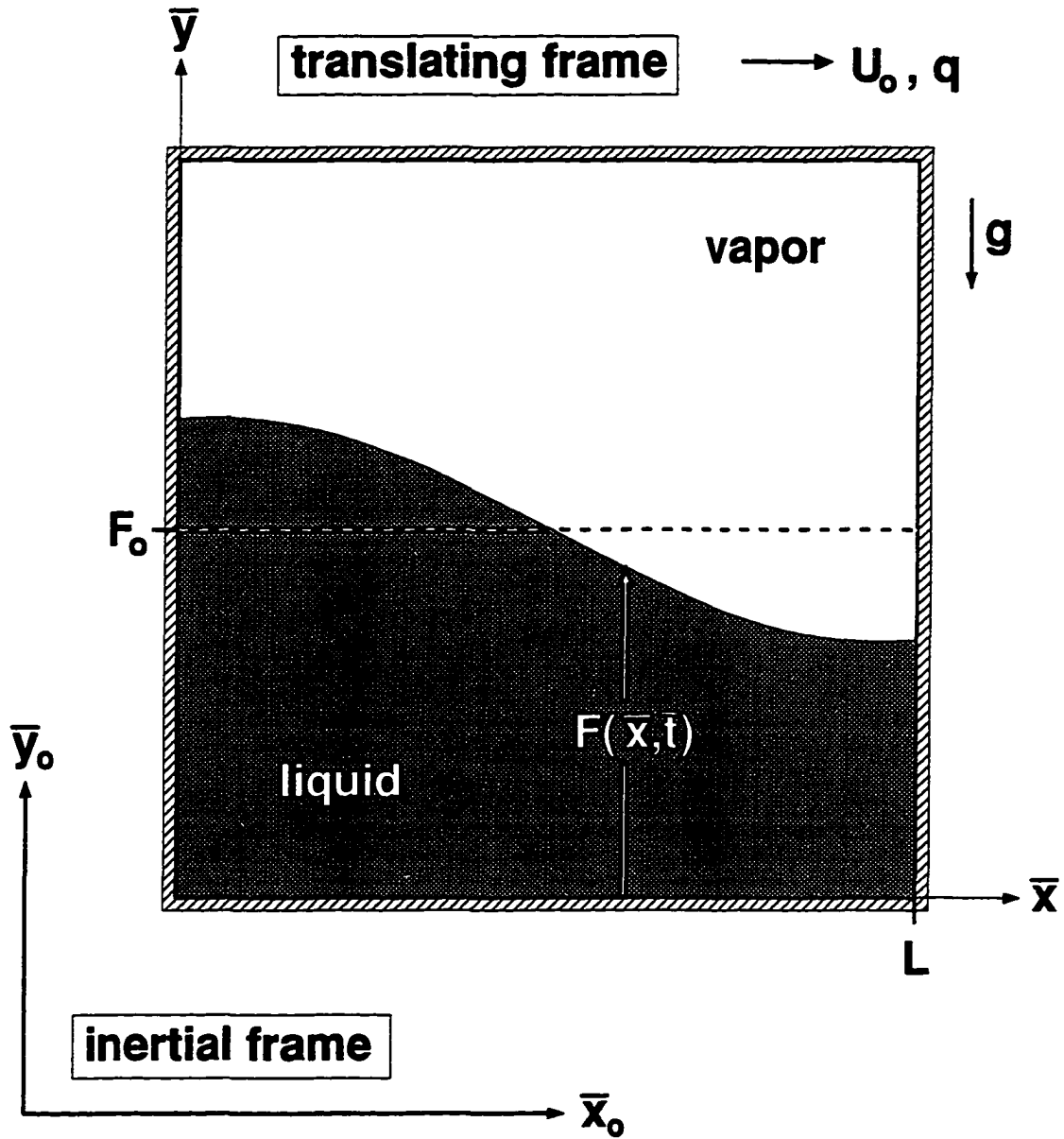


Figure 3.1: Translating Rectangular Container

into the model through the boundary conditions. The cross-differentiation of the momentum equations used in deriving the vorticity transport equation eliminates both pressure and conservative body force terms from the governing equations themselves. These terms can be incorporated into the model through the use of a free-surface boundary condition based on the tangential momentum equation. Although this approach eliminates the need for a pressure field calculation its implementation is very tricky and highly susceptible to truncation errors.

Three separate variable transformations are used in this formulation. The first one is used to change the frame of reference so that the coordinate system stays fixed with respect to the container. The second transformation maps the free surface, whatever its shape, into a straight horizontal line. The third transformation regularizes the formulation at the moment translation of the container begins. This enables the calculation of the correct pressure and velocity fields especially for impulsive start ($U_o \neq 0$) cases.

3.1 Dimensional Governing Equations

The motion of the incompressible Newtonian liquid within the moving container can be fully described by the Navier-Stokes equations. These equations are suitable for the description of the fluid motion in an inertial frame of reference (\bar{x}_o, \bar{y}_o) . However the solution of the problem in this frame is complicated by the motion of the container. Application of boundary conditions is more difficult and the ability to gain physical insight to the solution is reduced. A more suitable reference frame for the solution of the problem is frame (\bar{x}, \bar{y}) , see Figure 3.1, which is fixed with respect to the container. Under the assumption of constant horizontal acceleration, q , to the right, and constant initial horizontal velocity, U_o , the coordinate transformation from $(\bar{x}_o, \bar{y}_o, \bar{t}_o)$ to $(\bar{x}, \bar{y}, \bar{t})$ space is given by:

$$\begin{pmatrix} \bar{x} \\ \bar{y} \\ \bar{t} \end{pmatrix} = \begin{pmatrix} \bar{x}_o - U_o \bar{t}_o - \frac{1}{2} q \bar{t}_o^2 \\ \bar{y}_o \\ \bar{t}_o \end{pmatrix} \quad (3.2)$$

Substitution of equation (3.2) into the standard form of the Navier-Stokes equations, written for the inertial frame of reference $(\bar{x}_o, \bar{y}_o, \bar{t}_o)$, results in:

$$\frac{d\bar{u}}{d\bar{t}} = -\frac{1}{\rho} \frac{\partial \bar{p}}{\partial \bar{x}} - q + \nu \bar{\nabla}^2 \bar{u} \quad (3.3a)$$

$$\frac{d\bar{v}}{d\bar{t}} = -\frac{1}{\rho} \frac{\partial \bar{p}}{\partial \bar{y}} - g + \nu \bar{\nabla}^2 \bar{v} \quad (3.3b)$$

$$\frac{\partial \bar{u}}{\partial \bar{x}} + \frac{\partial \bar{v}}{\partial \bar{y}} = 0 \quad (3.3c)$$

where ρ is the liquid density, ν is the kinematic viscosity. The *del* operator and the total, also known as material or substantial, derivative operator are given by:

$$\bar{\nabla}^2 = \frac{\partial^2}{\partial \bar{x}^2} + \frac{\partial^2}{\partial \bar{y}^2}$$

$$\frac{d}{d\bar{t}} = \frac{\partial}{\partial \bar{t}} + \bar{u} \frac{\partial}{\partial \bar{x}} + \bar{v} \frac{\partial}{\partial \bar{y}}$$

The dependent variables \bar{p} , \bar{u} , and \bar{v} , in equation (3.3) represent respectively the pressure, the horizontal component, and the vertical component of the velocity. They are related to their respective values in the inertial coordinate frame by:

$$\begin{pmatrix} \bar{u} \\ \bar{v} \\ \bar{p} \end{pmatrix} = \begin{pmatrix} \bar{u}_o - U_o - q\bar{t}_o \\ \bar{v}_o \\ \bar{p}_o \end{pmatrix} \quad (3.4)$$

3.1.1 Pressure Poisson Equation

The necessary physics required to describe the liquid flow within the container are included in equations (3.3a-c). When coupled with an appropriate set of initial and boundary conditions these equations can fully describe the solution to the problem. However, at the present time no general analytical solution to these equations is known. Therefore, to obtain a solution some form of a numerical approximation method needs to be implemented. Since the pressure does not appear explicitly, that is in the form of a pressure equation, in equations (3.3a-c), the numerical solution of these equations in their present form is made more difficult to obtain an accurate solution.

Two types of methods have traditionally been used in deriving a pressure equation. The first involves the use of some pseudo-equation of state to couple the pressure and density, which when substituted into a simplified form of the unsteady compressible continuity equation yields an equation for the pressure. This is known as the artificial compressibility method and has been first introduced by Chorin, [50]. The second approach is based on using the momentum equations rather than the continuity equation in deriving an equation for the pressure. This is accomplished by taking the gradient

of the momentum equations which yields a Poisson equation for the pressure. The use of a Poisson equation for the calculation of the pressure field was first introduced by Welch and Harlow, [55]. The main advantage of this method is that it brings out the elliptic nature of the pressure field. Taking the gradient of equations (3.3a) and (3.3b) yields:

$$\frac{1}{\rho} \bar{\nabla}^2 \bar{p} = 2\bar{J}(\bar{u}, \bar{v}) - \left(\frac{d\bar{D}}{d\bar{t}} + \bar{D}^2 - \nu \bar{\nabla}^2 \bar{D} \right) \quad (3.5)$$

where,

$$\bar{D} = \frac{\partial \bar{u}}{\partial \bar{x}} + \frac{\partial \bar{v}}{\partial \bar{y}} \quad (3.6)$$

and,

$$\bar{J}(\bar{u}, \bar{v}) = \frac{\partial \bar{u}}{\partial \bar{x}} \frac{\partial \bar{v}}{\partial \bar{y}} - \frac{\partial \bar{u}}{\partial \bar{y}} \frac{\partial \bar{v}}{\partial \bar{x}} \quad (3.7)$$

Note that although the dilatation, \bar{D} , is identically zero by continuity (3.3c), the dilatation terms are retained in the pressure Poisson equation at this point in the formulation. Their significance depends on the numerical method used to solve equation (3.5). For explicit marching schemes they provide stability to the numerical method. The precise implementation of equation (3.5) will be discussed in detail when the numerical method used in this study is presented.

3.1.2 Free Surface Kinematic Condition

A final governing equation is needed to determine the position of the free surface. The general kinematic condition, which was originally proved by Lord Kelvin, is used. This condition states that the total derivative of the function used to describe the position of the free surface be equal to zero, $d\bar{F}/d\bar{t} = 0$. Physically, this condition means that if a fluid particle is on the free surface at any time, then it must remain there for all time. This is to be expected, provided that the motion is continuous, because the free surface is a material surface. That is, no fluid particles can cross the free surface as its position is determined by the motion of particles on it. Substitution of $\bar{F}(\bar{x}, \bar{t})$ into the general kinematic condition, followed by coordinate transformation into noninertial space as defined by equation (3.2), leads to:

$$\frac{\partial \bar{F}}{\partial \bar{t}} = \bar{v} - \bar{u} \frac{\partial \bar{F}}{\partial \bar{x}} \quad \text{along } \bar{y} = \bar{F} \quad (3.8)$$

It can be easily shown that kinematic equation remains invariant in form under successive coordinate transformations provided that the transformed velocity components are referenced with respect to the moving frames such that under a no-slip condition at the wall they vanish.

3.1.3 Boundary Conditions

The solution of the governing equations requires the specification of boundary conditions for the dependent variables \bar{u} , \bar{v} , and \bar{p} . The container walls are treated as impermeable no-slip boundaries. Consequently, the normal and tangential components of the velocity are set equal to zero along the walls. The pressure values along the walls are calculated from a reduced form of the corresponding normal momentum equation. This leads to the following set of conditions:

$$\bar{u} = \bar{v} = 0 \quad \text{along} \quad \bar{x} = 0 \quad \text{and} \quad \bar{x} = L \quad (3.9a)$$

$$\bar{u} = \bar{v} = 0 \quad \text{along} \quad \bar{y} = 0 \quad (3.9b)$$

$$\frac{1}{\rho} \frac{\partial \bar{p}}{\partial \bar{x}} = -q + \nu \frac{\partial^2 \bar{u}}{\partial \bar{x}^2} \quad \text{along} \quad \bar{x} = 0 \quad \text{and} \quad \bar{x} = L \quad (3.9c)$$

$$\frac{1}{\rho} \frac{\partial \bar{p}}{\partial \bar{y}} = -g + \nu \frac{\partial^2 \bar{v}}{\partial \bar{y}^2} \quad \text{along} \quad \bar{y} = 0 \quad (3.9d)$$

The free surface can be viewed as a fluid interface separating the liquid and the vapor enclosed within the container. The term *vapor* is used here to refer to the gas existing within the container, be it atmospheric air, the vapor phase of the liquid, or a mixture of the two. On a microscale, a fluid interface is a thin region, extending several intermolecular distances, where the liquid and vapor phases coexist. Within this interfacial region, fluid properties are a combination of the properties of the liquid and vapor phases. However, on a macroscale, a scale appropriate for the adequate resolution of the liquid flow, the interface is approximated as a region of zero thickness. To ensure continuity in the velocity field, the condition that needs to be enforced is that fluid particles on either side of the interface experience the same total acceleration. This can be accomplished by requiring that the stress tensor be continuous across the interface. Separating the stress tensor into normal and tangential components yields two equations. These equations are then simplified based on the assumption that the viscosity of the vapor is several orders of magnitude smaller than that of the liquid.

Thus, ignoring terms that involve the vapor viscosity yields the following *free surface dynamic conditions*:

$$\frac{\partial \bar{U}_\tau}{\partial n} - \kappa \bar{U}_\tau + \frac{\partial \bar{U}_n}{\partial \tau} = 0 \quad (3.10)$$

$$\bar{p} - \bar{p}_o = 2\mu \frac{\partial \bar{U}_n}{\partial n} + \kappa \mathcal{Y} \quad (3.11)$$

where \bar{U}_n and \bar{U}_τ represent the normal and tangential velocity components at the free surface and they are defined in terms of the normal, \bar{e}_n , and tangential, \bar{e}_τ , unit vectors at the free surface, see Figure 3.2, by:

$$U_n = \frac{-\bar{F}_x \bar{u} + \bar{v}}{\sqrt{1 + \bar{F}_x^2}} \quad \text{and} \quad U_\tau = \frac{\bar{u} + \bar{F}_x \bar{v}}{\sqrt{1 + \bar{F}_x^2}} \quad (3.12)$$

$$\text{with } \bar{e}_n = \frac{-\bar{F}_x \bar{i} + \bar{j}}{\sqrt{1 + \bar{F}_x^2}} \quad \text{and} \quad \bar{e}_\tau = \frac{\bar{i} + \bar{F}_x \bar{j}}{\sqrt{1 + \bar{F}_x^2}}$$

$$\text{and } \kappa = -\frac{\bar{F}_{xx}}{(1 + \bar{F}_x^2)^{\frac{3}{2}}}, \quad \bar{F}_x = \frac{\partial \bar{F}}{\partial \bar{x}} \quad \text{and} \quad \bar{F}_{xx} = \frac{\partial^2 \bar{F}}{\partial \bar{x}^2}$$

Here μ is the absolute viscosity of the liquid, ($\mu = \rho\nu$), \mathcal{Y} is the coefficient of surface tension for the liquid-vapor interface, and \bar{p}_o is the equilibrium vapor phase pressure. The local free surface curvature is κ which is defined in terms of the local slope, \bar{F}_x , and \bar{F}_{xx} .

The dynamic free surface conditions are expressed in terms of local orthogonal curvilinear coordinates, (τ, n) . The zero tangential stress condition, equation (3.10), implies that the stress exerted by the vapor-phase on the liquid-phase in a direction tangential to the free surface is negligible. This is a reasonable assumption provided that the forces driving the flow in the two phases are of the same order of magnitude. That is, the vapor flow is not driving the liquid flow. The normal stress condition, equation (3.11), implies that no unbalanced stresses should exist normal to the free surface. That is, any discontinuity in the pressure across the free surface should be balanced by the viscous component of the stress. Equations (3.10) and (3.11) can be made more useful when transformed into (\bar{x}, \bar{y}) coordinates. The details of this transformation are given in Appendix A. The resulting equations are:

$$(1 - \bar{F}_x^2) \left(\frac{\partial \bar{u}}{\partial \bar{y}} + \frac{\partial \bar{v}}{\partial \bar{x}} \right) - 2 \bar{F}_x \left(\frac{\partial \bar{u}}{\partial \bar{x}} - \frac{\partial \bar{v}}{\partial \bar{y}} \right) = 0 \quad (3.13a)$$

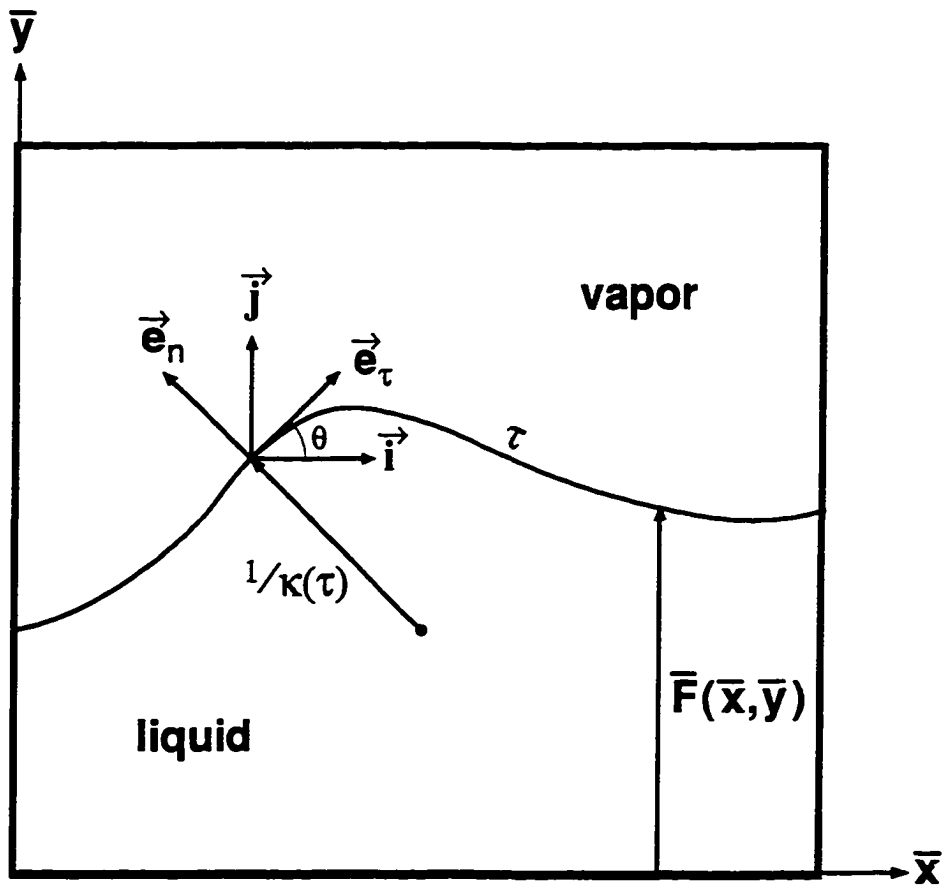


Figure 3.2: Free Surface Curvilinear Coordinates

$$\bar{p} - \bar{p}_o = \frac{\mu}{1 + \bar{F}_x^2} \left[\left(\frac{\partial \bar{v}}{\partial \bar{y}} - \bar{F}_x \frac{\partial \bar{v}}{\partial \bar{x}} \right) - \bar{F}_x \left(\frac{\partial \bar{u}}{\partial \bar{y}} - \bar{F}_x \frac{\partial \bar{u}}{\partial \bar{x}} \right) \right] + \kappa \mathcal{Y} \quad (3.13b)$$

The horizontal velocity component, \bar{u} , is determined from equation (3.13a), while equation (3.13b) is used to calculate the pressure at the free surface. The vertical component of the velocity, \bar{v} , at the free surface is determined from the continuity equation,

$$\frac{\partial \bar{v}}{\partial \bar{y}} = -\frac{\partial \bar{u}}{\partial \bar{x}} \quad (3.13c)$$

thus providing boundary conditions at the free surface for all of the dependent variables.

3.2 Initial Conditions

At $\bar{t} = 0$, the container experiences an abrupt change in either its horizontal velocity, \bar{U}_o , or its acceleration, q , with respect to the inertial coordinate frame, (\bar{x}_o, \bar{y}_o) . In order to derive the correct set of initial condition equations for the problem, the state of the liquid within the container at $\bar{t} = 0$, must be carefully examined. The following notation will be implemented in deriving this set of equations. Let $\bar{t} = 0^-$, denote the limit from below, or left limit, as $\bar{t} \rightarrow 0$. The liquid within the container is assumed to remain in a state of hydrostatic equilibrium up to this point. Thus, the initial conditions of the problem at this time are:

$$\left[\bar{u}^-, \bar{v}^-, \bar{p}^-, \bar{F}^- \right] = \left[-\bar{U}_o, 0, \rho g (\bar{F}_o - \bar{y}), \bar{F}_o \right] \quad \text{at } \bar{t} = 0^- \quad (3.14)$$

Note that the horizontal velocity component is equal to $\bar{u}^- = -\bar{U}_o$ because it is measured with respect to the moving container.

Let $\bar{t} = 0^+$, denote the limit from above, or right limit, as $\bar{t} \rightarrow 0$. This represents the time immediately following the start of the container motion. The state of the liquid within the container at this time, $\bar{t} = 0^+$, is different from that which existed at $\bar{t} = 0^-$. That is,

$$\left[\bar{u}^+, \bar{v}^+, \bar{p}^+, \bar{F}^+ \right] \neq \left[\bar{u}^-, \bar{v}^-, \bar{p}^-, \bar{F}^- \right]$$

and the initial conditions as given in equation (3.14) are incorrect in describing the state of the liquid at time $\bar{t} = 0^+$. To demonstrate this, consider a case for which $\bar{U}_o = 0$, and $q > 0$. The speed of the container, which is equal to $q\bar{t}$, is still zero at

time, $\bar{t}=0^+$. Consequently, one would expect the velocity field to be zero everywhere, ($\bar{u}^+ = 0, \bar{v}^+ = 0$) for all (\bar{x}, \bar{y}) . This implies that the momentum equations (3.3a,b) reduce to the following forms,

$$\frac{1}{\rho} \frac{\partial \bar{p}^+}{\partial \bar{x}} = -q \quad \text{and,} \quad \frac{1}{\rho} \frac{\partial \bar{p}^+}{\partial \bar{y}} = -g \quad (3.15)$$

which are inconsistent with a hydrostatic pressure field, $\bar{p}^- = \rho g(\bar{F}_o - \bar{y})$. Therefore, the pressure field at time, $\bar{t}=0^+$, has to differ from the hydrostatic field that existed immediately before, at time $\bar{t}=0^-$. In fact, the pressure field at $\bar{t}=0$ is discontinuous for $q \neq 0$, and it is singular for $\bar{U}_o \neq 0$. This is consistent with the liquid incompressibility assumption which implies an instantaneous adjustment of the pressure to imposed external forces.

3.2.1 Characteristic Scales

The sudden changes in the acceleration and velocity of the container at time $\bar{t}=0$ lead to discontinuities in the pressure and velocity fields of the liquid. To determine the proper, non-singular, initial conditions for the problem the immediate response of the liquid to the sudden changes in the forcing conditions must be examined. The acceleration of the container with respect to the inertial coordinate frame \bar{x}_o can be expressed as,

$$\frac{d^2 \bar{x}}{d\bar{t}^2} = q H(\bar{t}) + \bar{U}_o \delta(\bar{t}) \quad (3.16)$$

where q and \bar{U}_o represent the step changes in the container acceleration and velocity respectively. Here, $H(\bar{t})$ denotes the Heavyside function, and $\delta(\bar{t})$ denotes it's derivative, the Dirac function. They are defined by,

$$H(\bar{t} - \bar{t}_*) \equiv \begin{cases} 0 & \text{if } \bar{t} < \bar{t}_*^- \\ 1 & \text{if } \bar{t} > \bar{t}_*^+ \end{cases} \quad (3.17a)$$

and

$$\delta(\bar{t} - \bar{t}_*) \equiv \lim_{\epsilon \rightarrow 0} \frac{1}{\sqrt{\pi\epsilon}} e^{-(\bar{t}-\bar{t}_*)^2/\epsilon} \quad (3.17b)$$

The first term on the right hand side of equation (3.16) represents the step change in the acceleration of the container from a zero value at time $\bar{t}=0^-$ to a value of q at time $\bar{t}=0^+$. The second term in equation (3.16) represents the impulse or "spike" in the container acceleration necessary in order to produce a step change in the container

velocity from a zero value to a value of \bar{U}_o . The initial conditions for the problem need to be specified at time $\bar{t}=0^+$ in order to avoid singularities caused by the discontinuities in the container velocity and acceleration. Careful examination of the characteristic scales of the dependent and independent variables at time $\bar{t}=0$ leads to a simplified set of equations for the initial conditions.

The horizontal speed of the container is given by $(\bar{U}_o + q\bar{t})$. Thus the change in the horizontal velocity of the fluid from $\bar{t}=0^-$ to $\bar{t}=0^+$, can be expected to be of the same order, $\Delta\bar{u} \sim \bar{U}_o + q\bar{t}$. By continuity, $\Delta\bar{v} \sim \Delta\bar{u}$, provided that the aspect ratio of the container is of order one. The balance of terms in the momentum equations then takes the following form,

$$\underbrace{\frac{\partial\bar{u}}{\partial\bar{t}}}_{\sim \mathcal{O}\left(\frac{\Delta\bar{u}}{\Delta\bar{t}}\right)} + \underbrace{\bar{u}\frac{\partial\bar{u}}{\partial\bar{x}} + \bar{v}\frac{\partial\bar{u}}{\partial\bar{y}}}_{\sim \mathcal{O}\left(\frac{\Delta\bar{u}^2}{L}\right)} = - \underbrace{\frac{1}{\rho}\frac{\partial\bar{p}}{\partial\bar{x}}}_{\sim \mathcal{O}\left(\frac{\Delta\bar{p}}{\rho L}\right)} + q + \underbrace{\nu\left(\frac{\partial^2\bar{u}}{\partial\bar{x}^2} + \frac{\partial^2\bar{u}}{\partial\bar{y}^2}\right)}_{\sim \mathcal{O}\left(\frac{\nu\Delta\bar{u}}{L^2}\right)} \quad (3.18)$$

where L is the width of the container and is assumed to be of order one. Here, only the horizontal component of the momentum equation is shown since the same scaling holds for the vertical component. If $q \neq 0$ and $\bar{U}_o=0$, then the dominant terms in the are of order, $\sim \mathcal{O}(q)$. The momentum equations reduce to a balance between the acceleration, pressure gradient, and body force terms. The fluid experiences a non zero acceleration but in the limit as $\bar{t} \rightarrow 0^+$ the change in the velocity field is negligible, $(\bar{u}, \bar{v}) \sim q\bar{t} \rightarrow 0$. Thus, a step change in the container acceleration results in the immediate adjustment of the pressure field with no change in the velocity field. In the absence of curvature and viscous effects the free surface can not sustain a tangential pressure gradient. This leads to a pressure field at time $\bar{t}=0^+$, which is not in equilibrium with the body forces, and thus drives the liquid motion for $\bar{t} > 0^+$. The solution for the dependent variables for $q \neq 0$ and $\bar{U}_o=0$ can then be obtained from,

$$[\bar{u}^+, \bar{v}^+, \bar{F}^+] = [0, 0, \bar{F}_o] \quad (3.19a)$$

$$\bar{\nabla}^2\bar{p}^+ = 0 \quad (3.19b)$$

subject to boundary conditions,

$$\bar{p}^+ = 0 \quad \text{at} \quad \bar{y} = \bar{F}_o \quad (3.19c)$$

$$\frac{\partial\bar{p}^+}{\partial\bar{y}} = -\rho g \quad \text{at} \quad \bar{y} = 0 \quad (3.19d)$$

$$\frac{\partial \bar{p}^+}{\partial \bar{x}} = -\rho q \quad \text{at} \quad \bar{x} = 0, L \quad (3.19e)$$

For a step increase in the velocity of the container the dominant terms in the momentum equations are of order $\sim \mathcal{O}(\bar{U}_o/\Delta \bar{t})$. The pressure gradient becomes the only term capable of balancing the acceleration term. The horizontal acceleration spike experienced by the fluid particles can be written in terms the Dirac function as,

$$\frac{\partial \bar{u}}{\partial \bar{t}} \Big|_{\bar{t}=0} = [\bar{u}^+(t^+, \bar{x}, \bar{y}) - \bar{u}^-(t^-, \bar{x}, \bar{y})] \delta(\bar{t}) \quad \text{at} \quad \bar{t}=0 \quad (3.20)$$

with a similar expression used for the vertical acceleration. With $\bar{u}^-(0^-, \bar{x}, \bar{y}) = -\bar{U}_o$, the momentum equations reduce to the following form,

$$(\bar{u}^+ - \bar{U}_o) \delta(\bar{0}) = -\frac{1}{\rho} \frac{\partial \bar{p}}{\partial \bar{x}} \Big|_{\bar{t}=0} \quad (3.21a)$$

$$\bar{v}^+ \delta(\bar{0}) = -\frac{1}{\rho} \frac{\partial \bar{p}}{\partial \bar{y}} \Big|_{\bar{t}=0} \quad (3.21b)$$

Integration of these equations in a small neighborhood of $\bar{t} = 0$, and introducing a *pressure impulse function* $\bar{\Pi}$, such that $\bar{p}(\bar{t}) = \bar{\Pi}(\bar{t})\delta(\bar{t})$ as $\bar{t} \rightarrow 0$, leads to the following solution for the dependent variables at time $\bar{t} = 0^+$,

$$\bar{F}^+ = \bar{F}_o. \quad (3.22a)$$

$$\bar{u}^+ = -\bar{U}_o - \frac{1}{\rho} \frac{\partial \bar{\Pi}}{\partial \bar{x}} \quad (3.22b)$$

$$\bar{v}^+ = -\frac{1}{\rho} \frac{\partial \bar{\Pi}}{\partial \bar{y}} \quad (3.22c)$$

$$\bar{\nabla}^2 \bar{\Pi} = 0 \quad (3.22d)$$

subject to

$$\bar{\Pi} = 0 \quad \text{at} \quad \bar{y} = \bar{F}_o \quad (3.22e)$$

$$\frac{\partial \bar{\Pi}}{\partial \bar{y}} = 0 \quad \text{at} \quad \bar{y} = 0 \quad (3.22f)$$

$$\frac{\partial \bar{\Pi}}{\partial \bar{x}} = -\rho U_o \quad \text{at} \quad \bar{x} = 0, L \quad (3.22g)$$

where, $\bar{\Pi}$, is the pressure impulse function. The behavior of the pressure variable, \bar{p} , in the neighborhood of the initial singularity at $\bar{t}=0$ can be described in terms of $\bar{\Pi}$ by the following relation,

$$\bar{p}(t) = (1 - H(\bar{t} + \bar{t}^-)) \bar{p}^- + \bar{\Pi} \delta(0) + H(\bar{t} - \bar{t}^+) \bar{p}^+ \quad (3.22h)$$

where the three terms on the right hand side of equation (3.22h) represent respectively, the hydrostatic pressure field existing prior the movement of the container, the pressure impulse experienced by the liquid at $\bar{t}=0$ as a result of the impulsive start of motion, and the pressure field immediately following the start of motion.

Thus, as a result of a step increase in the velocity of the container, the liquid experiences a pressure impulse of order $\sim \mathcal{O}(\rho L \bar{U}_o / \bar{t})$ as $\bar{t} \rightarrow 0$, which results in an irrotational velocity field at $\bar{t}=0^+$. The momentum equations at time $\bar{t}=0^+$, immediately after the impulsive start, indicate a prevailing balance of order, $\sim \mathcal{O}(\bar{U}_o^2 / L)$. Thus, the liquid motion is initially driven by advection.

It should be noted that due to the loss of the viscous terms from the initial condition equations at $\bar{t}=0$, the no-slip boundary conditions along the container walls can not be fully satisfied. This implies the existence of boundary layers of thickness $\bar{\delta}$ along the container walls, where the viscous effects become of the same order of magnitude as the liquid acceleration. Based on the above scaling it can be shown that $\bar{\delta} \sim \sqrt{\nu \bar{t}}$. Similarly, the zero tangential stress condition at the free surface is not satisfied by the solution to equations (3.21) which are inviscid in nature. A viscous boundary layer, of the same thickness $\bar{\delta}$, is needed along the free surface to allow for the boundary conditions to be satisfied at time, $\bar{t}=0^+$. Similarity solutions for the flow in these boundary layers are given in Appendix B. However, for the numerical solution of the problem the initial irrotational velocity field, corrected for no-slip at the walls, provides an adequate initial condition for the velocity. The pressure field at $\bar{t}=0^+$ can also be approximately determined from the irrotational core flow. The pressure change across the boundary layers is small compared to the hydrostatic pressure scale,

$$\frac{\Delta \bar{p}^+}{\rho L g} \sim \frac{\nu \bar{U}_o}{L^2 g}$$

and can be neglected. Thus, for $\bar{U}_o \neq 0$, the pressure field at $\bar{t}=0^+$ can be approximated by the solution of the following Poisson equation,

$$\bar{\nabla}^2 \bar{p}^+ = 2\bar{J}(\bar{u}, \bar{v}) \quad (3.22i)$$

subject to boundary conditions,

$$\bar{p}^+ = 0 \quad \text{at} \quad \bar{y} = \bar{F}_o \quad (3.22j)$$

$$\frac{\partial \bar{p}^+}{\partial \bar{y}} = -\rho g \quad \text{at} \quad \bar{y} = 0 \quad (3.22k)$$

$$\frac{\partial \bar{p}^+}{\partial \bar{x}} = -\rho q \quad \text{at} \quad \bar{x} = 0, L \quad (3.22l)$$

3.3 Dimensionless Formulation

A more general set of governing equations is obtained by casting the developed equations in dimensionless form. The dimensionless variables are selected such that the domain of analysis is normalized and the resulting number of dimensionless parameters influencing the solution is minimized.

The liquid density, ρ , a characteristic length of the container, L , and the acceleration due to gravity, g , are used to define the following primary Mass-Length-Time scales:

- mass $M \sim \rho L^3$ (3.23a)

- length L (3.23b)

- time $\tau \sim \sqrt{L/g}$ (3.23c)

Derived from these are the following characteristic scales used in formulating dimensionless dependent variables:

- velocity $\mathcal{U} \sim \sqrt{Lg}$ (3.23d)

- pressure $\mathcal{P} \sim \rho Lg$ (3.23e)

The characteristic velocity scale, \mathcal{U} , is equivalent to the wave speed, *celerity*, determined from shallow water wave theory, while τ represents the time interval for a wave disturbance to travel across the container, and \mathcal{P} an Euler pressure scale based on \mathcal{U} .

The dimensionless independent variables of the problem are formulated to define a coordinate transformation that produces a natural coordinate system for the domain of analysis. This simple algebraic stretching is defined by:

$$(x, y, t) = \left(\frac{\bar{x}}{L}, \frac{\bar{y}}{LF}, \frac{\bar{t}}{\sqrt{L/g}} \right) \quad (3.24)$$

where $F(x, t) = \bar{F}(\bar{x}, \bar{t})/L$, called the dimensionless gap function, is simply the dimensionless free surface position.

The motion of the liquid is determined by five similarity parameters that emerge from the nondimensionalization. The first two of these parameters, are the dimensionless horizontal acceleration, Q , and the dimensionless initial horizontal velocity, U_o , which pertain information on the motion of the container relative to the inertial frame of reference. They are defined as,

$$Q \equiv \frac{q}{g} \quad \text{dimensionless horizontal acceleration} \quad (3.25a)$$

$$U_o \equiv \frac{\bar{U}_o}{\sqrt{Lg}} \quad \text{dimensionless initial velocity} \quad (3.25b)$$

The next two parameters are related to the physical properties of the liquid. These are the Galileo number, Ga , and the Bond number, Bo , defined as,

$$Ga \equiv \frac{L^3 g}{\nu^2} \quad \text{Galileo number} \quad (3.25c)$$

$$Bo \equiv \frac{\rho g L^2}{\gamma} \quad \text{Bond number} \quad (3.25d)$$

The Galileo number represents a ratio of body to viscous forces. The dimensionless Galileo number can also be viewed as being analogous to the square of a Reynolds number based on the characteristic velocity scale, \mathcal{U} . The Bond number represents a ratio of body to surface tension forces. It can also be expressed as the ratio of Weber to Froude numbers, the two dimensionless groups commonly associated with free surface flows. However, with the characteristic velocity and time scales used here, the Froude number does not emerge as an independent similarity parameter.

The final similarity parameter pertains information on the geometry of the liquid region. It is the initial aspect ratio of the liquid, and is simply defined as,

$$F_o \equiv \bar{F}_o/L \quad \text{initial liquid aspect ratio} \quad (3.25e)$$

3.3.1 Dimensionless Governing Equations

Based on the scales defined in equation (3.23) the following dimensionless dependent variables are formulated:

$$(u, v, p, D) \equiv \left(\frac{\bar{u}}{\sqrt{Lg}}, \frac{\bar{v}}{\sqrt{Lg}}, \frac{\bar{p} - p_o}{\rho Lg}, \frac{\bar{D}}{\sqrt{g/L}} \right) \quad (3.26)$$

Using the above variable definitions and based on the coordinate transformation defined by equation (3.24), the dimensionless governing equations become:

x-momentum equation:

$$\begin{aligned} \frac{\partial u}{\partial t} + u \frac{\partial u}{\partial x} + \frac{1}{F} (v - yF_x u - y\dot{F}) \frac{\partial u}{\partial y} \\ = - \left(\frac{\partial p}{\partial x} - \frac{yF_x}{F} \frac{\partial p}{\partial y} \right) - Q + \frac{1}{\sqrt{Ga}} (\nabla^2 - \mathcal{N}) u \end{aligned} \quad (3.27a)$$

y-momentum equation:

$$\begin{aligned} \frac{\partial v}{\partial t} + u \frac{\partial v}{\partial x} + \frac{1}{F} (v - yF_x u - y\dot{F}) \frac{\partial v}{\partial y} \\ = - \frac{1}{F} \frac{\partial p}{\partial y} - 1 + \frac{1}{\sqrt{Ga}} (\nabla^2 - \mathcal{N}) v \end{aligned} \quad (3.27b)$$

pressure Poisson equation:

$$\begin{aligned} (\nabla^2 - \mathcal{N}) p = \frac{2}{F} J(u, v) - \frac{\partial D}{\partial t} - u \frac{\partial D}{\partial x} \\ - \frac{1}{F} (v - yF_x u - y\dot{F}) \frac{\partial D}{\partial y} - D^2 + \frac{1}{\sqrt{Ga}} (\nabla^2 - \mathcal{N}) D \end{aligned} \quad (3.27c)$$

continuity equation (dilatation):

$$\frac{\partial u}{\partial x} - \frac{yF_x}{F} \frac{\partial u}{\partial y} + \frac{1}{F} \frac{\partial v}{\partial y} = D \quad (3.27d)$$

kinematic condition:

$$\dot{F} = v - F_x u \quad \text{along } y = 1 \quad (3.27e)$$

where

$$\nabla^2 = \frac{\partial^2}{\partial x^2} + \frac{1}{F^2} \frac{\partial^2}{\partial y^2}$$

$$\mathcal{N} = \left(\frac{2yF_x}{F} \right) \frac{\partial^2}{\partial x \partial y} - \left(\frac{2F_x^2}{F^2} - \frac{F_{xx}}{F} \right) y \frac{\partial}{\partial y} - \left(\frac{yF_x}{F} \right)^2 \frac{\partial^2}{\partial y^2}$$

$$J(u, v) = \frac{\partial u}{\partial x} \frac{\partial v}{\partial y} - \frac{\partial u}{\partial y} \frac{\partial v}{\partial x}$$

with

$$F_x = \frac{\partial F}{\partial x}, \quad F_{xx} = \frac{\partial^2 F}{\partial x^2}, \quad \text{and} \quad \dot{F} = \frac{\partial F}{\partial t}$$

Equation (3.27d) defines the dimensionless dilatation, $D = \bar{D}/\sqrt{g/L}$. Continuity requires $D \equiv 0$. Equation (3.27e) is the kinematic condition for the position of the free surface. It provides the governing equation for the gap function, $F(x, t)$.

Note that a number of new terms appear in the governing equations as these are transformed into dimensionless form. In the transformed (x, y) space, the free surface is both immobilized and normalized. Thus, all the information pertaining to the motion and shape of the free surface in the physical space, (\bar{x}, \bar{y}) , has been passed onto the normalized (x, y) space in the form of these new terms. The substantial derivative in (x, y) space takes the form:

$$\frac{d}{dt} = \left[\frac{\partial}{\partial t} + u \frac{\partial}{\partial x} + \frac{v}{F} \frac{\partial}{\partial y} \right] - \left[\left(\frac{y\dot{F}}{F} + \frac{yF_x u}{F} \right) \frac{\partial}{\partial y} \right] \quad (3.28)$$

The second bracketed term on the right hand side of the above equation contains two new convective terms. The $y\dot{F}/F$ term represents a convective effect due to the actual movement of the free surface, while the $yF_x u/F$ term represents a convective effect due to the irregular shape of the free surface. The irregular shape of the free surface also contributes to diffusive effects which are grouped in the second order \mathcal{N} operator. Note that F , F_x , and F_{xx} must be singly valued and well defined (one-to-one) for the coordinate transformation (3.24) and its inverse to be well behaved.

3.3.2 Dimensionless Boundary Conditions

Substitution of the dimensionless variables scales defined in (3.26) and the transformation defined by (3.24) into equations (3.9) (3.13) yields the following dimensionless boundary conditions:

along $x=0$ and $x=1$:

$$u = v = 0 \quad (3.29a)$$

$$\frac{\partial p}{\partial x} = \frac{yF_x}{F} \frac{\partial p}{\partial y} - Q + \frac{1}{\sqrt{Ga}} \frac{\partial^2 u}{\partial x^2} \quad (3.29b)$$

along $y = 0$:

$$u = v = 0 \quad (3.29c)$$

$$\frac{1}{F} \frac{\partial p}{\partial y} = -1 + \frac{1}{\sqrt{Ga}} \frac{\partial^2 v}{\partial y^2} \quad (3.29d)$$

along $y = 1$:

$$\frac{1}{F} (1 + F_x^2)^2 \frac{\partial u}{\partial y} = F_x (3 + F_x^2) \frac{\partial u}{\partial x} - (1 - F_x^2) \frac{\partial v}{\partial x} \quad (3.29e)$$

$$\frac{1}{F} \frac{\partial v}{\partial y} = \frac{F_x}{F} \frac{\partial u}{\partial y} - \frac{\partial u}{\partial x} \quad (3.29f)$$

$$p = \frac{2}{\sqrt{Ga}} \left[\frac{1}{F} \left(\frac{\partial v}{\partial y} - F_x \frac{\partial u}{\partial y} \right) - \frac{F_x}{1 + F_x^2} \left(\frac{\partial v}{\partial x} - F_x \frac{\partial u}{\partial x} \right) \right] + \frac{1}{Bo} \kappa \quad (3.29g)$$

Equation (3.29e) is the zero tangential stress condition and is used to determine u along the free surface. The continuity equation is rearranged into form (3.29f) and is used to determine the vertical component of the velocity along the free surface. Pressure values along the free surface are set according to equation (3.29g), which results from the normal stress condition.

3.4 Dimensionless Initial Conditions

The present model, which is based on the incompressible Navier-Stokes equations, is parabolic in terms of the velocity and purely elliptic in terms of the pressure. This implies that for the successful marching of the governing equations only information on the velocity field is needed from previous time levels. Thus, based on the scaling of the governing equations, the minimum requirement for the initial conditions is the correct determination of the velocity field at time, $t = 0^+$, to order $\sim \mathcal{O}(\sqrt{Lg})$.

The two types of forcing conditions considered here stem from sudden changes in the container acceleration and velocity at time $t = 0$. For the case of a sudden container acceleration, $Q > 0$, the pressure field *instantaneously* adjusts to the new apparent accelerations experienced by the liquid without any change occurring in the velocity field. Thus, the liquid is still motionless at time $t = 0^+$ if $U_o = 0$. For an

impulsive container start, $U_o > 0$, the liquid experiences a pressure impulse Π at time $t=0$, which results in a non-zero velocity field at time $t=0^+$. This initial velocity field can be determined from the solution of a simplified form of the governing equations,

$$F(0^+, x) = F_o \quad (3.30a)$$

$$u^+ = -U_o - \frac{\partial \Pi}{\partial x} \quad (3.30b)$$

$$v^+ = -\frac{1}{F_o} \frac{\partial \Pi}{\partial y} \quad (3.30c)$$

where, the pressure impulse is determined by the solution of the following Laplace equation,

$$\frac{\partial^2 \Pi}{\partial x^2} + \frac{1}{F_o^2} \frac{\partial^2 \Pi}{\partial y^2} = 0 \quad (3.30d)$$

subject to boundary conditions,

$$\frac{\partial \Pi}{\partial x} = -U_o \quad \text{along } x = 0 \text{ and } x = 1 \quad (3.30e)$$

$$\frac{1}{F_o} \frac{\partial \Pi}{\partial y} = 0 \quad \text{along } y = 0 \quad (3.30f)$$

$$\Pi = 0 \quad \text{at } y = 1 \quad (3.30g)$$

For $U_o > 0$, the pressure field at time $t=0^+$ must be determined from the solution of the full pressure Poisson equation,

$$\frac{\partial^2 p^+}{\partial x^2} + \frac{1}{F_o^2} \frac{\partial^2 p^+}{\partial y^2} = \frac{2}{F_o} \left(\frac{\partial u^+}{\partial x} \frac{\partial v^+}{\partial y} - \frac{\partial u^+}{\partial y} \frac{\partial v^+}{\partial x} \right) \quad (3.31a)$$

subject to the following boundary conditions,

$$\frac{\partial p^+}{\partial x} = -Q \quad \text{along } x = 0 \text{ and } x = 1 \quad (3.31b)$$

$$\frac{1}{F_o} \frac{\partial p^+}{\partial y} = 0 \quad \text{along } y = 0 \quad (3.31c)$$

$$p^+ = 0 \quad \text{along } y = 1 \quad (3.31d)$$

Using separation of variables equation (3.30d) can be solved analytically for the pressure impulse to obtain,

$$\Pi = U_o \left(\frac{1}{2} - x \right) - \sum_{m=0}^{\infty} b_m \cos X_m \cosh Y_m \quad (3.32a)$$

which can be substituted into equations (3.30b,c) to yield the initial velocity field in terms of,

$$u^+ = - \sum_{m=0}^{\infty} b_m (2m + 1) \pi \sin X_m \cosh Y_m \quad (3.32b)$$

$$v^+ = \sum_{m=0}^{\infty} b_m (2m + 1) \pi \cos X_m \sinh Y_m \quad (3.32c)$$

where

$$b_m = \frac{4U_o}{\pi^2(2m + 1)^2 \cosh [(2m + 1)\pi F_o]} \quad (3.32d)$$

$$X_m = (2m + 1)\pi x \quad \text{and} \quad Y_m = F_o(2m + 1)\pi y \quad (3.32e)$$

For cases involving only a sudden container acceleration, $U_o = 0$, equation (3.31) reduces to a simple Laplace equation. An analytical solution for the pressure field can then be determined using separation of variables to obtain,

$$p^+ = F_o(1 - y) + Q \left(\frac{1}{2} - x \right) - \sum_{m=0}^{\infty} b_m^* \cos X_m \cosh Y_m \quad (3.33a)$$

with X_m and Y_m as previously defined and,

$$b_m^* = \frac{4Q}{\pi^2(2m + 1)^2 \cosh [(2m + 1)\pi F_o]}$$

As indicated in the preceding analysis, the above inviscid solution for the pressure and velocity fields when $U_o \neq 0$ is correct only in the core of the flow. The no-slip condition at the walls is not fully satisfied as only the normal velocity components vanish at the wall. For a complete description of the flow at time, $t = 0^+$, the flow within boundary layers that emerge along the walls and the free surface should be determined (see Appendix B). The boundary layer thickness, δ , initially grows as the square root of time, $\delta \sim t^{\frac{1}{2}} G a^{\frac{1}{4}}$. The boundary layer flow at $t = 0^+$ is driven by the irrotational core flow. It is uncoupled from the core flow, and based on the scaling used for the dependent and independent variables in the governing equations its explicit determination becomes unnecessary. The inviscid solution, described in terms of (3.30a), (3.32b,c), and the solution of equation (3.31), with the tangential velocity components set equal to zero at the walls, provides the correct set of initial conditions for the full governing equations.

The nature of the state of the liquid at $t = 0^+$ can be better understood by examining sample solutions shown for a half filled container, $F_o = 0.5$, in Figure 3.3. The pressure field for a case with $Q = 0.2$ and $U_o = 0$ is shown in Figure 3.3(a). As a result of the sudden acceleration experienced by the fluid, the pressure rises at the lower left corner and falls at the right corner of the container. This causes the fluid to rise on left side and fall on the right side of the container for $t > 0^+$. The pressure impulse, Π , for a case with $U_o = 0.2$ is shown in Figure 3.3(b). Note that $\Pi > 0$ in the left half of the container and $\Pi < 0$ in the right half of the container. The horizontal gradients are symmetric about the mid plane, while the vertical gradients are negative in the left half and positive in the right half of the fluid. The velocity field produced by the action of this pressure impulse is shown in Figure 3.3(c). The motion of the fluid is in a clockwise direction everywhere. It is distinctly different from the condition ($u = -U_o, v = 0$) which is valid only at $t = 0^-$. The magnitude of U_o is drawn to scale at the top right corner. Note that the magnitude of the resulting velocity at the two ends of the free surface is roughly three times that of the container velocity. The resulting pressure field, with $Q = 0$, is shown in Figure 3.3(d). Note that the pressure field reveals the subsequent asymmetry of the velocity for $t > 0^+$. The horizontal pressure gradients are negative in the left, and positive in the right half of the fluid. The vertical pressure gradients are negative everywhere. Their combined effect is to turn the flow more towards the vertical direction in the left half, while turning the flow more towards the horizontal direction in the right half of the container. Thus the free surface will tend to rise more along the left wall than it would drop along the right wall.

3.5 Inviscid Irrotational Model

A model based on potential flow is also developed to describe the liquid flow within the moving container. The governing equations can be significantly simplified by assuming the resulting flow to be both inviscid and irrotational. This potential model, which is valid in the limit of vanishing liquid viscosity, will be used for the study of some of the problem parameters, and as a comparison tool for the full model.

Based on potential theory, the velocity is defined in terms of the gradient of the velocity potential, $\bar{\phi}$. In dimensionless form, using the same dependent and independent variables as in the governing equations, while using $L^{\frac{3}{2}}g^{\frac{1}{2}}$ as the scale for $\bar{\phi}$, the

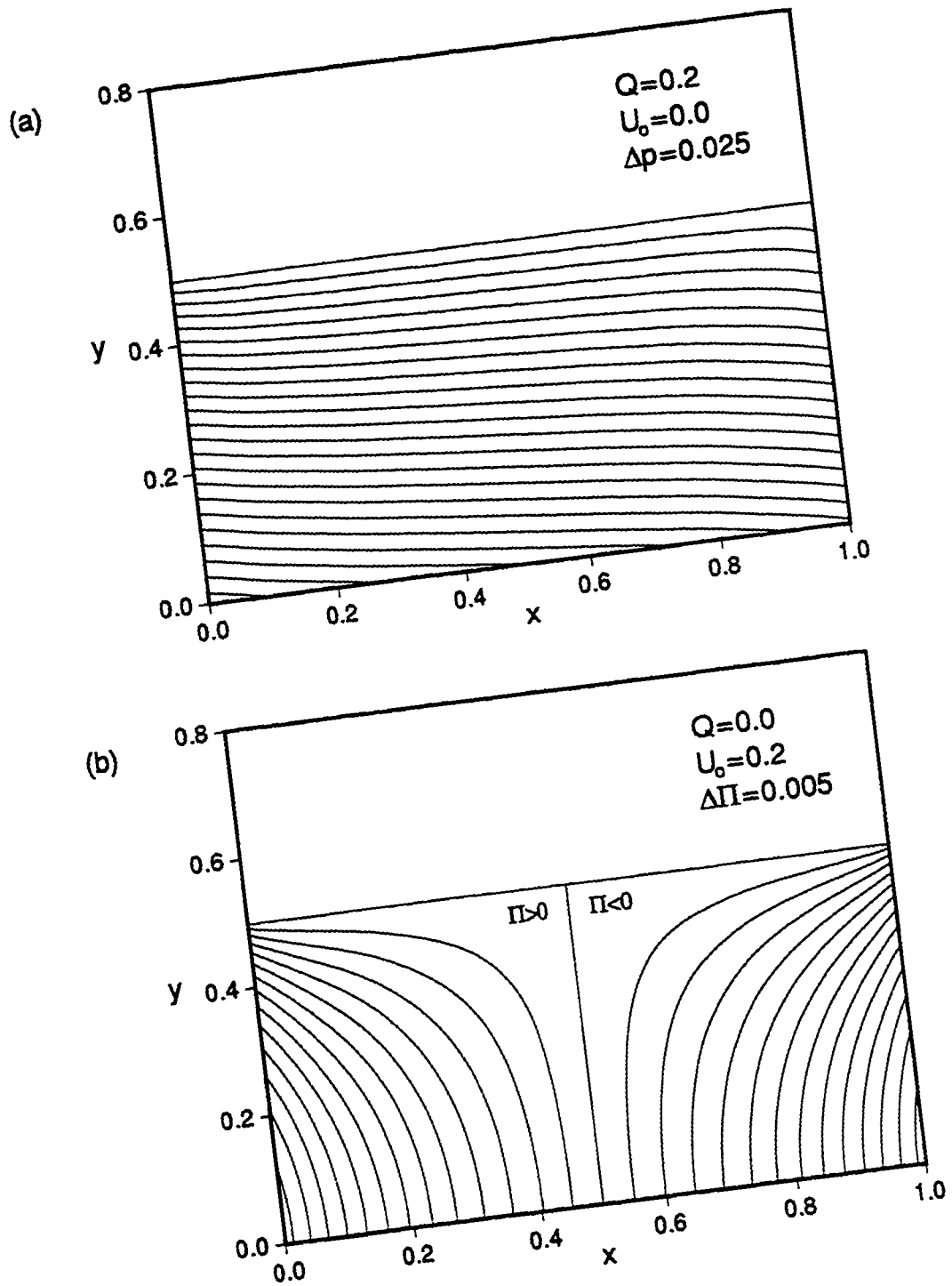


Figure 3.3: Initial Conditions Solution

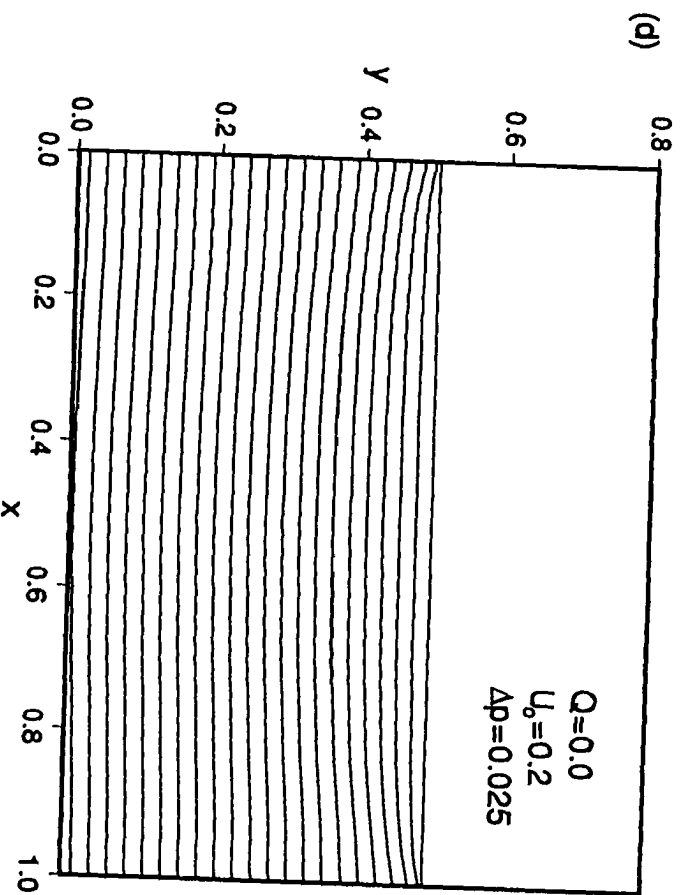
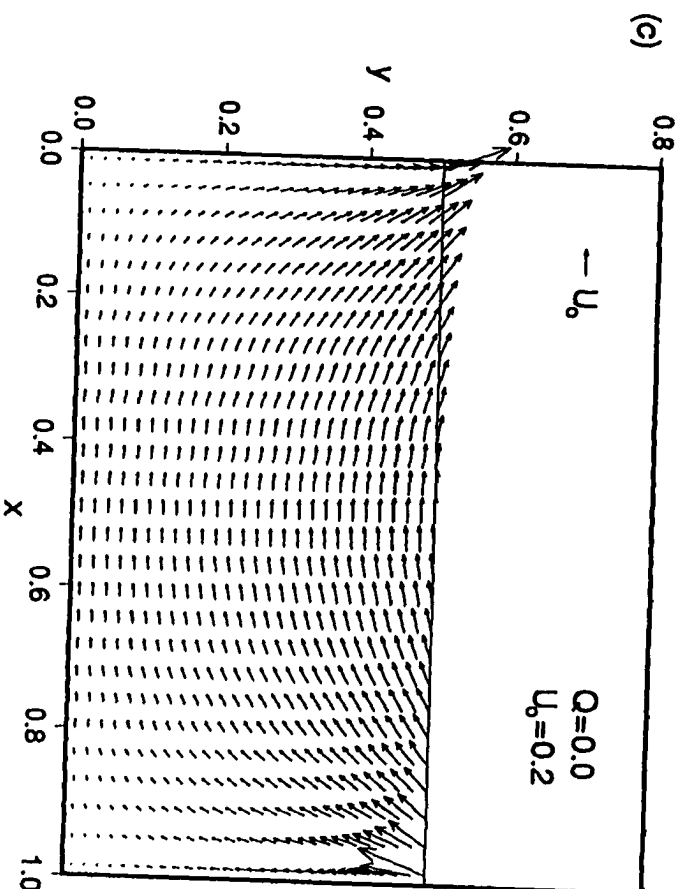


Figure 3.3 (Continued)

velocity components are defined as:

$$u = \frac{\partial \phi}{\partial x} - \frac{yF_x}{F} \frac{\partial \phi}{\partial y} \quad (3.34a)$$

$$v = \frac{1}{F} \frac{\partial \phi}{\partial y} \quad (3.34b)$$

Substitution of the above definitions into the continuity equation yields the following elliptic equation for the velocity potential:

$$(\nabla^2 - \mathcal{N}) \phi = 0 \quad (3.34c)$$

Equation (3.34b) is subject to impermeability boundary conditions along the solid walls:

$$u = 0 \quad \text{along } x = 0 \text{ and } x = 1 \quad (3.34d)$$

$$v = 0 \quad \text{along } y = 0 \quad (3.34e)$$

Using the definition of the potential, along with the assumption of irrotationality, the momentum equations are simplified and integrated along the free surface to yield the following Bernoulli equation, which provides the needed free surface boundary condition:

$$\frac{\partial \phi}{\partial t} = \frac{y\dot{F}}{F} \frac{\partial \phi}{\partial y} - \frac{1}{2} (u^2 + v^2) - Q \left(x - \frac{1}{2} \right) - (F - F_o) - \frac{1}{Bo} \kappa \quad (3.34f)$$

The first term on the right hand side of equation (3.34f) represents a convective effect resulting from the coordinate transformation. The remaining terms represent contributions to the velocity potential in the form of, kinetic energy, potential energy due to the apparent acceleration Q , gravitational potential energy, and surface tension effects.

The initial condition for the potential model is found by taking the limit of equations (3.34a-f) as time, $t \rightarrow 0^+$. Using separation of variables to solve the resulting set of equations yields the following initial condition for ϕ :

$$\phi = \sum_{m=0}^{\infty} b_m \cos X_m \cosh Y_m \quad (3.34g)$$

where, b_m , X_m , and Y_m , have been previously defined in equations (3.32d,e).

3.6 Streamfunction-Vorticity Formulation

One of the drawbacks of a primitive variable formulation for the incompressible Navier-Stokes equations is that the zero divergence condition of the velocity field is enforced in an implicit rather than an explicit manner. By contrast, a streamfunction vorticity formulation leads to solutions that are necessarily divergence free. This was the primary reason for considering a streamfunction vorticity formulation for the present problem. However, the development of a model based on a streamfunction vorticity formulation turned out to be more challenging than anticipated. A brief description of the formulation is included here, primarily because it provides an alternative way to examine the free surface model.

The basic difficulty encountered in developing the model stems from the very nature of the vorticity transport equation. The cross-differentiation of the momentum equations, used in deriving the vorticity equation, eliminates all the conservative, or potential, terms from the governing equations. However, for the present problem the flow is driven by a balance between the convective and the potential terms. The governing equations in terms of the streamfunction, \bar{f} , and the vorticity, $\bar{\omega}$, are given below in dimensionless form,

vorticity transport equation:

$$\frac{\partial \omega}{\partial t} + u \frac{\partial \omega}{\partial x} + \frac{1}{F} (v - yF_x u - y\dot{F}) \frac{\partial \omega}{\partial y} = \frac{1}{\sqrt{Ga}} (\nabla^2 - \mathcal{N}) \omega \quad (3.35a)$$

streamfunction equation:

$$(\nabla^2 - \mathcal{N}) f = -\omega \quad (3.35b)$$

kinematic condition:

$$\dot{F} = \frac{\partial f}{\partial x} \quad \text{along } y = 1 \quad (3.35c)$$

with boundary conditions along the container walls,

$$\omega = -\frac{\partial^2 f}{\partial x^2} \quad \text{and} \quad f = 0 \quad \text{along } x = 0 \quad \text{and} \quad x = 1 \quad (3.35d)$$

$$\omega = -\frac{1}{F^2} \frac{\partial^2 f}{\partial y^2} \quad \text{and} \quad f = 0 \quad \text{along } y = 0 \quad (3.35e)$$

where the velocity components are given in terms of the streamfunction by,

$$u = -\frac{1}{F} \frac{\partial f}{\partial y} \quad \text{and} \quad v = \frac{\partial f}{\partial x} + yF_x u \quad (3.35f)$$

The same scales have been utilized in the nondimensionalization of these equations. The dimensionless streamfunction and vorticity are defined by $f = \bar{f}/L^{\frac{3}{2}}g^{\frac{1}{2}}$, and $\omega = \bar{\omega}/\sqrt{g/L}$.

The remaining conditions that need to be specified are the boundary conditions at the free surface. In addition to enforcing the zero stress conditions at the free surface, these boundary conditions must also introduce into the governing equations the forcing experienced by the liquid. Note that the apparent acceleration Q is absent from the governing equations. Furthermore, for $U_o \neq 0$, the initial velocity field is mostly irrotational. Although this initial velocity field can be described in terms of the streamfunction at time $t=0^+$, no information is passed to the governing equations for $t > 0$ since the governing equations are only parabolic in terms of the vorticity. Thus, the free surface boundary conditions must also introduce into the governing equations any irrotational component of the flowfield.

To accomplish all of these objectives, a boundary condition for the streamfunction in terms of the momentum equations must be used. Note that if the velocity field and the free surface position are known, then the pressure along the free surface can be determined by the normal stress condition, (3.29g). Thus, formulating an equation for the conservation of momentum in the tangential direction eliminates the need for the explicit calculation of the entire pressure field. Eliminating the pressure gradient in the vertical direction from the two momentum equations, equations (3.27a,b), leads to the following equation,

$$\begin{aligned} \left(\frac{\partial u}{\partial t} + F_x \frac{\partial v}{\partial t} \right) + u \left(\frac{\partial u}{\partial x} + F_x \frac{\partial v}{\partial x} \right) \\ = -\frac{\partial p}{\partial x} - (Q + F_x) + \frac{1}{\sqrt{Ga}} \left(\frac{1 + F_x^2}{F} \frac{\partial \omega}{\partial y} - F_x \frac{\partial \omega}{\partial x} \right) \end{aligned} \quad (3.36a)$$

The above equation can be further manipulated into a form more appropriate for solution by noting that along the free surface $v = \dot{F} + F_x u$. This leads to,

$$\begin{aligned} \frac{\partial u}{\partial t} + u \frac{\partial u}{\partial x} + \frac{F_x}{1 + F_x^2} \left(\ddot{F} + 2\dot{F}_x u + F_{xx} u^2 \right) = \\ = -\frac{1}{1 + F_x^2} \frac{\partial p}{\partial x} - \frac{Q + F_x}{1 + F_x^2} + \frac{1}{\sqrt{Ga}} \left(\frac{1}{F} \frac{\partial \omega}{\partial y} - \frac{F_x}{1 + F_x^2} \frac{\partial \omega}{\partial x} \right) \end{aligned} \quad (3.36b)$$

This equation provides a boundary condition for the streamfunction in terms of the horizontal velocity component along the free surface. It enforces the normal stress

condition but in its present form it does not enforce the zero tangential stress condition. This must be incorporated into the vorticity boundary condition. The tangential stress and the vorticity along the free surface can be written in terms of the orthogonal curvilinear coordinate system introduced in equation (3.12) as,

$$\begin{aligned}\frac{\partial \bar{u}_\tau}{\partial n} - \kappa \bar{u}_\tau + \frac{\partial \bar{u}_n}{\partial \tau} &= 0 & (\text{tangential stress}) \\ \frac{\partial \bar{u}_\tau}{\partial n} + \kappa \bar{u}_\tau - \frac{\partial \bar{u}_n}{\partial \tau} &= \bar{\omega} & (\text{free surface vorticity})\end{aligned}$$

These two equations can be combined to yield the following boundary condition for the vorticity at the free surface,

$$\bar{\omega} = -2 \frac{\partial \bar{u}_n}{\partial \tau} + 2\kappa \bar{u}_\tau \quad \text{along } \bar{y} = \bar{F} \quad (3.37a)$$

Noting that along the free surface $\bar{u}_n = \dot{\bar{F}} / \sqrt{1 + \bar{F}_x^2}$, the above equation can be written in dimensionless form as,

$$\omega = \frac{2}{1 + F_x^2} (\dot{F}_x + F_{xx}u) \quad (3.37b)$$

Thus, the free surface of a viscous fluid can not undergo a change in shape, $\dot{F}_x \neq 0$, without generating vorticity. This raises the question as to why formulations which are based on the velocity potential, and thus assume an irrotational flow, have generally been proven to yield a reasonable description of wave dynamics. Recall that the position of the free surface is determined by the motion of the fluid particles that lie on it. Thus, no convection of fluid properties can occur across the free surface. Note that the convective terms in the y -direction do not appear in the tangential momentum equation, (3.36). As a result, viscous diffusion becomes the sole mechanism through which free surface vorticity can enter the interior flow. In the limit of vanishing liquid viscosity, $\nu \rightarrow 0$, vorticity generated at the free surface remains on the free surface.

3.7 Steady State Condition

The ultimate steady state of the system may be considered a hydrostatic state with respect to the combined body force acceleration, $(q\vec{i} + g\vec{j})$. It may be easily found in closed form by direct integration of the momentum equations. In dimensionless form, the result is:

$$\lim_{t \rightarrow \infty} u = 0 \quad \text{and} \quad \lim_{t \rightarrow \infty} v = 0 \quad (3.38a)$$

$$\lim_{t \rightarrow \infty} F = F_o + Q \left(\frac{1}{2} - x \right) \quad (3.38b)$$

$$\lim_{t \rightarrow \infty} p = (F_o - y) + Q \left(\frac{1}{2} - x \right) \quad (3.38c)$$

The final conditions have been written as limits rather than as equalities because the system approaches them asymptotically, through the mechanism of viscous damping.

3.8 First Law Analysis

A model based on the Navier Stokes equations has been established, which is capable of capturing in detail the liquid flow within the moving container. The modeling equations are non-linear and quite complicated. A total of five dimensionless similarity parameters, capable of influencing the flow, have been identified. Inevitably, solutions to the problem will also be complicated and difficult to analyze. However, despite the complexity of the fluid motions, viewed from a *global perspective* in terms of an energy balance the sloshing liquid behaves much like a damped second order system.

Based on the first law of thermodynamics, the energy conservation principle can be stated as: *the change in stored energy of a closed system during a process is fixed by the end states of the system and is independent of the details of the process.* The application of this principle to the liquid system will be based on the assumption that the sloshing process is adiabatic. Thus, any change in the total energy of the system, \bar{E} , must be interpreted to be the result of a work interaction, \bar{W} , between the liquid system and its surroundings. Furthermore, the internal energy of the liquid is assumed to change only as a result of viscous dissipation, and, that this change occurs from an initial reference state at $\bar{t} = 0$ which is taken to be equal to zero. Based on these assumptions the first law can be expressed as:

$$\bar{E}(\bar{t}) - \bar{E}_o = \bar{W}(\bar{t}) \quad (3.39a)$$

where $\bar{W}(\bar{t})$ represents the net work done by the liquid on its surroundings, and $\bar{E}(\bar{t})$ the total energy of the system at some time, \bar{t} . The initial energy of the system is represented by \bar{E}_o , where $\bar{E}_o \equiv \bar{E}(0)$. The total energy of the system is determined by the sum of the contributions from the following four components,

$$\bar{E}(\bar{t}) = \bar{E}_k(\bar{t}) + \bar{E}_p(\bar{t}) + \bar{E}_d(\bar{t}) + \bar{E}_S(\bar{t}) \quad (3.39b)$$

where \bar{E}_k represents the kinetic, and \bar{E}_p the potential energy of the system. The change in the internal energy of the system due to viscous dissipation is represented by \bar{E}_d .

The last term, \bar{E}_S , is a surface energy term, and it represents the contribution to the total energy of the system by the moving boundary.

The first law analysis of the liquid up to this point focused on general principles. The liquid system has been defined very loosely, and as result, the two terms, \bar{E}_S and \bar{W} , which appear in equation (3.39b) have not yet been clearly defined. However, before proceeding with the analysis, it may be helpful to reiterate the following two points:

1. The free surface of the liquid represents a modeling approximation for the interfacial region separating the liquid and gas phases. Based on this approximation, the interfacial region is treated as a material surface of zero thickness and mass. The requirement that the normal stress must remain continuous across the interface, leads to a pressure jump across the free surface of the liquid. A uniform pressure, equal to p_o , exists on the gas side of the free surface. The pressure difference on the liquid side, $\bar{p} - p_o$, is given by equation (3.10b). It is the sum of a viscous stress component and the contribution from surface tension effects.
2. The origin of surface tension can be traced to differences in the intermolecular structure and the cohesive forces present in each of the two bulk phases that are separated by a fluid interface. Liquid molecules that lie in the proximity of a boundary with a gaseous phase experience an unbalanced cohesive force directed away from the interface. Thus, for a given liquid volume, the tendency of the interface is to contract. Surface tension effects make a contribution to the total free Helmholtz energy associated with the interface. If the deformation of the interface occurs at a slow rate compared to the random motions of molecules in the bulk phases, the interfacial region can be assumed to be in a quasi-equilibrium state. It then follows that the contribution of surface tension to the Helmholtz energy depends only on the shape of the interfacial region.

The existence of a net pressure difference across the free surface of the liquid implies that the liquid must do some *expansion work* in deforming this boundary. The rate at which work is done in displacing an incremental section of the free surface, of area dA , is given by the dot product of the net pressure force acting on the liquid, $d\vec{F} = (\bar{p} - p_o)d\vec{A}$, and the local velocity vector at the surface, $(\bar{u}\vec{i} + \bar{v}\vec{j})$. This leads to the following integral expression for the total expansion work done by the liquid in

deforming the free boundary,

$$\bar{W} = \int_0^{\bar{t}} \int_0^L (\bar{p} - p_o) \dot{\bar{F}} d\bar{x} d\bar{t} \quad (3.40)$$

If the interfacial region is considered to be a part of the surroundings, rather than the liquid system, then the liquid interacts with the surroundings, and this interaction is in the form of expansion work needed in displacing the free surface. In this case, the surface energy component is equal to zero, $\bar{E}_S = 0$. However, if the interfacial region is considered to be a part of the liquid system, then, the work required in displacing the free surface against a constant pressure force, $p_o dA$, is equal to zero, $\bar{W} = 0$. In this case, the liquid becomes an *isolated system*. Furthermore, the surface energy component can not be equal to zero, $\bar{E}_S \neq 0$.

These two different and equally valid approaches suggest that the two terms, \bar{W} and \bar{E}_S , are physically related. This can be made more clear by considering an alternative system consisting solely of the interfacial region. The expansion work done by the liquid in displacing its free surface, \bar{W} , represents the net work input into the interfacial region. Since the interfacial region is treated as a material surface of zero mass, its kinetic and potential energy components are also equal to zero. Thus, any change in the total energy of this region must be due to changes in either its internal or its surface energy. The total expansion work \bar{W} can be separated into a component which represents the work done against the viscous contribution to the net pressure force, denoted by \bar{W}_v , and a component which represents the work done against the surface tension contribution, denoted by \bar{W}_s . As a result of the work done on the interfacial region, its internal energy changes by an amount, $\bar{E}_v = \bar{W}_v$, due to viscous dissipation. The remaining fraction of the work input, leads to an increase in the free Helmholtz energy of the interface, $\bar{E}_s = \bar{W}_s$, due to the surface tension effects.

Thus, the first law analysis of the liquid system leads to the following two alternative expressions for the energy conservation principle,

$$\bar{E}_k(\bar{t}) + \bar{E}_p(\bar{t}) + \bar{E}_d(\bar{t}) + \bar{E}_v(\bar{t}) + \bar{E}_s(\bar{t}) - \bar{E}_o = 0 \quad (3.41a)$$

or,

$$\bar{E}_k(\bar{t}) + \bar{E}_p(\bar{t}) + \bar{E}_d(\bar{t}) - \bar{E}_o = -\bar{W}_v(\bar{t}) - \bar{W}_s(\bar{t}) \quad (3.41b)$$

depending on whether the free surface is treated as part of the liquid system as in equation (3.41a), or, as part of the surroundings as in equation (3.41b). Regardless of

the approach, the process of deforming the free boundary of the liquid is accompanied by an energy loss due to viscous dissipation, \bar{E}_v , and by a change in the free Helmholtz energy of the surface, \bar{E}_s , due to surface tension effects. The later term, \bar{E}_s , can be viewed as a conservative mechanism through which energy can be *stored* and *released* from the interfacial region.

Integral expressions for each of the components that enter into the energy balance have been derived in terms of moving coordinates, (\bar{x}, \bar{y}) . These expressions are given in dimensionless form below, where $(\rho L^3 g)$ has been used as the per unit depth energy scale, and each of the components has been normalized with respect to the dimensionless initial energy of the system, E_o .

kinetic energy:

$$E_k = \frac{\bar{E}_k}{\rho L^3 g E_o} = \frac{1}{E_o} \int_0^1 \int_0^1 \frac{1}{2} (u^2 + v^2) F dx dy \quad (3.42a)$$

potential energy:

$$E_p = \frac{\bar{E}_p}{\rho L^3 g E_o} = \frac{1}{E_o} \left[\frac{Q^2}{24} + QV \left(X_{cg} - \frac{1}{2} \right) + V^2 \left(Y_{cg} - \frac{1}{2} \right) \right] \quad (3.42b)$$

viscous dissipation:

$$E_d = \frac{\bar{E}_d}{\rho L^3 g E_o} = \frac{1}{E_o} \frac{1}{\sqrt{Ga}} \int_{0^+}^t \int_0^1 \int_0^1 \Phi F dx dy dt \quad (3.42c)$$

surface dissipation:

$$E_v = \frac{\bar{E}_{sv}}{\rho L^3 g E_o} = \frac{1}{E_o} \frac{2}{\sqrt{Ga}} \int_{0^+}^t \int_0^1 U_{n,n} \dot{F} dx dt \quad (3.42d)$$

surface storage:

$$E_s = \frac{\bar{E}_{st}}{\rho L^3 g E_o} = \frac{1}{E_o} \frac{1}{Bo} \int_{0^+}^t \int_0^1 \kappa \dot{F} dx dt \quad (3.42e)$$

Here V represents the dimensionless volume of the liquid, and is defined by,

$$V = \frac{\bar{V}}{L^2} = \int_0^1 F dx \quad (3.43a)$$

Note that in the absence of numerical error, the calculated value of V should remain numerically equal to F_o . The dimensionless coordinates of the center of gravity of the liquid are given by:

$$X_{cg} = \frac{\bar{X}_{cg}}{L} = \frac{1}{V} \int_0^1 F x dx \quad (3.43b)$$

$$Y_{cg} = \frac{\bar{Y}_{cg}}{L F_o} = \frac{1}{2V^2} \int_0^1 F^2 dx \quad (3.43c)$$

The quantity Φ is the dissipation function. It represents the heat equivalent of the rate at which mechanical energy is lost in the process of deformation of the liquid by viscosity. In dimensionless form it is given by:

$$\Phi = 2 \left(\frac{\partial u}{\partial x} - \frac{y F_x \partial u}{F \partial y} \right)^2 + 2 \left(\frac{1}{F} \frac{\partial v}{\partial y} \right)^2 + \left(\frac{1}{F} \frac{\partial u}{\partial y} + \frac{\partial v}{\partial x} - \frac{y F_x \partial v}{F \partial y} \right)^2 \quad (3.43d)$$

Finally, the quantity $\mathcal{U}_{n,n}$ represents the dimensionless normal velocity gradient at the free surface, and is given by:

$$\mathcal{U}_{n,n} = \frac{\bar{\mathcal{U}}_{n,n}}{\sqrt{Lg}} = \frac{1}{F} \left(\frac{\partial v}{\partial y} - F_x \frac{\partial u}{\partial y} \right) - \frac{F_x}{1 + F_x^2} \left(\frac{\partial v}{\partial x} - F_x \frac{\partial u}{\partial x} \right) \quad (3.43e)$$

The steady state condition is used as the reference state for the potential energy calculation of the system. The three terms appearing inside the brackets on the right hand side of equation (3.42b), represent, from left to right, the initial potential energy of the system, the contribution due to the apparent horizontal acceleration Q , and the contribution due to the gravitational acceleration. The sum of equations (3.42d) and (3.42e) is the net change in the energy of the interfacial region due to viscous and surface tension effects.

The initial horizontal free surface position is taken as a reference state for the surface tension component, such that $E_s(0) = 0$. The initial energy available to the system, E_o , is the sum of the potential energy due to the sudden horizontal acceleration, Q , and the kinetic energy due to the impulsive velocity of the container, U_o . Using the analytical solution for the velocity field at time, $t=0^+$, and the initial value of the gap function, $F = F_o$, the initial energy can be calculated to be:

$$E_o = \frac{\bar{E}_o}{\rho L^3 g} = \frac{Q^2}{24} + \frac{4U_o^2}{\pi^3} \sum_{m=0}^{\infty} \frac{\tanh[\pi(2m+1)F_o]}{(2m+1)^3} \quad (3.43f)$$

The amount of energy available to the liquid at $t=0^+$, in the form of potential energy, is equal to $Q^2/24$. This result is independent of the amount of liquid within the container, provided that for a given value of Q , there is sufficient fluid in the container to keep the bottom wall covered at steady state. However, the initial amount of energy available to the liquid in the form of kinetic energy, shows a strong dependence on the liquid aspect ratio, F_o .

The effect of the liquid aspect ratio, F_o , on the initial energy of the system, E_o , is depicted in Figure 3.4, in terms of two curves. Both of these curves correspond to cases with values of $Q = 0$, such that initially only kinetic energy is present in the system.

In order to isolate the effects of F_o on E_o , E_o is normalized by dividing it by the square of the container velocity, U_o . This is shown in the figure by the dashed line. For a given value of U_o , E_o behaves much like the hyperbolic tangent of F_o . It increases from a zero value at $F_o = 0$, to reach asymptotically an upper limit of approximately 0.1356. For aspect ratios greater than approximately one, the effect of F_o on E_o is virtually negligible. This implies that for a given container velocity, the initial liquid kinetic energy becomes constant and independent of the volume of fluid within the container.

The solid line in the figure depicts the variation of E_o/E_o^* with respect to F_o . Here, the scale used to normalize E_o is equal to $E_o^* = F_o U_o^2 / 2$. It represents the maximum kinetic energy that the liquid can have if it were to move as a rigid body. Note the limiting behavior of E_o/E_o^* . In the limit as $F_o \rightarrow 0$, $E_o/E_o^* \rightarrow 1$, and as $F_o \rightarrow \infty$, $E_o/E_o^* \rightarrow 0$. Since the energy balance was carried out with respect to the moving coordinate frame, a kinetic energy value of zero implies that the liquid moves along with the container as a rigid body. Thus, in the upper limit as $F_o \rightarrow \infty$, the container appears as two moving semi infinite parallel plates, whereas, in the lower limit as $F_o \rightarrow 0$, the container appears as an impulsively started flat plate.

All of the components appearing in the energy balance can be determined explicitly. This provides means to analyze the sloshing motion based on the first law, but also to monitor the accuracy of the numerical solution. To accomplish this, a dimensionless error component is introduced, E_r , and is defined by the first law as:

$$E_r = (E_k + E_p + E_d + E_v + E_s) - 1 \quad (3.43g)$$

3.9 Coupling of Fluid and Vehicular Dynamics

Sloshing problems deal with the motion of liquids within some form of a *containing* structure such as vehicle. The forcing of the liquid is generally brought about by the motion of the vehicle. Therefore, it becomes a matter of practical concern to explore the dynamic interaction of the sloshing liquid with the vehicle.

Since the forcing of the liquid is determined by the motion of the vehicle, the

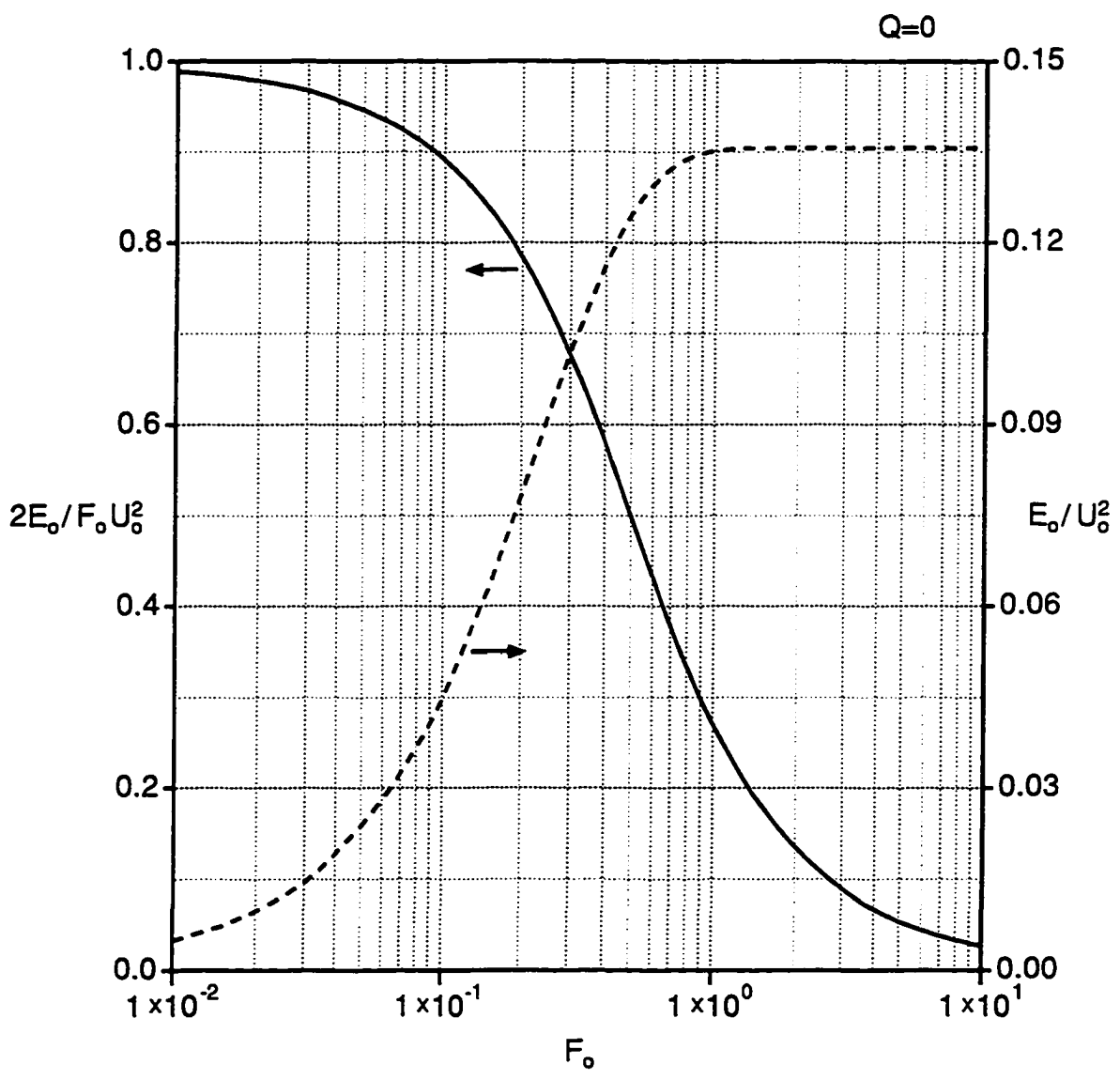


Figure 3.4: Initial Liquid Kinetic Energy

equations that govern the motion of the liquid are strongly coupled to the equations that govern the motion of the vehicle. The solution of the combined set of liquid and solid equations becomes more difficult as a result of this strong coupling. To obtain an accurate numerical solution it generally requires the use of an algorithm that provides for the implicit coupling of the solid and liquid equations. This represents an expensive approach, considering that the solution of the liquid equations is already computationally intensive, even in the absence of any interaction with the enclosing structure. The purpose of the following analysis is to examine the dynamic interaction between the liquid and the enclosing solid structure, and to develop an alternative approach to the straight forward implicit solution of the combined set of equations.

To accomplish this task, consider a very simple extension to the standard model that was presented earlier in this chapter. Let the rectangular container be considered to be a part of a moving vehicle, such as a truck. Assuming that this truck travels along a straight path, Newton's second law requires,

$$\bar{M} \frac{\partial^2 \bar{x}}{\partial t^2} = \bar{T}_1 + \bar{T}_2 \quad (3.44)$$

where, \bar{M} denotes the mass of the vehicle without the liquid. The net force exerted by the liquid on the truck is denoted by \bar{T}_2 , while all other forces acting on the vehicle are represented in terms of a net external thrust \bar{T}_1 , as shown in Figure 3.5.

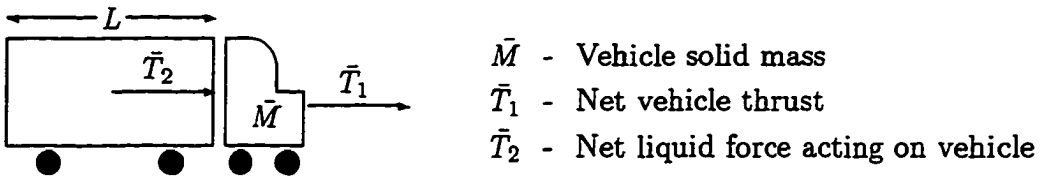


Figure 3.5: Forces on an Accelerating Vehicle

The net horizontal force exerted by the liquid on the container can be determined by considering the pressure forces along the container side walls and the shear force along the bottom container wall. These forces can be calculated in dimensionless form by,

$$T_\ell \equiv \frac{\bar{T}_\ell}{\rho L^2 g} = -F(t, 0) \int_0^1 p(t, 0, y) dy \quad \text{left wall} \quad (3.45a)$$

$$T_r \equiv \frac{\bar{T}_r}{\rho L^2 g} = F(t, 1) \int_0^1 p(t, 1, y) dy \quad \text{right wall} \quad (3.45b)$$

$$T_b \equiv \frac{\bar{T}_b}{\rho L^2 g} = \frac{1}{\sqrt{Ga}} \int_0^1 \frac{1}{F} \frac{\partial u}{\partial y} \Big|_{y=0} dx \quad \text{bottom wall} \quad (3.45c)$$

where the net liquid force is given by, $T_2 = T_\ell + T_r + T_b$.

In order to remain consistent with the notation used earlier in this study, let the instantaneous dimensionless horizontal acceleration of the vehicle to be denoted by Q ,

$$Q(t) \equiv \frac{q(\bar{t})}{g} = \frac{1}{g} \frac{d^2 \bar{x}}{d \bar{t}^2} \quad (3.46)$$

As a result of the acceleration of the container with respect to the inertial coordinate frame, the liquid experiences an apparent body force equal to $-Q(t)$. Equation (3.44) can be rewritten in terms of Q as,

$$M Q(t) = T_1(t) + T_2(t) \quad (3.47)$$

For the simple model considered here, equation (3.47) provides the necessary coupling between the dynamics of the liquid and those of the vehicle. It can be solved for the acceleration, $Q(t)$, and along with the governing equations for the liquid it provides the necessary closure to the problem. However, the numerical solution of equation (3.47) requires the use of an implicit algorithm. If this equation is coupled explicitly to the liquid equations, then the solution exhibits oscillations, and for cases that the solid mass of the vehicle is small compared to that of the liquid, $M \ll F_o$, the solution diverges.

An alternative form of equation (3.47) can be developed by examining the interaction between the liquid and the vehicle more closely. The magnitude of the horizontal liquid force, T_2 , is a function of all of the dependent variables of the problem, (u, v, p, F) , as well as the horizontal vehicle acceleration, Q . Consider how the liquid responds to a sudden change in the motion of the vehicle. Let the external thrust acting on the vehicle undergo a sudden change at some time, t , such that $T_1(t^+) = T_1(t^-) + \Delta T_1$. Also let the solution of the problem be known at time t^- , just prior to the sudden change in the external thrust, and let it be denoted by (u^-, v^-, p^-, F^-) and Q^- . Let Q^+ denote the unknown acceleration of the vehicle at t^+ , immediately following the sudden change in T_1 . Given that the change in the external thrust of the vehicle occurs

suddenly, $(t^+ - t^-) \rightarrow 0$, neither the velocity field, (u^+, v^+) , or the position of the free surface, F^+ , change by t^+ . Thus,

$$(u^+, v^+, F^+) = (u^-, v^-, F^-) \quad (3.48)$$

However, since the acceleration of the vehicle, Q^+ , is different than Q^- , and hence the liquid experiences a different apparent horizontal body force at t^+ , the pressure field will also be different at t^+ . The new pressure field, p^+ , can be evaluated using superposition. The pressure variable can be separated into two components, with one component, \hat{p} , accounting solely for the pressure contribution due to the apparent body force, $Q(t)$, and another component, \check{p} , accounting for all remaining contributions from inertial, viscous, gravitational, and surface tension effects. The pressure component, \hat{p} , can be determined from the solution of the following elliptic equation,

$$(\nabla^2 - \mathcal{N}) \hat{\mathcal{P}} = 0 \quad (3.49a)$$

subject to boundary conditions,

$$\frac{\partial \hat{\mathcal{P}}}{\partial x} - \frac{yF_x}{F} \frac{\partial \hat{\mathcal{P}}}{\partial y} = -1 \quad \text{along } x = 0 \quad \text{and} \quad x = 1 \quad (3.49b)$$

$$\frac{\partial \hat{\mathcal{P}}}{\partial y} = 0 \quad \text{along } y = 0 \quad \text{and,} \quad \hat{\mathcal{P}} = 0 \quad \text{along } y = 1 \quad (3.49c)$$

where,

$$\hat{\mathcal{P}} \equiv \frac{\hat{p}}{Q} \quad (3.49d)$$

Note that equation (3.49) in terms of the redefined variable $\hat{\mathcal{P}}$ becomes independent of Q . The pressure field \hat{p} is simply proportional to the magnitude of the apparent body force, Q . The pressure field within the container at any time t , is given by the superposition of,

$$p(t, x, y) = Q(t) \hat{\mathcal{P}}(t, x, y) + \check{p}(t, x, y) \quad (3.50)$$

An equation for \check{p} can be developed such that its superposition with equation (3.49) will lead to the full pressure Poisson equation (3.27c), subject to boundary conditions (3.29b, d, g), which is used for the solution of the pressure variable, p . However, this is unnecessary since both p and $\hat{\mathcal{P}}$ will generally be calculated as part of the solution, and equation (3.50) can then be solved for \check{p} .

The net horizontal force exerted by the liquid on the vehicle, T_2 , can also be separated into two corresponding components,

$$T_2 = \hat{T}_2 + \check{T}_2 \quad (3.51a)$$

where,

$$\hat{T}_2 = [T_\ell(\hat{\mathcal{P}}) + T_r(\hat{\mathcal{P}})] Q \quad (3.51b)$$

$$\check{T}_2 = T_\ell(\check{p}) + T_r(\check{p}) + T_b(u) \quad (3.51c)$$

Here, T_ℓ , T_r , and T_b represent the integral expressions defined in equation (3.45). The shear force along the bottom wall is taken to be part of \check{T}_2 . Equation (3.51b) can be rewritten in the following form,

$$\hat{T}_2 = -\mathcal{M}_a Q \quad (3.52)$$

The *apparent mass* of the liquid, \mathcal{M}_a , is a function of only $F(t, x)$. Therefore, \mathcal{M}_a represents a *geometrical factor* which depends solely on the configuration of the liquid within the container.

The pressure field, p^+ , immediately following the sudden change in T_1 can be determined from equation (3.50) according to,

$$p^+ = \hat{\mathcal{P}}^+ Q^+ + \check{p}^+ \quad (3.53a)$$

However, since $\hat{\mathcal{P}}$ depends solely on F , and \check{p} on (u, v, F) , then based on equation (3.48) they do not change by t^+ . The pressure field at t^+ can be rewritten as,

$$p^+ = \hat{\mathcal{P}}^- Q^+ + \check{p}^- \quad (3.53b)$$

It also follows from equation (3.50) that $p^- = \hat{\mathcal{P}}^- Q^- + \check{p}^-$. Solving for \check{p}^- and substituting into equation (3.53b) leads to,

$$p^+ = p^- + \hat{\mathcal{P}}^- (Q^+ - Q^-) \quad (3.53c)$$

Thus, a sudden change in the apparent body force, $(Q^+ - Q^-)$, causes an equally sudden change in the pressure field. The corresponding change in the liquid force, T_2 can also be determined in terms of the apparent mass, \mathcal{M}_a . The horizontal liquid force T_2^+ can be written based on equation (3.51) as,

$$T_2^+ = \check{T}_2^+ - \mathcal{M}_a^+ Q^+ \quad (3.54a)$$

It follows from equation (3.48), and with $\check{p}^+ = \check{p}^-$, that $\mathcal{M}_a^+ = \mathcal{M}_a^-$, and also, $\check{T}_2^+ = \check{T}_2^-$. Furthermore, $\check{T}_2^- = T_2^- + \mathcal{M}_a^- Q^-$, which leads to,

$$T_2^+ = T_2^- - \mathcal{M}_a^- (Q^+ - Q^-) \quad (3.54b)$$

The acceleration of the vehicle, Q^+ , immediately following the sudden change in T_1 , can be written in terms of equation (3.47) as,

$$MQ^+ = T_1^+ + T_2^+$$

Substituting the expression for T_2^+ given in equation (3.54), and rearranging leads to the following expression for Q^+ ,

$$(M + \mathcal{M}_a^-) Q^+ = T_1^+ + T_2^- + \mathcal{M}_a^- Q^- \quad (3.55)$$

Equation (3.55) been developed by considering how the liquid reacts to a sudden change in the acceleration of the vehicle, Q . Assuming that the dimensionless variables $(u, v, p, F, Q) \sim \mathcal{O}(1)$, it can be shown using order of magnitude analysis that a change of $\mathcal{O}(\Delta Q)$ in the vehicle acceleration at time, t , causes an immediate pressure change of $\mathcal{O}(\Delta \check{p}) \sim \mathcal{O}(\Delta Q)$ due to the elliptic readjustment of the pressure field. It is followed by a more gradual adjustment of $\Delta \check{p} \sim \mathcal{O}(\Delta Q \cdot \Delta t)$ as inertial, gravitational, viscous, and surface tension effects contribute more slowly to the pressure field.

Equation (3.55) represents an alternative to the description of Newton's second law as given in equation (3.47). A numerical algorithm for the solution of the problem can be constructed based on either one of these two equations. During the course of a numerical solution, Newton's law will be used to provided an updated value for Q^{k+1} , based on set of input, or known, parameters at level k . This can be done according to either equation (3.47),

$$Q^{k+1} = \left(\frac{T_1 + T_2}{M} \right)^k \quad (3.56)$$

or equation (3.55),

$$Q^{k+1} = \left(\frac{T_1 + T_2 + \mathcal{M}_a Q}{M + \mathcal{M}_a} \right)^k \quad (3.57)$$

where, for an implicitly coupled scheme, k represents the iteration level at a given (constant) time level, and for an explicitly coupled scheme, k represents a discrete time level.

The interaction between the liquid and the vehicle is partly built into equation (3.57) in terms of the apparent mass, \mathcal{M}_a . It gives it with the ability to anticipate the inevitable and instantaneous change in the magnitude of the liquid force component, \hat{T}_2 , which occurs in response to any change in the acceleration of the vehicle, Q . The lack of this property from equation (3.56) causes it to underestimate the liquid force at level k , and thus, to overestimate the value of Q^{k+1} . With an overestimated Q^{k+1} , T_2^{k+1} becomes unrealistically high, leading to an overcorrection at the next level for Q^{k+2} . Numerical solutions based on equation (3.56) exhibit oscillations in the calculated values of Q . When the equations are solved implicitly, this behavior can be eliminated by underrelaxing the value of Q predicted by equation (3.56). However, if the equations are solved explicitly, this behavior can not be corrected and leads to the accumulation of error in the solution. The magnitude of these oscillations increases as the solid mass of the vehicle becomes smaller compared to that of the liquid, and as $M/F_o \rightarrow 0$ the explicit solution based on equation (3.56) diverges.

A numerical algorithm based on equation (3.57) does not suffer from this behavior. For an implicit scheme, the algorithm based on \mathcal{M}_a provides for much faster convergence rates. Note that as the iterations converge, $Q^{k+1} \rightarrow Q^k$, and equation (3.57) reduces to the same form as equation (3.56). But more important, an explicit algorithm can be constructed in terms of equation (3.57) which is not only stable but also significantly faster than the implicit one. Changes in the vehicle acceleration cause immediate changes in the liquid force component \hat{T}_2 as a result of the liquid incompressibility assumption. The change in \hat{T}_2 is incorporated into the calculation of Q at the same time level. Effects of order $\mathcal{O}(\Delta t)$, arising from the subsequent adjustment of the flowfield, in terms of \tilde{T}_2 , are incorporated into the calculation of Q at the next time level.

The initial horizontal force exerted by the liquid on the container at time $t = 0^+$, for a case with $U_o = 0$, can be determined from the initial condition for pressure, p^+ , given by equation (3.33). Since at $t = 0^+$, the liquid is still in a motionless state, $(u^+, v^+) = 0$, and the free surface is still at its initial horizontal position, $F^+ = F_o$, the pressure p^+ , differs from \hat{p}^+ only by a hydrostatic contribution due to gravity, $\check{p}^+ = (1 - y)F_o$. Substituting \hat{p}^+ into equations (3.45) the force component \hat{T}_2^+ can be calculated and used to obtain the following result for the initial value of the apparent

mass of the liquid, \mathcal{M}_a^+ :

$$\mathcal{M}_a^+ \equiv \mathcal{M}_a(0^+) = F_o - \frac{8}{\pi^3} \sum_{m=1}^{m=\infty} \frac{\tanh[(2m+1)\pi F_o]}{(2m+1)^3} \quad (3.58)$$

The dependence of the apparent liquid mass, \mathcal{M}_a^+ , on the initial liquid aspect ratio, F_o , is shown in Figure 3.6. Using residue theory to evaluate the summation in equation (3.58), the limiting behavior of \mathcal{M}_a^+ with respect to F_o can be shown to be equal to,

$$\lim_{F_o \rightarrow 0} \frac{\mathcal{M}_a^+}{F_o} = 0 \quad \text{and} \quad \lim_{F_o \rightarrow \infty} \frac{\mathcal{M}_a^+}{F_o} = 1$$

Thus, as $F_o \rightarrow 0$, the container approaches the flat plate approximation, with the liquid offering no resistance. The resulting acceleration is determined solely by the mass of the container, M . In the opposite limit, $F_o \rightarrow \infty$, the fluid behaves as a rigid body. The apparent mass at steady state is determined by the final position of the free surface.

If a constant force T_1 is applied to the vehicle, such that it would result in a constant vehicle acceleration equal to Q_∞ at steady state, where the liquid moves as a rigid body of mass F_o , then the magnitude of this force is given by $T_1 = (M + F_o)Q_\infty$. The initial acceleration of the vehicle can be determined from equation (3.55), by noting that Q^- and T_2^- , which correspond to the hydrostatic equilibrium state of the liquid at $t = 0^-$, are equal to zero. This leads to the following result for the initial acceleration of the vehicle,

$$Q(0^+) = \left(\frac{M + F_o}{M + \mathcal{M}_a^+} \right) Q(\infty) \quad (3.59)$$

Note that if the mass of the vehicle is much greater than that of the liquid, $M \gg F_o$, then the effect of the liquid is negligible, and $Q(0^+) \approx Q_\infty$. On the other hand, if $M \ll F_o$, the initial vehicle acceleration is greater than Q_∞ , and $Q(0^+) \approx Q_\infty/\mathcal{M}_a$. For a half filled container, $F_o = 0.5$, this turns out to be about twice the final acceleration, $Q(0^+) \approx 2Q_\infty$.

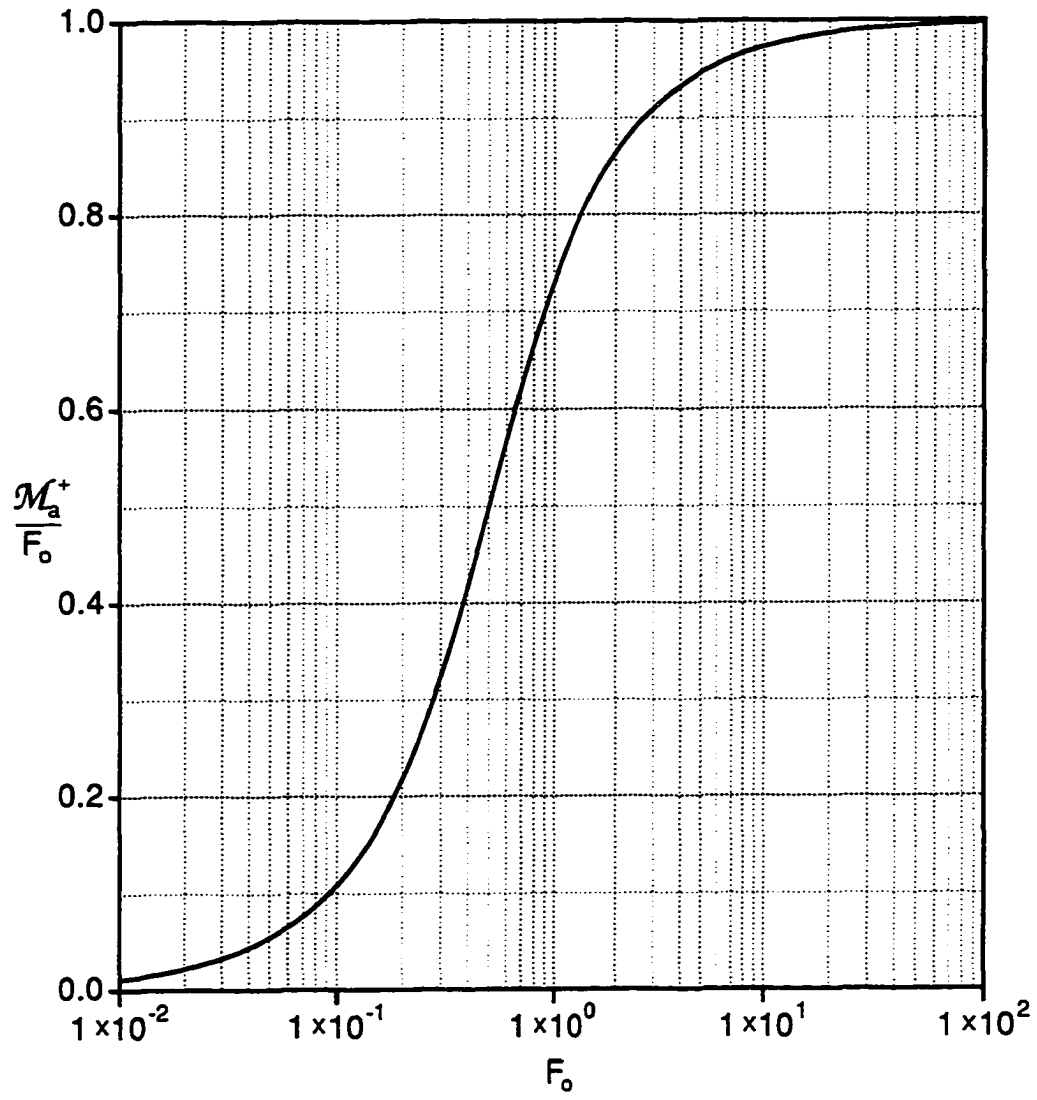


Figure 3.6: Apparent Liquid Mass at $t = 0^+$

4. NUMERICAL METHOD

The equations governing the motion of an incompressible viscous fluid within a moving rectangular container have been formulated in the previous chapter. Equations (3.27a-e), boundary conditions (3.29a-g), and initial conditions (3.30a-g, 3.31a-d) provide a complete description of the motion of the liquid from the moment the container begins to move. However, at the present time, the determination of a general analytical solution for this problem is an intractable task. Consequently, a numerical method based on finite differences is used to solve the problem. In this numerical approach, each of the derivatives in the governing equations is replaced by an approximate finite difference expression at selected points in the physical problem domain. Collectively, these points define the computational grid. Thus, the solution of the problem is obtained by solving the resulting system of simultaneous non-linear algebraic equations.

In this primitive variable approach, the governing equations are discretized on a variable increment, non-staggered grid using second order accurate implicit differencing. The momentum and kinematic condition equations are solved for the dependent variables, u , v , and F . A Poisson equation is solved for the pressure variable, p , using an iterative pressure updating scheme which implicitly satisfies the continuity equation. One of the advantages of the physical model developed here is its relative geometrical simplicity. This allows for an in depth investigation of the physics of liquid sloshing in moving containers, as well as the study of the numerical techniques that are used to approximate them. First, the accuracy of the time discretization is investigated through the use of both a first and a second order accurate time differencing. Due to the periodic nature of the liquid flow, the time truncation error needs to be carefully monitored for accurate long term solutions. Second, the effects of an explicit rather than implicit calculation for the free surface position are also investigated. As more complex geometries are considered, the use of an adaptive grid requiring the solution of extra grid equations becomes likely. In such a case, the explicit solution

of the kinematic equation significantly reduces the overall computational effort as the grid equations are solved only once per time step. Third, the approximation of the free surface position at the contact line is investigated. The lack of a physical model for the description of the flow in the vicinity of a contact points necessitates the use of approximations. The effectiveness of these approximations and their overall effect on the dynamics of the problem will be considered. Finally, several variations in the algorithm used for the solution of the equations will also be considered.

4.1 Grid Generation

The finite difference expressions used to approximate the derivative terms in the governing equations are derived from Taylor series expansions about the grid points. The accuracy of these finite difference approximations depends on the spacing between the grid points. When large gradients are present, it is essential that this spacing is kept sufficiently small to ensure a good approximation. However, the total number of grid points that can be used is limited by the computational effort that is required to solve the resulting system of equations. Consequently, the use of a variable increment grid provides means for minimizing the total number of grid points used, and yet maintaining a desired degree of accuracy by clustering grid points where large gradients are expected to exist.

An algebraic stretching transformation, based on a family of grid stretching transformations proposed by Roberts (see [67]), is used to determine the grid point distribution. This transformation, which maps the normalized (x, y) space onto a uniform, unit spaced (ξ, η) space, is given by:

$$x(\xi) = \frac{(\beta_1 + 1)(\beta_1^*)^{\frac{2\xi}{NX-1}-1} - (\beta_1 - 1)}{2 \left[1 + (\beta_1^*)^{\frac{2\xi}{NX-1}-1} \right]} \quad 0 \leq \xi \leq NX - 1 \quad (4.1a)$$

$$y(\eta) = \frac{(\beta_2 + 1)(\beta_2^*)^{\frac{2\eta}{NY-1}-1} - (\beta_2 - 1)}{2 \left[1 + (\beta_2^*)^{\frac{2\eta}{NY-1}-1} \right]} \quad 0 \leq \eta \leq NY - 1 \quad (4.1b)$$

where

$$\beta_1^* = \frac{\beta_1 + 1}{\beta_1 - 1} \quad \text{and} \quad \beta_2^* = \frac{\beta_2 + 1}{\beta_2 - 1}$$

Here, the parameters NX and NY represent the total number of grid points in the x and y directions respectively. The parameters β_1 and β_2 control the clustering of

the grid points. For very large values of β , $\lim \beta \rightarrow \infty$, the grid becomes uniformly spaced in (x, y) space. As the value of β decreases towards unity the grid lines become increasingly clustered about $x=0$ and $x=1$.

A typical grid, with $\beta_1 = 1.1$ and $\beta_2 = 1.1$, used for the solution of the problem is shown in Figure 4.1. The distribution of the grid points in the physical, (\bar{x}, \bar{y}) , and normalized (x, y) , spaces are shown in Figures 4.1(a) and 4.1(b) respectively. With decreasing liquid viscosity (Ga increasing), frictional effects become more distinctly confined in boundary layers that form along the container walls. To resolve the large velocity gradients associated with these layers the grid lines are clustered near the walls. The grid is also clustered near the free surface. This is done to resolve frictional effects associated with the formation of a viscous layer along the free surface. Furthermore, the strongest fluid motion typically occurs near the free surface.

The grid is also shown in Figure 4.1(c) in terms of (ξ, η) coordinates. In order to simplify the resulting finite difference equations, the transformation defined by equation (4.1) has been set up to map the grid onto (ξ, η) space, such that the spacing between adjacent grid points is not only uniform but also equal to unity. Thus, the resulting computational domain is a rectangle, the size of which is determined by the number of grid points used in the ξ and η directions.

4.2 Transformation of Equations onto (ξ, η) Space

The governing equations are transformed from (x, y) space onto (ξ, η) space using the chain-rule. This involves replacing the derivative terms in these equations with the following expressions in terms of the (ξ, η) coordinates:

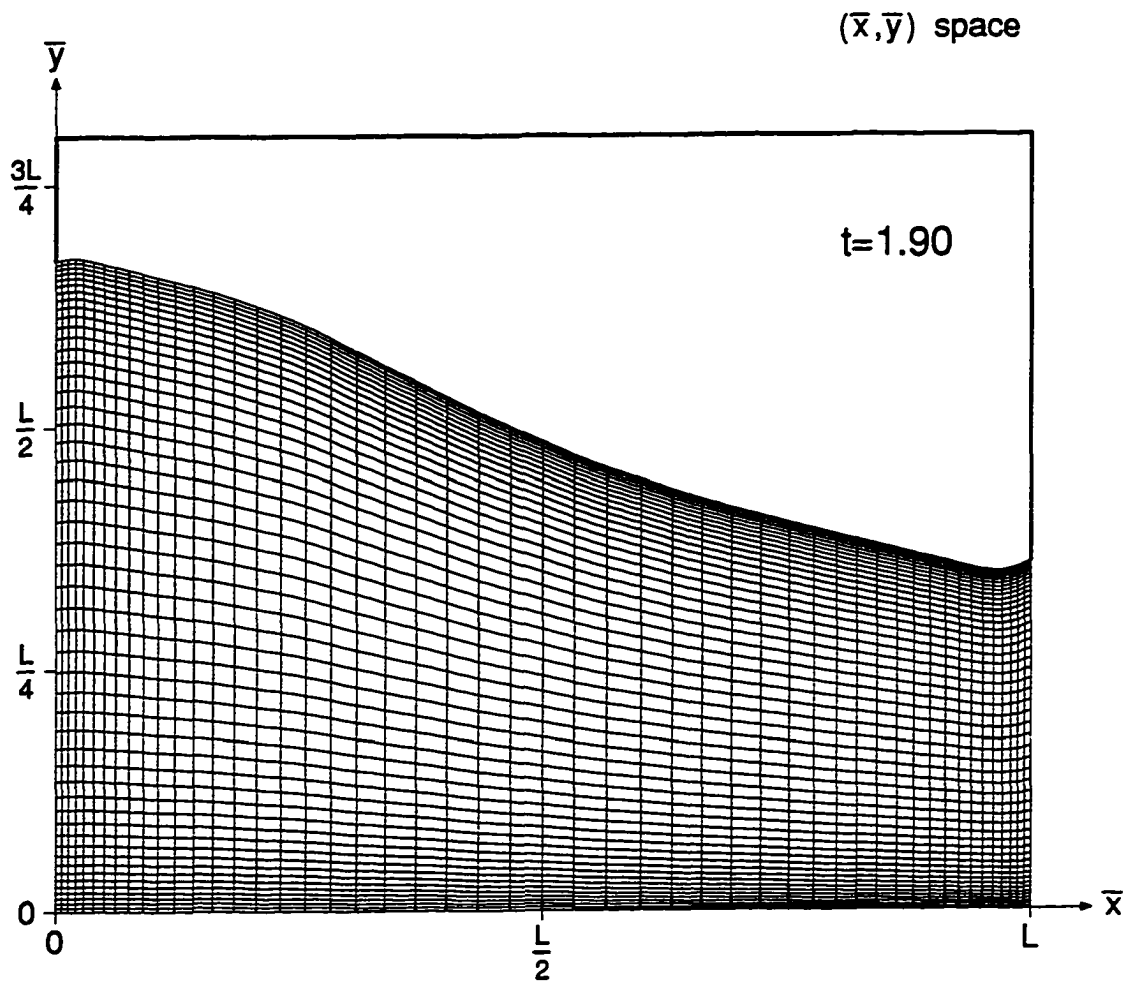
$$\frac{\partial}{\partial x} = \xi_x \frac{\partial}{\partial \xi} \quad (4.2a)$$

$$\frac{\partial}{\partial y} = \eta_y \frac{\partial}{\partial \eta} \quad (4.2b)$$

$$\frac{\partial^2}{\partial x^2} = \xi_x^2 \frac{\partial^2}{\partial \xi^2} + \xi_{xx} \frac{\partial}{\partial \xi} \quad (4.2c)$$

$$\frac{\partial^2}{\partial y^2} = \eta_y^2 \frac{\partial^2}{\partial \eta^2} + \eta_{yy} \frac{\partial}{\partial \eta} \quad (4.2d)$$

(a)



$NX=51$
 $NY=51$
 $\beta_1=1.100$
 $\beta_2=1.100$

$F_o=0.5$
 $Q=0.2$
 $U_o=0.0$
 $Ga=10^6$
 $Bo=\infty$

Figure 4.1: Grid Generation

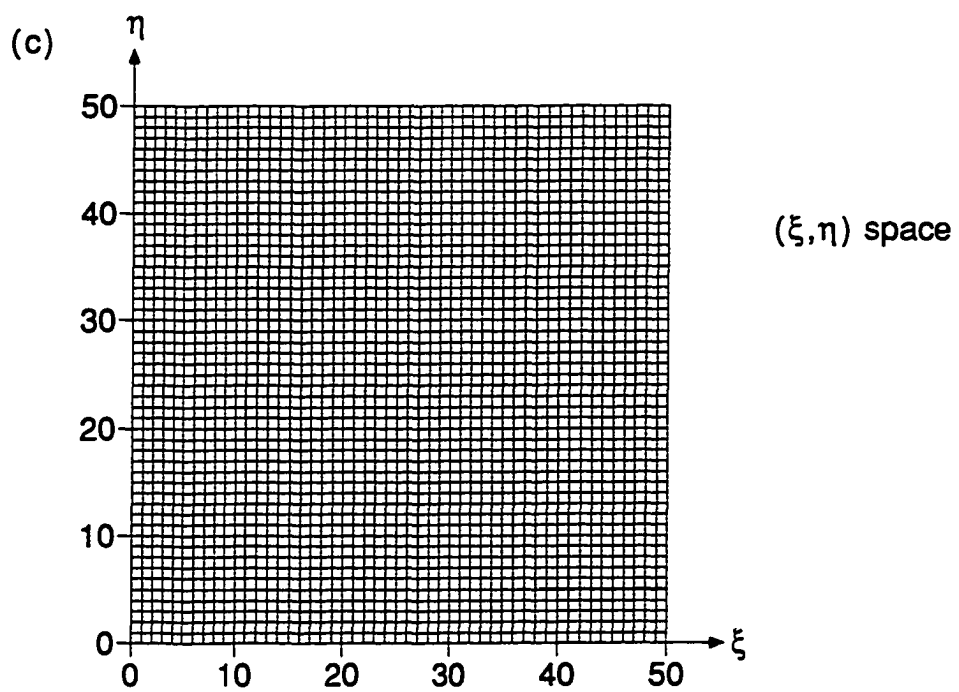
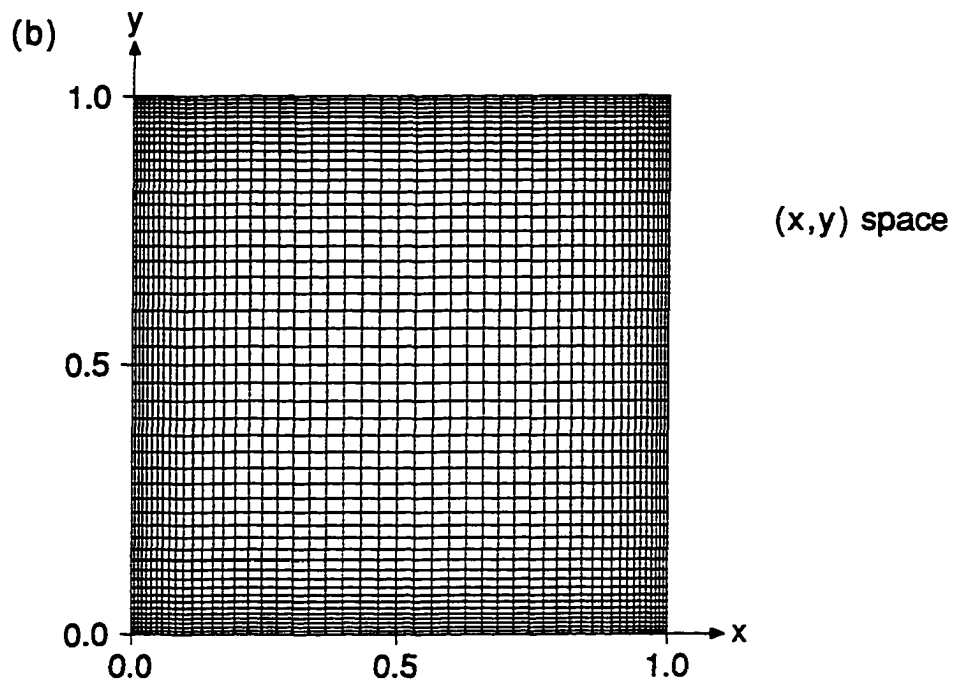


Figure 4.1 (Continued)

where the ξ_x , η_y , ξ_{xx} , and η_{yy} , represent the transformation metrics and are defined by,

$$\xi_x = \frac{\partial \xi}{\partial x}, \quad \xi_{xx} = \frac{\partial^2 \xi}{\partial x^2}, \quad \eta_y = \frac{\partial \eta}{\partial y}, \quad \text{and} \quad \eta_{yy} = \frac{\partial^2 \eta}{\partial y^2} \quad (4.3)$$

The transformation metrics can be evaluated analytically by inverting the transformation defined in equation (4.1) to obtain expressions for $\xi(x)$ and $\eta(y)$ which are then differentiated to yield:

$$\xi_x = \frac{2 \beta_1 (NX - 1)}{[\beta_1^2 - (2x - 1)^2] \ln(\beta_1^*)} \quad (4.4a)$$

$$\xi_{xx} = \frac{4(2x - 1)\xi_x}{\beta_1^2 - (2x - 1)^2} \quad (4.4b)$$

$$\eta_y = \frac{2 \beta_2 (NY - 1)}{[\beta_2^2 - (2y - 1)^2] \ln(\beta_2^*)} \quad (4.4c)$$

$$\eta_{yy} = \frac{4(2y - 1)\eta_y}{\beta_2^2 - (2y - 1)^2} \quad (4.4d)$$

Alternatively, the metrics can be evaluated numerically in a matter that is consistent with the differencing used in the governing equations. However, based on numerical experimentation, it was determined that the analytic evaluation of the metrics, using equations (4.4a-d), yields the most accurate results when used in conjunction with centered differences in the governing equations. Thus, in transforming the equations, only derivatives that were subsequently approximated by centered difference equations were converted onto (ξ, η) space. Along the domain boundaries, it was determined that the best representation of normal derivatives was obtained by using variable increment one-sided differences in terms of (x, y) coordinates.

4.2.1 Discretization of the Momentum Equations

Using the chain-rule expressions defined in (4.2), the two momentum equations, (3.27a, b), are transformed onto (ξ, η) space and arranged in the following non conservative form, suitable for discretization:

$$\frac{\partial u}{\partial t} = C_\xi \frac{\partial u}{\partial \xi} + C_\eta \frac{\partial u}{\partial \eta} + C_{\xi\xi} \frac{\partial^2 u}{\partial \xi^2} + C_{\eta\eta} \frac{\partial^2 u}{\partial \eta^2} + C_{\xi\eta} \frac{\partial^2 u}{\partial \xi \partial \eta} + S_u \quad (4.5a)$$

$$\frac{\partial v}{\partial t} = C_\xi \frac{\partial v}{\partial \xi} + C_\eta \frac{\partial v}{\partial \eta} + C_{\xi\xi} \frac{\partial^2 v}{\partial \xi^2} + C_{\eta\eta} \frac{\partial^2 v}{\partial \eta^2} + C_{\xi\eta} \frac{\partial^2 v}{\partial \xi \partial \eta} + S_v \quad (4.5b)$$

where

$$C_\xi = -u + \frac{\xi_{xx}}{\sqrt{Ga}} \quad (4.5c)$$

$$C_\eta = -\frac{1}{F} (v - y\xi_x F_\xi u - y\dot{F}) + \frac{y\eta_y}{\sqrt{Ga}} \left(\frac{2\xi_x^2 F_\xi^2}{F^2} - \frac{\xi_x^2 F_{\xi\xi} + \xi_{xx} F_\xi}{F} \right) + \frac{1}{\sqrt{Ga}} \frac{\eta_{yy}}{F^2} [1 + (y\xi_x F_\xi)^2] \quad (4.5d)$$

$$C_{\xi\xi} = \frac{\xi_x^2}{\sqrt{Ga}} \quad (4.5e)$$

$$C_{\eta\eta} = \frac{1}{\sqrt{Ga}} \frac{\eta_y^2}{F^2} [1 + (y\xi_x F_\xi)^2] \quad (4.5f)$$

$$C_{\xi\eta} = -\frac{1}{\sqrt{Ga}} \frac{y\eta_y \xi_x^2 F_\xi}{F} \quad (4.5g)$$

and

$$S_u = -\xi_x \left(\frac{\partial p}{\partial \xi} - \frac{y\eta_y F_\xi}{F} \frac{\partial p}{\partial \eta} \right) - Q \quad (4.5h)$$

$$S_v = -\frac{\eta_y}{F} \frac{\partial p}{\partial \eta} - 1 \quad (4.5i)$$

The momentum equations are discretized using second order accurate centered differences to approximate the spatial derivatives. The temporal derivatives are approximated using either a first or a second order accurate one sided differences. Thus, based on the time differencing, two algorithms emerge which will be subsequently referred to as the *first order* and the *second order* methods. Southwell's notation is used for the immediate neighborhood of a typical node (see Figure 4.2). The horizontal increments in front and behind the typical node are denoted by h_f and h_b respectively. The vertical increments in front (top) and behind (below) the typical node are denoted by k_f and k_b respectively. Note that these increments are measured in terms of the (x, y) coordinates. In (ξ, η) space increments between adjacent nodes are equal to unity. Thus, the traditional centered differences, and the temporal differencing used in the discretization scheme become:

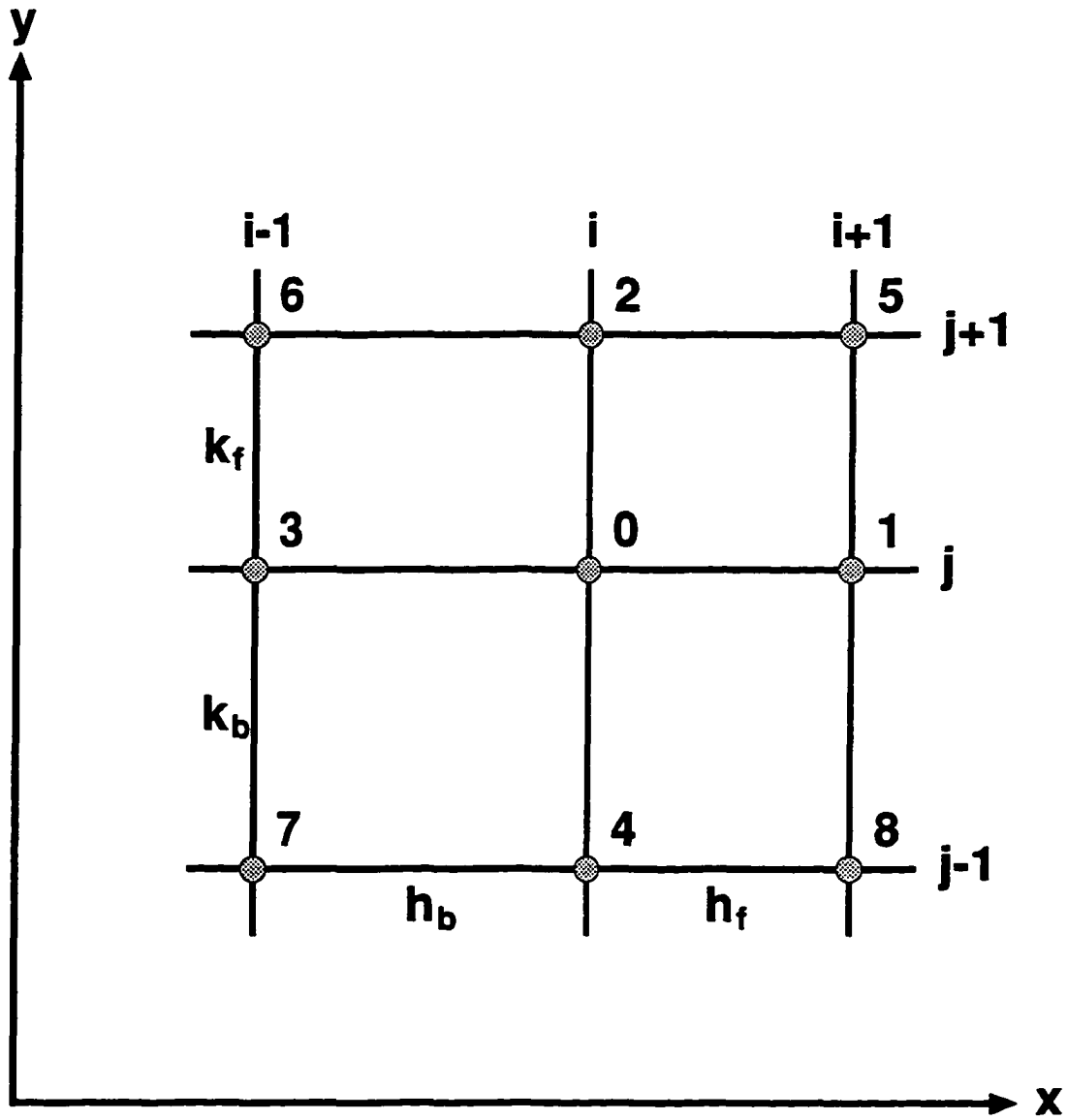


Figure 4.2: Grid Star Definition

$$\left. \frac{\partial U}{\partial \xi} \right|_0 = \frac{1}{2} (U_1 - U_3) \quad (4.6a)$$

$$\left. \frac{\partial^2 U}{\partial \xi^2} \right|_0 = U_1 - 2U_0 + U_3 \quad (4.6b)$$

$$\left. \frac{\partial U}{\partial t} \right|_0^n = \frac{1}{\Delta t} \left[\left(1 + \frac{\alpha}{2}\right) U_0^n - (1 + \alpha) U_0^{n-1} + \frac{\alpha}{2} U_0^{n-2} \right] \quad (4.6c)$$

where

$$\alpha = \begin{cases} 0 & \text{first order method} \\ 1 & \text{second order method} \end{cases}$$

Here, superscript n is used to denote the time level, and Δt the time increment such that, $t = n \Delta t$. Similar expressions for centered differences in the η direction are used.

To enhance the stability of the method by improving the diagonal dominance of the coefficient matrix, the convective terms are split into a first order upwind difference term plus a second order correction term [66]. Thus, a typical convective term is differenced according to:

$$\begin{aligned} C_\xi \left. \frac{\partial u}{\partial \xi} \right|_0^{n+1, m+1} &= \left[C_\xi^+ (u_1 - u_0) + C_\xi^- (u_3 - u_0) \right]^{n+1, m+1} \\ &\quad - \frac{1}{2} (C_\xi^+ + C_\xi^-) [u_1 - 2u_0 + u_3]^{n+1, m} \end{aligned} \quad (4.7a)$$

where

$$C_\xi^+ = \frac{|C_\xi| + C_\xi}{2} \quad \text{and,} \quad C_\xi^- = \frac{|C_\xi| - C_\xi}{2} \quad (4.7b)$$

Here, superscript m is used to denote the iteration level for the SOR or SLOR method. The upwind term is evaluated using current information at the $m + 1$ level, while the second order correction term is evaluated using information from the previous iteration level, m .

Using the finite difference equations defined in (4.6a-c) and the convective term differencing described in (4.7) the momentum equations (4.5a,b) take the following form for $\Phi = (u, v)$:

$$\begin{aligned} C_0 \Phi_0^{n+1} &= \left(\frac{1 + \alpha}{\Delta t} \right) \Phi_0^n - \left(\frac{\alpha}{2 \Delta t} \right) \Phi_0^{n-1} + C_1 \Phi_1^{n+1} + C_2 \Phi_2^{n+1} + \\ &\quad C_3 \Phi_3^{n+1} + C_4 \Phi_4^{n+1} + \mathcal{X}_\Phi^{n+1, m} + \mathcal{E}_\Phi^{n+1, m} + S_\Phi^{n+1, k+1} \end{aligned} \quad (4.8a)$$

where

$$C_0 = \left(\frac{2 + \alpha}{2 \Delta t} \right) + C_\xi^+ + C_\xi^- + C_\eta^+ + C_\eta^- + 2C_{\xi\xi} + 2C_{\eta\eta} \quad (4.8b)$$

$$C_1 = C_\xi^+ + C_{\xi\xi} \quad (4.8c)$$

$$C_2 = C_\eta^+ + C_{\eta\eta} \quad (4.8d)$$

$$C_3 = C_\xi^- + C_{\xi\xi} \quad (4.8e)$$

$$C_4 = C_\eta^- + C_{\eta\eta} \quad (4.8f)$$

$$\mathcal{X}_\Phi^{n+1,m} = -\frac{1}{4} C_{\xi\eta} (\Phi_5 + \Phi_7 - \Phi_6 - \Phi_8)^{n+1,m} \quad (4.8g)$$

$$\begin{aligned} \mathcal{E}_\Phi^{n+1,m} = & -\frac{1}{2} (C_\xi^+ + C_\xi^-) [\Phi_1 - 2\Phi_0 + \Phi_3]^{n+1,m} \\ & -\frac{1}{2} (C_\eta^+ + C_\eta^-) [\Phi_2 - 2\Phi_0 + \Phi_4]^{n+1,m} \end{aligned} \quad (4.8h)$$

$$S_u^{n+1,k+1} = -\frac{\xi_x}{2} (P_1 - P_3)^{n+1,k+1} + \frac{y\xi_x\eta_y F_\xi}{2F} (P_2 - P_4)^{n+1,k+1} - Q \quad (4.8i)$$

$$S_v^{n+1,k+1} = -\frac{\eta_y}{2F} (P_2 - P_4)^{n+1,k+1} - 1 \quad (4.8j)$$

Here, superscript k is used to denote the update level of the pressure solution. A pressure update level k indicates that the pressure field has been corrected (updated) k times for the given time step. The pressure gradients appearing in the source terms, S_Φ , are evaluated using the most currently available pressure values at update level $k + 1$. In addition to the second order correction terms, \mathcal{E}_Φ , the cross derivative term, \mathcal{X}_Φ , is also evaluated at the previous iteration level m .

4.2.2 Setup of the Pressure Correction Scheme

The solution of the incompressible Navier-Stokes equations in terms of primitive variables is hindered by the absence of an equation for the direct calculation of one the dependent variables of the problem, namely the pressure, p . Using information on the velocity field, which is overspecified in terms of both the momentum and the continuity equations, an equation that can be used for the calculation of the pressure must be derived.

Generally, one of two approaches is used in developing a pressure equation. In the Artificial Compressibility Method (ACM), a pressure equation is obtained by introducing a pseudo equation of state for the fluid. When used in conjunction with an unsteady form of the continuity equation this approach leads to a simple parabolic equation for the pressure of the form,

$$\frac{\partial p}{\partial t} + cD = 0 \quad (4.9)$$

where c represents constant parameters arising from the specific form of the utilized equation of state. This equation can be used as the starting point for the development of a numerical scheme for the solution of the governing equations. However, in its present form this equation is physically implausible because it suggests a parabolic behavior for the pressure field which is inconsistent with the incompressibility assumption.

The alternative approach is the use of a Pressure Poisson Method (PPM). The PPM, as its name implies, relies on a Pressure Poisson Equation (PPE) for the calculation of the pressure field. The pressure equation which is derived from the momentum equations utilizes principles already embodied in the governing equations. Thus, it provides a more fundamental starting point in the development of a numerical algorithm for the solution of the incompressible equations. A Poisson equation for the pressure has been derived in the previous chapter (see equation 3.27c) and is rewritten here in the following form:

$$\left(\nabla^2 - \mathcal{N}\right) p = \frac{2}{F} J(u, v) - \frac{\partial D}{\partial t} - T_s \quad (4.10a)$$

where,

$$T_s = u \frac{\partial D}{\partial x} + \frac{1}{F} \left(v - yF_x u - y\dot{F} \right) \frac{\partial D}{\partial y} + D^2 - \frac{1}{\sqrt{Ga}} \left(\nabla^2 - \mathcal{N} \right) D \quad (4.10b)$$

The left hand side of the above equation represents the elliptic operator transformed in (x, y) space. The right hand side of the equation consists of three terms which collectively represent the source term for the Poisson equation, S_p . Note that the Jacobian term is the only term that does not vanish for $D=0$. Given a velocity field that satisfies the divergence free condition S_p reduces to the Jacobian term, and the pressure field can then be readily determined by the solution of the Poisson equation. The remaining terms in the pressure source term contain derivatives of the dilatation, D , and consequently vanish as $D \rightarrow 0$. However, since the solution of the equations

does not enforce mass conservation directly, at least some of these dilatation terms must be retained in the equation. These terms are needed in building a numerical algorithm which will correct the pressure field for non zero dilatation values.

The precise use of the dilatation terms to correct the pressure field for non-zero dilatation depends on the numerical method used for the solution of the governing equations. One of the earliest applications of the PPM method was demonstrated by Harlow and Welch, [70], in conjunction with their Marker and Cell method (MAC). In the MAC method, an algebraic form of the pressure Poisson equation was used which was derived directly from the finite difference representation of the momentum equations. The explicit time differencing, which was used with the momentum equations, enabled the Poisson equation to be treated as a parabolic equation in terms of the dilatation. The time derivative of the dilatation was differenced according to:

$$\frac{\partial D}{\partial t} = \frac{D^{n+1} - D^n}{\Delta t} \quad (4.11)$$

A Poisson equation was then formed by solving for D^{n+1} and setting it equal to zero. Thus, in marching the governing equations from time level n to time level $n + 1$, a Poisson equation was solved for the pressure which provided for the correction of the pressure field based on non-zero dilatation values at the previous time level, n . Based on this parabolic differencing scheme, the pressure and velocity fields remain continuously out of phase. As a result, the time accuracy of the method suffers. This could lead to significant error accumulation if the MAC method is applied to problems where the forcing conditions dictate abrupt pressure changes.

The purely elliptic pressure equation makes the solution of the incompressible equations more difficult. Due to the lack of any parabolic pressure terms, an attempt to solve the equations directly leads to a slow but continuous drifting of the solution without ever reaching a converged, divergence free, solution. A popular algorithm, which deals with this problem, is the SIMPLE method introduced by Patankar, [49]. In the SIMPLE method, as well as in most of its derivatives, the pressure Poisson equation is solved for a pressure correction rather than the pressure variable itself. This pressure correction is either added to the pressure field directly, or alternatively is used to calculate inviscid velocity corrections. The use of this form of the superposition principle in obtaining the solution complicates the method by making the application of boundary conditions more cumbersome and prone to errors.

In the present study a somewhat different approach is used in building an algorithm for the solution of the incompressible equations. As a first step, the right hand

side of equation (4.10a) is simplified. Consider the physical relation between the pressure, p , and the dilatation, D . If the dilatation is evaluated at a given point in the flowfield and yields a positive value, $D > 0$, then this would imply the existence of a net outflow from an infinitesimal control surface surrounding that point. In contrast, negative dilatation values, $D < 0$, imply a net inflow into the control volume. Thus, to correct the flow field at that point the pressure must be lowered for $D > 0$ and raised for values of $D < 0$. The time derivative of the dilatation, \dot{D} , is the only term on the right hand side of equation (4.10a) which can be easily rearranged into a form that will provide a correction to the pressure for non-zero dilatation values. The Jacobian term does not appear to provide a positive contribution to the pressure correction process, while the effect of the spatial dilatation terms, denoted by T_s , is very insignificant. Consequently, both terms are dropped from the equation in favor of simplicity. This leads to a simplified pressure Poisson equation of the form:

$$(\nabla^2 - \mathcal{N})p = -\frac{\partial D}{\partial t} \quad (4.12)$$

Note that the iterative correction of the pressure field can be built directly into the Poisson equation by forming the difference of the elliptic operator between two consecutive pressure update levels. This leads to the following equation,

$$[(\nabla^2 - \mathcal{N})p]^{n+1,k+1} - [(\nabla^2 - \mathcal{N})p]^{n+1,k} = -\dot{D}^{n+1,k+1} + \dot{D}^{n+1,k} \quad (4.13)$$

where as previously noted, superscript k is used to denote the pressure update level, and superscript n the time level. The evaluation of the time derivatives of the dilatation must be consistent with the incompressibility assumption. Thus, values of the dilatation at time levels other than $n + 1$ are eliminated from the pressure Poisson equation. Solving the equation for $D^{n+1,k+1}$ and setting it equal to zero yields,

$$[(\nabla^2 - \mathcal{N})p]^{n+1,k+1} = [(\nabla^2 - \mathcal{N})p]^{n+1,k} - \frac{D^{n+1,k}}{\Delta t} \quad (4.14)$$

Note that this equation can be rearranged into the following form which is both more understandable and more suitable for its numerical solution,

$$[(\nabla^2 - \mathcal{N})p]^{n+1,k+1} = S_p^{n+1,k+1} \quad (4.15a)$$

where the pressure source term is now given by,

$$S_p^{n+1,k+1} = S_p^{n+1,k} + \frac{D^{n+1,k}}{\Delta t} \quad (4.15b)$$

Thus, in the approach developed here for the solution of the incompressible equations, the pressure correction scheme described in terms of equation (4.15) seeks to iteratively build the pressure source term, S_p , in order to achieve a solution that satisfies the divergence free condition.

Note that when the ACM method is used for the solution of the unsteady equations the time derivative of the pressure which appears in equation (4.9) must be replaced by a derivative in terms of a pseudo-time. This becomes necessary due to the incompressibility assumption which precludes the parabolic behavior of the pressure. Under these circumstances, the finite difference representation of equation (4.9) takes the form,

$$p^{n+1,k+1} = p^{n+1,k} - c \Delta\tau D^{n+1,k} \quad (4.16)$$

where $\Delta\tau$ may be taken to represent the marching step in terms of the pseudo-time. The resulting pressure equation used by the ACM method is similar in form with equation (4.14), the pressure Poisson equation developed in this study. The two equations can be made identical if the pressure variable in the above equation is replaced by the elliptic pressure operator. The only apparent advantage of equation (4.16) is its simplicity. Equation (4.14) can be easily rearranged into a form that is suitable for its direct solution and it offers the reassurance of preserving the elliptic character of the pressure field.

4.2.3 Discretization of the Pressure Poisson Equation

The discretization of the pressure equation is carried out following the same procedure that was used for the momentum equations. The pressure Poisson equation, (4.15), is transformed onto (ξ, η) space and rearranged into the following form suitable for discretization:

$$C_\xi^* \frac{\partial p}{\partial \xi} + C_\eta^* \frac{\partial p}{\partial \eta} + C_{\xi\xi}^* \frac{\partial^2 p}{\partial \xi^2} + C_{\eta\eta}^* \frac{\partial^2 p}{\partial \eta^2} + C_{\xi\eta}^* \frac{\partial^2 p}{\partial \xi \partial \eta} + S_p = 0 \quad (4.17a)$$

where

$$C_\xi^* = \xi_{xx} \quad (4.17b)$$

$$C_\eta^* = y\eta_y \left(\frac{2\xi_x^2 F_\xi^2}{F^2} - \frac{\xi_x^2 F_{\xi\xi} + \xi_{xx} F_\xi}{F} \right) + \frac{\eta_{yy}}{F^2} [1 + (y\xi_x F_\xi)^2] \quad (4.17c)$$

$$C_{\xi\xi}^* = \xi_x^2 \quad (4.17d)$$

$$C_{\eta\eta}^* = \frac{\eta_y^2}{F^2} [1 + (y \xi_x F_\xi)^2] \quad (4.17e)$$

and

$$C_{\xi\eta}^* = -\frac{y \eta_y \xi_x^2 F_\xi}{F} \quad (4.17f)$$

The pressure equation is finite differenced using the centered difference equations defined in (4.6) and the convective term differencing which was outlined in (4.7). The finite difference representation of the pressure Poisson equation takes the following form:

$$\begin{aligned} C_0^* p_0^{k+1} = C_1^* p_1^{k+1} + C_2^* p_2^{k+1} + C_3^* p_3^{k+1} + C_4^* p_4^{k+1} \\ + \chi_p^{k+1,m} + \mathcal{E}_p^{k+1,m} + S_p^{k+1} \end{aligned} \quad (4.18a)$$

where

$$C_0^* = C_{\xi\xi}^{*+} + C_{\xi\xi}^{*-} + C_{\eta\eta}^{*+} + C_{\eta\eta}^{*-} + 2C_{\xi\xi}^* + 2C_{\eta\eta}^* \quad (4.18b)$$

$$C_1^* = C_{\xi\xi}^{*+} + C_{\xi\xi}^* \quad (4.18c)$$

$$C_2^* = C_{\eta\eta}^{*+} + C_{\eta\eta}^* \quad (4.18d)$$

$$C_3^* = C_{\xi\xi}^{*-} + C_{\xi\xi}^* \quad (4.18e)$$

$$C_4^* = C_{\eta\eta}^{*-} + C_{\eta\eta}^* \quad (4.18f)$$

$$\chi_p^{k+1,m} = -\frac{1}{4} C_{\xi\eta}^* (p_5 + p_7 - p_6 - p_8)^{k+1,m} \quad (4.18g)$$

$$\begin{aligned} \mathcal{E}_p^{k+1,m} = -\frac{1}{2} (C_{\xi\xi}^{*+} + C_{\xi\xi}^{*-}) [p_1 - 2p_0 + p_3]^{k+1,m} \\ - \frac{1}{2} (C_{\eta\eta}^{*+} + C_{\eta\eta}^{*-}) [p_2 - 2p_0 + p_4]^{k+1,m} \end{aligned} \quad (4.18h)$$

Note that the finite difference coefficients for the pressure equation depend only on the free surface position and the grid metrics. Consequently, they remain constant if the pressure and kinematic equation are solved uncoupled.

4.2.4 Discretization of the Kinematic Condition

The position of the free surface, F , at time level $n + 1$, is determined by the finite difference approximation of the kinematic condition. The kinematic condition, which was given in the previous chapter as equation (3.27e), is differenced as follows:

$$\left. \frac{\partial F}{\partial t} \right|_i^{n+1} = v_i^\ell - u_i^\ell \left. \frac{\partial F}{\partial x} \right|_i^{n+1} \quad (4.19)$$

where u^ℓ and v^ℓ will be defined shortly. The time derivative of F at time level $n + 1$ and grid position i is approximated by,

$$\left. \frac{\partial F}{\partial t} \right|_i^{n+1} = \frac{1}{\Delta t} \left[\left(1 + \frac{\alpha}{2}\right) F_i^{n+1} - (1 + \alpha) F_i^n + \frac{\alpha}{2} F_i^{n-1} \right] \quad (4.20)$$

using a differencing scheme which is identical with the one used in the momentum equations (see equation 4.5). The convective term is upwind differenced according to,

$$u_i^\ell \left. \frac{\partial F}{\partial x} \right|_i^{n+1} = \left[\frac{u + |u|}{2} \right]_i^\ell \mathcal{D}_f(F_i^{n+1}) + \left[\frac{u - |u|}{2} \right]_i^\ell \mathcal{D}_b(F_i^{n+1}) \quad (4.21)$$

where here, \mathcal{D}_f and \mathcal{D}_b denote the standard three point, second order accurate forward and backward finite difference approximations.

Physically, the position of the free surface is determined by the interaction of various waveforms that become excited within the container as a result of the applied forcing. The upwind differencing of the convective term in the kinematic equation yields results that are physically more realistic than those obtained from a centered differenced scheme. In particular, upwind differencing seems to prevent the smearing of short wavelength components in the interior of the surface, while providing a better model for the reflection of all waves from the container walls.

The final consideration entering into the integration of the kinematic condition deals with the selection of appropriate values for the velocity components. Thus, based on the values used for u^ℓ and v^ℓ in equation (4.19) the following three possibilities are considered here:

$$u^\ell = \begin{cases} u^{n+1} & \text{implicit method} \\ u^n & \text{explicit method} \\ \frac{5}{2} u^n - 2 u^{n-1} + \frac{1}{2} u^{n-2} & \text{predictive method} \end{cases} \quad (4.22)$$

where similar expressions are implied for v^ℓ . Note that the free surface represents a moving boundary and as such it defines the computational domain. Thus, the computational grid needs to be adjusted whenever the position of the free surface changes.

The implicit solution of the kinematic equation will generally require multiple grid adjustments per time step. If the grid generation scheme requires the solution of additional equations this can lead to a significant expenditure in terms of computational resources. The explicit integration of the kinematic equation alleviates this problem since it requires a single grid adjustment per time step. However, this is done at the expense of the long term accuracy of the method. The predictive method is investigated as means of improving the accuracy of the explicit integration. The free surface velocities at time level $n + 1$ are predicted from previous values using second order accurate extrapolation. The kinematic equation is then solved explicitly based on these predicted values. This approach may also be used as an acceleration technique for an implicit scheme.

It should be noted that the current model is used to investigate only the relative accuracy of these three schemes. Comparisons in terms of computational requirements are meaningless. This is due to the fact that the normalized coordinate transformation, used in conjunction with an algebraic grid generation, render the grid and its associated metrics invariant throughout the solution of the problem. As a result, for the model presented here, the difference between the explicit and implicit methods in terms of computational time requirements for the solution of a problem are very small. The explicit method is approximately one percent faster than the implicit method.

4.2.5 Discretization of the Boundary and Initial Conditions

As a general rule, the boundary conditions are discretized using centered differences for derivatives tangential to the boundaries and second order accurate, 3-point, one-sided differences for derivatives normal to the boundaries.

Along the container walls, the velocity components are set equal to zero based on the no-slip condition. The viscous terms entering the pressure boundary conditions are approximated using second order accurate finite difference representations, derived from Taylor series expansions. Along the left container wall, ($x =$ or $z = 1$), this results in the following finite difference approximation,

$$\left. \frac{\partial^2 u}{\partial x^2} \right|_{z=1} = \left(\frac{h_1 + h_2}{h_1^2 h_2} \right) u_2 - \left(\frac{h_1}{(h_1 + h_2)^2 h_2} \right) u_3 + \mathcal{O}[h_1(h_1 + h_2)] \quad (4.23)$$

where here h_1 and h_2 represent respectively the first and second grid increments from the wall. Similar expressions are used for the viscous terms along the remaining solid boundaries.

The discretization of the boundary conditions along the free surface is straight forward with the exception of the contact points at the walls. In particular, the no-slip condition that the tangential velocity component vanish at the wall appears inconsistent with the kinematic condition that fluid particles on the free surface remain on the free surface. The precise physics that govern the motion of the contact points are far from been clearly understood. The description of this flow represents an entire new area of study all in itself.

Several approximation techniques dealing with the motion of the contact points have been investigated in the course of this study. The results of this investigation suggest that the precise form of approximation used at the contact point does not have a significant effect on the solution away from the wall. Based on these conclusions, the free surface position at the contact points is determined by requiring that the free surface slope at wall be equal to zero.

The velocity components associated with the contact points must also be prescribed since they enter into the finite difference representation of the governing equations and the free surface conditions. It may be easily seen that the horizontal velocity component, being normal to the wall, must vanish at the contact points. The vertical velocity component, which is tangential to the wall, and should also vanish based on the no-slip condition, can not do so from a kinematic standpoint if the contact point is allowed to move up and down the wall. Thus the contact point is treated numerically as follows. In the momentum equations, where the contact point velocities are needed for the evaluation of cross-derivatives in the viscous diffusion terms, the contact point is assumed to satisfy the no-slip condition ($u = 0, v = 0$). In the finite difference representation of the free surface conditions, velocity values at the contact points are set based on the kinematic assumption that the point moves along with the free surface. This leads to the condition ($u = 0, v = \dot{F}$). This approach, which leads to dual values for the vertical velocity component at the contact points, appears to work well.

4.3 Computational Procedure

The discretization process, whereby each of the derivatives that appear in the governing equations and boundary conditions is replaced by a finite difference approximation, converts the continuous problem which is described in terms of partial differential equations into a discrete one described by a set of non-linear simultaneous algebraic equations. An approximation to the exact solution of the problem can be

obtained by the solution of this set of algebraic equations.

Several iterative methods are available for the solution of the algebraic equations. Algorithms based on Gauss-Siedel, SOR (Successive Overrelaxation), SLOR (Successive Line Overrelaxation), and ADI (Alternative Direction Implicit) methods were developed and tested. A simple SOR method, based on Gauss-Siedel iterations, proved to be the most suitable choice for the solution of the momentum and kinematic equations. For the solution of the pressure equation both the SOR and SLOR methods proved to be consistently more efficient than the ADI method. A comparison between the SOR and SLOR methods yielded similar performance results. Algorithms based on both methods have been used during the course of this study but the majority of the results were calculated using the SOR method for the solution of the pressure equation.

4.3.1 Relaxation Parameters

The use of relaxation techniques is a common tool used in speeding up the convergence of the numerical solution. For the present model, the pressure equation is solved uncoupled from the momentum equations. This allows for the optimization of the overrelaxation used for the solution of the Poisson equation. Relaxation parameters in the range 1.75 – 1.85 proved to yield the fastest convergence rates. For the solution of the momentum equations and kinematic condition a slight underrelaxation proved beneficial at higher Galileo values. Relaxation parameters in the range 0.80 – 1.00 have been utilized.

An additional relaxation parameter was used in the updating of the pressure source term. To accommodate this relaxation, equation (4.15b) has been rewritten in the form,

$$S_p^{k+1} = S_p^k + \frac{1}{\Delta t} [\omega D^k + (1 - \omega) D^{k-1}] \quad (4.24)$$

where values of the relaxation parameter ω in the range $0.6 \leq \omega \leq 0.8$ were used. Overall the underrelaxation of the pressure source term did not appear to alter significantly the number of required pressure iterations. However, it was found helpful in ensuring the monotonic decrease of the maximum residual dilatation value towards zero.

4.3.2 Convergence Criteria

The governing equations are solved numerically using an iterative algorithm. Two different types of conditions are used to establish the convergence of the solution. The convergence of each of the governing equations, that is the momentum equations, the pressure Poisson equation, and the kinematic condition, is based on the following criterion:

$$\left| \frac{\phi_{i,j}^{n+1,m+1} - \phi_{i,j}^{n+1,m}}{\max(\phi_{i,j}^{n+1,m+1})} \right| < \epsilon_1 \quad \text{for} \quad \phi = \{u, v, p, F\} \quad (4.25)$$

where, $\epsilon_1 = 10^{-7}$ was a typical value used during the calculations.

In addition to the convergence of each of the individual governing equations the solution must also satisfy, to within some acceptable limits, the divergence free condition, $D = 0$. It is important to note that the magnitude of the dilatation does not provide a physically meaningful measure as to how well mass conservation is enforced. The magnitude of the dilatation is proportional to the strength of the flow. Thus, a criterion based on the requirement that the maximum value of the dilatation remains smaller than a prescribed value is dangerous because it does not ensure the uniform convergence of the solution throughout the spatial and time domains of the problem. The strength of the flow varies spatially, with flow along the bottom container wall being much weaker than the free surface flow. Furthermore, the strength of the flow will generally exhibit a damped sinusoidal time behavior. To address these considerations, the convergence criterion used in enforcing the divergence free condition must be based on velocities local to each grid cell.

Note that a non zero value of the dilatation represents an imbalance between the various gradients present in the expression for the divergence of the velocity. If Δz is used to represent a characteristic dimension of a given grid cell, then a velocity correction of order $\Delta w \sim D\Delta z$ is necessary to achieve mass conservation. Taking Δz to be the geometric mean of the two cell dimensions, $\Delta z = \sqrt{\Delta x \Delta y}$, the ratio of this velocity correction Δw and the local fluid speed is used to formulate a *Normalized Dilatation*, denoted by \mathcal{D} , and defined in terms of (ξ, η) coordinates by:

$$\mathcal{D}_{i,j} \equiv \sqrt{\frac{F_i D_{i,j}^2}{\xi_{x_i} \eta_{y_j} (u_{i,j}^2 + v_{i,j}^2)}} \quad (4.26)$$

The normalized dilatation, \mathcal{D} , represents the fraction by which the local speed must be altered to enforce mass conservation. Thus, a physically meaningful convergence criterion for enforcing the divergence free condition of the velocity field, can be

constructed in terms of \mathcal{D} . The convergence of the solution was based on the following condition,

$$\max(\mathcal{D}_{i,j}) < \epsilon_2 \quad (4.27)$$

where $\epsilon_2 = 10^{-4}$ was a typical value used during the computations.

4.3.3 Outline of Solution Algorithm

The marching of the solution from time level n to time level $n + 1$, where $t^{n+1} = t^n + \Delta t$, is carried out based on the algorithm outlined in Figure 4.3. The converged solution at the previous time level, n , is used to initialize all of the dependent variables at the beginning of the iterative cycle. The pressure update level, k , is set equal to zero, and the pressure field at the previous time level is used for the solution of the momentum equations during the first pass, $k = 0$.

The position of the free surface is calculated as part of the momentum solution. The momentum equations and kinematic condition are iterated using an SOR algorithm until convergence condition (4.25) is satisfied. With a converged momentum solution the value of the dilatation, D , is evaluated, and used to calculate the normalized dilatation, \mathcal{D} . If the maximum value of \mathcal{D} is too large such that condition (4.27) is not satisfied, then a pressure correction or update becomes necessary. Note that the algorithm is set up to perform at least one pressure correction at each time step. If a pressure correction is required, the pressure source term, S_p , is updated according to equation (4.24), and the pressure Poisson equation is solved iteratively using either an SOR or SLOR algorithm. The new pressure field serves as the basis for a new momentum solution, and the cycle is repeated until the solution converges.

The main advantage of this method for the specific problem under consideration here, is that the momentum and pressure equations are solved separately. This allows for the optimization of both the pressure and momentum solutions. The solution of the problem exhibits a periodic time behavior. To preserve the long term accuracy of the solution the size of the time step used in marching the equations must be kept small. As a result, the velocity field does not change significantly between successive time steps and thus the effort required in solving the momentum equations is relatively small. This is illustrated in Figure 4.4 for the solution of a case with $F_o = 0.5$, $Q = 0.2$, $U_o = 0$, $Ga = 10^7$, and $Bo = \infty$, which was carried out on a 31×31 grid with the time step set equal to $\Delta t = 0.002$. Both the momentum and pressure equations were solved

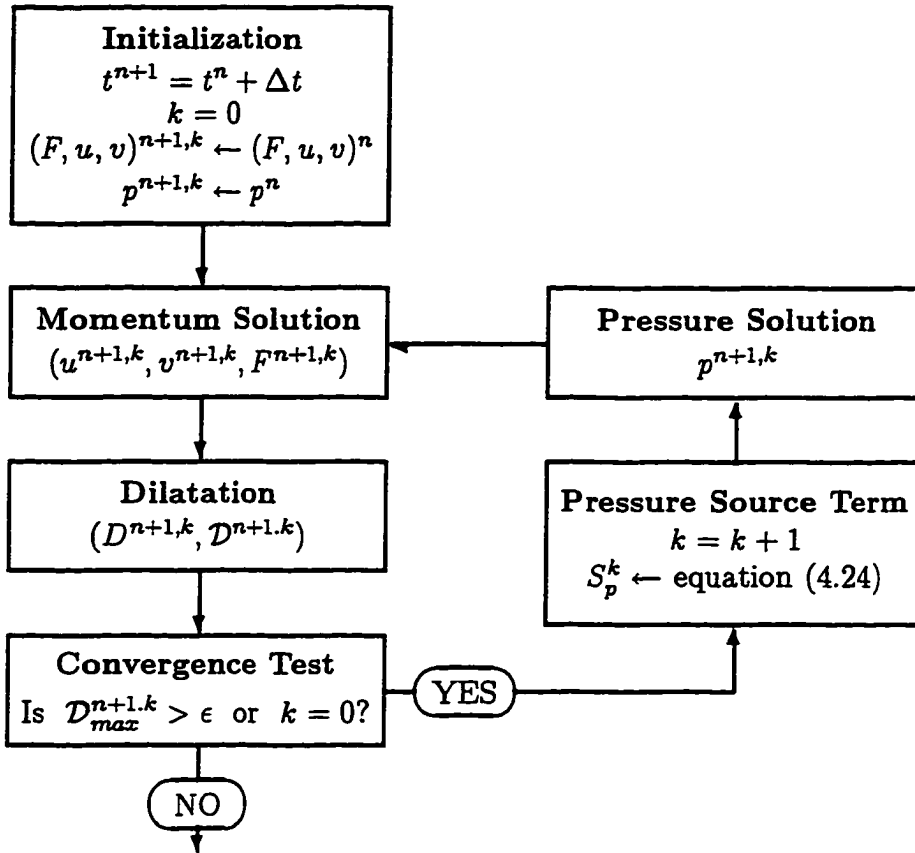


Figure 4.3: Iterative Solution Cycle

using the SOR method. The convergence history of the method is depicted in terms of the total number of iterations per time step required for the solution of the momentum equations, denoted by NITM and shown in part (a), and the pressure equation, denoted by NITP and shown in part (b). Both NITM and NITP are shown on a per five time step average in order to reduce oscillations in their values and thus make the figure more legible. These oscillations are the result of the method requiring a different number of pressure updates or corrections, NPU, between successive time steps. This in turn causes significant variations in the number of pressure and momentum iterations between successive time steps which appear as oscillations in the figure. In general, one or two pressure corrections are sufficient in reducing the residual dilatation values to within acceptable limits. The number of required pressure corrections, NPU, increases to as high as fifteen in certain intervals of the flow, but the average remains small, at $NPU = 1.73$. An average of $NITM = 19.2$ iterations are needed for the solution of the

momentum equations while the solution of the pressure equation requires an average of $NITP = 321$ iterations.

The variations in the number of iterations required for the solution of the equations can be linked to changes that occur in the flowfield. The fluid, which initially is motionless, is set into a periodic motion in response to the applied acceleration Q . As the fluid begins to rise along the left container wall a viscous flowfield starts to develop. By time $t \approx 0.3$, the flowfield has been well defined and is characterized by a pattern of strong free surface flow that pushes the liquid up the left wall. Initially, $NITP$ increases as the flowfield develops, and then it begins to decrease when the well defined flow pattern has been established. At approximately $t \approx 1.0$, a secondary flowfield appears in the vicinity of the lower corners of the container. This secondary flowfield consists of small regions of weak reversed flow. The sudden jump in the value of $NITP$ at this time is caused by the difference in the strengths of the primary and secondary flow. Before the weak secondary flow can be resolved, the primary flowfield near the free surface has to become sufficiently divergence free. As a result, extra pressure updates become necessary to converge the solution. It should be noted that if the convergence criterion is based on the maximum value of the dilatation rather than the normalized dilatation the secondary flow does not get resolved and the value of $NITP$ continues to decrease in this region. Beyond $t \approx 1.0$, the strength of the primary flow begins to decrease as the fluid continues to approach the point of maximum elevation. The difference in the strength of the primary and secondary flows becomes smaller, and it is reflected in the figure by the decrease in the value of $NITP$. At $t \approx 1.9$ the liquid has reached the point of maximum elevation, and from a global perspective it comes to rest before it starts descending along the left wall. The flowfield at this time is extremely weak and a consistent flow pattern can not be identified. This causes a significant increase in the number of pressure updates required for the convergence of the solution. It is reflected in the figure by the increase in the value of $NITP$, and even more clearly by the jump in the value of $NITM$.

The same case as shown in Figure 4.4 has also been solved using the SLOR method for the pressure Poisson equation. By time $t = 1.0$, the SLOR method required a total of 26.05% fewer iterations than the SOR method. However, the corresponding reduction in the required computation time was only 0.66%. The same comparison at time, $t = 2.0$, revealed a 23.87% reduction in the number of iterations which resulted in a 1.60% increase in the computation time. Thus, despite a significant reduction in the

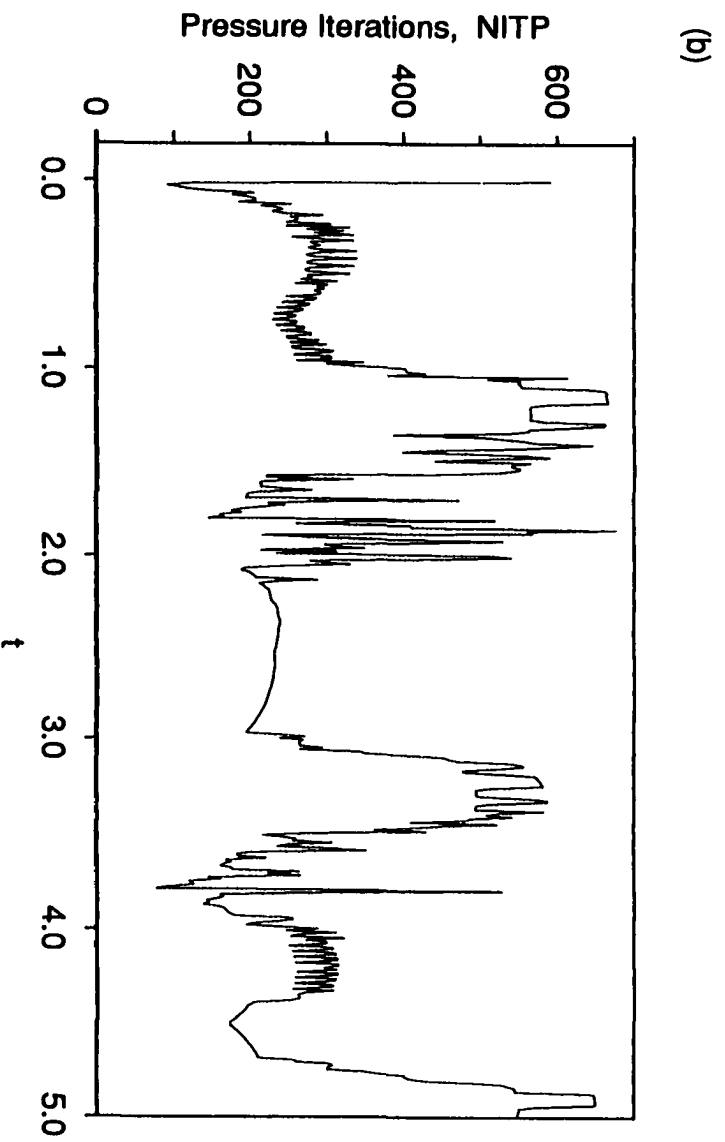
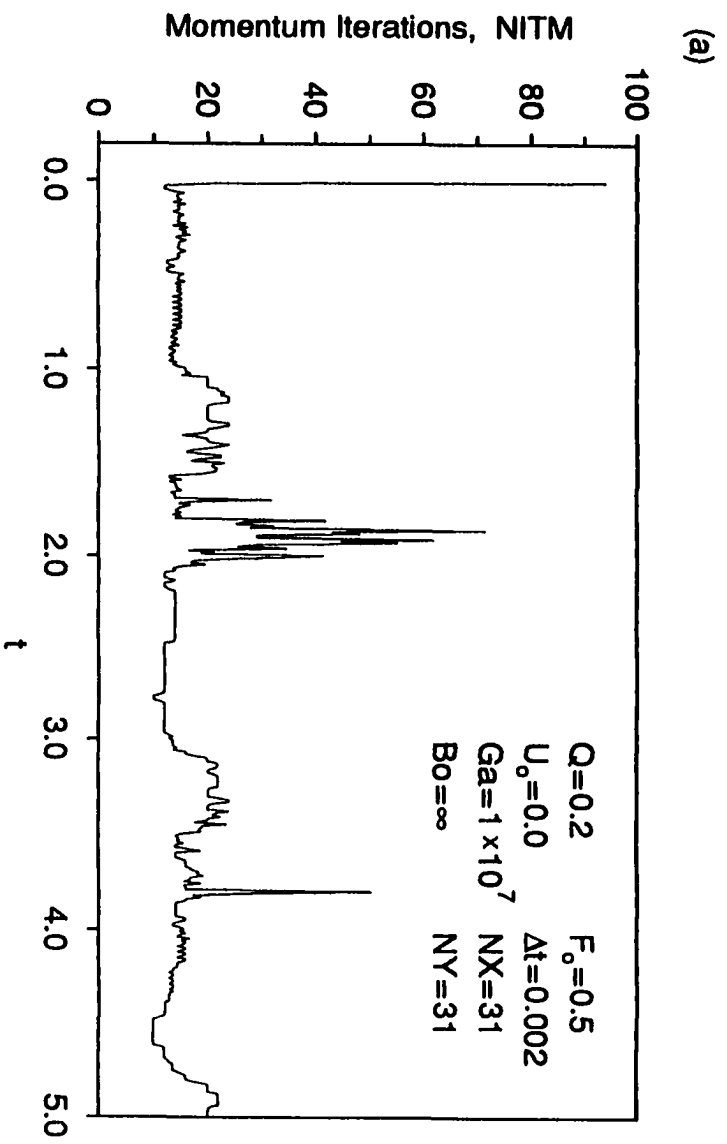


Figure 4.4: Iterative Convergence History

number of required pressure iterations the performance of the SOR and SLOR methods in terms of required computation time remains indistinguishable. Note that when the momentum and pressure equations are solved uncoupled, during the course of a given pressure update the value of the pressure along the free surface as well as the value of the pressure gradients along the walls remain constant. In addition, the finite difference coefficients depend only on the grid metrics and the free surface position and thus they can be evaluated beforehand and stored. As result, an SOR iteration at any given grid point can be accomplished in terms of single code statement. For the SLOR method approximately the same effort is required in setting up the constant vector of the tridiagonal solver.

An attempt to solve the momentum and pressure equations iteratively coupled, rather than in separate steps, results in a significantly slower algorithm. Although the number of iterations required by the coupled scheme is considerably less than NITP, it is also sufficiently higher than NITM such that the increase in momentum iterations nearly doubles the required computation time. It should be noted that a pressure iteration for the uncoupled solution of the equations is nearly 5.2 times faster than a corresponding momentum iteration.

4.4 Evaluation of the Method

Some of the aspects that enter into the numerical model for the sloshing liquid problem are investigated here. The truncation error of the method due to the spatial discretization is investigated. The accuracy of methods based on first and second order time differencing are considered. The kinematic equation is integrated using both explicit and implicit schemes. The effects of the approximations used at the contact points are evaluated. Results from a comparison between the pressure Poisson method and the artificial compressibility method are also presented.

4.4.1 Spatial Truncation Error Behavior

For a consistently differenced scheme, the accuracy of the numerical solution increases with increasing grid resolution. However, the degree of feasible grid refinement that can be provided for the solution of the problem is limited by the amount of available computational and time resources.

Given a limited number of grid points that can be used for the solution of the

problem, grid stretching transformation techniques provide means for optimizing the placement of grid points in the physical (x, y) problem domain. For the present model, the transformation defined in terms of equation (4.1) clusters the grid points along the domain boundaries. This improves the accuracy of the momentum solution by providing a better resolution of the viscous and free surface effects. At the same time, the spacing of grid points in the computational (ξ, η) domain remains uniform, thus preserving the second order truncation error behavior of the method.

The effect of grid stretching on the truncation error of the method are investigated in Figure 4.5. The value of the pressure at the left lower corner of the container at time $t = 0^+$ can be determined exactly from the analytical solution given by equation (3.33). This value, p_{max} , which also happens to represent the maximum pressure value at time $t = 0^+$, is compared to a corresponding value obtained from the numerical solution of the pressure equation for the conditions indicated on Figure 4.5, ($Q = 0.2$, $U_o = 0$, $F_o = 0.5$). The percent error in p_{max} is plotted against the dimensionless grid stretching parameter, β , for five different grids, ranging in size from 11×11 to 51×51 . Here, the same grid distribution is used in both the x and y directions, $\beta_1 = \beta_2 = \beta$. Recall that based on the grid transformation defined in equation (4.1), the grid point distribution in the (x, y) space is controlled by this parameter β . As $\beta \rightarrow \infty$ the resulting grid becomes uniformly spaced, while as $\beta \rightarrow 1$ the grid points become increasingly clustered at the boundaries of the domain (see Figure 4.1).

Note that the same order of magnitude pressure gradients exist throughout the liquid at time $t = 0$. As a result, the solution of the pressure equation does not benefit from any degree of grid stretching. If excessive grid stretching is used with a coarse grid then the solution can be easily compromised by a large error. The second order truncation error behavior of the method can be easily verified by examining the solution at any given value of β . For a value of $\beta = 1.10$, the error associated with the 11×11 grid is 3.93%. The error decreases to 0.95% for the 21×21 grid and to 0.22% for the 41×41 grid. This is consistent with the behavior of a second order method where a fourfold decrease in the error can be expected by doubling the grid resolution. It should be noted that all of the results presented in this study were calculated using values for the stretching parameters that were $\beta \geq 1.1$.

The second order truncation error behavior of the method under successive grid refinement is also depicted in Figure 4.6. Here, the value of the kinetic energy of the liquid, E_k , at time $t = 0.901$ is plotted as a function of the number of horizontal grid

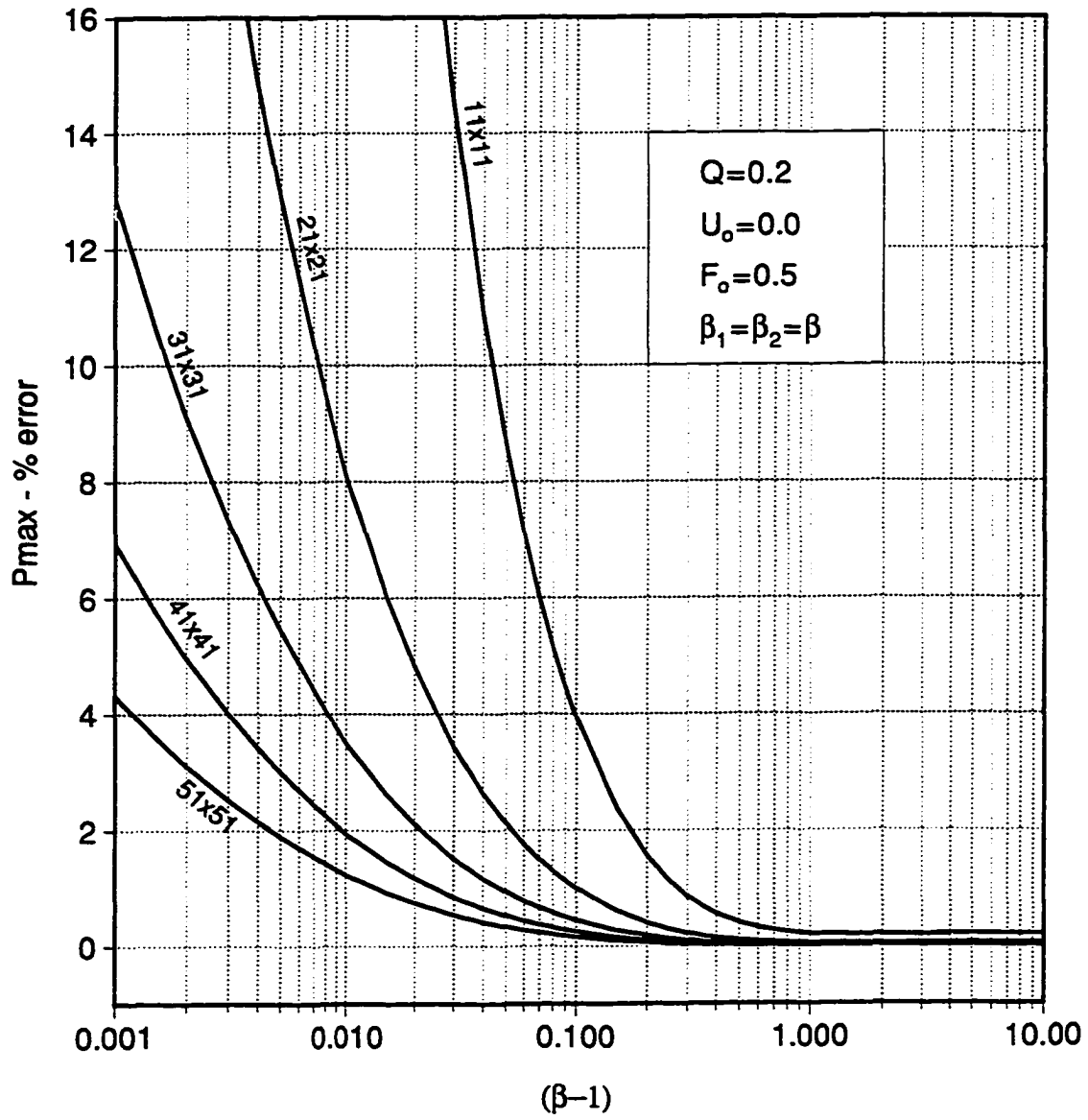


Figure 4.5: Effect of Grid Stretching

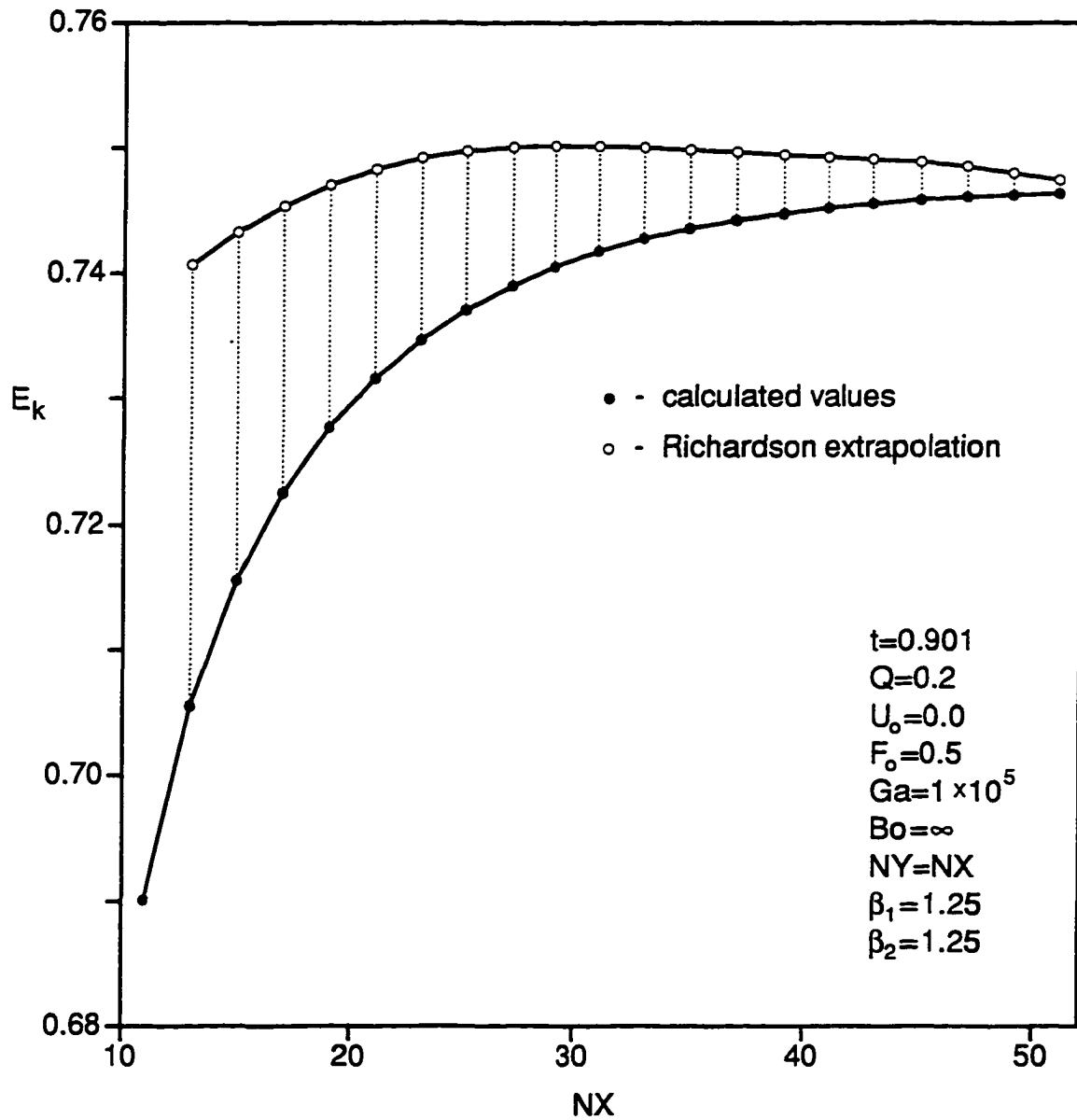


Figure 4.6: Grid Refinement and Spatial Truncation Error

points, NX , used in the calculation. The same number of grid points was also used in the vertical direction, $NY = NX$. The calculated values of E_k are indicated in the figure by the solid bullets. Note that as NX increases the value of E_k approaches a constant value asymptotically. The hollow bullets shown in Figure 4.6 represent predictions of the exact value of E_k based upon Richardson extrapolation. Assuming that the method is second order accurate, then a parabolic behavior can be postulated for the error associated with any calculated quantity, Φ , of the form,

$$\Phi|_{\text{calculated}} = \Phi|_{\text{exact}} + C \bar{h}^2$$

where C represents a constant and \bar{h} some measure of the average grid resolution. Based on this assumed error behavior, the exact value of Φ can be *predicted* given any two values Φ_1 and Φ_2 from the formula,

$$\Phi_p = \frac{\bar{h}_2^2 \Phi_1 - \bar{h}_1^2 \Phi_2}{\bar{h}_2^2 - \bar{h}_1^2} \quad (\text{Richardson extrapolation}) \quad (4.28)$$

Using the average grid spacing for \bar{h}_1 and \bar{h}_2 the above formula was used to calculate the predicted values of the kinetic energy shown in the figure. Each of these predicted values corresponds to the calculated value at the same value of NX , which is also connected to it with the dashed line, and the value immediately to the left of it. The values predicted by this formula provide a fairly good estimate of the exact value of E_k at any given grid resolution. Consequently, this formula can be used to obtain at least an order of magnitude estimate of the spatial truncation error associated with coarse grid solutions.

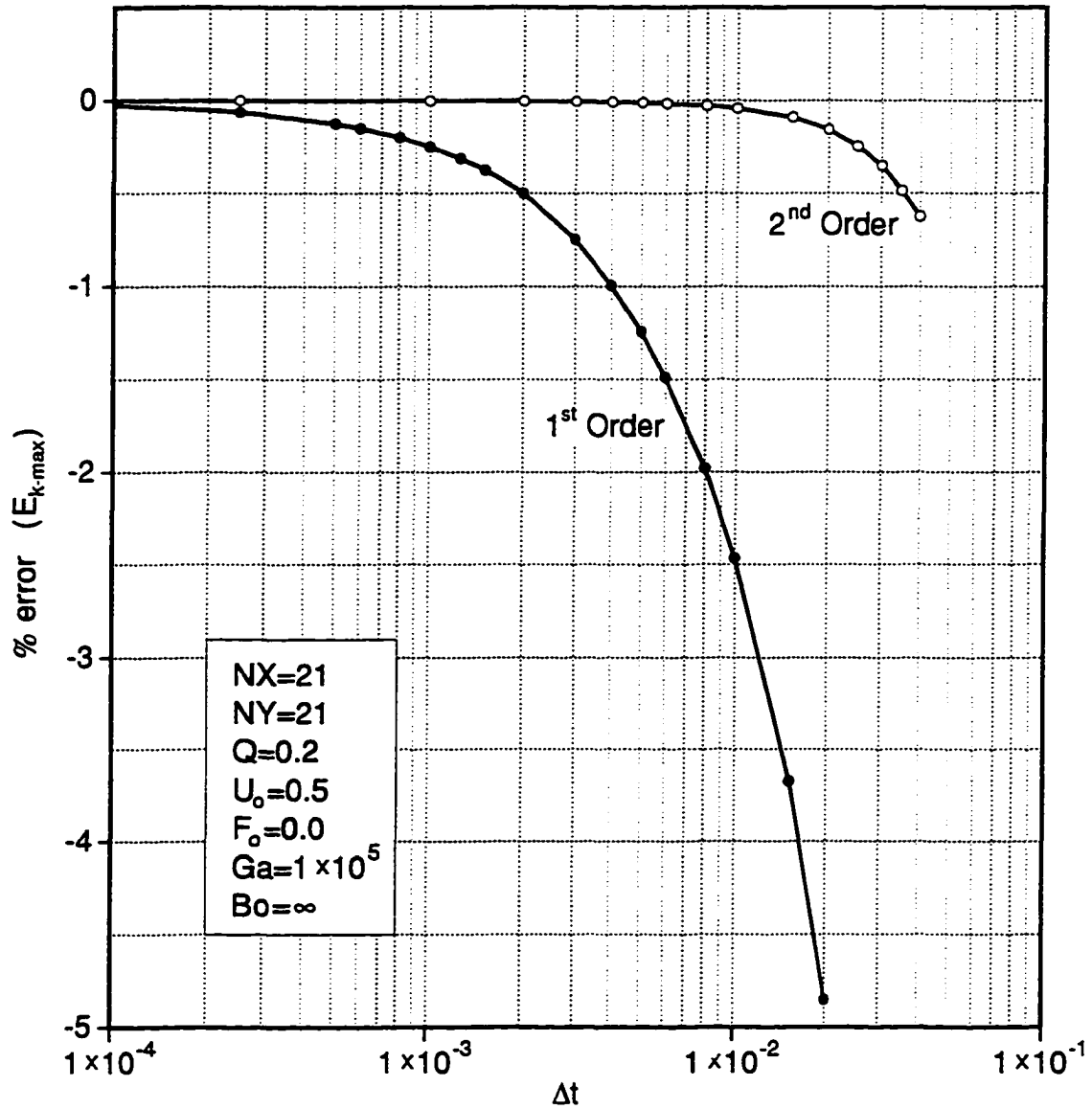
4.4.2 Time Differencing

The analysis of the periodic behavior of the liquid motion which occurs in response to the imposed forcing conditions requires that the numerical solution must remain accurate for intervals extending to large values of time. Based on the setup of the numerical method the two factors which influence the long term accuracy of the solution are the truncation error order of the method and the actual size of the time step, Δt , used in integrating the equations. Recall that based on the finite difference approximation introduced in equation (4.6), the order of the time differencing is determined by the value of the parameter α . A value of $\alpha = 0$ results in the approximation of all time derivatives by a first order difference, while for value of $\alpha = 1$ the time differencing becomes second order.

The truncation error behavior under time step refinement for the two methods is depicted in Figure 4.7 for a case with dimensionless parameters $F_o = 0.5$, $Q = 0.2$, $U_o = 0$, $Ga = 10^7$, and $Bo = \infty$. The applied acceleration Q causes the liquid which is initially stationary to be set into a periodic motion about the new equilibrium position. As it begins to rise along the left container wall its kinetic energy begins to increase and it experiences a local maximum, E_{k-max} , at an approximate time of $t = 0.9$. The truncation error of the method is examined in Figure 4.7 by comparing the percent error in the magnitude of this *first* kinetic energy maximum for different values of Δt . The result from the second order method with $\Delta t = 0.0001$ is used as the basis for the calculation of the error. It becomes evident from the figure that the first order method results in significant error even at reasonably small values of Δt . A value of $\Delta t = 0.002$, which implies that each period of oscillation will be resolved into approximately 1900 time steps, yields an error of 0.5% after only 1/4 of a period. In contrast, the error associated with the second order method is much smaller, and it remains small for all reasonable time step sizes, $0.001 \leq \Delta t \leq 0.01$.

The long term truncation error of the first and second order methods is examined in Figure 4.8. For the case under consideration here, the value of the Galileo number has been increased to $Ga = 10^8$ while the rest of the dimensionless parameters remain the same. The percent error in the magnitude of the local maxima of the kinetic energy distribution is plotted as a function of time. The solution from the second order accurate method with $\Delta t = 0.001$ serves as the basis for the calculation of the error. The behavior of the first order method is shown in part (a) for three different time step sizes. Note the almost linear accumulation of truncation error with time. Even with a small time step size of $\Delta t = 0.001$, the error associated with the first order method increases by approximately a full percentage point for every period of oscillation. The behavior of the second order method is shown in part (b). The error accumulation for the second order method occurs at a much slower rate. Based on this initial rate, the error of the second order method with $\Delta t = 0.005$ will remain less than 1% for values of $t < 480$.

Based on the above comparisons the need for at least a second order accurate time differencing is unquestionable. The last consideration with respect to the time accuracy of the calculations concerns the size of the time step. Although smaller values of Δt are preferable, the resulting number of steps required in marching the solution increases, and thus the computation time may also increase. The effect of the size of

Figure 4.7: Effect of Δt on the Truncation Error

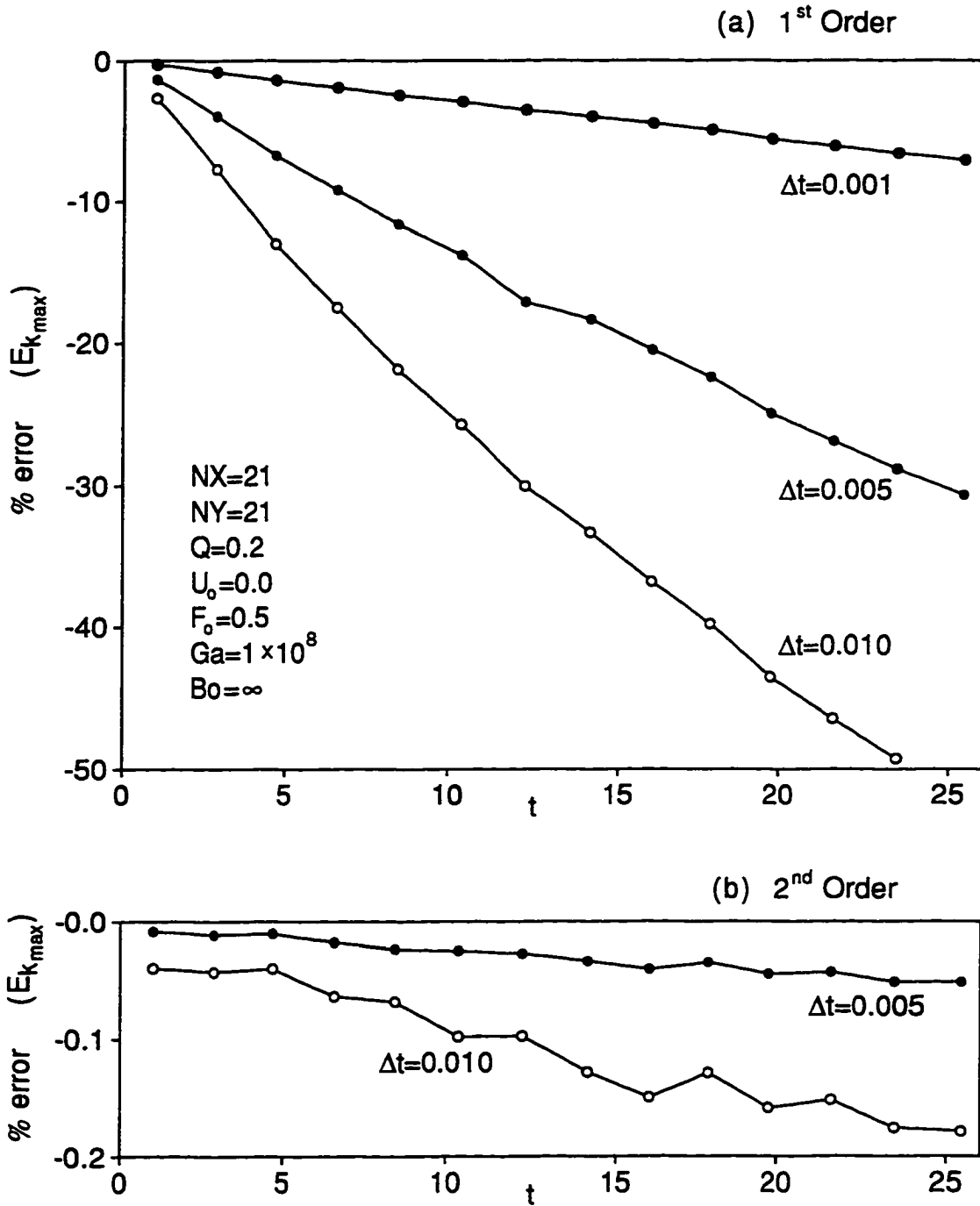


Figure 4.8: Long Term Accuracy of the Solution

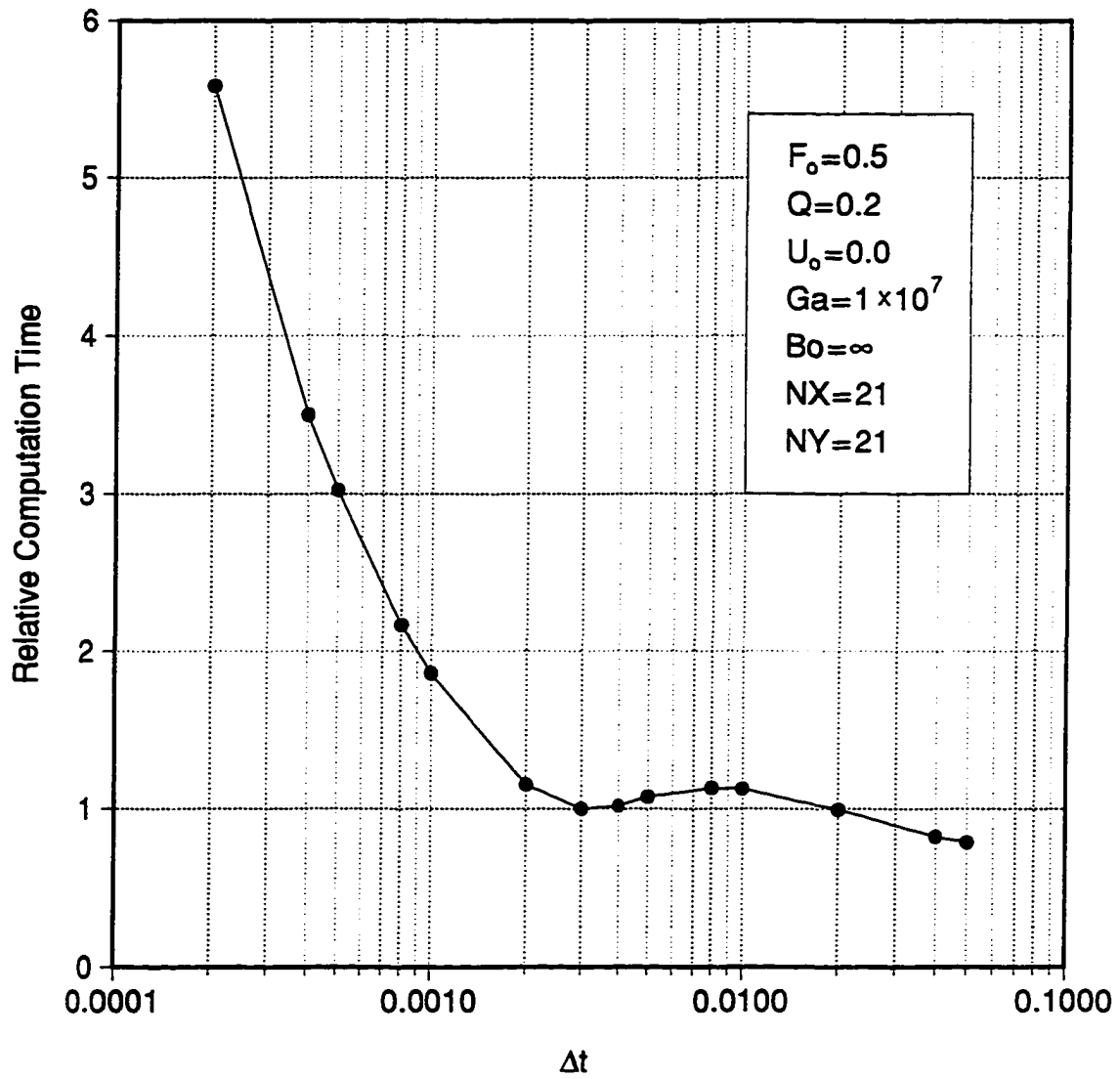
the time step on the required computation time is depicted in Figure 4.9. Here, the time required for the solution of the problem has been normalized with respect to the result obtained with $\Delta t = 0.003$. Note that the required time remains fairly constant for time steps as small as $\Delta t = 0.002$. Consequently, the size of the time step can be made sufficiently small to address accuracy considerations without experiencing a significant penalty in terms of computation time requirements.

4.4.3 Integration of the Kinematic Equation

The position of the free surface, $F(x, t)$, is determined by the solution of the kinematic condition. The free surface represents a moving boundary, and as such its position must be known in order to define the problem domain. The implicit integration of the kinematic condition would generally require multiple grid adjustments as the position of the free surface changes continually during the solution process. An explicit integration allows the determination of the free surface position prior to the solution of the remaining governing equations, and thus the grid need only be adjusted once.

The finite difference representation of the kinematic condition was set up in equation (4.19) to allow the investigation of three different methods that can be used for its solution. In addition to standard implicit and explicit representations, a modified explicit method, termed the *predictive* method, which is based on extrapolated values of the velocity components at the free surface is also considered. The performance of these three methods is examined in Figure 4.10 for a case with $F_o = 0.5$, $Q = 0.2$, $U_o = 0$, $Ga = 10^7$, and $Bo = \infty$, which was solved on 21×21 grid using a time step equal to $\Delta t = 0.01$.

In part (a) of the figure the comparison is in terms of a global mass conservation. The percent error in the calculation of the dimensionless liquid volume, V , is shown as a function of time. Note that in the absence of numerical error, the value of the dimensionless liquid volume should remain constant and equal to the initial liquid depth, $V(t) = F_o$. The error associated with the explicit method, shown in terms of the solid line, grows to approximately 0.8% after the elapse of five periods of oscillation. The error of the predictive method, shown in terms of the dashed line, is four times smaller. The error associated with the implicit method is not shown directly on the figure. It is nearly identical to the error of the predictive method and based on the scale used for the figure, if drawn it will coincide with the dashed line. The excellent improvement provided by the predictive method is also illustrated in part (b) of the

Figure 4.9: Required Computation Time vs Δt

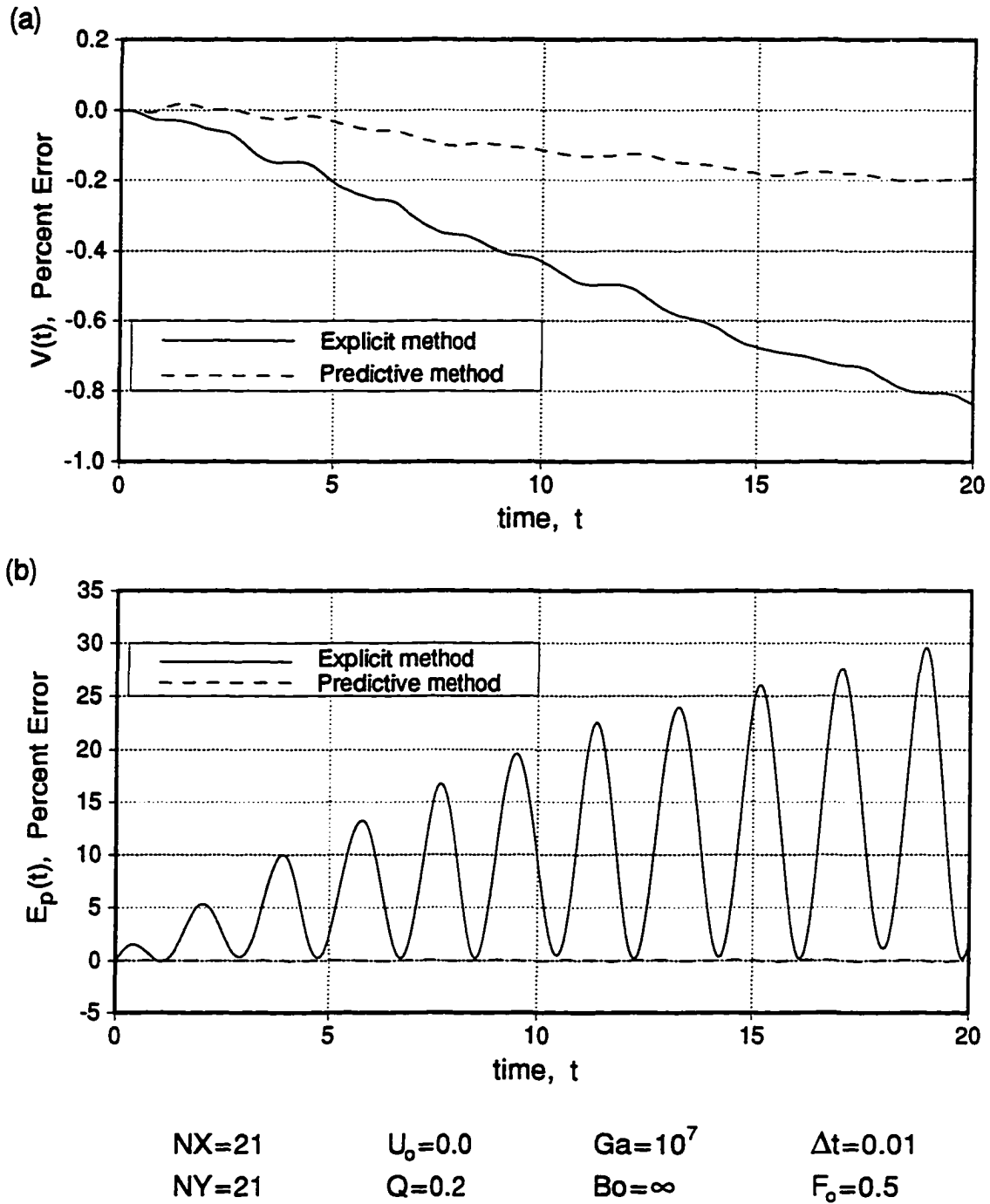


Figure 4.10: Integration of the Kinematic Condition

figure. Here, the comparison is terms of the potential energy of liquid, E_p . The result obtained by the implicit method is used as the basis for the calculation of the error. The error of the predictive method is negligible, which implies that the variation of the free surface velocity components is sufficiently smooth that they can be predicted to within a high degree of accuracy by second order extrapolation. The error accumulation demonstrated by the explicit method is significantly high to render the method unreliable for long term calculations.

The implicit method has been used for the calculation of all of the results that will be presented in this study. The analytic coordinate transformation, which was used to map the (\bar{x}, \bar{y}) space onto the (x, y) space, results in a computational domain that remains invariant with respect to the free surface position. The transformation metrics in the (ξ, η) space need only be calculated once, while the computational effort required for updating the metrics in (x, y) space represents a very small fraction of the total effort. As a result the use of the predictive or explicit methods results in negligible savings in terms of computation time.

The performance of the predictive method when applied to three dimensional problems is not quite as impressive. However, it continues to offer a significant improvement over the explicit method. It has been successfully implemented as the predictive step of a two-step, predictive-corrective algorithm which will be presented in conjunction with the three dimensional model.

4.4.4 Free Surface Position at the Contact Point

The position of the free surface is determined by the motion of fluid particles that lie on it. At the contact points, which are defined by the intersection of the free surface with the container walls, the velocity of the fluid is assumed to be equal to zero in accordance with the no-slip condition. As a result of the no-slip boundary condition the free surface becomes *pinned* at the walls. This leads to the formation of *thin film like regions* along the walls which tend to cause resolution problems for the numerical method.

Although this film formation may be a realistic effect contributing to the mechanics of motion for the contact line it is also very difficult to describe. Once these regions develop, a local embedded grid is usually required for the solution of the equations in these regions. Furthermore, the precise physics which governs the motion of a contact line is not yet well understood. It is more than likely that the motion of a contact

line can not even be fully described in terms of continuum mechanics. An asymptotic boundary layer rescaling of the equations in this region does not alleviate the problem since a physical model for the *slipping* of the contact line would still be needed. Due to the lack of such a physical model for the description of the flow in this region it becomes necessary to use some form of an approximation technique in determining the position of the free surface at the wall.

Several techniques have been investigated for the approximation of the free surface position at the contact points. The purpose of this investigation was to identify suitable methods that can be used for the approximation, and more important, to ascertain the overall effect of these approximations on the dynamics of the problem. Based on a control volume approach, approximations for the free surface position have been derived and tested using mass, momentum, and energy conservation principles. Extrapolation techniques have been used to approximate the wall position of the free surface from interior values. Methods that enforce a specific behavior for the free surface profile at the wall, such as a zero slope approximation, have also been considered.

Each of these types of methods provided approximations which exhibited varying degrees of success. Methods that were derived from a control volume approach tended to reinforce the viscous velocity profile near the wall, and thus lead to the formation of film like regions. Approximations based on extrapolation methods appeared to work somewhat better. A second order extrapolation worked reasonably for a rising surface, but failed to work as well for a falling surface which appeared to be more prone to film formation. Extrapolations of higher order lead to the formation of more profound film regions. The formation of film like regions can be effectively eliminated by the use of methods that prescribe the surface profile at the wall. Methods based on zero slope and zero curvature were examined, and the zero slope method appeared to yield a physically better approximation throughout the calculations. It should also be pointed out that approximations based on methods which are prone to the formation of film regions tend to become worse under grid refinement.

There is a significant variation in the predictions for the free surface position at wall as obtained by each of these methods. However, the precise wall position of the free surface does not appear to have a strong influence on the overall dynamics of the problem. This is illustrated by the free surface profiles shown in Figure 4.11 for a case with $F_o = 0.5$, $Q = 0.2$, $U_o = 0$, $Ga = 10^{-5}$, and $Bo = \infty$. The four profiles shown in the figure were obtained using methods based on control volume mass conservation,

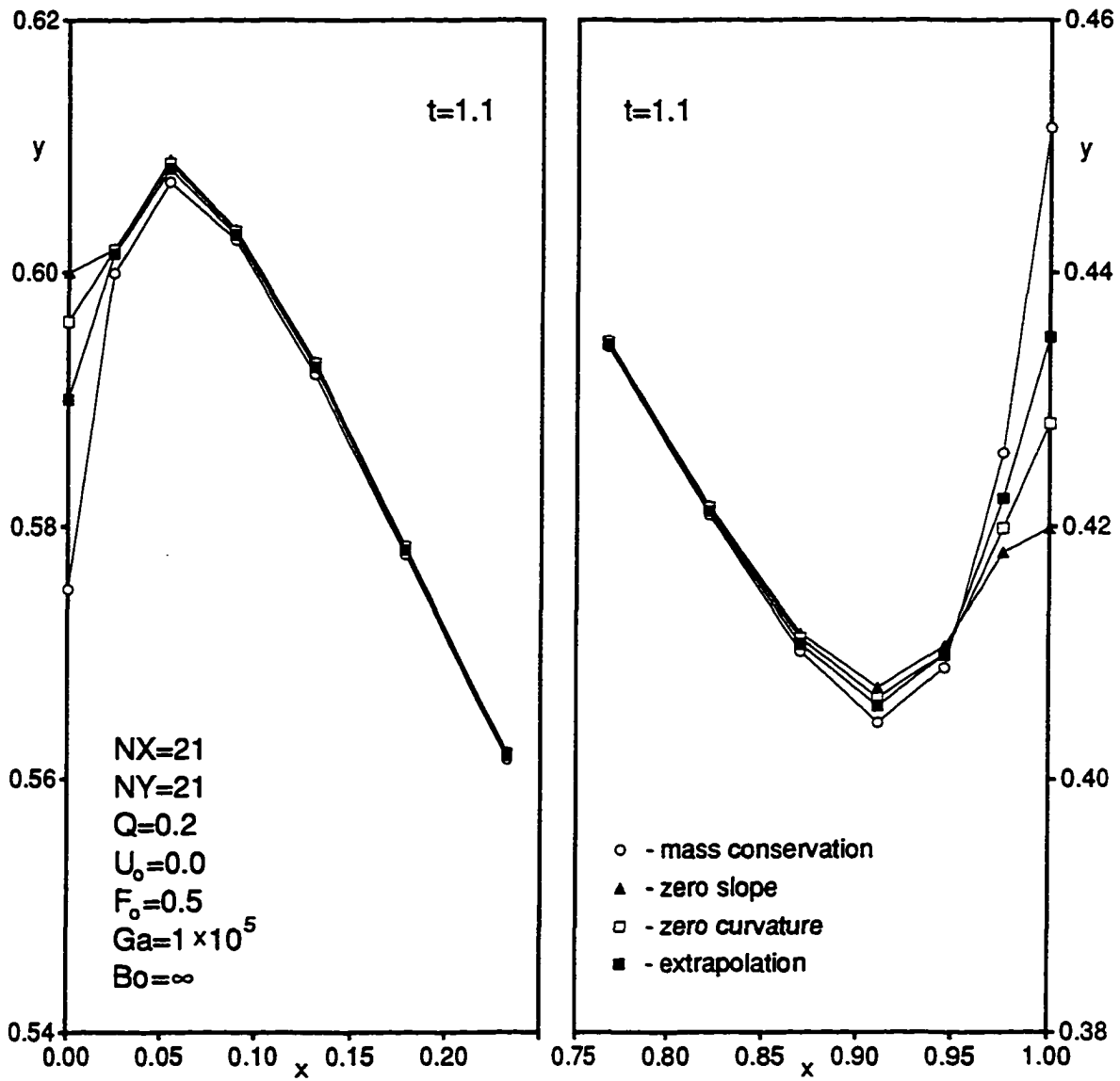


Figure 4.11: Contact Point Movement

second order extrapolation, zero curvature at the wall, and zero slope at the wall.

Despite a 5.0% variation in the value of F at the left wall, and a 6.3% variation at the right wall, the variation is significantly smaller at interior points. At the left wall, where the free surface is rising at $t = 1.1$, the variation at the grid point adjacent to the wall is only 0.38%. At the right wall, where the free surface is falling, the film like formation is more profound which causes a somewhat greater variation in the interior values of F . However, this variation remains confined to the immediate vicinity of the wall and it does not appear to have a strong influence on the value of F away from the wall. If the grid is refined at the walls, the effects of the approximation remain confined to the same number of grid points. As a result, under grid refinement, control volume and extrapolation type methods lead to increasingly steeper free surface profiles. In contrast, the zero slope approximation yields increasingly smoother profiles under grid refinement.

Methods that capture the film formation are significantly slower and more difficult to implement than methods which prescribe the shape of the free surface at the wall. Since the effect of these approximations on the dynamics of the liquid away from the wall is small, the zero slope approximation has been implemented for the determination of the free surface position at the contact points. This choice is based on the overall robustness and computational efficiency of the zero slope approximation.

4.4.5 Pressure Solution

A comparison between the Artificial Compressibility Method (ACM) and the Pressure Poisson Method (PPM) has been carried out as part of an investigation to ascertain the efficiency of schemes that are based on the coupled solution of the momentum and pressure equations. The pressure correction scheme developed in this study, was compared with an ACM algorithm which was based on the coupled iterative solution of the kinematic equation, the momentum equations, and the parabolic pressure equation as outlined in (4.15). The value of the constant parameter, c , in equation (4.16) was adjusted to obtain the fastest convergence rates for the algorithm. The results of this comparison are summarized in terms of Figure 4.12. In part (a) of the figure the comparison is in terms of the root mean square value of the residual dilatation, D_{rms} . The solution of the equations was based on a convergence criterion which required that the maximum value of dilatation, D_{max} , remain smaller than 10^{-3} . This was done to facilitate the comparison in terms of D_{rms} , since the usual convergence criterion

in terms of the normalized dilatation, \mathcal{D} , results in values of D_{max} , and consequently D_{rms} , that vary significantly throughout the calculation.

The loss of the elliptic operator from equation (4.16), which is used to calculate the pressure in the ACM method, results in average residual dilatation values for the ACM method that are larger than those obtained by the PPM method by a factor of three to four. An inspection of the spatial distribution of the dilatation, $D(x, y)$, reveals that in the core of the flow, the PPM method results in dilatation values which are smaller than the convergence constraint by nearly two orders of magnitude. The ACM method results in a more even distribution for $D(x, y)$, with core values that are only an order of magnitude smaller than the convergence constraint.

It should also be noted, that as the liquid becomes less viscous, $Ga \rightarrow \infty$, the ACM method requires the use of some form of elliptic smoothing in order to prevent the appearance of wiggles, or spatial oscillations, in the pressure field. The elliptic character of the pressure field is not enforced directly by the equation that is used to calculate it. Instead, the method relies upon the momentum equations for the implicit enforcement of the elliptic property of the pressure field. As a result, this approach begins to fail as viscous diffusion effects become weaker.

A comparison in terms of the time required for the solution of the problem is shown in part (b) of the figure. If an iterative method is used for the solution of the problem, then the ACM method appears to be slower than the PPM method by a factor of two. When the momentum and pressure equations are solved iteratively coupled, then local transient iterative errors get spread through pressure effects on to larger regions of the flowfield. This causes a significant increase in the number of required momentum iterations, and despite a decrease in the number of pressure iterations the method becomes significantly slower. That is the primary reason for the ACM being slower than the PPM method here.

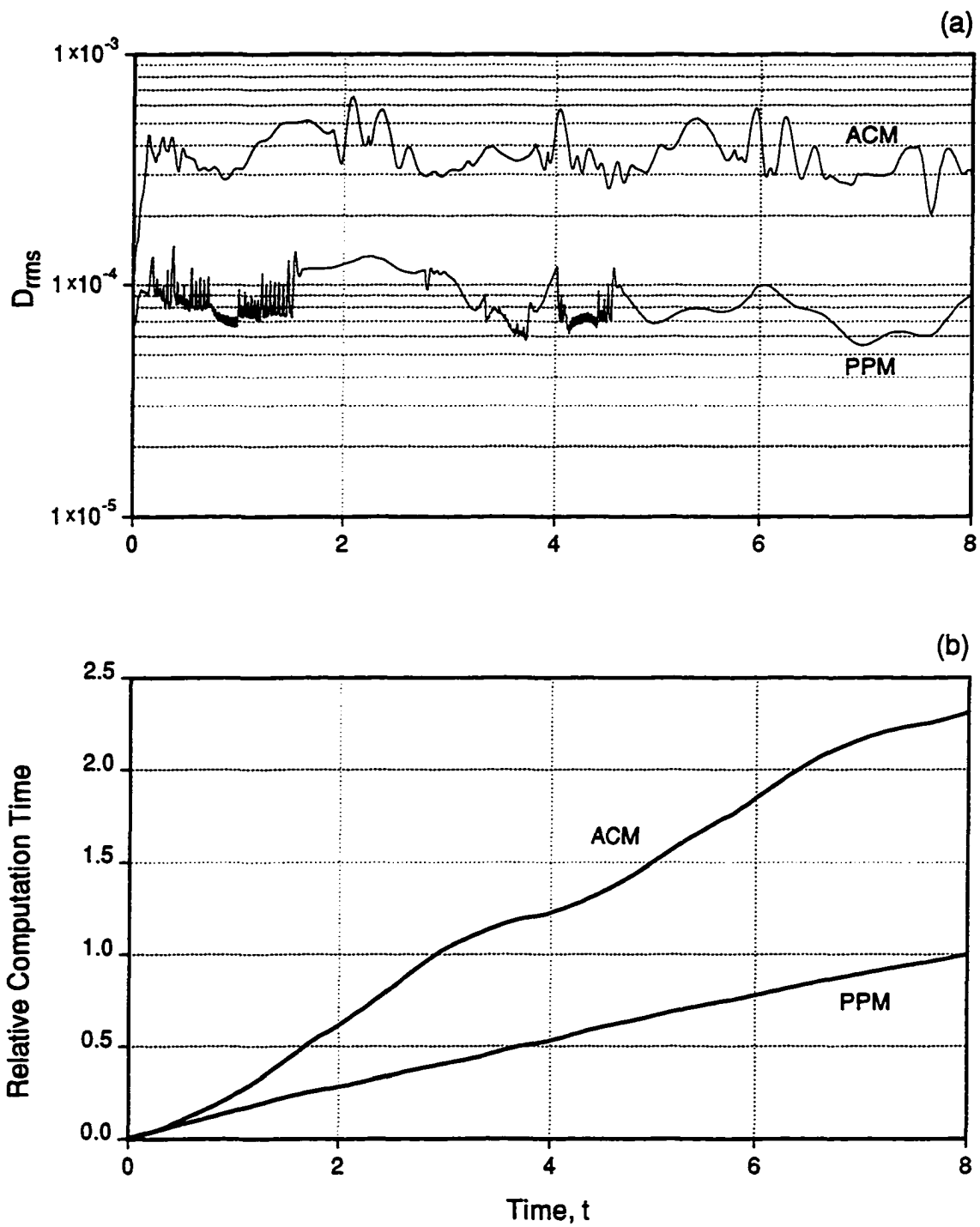


Figure 4.12: A Comparison of ACM and PPM Methods

5. RESULTS

A numerical model has been developed to investigate the effects of liquid viscosity, surface tension, forcing conditions, and the initial liquid geometry on the dynamics of the sloshing liquid. Based on the scales used for the nondimensionalization of the dependent and independent variables, five similarity parameters have been identified:

- *Liquid geometry effects* $\iff F_o$ (equation 3.25e)
- *Forcing condition effects* $\iff \begin{cases} Q & \text{(equation 3.25a)} \\ U_o & \text{(equation 3.25b)} \end{cases}$
- *Viscous effects* $\iff Ga$ (equation 3.25c)
- *Surface tension effects* $\iff Bo$ (equation 3.25d)

The dimensionless liquid aspect ratio, or initial liquid depth, F_o , represents the geometry of the problem domain. It has a strong effect on the period of oscillation and a secondary effect on the rate of viscous dissipation. The motion of the container with respect to the inertial frame of reference, and the subsequent forcing of the liquid, are described in terms of the dimensionless horizontal acceleration, Q , and the initial velocity step change, U_o . The forcing conditions have only a minor effect on the period of oscillation.

The remaining two parameters relate the physical properties of the liquid to the forcing conditions. The dimensionless Galileo number, Ga , has a dominating effect on the viscous dissipation rate and a minor effect on the period of oscillation. It is inversely proportional to the square of the kinematic viscosity, ν , and thus its value *decreases* with increasing liquid viscosity. In order to gain a feel for the value of Ga , Table 5.1 lists representative values of it for various fluids assuming a container size of $L = 0.1$ m.

The dimensionless Bond number, Bo , has a strong effect on the period of oscillation and a weaker effect on the rate of viscous dissipation. It is inversely proportional to the coefficient of surface tension, Υ , and thus its value decreases with an increasing coefficient of surface tension. However, the coefficient of surface tension for most

Table 5.1: Representative Values of Ga for Various Fluids^a with $L = 0.1$ m

Fluid	Liquid Hg	Water	Air	SAE 10W Oil	Glycerin
Ga	10^{12}	10^{10}	10^8	10^6	10^4

^aKinematic viscosities at 20° C and 1 atm.

common liquids in contact with air is generally of the same order of magnitude, with $\Upsilon \sim 10^{-2}$ N/m. Consequently, the significance of surface tension effects is dictated by factors other than the physical properties of the liquid. If either the characteristic container dimension, L , or the *effective* gravitational acceleration acting on the liquid, g , are sufficiently small then surface tension effects could become significant. Thus, it is important to consider the changes in the dynamic response of the liquid in a surface tension dominated regime. For example, the characteristic value of the Bond number, for an experiment carried out on the surface of the earth using water as the fluid and a container size of $L = 0.1$ m, is equal to $Bo = 1350$. If the same experiment was performed at middeck of the orbiting space shuttle, where acceleration jitters are small and the effective acceleration is of order $10^{-4}g$, then the value of the Bond number will be of order $Bo \sim 0.1$, which is characteristic of container size of $L = 1$ mm on the earth surface.

In an effort to carefully assess the effect of all of the similarity parameters on the dynamics of the sloshing liquid numerous cases were considered. These solutions were calculated using combinations of the similarity parameters in the range:

Liquid depth: $0.001 \leq F_o \leq 1.00$

Horizontal acceleration: $0.001 \leq Q \leq 0.40$

Initial velocity: $0.001 \leq U_o \leq 0.20$

Galileo number: $10^4 \leq Ga \leq 10^{10}$ and $Ga = \infty$ (inviscid limit)

Bond number: $10^{-4} \leq Bo \leq \infty$

The remainder of this chapter is dedicated to the presentation of sample results from these calculations. This presentation is divided into two parts. In the first part, the liquid flow is analyzed from a kinematic point of view. Detailed analysis of the velocity and pressure fields for characteristic cases will be given. In the second part, the sloshing

Table 5.2: Cases Considered for Kinematic Analysis

Case #	F_o	Q	U_o	Ga	Bo
1	0.50	0.20	0.00	10^6	∞
2	0.30	0.00	0.15	10^6	∞
3	0.50	0.20	0.00	10^{10}	∞
4a	0.50	0.20	0.00	10^8	20
4b	0.50	0.20	0.00	10^8	∞
5a	0.30	0.20	0.00	10^7	∞
5b	0.50	0.20	0.00	10^7	∞
5c	0.80	0.20	0.00	10^7	∞

liquid is analyzed as a *dynamical system*. The response of this system to the various parameters will be carefully examined, and the results of a parametric study, focusing on the period of oscillation and the viscous dissipation rate, will be presented.

5.1 Kinematic Description of the Liquid Sloshing

The motion of the sloshing liquid within the moving container is considered here. Using a combination of velocity, pressure, and vorticity plots the flowfield is carefully analyzed from a kinematic perspective. Information on the transient free surface position will also be provided. To ascertain the effects of the various similarity parameters on the kinematic response of the sloshing liquid a total of eight cases will be considered. All of these cases are identified and summarized in Table 5.2.

The first case shown in Table 5.2, Case 1, is used to analyze the flow which occurs in response to a sudden container acceleration. Furthermore, based on the value of the Galileo number used in this case, $Ga = 10^6$, significant viscous effects are present. The transient decay of the flow towards a steady state condition is examined. The response of the liquid to an impulsive container start is examined in Case 2. Changes which occur in the flowfield as the liquid becomes less viscous are examined by comparing Case 3, for which $Ga = 10^{10}$, with Case 1. The effects of surface tension on the flowfield are analyzed by comparing the solutions of Cases 4a and b. The effect of the initial liquid depth on the flowfield is analyzed by comparing the velocity profiles obtained using different values of F_o as indicated in Cases 5a, b, and c.

5.1.1 Case 1: Liquid Flow in an Accelerating Container

The case under consideration here, Case 1, is used to examine the kinematic response of the liquid to a sudden container acceleration. The dimensionless parameters which describe Case 1 are listed in Table 5.2. Based on this set of similarity parameters, this case is representative of the sloshing of a viscous liquid, such as SAE 10W oil, in a container of characteristic dimension $L \approx 0.1 \text{ m}$.

The step change in the acceleration of the container at $t=0$, causes an *instantaneous* adjustment in the hydrostatic pressure field which existed for $t < 0$. As a result, the liquid is set into motion by the action of unbalanced surface and body forces. The transient evolution of the flowfield for this case is depicted in Figure 5.1. Here, the velocity vector is plotted in terms of its components, $\vec{V} = u\vec{i} + v\vec{j}$, at selected time intervals. At time $t=0$, the fluid is still motionless. This is shown in Figure 5.1(a) where the velocity vectors have been reduced to points. Note that Figure 5.1(a) also provides some information on the distribution of the grid used for the solution of Case 1. Approximately one fourth of the total grid points are visible since the velocity vectors are shown only at odd rows and even columns of the grid. For $t > 0$, the magnitude of the velocity increases and a distinct flow pattern begins to emerge. The fluid moves from the right to the left side of the container with the strongest flow occurring along the free surface. The nearly horizontal flow which exists near the centerline of the container, $x \approx 0.5$, turns into nearly vertical flow along the two container side walls. The free surface begins to rise along the left wall and to fall along the right wall. By $t = 0.40$, this pattern has been well established. Viscous shear layers have developed along each of the container walls. As a result, the motion of the free surface along the side walls is being retarded.

At time $t = 0.90$, the liquid is approximately in a state of maximum kinetic energy. Nearly 11% of the available energy of the system, E_A (see equation 5.4b), has already been dissipated by this time. The free surface, which is close to its equilibrium position, given by a line of slope $-Q$, continues to rise toward a position of maximum elevation. However, as the surface rises above this equilibrium position the hydrostatic contribution to the pressure increases along the left side and decreases along the right side of the container. As a result of stronger pressure gradients opposing the *clockwise* motion of the liquid, the flow begins to decelerate. The motion of the liquid near the corners of the container, which is generally weak, becomes easily reversed. This leads to the formation of very weak regions of recirculating flow at each of the two

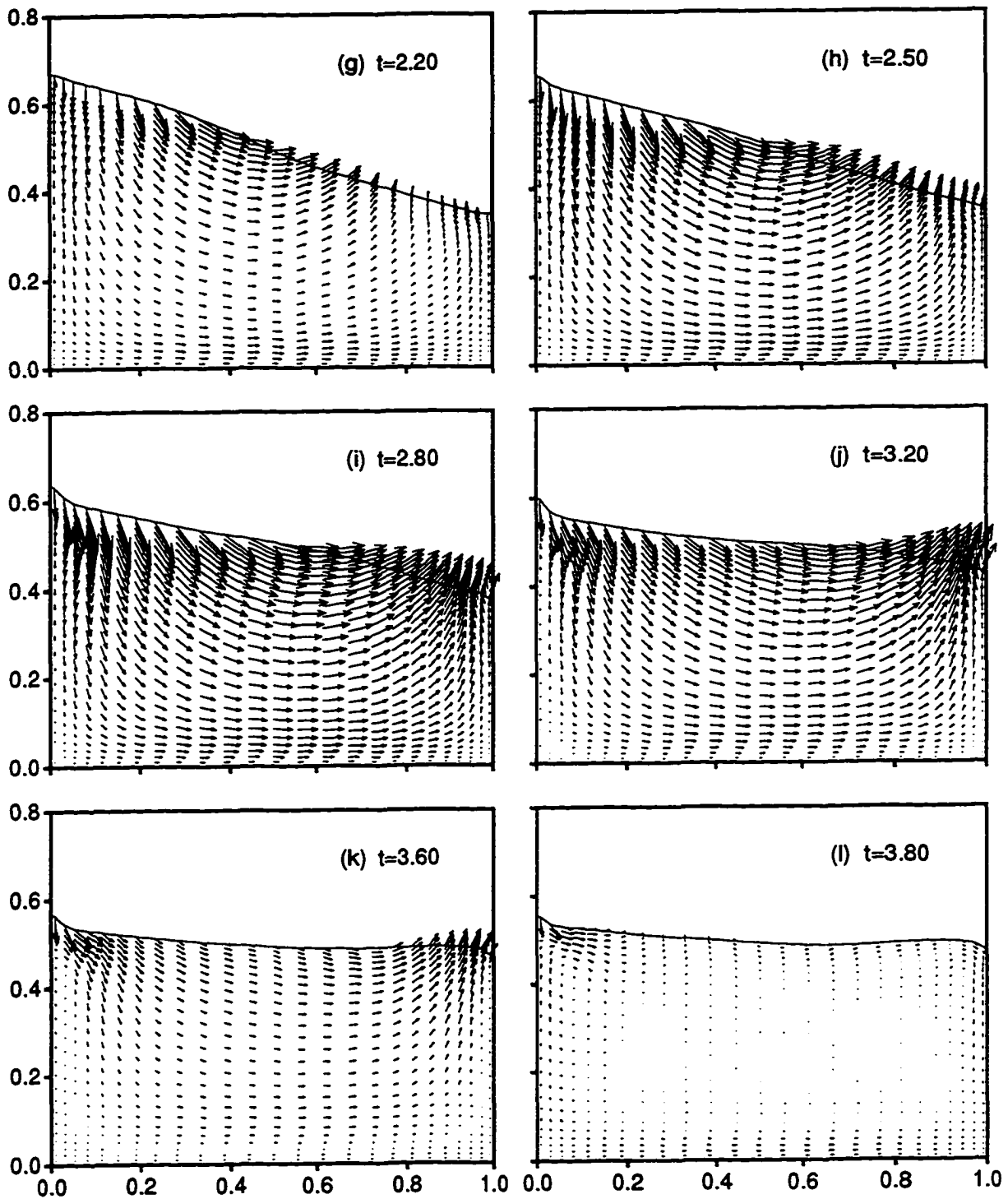


Figure 5.1 (Continued)

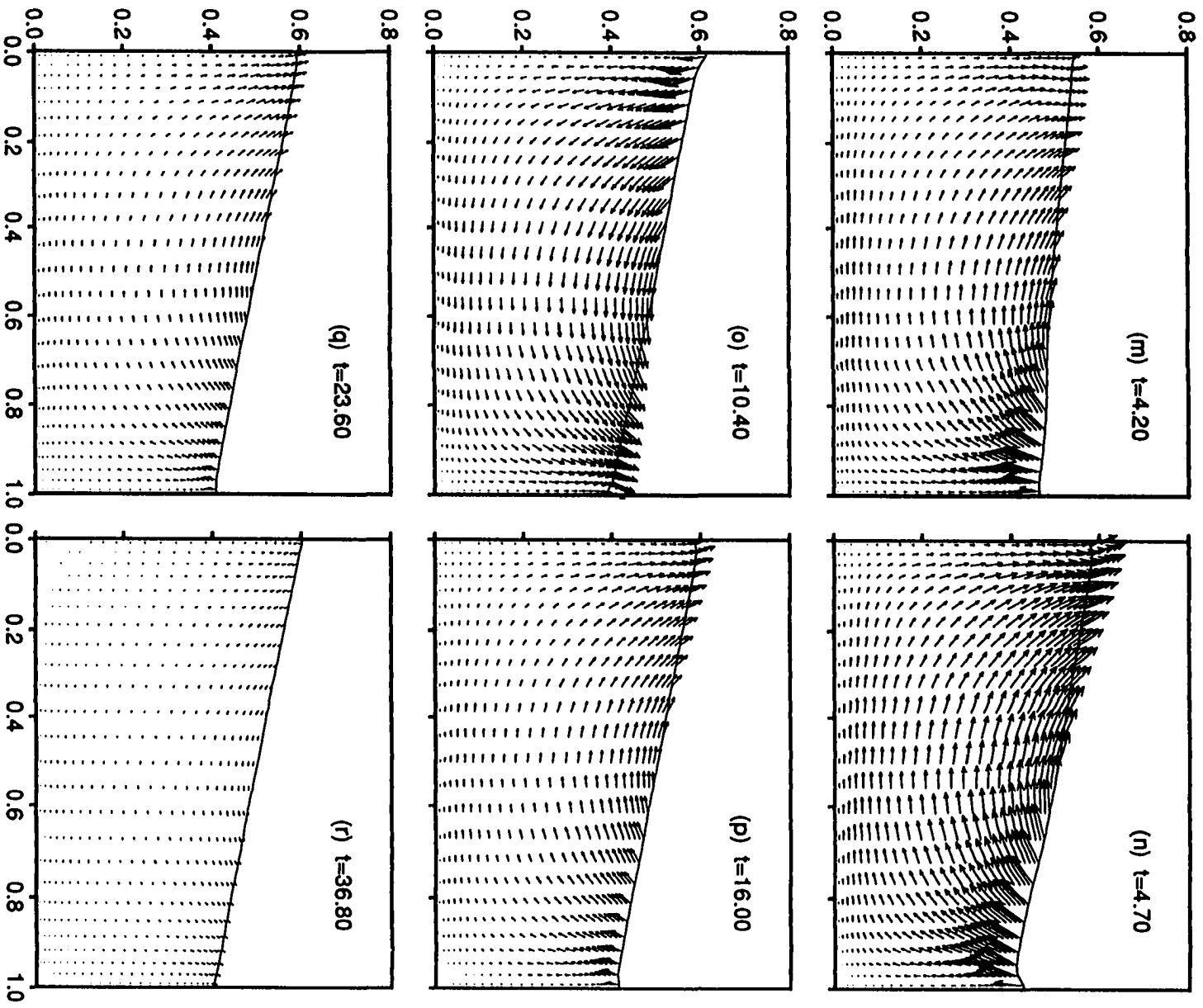


Figure 5.1 (Continued)

container corners shortly after $t \approx 0.9$. The flow in the core of the liquid continues to decelerate and by $t = 1.60$, the recirculating flow regions, although they are still weak, they have grown in size and merged along the bottom container wall. In Figure 5.1(f), $t = 1.90$, the free surface is very close to a position of maximum elevation. The pattern of *clockwise* flow which existed earlier has now been significantly altered. The flow in the core of the liquid is fairly weak. The strongest flow occurs at the right contact point. Here, the free surface whose fall along the wall has been slowed down by viscous drag, is now in the process of catching up. The reversed, *counterclockwise* flow, has gained more strength and it now extends along the entire solid boundary.

The first half cycle of the sloshing process, where the liquid rises from its initial horizontal position to a position of maximum elevation, has been depicted in Figures 5.1(a-f). Figures 5.1(g-l) depict the preceding sequence of events in reverse order as the liquid descends back toward its initial position. By time $t = 2.20$, a well defined *counterclockwise* flow pattern has emerged as the liquid continues to fall toward its equilibrium position. At $t \approx 2.80$, the flow is once again near a state of maximum kinetic energy. The available energy of the liquid has been further reduced by viscous dissipation to approximately 71% of its original value. Once again, recirculating flow regions develop at the two corners, they grow in size and merge along the bottom wall by $t \approx 3.60$. In Figure 5.1(l) the liquid has just completed its first period of oscillation. The strongest flow occurs once again along the boundaries. The effect of viscous drag can now be seen at the left contact point. A clockwise flow pattern gets reestablished by $t = 4.20$, and as the liquid reaches the next state of maximum kinetic energy at $t \approx 4.70$, nearly 46% of its available energy has been dissipated.

Figures 5.1(o-p) depict the flowfield at later times. In each of these figures the liquid is a state of maximum kinetic energy. At $t \approx 10.40$, the liquid is in the process of falling towards a position of minimum elevation which will mark the completion of three cycles. Viscous dissipation has increased to nearly 75%. Having completed four full cycles, the liquid is once again rising at $t = 16.0$ with approximately 12.5% of its original energy left. The available energy is reduced to about 4.8% by $t \approx 23.60$, with the fluid rising after the completion of six full cycles. At $t = 36.80$, the liquid is in the process of falling toward a low elevation position for the tenth time. After nearly ten periods of oscillation less than 0.1% of the original energy remains in the system. The global clockwise-counterclockwise pattern which existed earlier is no longer clearly evident. The flowfield is now dominated by local regions of weak free surface flow as

minor adjustments in the free surface position take place.

The pressure field associated with Case 1 is depicted in Figure 5.2 in terms of a series of contour plots. The spacing between adjacent isobars is $\Delta p = 0.02$. The initial pressure distribution at $t = 0$, immediately following the application of the horizontal acceleration, Q , is shown in Figure 5.2(a). Note that the horizontal hydrostatic isobars which existed prior to the application of the forcing have instantaneously adjusted to the apparent acceleration. This initial pressure distribution is dictated by the geometrical configuration of the liquid. A *flat stationary* free surface can not support any pressure gradients along it. Thus, the free surface remains at zero pressure which in turn causes the bending of the isobars, especially those closest to the surface. With the pressure rising at the left half and dropping at the right half of the container the liquid is set into motion. Note the effects of viscous drag on the free surface profile next to the container walls. They become especially profound for a *falling* free surface. As viscous drag acts to retard the motion of the free surface in the vicinity of the wall, a small triangular region of slight negative pressure appears next to the receding contact point. These regions of negative pressure, seen in Figures 5.2(b-f) for the right wall and Figures 5.2(g-j) for the left wall, are caused by the very shape of the free surface profile at the wall. Note that the negative pressure levels encountered here are very small and they remain well above the critical cavitation pressure. Although their overall effect on the interior flowfield is negligible, they play an important role in the local dynamics of the contact point. A receding free surface is generally curved upwards at the wall primarily due to viscous effects. Note for example the free surface profile at the right wall in Figure 5.2(c). The formation of a negative pressure region immediately beneath it exerts a normal suction force on the free surface. As a result of this negative pressure force, the free surface tends to become increasingly curved at the wall. This leads to the formation of a thin film region along the wall. Although this sequence of events appears to be physically meaningful, and possibly a viable mechanism leading to film formation, it also leads to the various numerical difficulties which have been discussed in section 4.4.4.

Once the sloshing of the liquid begins, $t \geq 0$, the pressure field remains for the most part qualitatively unchanged. The liquid experiences a leftward body force due to the apparent acceleration, Q . The pressure field exerts surface forces which are generally directed to the right. The magnitude of the surface forces increases as the liquid rises along the left wall. Figure 5.2(c) depicts the pressure field at $t = 0.90$. Here, the liquid

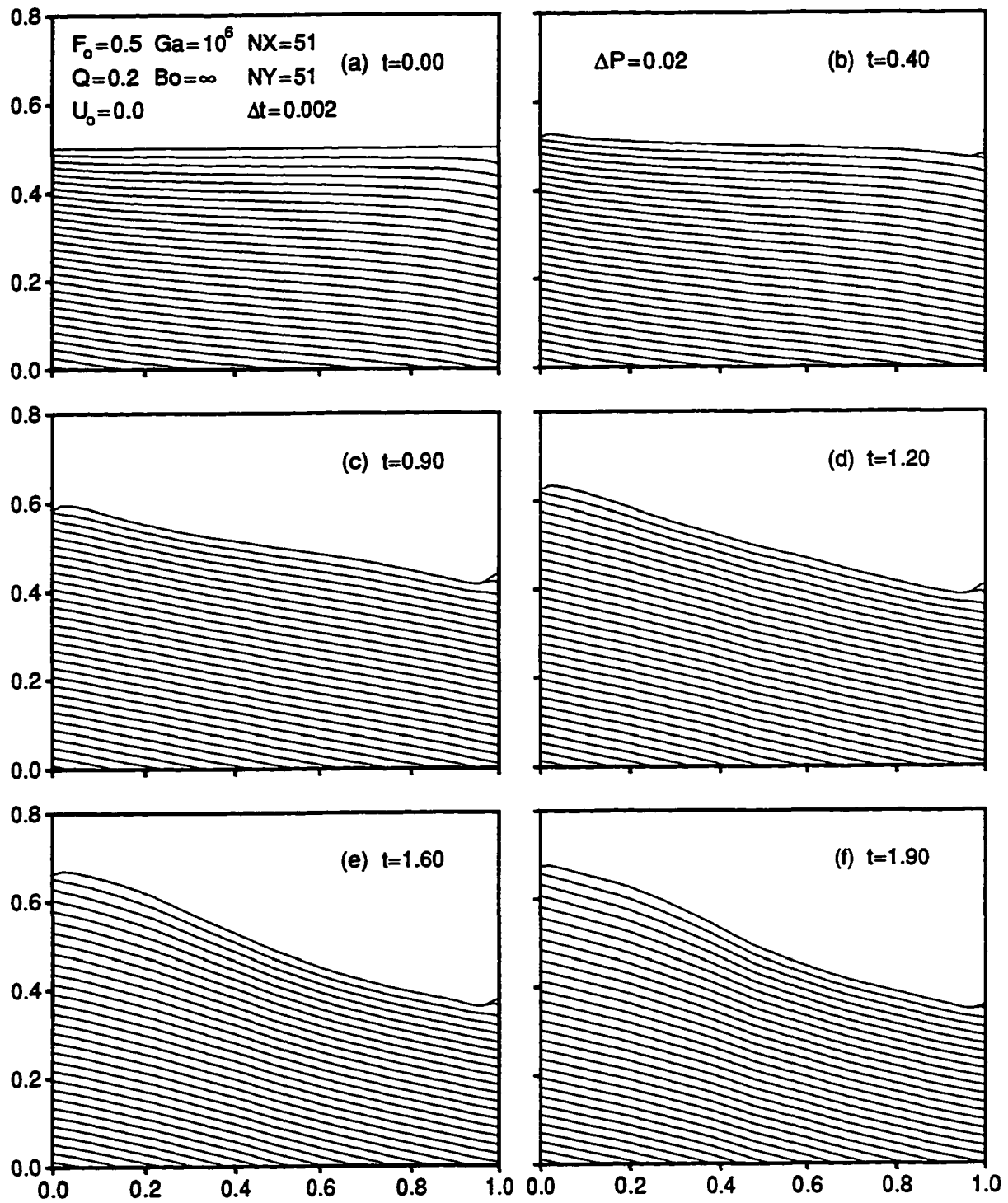


Figure 5.2: Pressure Field for $Q = 0.2$, $F_o = 0.5$, $Ga = 10^6$, and $Bo = \infty$

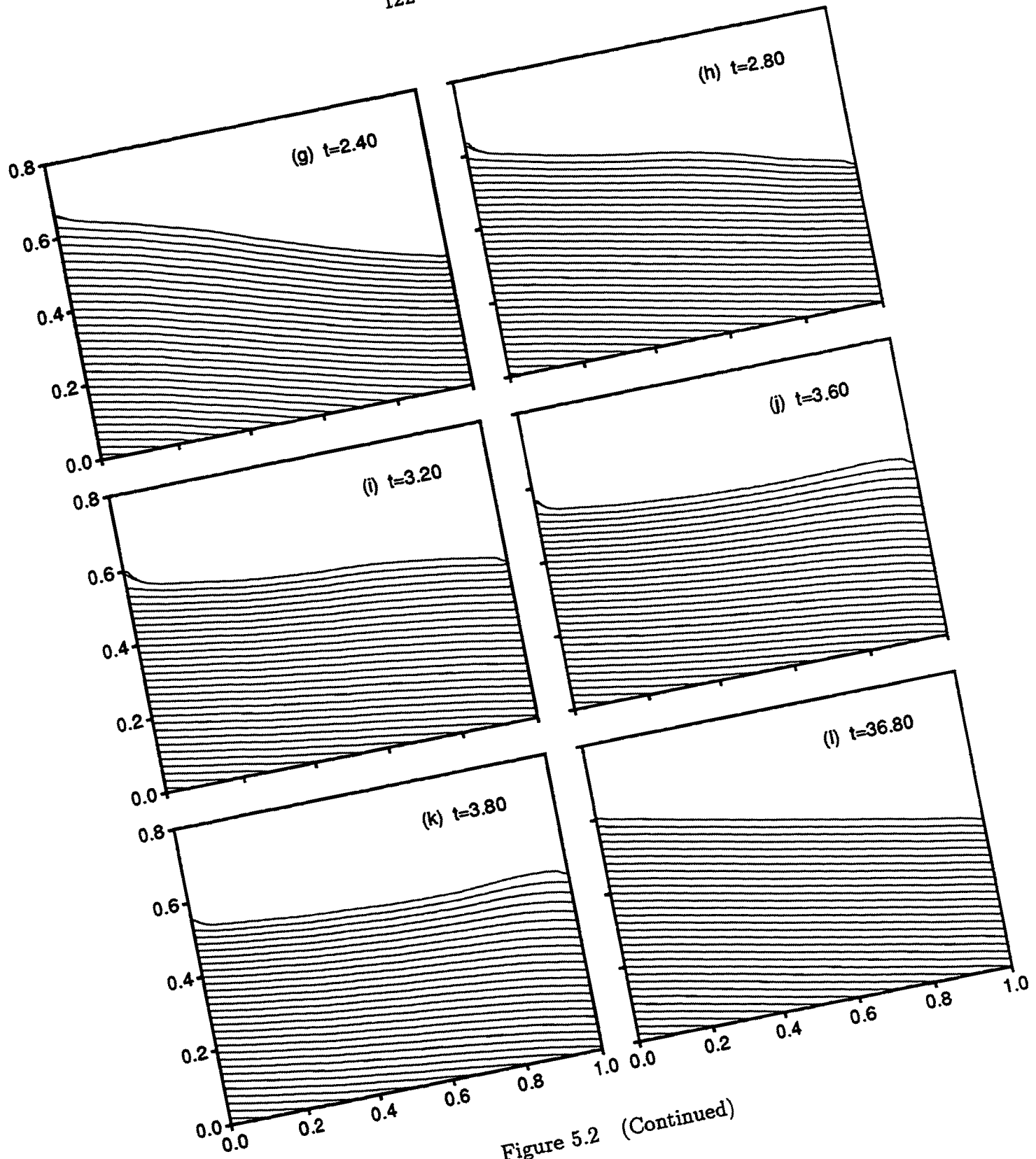


Figure 5.2 (Continued)

is in the vicinity of the equilibrium position for the first time. Note the similarity of this field with the field depicted in Figure 5.2(h) at $t = 2.80$, when the liquid is once again in the vicinity of the equilibrium position. Minor differences which exist between these two fields are confined to the vicinity of the free surface. Both of these fields look very much the like the final steady state field, depicted in Figure 5.2(l).

The sloshing of the viscous liquid of Case 1 is also depicted in terms of the series of vorticity contour plots shown in Figure 5.3. The increment between adjacent lines of constant vorticity is given by $\Delta\omega = 0.2$. Lines that correspond to values of zero vorticity are drawn as heavier (thicker) lines in the figure. The direction of rotation for some of the interior points is also indicated on the figure. The vorticity field is determined according to the definition given in equation (3.35b). Based on this definition, positive values of ω are indicative of a counterclockwise (CCW) rotation while negative values of ω are indicative of a clockwise (CW) rotation.

Initially, the liquid is free of any vorticity and in a state of hydrostatic equilibrium. The application of the horizontal acceleration, Q , disturbs this hydrostatic equilibrium and causes the liquid to begin to accelerate under the action of unbalanced body and surface forces. As the liquid begins to move, vorticity is being generated at each of the container walls due to viscous shear. Vorticity is also being generated along the free surface. Recall that the free surface of a viscous fluid *must* generate vorticity if it undergoes a change in either its shape or its orientation. The *effective normal convection velocity* along each of the domain boundaries, including the free surface, is zero. Thus, viscous diffusion becomes the sole mechanism through which vorticity from the boundaries can enter the interior of the flowfield. The diffusion of vorticity from the boundaries into the adjacent liquid leads to the formation of viscous boundary layers, which are characterized by a high concentration of vorticity. The core of the flowfield remains for the most part irrotational until vorticity from the boundary layers gets further diffused or convected into the interior of the flowfield.

Figures 5.3(a-f) depict the flowfield for approximately the first half cycle of sloshing. The free surface, starting from its initial horizontal position at $t = 0$, rises along the left wall toward a position of maximum elevation which it reaches shortly after $t = 1.80$. The CW motion of the liquid adjacent to the walls early in the sloshing process results in the formation of regions of positive circulation each of container walls. A much weaker region of negative circulation also forms along the free surface. The viscous boundary layers and the nearly irrotational core of the flowfield are clearly

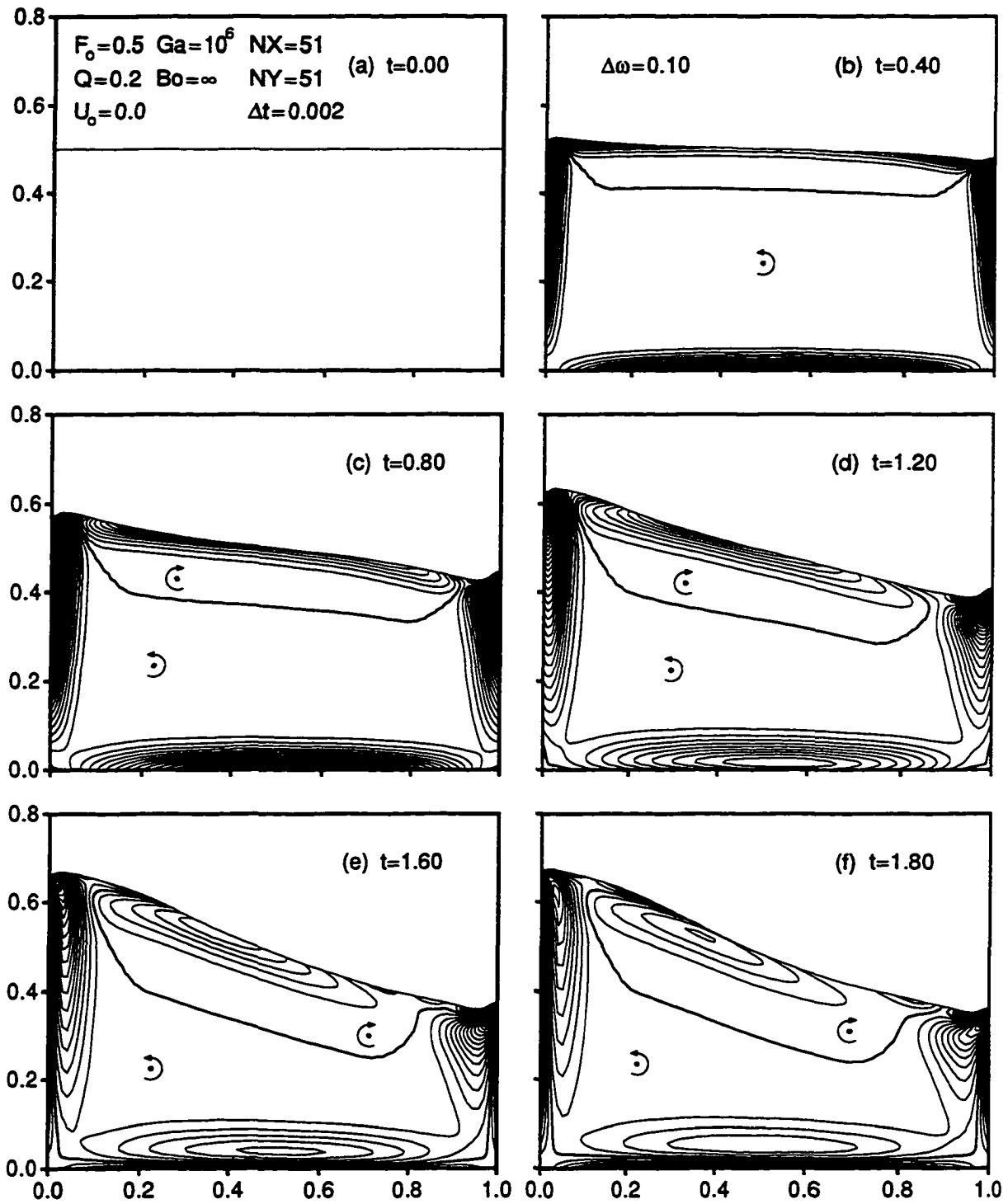


Figure 5.3: Vorticity Field for $Q = 0.2$, $F_o = 0.5$, $Ga = 10^6$, and $Bo = \infty$

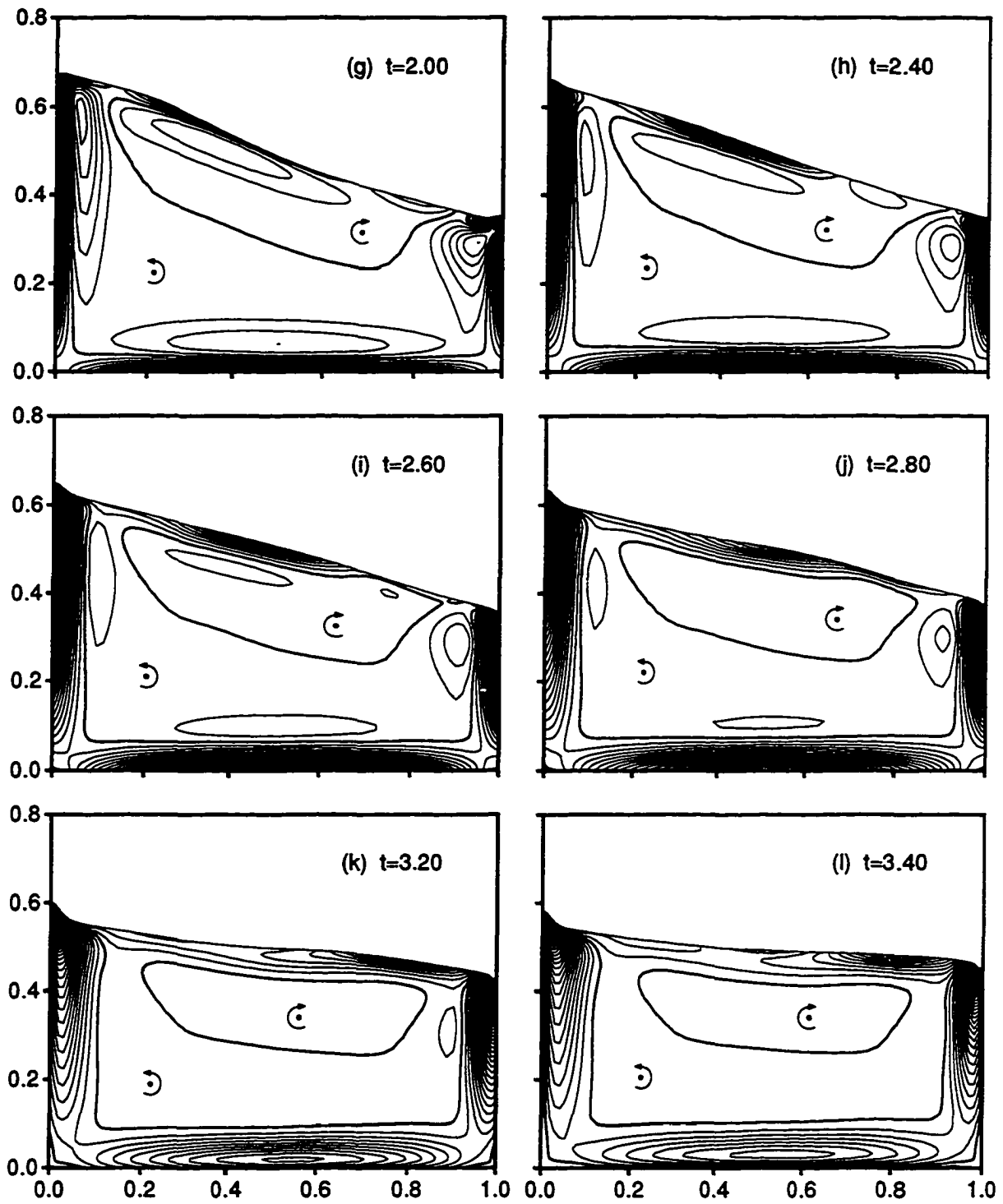


Figure 5.3 (Continued)

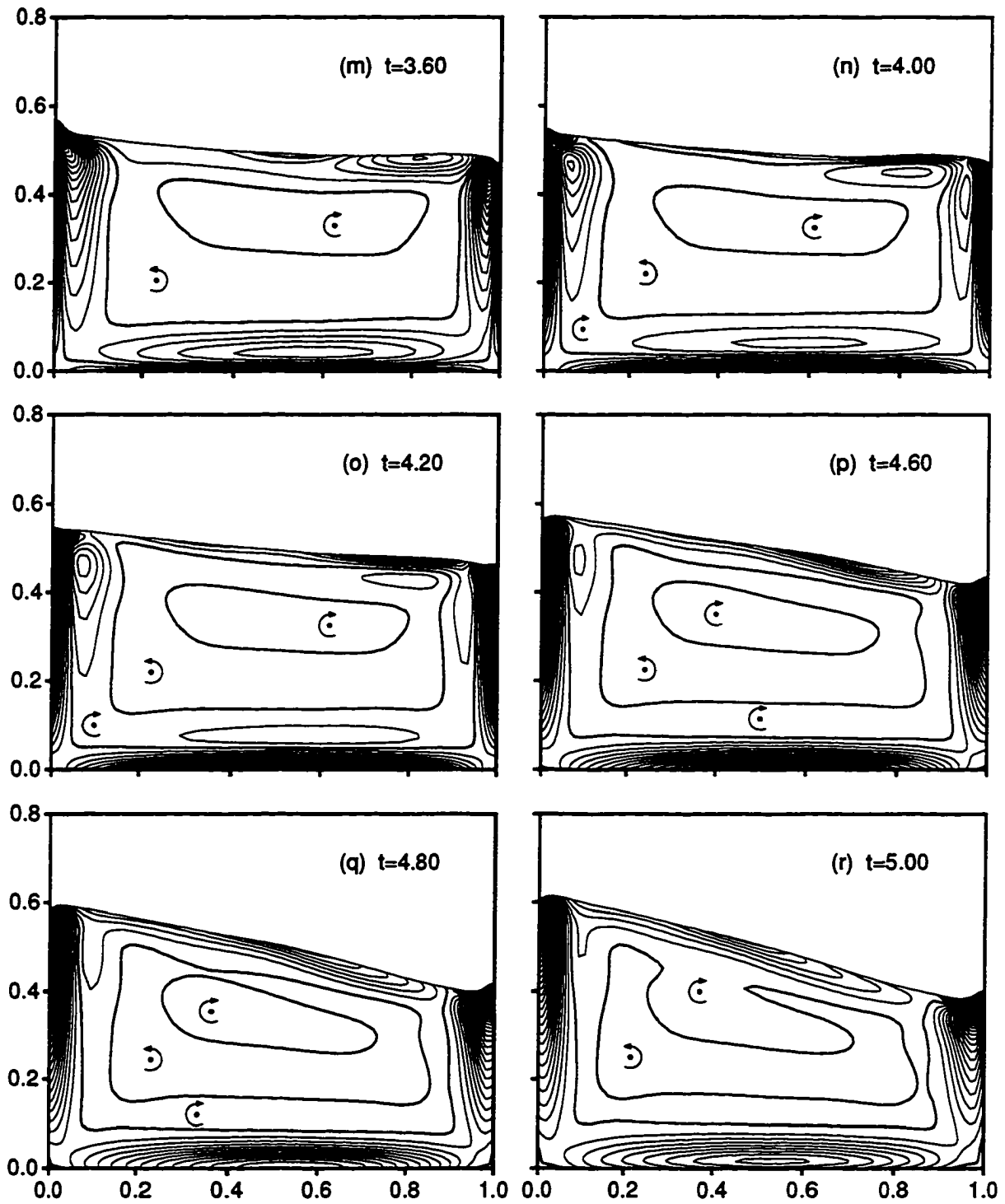


Figure 5.3 (Continued)

shown in Figure 5.3(b) for $t=0.40$.

The secondary recirculating flow and its interaction with the primary flowfield are also very nicely illustrated in the figure. By $t = 1.20$, small regions of negative vorticity are clearly visible at each of the container corners. These recirculating flow regions form as the net horizontal acceleration experienced by the liquid changes from a negative to a positive value at $t \approx 0.9$. Note that as the secondary negative circulation at the corners continues to increase in size and strength, the strength of the primary positive circulation decreases. By $t = 1.60$, the regions of secondary circulation have nearly merged along the bottom wall, and they have greatly extended upwards along the side walls. The negative circulation along the free surface has also decreased in strength, with secondary regions of positive circulation starting to develop near the two surface ends. By $t = 1.80$, the secondary circulation along the walls has gained further strength and grew in size covering the entire wall area. The initial regions of positive circulation have been dislodged from the walls and move further into the interior. The left region of secondary free surface circulation grows in strength and size and by $t = 2.60$ has completely dislodged the primary region of negative circulation. This sequence of events is repeated as the free surface of the liquid returns back toward its original horizontal position. Two new regions of positive circulation grow out of the two container corners and by $t = 3.60$ they displace the regions of negative circulation from container walls. Similarly, a region of negative circulation grows out of the right side of the free surface, dislodging the primary region of positive circulation shortly after $t \approx 4.0$. Thus, with each cycle of sloshing, two regions of opposite circulation are shed from each of the boundaries. They propagate into the interior of the flowfield where they get dissipated. Note that shortly after $t = 4.80$, the first region of positive circulation which was shed from the free surface merges with the second region shed from the walls, such that by $t = 5.00$ in Figure 5.3(r) these two regions become indistinguishable.

The effects of convection on the thickness of the boundary layers is also evident from this figure. For example, note that by $t = 1.20$ the boundary layer along the right wall of Figure 5.3(d) has grown somewhat thicker than the boundary layer on the left wall. Where along the right wall the diffusion process has been aided by the convection of vorticity away from the wall and into the interior of the flowfield, along the left wall the diffusion process has been opposed by the convection of vorticity into the wall.

5.1.2 Case 2: Liquid Flow in an Impulsively Started Container

The response of the liquid to an impulsive container start is examined in Case 2. For the case under consideration here, the container is filled to a dimensionless depth of $F_o=0.30$, and at $t=0$ it experiences a step change in its velocity to $U_o=0.15$. The remaining dimensionless parameters for Case 2 are listed in Table 5.2. Note that the values of the Galileo and Bond numbers used here match those used for Case 1. The magnitude of the initial sloshing energy, E_o , which is available to the liquid for this case is approximately 38% larger than the corresponding value of E_o for Case 1.

The velocity field for Case 2 is shown in Figure 5.4. Here, velocity vectors are plotted at every third row and third column of the 81×51 grid which was used for the solution of the problem. The scaling used for the plotting of the velocity vectors here is identical with the scaling used in Figure 5.1. The velocity field shown in Figure 5.4(a) was determined by the solution of the initial condition equations. The initial conditions for an impulsively started container have already been extensively discussed (section 3.2.1). As a result of the step change in the velocity of the container, the liquid experiences a pressure impulse, Π , which leads to the establishment of the non-zero velocity field shown in Figure 5.4(a) for $t = 0^+$. Note the very large initial velocities which exist at the two free surface ends near the walls. In response to these large velocities the free surface rises along the left wall and falls along the right wall at a rather rapid rate. By $t=0.40$, the free surface position along the walls is already very close to its maximum and minimum elevation values. Boundary layers have formed along each wall and are clearly visible in the figure.

The rapid rise of the free surface along the left wall results in the build up of hydrostatic pressure beneath it. As a result, the leftward liquid flow is pushed away from the wall and further into the interior of the container. At $t = 0.80$, the surface of the liquid is shown near a position of maximum elevation along the left wall and has actually just started to drop. A fairly strong leftward flow still remains in the interior of the container. The liquid reaches a state of maximum potential energy very shortly after $t = 1.00$. Even though the kinetic energy of the liquid is at a minimum state during this time the flowfield does not come to a complete halt. The very last remains of the original leftward flow pattern still exist in the interior of the container. Along the container walls recirculating flow regions have merged to form an extended region with positive circulation. Cells of localized free surface flow have also developed at the two surface ends. At the right wall the free surface position, which has been

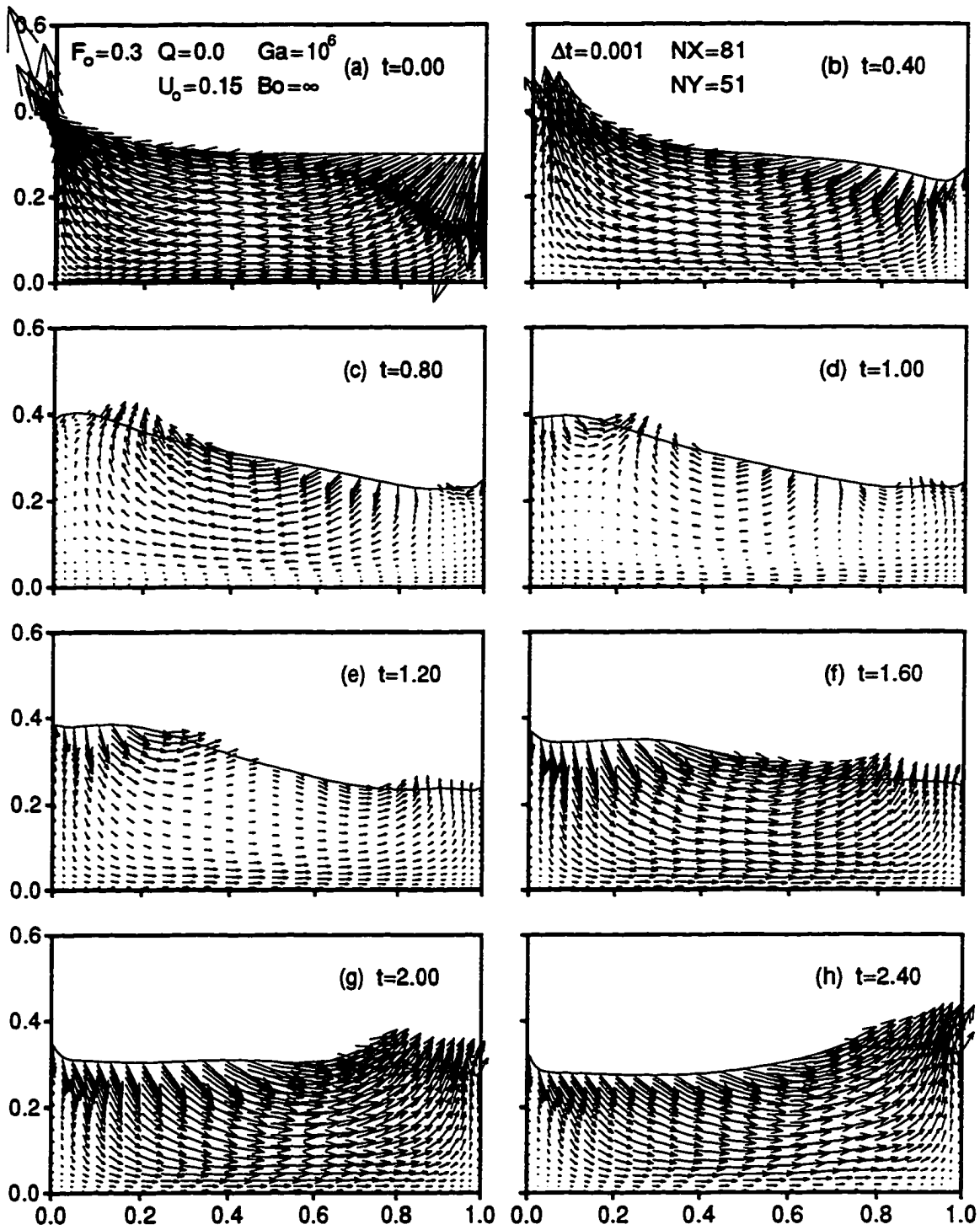


Figure 5.4: Velocity Field for $U_o = 0.15$, $F_o = 0.3$, $Ga = 10^6$, and $Bo = \infty$

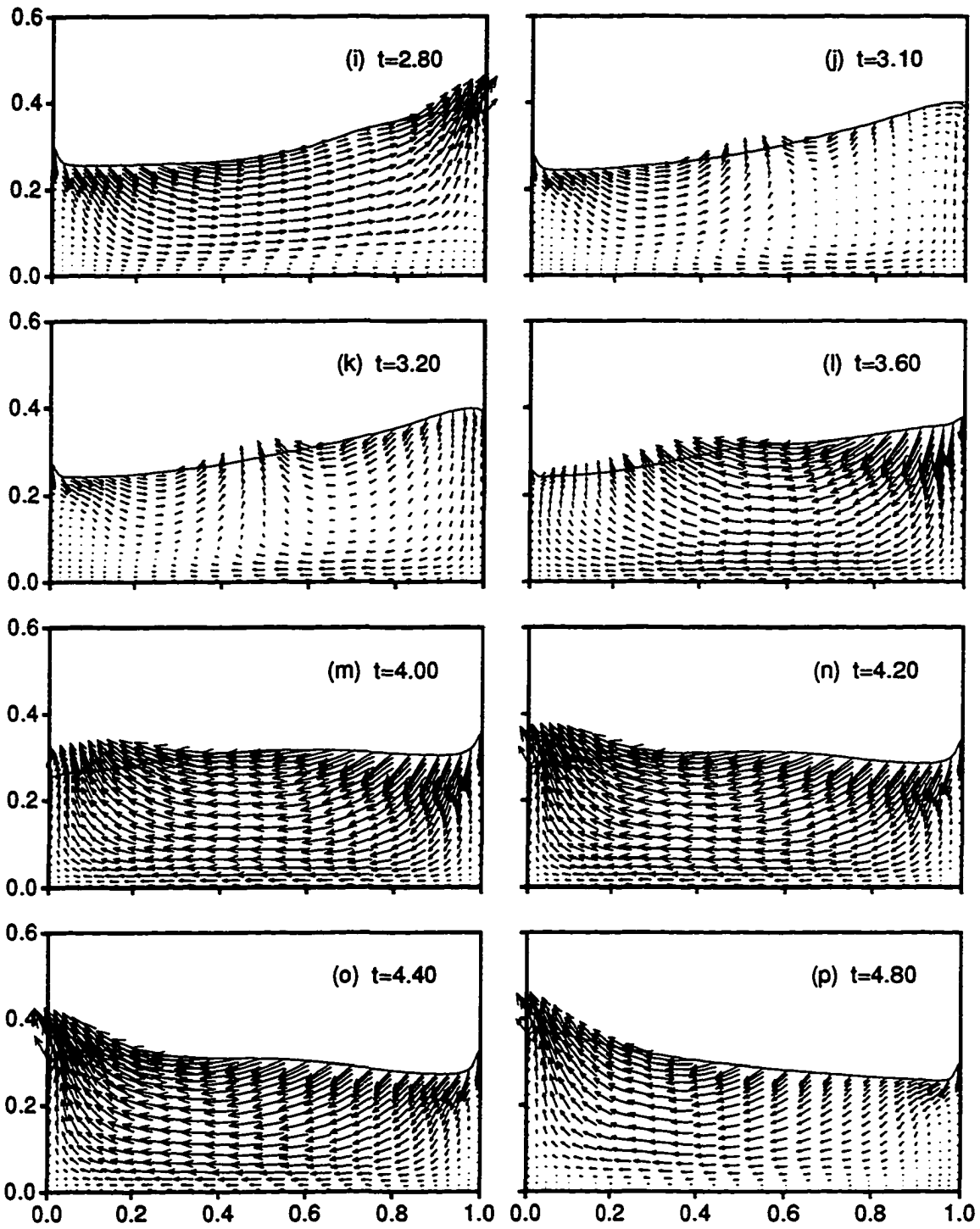


Figure 5.4 (Continued)

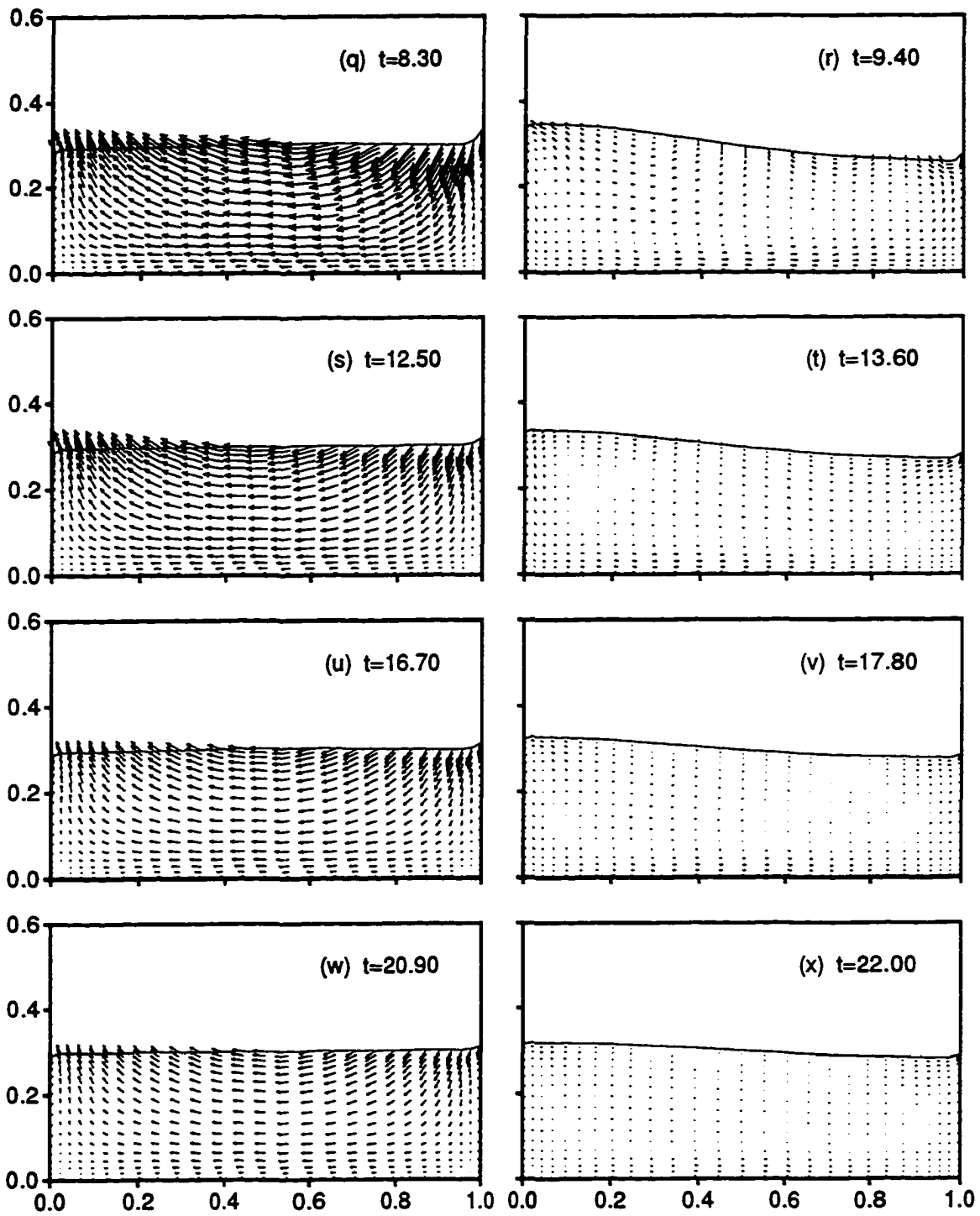


Figure 5.4 (Continued)

trailing due to viscous drag, is now in the process of catching up. Close to the left wall, where the free surface is in a position of maximum elevation, a cell of rightward flow has started to develop. As the free surface of the liquid starts to fall back toward its equilibrium position a rightward flow pattern begins to get established throughout the flowfield.

The liquid, having nearly completed the first half of a full cycle of sloshing, is shown in Figure 5.4(g) once again approaching a state of maximum kinetic energy. About 72% of the initial sloshing energy is still available at $t = 2.00$. A similar sequence of events is depicted in Figures 5.4(i-n) as the liquid rises and falls along the right wall to complete the second half of the cycle. The liquid reaches a state of minimum kinetic energy very shortly after $t = 3.10$. By $t = 4.20$, the first full cycle of sloshing has just been completed and the liquid starts to rise along the left wall with approximately 50% of its original energy left.

The effects of viscous dissipation on the flowfield are also depicted in the sequence of Figures 5.4(q-x). Note the decrease in the strength of the flowfield as well as in the elevation reached by the free surface as the available energy of the liquid continues to get dissipated. At $t = 8.30$, the flowfield is shown very near a state of maximum kinetic energy as the second cycle of sloshing is about to be completed. With approximately 26% of the initial energy remaining, the liquid rises along the left wall to reach the next position of maximum potential energy at $t \approx 9.40$. After the completion of three full cycles of sloshing at $t \approx 12.5$, the sloshing energy has dropped to under 14% of its original value and the corresponding state of maximum potential energy is reached at $t \approx 13.6$. The energy of the liquid continues to decrease, dropping to about 7.6% after the completion the fourth cycle of sloshing at $t \approx 16.70$, and to 4.1% after the completion of the fifth cycle at $t \approx 20.90$.

The transient pressure field for Case 2 is depicted in terms of a series of contour plots which are shown in Figure 5.5. The spacing between adjacent isobars is equal to $\Delta p = 0.02$. The initial pressure distribution at $t = 0^+$, which has been determined from the solution of the initial condition equations (3.31), is shown in Figure 5.5(a). Note that the initial flowfield in the interior of the container is irrotational. Thus, variations which occur across the pressure field at this time could also be determined from Bernoulli's equation.

The pressure adjacent to the left container wall increases as the liquid starts to rise above its equilibrium position. The vertical spacing between isobars that lie close

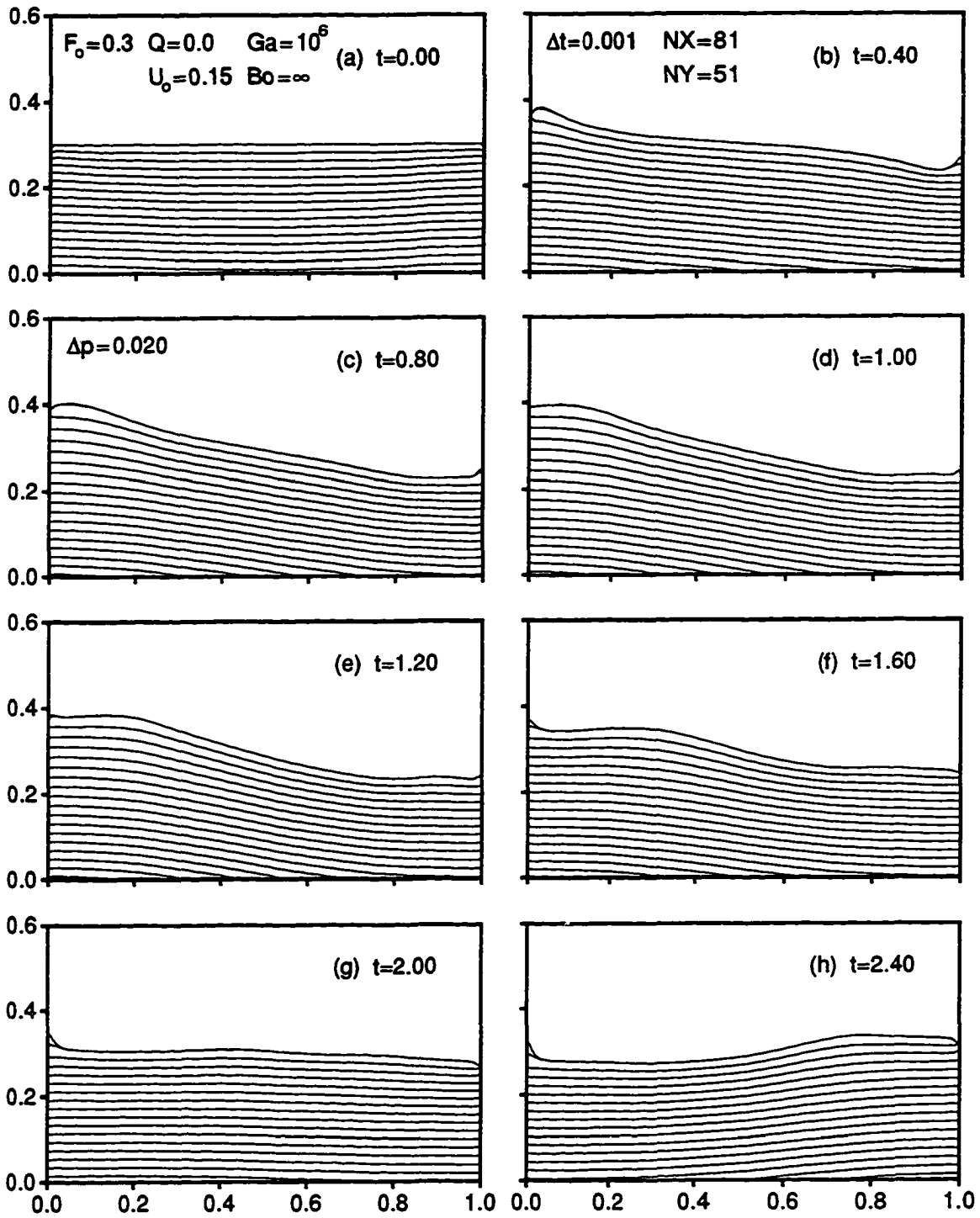


Figure 5.5: Pressure Field for $U_o = 0.15$, $F_o = 0.3$, $Ga = 10^6$, and $Bo = \infty$

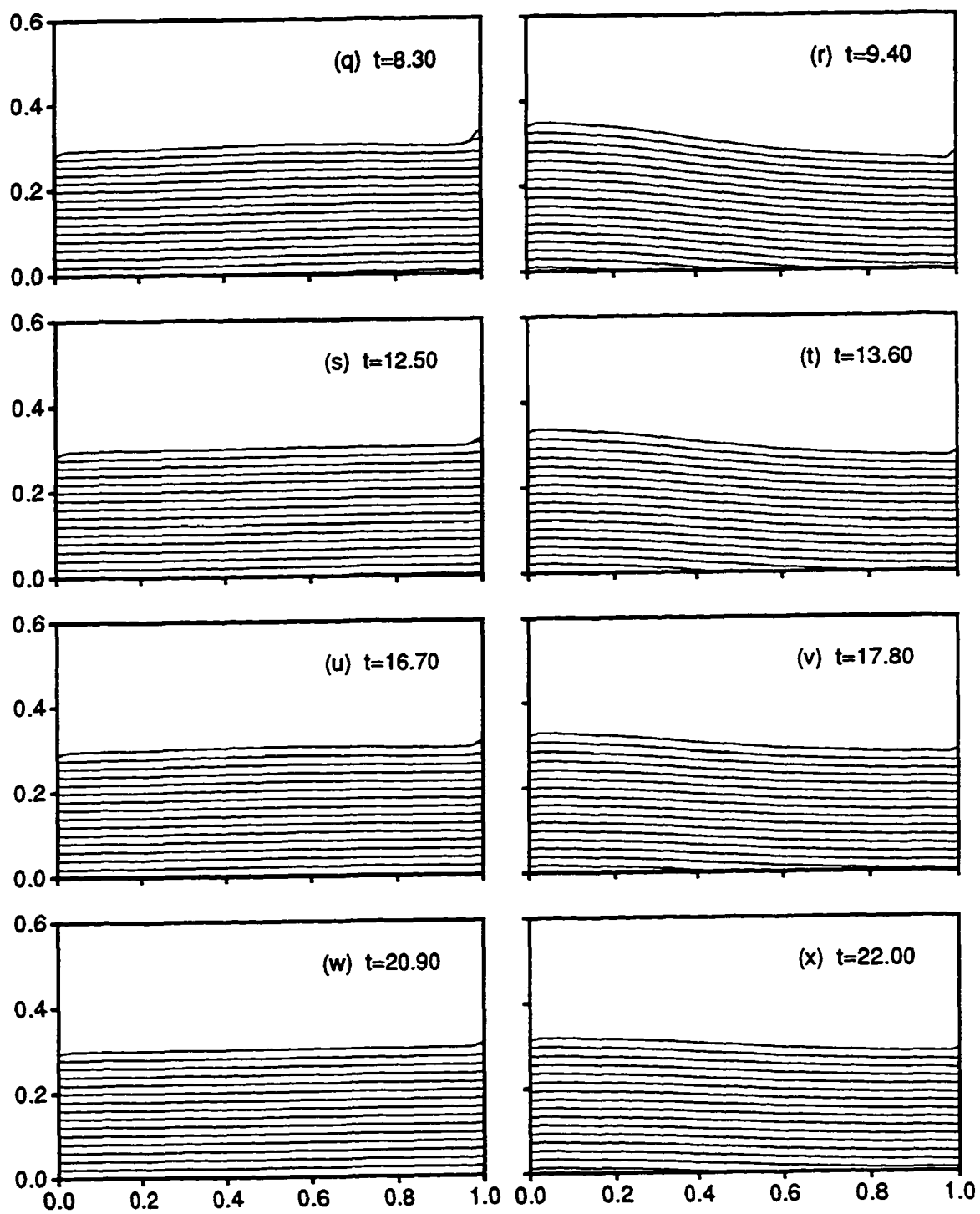


Figure 5.5 (Continued)

to the free surface also increases, indicating a decrease in the magnitude of the vertical pressure gradients which are acting on the liquid close to the free surface. As gravity acts to decelerate the upward motion of the liquid, the free surface reaches a position of maximum elevation on the left wall at $t \approx 0.80$, and then it starts to fall. Further away from the wall, the free surface continues to rise as the leftward liquid flow is redirected upwards by the pressure field.

The small regions of negative pressure which were encountered in Case 1 are also present here. These regions of slight negative pressure form underneath a receding contact point as result of the viscous drag which inhibits the fall of the free surface. They can be seen in Figures 5.5(b-c) and Figures 5.5(l-p) for the right contact point, and in Figures 5.5(f-j) for the left contact point.

Note that the pressure field of Figure 5.5 is dominated by hydrostatic contributions. This limits the amount of quantitative as well as qualitative information that can be extracted from this figure. The interaction between the pressure and velocity fields for this case can be ascertained more clearly and effectively by examining the hydrodynamic pressure distribution, $P_d = p - P_s$, where p the static pressure, and P_s is the hydrostatic component. The hydrostatic component represents the *apparent weight* of the liquid as a result of the body forces that are acting on it. The hydrodynamic pressure component is:

$$P_d = p + (F y - F_o) + Q(x - \frac{1}{2}) \quad (5.1)$$

Note that constant terms have been added to equation (5.1) such that in the limit as $t \rightarrow \infty$, $P_d \rightarrow 0$. Pressure gradients in terms of P_d represent the net acceleration experienced by the liquid as a result of both surface and body forces.

The sloshing of the liquid which occurs in response to the initial impulse experienced by the container is driven by a dynamic balance between the inertial and the hydrodynamic pressure forces, with the liquid reaching its ultimate steady state condition under the action of the viscous forces. This dynamic interaction is very nicely depicted in terms of the hydrodynamic pressure field shown in Figure 5.6. The spacing between adjacent lines of constant hydrodynamic pressure is equal to $\Delta P_d = 0.002$. A heavier (thicker) line is used to denote lines of zero pressure. In addition, regions of high (positive) and low (negative) hydrodynamic pressure are identified by the symbols located just above the free surface.

The initial hydrodynamic pressure field which exists within the container immediately after the application of the impulse is shown in Figure 5.6(a). Recall that

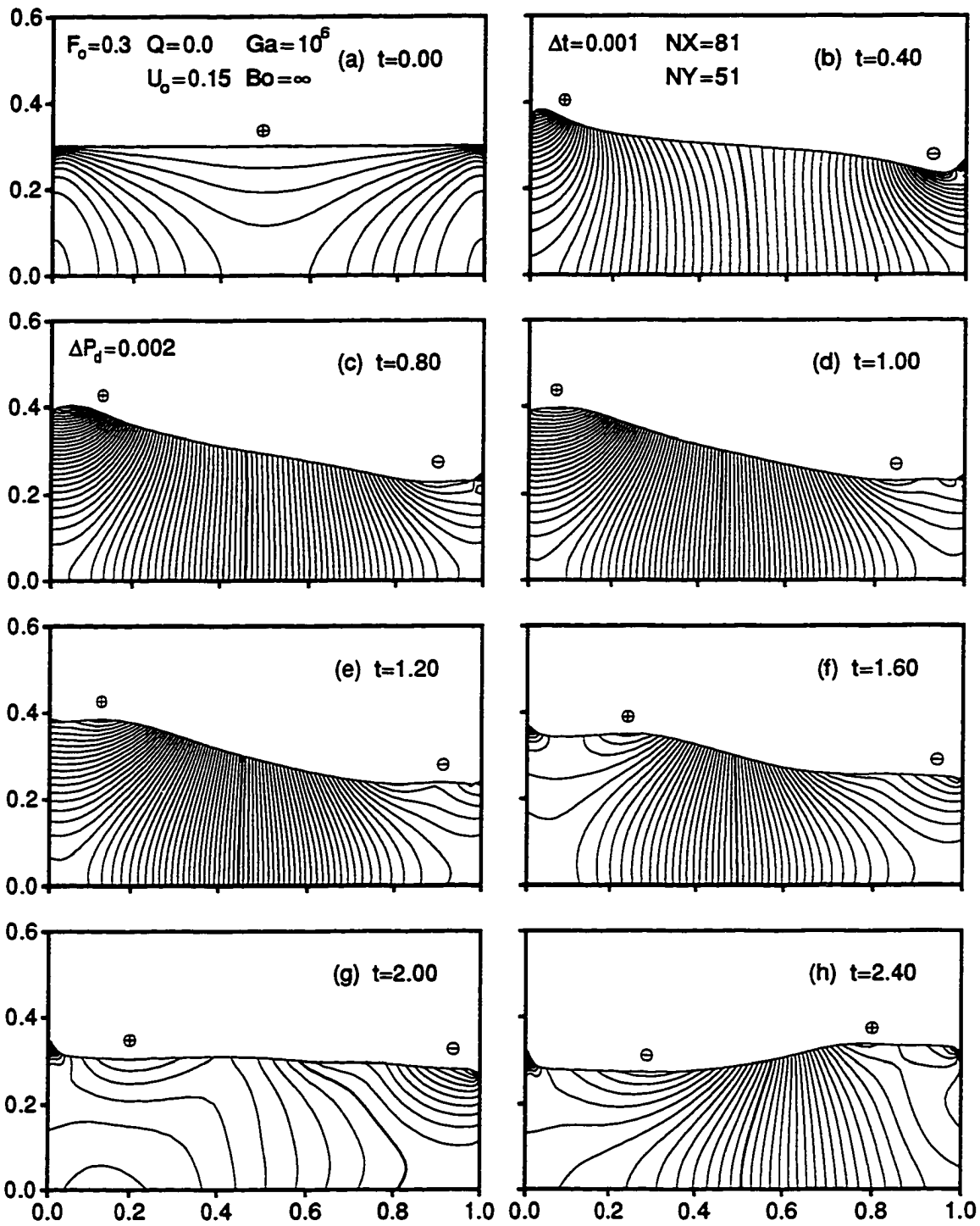


Figure 5.6: Hydrodynamic Pressure for $U_o = 0.15$, $F_o = 0.3$, $Ga = 10^6$, and $Bo = \infty$

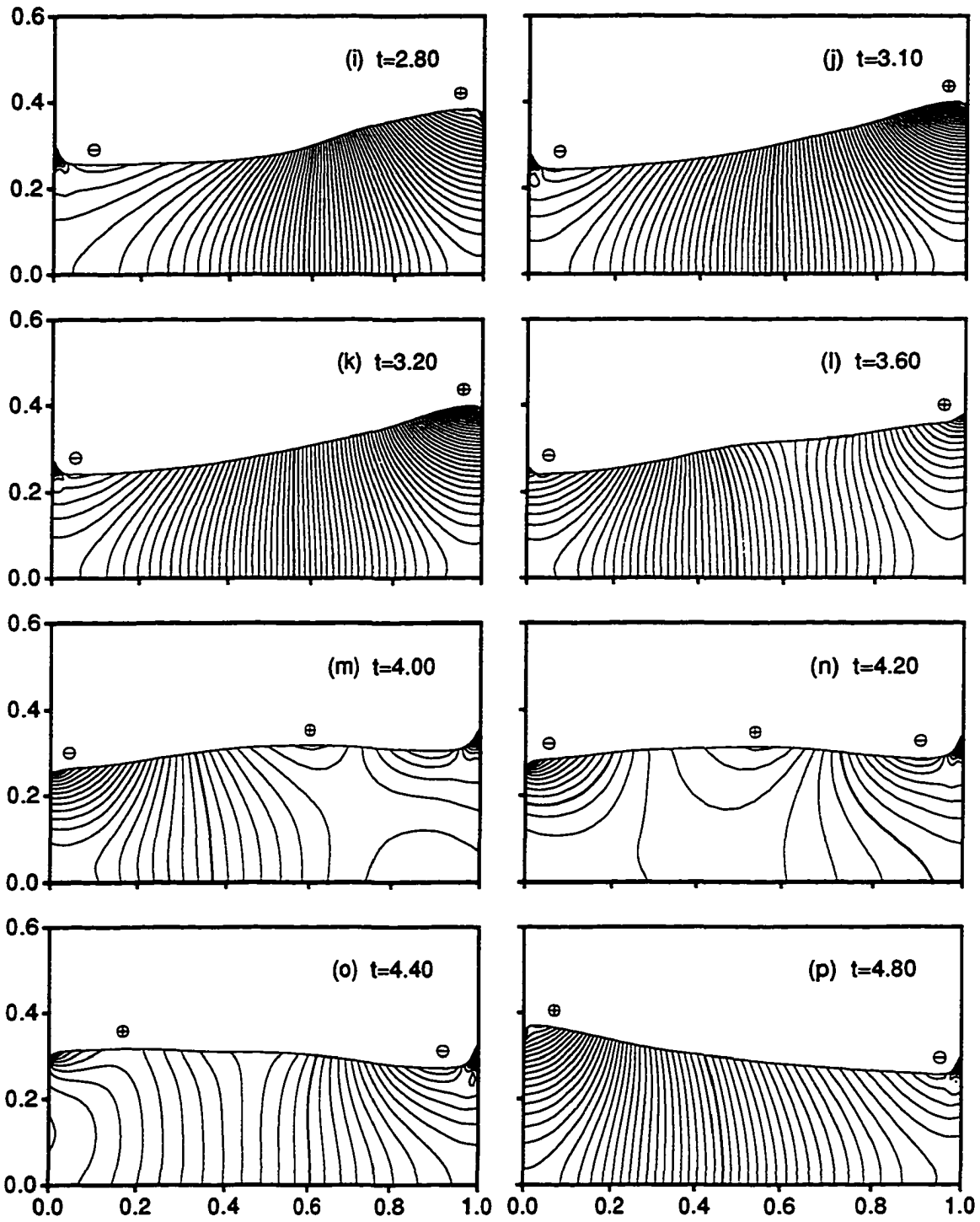


Figure 5.6 (Continued)

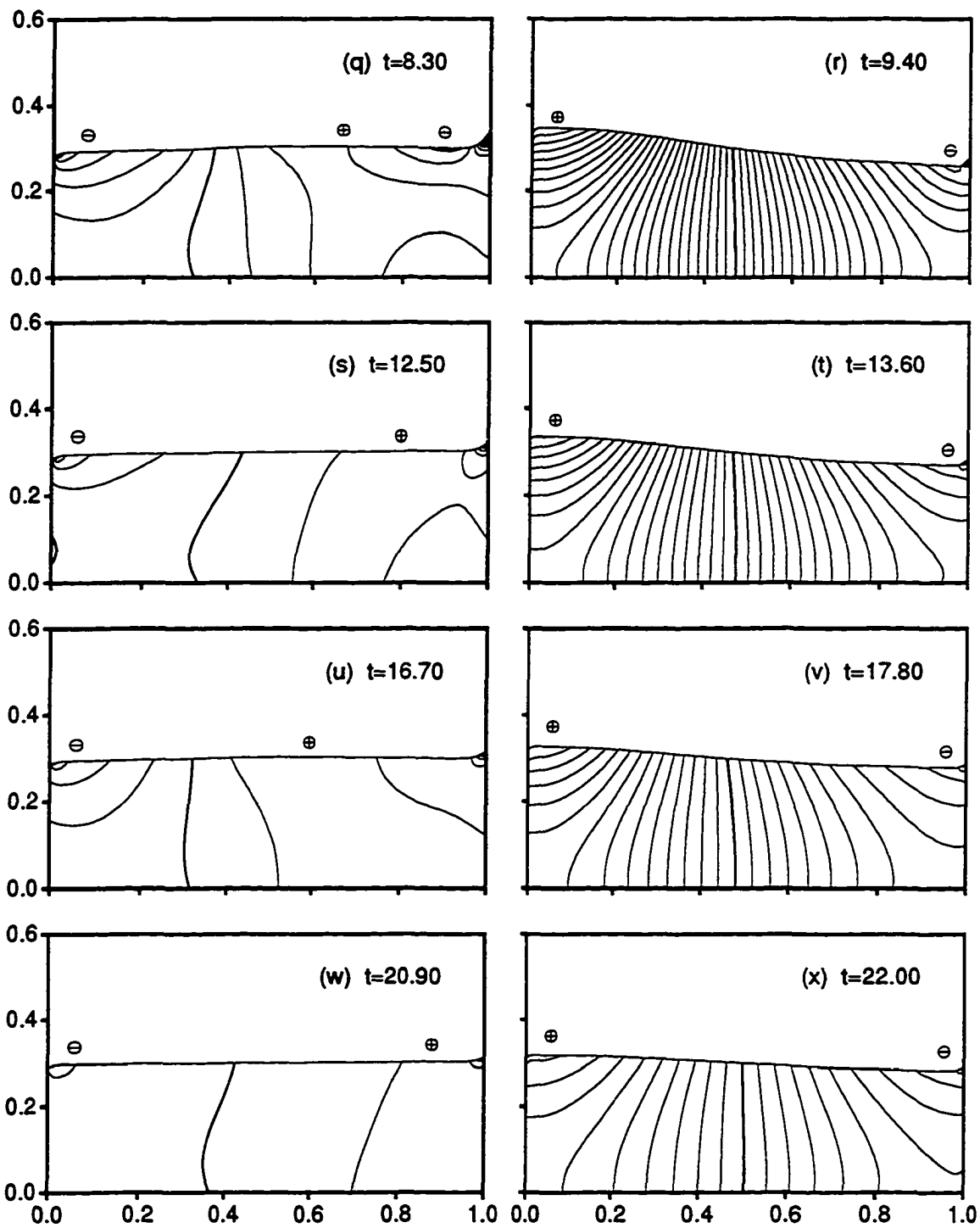


Figure 5.6 (Continued)

the initial flowfield in the interior of the container is irrotational. Consequently, any variations which occur across the pressure field reflect a simple balance between the pressure and the kinetic energy of the liquid and can be described by Bernoulli's equation. With $Q = 0$, the hydrodynamic pressure across the free surface of the liquid is uniform and equal to $P_d = 0$.¹ The pressure field is symmetric about the container mid-plane at $x = 0.5$, with the highest pressure values occurring at the lower corners of the container where the liquid is stagnant. The strongest pressure gradients occur near the two free surface ends in response to the rapid decrease in the kinetic energy of the liquid with depth.

The pattern of the hydrodynamic pressure lines of Figure 5.6(a) changes as the liquid surface moves away from initial horizontal position. A new pattern gets established which is depicted in Figures 5.6(b-f). It is characterized by pressure lines that are nearly vertically oriented in the center of the container while becoming more horizontally oriented near the two free surface ends. The hydrodynamic pressure increases along the left side of the container and decreases along the right side as the liquid moves further away from its equilibrium position. The resulting adverse pressure gradients reverse the direction of the liquid flow at $t \approx 1.00$. As the liquid approaches the horizontal position at $t = 2.00$ and regains some of its inertia the pressure lines become once again sparsely spaced.

A similar sequence of events is depicted in Figures 5.6(h-o). Here, the liquid is carried by its inertia past the equilibrium horizontal position and begins to rise along the right container wall. The hydrodynamic pressure increases along the right side and decreases along the left side of the container resulting in pressure gradients which resist this departure of the liquid from its equilibrium position. The action of these adverse gradients slow down and reverse the flow with the liquid returning back toward the equilibrium position by $t = 4.20$.

The effects of viscous dissipation on the hydrodynamic pressure field are illustrated in the sequence of Figures 5.6(q-x). At $t = 8.30$, the liquid is approaching its equilibrium position from the right as is about to complete the second full cycle of sloshing. The spacing of the pressure lines is sparse since the liquid is in a state of maximum inertia. It continues past the equilibrium position reaching a position of maximum elevation along the left wall by $t \approx 9.40$. Here, with the liquid being near a position of maximum departure from the equilibrium, the pressure gradients are at their maximum strength.

¹Based on the definition of P_d given in equation (5.1).

5.1.3 Case 3: Liquid Flow at Higher Galileo Numbers.

The sloshing of the liquid due to a step change in the horizontal acceleration experienced by the container has been presented in detail in Case 1. The case under consideration here, Case 3, deals with changes which occur in the flowfield as a result of a *lower* liquid viscosity. The dimensionless parameters which define both of these cases are listed in Table 5.2. Note that, with the exception of the Galileo number, the remaining similarity parameters for this case are identical with those of Case 1. Where the value of the Galileo number used in Case 1, $Ga = 10^6$, is representative of a viscous liquid such as SAE-10W oil, the value of the Galileo number used here, $Ga = 10^{10}$, is more representative of a less viscous liquid such as water.²

A series of velocity and pressure field plots are used to depict the development of the flowfield for this case. In Figure 5.7, the velocity vector is plotted at alternating rows and columns of the 81×81 computational grid which was used for the solution of the problem. The pressure distribution within the liquid is shown in Figure 5.8. Isobars that correspond to a zero pressure value are drawn using a heavier weight line. Tiny regions of slight negative pressure may be seen along the free surface of the liquid throughout Figure 5.8. The negative pressure is the result of the normal stress condition, see equation (3.29g), and its magnitude in the interior of the surface remains of order $1/\sqrt{Ga}$. The scaling factor used in plotting the velocity vector in Figure 5.7, and the spacing between adjacent isobars in Figure 5.8, are identical with those used in Figures 5.1 & 5.2, the two corresponding figures depicting the flowfield of Case 1.

The flowfield for the first period of oscillation is depicted in parts (a-k) of the two figures. Although the general structure of the flowfield remains very similar to that of Case 1, some changes are evident as a result of the lower liquid viscosity. Viscous effects are now confined to much thinner boundary layers along the container walls. The boundary layer along the bottom wall is very nicely depicted in Figure 5.7(d). The lower liquid viscosity also alters the shape of the free surface. The extent to which viscous drag retards the motion of the surface along the walls has been significantly reduced compared to that of Case 1.

As a result of the lower drag, the liquid rises more rapidly near the left wall. By time $t = 0.5$, a small crest has formed in the immediate vicinity of the left wall. Viscous effects act to flatten the free surface profile at the wall. The formation of this

²Assuming a characteristic container dimension $L \sim 0.1m$.

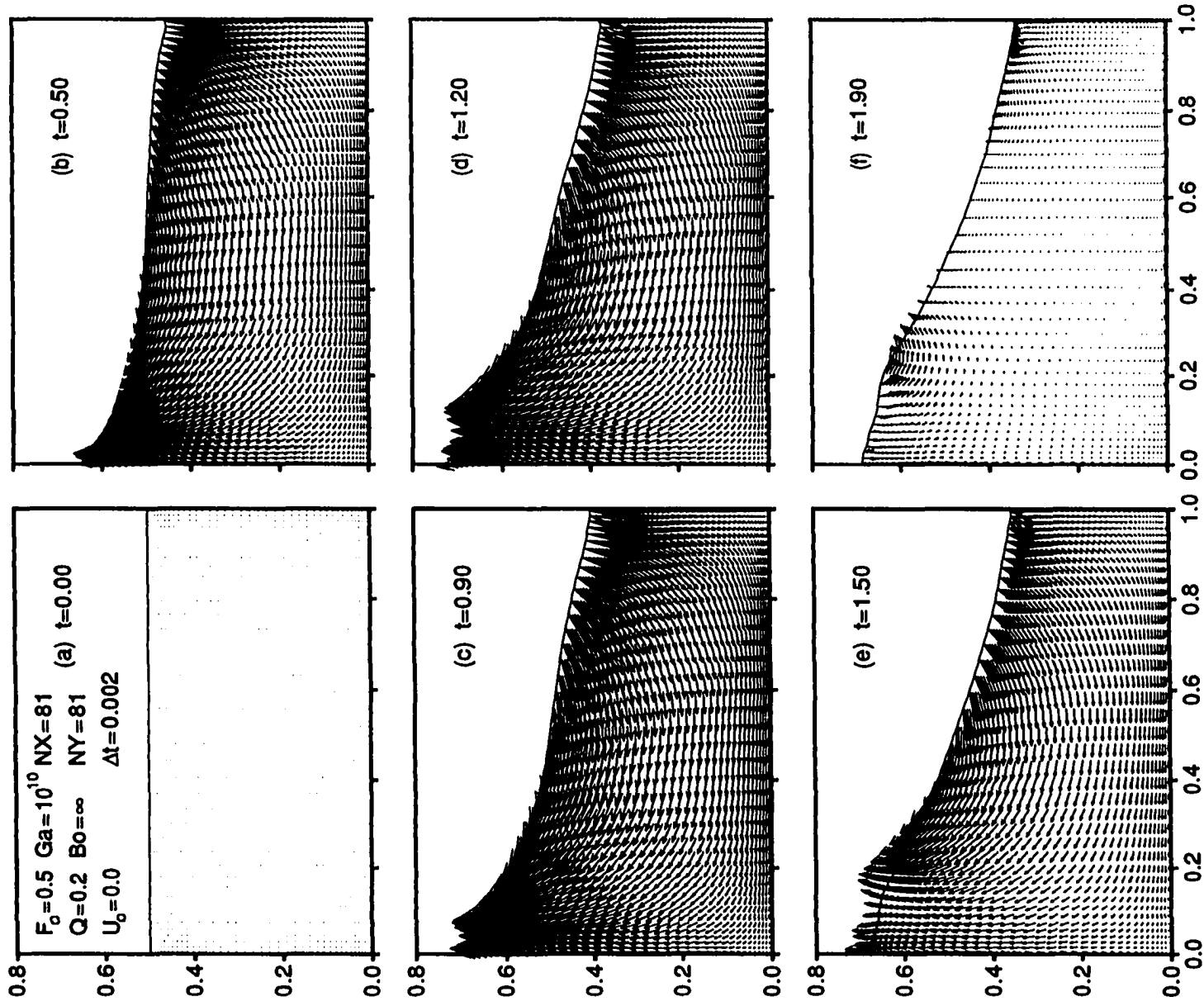


Figure 5.7: Velocity Field for $Q = 0.2$, $F_o = 0.5$, $Ga = 10^{10}$, and $Bo = \infty$

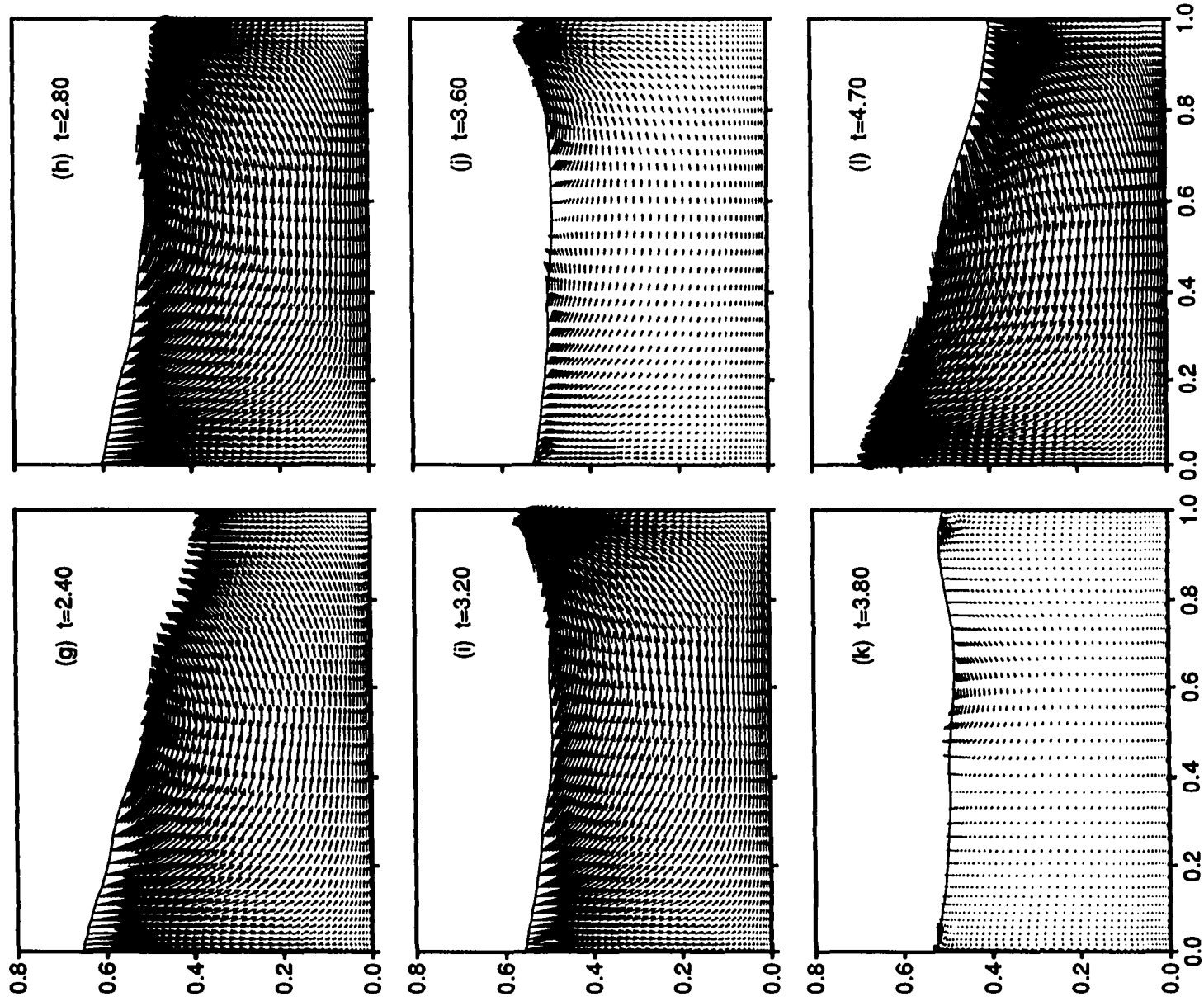


Figure 5.7 (Continued)

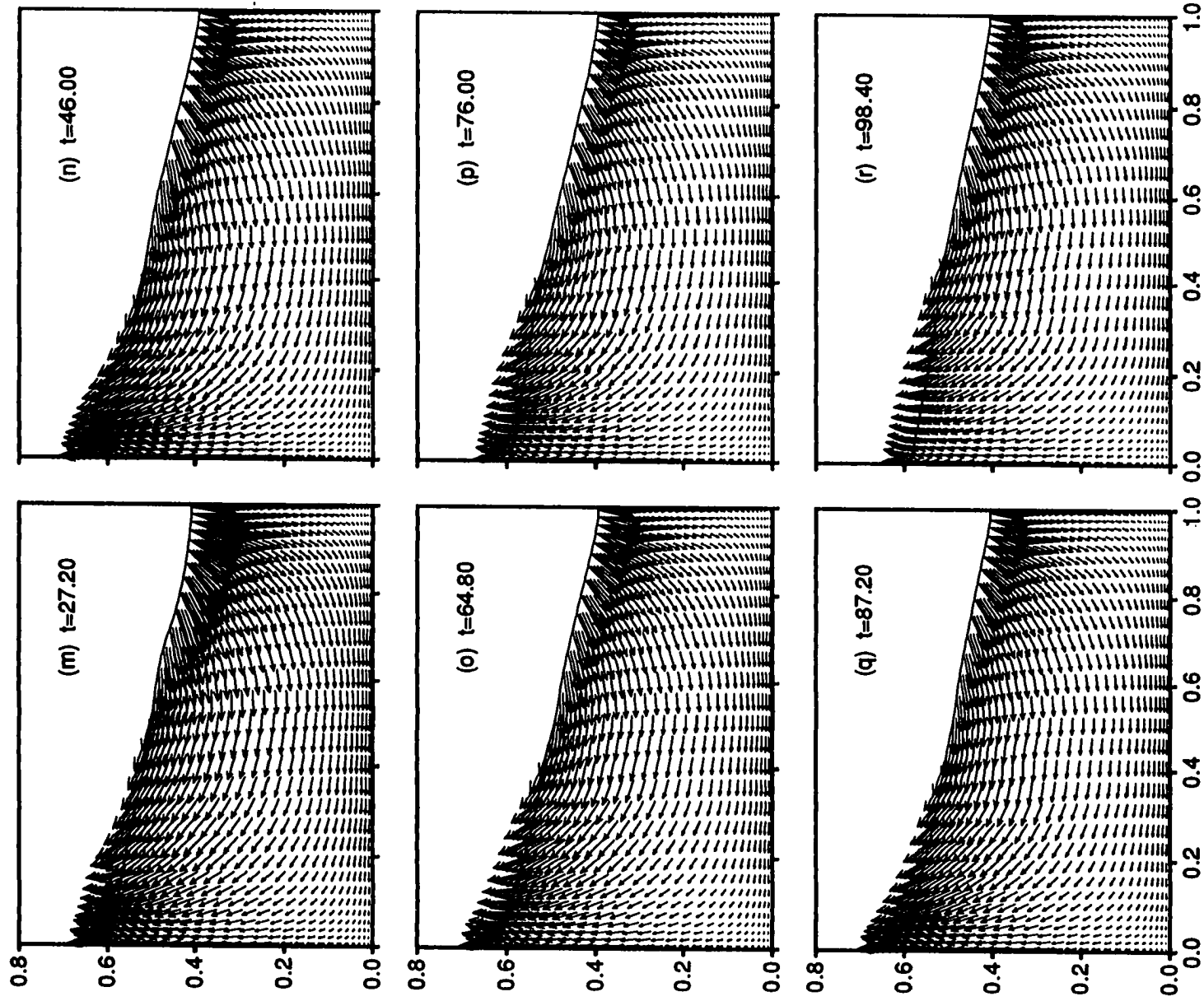


Figure 5.7 (Continued)

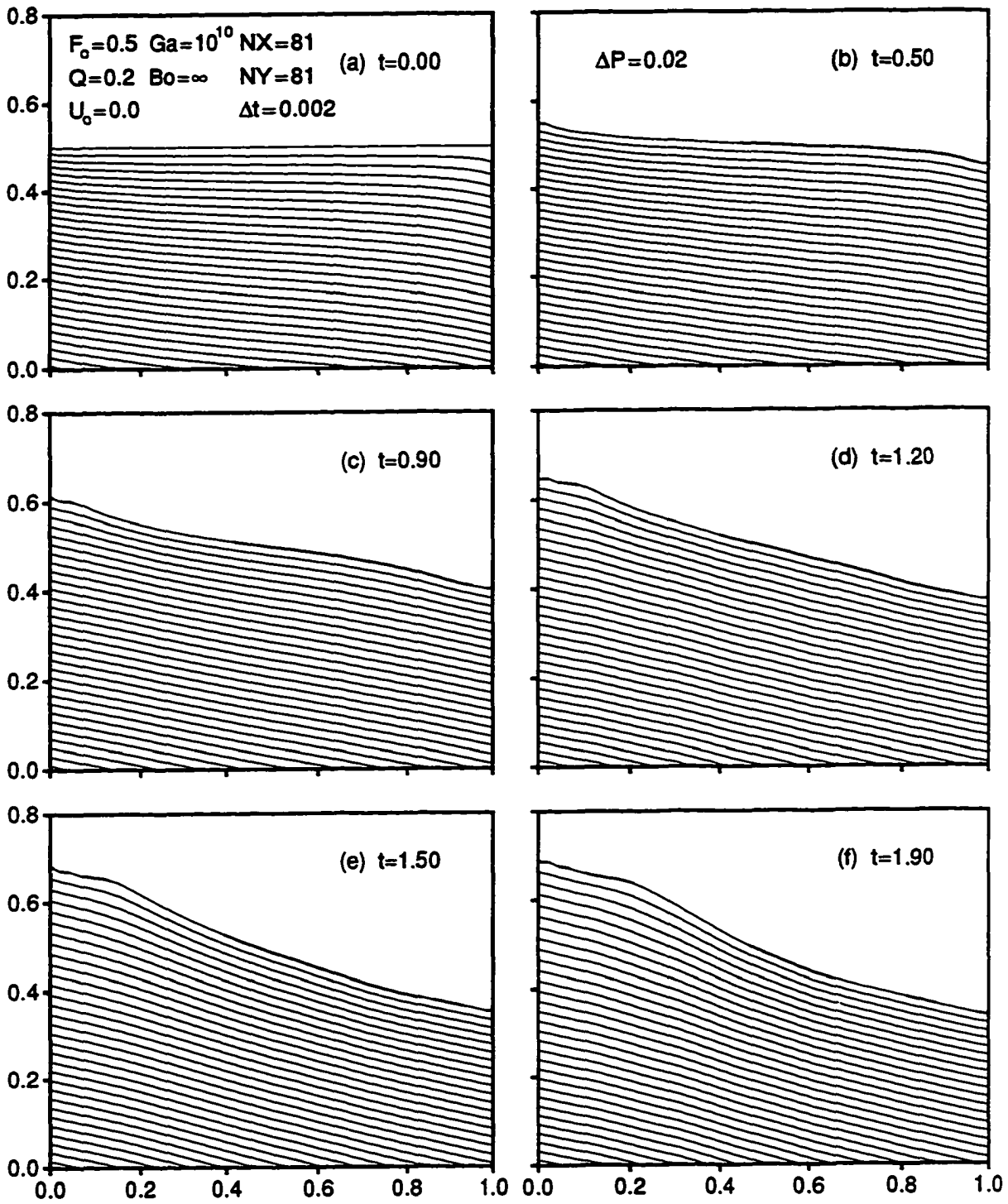


Figure 5.8: Pressure Field for $Q = 0.2$, $F_o = 0.5$, $Ga = 10^{10}$, and $Bo = \infty$

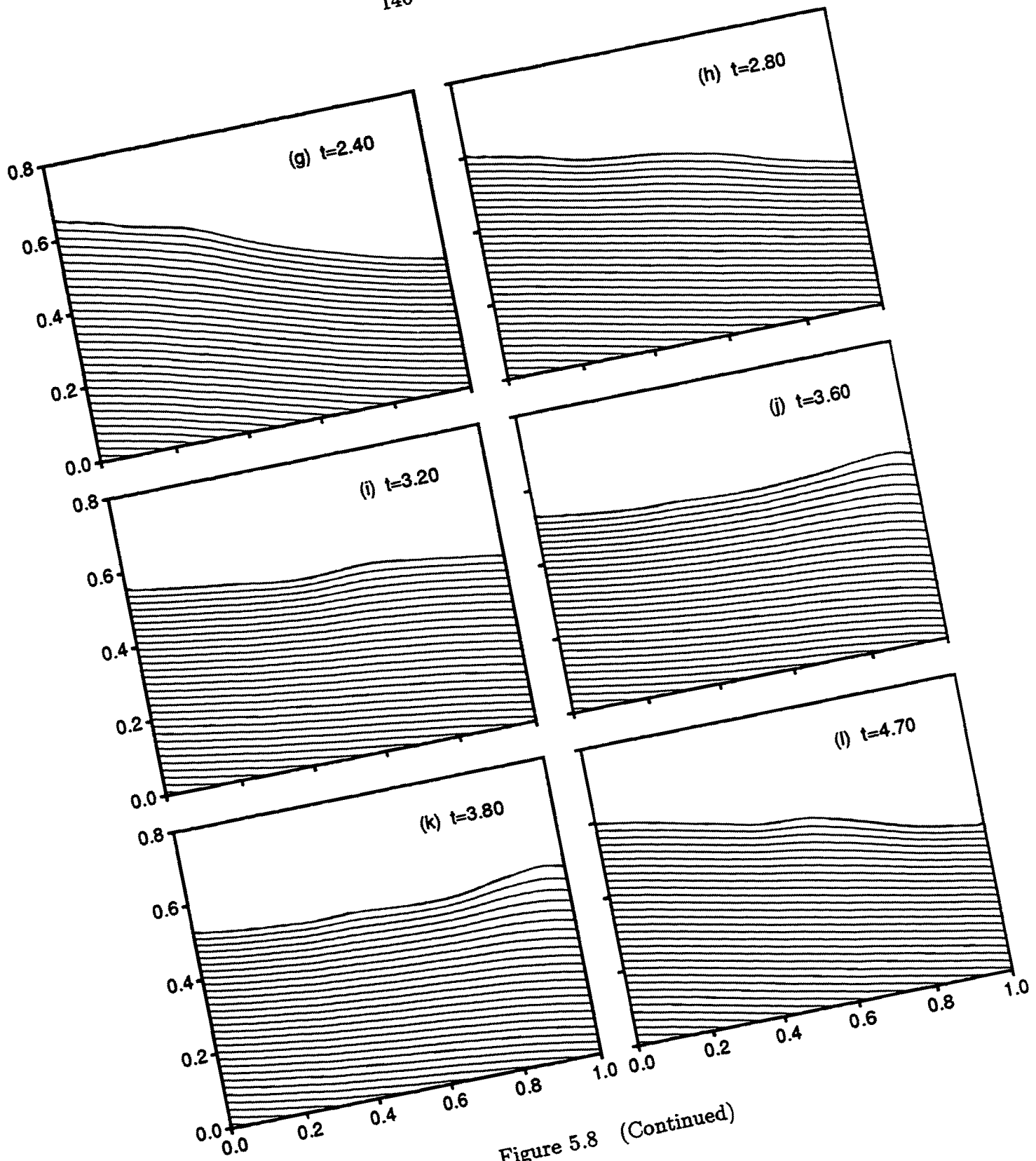


Figure 5.8 (Continued)

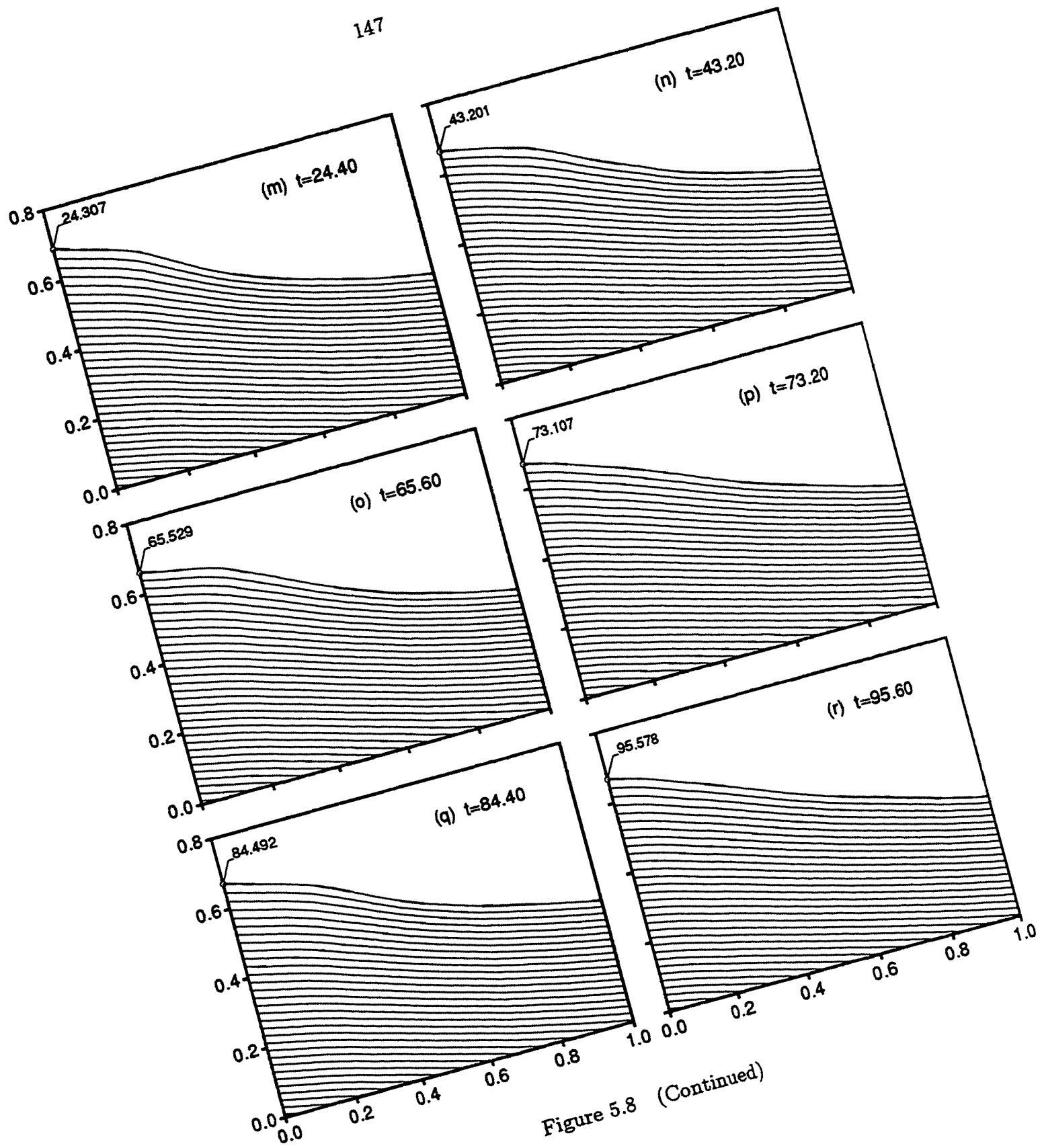


Figure 5.8 (Continued)

small crest next to the left wall contributes to a mechanism through which secondary waveforms get generated at the surface. The pressure rise beneath this peak, due to hydrostatic contributions, causes the slight upward bending of the isobars that lie close to the surface. This gives rise to locally stronger horizontal pressure gradients at a small distance from the left wall, and on the downhill side of this crest. The effect of this local pressure rise on the flowfield is clearly depicted in Figures 5.7(b-e). Part of the upward flow along the left wall, experiencing surface forces that are directed to the right, turns away from the wall and toward the interior of the container. This leads to the formation of a secondary waveform near the top of the free surface. This waveform, which at time $t = 0.90$ is located at $x \approx 0.06$, begins to slide down the free surface driven by a balance between body and surface forces. Viscous effects act to reduce its amplitude and to broaden its breadth as it moves along the surface.

By time $t = 1.90$, the liquid has reached its maximum elevation along the left container wall and it is in a state of minimum kinetic energy. The most prevailing feature of the flowfield at this time, which is shown in Figure 5.7(f), is the surface flow associated with the motion of the secondary waveform. The waveform, which is now located at $x \approx 0.22$, continues to slide down the free surface. The corresponding pressure field at $t = 1.90$ is shown in Figure 5.8(f). The pressure at the surface is positive on the leading side and negative on the trailing side of the secondary waveform. With the free surface returning back near its equilibrium position at $t = 2.80$, the flowfield is in a state of maximum kinetic energy. The secondary waveform has moved past the container mid-plane and is now located at $x \approx 0.55$. It continues to lose strength as it moves further toward the right container wall, and as the first cycle of sloshing is completed at $t \approx 3.80$, it becomes absorbed by the flow reflected off the right container wall.

The long term effects of the liquid viscosity on the flowfield are illustrated in parts (m-r) of the two figures. In each of the velocity fields depicted in Figures 5.7(m-r) the liquid is approximately in a state of maximum kinetic energy as it rises past its equilibrium position having completed 7, 12, 17, 20, 23, and 26 full cycles of sloshing. Compared to the results of Case 1 for $Ga = 10^6$, where approximately 38% of the total energy of the liquid was dissipated within the first cycle, and 99% after ten cycles, the damping rate experienced by the flowfield here, for $Ga = 10^{10}$, is significantly lower. Less than 2% of the sloshing energy is dissipated within the first cycle, and after somewhat more than 26 cycles the flowfield of Figure 5.7(r) still possesses about 55%

of its initial energy.

Each of the pressure fields shown in Figures 5.8(m-r) depicts the liquid near a position of maximum potential energy. The free surface has risen to approximately its highest elevation along the left wall having already completed 6, 11, 17, 19, 22, and 25 full cycles of sloshing. The maximum elevation reached by the surface during each of these cycles is marked on the left wall, while the corresponding value of time that this occurs is also indicated. The slow rate at which the amplitude of the sloshing motion decreases is clearly evident from this sequence of figures. This slow damping rate, coupled with the fact that the free surface profile does not remain *similar* from cycle to cycle, leads to a non-monotonic decrease in the amplitude of sloshing. For example, the maximum elevation reached by the surface during the 26th cycle of Figure 5.8(r) is slightly higher than the elevation reached during the 12th cycle of Figure 5.8(n). Thus, even though the available energy of the flowfield at $t = 95.60$ is about 20% less than that at $t = 43.20$, a *flatter* free surface profile causes the liquid to rise to a slightly higher elevation.

More detailed information on the free surface profile is given in the next two figures. Figure 5.9 is a three dimensional plot of $F(x, t)$, the function used to describe the free surface position. This figure provides a nice qualitative and quantitative picture of the sloshing process for both the $Ga = 10^6$ and the $Ga = 10^{10}$ results. Figure 5.10, which is a two dimensional projection of lines of constant elevation, provides additional information on the surface position. The reference elevation, which is drawn in terms of a heavier weight line, corresponds to the initial surface elevation of $F_o = 0.5$. The dramatic difference in the dissipation rate between the two cases is clearly demonstrated by these two figures. It is also evident that once the sloshing process begins, the free surface does not return to the exact same position twice. The liquid flow, which exhibits a quasi-periodic behavior, yields non-similar free surface profiles. Note for example the solution for $Ga = 10^{10}$ in Figure 5.9(b). The elevation reached by the free surface during cycles 6 and 12 is noticeably less than that reached during the adjacent cycles.

The quasi-periodic characteristics of the flow are determined for the most part by the first sloshing *mode*. In the context used here, the n^{th} mode, F_n , refers to the coefficient of the n^{th} harmonic term in a Fourier series expansion of $F(x, t)$ based on

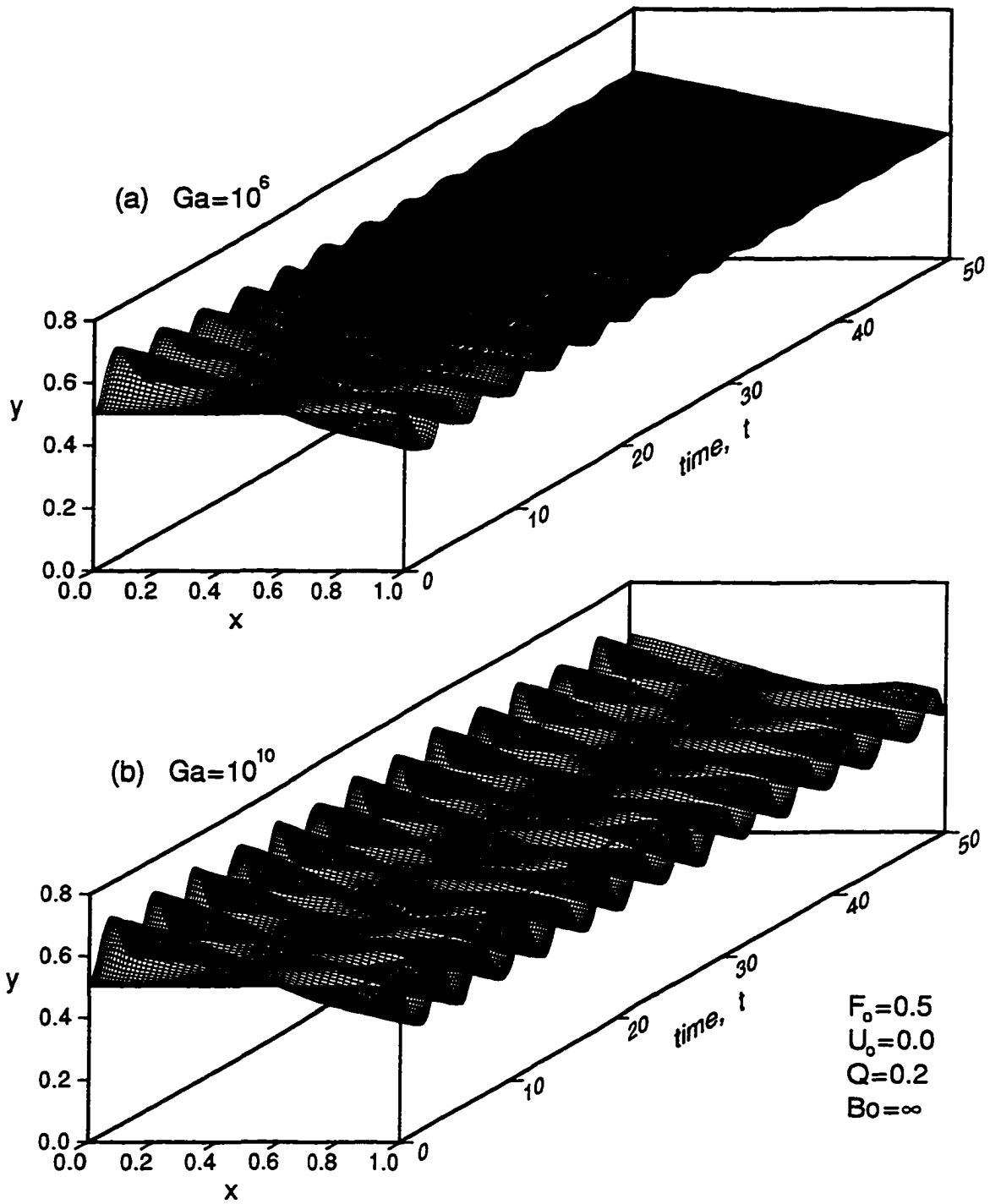


Figure 5.9: Free Surface Evolution for Cases 1 and 3

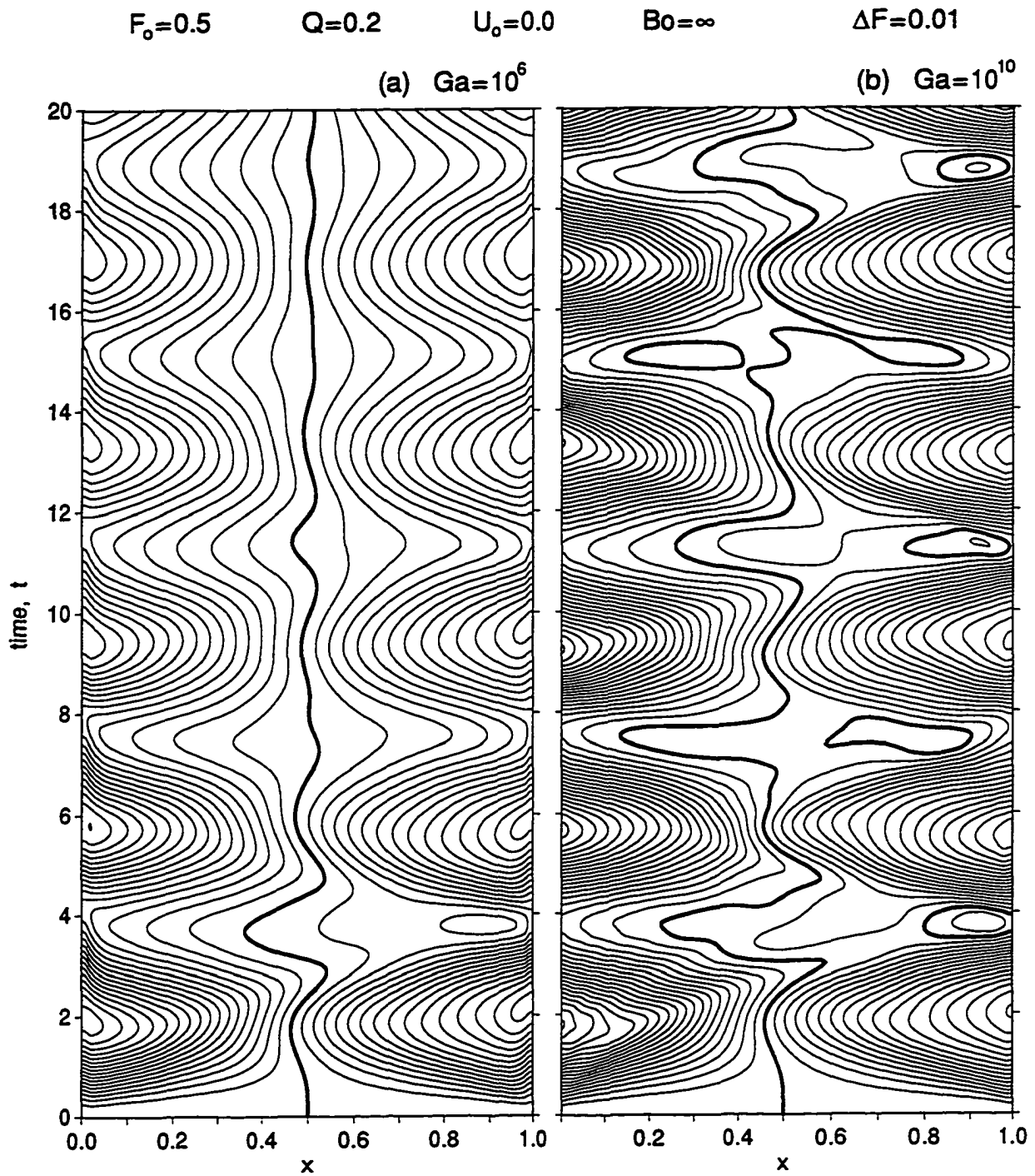


Figure 5.10: Free Surface Elevation Maps for Cases 1 and 3

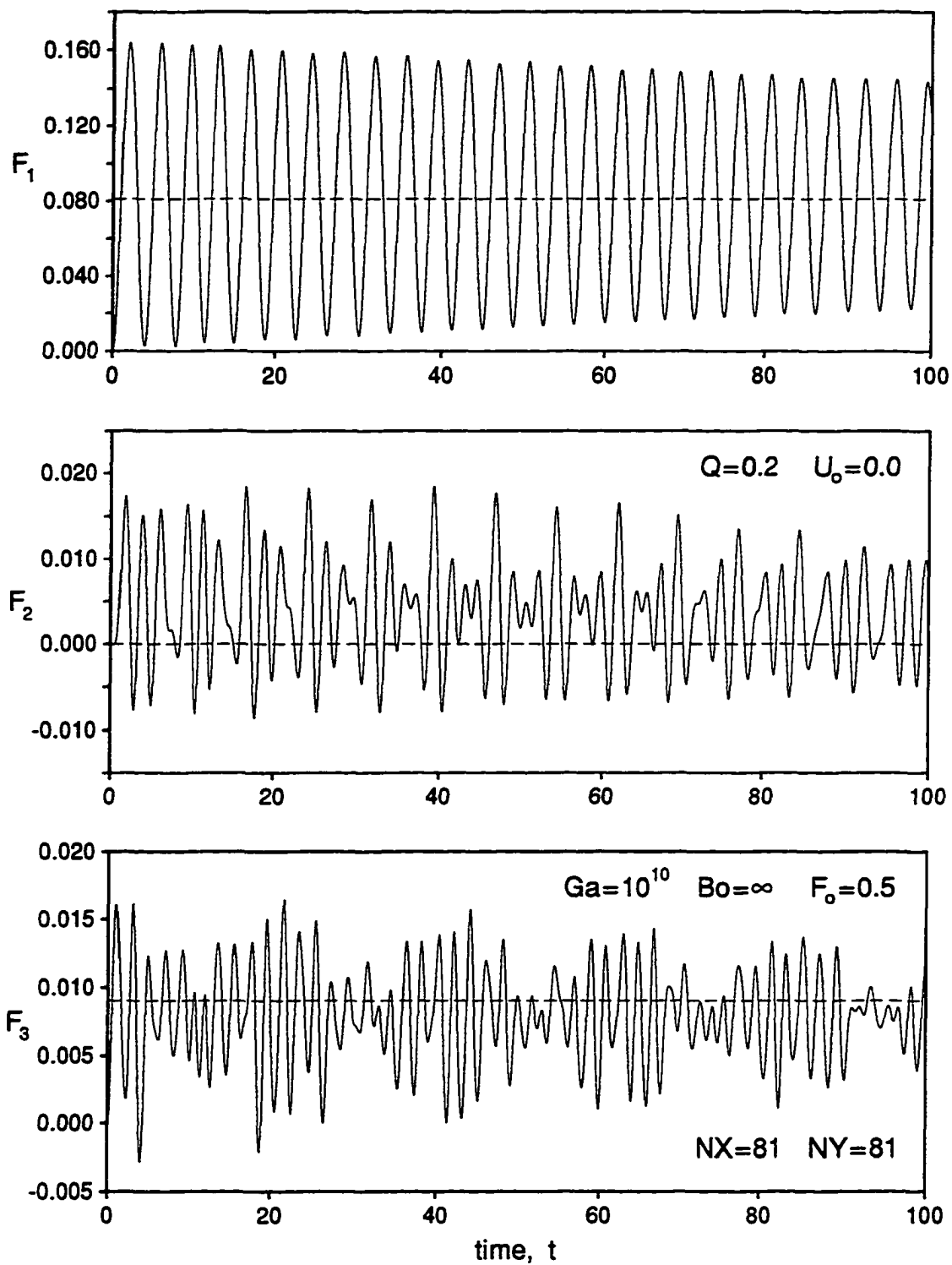


Figure 5.11: First Three Modes of Sloshing for Case 3

the following relation:

$$F(x, t) = \sum_{n=0}^{\infty} F_n(t) \cos(n\pi x) \quad (5.2)$$

The first three modes of sloshing for Case 3 are shown in Figure 5.11. A dashed line is used to denote the limiting value for each mode, $F_n(\infty)$. The amplitude of the first mode, F_1 , is about an order of magnitude larger than that of the remaining modes. Consequently, the general shape of the free surface as well as the fundamental frequency associated with the flow are dominated by the first mode. The structure of the second and third modes are less well defined. The second mode, F_2 , exhibits a quasi-periodic pattern which extends over two-cycle time intervals, while the quasi-periodic pattern exhibited by the third mode, F_3 , encompasses nearly a six cycle interval.

5.1.4 Case 4: Effects of Surface Tension

The primary focus of the discussion here is Case 4a which is listed in Table 5.2. It involves the flow in an accelerating container, $Q=0.2$, in the presence of significant surface tension effects, $Bo = 20$. Comparisons will be drawn with Case 4b, which involves a flow under similar conditions but in the absence of any surface tension effects, $Bo = \infty$.

The equilibrium position of the liquid with respect to the body forces changes at $t = 0$ as a consequence of the horizontal acceleration component, Q . As a result, the liquid experiences a restoring force which tends to move it away from its initial horizontal position and toward an equilibrium position with respect to the new net body force. Along the free surface, surface tension leads to a variable force which is determined by the local curvature (see equation 3.29g). This force acts as an additional restoring force which tends to prevent the liquid from departing its initial horizontal position which minimizes the free surface energy. For a Bond number value of $Bo = 20$, the magnitude of the surface tension force is comparable to that of the body forces acting on the liquid. As a result of these dual and competing restoring forces experienced by the liquid, the flow becomes more intriguing and considerably less predictable.

The development of the flowfield for Case 4a is depicted in the next three figures in terms of a series of velocity, pressure and hydrodynamic pressure field plots. The velocity vector is plotted in Figure 5.12 at alternating rows and columns of the 51×51 grid which was used for the solution of the problem. The pressure field is shown in

Figure 5.13, where a heavier weight line is used to indicate the zero value isobars. The hydrodynamic pressure, P_d , defined by equation (5.1), is shown in Figure 5.14. In addition to the use of a heavier weight line to indicate the zero value contours, regions of negative and positive hydrodynamic pressure are also identified by the symbols located just above the free surface.

Parts (a-h) in each of these three figures span the development of the flowfield over the first cycle of sloshing. Initially, at $t=0$, the liquid is still motionless. All of its available energy, E_A , is in the form of potential energy with respect to the body forces. The initial acceleration experienced by the liquid is given in terms of the gradients of the hydrodynamic pressure, which combines the effects due to body and surface forces. As the liquid begins to move part of its available energy is used in moving the free surface. The flowfield undergoes through a state of maximum kinetic energy shortly before $t = 0.80$, and begins to slow down as the magnitude of the restoring force due to surface tension exceeds that of the restoring force due to the body forces. The free surface rises slightly above the equilibrium position as the liquid comes to a near halt at $t \approx 1.60$. At this time, the available energy of the liquid has decreased by approximately 2.3% due to viscous dissipation in the interior of the flowfield, E_d , and viscous dissipation at the free surface, E_v ³. Approximately 84% of the initial energy of the liquid has been used in moving the free surface to this position against the surface tension forces, $E_s \approx 0.84$. The hydrodynamic pressure field at this time is dominated by surface tension forces since the liquid is nearly at rest and fairly close to its equilibrium position with respect to the body forces. The flow is reversed, and the liquid begins to move back toward its initial position. During the second half of the cycle, the pressure forces along the free surface now do work on the liquid. The liquid returns close to its initial position, marking the completion of the first cycle, shortly after $t = 3.10$. Nearly all of the stored surface tension energy is transferred back into the flowfield, $E_s \approx 0.09$. Note that, once the sloshing process begins, the free surface is never again precisely in a horizontal flat position, and thus the term E_s does not completely vanish.

During the first cycle, the maximum elevation reached by the free surface was only, $F_{max} = 0.610$. This is considerably lower than $F_{max} = 0.687$, the maximum elevation reached by the surface in the absence of surface tension effects of Case 4b.

³Definitions of the various energy components, E_d , E_v , E_s , etc. are given in section 3.8

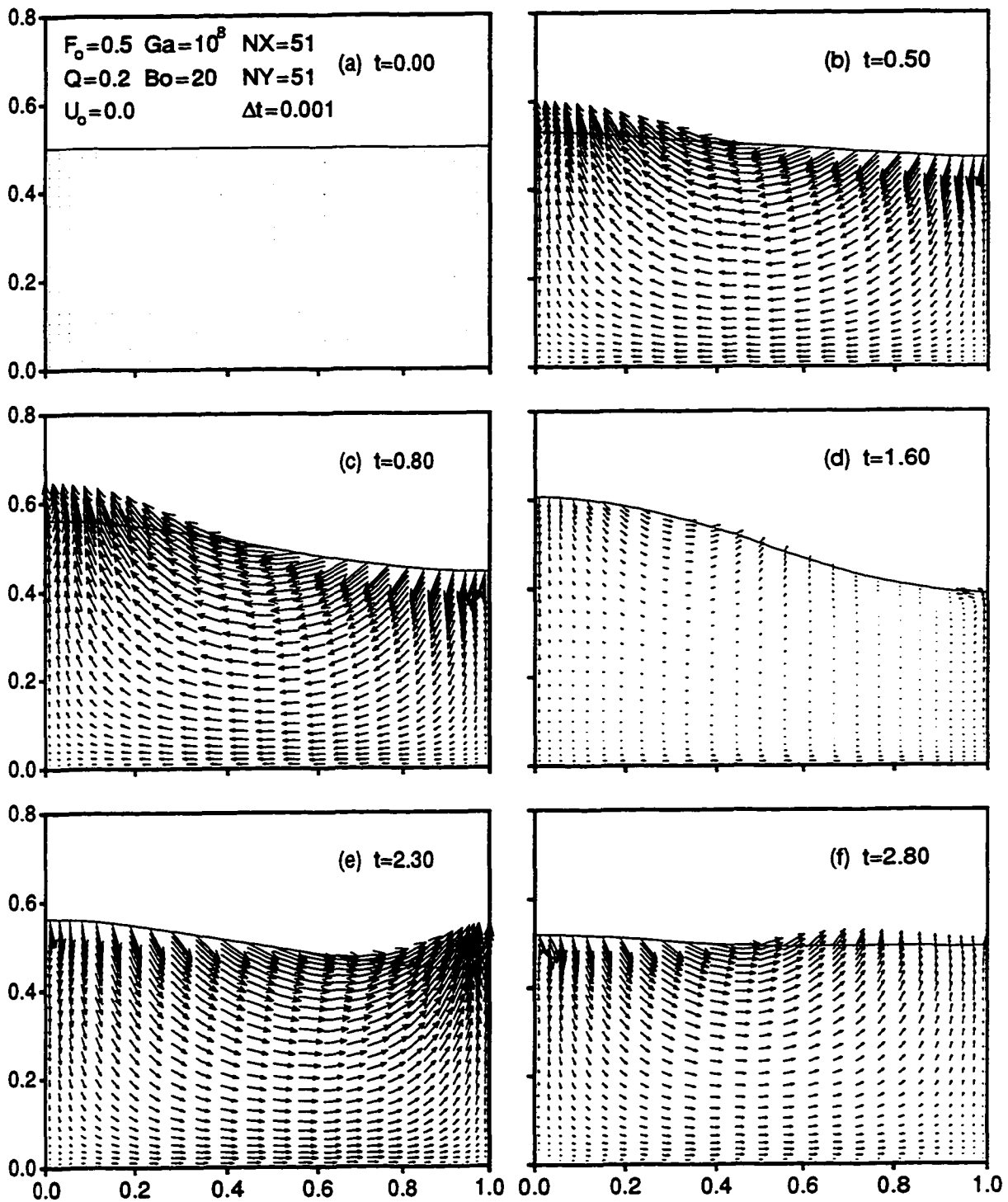


Figure 5.12: Velocity Field for $Q = 0.2$, $F_o = 0.5$, $Ga = 10^8$, and $Bo = 20$

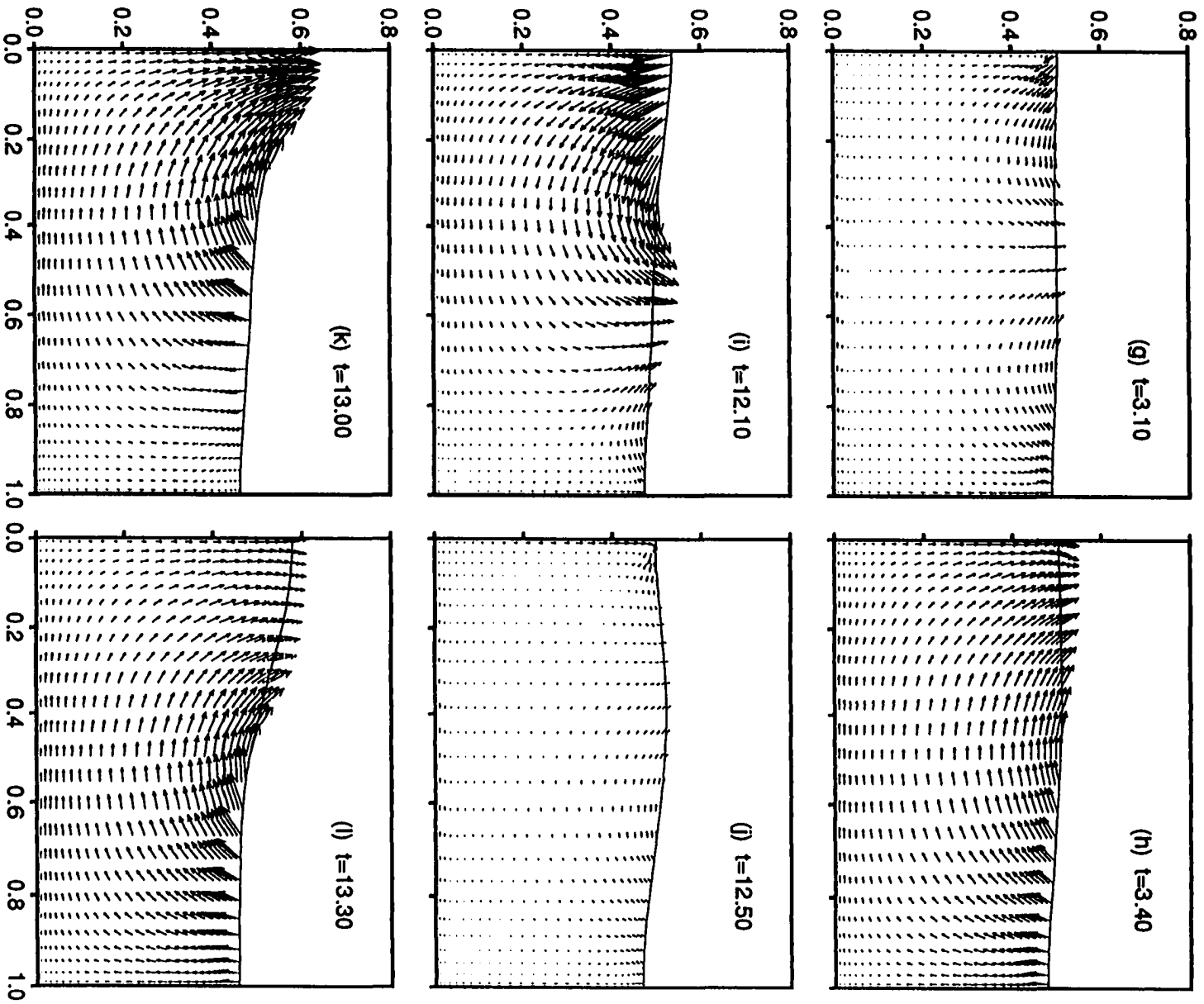


Figure 5.12 (Continued)

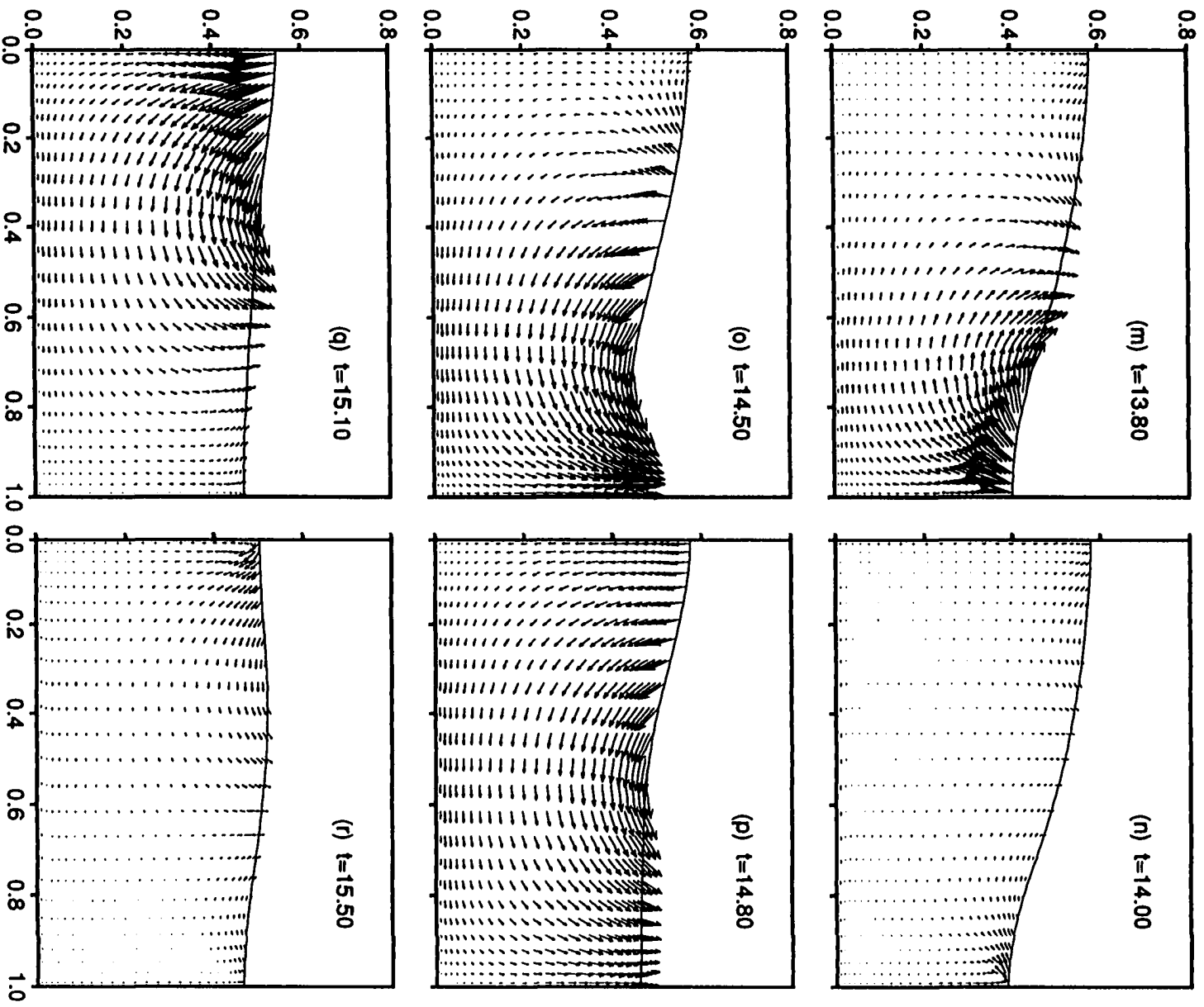
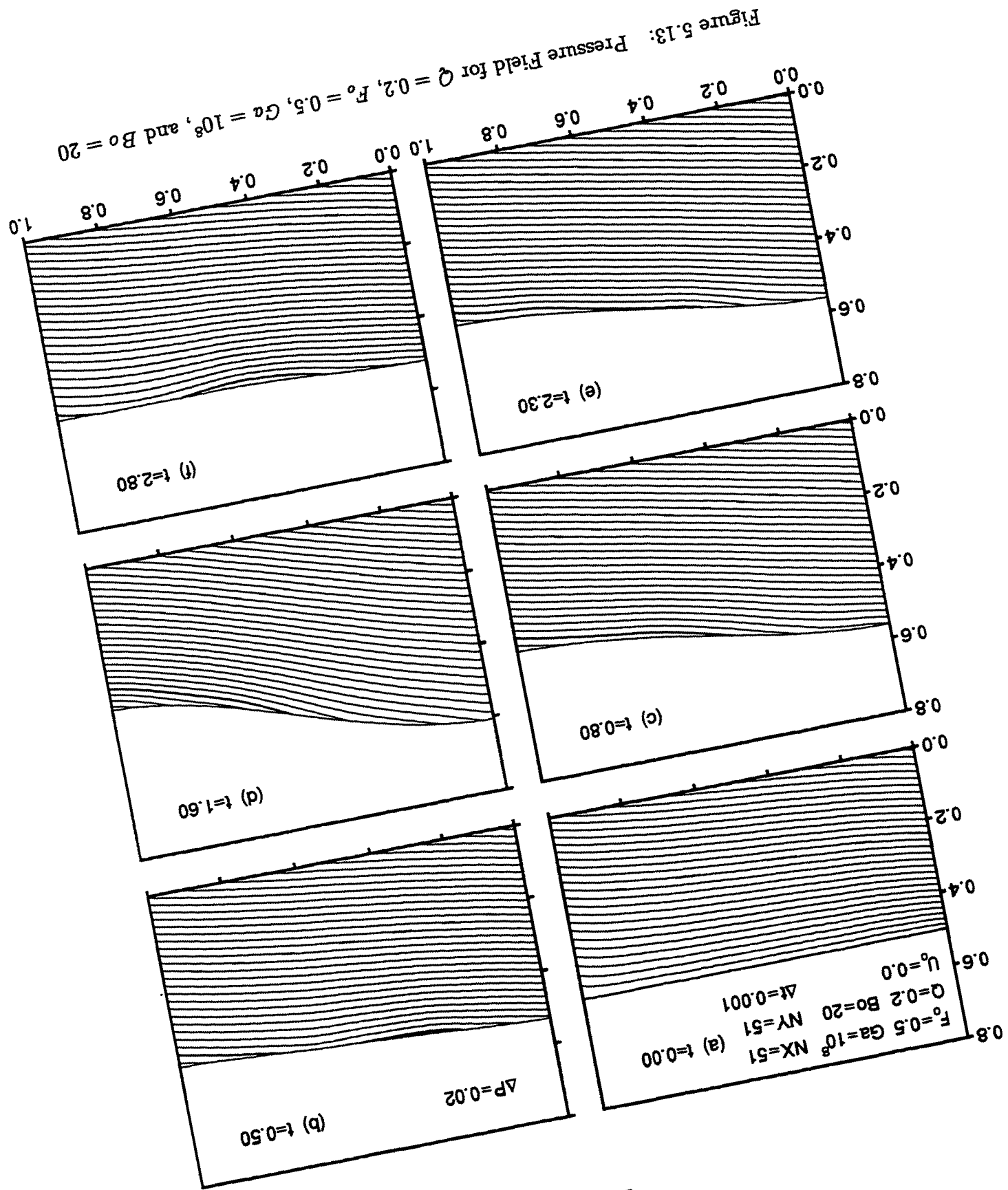


Figure 5.12 (Continued)



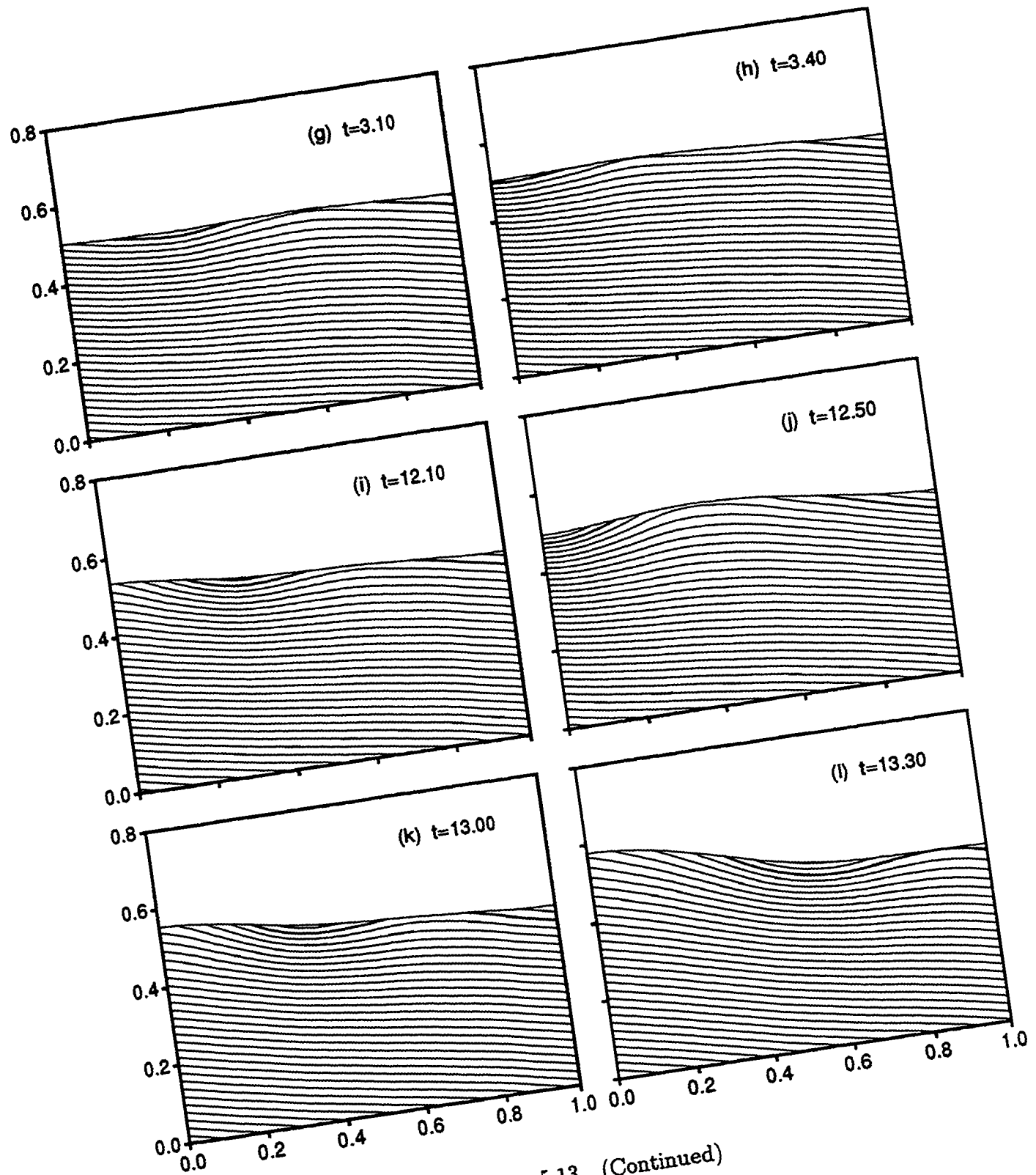


Figure 5.13 (Continued)

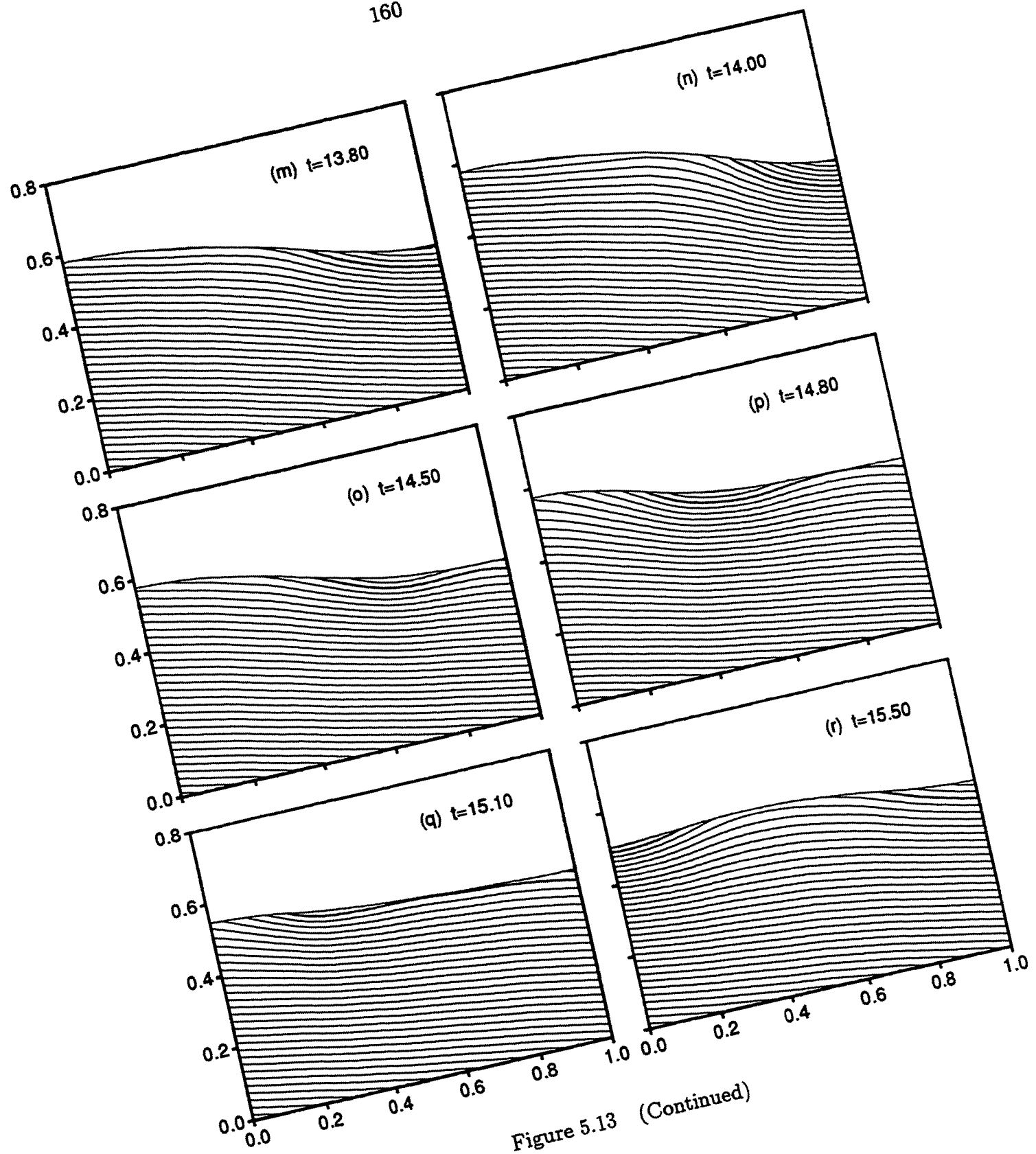


Figure 5.13 (Continued)

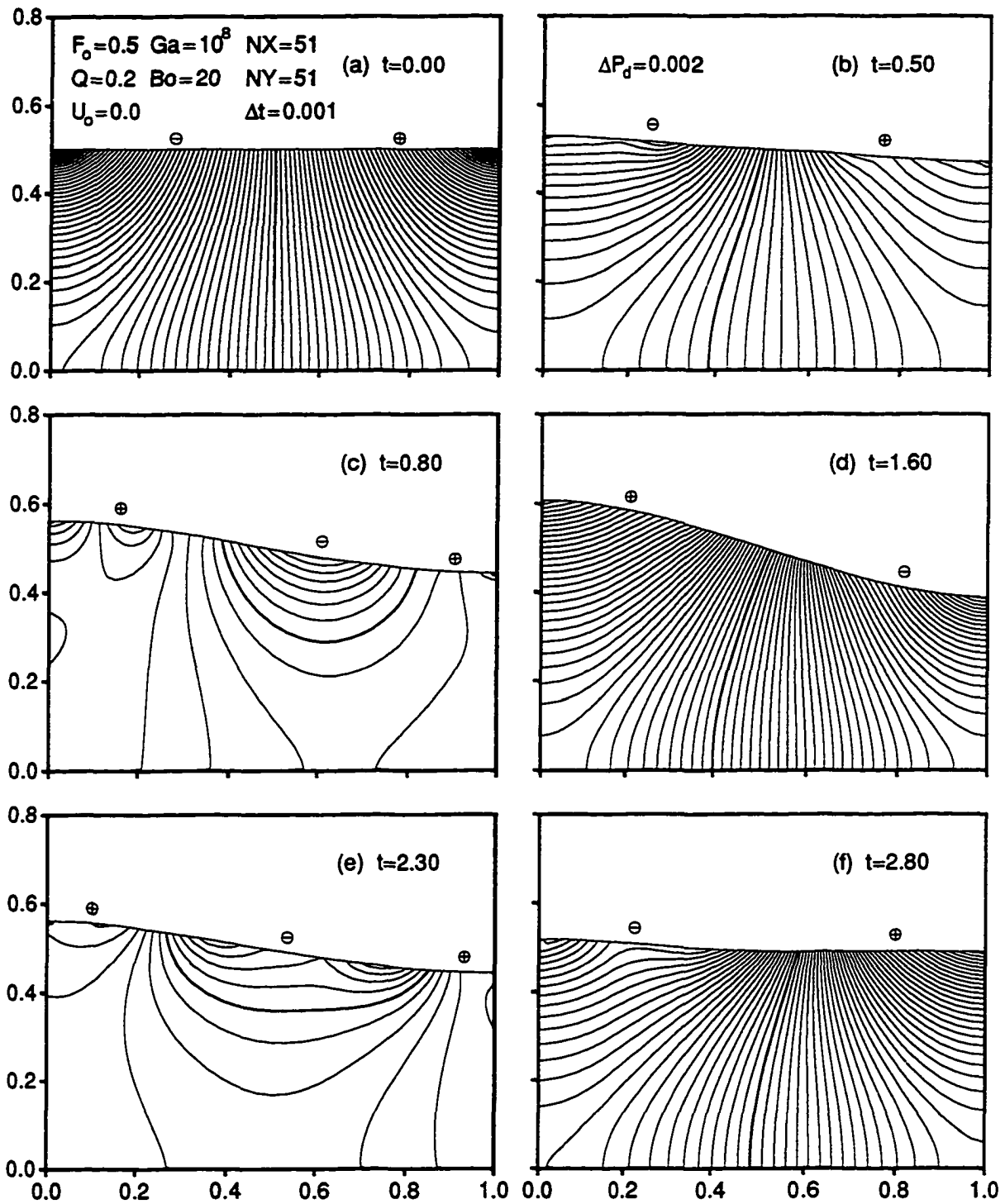


Figure 5.14: Hydrodynamic Pressure for $Q = 0.2$, $F_o = 0.5$, $Ga = 10^8$, and $Bo = 20$

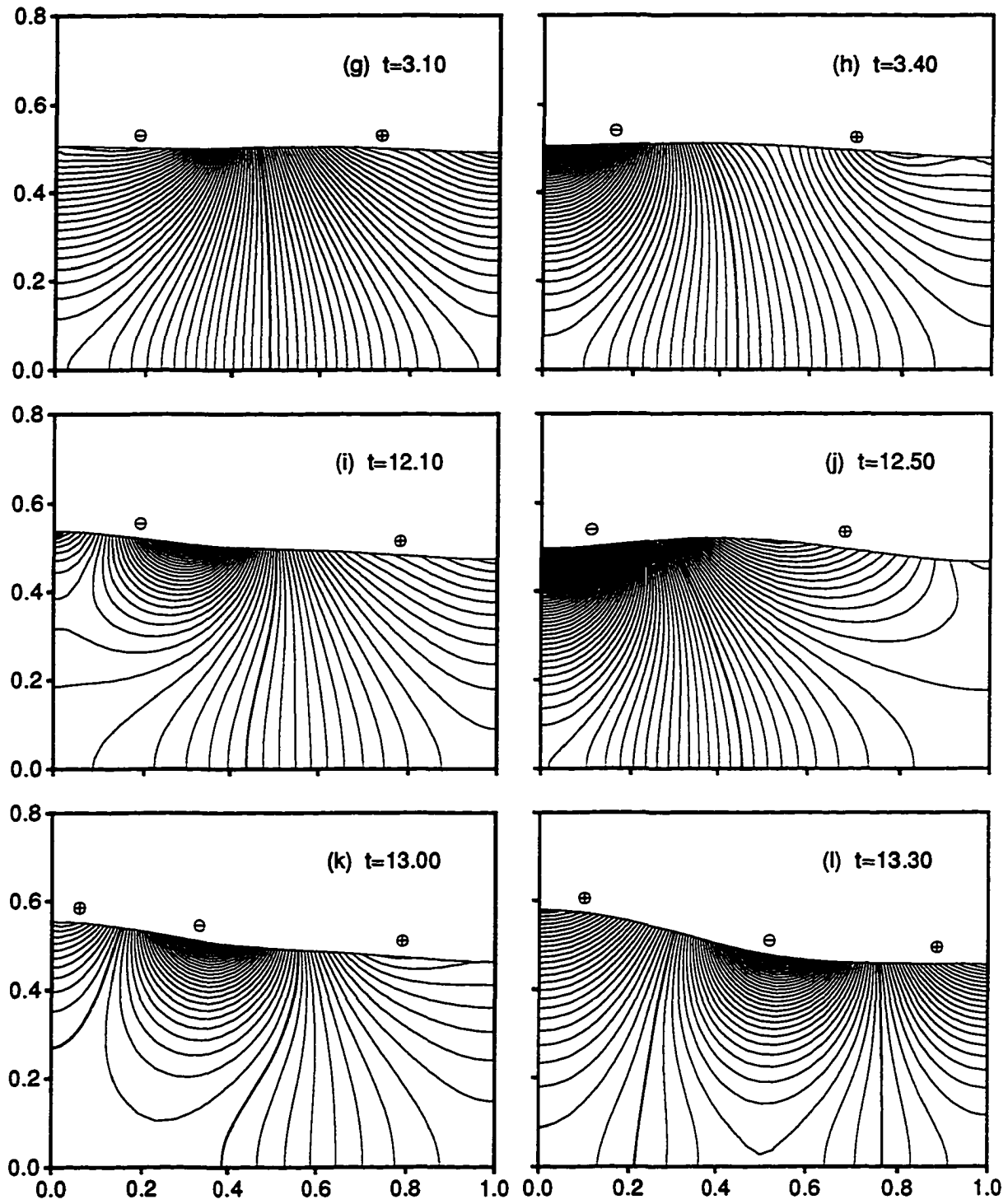


Figure 5.14 (Continued)

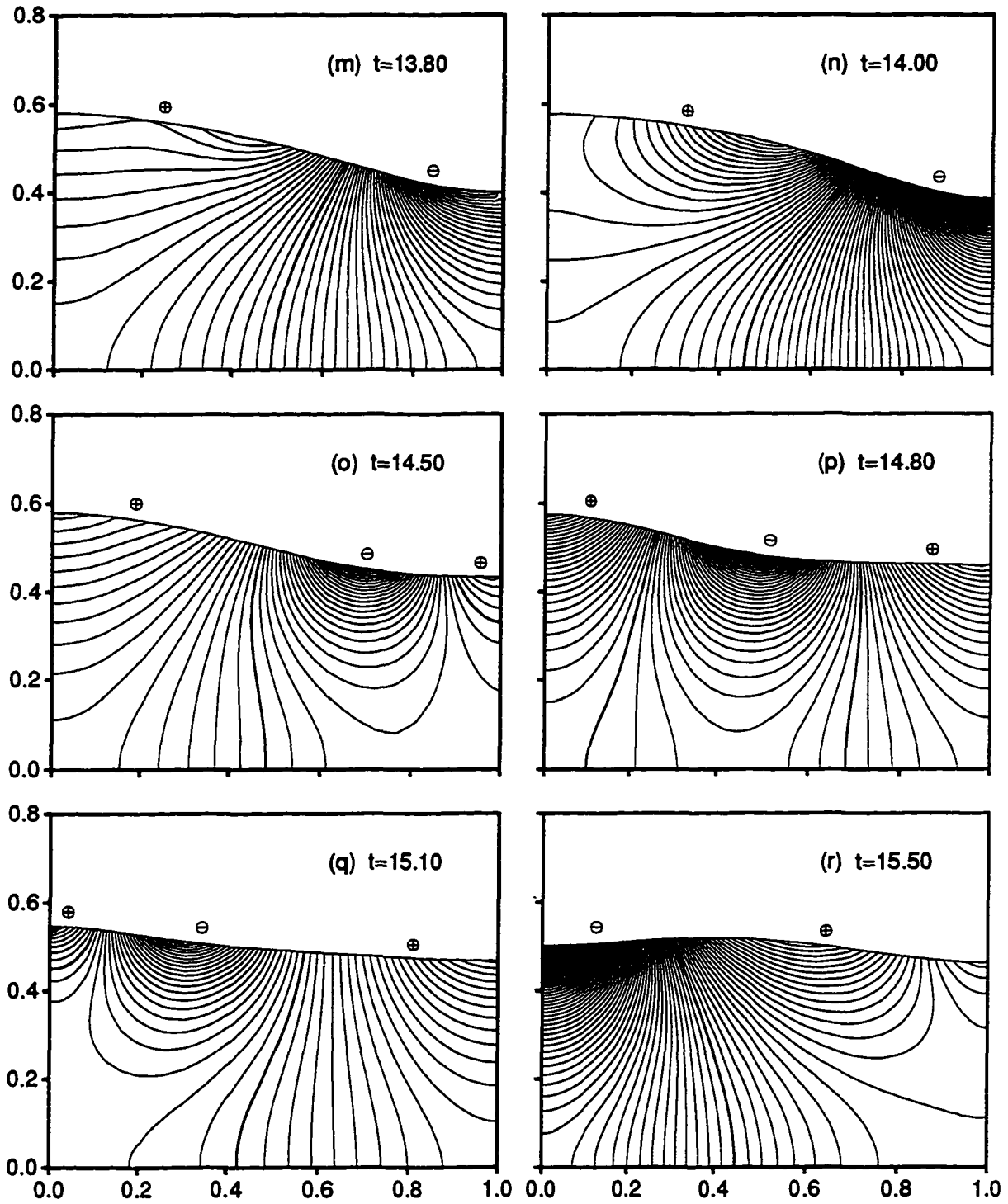


Figure 5.14 (Continued)

The period has also been substantially shortened to $T = 3.1035$, as compared to a value of $T = 3.7695$ for Case 4b. Nevertheless, the motion of the liquid during the first cycle has remained qualitatively similar to that which was encountered in Cases 1 and 3. Sloshing was still dominated by the *first mode*, with the surface rising on one side of the container while falling on the other side.

The remainder of each of Figures 5.12, 5.13, and 5.14, parts (i-r), cover the development of the flowfield over the fifth cycle of sloshing. The liquid at $t = 12.10$ is in the process of returning toward the initial position to complete the fourth cycle. At the end of the fourth cycle, $t \approx 12.50$, the free surface actually overshoots its initial position, forming a swell, which is centered somewhat to the left of the center of the surface. This leads to a region of high surface pressure in the interior and two regions of low pressure located next to the walls. This pressure field, coupled with the body forces experienced by the liquid in this configuration, lead to the hydrodynamic pressure field shown in Figure 5.14(j). Note the clustering of the hydrodynamic pressure lines beneath the free surface in the vicinity of the left wall. The stronger forces experienced by the liquid in this region lead to the formation of a local cell of strong surface flow. The surface starts to rise rapidly next to the left wall, while at the same time a large section of the surface next to the right wall remains comparatively stationary. As the surface rises on the left side, its curvature causes the surface pressure to increase, thus causing the flow cell to start moving toward the right side of the container. The liquid approaches the equilibrium position with respect to the body forces and comes to a near halt shortly after $t = 14.00$. In this configuration, the surface curvature causes a strong pressure drop next the right wall. A cell of locally strong flow now forms next to the right wall and travels to the left along the surface during the second half of the cycle. At the end of the cycle, $t \approx 15.50$, the flowfield appears to be qualitatively similar to that which existed at the beginning of the cycle, $t \approx 12.50$.

The flowfield of Case 4a, undergoes a gradual and continuous transition between the two flow patterns observed during the first and the fifth cycles. This behavior is illustrated in Figure 5.15, which depicts the variation in the amplitude of the first three modes of oscillation, F_1 , F_2 , and F_3 (see equation 5.2). The solid lines depict the result for Case 4a with $Bo = 20$, while the result of Case 4b for $Bo = \infty$ is depicted by the dashed lines. The amplitude of the second mode, F_2 , increases when the free surface exhibits some degree of even symmetry with respect to the container mid-plane. For example, the interior swells formed by the free surface at the beginning and the end

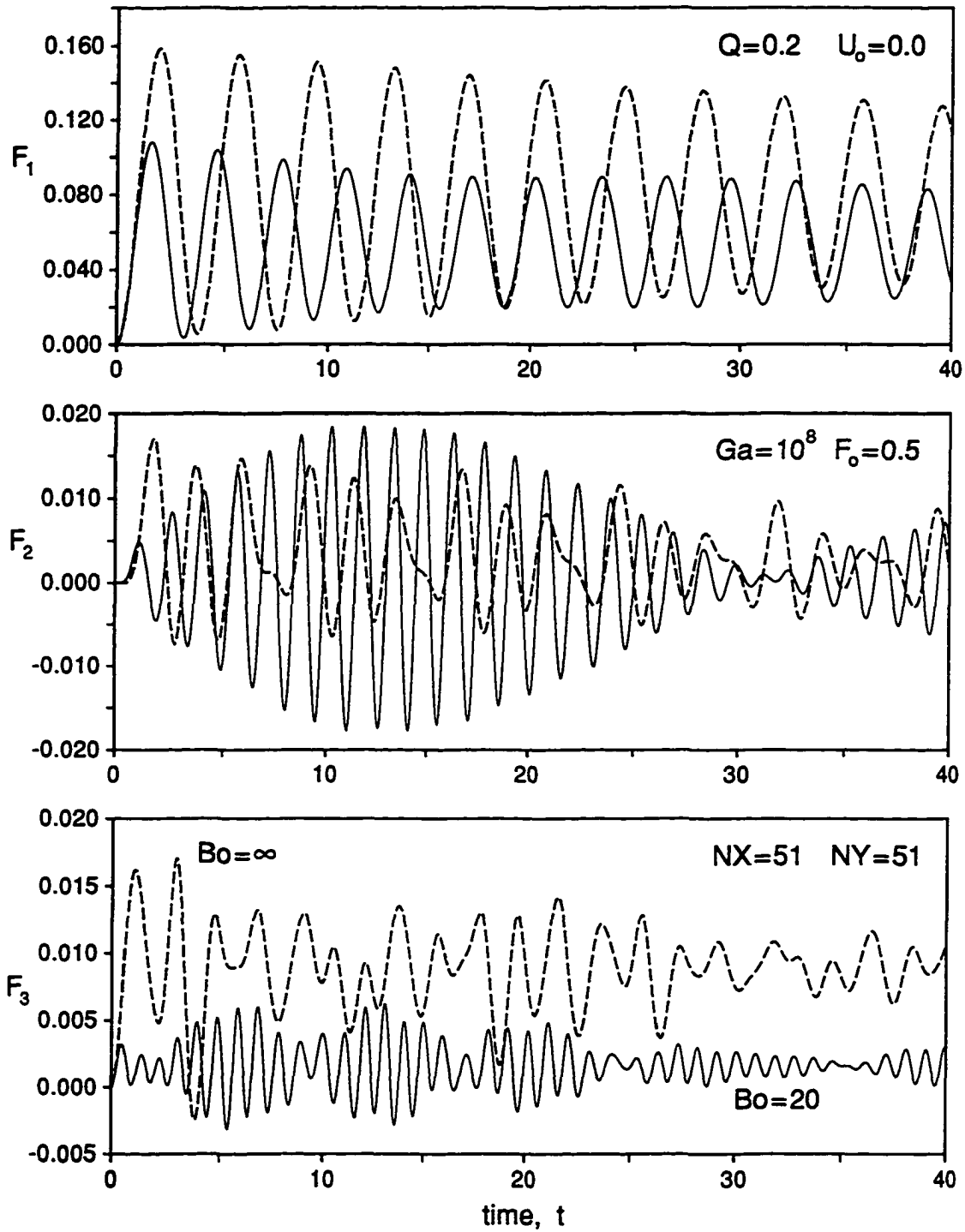


Figure 5.15: First Three Modes of Sloshing for Case 4

of the fifth cycle, correspond to local minima of F_2 . The maxima of F_2 occur when the free surface is close to the equilibrium position with respect to the body forces. The even symmetry of the surface leads to pressure forces along the surface which also exhibit even symmetry, and play an important role in driving the flow pattern of the fifth cycle. The transition of the flowfield from a regime dominated by the first mode, to one with significant second mode contributions, and back to a first mode regime, spans a ten cycle interval.

The evolution of the free surface position for Cases 4a and b is shown in the next two figures. Figure 5.16 is a three dimensional plot of $F(x, t)$, the function describing the free surface position. It provides a qualitative picture of the increase in the frequency, and decrease in the amplitude of sloshing which occur as a result of surface tension effects. Figure 5.17 is a two dimensional projection of lines of constant surface elevation. A reference elevation corresponding to the initial depth of $F = 0.5$ is drawn in terms of a heavier weight line. This figure provides more quantitative information on the position of the free surface. Note the effect of the changing flow pattern and increase in frequency on the motion of the free surface. The velocity of the surface, which can be derived by the spacing of the lines, indicates that as the second mode becomes excited at least some portion of the free surface is always in motion, such that the free surface does not come to a uniform halt.

5.1.5 Case 5: Effects of Liquid Depth

These effects are ascertained by comparing the horizontal velocity profile, u , at the container mid-plane, $x = 0.5$, for three different values of the initial liquid depth, $F_o = 0.2, 0.5$, and 0.8 . These values correspond to Cases 5a, b, and c from Table 5.2. In each case, the forcing of the liquid is given by $Q = 0.1$, and the same set of values are used for the remaining similarity parameters.

The horizontal velocity profiles for these three cases are shown in Figure 5.18(a-c). In each case, the liquid is in a state of maximum kinetic energy as the free surface passes through its equilibrium position for the first time. For an initial liquid depth of $F_o = 0.8$, this state occurs at $t = 0.890$. However, with the period, T , increasing with decreasing liquid depth, it takes substantially longer for the flow with $F_o = 0.2$ to reach this state at $t = 1.194$.

For a horizontally accelerating container, the slope of the equilibrium position of the free surface is independent of the initial depth, F_o , and equal to $-Q$. This

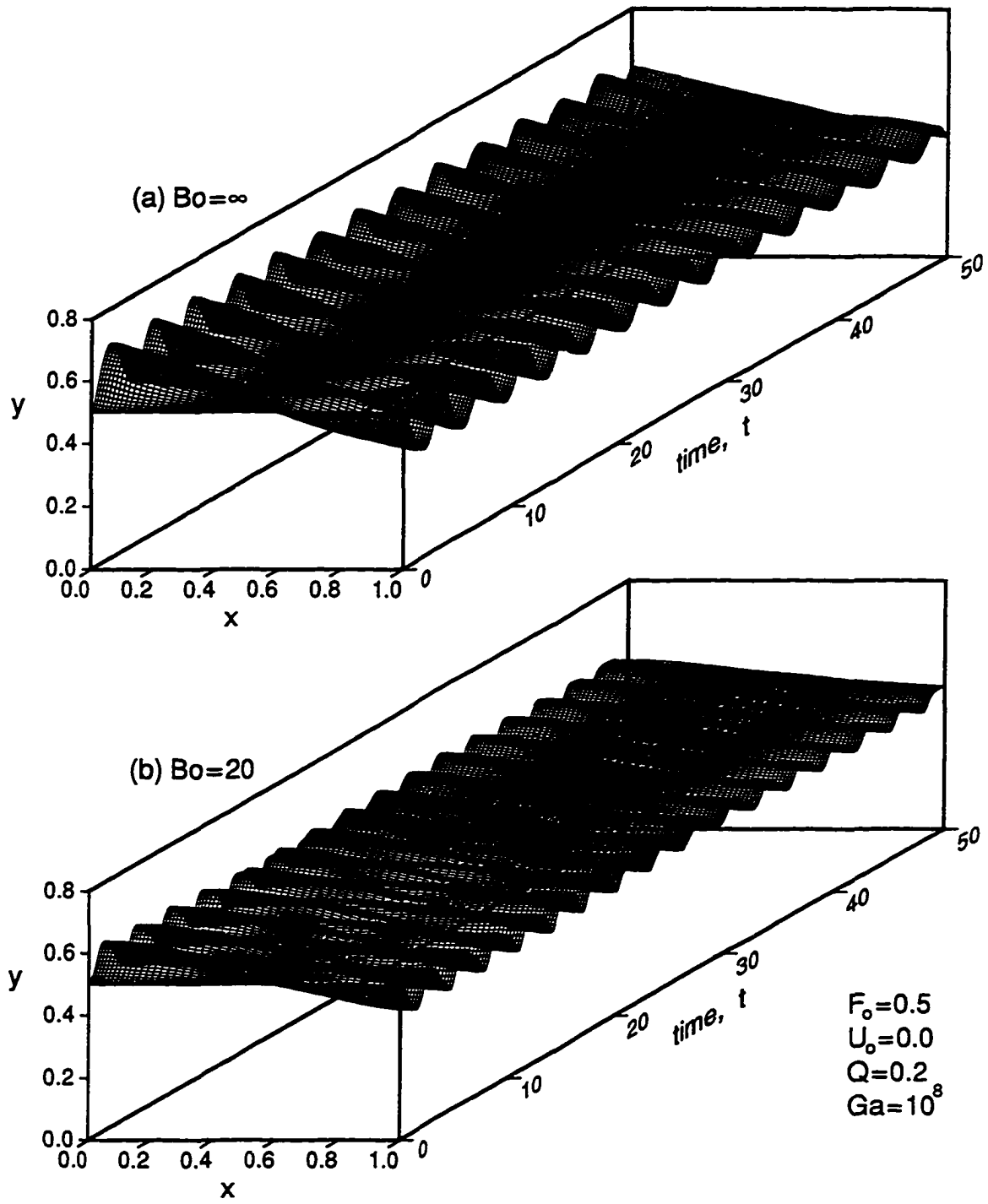


Figure 5.16: Free Surface Evolution for Case 4

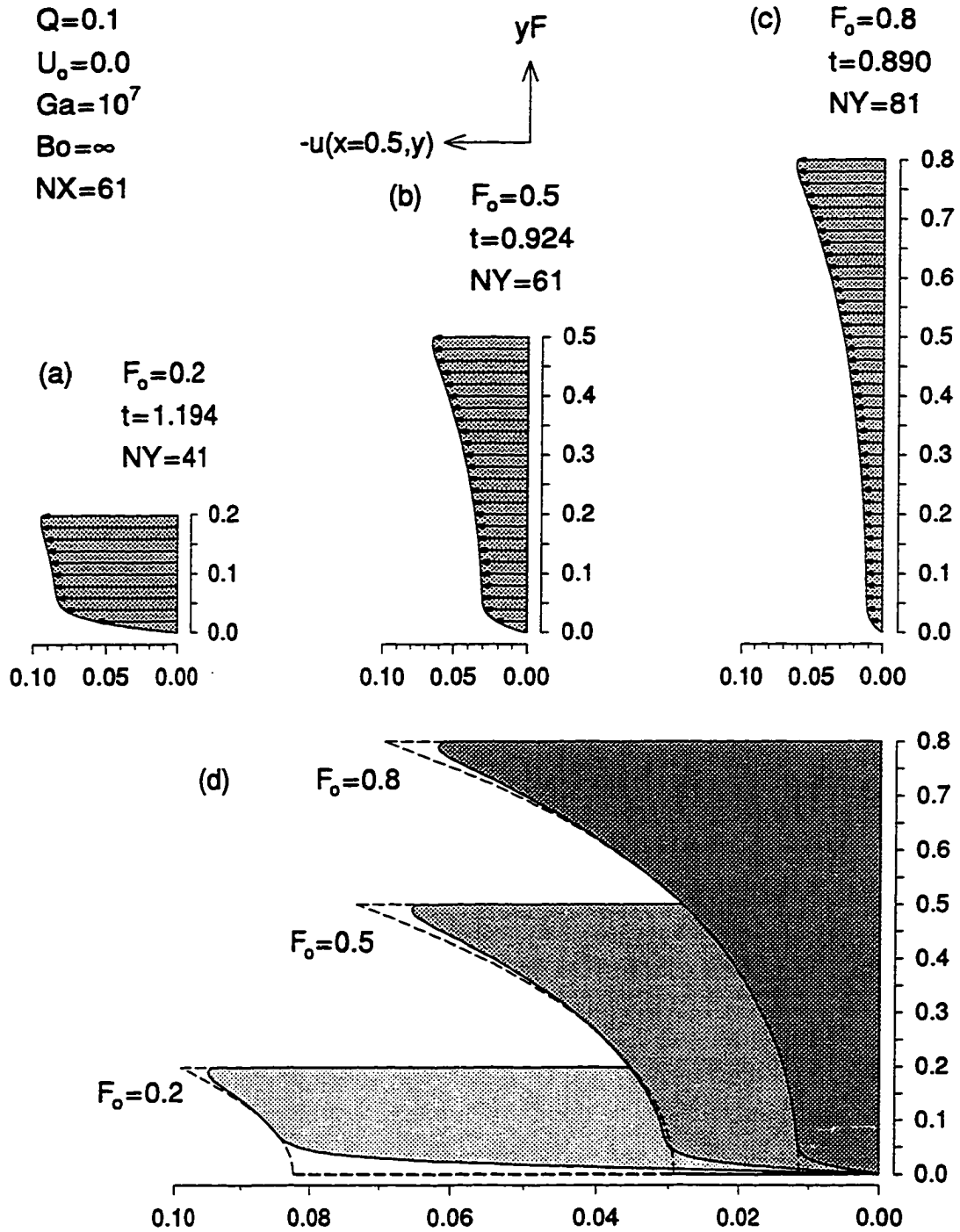


Figure 5.18: Centerline Velocity Profiles for Case 5

implies that the liquid volume which must be displaced from the right to the left side of the container as the free surface moves from its initial to its equilibrium position is the same for all three cases. Consequently, the magnitude of the average horizontal velocity, u_{ave} , must increase as the liquid becomes more shallow. The average velocity must also increase as the period of oscillation, T , becomes shorter. Numerical values for the product of $u_{ave}F_oT$, calculated for the three profiles shown in Figure 5.18, exhibit only a 0.4% variation.

Where at $F_o = 0.8$, the bottom half of the profile accounts for approximately 11.5% of the kinetic energy flowing through the $x = 0.5$ plane, this fraction increases to 27.8% at $F_o = 0.5$, and to 41.6% at $F_o = 0.2$. As the liquid becomes more shallow, the interior of the horizontal velocity profile becomes increasingly more uniform, thus moving the flow closer to the bottom boundary. This leads to a significant increase in the magnitude of the local shear stress at the bottom wall. Compared to the magnitude of the shear stress for $F_o = 0.8$, the shear stress is larger by a factor of 2.6 at $F_o = 0.5$, and by a factor of 6.9 at $F_o = 0.2$.

In Figure 5.18(d) the shape of each of these three profiles is compared to the shape suggested by the analytical result of the *linearized gravity wave theory*. The analytical result for the horizontal velocity profile, see [4], is rearranged into the following form by eliminating its dependence on time, t , and on wave position, x , to yield,

$$u_a(y) = C \frac{\cosh(\pi F_o y)}{\sinh(\pi F_o)} \quad (5.3)$$

where C is a constant which depends on several parameters such as the amplitude, wavelength, and phase speed of the wave. For the analytical profiles of u_a , which are drawn in the figure in terms of the dashed lines, the value of C was selected by matching the analytical and numerical profiles at their mid-point, $y = 0.5$. Despite the fact that the analytical profiles are valid for inviscid irrotational flow of waves with a vanishingly small amplitude compared to their wavelength, the agreement with the shape of the numerical profiles away from the top and bottom boundaries is excellent.

5.2 Parametric Effects on Sloshing

Despite the complexity of the flowfield the response of the sloshing liquid to the forcing conditions can be approximated from a *global prospective* as that of a simple dynamical system. Several models, based on equivalent mechanical systems, have been used in the course of study of sloshing problems. These include models ranging

in complexity from simple pendulum approximations to more elaborate composite systems using multiple equivalent masses and torsional springs.

In the absence of viscous effects, $Ga \rightarrow 0$, and surface tension effects, $Bo \rightarrow \infty$, the liquid behaves like an undamped second order system. An equivalent mechanical model based on a simple pendulum provides a reasonable approximation. The two forcing conditions under consideration here, described in terms of Q and U_o , lead to different initial conditions for the system.

The sudden acceleration of the container results in an apparent horizontal acceleration, Q , acting on the liquid mass. This causes a shift in the hydrostatic equilibrium position of the liquid which is now determined by the net acceleration acting on the fluid, given by $\vec{a} = -Q\vec{i} - \vec{j}$. The initial condition for the liquid at time $t=0$, described by a zero velocity and a horizontal free surface position, represents a displacement of the liquid mass from this equilibrium position. The liquid is set into motion under the action of a restoring force which consists of a vertical component in terms of the acceleration due to gravity, and a horizontal component in terms of the apparent acceleration, Q .

A step change in the velocity of the container at time, $t=0$, results in a non zero initial velocity field for the liquid. This causes the liquid mass to be displaced from its equilibrium position, which for $Q=0$ is determined only by the acceleration due to gravity.

Where viscous effects introduce damping into the system, surface tension effects can significantly alter the dynamic behavior of the system. The local curvature of the free surface leads to non-zero pressure forces acting along it. As a result of these surface forces the liquid must use some of its available energy in deforming its free surface. This energy is stored in the interfacial region as free energy. In the absence of losses due to contact angle hysteresis effects, it is returned to the flowfield when the liquid surface returns back to its original position. The rate at which the interfacial energy changes is determined locally by the free surface curvature and velocity. Consequently, this *potential energy storage* can not be accurately determined from a global prospective such as the position of the center of mass of the liquid. Thus, the use of equivalent mechanical systems to model surface tension effects, such as a torsional spring, are not very accurate.

Surface tension effects lead to an additional, non-linear, restoring force acting on the system. This force tends to return the liquid back to an equilibrium position which

minimizes the free surface energy. Thus the equilibrium position for the surface tension energy is represented by the initial horizontal position of the free surface. For cases with $Q = 0$, the restoring force due to surface tension reinforces the restoring body force in terms of gravity. However, for cases with $Q \neq 0$, the restoring force due to surface tension acts along a direction that is different from that of the restoring force due to net the body force. In this case the dynamic response of the system becomes more unpredictable. The equilibrium position of the free surface, which is reached through the action of viscous dissipation as time $t \rightarrow \infty$, is different from that determined by a hydrostatic force balance based solely on the body forces. The steady state free surface position is not flat, and cannot be determined in advance.

The analysis of the sloshing liquid as a dynamic system will be carried out using energy conservation principles. A detailed, first law analysis of the system was presented in section 3.8. It lead to the derivation of a set of equations which can used for the calculation of each of the following energy components:

- E_k : kinetic energy
- E_p : potential energy (due to body forces only)
- E_s : surface tension energy storage
- E_d : viscous dissipation energy component
- E_v : viscous surface dissipation component

The total energy of the system is given by the sum of each of the above energy components according to,

$$E(t) = E_A(t) + E_D(t) = 1 \quad (5.4a)$$

where E_A represents the amount of available energy of the system, and is given by,

$$E_A(t) = E_k(t) + E_p(t) + E_s(t) \quad (5.4b)$$

and E_D represents the total amount of viscous energy dissipation given by the sum of viscous dissipation in the interior of the flowfield and the viscous dissipation at the free surface,

$$E_D(t) = E_d(t) + E_v(t) \quad (5.4c)$$

Under the action of viscous dissipation the system reaches an equilibrium, *steady state*, condition in the limit as $t \rightarrow \infty$. The limiting values of the available and dissipated energy components of the system are given by,

$$\lim_{t \rightarrow \infty} E_A = E_p(\infty) + E_s(\infty) \equiv E_R \quad (5.5a)$$

and

$$\lim_{t \rightarrow \infty} E_D = E_d(\infty) + E_v(\infty) = 1 - E_R \quad (5.5b)$$

where E_R represents the residual amount of available energy which is left in the system. As a final note on the first law analysis, the following two points are reiterated here in order to clarify the presentation and discussion of results which will follow:

1. The energy balance of the system was carried out with respect to the moving frame, (x, y) . Consequently, a state of zero kinetic energy, $E_k = 0$, implies that the liquid is moving along with the container as a rigid body.
2. The potential energy of the system was formulated with respect to an equilibrium position determined solely by the net body force. Consequently, a state of zero potential energy, $E_p = 0$, implies that the center of mass of the liquid lies in a position for which the net body force torque is equal to zero. In the presence of surface tension effects this position does not necessarily represent an equilibrium position for the system.

The parametric study on the effects of the various similarity parameters on the dynamics of the sloshing liquid will focus for the most part on the period of oscillation, T , and the rate of viscous damping. The period of the system will be determined by examining the transient behavior of the kinetic energy of the liquid. For a second order system, the rate of viscous damping can be expected to obey a simple exponential relation of the form,

$$E_A^n = (1 - E_R) 10^{-\tau t} + E_R \quad (5.6)$$

where, τ , is used to denote the *modulus of decay*. Note that the continuous rate of viscous dissipation does not remain constant through any given period of oscillation. Regression analysis will be used to determine the modulus of decay, τ , based on the above relation, where E_A^n is used to denote a set of discrete values of the available energy of the system, taken at points corresponding to states of maximum kinetic energy.

5.2.1 Effects of Initial Liquid Depth

The initial liquid depth, F_o , is the sole dimensionless parameter that defines the geometry of the problem. Some of the effects attributed to F_o have already been

identified and discussed. Recall for example that the apparent mass of the liquid, \mathcal{M}_a , which represents the resistance offered by the liquid to the applied forcing, depends strongly and non-linearly on the value of F_o (see Figure 3.6).

For a sudden container acceleration, $Q \neq 0$, the initial energy available to the liquid, E_o , is in the form of potential energy and is generally⁴ independent of the liquid depth. However, for a step change in the velocity of the container, $U_o \neq 0$, the initial energy of the system, E_o , is in the form of kinetic energy and it was shown to depend non-linearly on the magnitude of F_o (see Figure 3.4).

The effect of the initial liquid depth, F_o , on the period of oscillation, T , is shown in Figure 5.19. Numerical results for the magnitude of T were calculated at several values of F_o , and are shown in the figure in terms of the solid bullets. The remaining similarity parameters were held constant at $Q = 0.05$, $U_o = 0$, $Ga = 10^6$, and $Bo = \infty$. The present result is compared to an analytical solution which is drawn in the figure as a solid line. This analytical result is derived from the solution of the linearized potential flow equations. It is valid for irrotational flow, $Ga \rightarrow \infty$, with no surface tension effects taken into consideration, $Bo \rightarrow \infty$, and for an infinitesimal amplitude of sloshing, $(Q, U_o) \rightarrow 0$. Under these conditions the period of oscillation predicted by the analytical result, T_a , is given by,

$$T_a(F_o) = \sqrt{\frac{4\pi}{\tanh \pi F_o}} \quad \text{for} \quad \lim Ga \rightarrow \infty \quad \text{and} \quad \lim(Q, U_o) \rightarrow 0 \quad (5.7)$$

Note that the functional dependence of the period on the liquid depth, as depicted by the numerical result, is in excellent agreement with the behavior described by the analytical solution. In the limit as $F_o \rightarrow \infty$, the period of oscillation becomes independent of the depth, $T_a \rightarrow 2\sqrt{\pi}$, while as $F_o \rightarrow 0$ the period increases with decreasing liquid depth according to $T_a \rightarrow 2/\sqrt{F_o}$. Note that numerical results shown in the figure correspond to a solution for which significant viscous effects are present. Viscous effects appear to cause the shifting of the analytical curve both to the right and upwards. Thus for a Galileo value of $Ga = 10^6$, this leads to periods which are longer by 1.1% at $F_o = 1.00$, and by as much as 6.2% at $F_o = 0.15$. The increased deviation of the numerical result from the predicted analytical value, which occurs at lower liquid depths, is due the strengthening of viscous effects as $F_o \rightarrow 0$.

The effect of the liquid depth on the rate of viscous dissipation is shown in Figure 5.20. Using the same set of similarity parameters as above, the modulus of decay,

⁴Provided the bottom wall remains covered as $t \rightarrow \infty$.

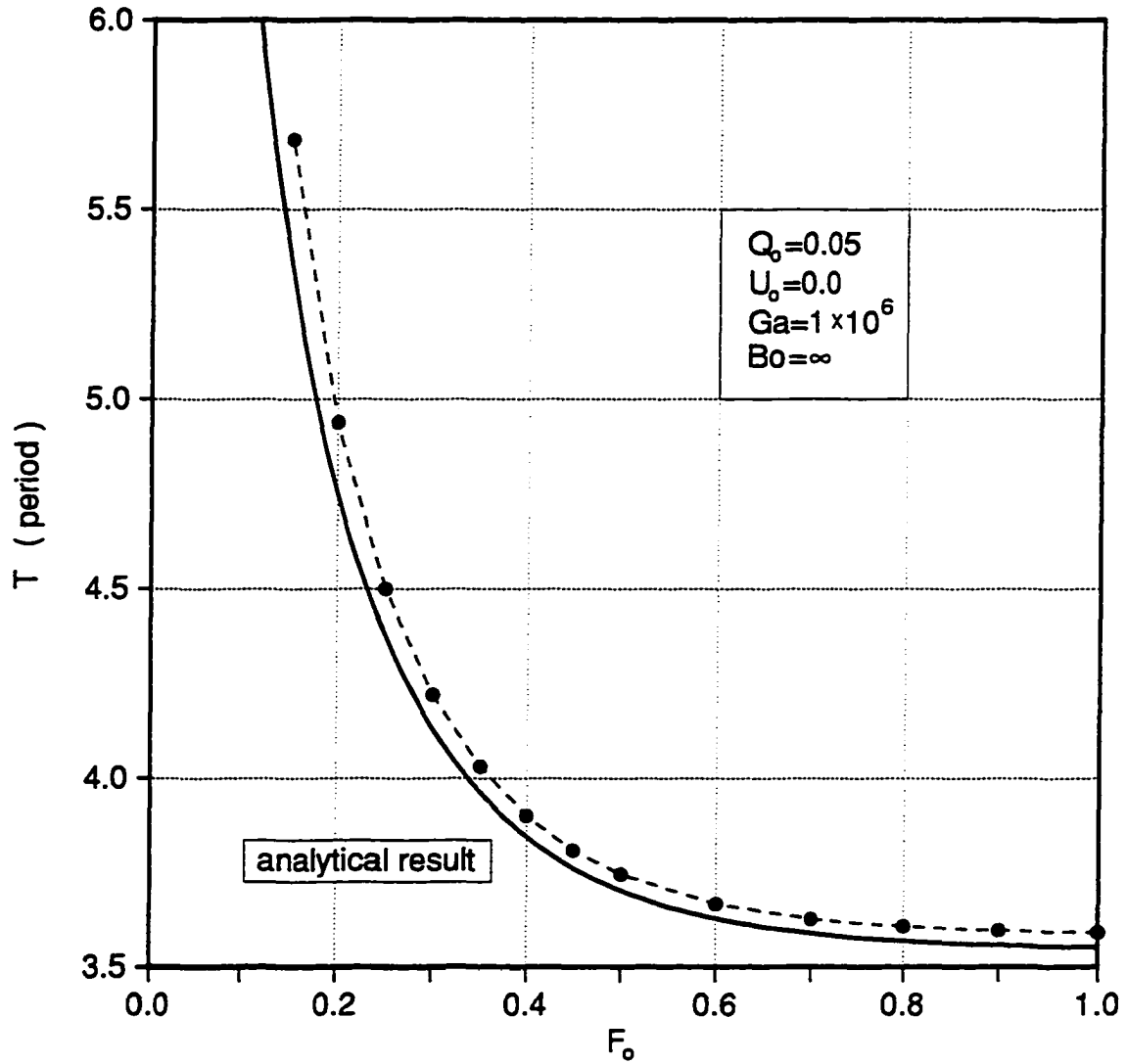


Figure 5.19: Effect of Initial Liquid Depth, F_o , on the Period, T

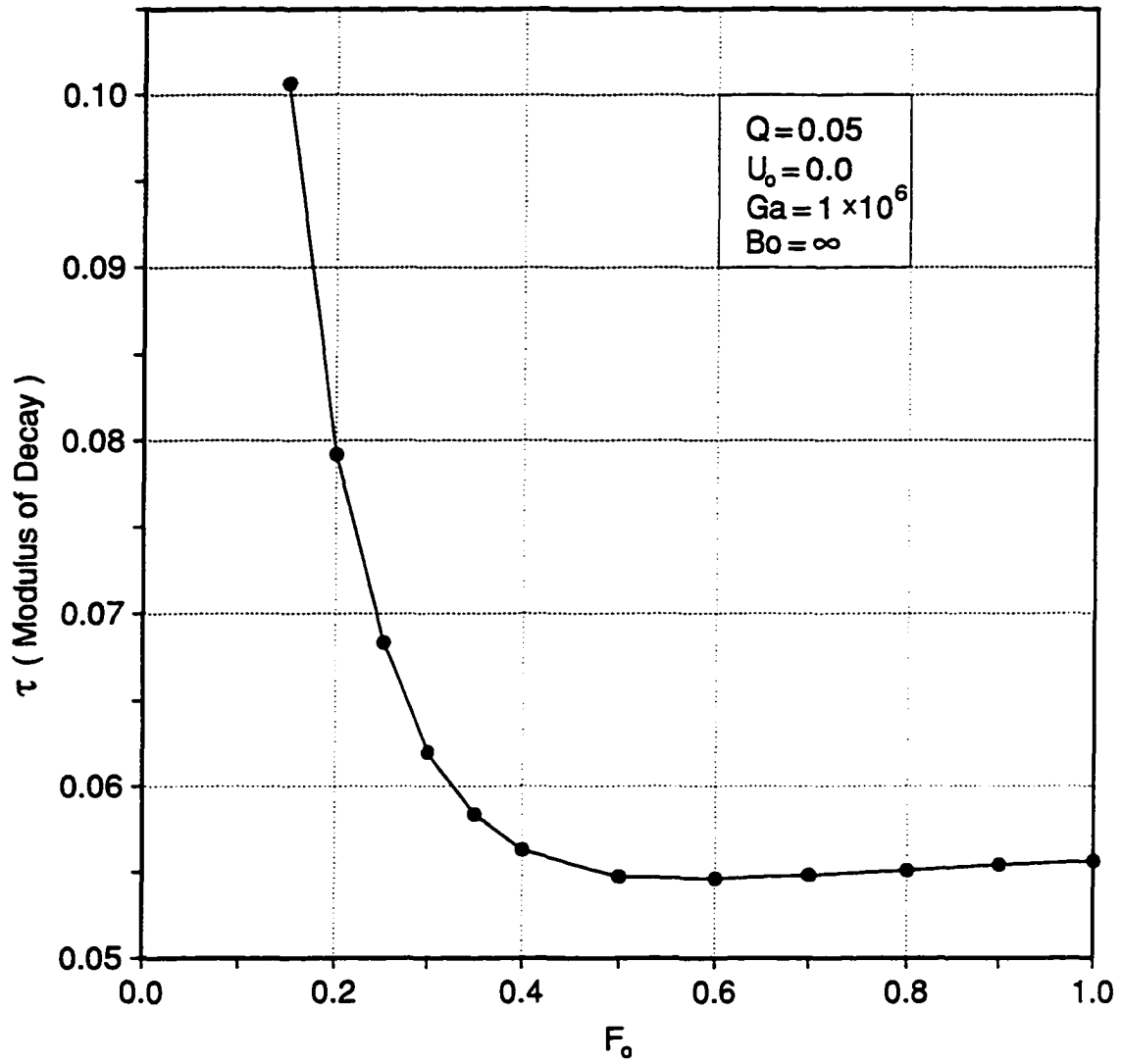


Figure 5.20: Effect of Initial Liquid depth, F_o , on the Dissipation Rate, τ

τ , is determined according to equation (5.6), and plotted against the liquid depth, F_o . Note that the minimum value of τ occurs at approximately $F_o \approx 0.5$. The rate of viscous dissipation increases very rapidly at smaller values of F_o , but it also increases, albeit at a very slow rate, at larger values of F_o . An aspect ratio of $F_o = 0.5$, corresponds to the geometrical configuration which offers the least resistance to the liquid flow. Note that for smaller values of F_o , the free surface position moves closer to the bottom boundary, which forces the streamlines to become more densely spaced and squeezed against the lower container wall. This leads to an increased dissipation due to boundary layer effects along the bottom boundary. For large values of F_o , the streamlines along the centerline of the container have room to expand to increasing depths which lowers the dissipation from the bottom boundary. However, with the increasing expansion of the flow to higher depths the streamlines become increasingly squeezed against the container side walls. Thus, even though the dissipation from the lower wall decreases with an increasing liquid depth, the dissipation from the side wall increases sufficiently to cause a small increase in the overall rate of viscous dissipation. From a global perspective, the center of mass of the liquid is undergoing a rotation about a point located approximately at center of the free surface, ($\bar{x} \approx L/2, \bar{y} \approx F_o/2$). An aspect ratio of $F_o = 0.5$, places each of the container walls at an equal distance from this point of rotation, and it appears to minimize the overall dissipative effects. It is interesting to note, that $F_o = 0.5$ also corresponds to the geometrical configuration which minimizes the wall surface for any given amount of liquid volume (dimensional volume, $\bar{V} = L\bar{F}_o$).

The rate of viscous dissipation from each of the container walls can be evaluated on a per unit area basis by the integral of the viscous dissipation function, Φ , which was defined in equation (3.43d). In general, the highest local dissipation rates occur in the vicinity of the contact points. For $F_o = 0.8$, the dissipation from the two side walls accounts for nearly 98% of the total dissipation from all three walls. The contribution from the bottom wall increases to about 13% for $F_o = 0.5$, and it becomes dominant for $F_o = 0.2$, accounting for nearly 74% of the overall dissipation rate from the walls.

5.2.1.1 Truncation Error Estimate The results presented in this section were calculated using computational grids ranging in size from a 41×41 grid for small values of F_o to a 41×61 grid for large values of F_o . The size of the time step used during the calculation was equal to $\Delta t = 0.001$. The results for T represent a 10 cycle average

while the modulus of decay was calculated by regression analysis from approximately 20 points over the same time interval. Grid refinement studies have been carried out to assess the truncation error of the results. It is estimated that the maximum error for the period of oscillation in Figure 5.19 is less than 0.1%, while the error for the modulus of decay in Figure 5.20 is on the order of 2.4%.

5.2.2 Effects of Forcing Conditions

The two forcing conditions under consideration in the present study are described in terms of the two similarity parameters, Q and U_o . A sudden container acceleration results in an apparent horizontal acceleration of magnitude Q which is acting on the liquid. A step change of magnitude U_o in the velocity of the container results in a non-zero initial velocity for the liquid. In the absence of surface tension effects, $Bo \rightarrow \infty$, which will be examined later, the dynamic response of the liquid to the two types of forcing conditions is quite similar.

The effect of the magnitude of forcing on the period of oscillation is shown in Figure 5.21. Here, calculated results for the period, T , are plotted as a function of the apparent acceleration, Q . Note that in addition to a set of data points which was obtained with $Ga = 10^6$, and is represented in the figure by the solid bullets, a similar set of results was obtained using the potential code for $Ga = \infty$, and is represented by the white bullets. The values of the remaining similarity parameters were held constant during these calculations with $F_o = 0.5$, $U_o = 0$, and $Bo = \infty$. These results are also compared to the linearized (small amplitude) analytical solution of equation (5.7) which is drawn in the figure as a solid horizontal line. The analytical result for the period of oscillation is valid in the double limit of $Ga \rightarrow \infty$ and $Q \rightarrow 0$ and is equal to $T_a = 3.7016$. At small values of Q , both the viscous and inviscid results for the period of oscillation are independent of the value of Q . Results obtained from the potential flow model for inviscid flow differ from the analytical solution by only 0.044% at small values of Q . The period of the viscous solution, which also remains constant at small values of Q , is longer by approximately 1.10%. Liquid viscosity causes the period of oscillation to increase. Its effects on T will be presented in the following section. For larger values of Q non-linear effects are significant and the period of oscillation becomes longer than the value predicted by the linearized analytical solution. Note that non-linear effects, caused by a finite amplitude of sloshing begin to manifest themselves for values of Q as small as 0.02. The period of oscillation for both the viscous and

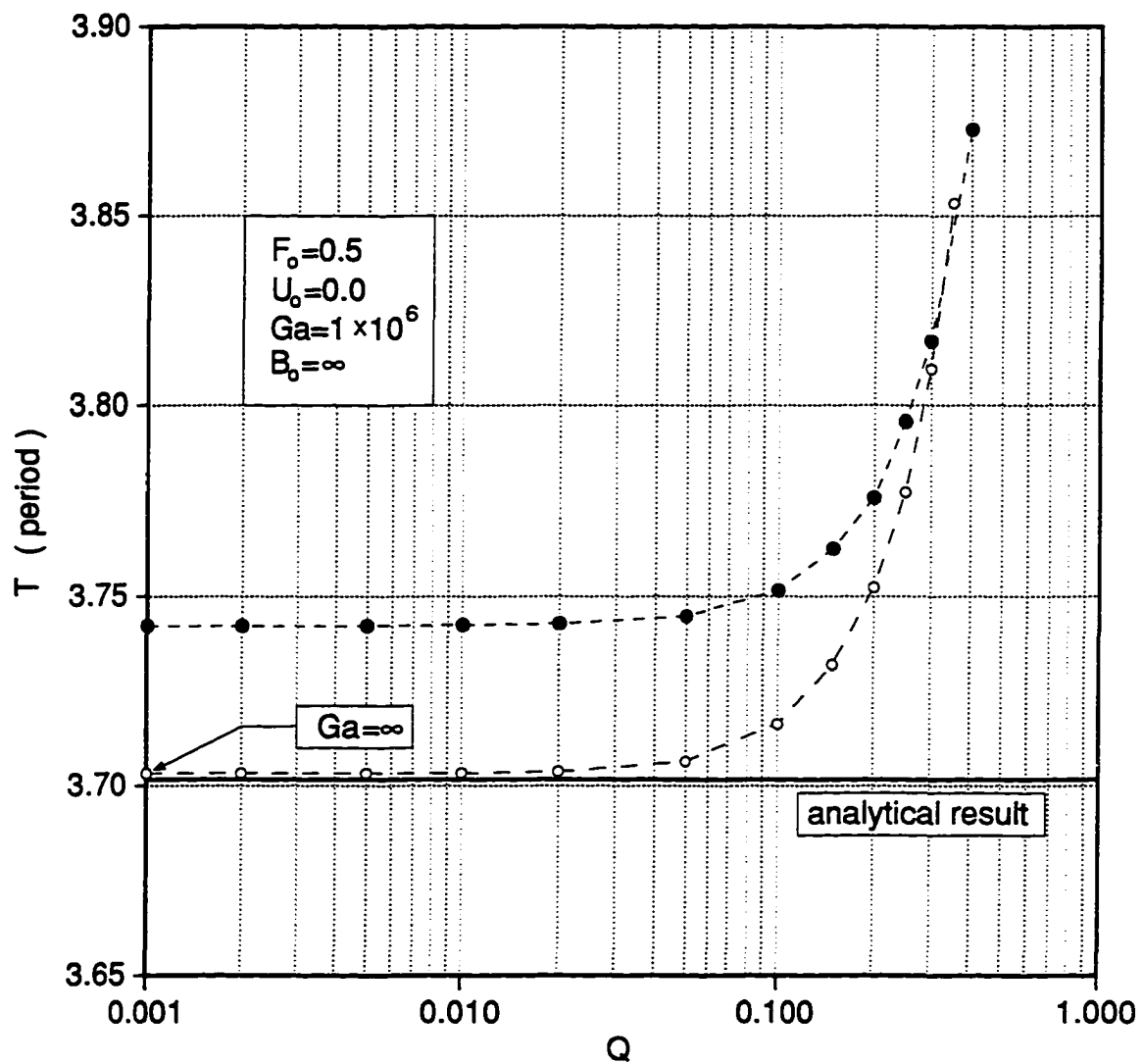


Figure 5.21: Effect of Apparent Acceleration, Q , on the Period, T

the inviscid solutions becomes longer as the magnitude of the apparent acceleration increases above $Q > 0.02$.

A similar behavior was demonstrated by the period of oscillation for cases with $U_o \neq 0$. Numerical values for T , calculated using small values of U_o , were for all practical purposes identical with those obtained at corresponding values of Q . For cases with $U_o \neq 0$, the increase in the value of T due to finite amplitude of sloshing effects can be very closely correlated to the corresponding increase obtained for cases with $Q \neq 0$, if this correlation is carried out in terms of the total energy of the system. The total energy of the system determines the extent of non-linear effects, and is generally different for equal values of Q and U_o . For an aspect ratio of $F_o = 0.5$, the magnitude of U_o which will yield the same energy as a case calculated with $Q \neq 0$, is given by $U_o = \sqrt{5}Q/3$.

Unlike the effect on the period of oscillation the magnitude of the apparent acceleration, Q , appears to have an insignificant effect on the rate of viscous dissipation. The dissipation of the available energy of the system, E_A , which for $Bo \rightarrow \infty$ is given by the sum of the kinetic and potential energy components, is shown in Figure 5.22 for some of the cases which were considered above. All of the data points shown on the figure correspond to those states for which the kinetic energy of the system is at a maximum. This is done in order to isolate the exponential decay of E_A from periodic variations. In general, the rate at which the available energy of the system is dissipated is determined by an exponential factor in terms of the modulus of decay and a periodic factor which accounts for variations which occur at different stages of any given cycle. For example, the rate of dissipation is approximately maximum when the kinetic energy of the system is at a maximum and drops to nearly zero when the kinetic energy of the system is at a minimum.

Note that solid line drawn on the figure represents well all sets of data points calculated with different values of Q . Furthermore, it does not appear that the small deviations which exist in the rate of viscous dissipation at different values of Q follow a clear pattern. That is, the highest rate of dissipation appears to occur for $Q = 0.3$, the highest value of Q considered, while the second fastest rate occurs for $Q = 0.01$, the smallest of the values considered. A similar behavior was also observed for forcing conditions in terms of U_o . The effect of the magnitude of the forcing conditions on the rate of viscous dissipation appears to be negligible.

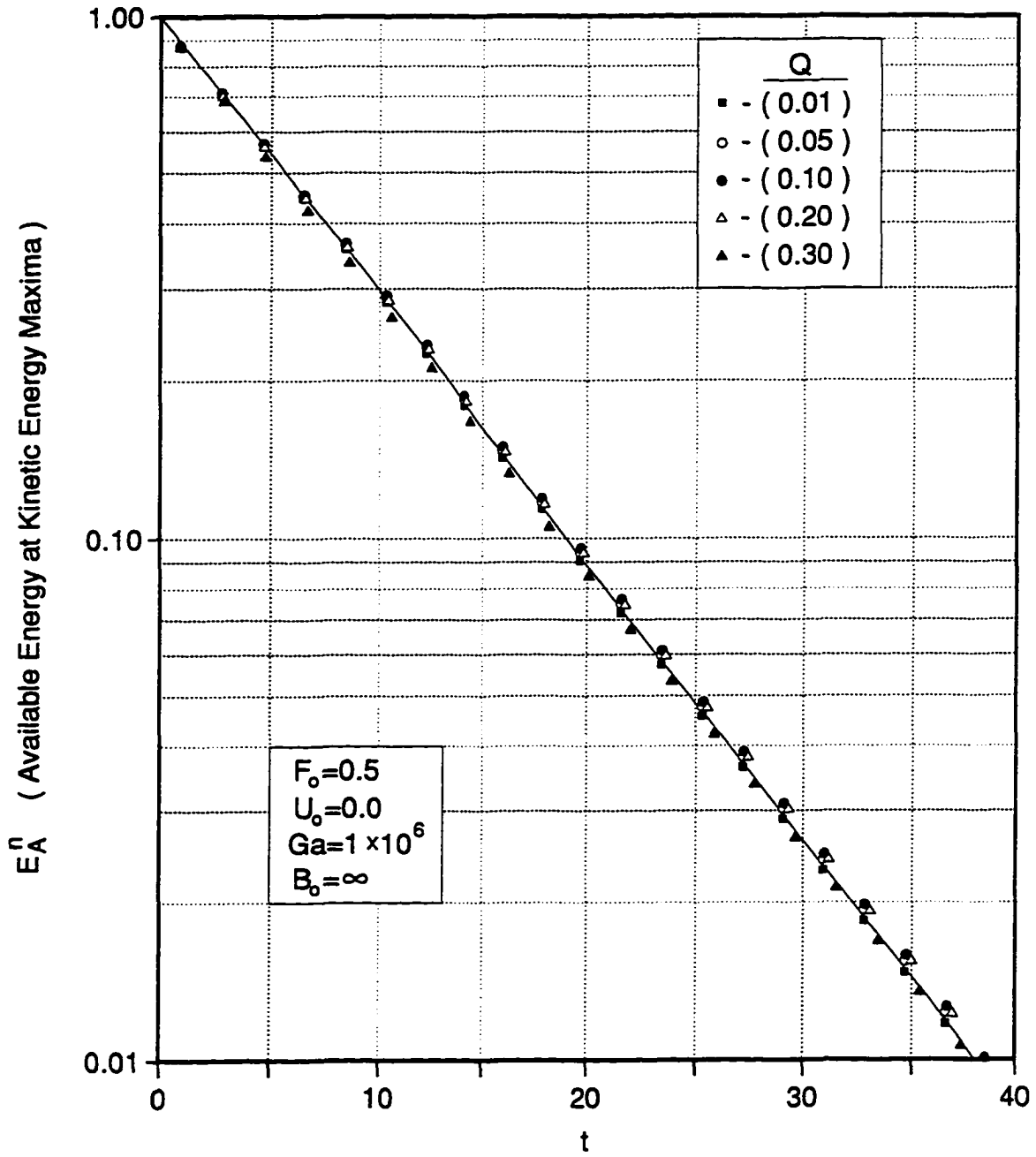


Figure 5.22: Effect of Apparent Acceleration, Q , on the Viscous Dissipation Rate

5.2.2.1 Truncation Error Estimate Results presented in this section were calculated using a 41×41 grid with a time step of $\Delta t = 0.001$. Based on a truncation error study which was carried out for a value of $Q = 0.2$, the truncation error of the results for the period of oscillation is estimated to be less than 0.10% for the viscous results and somewhat smaller for the irrotational results. The periods of oscillation, T , shown on Figure 5.21, were based on a 10 cycle average.

5.2.3 Effects of Liquid Viscosity

The viscosity of the liquid, and hence the Galileo number, have a profound effect on the dynamics of the sloshing liquid system. For the range of cases considered here, $10^4 \leq Ga \leq 10^{10}$, the rate of viscous dissipation changes by about two orders of magnitude. The period of oscillation for the liquid, T , is also affected by the value of the Galileo number, but to a much lesser degree.

To ascertain the effects of the Galileo number, Ga , on the period of oscillation, T , and the modulus of decay, τ , several cases were considered at selected values of Ga . For each of these cases, the remaining similarity parameters were held constant at $Q = 0.2$, $U_o = 0$, $F_o = 0.5$, and $Bo = \infty$. Furthermore, at each Ga value, the solutions from at least three different size meshes were considered in order to establish the truncation error of the results.

The results for the period of oscillation, T , are summarized in Table 5.3. The value of the period for the first cycle is shown in the second column of the table. The length of the first cycle increases with as the flow becomes more viscous. Compared to the potential result for the period, $T_p = 3.7523$, which represents the inviscid limit with finite amplitude of sloshing effects present, the length of the first cycle increases by less than 0.2% at $Ga = 10^{10}$, and by as much as 2.4% at $Ga = 10^4$. In addition to the increase in T as Ga decreases, the period also changes with respect to time, t . Although this change is not necessarily monotonic from one cycle to the next, the trend of the average period, \bar{T} , is to decrease as the flow progresses. This trend is clearly depicted by the average period, \bar{T} , calculated over five cycle intervals, and shown in the remaining columns of Table 5.3. The decrease in \bar{T} occurs at a faster rate for more viscous cases. For cases with larger Ga values, the length of the average period, \bar{T} , eventually drops below that of the potential result, T_p .

Viscous effects manifest themselves in two distinct ways to cause the behavior exhibited by the period in Table 5.3. First, the decrease in the length of the period

Table 5.3: Average Period of Oscillation, \bar{T} , at Several Ga Values

Galileo Number Ga	Average Period over Cycles n to m , $\bar{T}[n, m]$				
	$\bar{T}[1 : 1]$	$\bar{T}[1 : 5]$	$\bar{T}[6 : 10]$	$\bar{T}[11 : 15]$	$\bar{T}[16 : 20]$
10^4	3.8457	3.8075			
10^5	3.8122	3.7902	3.7805		
10^6	3.7909	3.7792	3.7718		
10^7	3.7771	3.7701	3.7625		
10^8	3.7695	3.7618	3.7560	3.7533	
10^9	3.7635	3.7570	3.7529	3.7505	3.7476
10^{10}	3.7592	3.7548	3.7525	3.7517	3.7492

with respect to time, is the result of a reduction in the *effective amplitude* of sloshing with time due to damping. Second, the increase in the length of the period with decreasing Ga values is the result of a reduction in the *effective depth* of the liquid due to boundary layer effects. Consider as an example the case with $Ga = 10^{10}$. The initial cycle of the viscous result is longer than the potential result of $T_p = 3.7523$ by about 0.18%. Both of these results have been calculated with a value of $Q = 0.20$ and based on Figure 5.21 some finite amplitude of sloshing effects are present. The amplitude of sloshing is directly proportional to the horizontal acceleration Q . Unlike the potential case, for which the amplitude of sloshing remains of the same order throughout the flow, for the case with $Ga = 10^{10}$ the effective value of Q decreases with time due to damping. Thus, finite amplitude of sloshing effects also decrease, causing the period of the viscous case to eventually become shorter than that of the inviscid case.

Figure 5.23 helps illustrate both of these two effects. The numerical result for the first period, T , is depicted in the figure in terms of the solid bullets, connected by the dashed line. The solid line represents the potential result, T_p . The potential result of $T_p = 3.7523$ is adjusted at each Ga value to account for changes in the effective amplitude of sloshing and the effective liquid depth. The solid square symbols shown in Figure 5.23, represent an adjustment to the potential result for a reduction in the amplitude of sloshing due to damping. The amplitude of sloshing is proportional to the square root of the available energy of the liquid, E_A . In the presence of damping, this amplitude can be expressed in terms of an effective acceleration, \hat{Q} , which is calculated

according to the relation:

$$\hat{Q} = Q \sqrt{E_A} \quad (5.8)$$

Based on this relation, and using the value of E_A at the mid-point of the first cycle, a representative value for \hat{Q} is determined at each Ga value. The potential result is then adjusted using Figure 5.21 to determine the appropriate value of the period at the calculated value of \hat{Q} . Note that this adjustment becomes more significant as the damping rate increases.

The length of the period of oscillation is most sensitive to the depth of the liquid, F_o . The *displacement thickness* associated with the viscous layer along the bottom wall, causes a reduction in the effective depth of the liquid, \hat{F}_o . The thickness of the viscous layer, $\bar{\delta}$, is proportional to $\sqrt{\nu}$, where ν denotes the liquid viscosity. In dimensionless form this requires, $\delta \sim Ga^{-1/4}$. Thus, a value for the effective liquid depth can be approximated by,

$$\hat{F}_o = F_o - C Ga^{-1/4} \quad (5.9)$$

where C represents a constant, which here is set equal to $C = 1$. Using the above relation, a value of \hat{F}_o is calculated at each Ga value. It is then used to determine the factor by which the period increases as a result of the depth reduction, based on the analytical result for T_a , which is given in equation (5.7). The white square symbols in Figure 5.23 represent the potential result for the period, T_p , having been adjusted for both the reduction in the effective amplitude and effective depth of the liquid motion. In the presence of liquid viscosity, the period of oscillation increases due to a reduction in the effective depth of the liquid, and if finite amplitude of sloshing effects are present the period decreases with time.

The effect of liquid viscosity on the damping rate of the system is shown in Figure 5.24. Here, the modulus of decay, τ , is calculated by regression analysis based on equation (5.6), and is plotted as a function of the Galileo number, Ga . Multiple solutions, providing an increasing degree of grid resolution, were considered at each Ga value. This was done in order to establish an estimate for the order of the truncation error in the results. Grid sizes in the range of 21×21 to 81×81 nodes were used, and they are identified in Figure 5.24 by the various symbols. In addition to the numerical results, extrapolated values for τ , which are based on equation (4.28) are also included in the figure. These values represent a *best estimate* for the magnitude of τ at each Ga value. They also provide an estimate for the truncation error, which ranges from a

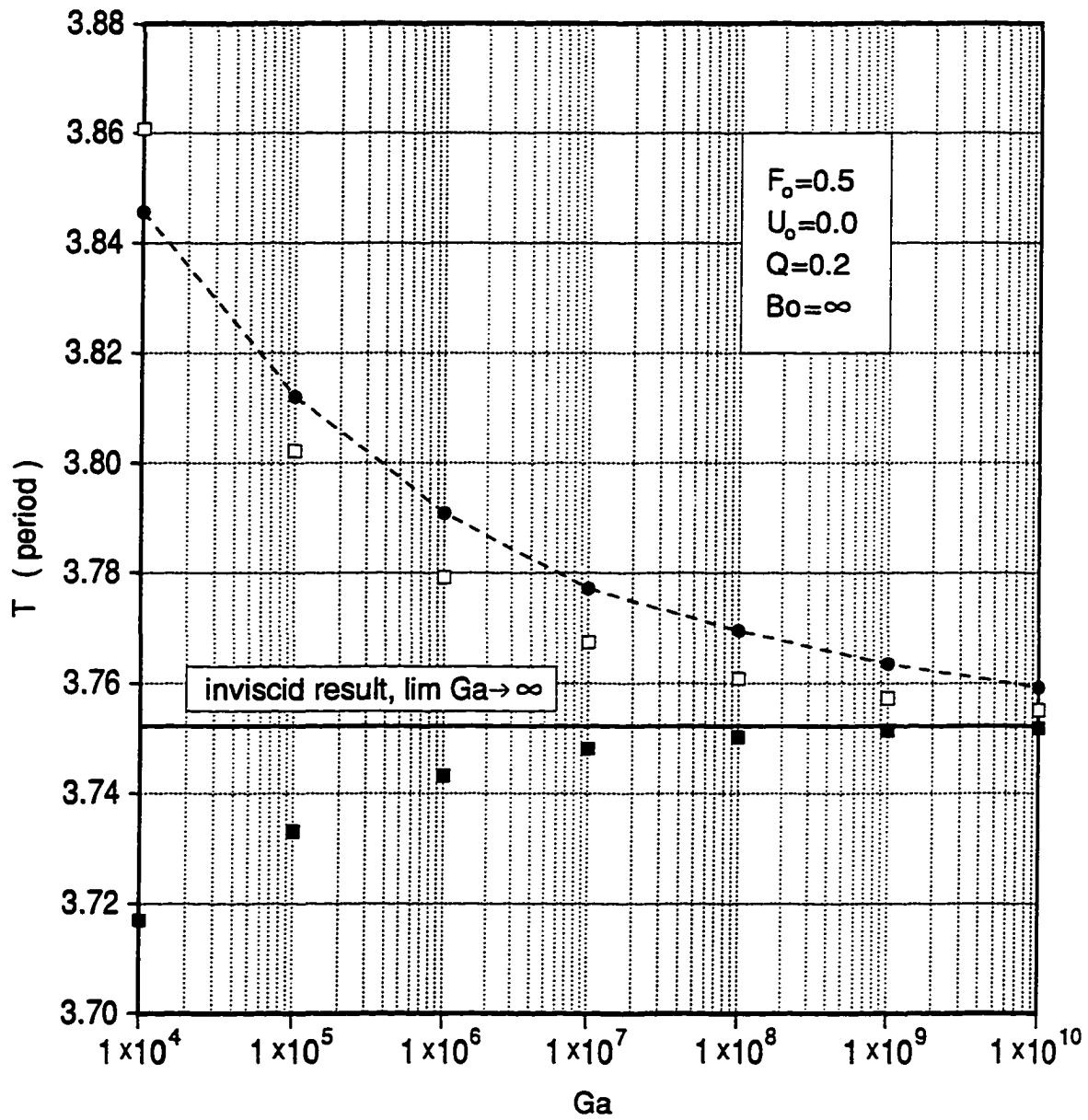


Figure 5.23: Effect of the Galileo Number, Ga , on the Period of Oscillation, T

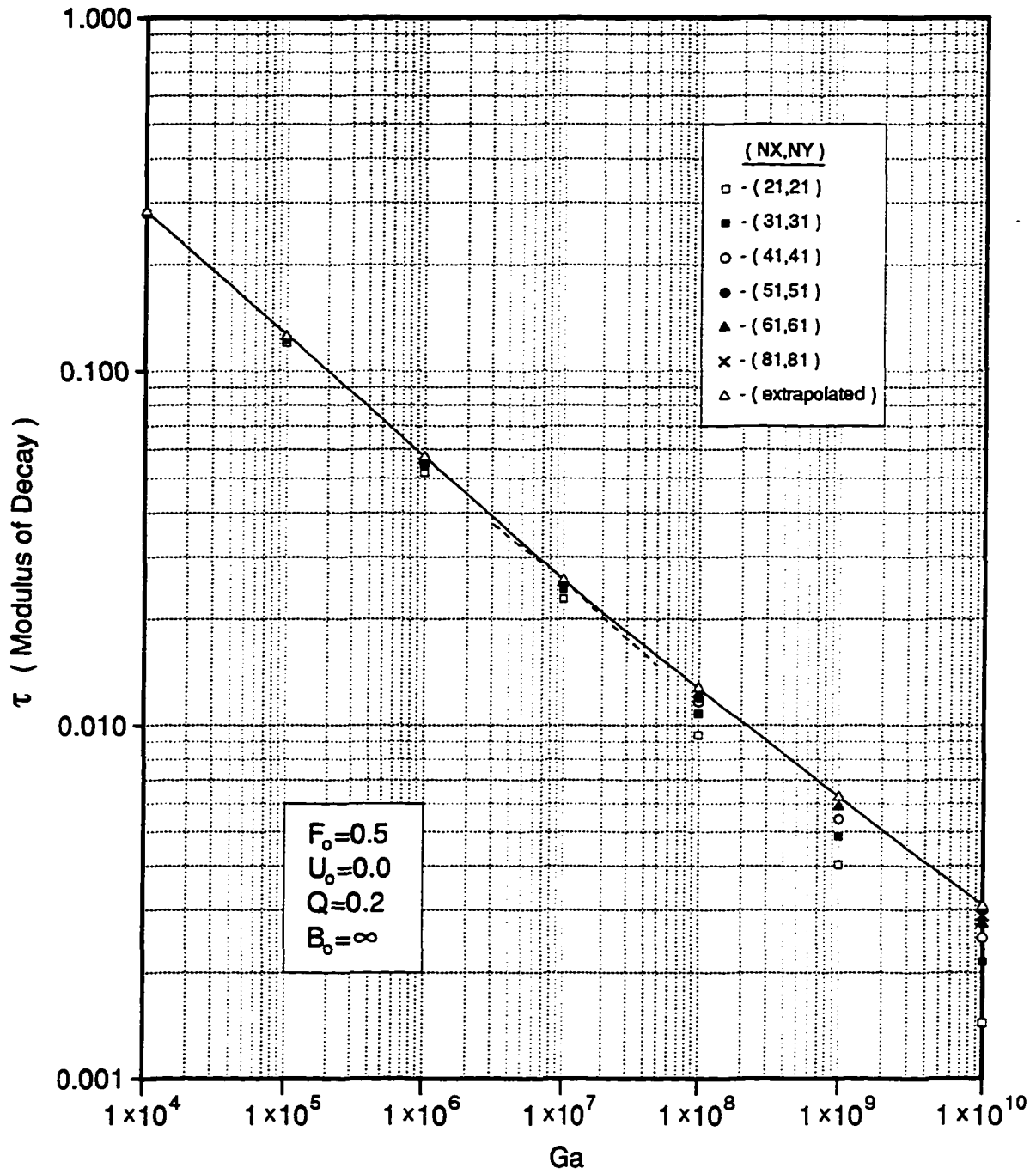


Figure 5.24: Effect of Galileo Number, Ga , on the Modulus of Decay, τ

minimum value of 0.5% at $Ga = 10^4$ to a maximum of 6.0% at $Ga = 10^9$. As the value of the Galileo number increases, and the liquid becomes less viscous, the character of the flowfield changes. Cells of local secondary flow develop along the free surface. As a result, grid refinement becomes essential in adequately resolving the flow along the free surface. It is strongly suspected, that the development of these secondary flow patterns along the surface of the liquid, also contributes to the behavior exhibited by τ in the figure. The numerical data for the modulus of decay, τ , can be represented with less than 2% deviation by the following relation:

$$\tau = \begin{cases} 6.823 Ga^{-0.346} & \text{for } 10^4 \leq Ga \leq 10^7 \\ 3.639 Ga^{-0.307} & \text{for } 10^7 < Ga \leq 10^{10} \end{cases} \quad (5.10)$$

It is believed that the decrease in the rate at which τ decreases with the value of the Galileo number, for $Ga > 10^7$, is the result of the secondary flow along the surface, which moves some of the available energy of the liquid away from the walls, thus leading to a decrease in the rate of dissipation.

An analytical solution for viscous, infinitesimal amplitude, deep water waves was given in [4]. This solution predicts an exponential damping in time for the displacement of the free surface from its equilibrium position, which leads to a modulus of decay for the displacement that is proportional to the liquid viscosity, ν . Since the energy of the system is proportional to the square of the displacement, this implies that the modulus of decay for the energy of the system should also be proportional to ν . In dimensionless form, this implies that $\tau \sim Ga^{-1/2}$.

5.2.4 Effects of Surface Tension

Some of the effects due to surface tension on the liquid flowfield and the position of the free surface have already been discussed in section 5.1.4. The focus in this section is on the changes which occur in the dynamic behavior of the liquid system as a result of surface tension effects.

Based on the two forcing conditions under consideration in this study, the liquid is set into motion either from an initial state of maximum potential energy for $Q > 0$, or, from an initial state of maximum kinetic energy for $U_o > 0$. The value of the dimensionless Bond number, Bo , determines the strength of the surface tension forces relative to that of the body forces that are acting on the liquid system. For $Bo \gg 1$, the dynamic behavior of the system is dominated by body forces, while for $Bo \ll 1$,

surface tension forces become dominant. The magnitude of the surface tension force is determined by the local curvature of the free surface. The resulting restoring force acts to minimize the free surface energy.

For cases with $U_o > 0$ and $Q = 0$, the restoring force due to surface tension acts in the same direction as the restoring force due to gravity. The effect of surface tension is to reduce the amplitude and the period of the liquid oscillations as $Bo \rightarrow 0$. However, the qualitative motion of the liquid for large and small Bo number cases remains similar.

For cases with $Q > 0$, the two restoring forces tend to work in different directions. The liquid is in equilibrium with respect to the net body force when the slope of its surface is equal to $-Q$. On the other hand, the liquid is in equilibrium with respect to the surface tension force if its surface remains horizontal. As a result of these two competing forces the dynamic response of the system becomes more complex and unpredictable. Since the force due to surface tension is determined by the local liquid surface curvature it is not uniform along this surface. As a result, additional modes and frequencies of oscillation become excited, thus making the liquid oscillations to appear to be more aperiodic. As $t \rightarrow \infty$, viscous damping brings the liquid in a position of static equilibrium. In this position, the liquid mass is in equilibrium with respect to both the body and the surface tension forces. However, this position of static equilibrium cannot be determined in advance since the force due to surface tension depends on the shape of the free surface.

In its initial horizontal position, the liquid is in a state of maximum potential energy, $E_p = 1.0$, experiencing only a net torque due to the body forces. The maximum elevation, F_{MAX} , reached by the free surface during a given case depends on the relative strength of the body and surface tension effects. This variation in F_{MAX} with respect to the Bond number, Bo , is depicted in Figure 5.25 for a set of cases calculated with $Q = 0.2$, $U_o = 0.0$, $F_o = 0.5$, and $Ga = \infty$. If surface tension effects are dominant the magnitude of the restoring force due to surface tension increases very rapidly as the liquid departs from the horizontal position and its surface becomes curved. As a result, the direction of motion is reversed well before the liquid reaches any appreciable height. If surface tension effects are negligible the liquid oscillates between positions of maximum kinetic and potential energy. In each of these two extreme regimes, the oscillations of the liquid mass remain quasi-periodic in nature, and very similar to those for a case with $U_o > 0$. At moderate values of the Bond number, $1 \leq Bo \leq 1000$,

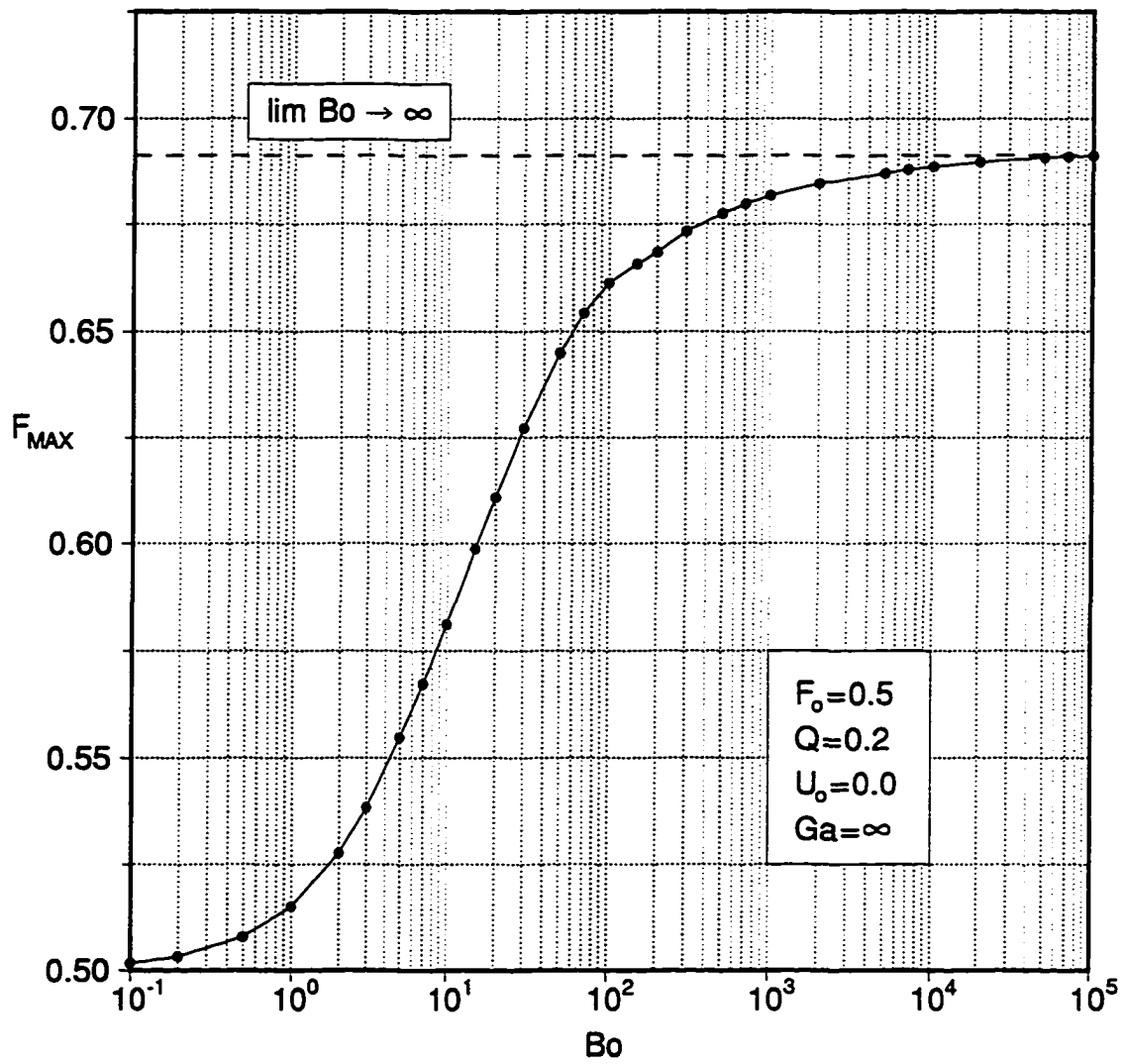


Figure 5.25: Effect of Bond Number on Surface Elevation

the maximum elevation reached by the liquid depends strongly on the value of Bo .

This behavior was previously examined in section 5.1.4, where the flowfield for Case 4 was analyzed from a kinematic perspective. The solution for Case 4 is examined here based on the First Law analysis of section 3.8. In Figure 5.26, the motion of the liquid is depicted in terms of an energy balance. The total energy of the system, E_t , is separated into five distinct components. These are, the kinetic energy E_k , the potential energy with respect to the net body force E_p , the viscous dissipation term E_d , and the two surface components E_v and E_s . The last two terms represent the total energy of the free surface of the liquid. The term E_v represents the increase in the internal energy of the free surface due to viscous dissipation, while E_s represents the free surface energy storage due to surface tension.

The motion of the liquid for this case is determined primarily by a pattern of interaction between the first two modes of oscillation. This pattern spans a ten cycle time interval, with the amplitude of the second mode gradually increasing to a maximum value and then decreasing back to a minimum. Furthermore, the frequency associated with the second mode is twice the fundamental frequency. As a result, the motion of the liquid in Figure 5.26 appears to be continually changing. The first cycle of sloshing is dominated by the first mode of oscillation. The liquid mass begins to accelerate away from its initial position of maximum potential energy, with E_k increasing to a maximum value of about 0.65 shortly before the liquid reaches the equilibrium position with respect to the body forces. During the first cycle, the surface tension component, E_s , varies approximately sinusoidal in time, increasing smoothly as the liquid moves away from the initial horizontal position, and decreasing in a similar fashion as the liquid returns back toward a horizontal position. The type of variation exhibited by E_s during the first cycle, can be reasonably approximated by an equivalent mechanical system which provides for energy *storage* and *release* based on the position of the liquid mass. However, finding a reasonable approximation in terms of an equivalent mechanical system becomes an increasingly difficult task as the amplitude of the second mode of oscillation increases. In the presence of second mode effects the variation of E_s becomes more complicated. Superimposed on the simple variation of the first mode, second mode effects cause the storage and release of additional energy at different stages of the cycle. As a result, the motion of the liquid becomes more abrupt, with the liquid accelerating and decelerating at faster rates.

As $t \rightarrow \infty$, viscous damping brings the system into a static equilibrium position.

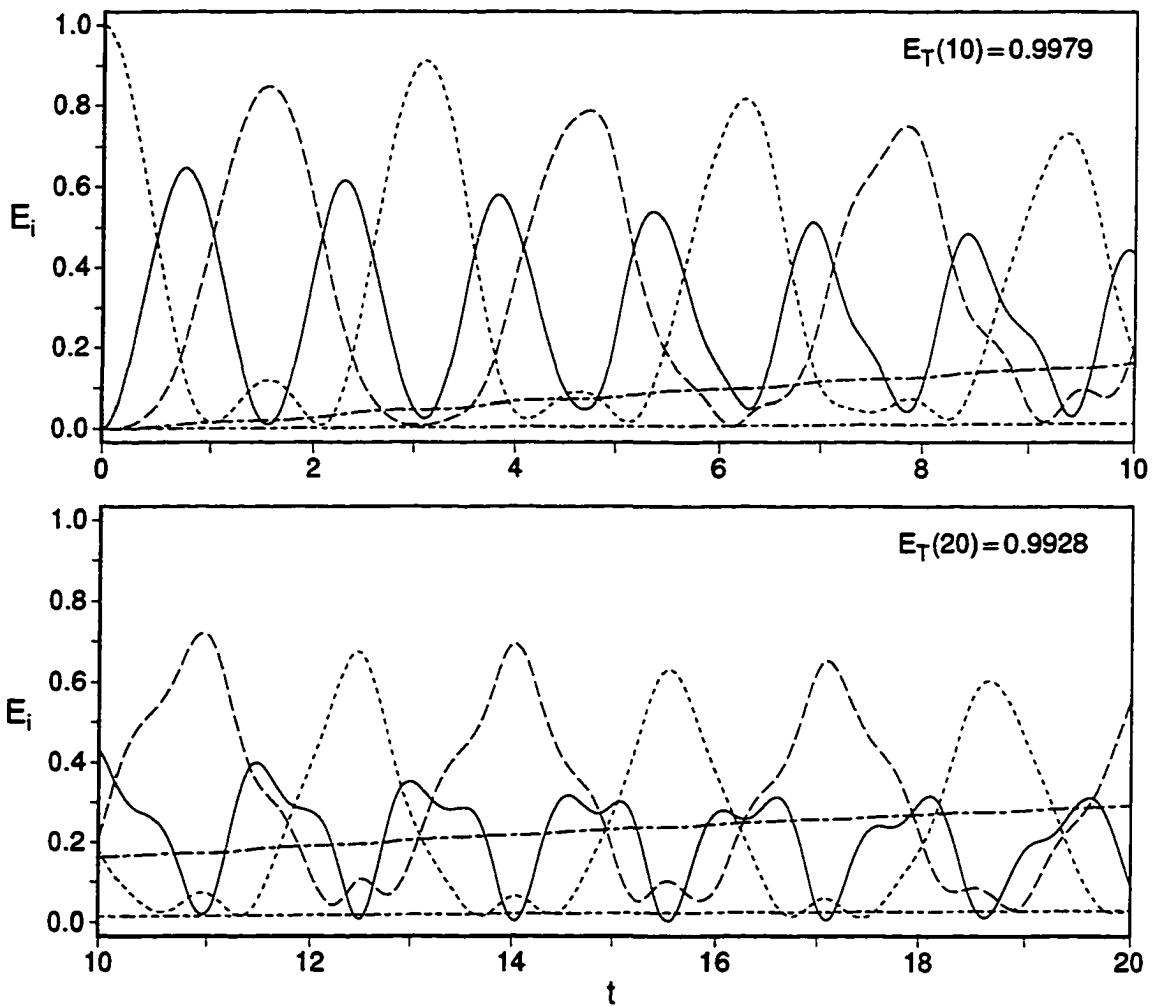
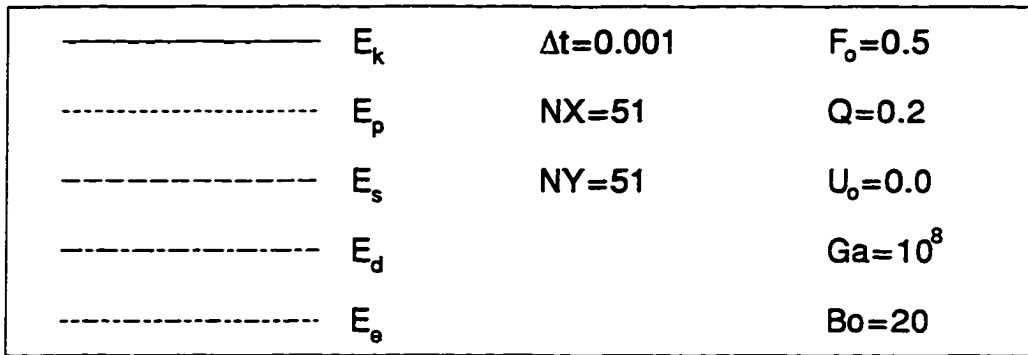


Figure 5.26: Energy Balance for $Bo = 20$ and $Ga = 10^8$

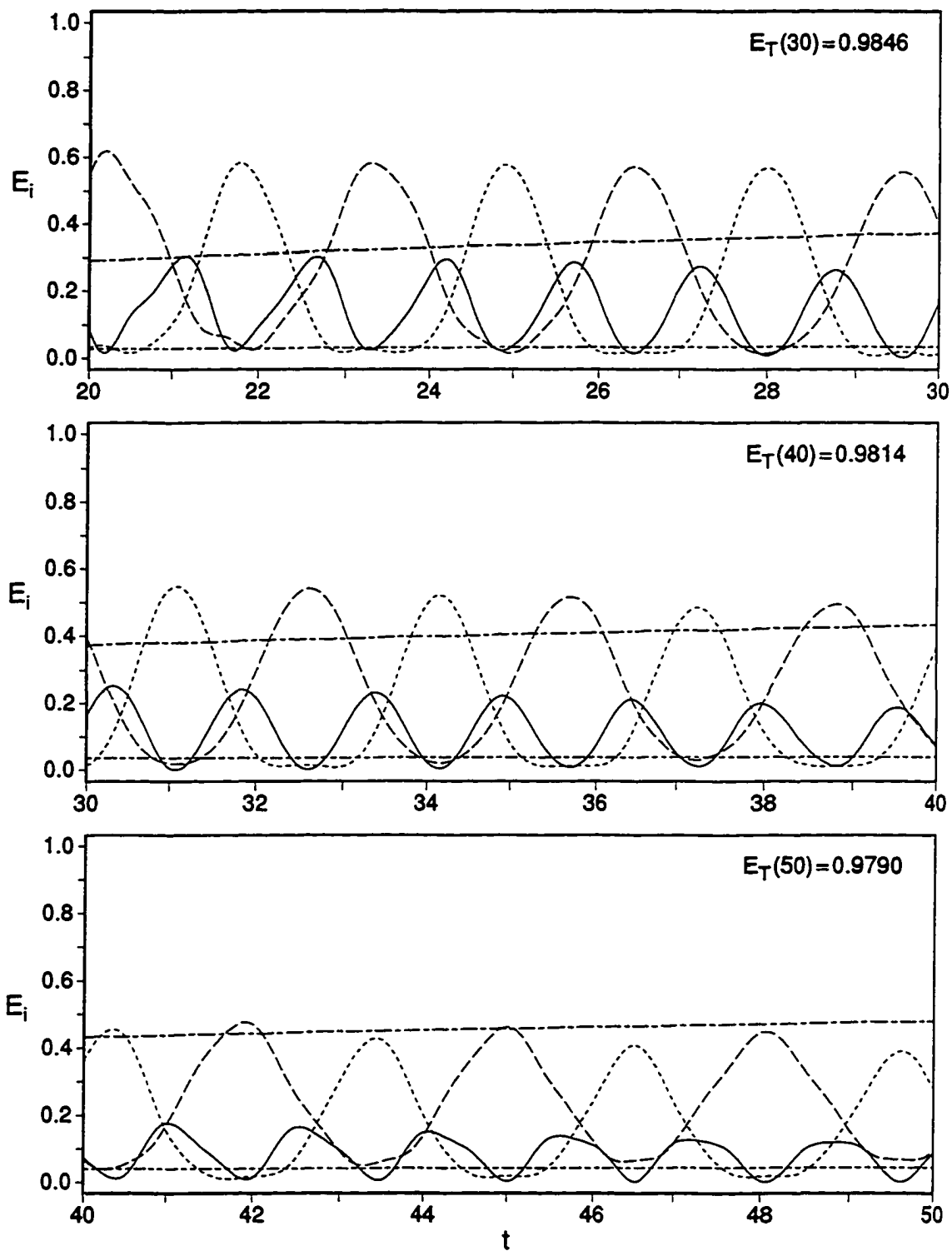


Figure 5.26 (Continued)

In this final position, the liquid mass is in equilibrium with both the body and surface tension forces. With $Bo = 20$, as the liquid reaches this position, nearly 71% of its initial energy would have been dissipated. The remaining 29% is left into the system as residual energy in the form of potential energy, E_p , and surface tension storage, E_s . Note that, the free surface dissipation term, E_v , remains approximately an order of magnitude smaller than E_d . This is typical of all cases considered in this study, where regardless of the values of Ga and Bo , viscous dissipation at the free surface accounts for 8 – 10% of the total dissipation.

The sum of these five components is equal to the total energy of the system, which in the absence of any error should remain constant, and equal to $E_t = 1$. With the governing equations having been differenced in their non-conservative form, the calculated value for E_t provides another measure of the truncation error present in the solution. A calculated value of the total energy of the system, E_t , is shown at the upper right corner of each time strip. Although, the rate at which the truncation error accumulates varies from cycle to cycle, as well as through the different stages of any given cycle, on average the total energy of the system decreases with time. Where the error in the value of E_t at $t = 10$ is only about 0.2%, by $t = 50$, it has increased to 2.1%.

In an effort to ascertain if liquid viscosity alters the basic structure of the liquid flow, the inviscid limit for Case 4 was also considered. This calculation was carried out based on the potential formulation of section 3.5. The solution is shown in terms of an energy balance in Figure 5.27. With the exception of dissipative effects, the motion of the liquid here, with $Ga = \infty$, remains qualitatively as well as quantitatively similar to that depicted in Figure 5.26 for $Ga = 10^8$.

In the absence of viscous effects, $Ga \rightarrow \infty$, the total energy of the system, E_t , is given by the sum of only three components. These components are the kinetic, E_k , potential, E_p , and surface tension, E_s . Since the total energy of the system must also remain constant, then only two of these three components are mutually independent. Thus, any two of these components can be used in defining an *energy space*. The motion of the liquid can then be represented in such a space by the path traced by the various energy states that the liquid system passes through during the course of the flow.

Figure 5.28 provides a summary of results obtained at several values of the Bond number. These results are shown here in terms of a series of paths, or trajectories, traced by the liquid in (E_p, E_k) space. In the absence of any surface tension effects,

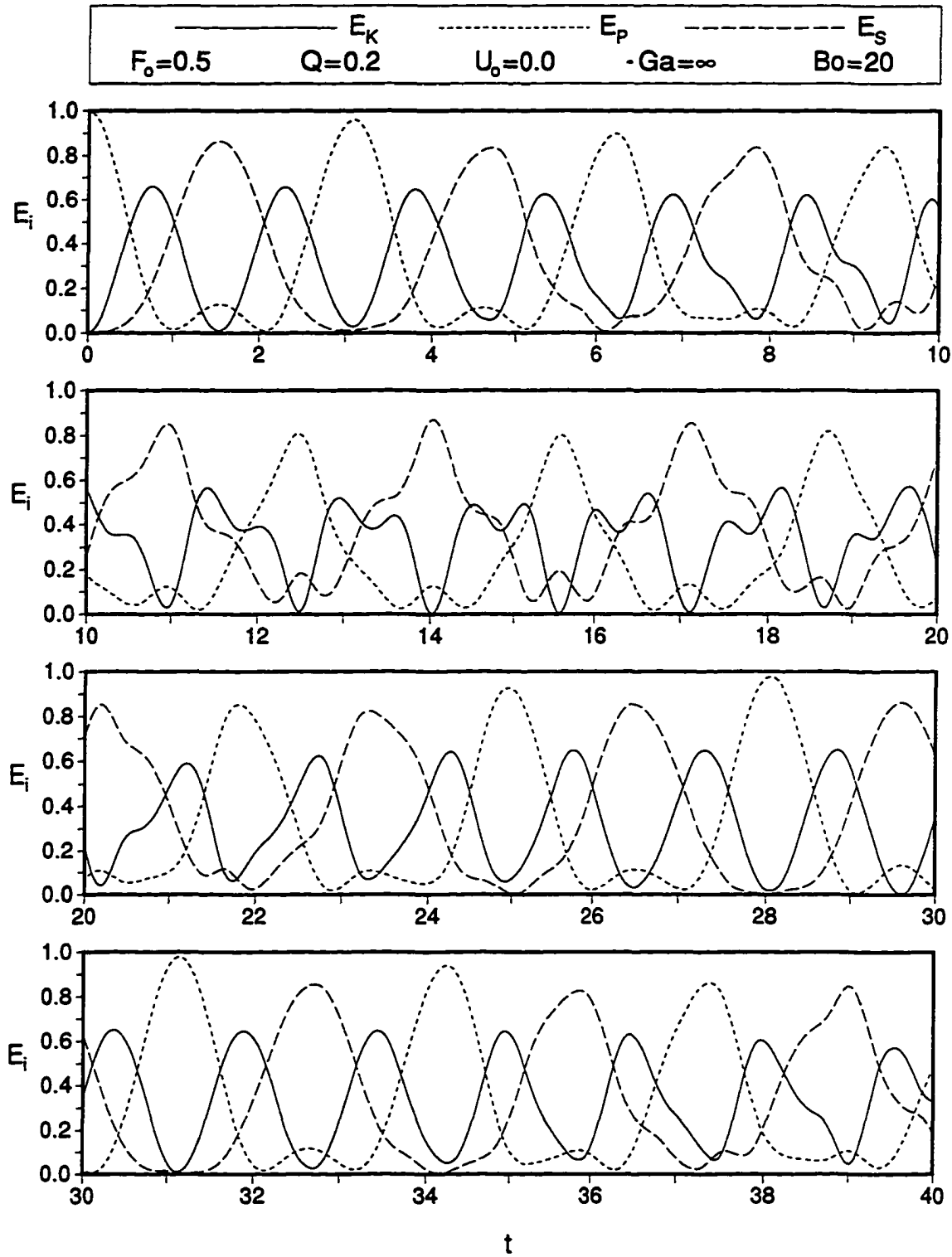


Figure 5.27: Energy Balance for $Bo = 20$ and $Ga = \infty$

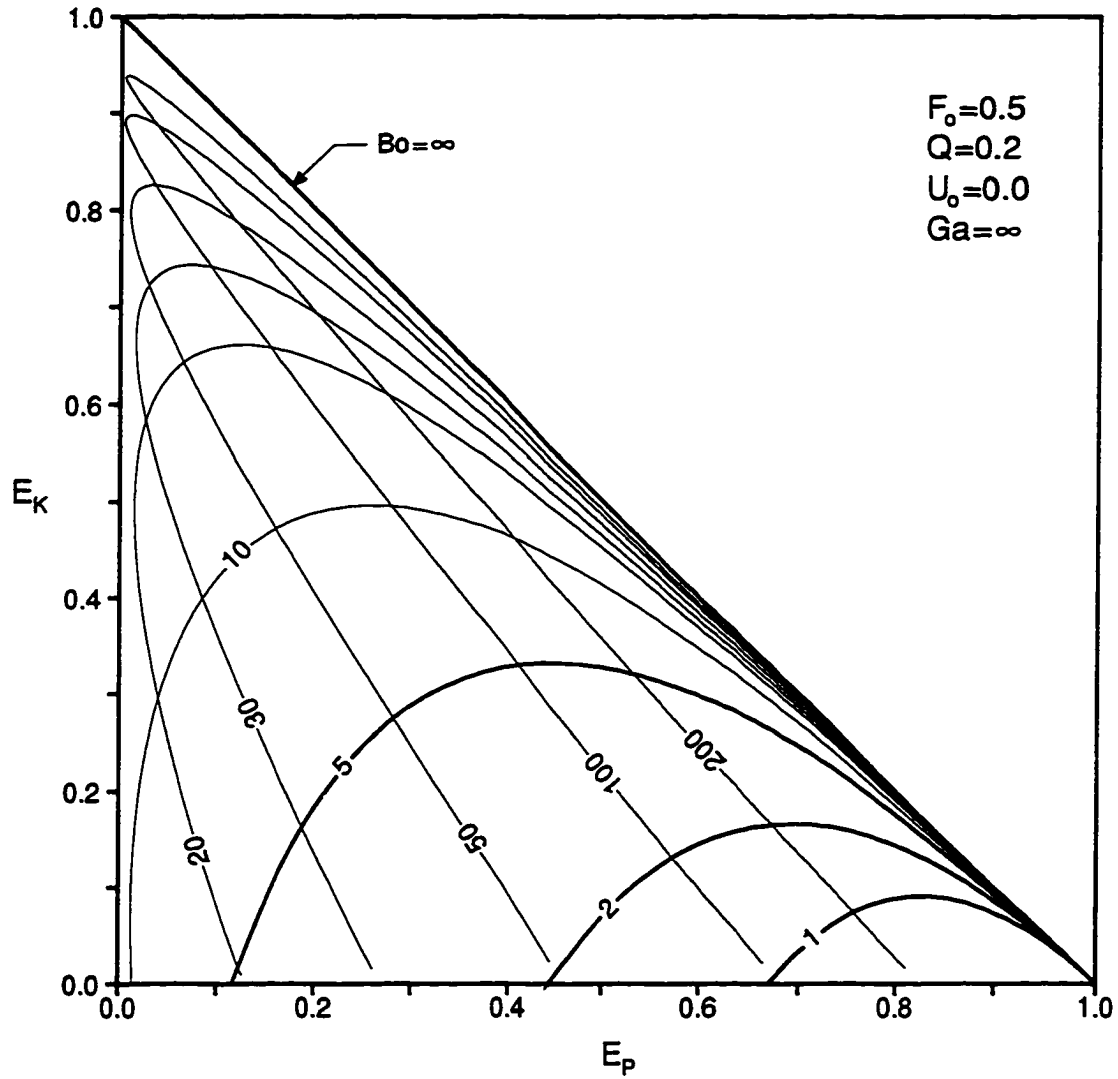


Figure 5.28: Trajectories of the Liquid System in (E_p, E_k) Space

$Bo \rightarrow \infty$, and thus $E_s \rightarrow 0$, all possible energy states that can be assumed by the system must fall on the line, $E_p + E_k = 1$. The initial position of the liquid is represented by the state $(1, 0)$. With $Bo = \infty$, the liquid also approaches this state when is in the position of maximum elevation. Thus, the liquid moves along this linear path from point $(1, 0)$ toward point $(0, 1)$ and back to point $(1, 0)$ twice every cycle, as it rises to a position of maximum elevation and falls back toward its initial position. For finite values of the Bond number, E_s generally continues to increase as the liquid moves further and further away from the horizontal position. As a result, the trajectories separate at the state of maximum kinetic energy, with the liquid following a unique path all the way to the position of maximum elevation. For $Bo \leq 10$ the liquid remains below the equilibrium position with respect to the body forces. As surface tension effects increase the trajectories traced by the liquid become more symmetric. In the limit, as $Bo \rightarrow 0$, the liquid surface becomes more and more *rigid*, and with $E_k \rightarrow 0$, the trajectories collapse toward the point $(1, 0)$.

The trajectories drawn in Figure 5.28 in terms of a heavier weight line, for $Bo = 1, 2, 5$, and $Bo = \infty$, are for all cycles of oscillation. In the remaining cases, $10 \leq Bo \leq 200$, *only characteristic trajectories* based upon the first mode oscillations of the liquid show this form. Within this range of Bond values, the excitation of additional modes and frequencies of oscillation leads to trajectories that continually change from one cycle to the next. The highest degree of variation in the paths traced by the liquid oscillations was observed in the range, $20 \leq Bo \leq 100$, with the trajectories for $Bo = 10$ and $Bo = 200$ almost being identical to the characteristic trajectories. Two examples of the actual trajectories traced by the liquid in this transition range, are shown in Figure 5.29 for $Bo = 20$, and in Figure 5.30 for $Bo = 50$.

As the liquid departs from its initial horizontal position, and its surface becomes curved, the energy of the liquid surface increases. This increase or storage of free surface energy is represented by the component E_s . In Figure 5.31, the maximum value of E_s , E_{s-max} , is plotted as a function of the Bond number. Four sets of data points are included in this figure. Two of these sets deal with a sudden container acceleration, $Q = 0.1$ and $Q = 0.2$, while the other two with an impulsive container start, $U_o = 0.1$ and $U_o = 0.2$. The variation in E_{s-max} differs based on the type of the forcing condition, but it appears to be indifferent to the magnitude of the forcing.

For the two cases with $U_o > 0$, E_{s-max} increases continuously with a decreasing value of the Bond number. Here, the system starts from an initial state of maximum

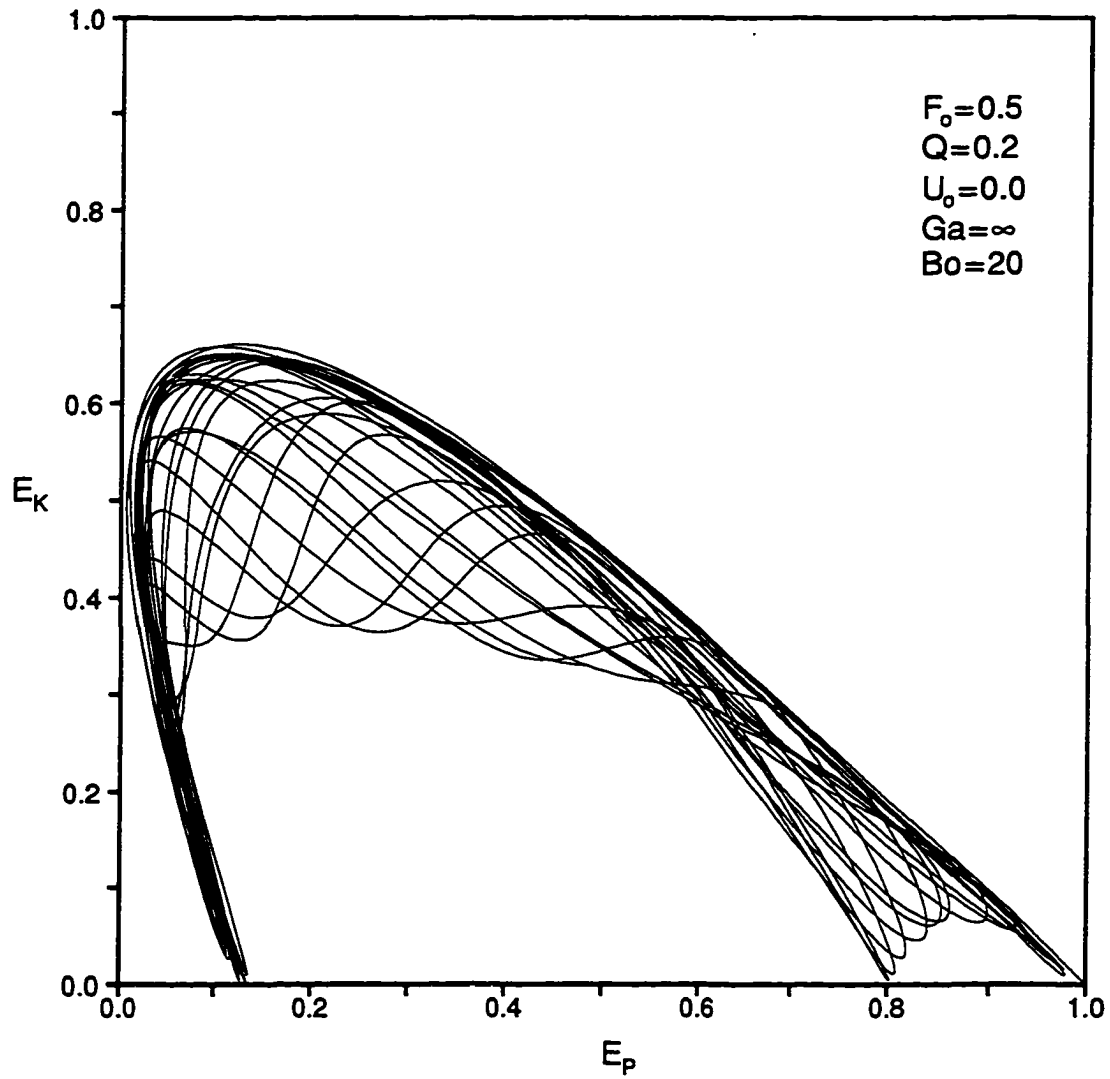


Figure 5.29: Liquid Oscillations in (E_p, E_k) Space at $Bo = 20$

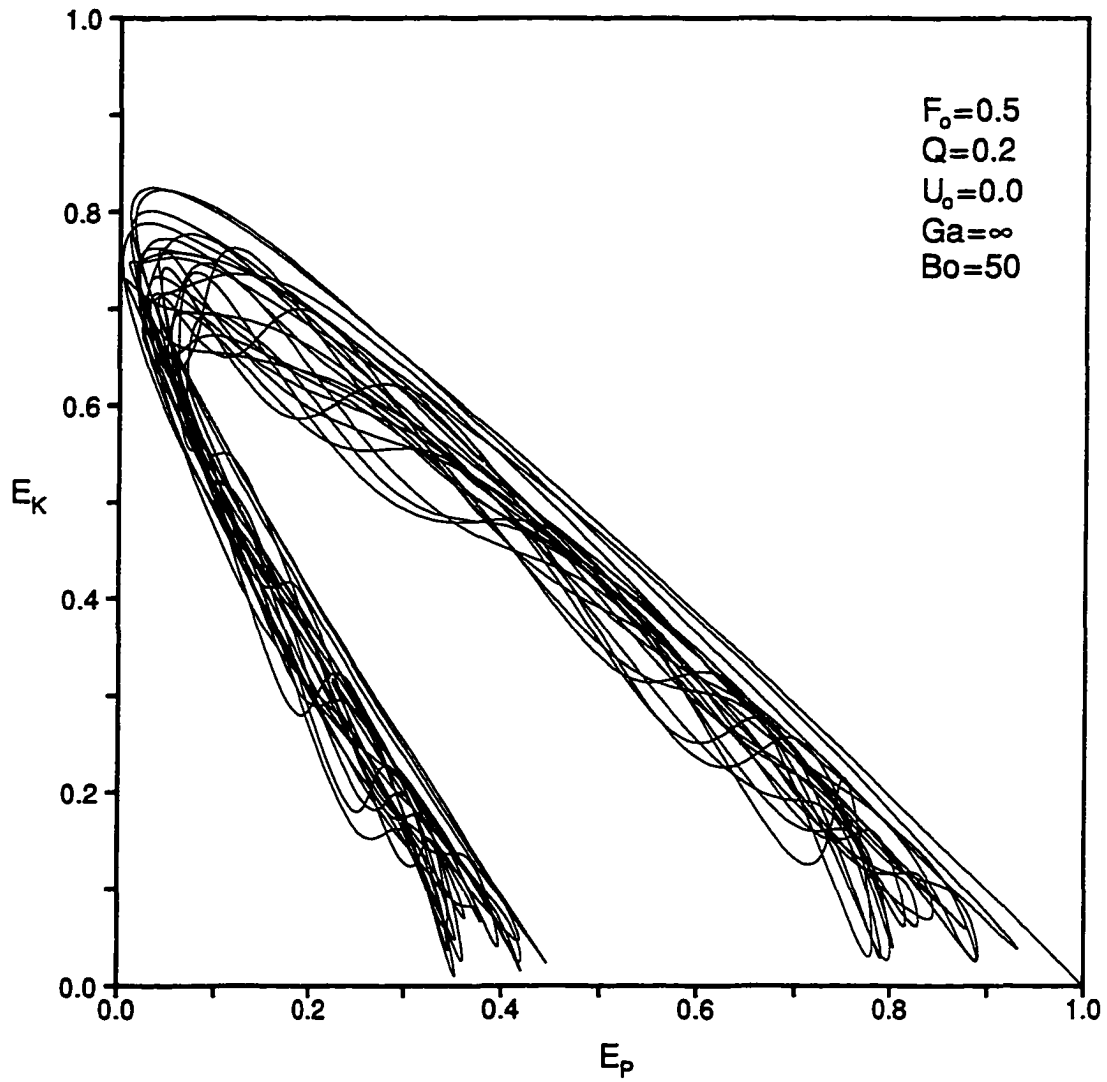


Figure 5.30: Liquid Oscillations in (E_p, E_k) Space at $Bo = 50$

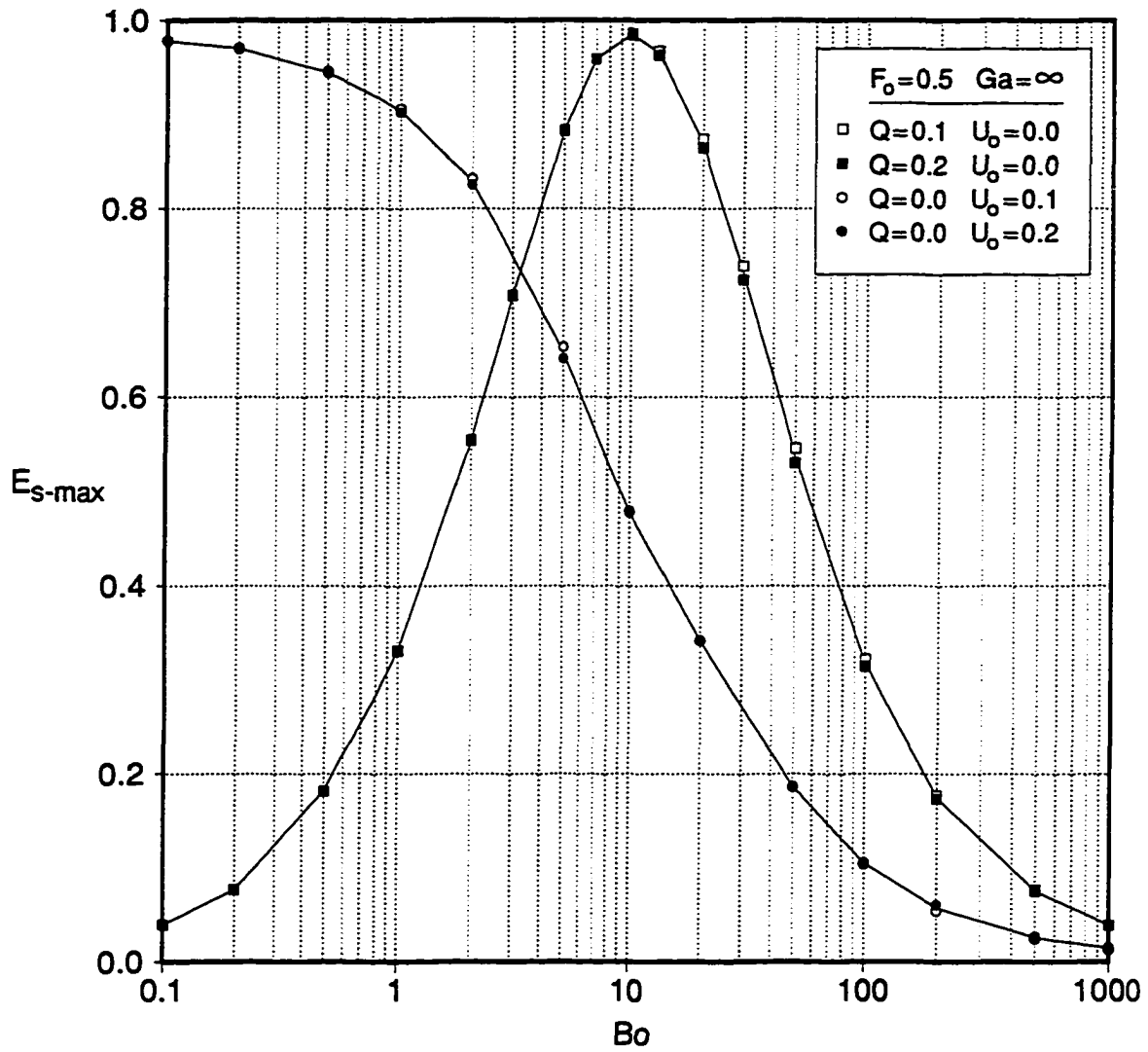


Figure 5.31: Maximum Surface Tension Energy Storage

kinetic energy, and carried by its initial inertia it moves away from the horizontal position. It reaches a position of maximum elevation before the combined force due to surface tension and body forces reverses its direction of motion. The maximum value of E_s occurs when the liquid is near this position of maximum elevation. In this position, the kinetic energy of the system is very small, and most of energy of the system is distributed between the potential, E_p , and surface tension, E_s , components. At $Bo=1000$, E_{s-max} accounts for only about 1.4% of the initial energy, with most of the system energy being in the form of potential energy. This increases to nearly 48% at $Bo=10$, and to just over 90% at $Bo=1$.

The variation of E_{s-max} is different for the two cases with $Q > 0$. Here, the liquid is driven away from its initial position by the net body force that is acting on it. The maximum elevation reached by the liquid depends on the relative strength of the body and surface tension forces. At large values of the Bond number, E_{s-max} increases with a decreasing Bond number. However, it reaches a maximum value of about 0.985 at $Bo=10$, and then it begins to decrease as Bo decreases further. At $Bo=10$, the liquid comes to a momentary rest in a position of maximum elevation which is very near the equilibrium position with respect to the body forces. Thus, most of the initial energy of the system which was in the form of potential energy, becomes stored as surface tension energy. For $Bo < 10$, the liquid does not reach the equilibrium position with respect to the body forces. As it reaches a position of maximum elevation, some of its initial energy remains in form of potential energy. As $Bo \rightarrow 0$, the maximum elevation reached the liquid continues to decrease, and with an increasing fraction of the system energy left in the form of potential energy, E_{s-max} decreases.

For cases with $Q > 0$, surface tension causes the static equilibrium position of the liquid to change. This position, which is reached by the liquid as $t \rightarrow \infty$ as a result of damping, is determined by both the body and surface tension forces that are acting on the liquid. In this equilibrium position, the surface of the liquid is curved, and located in between the initial horizontal position and the equilibrium position determined solely by the net body force. The static equilibrium position can not be uniquely determined in advance by a force balance, since the final shape of the free surface is unknown. Note for example, that the equilibrium position with respect to the body forces, given by a *flat* surface of slope equal to $-Q$, places the liquid in a position where it is in equilibrium with the body forces as well as with a zero surface tension force. However, this position represents an energy state which is inaccessible

to the liquid flow. Three profiles, depicting the position of the free surface at steady-state, $F(x, \infty)$, are shown in Figure 5.32. These correspond to values of the Bond number given by $Bo = 1, 10, \text{ and } 100$. The equilibrium position with respect to the body forces is also shown in terms of the dashed line. These profiles were calculated with $Ga = 10^6$, and steady state was assumed when the available energy of the system was reduced to below 0.001% of its initial value. Note that as surface tension effects become stronger, the liquid surface behaves more and more like a rigid surface. It tends to become more flat and to approach the initial horizontal position.

As a result of this shift in the equilibrium position of the liquid, the system reaches steady-state with some of its available energy, E_A , still left in it. This residual energy, E_R , is given by the sum of the final values of potential, $E_p(\infty)$, and the surface tension, $E_s(\infty)$, components. It is shown in Figure 5.33 as a function of the Bond number. As the equilibrium position of the liquid surface moves closer and closer to the horizontal position with a decreasing value of the Bond number, the residual energy, E_R , increases. In the limit, as $Bo \rightarrow \infty$, $E_R \rightarrow 1$. An infinitesimal displacement of the free surface, generates surface tension forces that are comparable in magnitude to the body forces. Thus, the liquid remains in its initial position, with all of its initial energy representing residual energy.

The changes which occur in the damping rate of the system, in the presence of surface tension effects, are illustrated in Figure 5.34. Here, the modulus of decay, τ , is calculated by regression analysis based on equation (5.6). It is further normalized by the value of τ obtained in the absence of surface tension effects with $Bo = \infty$, and plotted as a function of the Bond number. The modulus of decay increases as surface tension effects become stronger. And although this increase remains fairly small, less than 0.9%, for $Bo > 100$, it increases at a much faster rate for $Bo < 10$. As the surface of the liquid starts to behave more like a rigid surface, its movement causes relatively stronger flow to penetrate further into the liquid and closer to the container walls. As a result, the rate of viscous dissipation increases.

The effect of surface tension on the period of oscillation, T , is examined in Figure 5.35. Two sets of numerical results for T are included in the figure. They correspond to calculations carried out at $Ga = 10^6$ and $Ga = \infty$. The numerical results are compared to an analytical solution which is drawn in Figure 5.35 as a solid line. This analytical result is derived from the solution of the linearized potential flow equations. It is valid for irrotational flow, $Ga \rightarrow \infty$, and for an infinitesimal amplitude of sloshing,

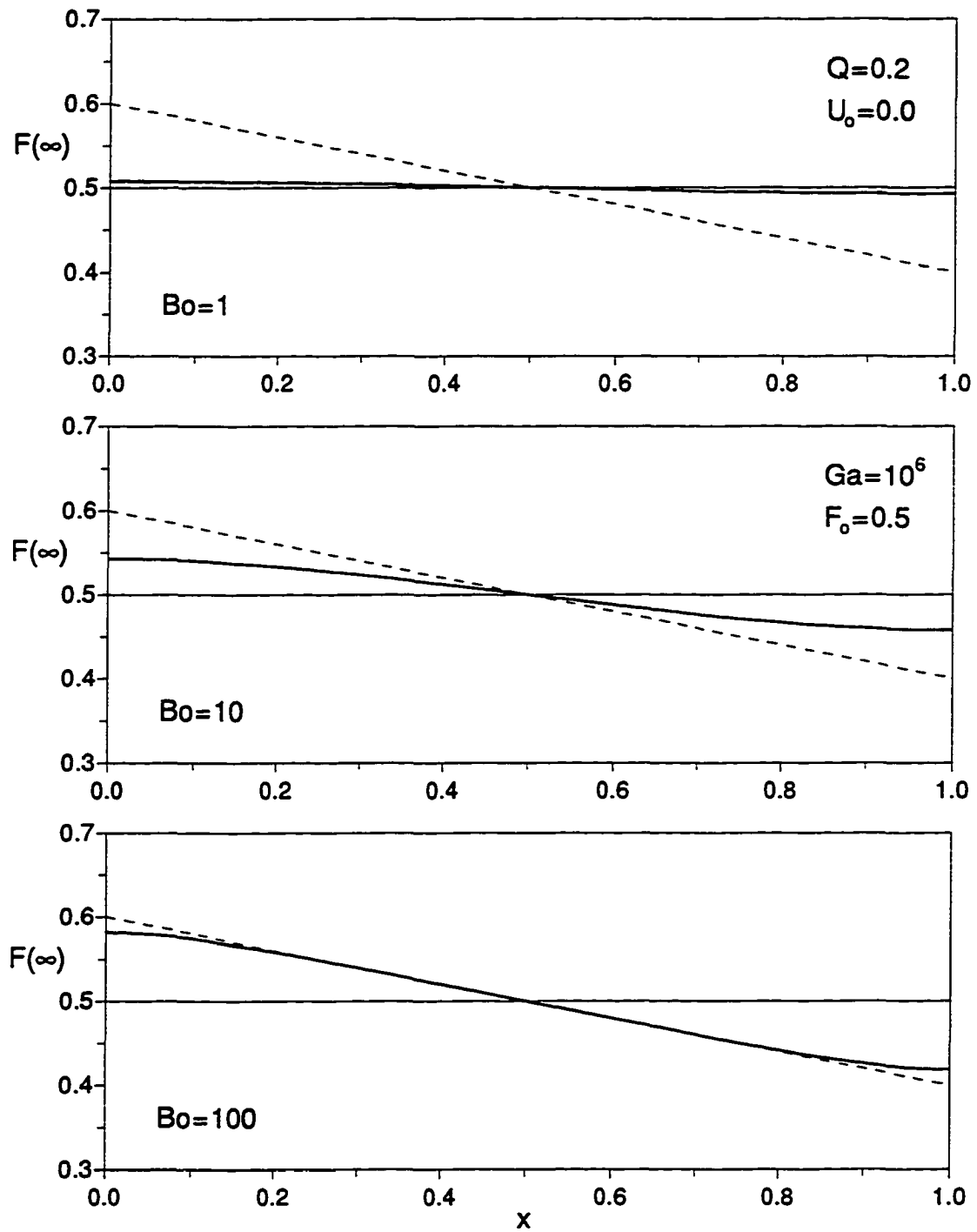


Figure 5.32: Free Surface Profiles at Static Equilibrium

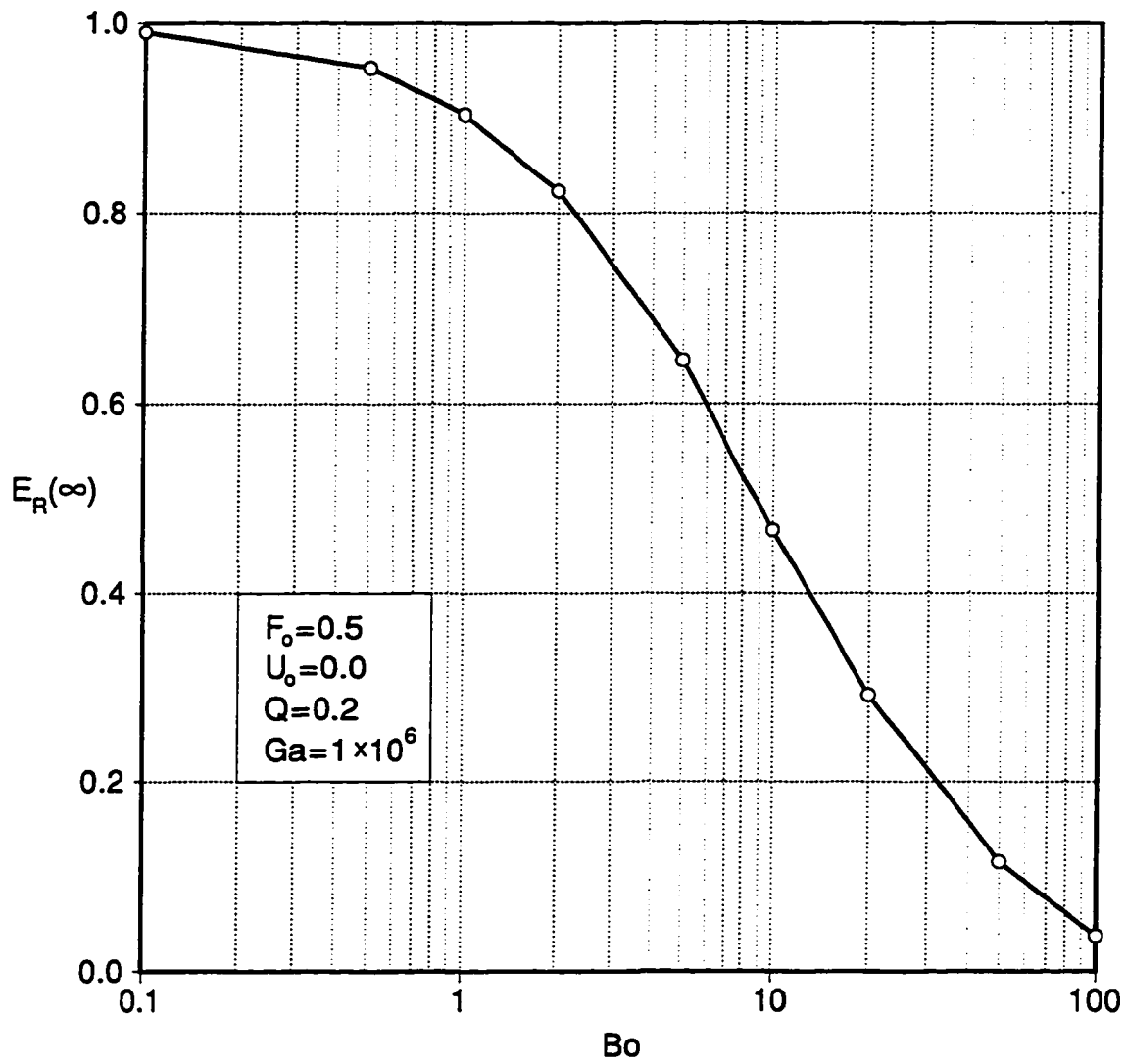


Figure 5.33: Residual System Energy at Static Equilibrium

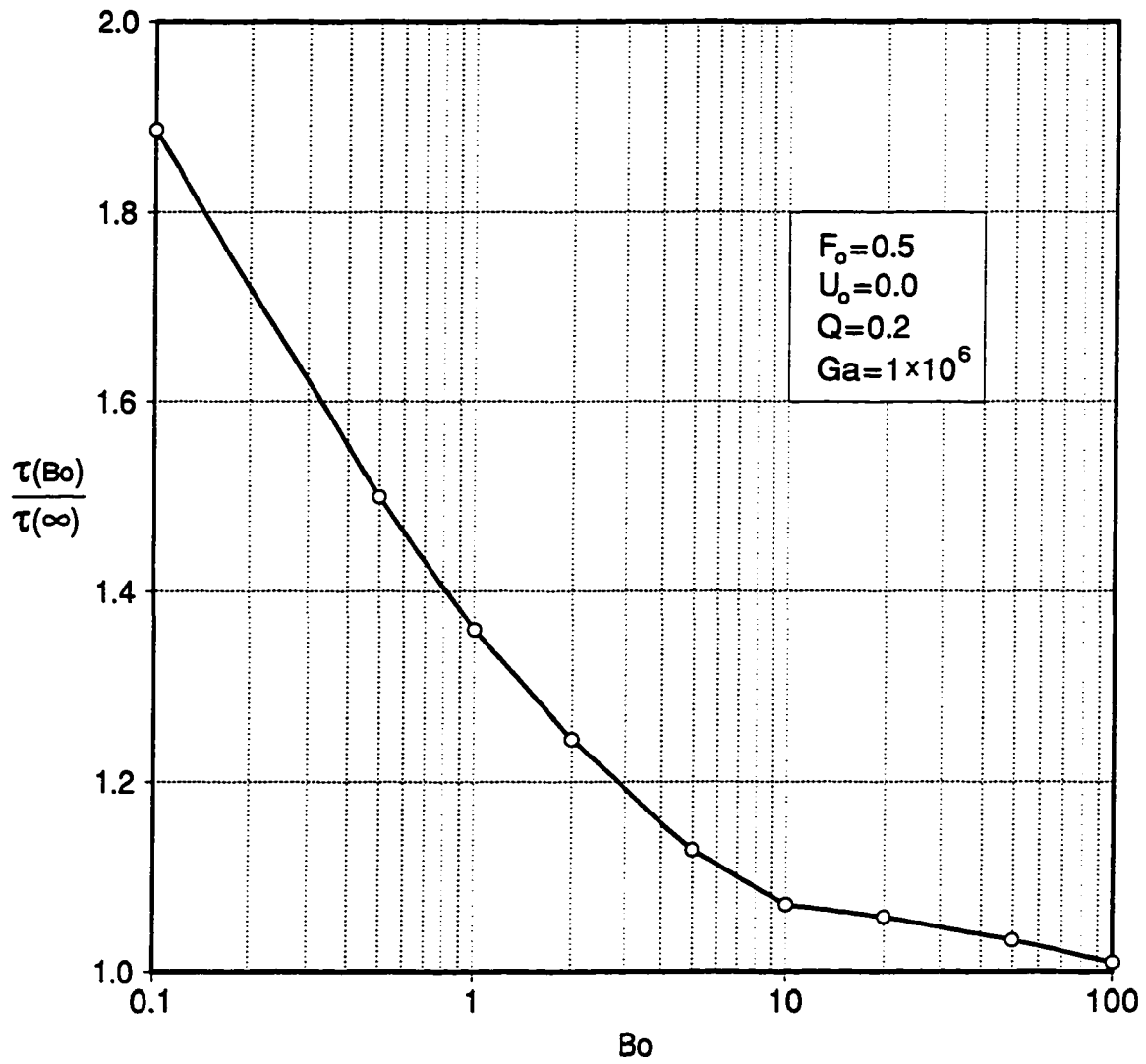


Figure 5.34: Effect of Bond Number on Viscous Dissipation

$(Q, U_o) \rightarrow 0$. The analytical solution, which is given in [4], is recast here into a slightly different form. This form is obtained by factoring out $T_a(\infty)$, the result predicted by the linearized theory in the absence of surface tension ($Bo = \infty$), and which is given in terms of equation (5.7). The period of oscillation at a given value of the Bond number, $T_a(Bo)$, can then be determined by:

$$\frac{T_a(Bo)}{T_a(\infty)} = \frac{1}{\sqrt{1 + \pi^2/Bo}} \quad \text{for } \lim Ga \rightarrow \infty \quad \text{and} \quad \lim(Q, U_o) \rightarrow 0 \quad (5.11)$$

Recall (sections 5.2.2 & 5.2.3) that both viscous and finite amplitude sloshing effects cause an increase in the magnitude of the period, T , as compared to the analytical prediction, T_a . Thus, in an effort to isolate the effects due to surface tension, the results in Figure 5.34 are plotted as the ratio of $T(Bo)$ to $T(\infty)$. Note that the numerical results, both viscous and inviscid, are in excellent agreement with the analytical solution. The decrease in T is less than 5% for $Bo > 100$.

5.3 Liquid Interaction with the Moving Container

The dynamic interaction of the sloshing liquid with the enclosing solid structure is considered here. This analysis is based on results that were obtained using the model which was presented in section 3.9. A quick overview of this model will be given here but the reader is encouraged to refer to Figure 3.5 and the accompanying discussion for the details.

The container enclosing the liquid is considered to be an integral part of a moving vehicle of total solid mass M . The motion of the vehicle is brought about by a specified external force (thrust) T_1 , which acts on the vehicle for $t > 0$. Inclusion of the net liquid force, T_2 , in the resulting equation of motion couples the dynamics of the liquid with those of the moving vehicle.

The liquid force, T_2 , depends upon the dependent variables (u, v, p, F) , as well as the net vehicle acceleration, $Q(t)$. The liquid experiences an equivalent apparent body force due to the instantaneous acceleration of the vehicle. Any change in the acceleration of the vehicle results in a corresponding change in the liquid body force Q .

A change in the net force acting on the vehicle, $T = T_1 + T_2$, leads to a change, ΔQ , in the horizontal body force acting on the liquid. The subsequent adjustment of the net horizontal liquid force, T_2 , occurs on two different time scales. The component of the liquid force, \hat{T}_2 , which is determined solely by the elliptic adjustment of the pressure

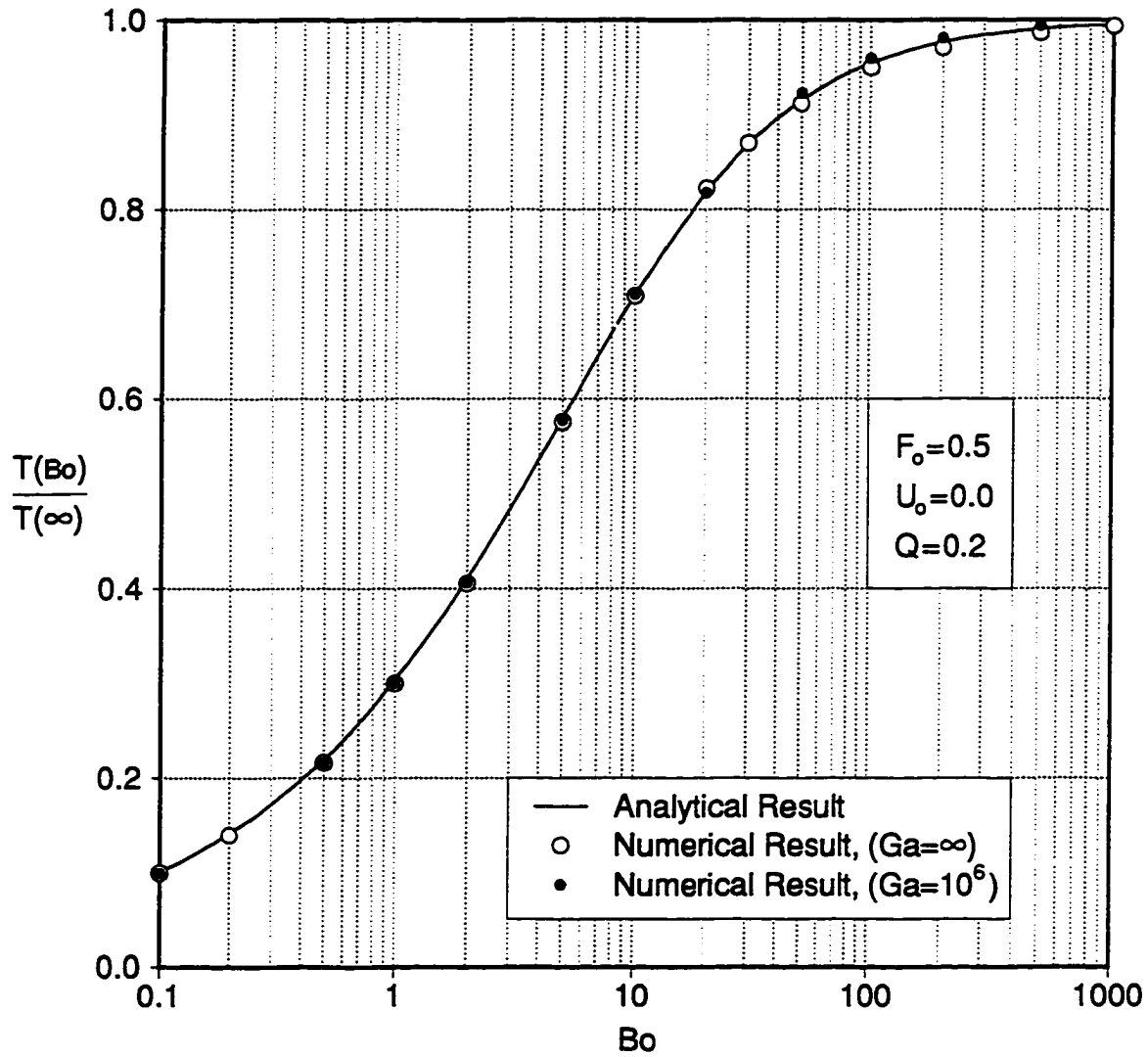


Figure 5.35: Effect of Bond Number on Period of Oscillation

field to the new body force, changes immediately and according to $\Delta\hat{T}_2 = -\mathcal{M}_a\Delta Q$. The component of the liquid force, \hat{T}_2 , which depends on the parabolic adjustment of the velocity field, changes linearly with time according to $\Delta\hat{T}_2 \sim -\Delta t \Delta Q$. Using the apparent liquid mass, \mathcal{M}_a , the change in the liquid force component \hat{T}_2 can be determined independently of the flowfield. Based on \mathcal{M}_a , equation (3.57) has been developed in section 3.9 as an alternative to equation (3.56), the standard representation of the equation of motion for the vehicle. The immediate change in the liquid force component \hat{T}_2 which occurs as a result of a change in the value of Q is already built into equation (3.57). The main advantage offered by this approach is that a numerical algorithm which is based on the explicit coupling of equation (3.57) with the liquid equations is stable. It is also significantly faster than an implicit algorithm which becomes necessary if the solution of the problem is based on equation (3.56). For the cases discussed below, the maximum increase in the amount of required computational time for the solution of the problem based on equation (3.57) was only about 11% when compared to the standard case of constant Q forcing.

The apparent mass, \mathcal{M}_a , is a function of $F(t, x)$ only. It represents a geometrical shape factor which measures the *instantaneous* resistance offered by the liquid to a change in the acceleration of the vehicle. The overall inertia of the liquid to the forcing imposed upon it by the motion of the vehicle can be measured in terms of the *effective mass* of the liquid, which is defined by the ratio of the net liquid force and the instantaneous vehicle acceleration:

$$\mathcal{M}_e \equiv -\frac{T_2}{Q} \quad (\text{effective liquid mass}) \quad (5.12)$$

Several cases were considered in evaluating the effects of coupling the dynamics of the liquid with those of the vehicle. For each of these cases, $F_o = 0.5$, $Gr = 10^7$, and $Bo = \infty$. The magnitude of the driving force, T_1 , was selected such that it would yield a final acceleration at steady state equal to $Q_\infty \equiv \lim_{t \rightarrow \infty} Q(t) = 0.2$. As a result, the driving force becomes a function of the vehicle mass, M , with its magnitude given by $T_1 = (M + F_o)Q_\infty$. Numerical solutions for several cases, ranging from $M = 0$ to $M = \infty$, were generated using a 41×41 computational grid and a time-step of size $\Delta t = 0.002$. The case represented here as corresponding to $M = \infty$, was actually calculated by setting the vehicle mass equal to 10^{25} . Due to the excessively large solid mass, the solution for this case was practically identical with the solution calculated using the standard model (constant Q model) which was presented in the first part of this chapter. The very small difference in the computational time requirements for

these two calculations suggests that the overhead associated simply with the solution of equation (3.49) and the calculation of \mathcal{M}_a is only about 0.9% of the total effort. The cases $M = 0.0$ and $M = 0.5$ were also solved using an implicit marching scheme with equation (3.56) providing the coupling with the vehicle dynamics. The computational time requirements for these calculations, when compared to those obtained by the explicit algorithm based on \mathcal{M}_a , were larger by a factor of 2.1 for the $M = 0.5$ and by a factor of 6.2 for the $M = 0.0$ calculations. Furthermore, an underrelaxation parameter of 0.4 at $M = 0.5$, and of 0.05 at $M = 0.0$ were necessary for stability.

The effects of the vehicle mass, M , on the dynamics of the system are summarized in Figure 5.36. The transient behavior of the apparent mass, \mathcal{M}_a , is shown in part (a) of the figure. Here, \mathcal{M}_a is normalized by the total, or rest, mass of the liquid, which in dimensionless form is numerically equal to F_o . A similar plot for the effective liquid mass, \mathcal{M}_e , is shown in part (b) of Figure 5.36. The horizontal force exerted by the liquid on the container, T_2 , is shown in part (c) of the figure, while part (d) depicts the transient vehicle acceleration, $Q(t)$, normalized by its steady state value, $Q(\infty)$.

Recall (section 3.9) that the apparent mass, \mathcal{M}_a , is a geometrical factor which is determined solely by the configuration of the liquid within the container. The following generalizations can be made about the effect of the free surface shape on the magnitude of \mathcal{M}_a . For a flat free surface, one that its position can be described by a straight line, \mathcal{M}_a is minimum at a zero slope with its magnitude increasing evenly for positive and negative slopes as the surface departs from the horizontal position. For a curved surface, a crest formation in the interior of the container leads to a decrease in the value of \mathcal{M}_a as some of the liquid gets displaced away from the container walls. Reversely, an interior surface trough leads to an increase in the value of \mathcal{M}_a . For each of the three cases shown in Figure 5.36(a), \mathcal{M}_a/F_o , starting from an initial value of 0.5, increases as the liquid rises along the left side of the container. It reaches a maximum value of approximately 0.557 for the $M = 0.0$ case during the first cycle of sloshing. As the liquid surface begins to fall back toward its initial position, the value of \mathcal{M}_a decreases. The behavior of \mathcal{M}_a is fairly similar for all three cases during that part of the cycle for which the liquid surface is sufficiently away from the horizontal position. When the liquid surface is near a position of minimum elevation, the behavior of \mathcal{M}_a shows significantly more variation, not only with respect to the value of M , but also from cycle to cycle. In this position, \mathcal{M}_a is largely determined by the curvature of the liquid surface. As a result, its magnitude is affected even by the small variations which occur

in the curvature of the free surface. At steady state, $t \rightarrow \infty$, the apparent mass differs from its initial value by less than 1.7%, as $\mathcal{M}_a/F_o \rightarrow 0.5083$.

Although the apparent mass of the liquid is very helpful in determining the dynamics of the system, it provides very limited information on the actual interaction between the liquid and the vehicle. To ascertain this interaction, the effective liquid mass, \mathcal{M}_e , the net horizontal liquid force acting on the vehicle, T_2 , and the acceleration of the vehicle, Q , are examined for three distinct values of the vehicle mass, M , in Figure 5.36(b-d). In two of these cases the behavior of the system is examined at the two limits of zero and infinite vehicle mass ($M = 0.0$ and $M = \infty$), while in the third case, $M = 0.5$, the mass of the vehicle is equal to that of the liquid.

The case with $M = \infty$ in Figure 5.36 represents the limit of a vehicle mass that is so overwhelmingly larger than the mass of the liquid, such that, any forces generated by the liquid have no impact in determining the motion of the vehicle. The acceleration of the vehicle, Q , is determined by the constant magnitude driving force, T_1 , and thus it remains constant throughout the sloshing process. The liquid force, T_2 , which acts in the negative direction, exhibits a quasi-periodic behavior. Its magnitude increases as the liquid rises and decreases as the liquid falls along the left container wall. As a result of the constant acceleration Q , the transient behavior of the effective mass is determined solely by the liquid force, $\mathcal{M}_e = -T_2/Q$. Viscous dissipation brings the system to a static equilibrium as $t \rightarrow \infty$. With the liquid moving as a rigid body at steady state, $\mathcal{M}_e/F_o \rightarrow 1$, the magnitude of the liquid force is determined by the final value of the vehicle acceleration, $T_2 \rightarrow -F_o Q(\infty)$. For each of the cases under consideration here which were calculated with $F_o = 0.5$ and $Q(\infty) = 0.2$ this corresponds to $T_2(\infty) = -0.1$.

The second case under consideration in Figure 5.36, deals with the opposite extreme scenario. Here, for $M = 0.0$, the mass of the vehicle is so small compared to that of the liquid, such that the motion of the vehicle is determined solely by the dynamic behavior of the liquid. The initial value of the effective liquid mass, which is determined by the initial liquid geometry, is equal to $\mathcal{M}_e(0^+) = 0.5F_o$. The liquid appears to be only half as *massive* at $t = 0$, than it does as $t \rightarrow \infty$. Consequently, the initial value of the acceleration is twice the steady state value, $Q(0^+) = 2Q(\infty)$. Note in Figure 5.36(c), that the variation in the magnitude of the liquid force T_2 decreases as the vehicle mass becomes smaller. For $M = 0.0$, the magnitude of the net horizontal force exerted by the liquid on the container becomes constant. Although at a first

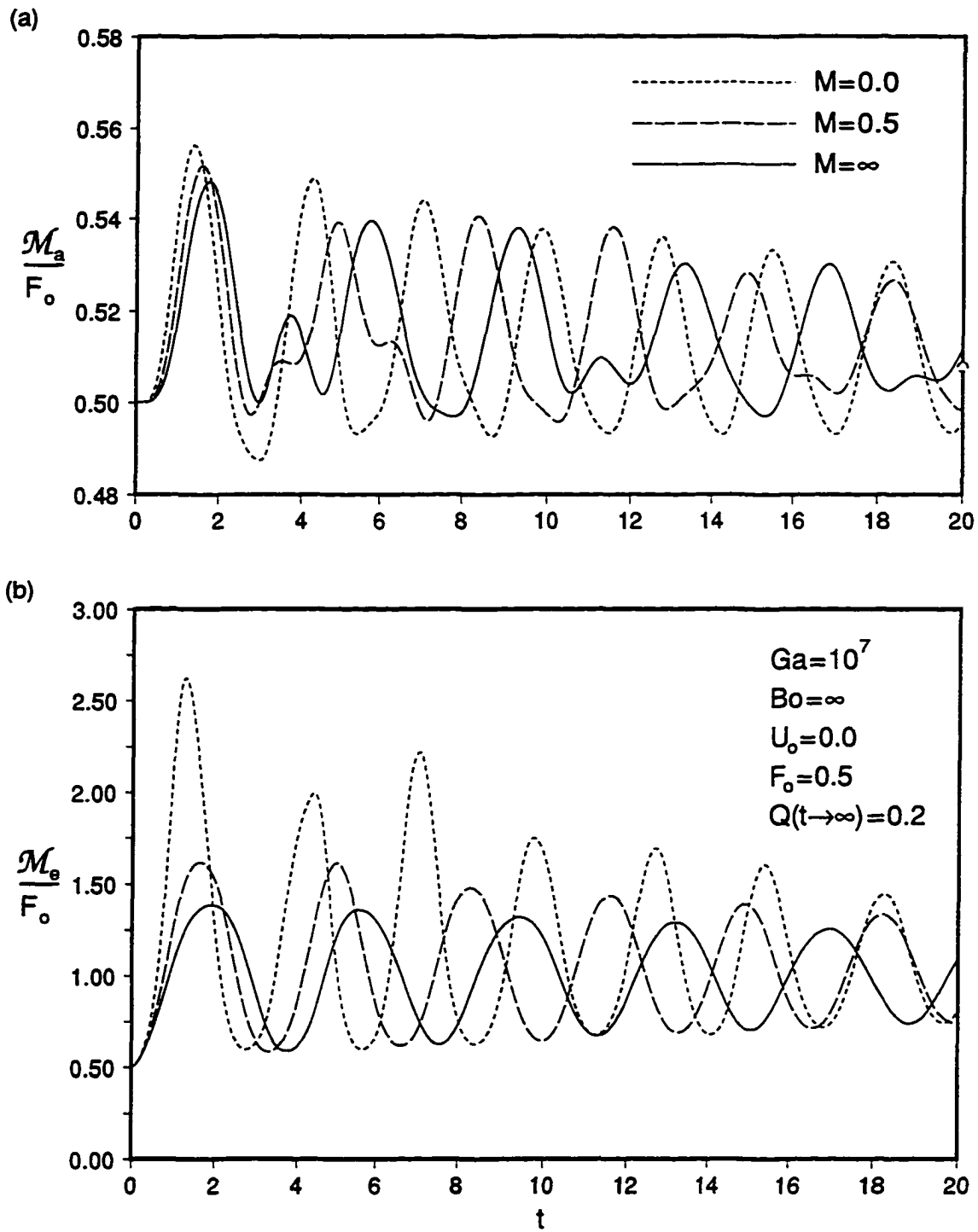


Figure 5.36: Effects of a Finite Vehicle Mass, M , on the Sloshing Dynamics

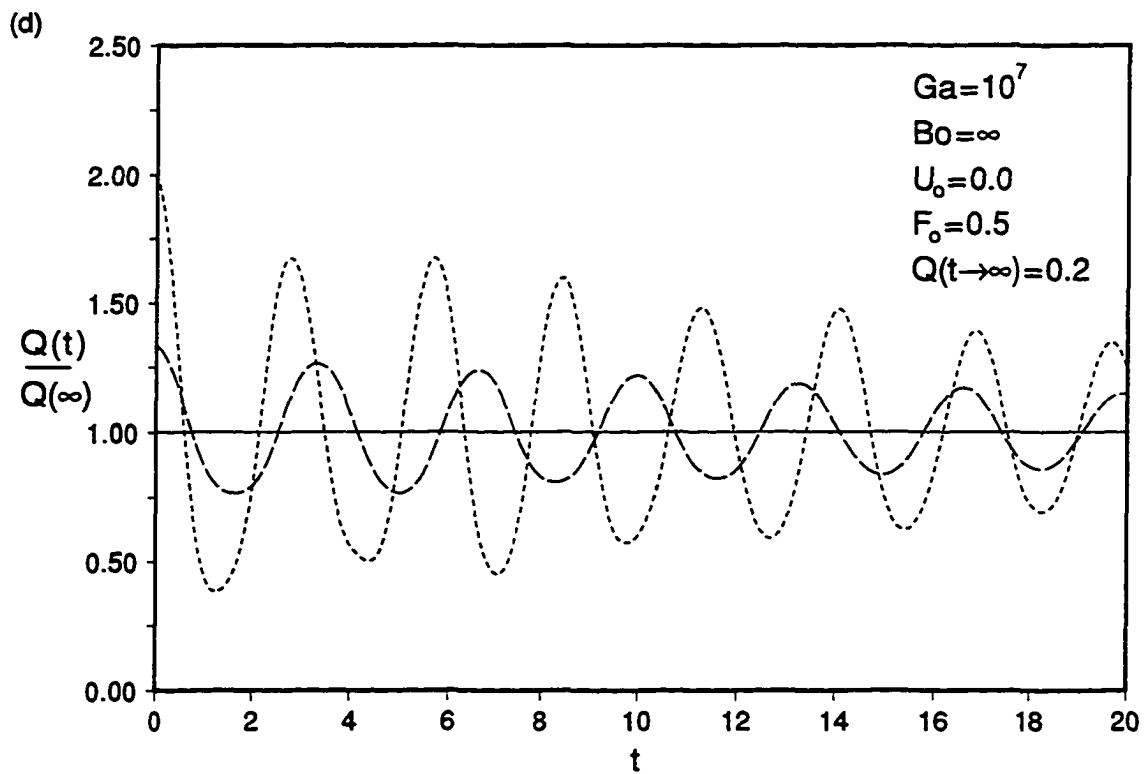
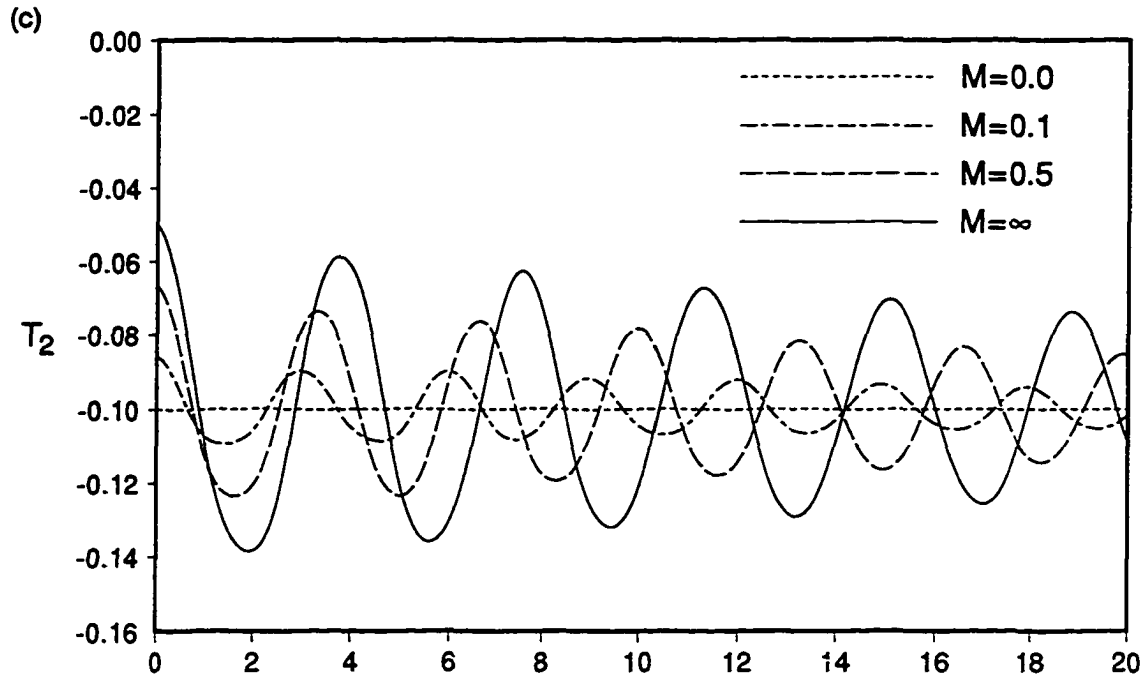


Figure 5.36 (Continued)

glance, this may appear to be a surprising result, it should not be an unexpected one. For the acceleration of the vehicle, Q , to remain bounded as $M \rightarrow 0$, the net force acting on the vehicle must also vanish, $(T_1 + T_2) \rightarrow 0$. In this case, the liquid exerts a horizontal force on the container equal to $T_2 = -0.1$, which is equal in magnitude and opposite in direction to the driving force T_1 . With T_2 being constant, the effective mass of the liquid, \mathcal{M}_e , becomes inversely proportional to the acceleration, Q . As the liquid surface rises along the left wall, Q decreases well below its steady state value, reaching a minimum of about 0.075 during the first cycle of sloshing. Based on the corresponding value of the effective mass, $\mathcal{M}_e \approx 2.67$, at this point the liquid appears to be more than two and half times heavier than it does at steady state.

The third case considered in Figure 5.36, $M = 0.5$, deals with the interaction between the vehicle and the liquid when the mass of the vehicle is equal to the rest mass of the liquid. As the liquid force, T_2 , increases in magnitude, the magnitude of the net force acting on the vehicle is reduced, thus, causing a decrease in the acceleration. The acceleration of the vehicle, Q , exhibits a quasi-periodic behavior, and it varies by as much as 33% from its steady state value of 0.2. With the vehicle absorbing some of the inertia of the liquid, by adjusting its acceleration to changes in the magnitude of the liquid force, the variation in the effective mass of the liquid is considerably reduced compared to those for case with $M = 0.0$.

The period of oscillation, T , is also affected by the interaction between the vehicle and the liquid. Although some of these effects can be deduced from Figure 5.36, they are also depicted in a more comprehensive way in Figure 5.37. In this figure, the period is plotted as a function of the vehicle *payload*, λ . The payload is simply defined as the ratio of the rest mass of the liquid and the solid mass of the vehicle, $\lambda \equiv F_o/M$. Note that in Figure 5.37, the period is normalized by the value obtained for with $\lambda = 0$. This value corresponds to the result of the standard case considered in this study, for which the apparent acceleration experienced by the liquid is constant. As the liquid payload increases, and the liquid begins to play a more active role in determining the dynamics of the system, the period of oscillation decreases. For $\lambda = 1$, the period is shorter by about 11.2%, compared to the corresponding value of T obtained for the standard case for negligible liquid effects, $\lambda = 0$. In the limit, as $\lambda \rightarrow \infty$, where the vehicle mass becomes negligible in comparison to the liquid mass, the period is shorter by 25.2%.

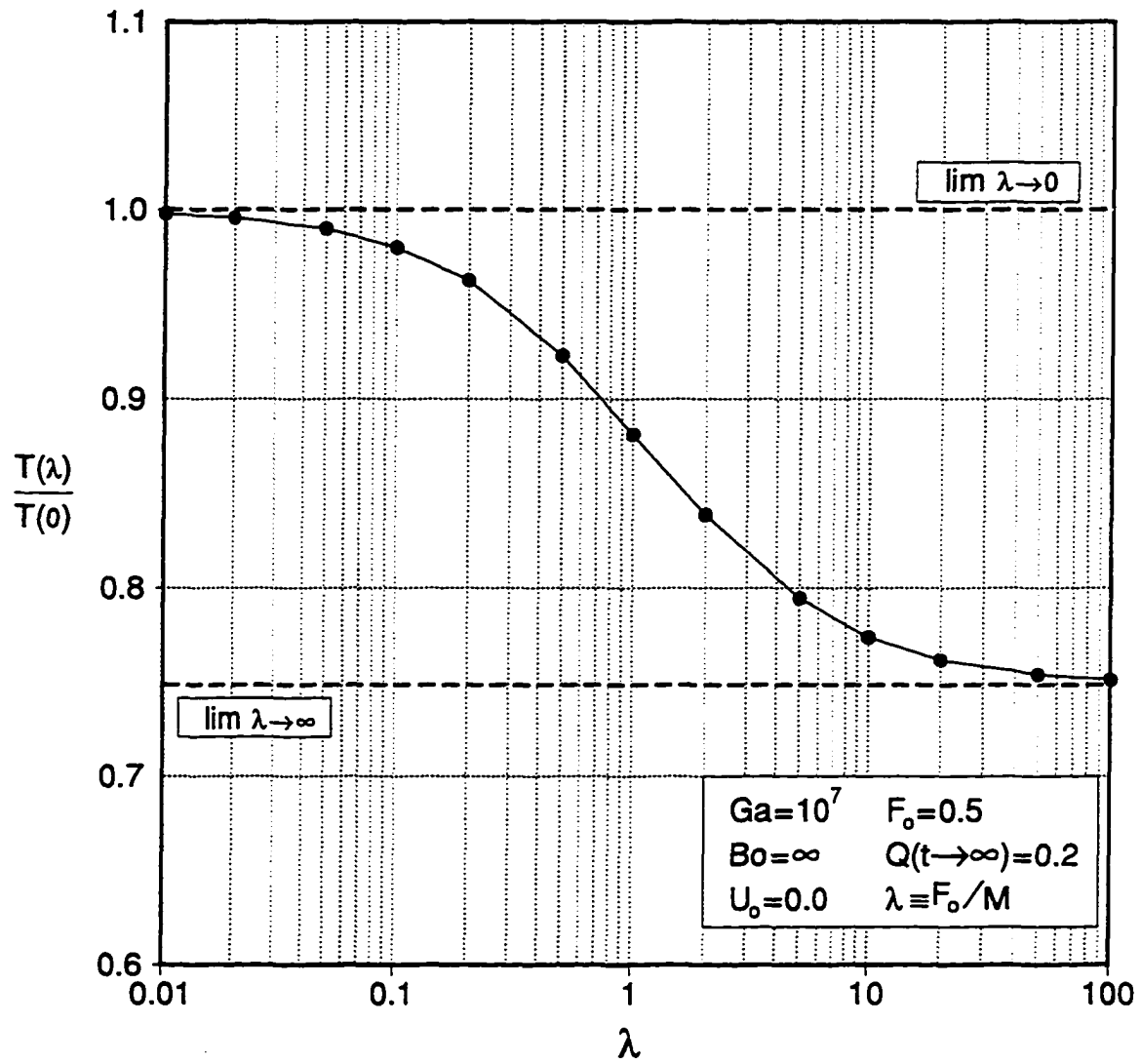


Figure 5.37: Effect of Vehicle Payload, λ , on the Period of Oscillation, T

PART II.

SLOSHING IN 3-D MOVING CONTAINERS

6. A GENERAL THREE DIMENSIONAL SLOSHING MODEL

A more general model is developed here, which may be used to study sloshing problems under a broader variety of forcing conditions. It deals with the sloshing of a viscous, incompressible liquid within three dimensional partially filled containers. The forcing of the liquid is induced by the motion of the container. This motion can be quite arbitrary, as the model allows for the superposition of multiple linear and angular time varying accelerations. The Navier Stokes equations are cast into a frame that is best suited for the description of the liquid motion. This is accomplished through a series of coordinate transformations which translate and rotate the frame of reference so as to match the accelerated frame of the container. The governing equations are finite differenced on a body fitted grid and solved using an implicit, iterative, second order accurate numerical method.

The initial motivation behind this work has been the need to describe the complex motion which occurs within liquid stores that are carried aboard spin-stabilized spacecraft. Certain configurations of spin-stabilized satellites, have in the past consistently demonstrated a nutational instability during the perigee phase of their burn. It has been suspected that this instability is initiated and sustained by the sloshing that occurs within the liquid stores, in response to the sudden axial thrust that is applied to the vehicle at the onset of the perigee burn. As a result of the initial scope of this work the development of the mathematical model is heavily influenced by forcing conditions that are characteristic of those experienced by spin-stabilized vehicles.

The general formulation of the model is presented in Chapter 7. The sequence of coordinate transformations, used in introducing the various aspects of the vehicle motion into the liquid equations, is presented. An additional transformation used in regularizing the physical domain of the problem prior to grid generation is also discussed. The numerical method used for the solution of the problem is also developed here.

Sample results from three representative cases are given in Chapter 8. A case

of sloshing in an impulsively translated rectangular container is presented. This case is a simple extension of the type of liquid flows that have been considered in the first part of this study. A case of axisymmetric spinup in a cylindrical container is presented next. This case was primarily selected because it allows for a comparison of the numerical result with experimental measurements. Finally, a full three dimensional spinup problem in a spherical container is considered.

7. FORMULATION OF THE 3D MODEL

A 3D numerical model for the description of the motion of a viscous liquid within a partially filled moving container is considered here. The container is assumed to be attached to a moving vehicle. The motion of the vehicle may be quite arbitrary, including both linear and angular time varying accelerations. The motion of the liquid within the container is the result of forcing imposed upon it by the motion of the vehicle.

A series of coordinate transformations is used to formulate the mathematical model for the problem. Each of these transformations introduces into the governing equations some aspect of the motion of the vehicle. A free surface tracking coordinate transformation is also utilized, which allows the free surface to be modeled under a variety of sloshing conditions without any modifications to the model. The resulting set of governing equations are finite-differenced on a body fitted grid, and solved using an implicit, iterative, second order accurate numerical method.

Some of the mathematical concepts, and most all of the numerical and computational techniques incorporated into the model, have been developed and tested using the two dimensional model. With the two dimensional model having been presented in considerable detail, here the presentation of the three dimensional model is fairly brief. The discussion that follows focuses mostly on issues that are unique to the three dimensional formulation. A more concise description of the 3D model can also be found in Kassinos and Prusa, 1990 (see [71]).

7.1 Mathematical Model

The sloshing of a viscous liquid inside a moving container is modeled using first principles. Equations describing the conservation of mass and linear momentum are formulated in a coordinate system that is moving along with the container. The selection of a *body fixed* coordinate system to describe the liquid motion was based on the simplicity of the resulting form of the boundary conditions and by the straightforward

interpretation of the numerical solution.

The motion of a fluid particle in an inertial frame of reference can be described by the Navier-Stokes equations. The incompressible three dimensional form of these equations can be written using index notation as:

$$\frac{\partial u_n}{\partial t} + u_i \frac{\partial u_n}{\partial x_i} = -\frac{1}{\rho} \frac{\partial p}{\partial x_n} - g_n + \nu \delta_{ij} \frac{\partial^2 u_n}{\partial x_i \partial x_j} \quad (7.1a)$$

$$\frac{\partial u_i}{\partial x_i} = 0 \quad (7.1b)$$

where u_i is the absolute velocity of a fluid particle,

g_i is the acceleration due to gravity,

p is the static pressure,

ρ is the fluid density,

and ν is the kinematic viscosity of the fluid.

In a body fixed coordinate system, information pertaining to the motion of the container is transferred from the boundary conditions to the governing equations as extra terms. These terms are to be determined by considering the motion of the container with respect to the inertial coordinate frame x . The container is assumed to be an integral part of the solid structure of a moving vehicle.

7.1.1 Linearly Accelerating Coordinate System

The effects of the rectilinear component of the vehicle acceleration on the liquid within the container are introduced into the governing equations by considering the following transformation. Let x_0 denote a coordinate system that is moving along with the vehicle. Its position with respect to the inertial frame x is denoted by ℓ as depicted in Figure 7.1. The dependent and independent variables in the new coordinate system can then be related to those of inertial system x , according to:

$$x_{0i} = x_i + \ell_i \quad \text{and} \quad t_0 = t \quad (7.2a)$$

$$u_{0i} \equiv u_j \frac{\partial x_{0i}}{\partial x_j} = u_i + \dot{\ell}_i \quad (\text{contravariant velocity}) \quad (7.2b)$$

Based on the notation used here, dotted and double dotted quantities represent respectively first and second time derivatives. The velocity vector, u_{0i} , is defined to

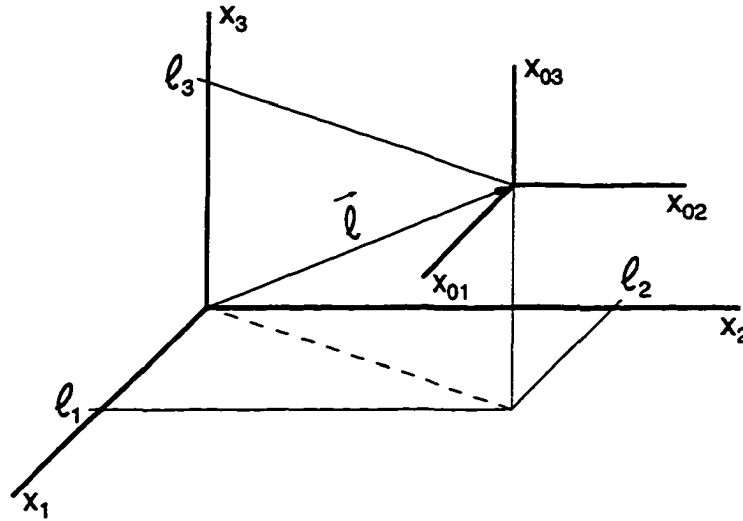


Figure 7.1: Linearly Accelerating Coordinate System, x_0

be *contravariant* with respect to the moving coordinate system, x_{0i} . Thus, the velocity of a given surface such as the container wall, which remains fixed relative to the moving coordinate frame becomes equal to zero. Substitution of equations (7.2) into equations (7.1) leads to the set of governing equations in coordinate frame x_0 :

$$\frac{\partial u_{0n}}{\partial t} + u_{0i} \frac{\partial u_{0n}}{\partial x_{0i}} = -\frac{1}{\rho} \frac{\partial p}{\partial x_{0n}} - g_{0n} + \nu \delta_{ij} \frac{\partial^2 u_{0n}}{\partial x_{0i} \partial x_{0j}} \quad (7.3a)$$

$$\frac{\partial u_{0i}}{\partial x_{0i}} = 0 \quad (7.3b)$$

where the body force term in the translating coordinate system is given by,

$$g_{0i} = g_i + \ddot{l}_i \quad (7.4)$$

Therefore, with the velocity defined with respect to the non-inertial frame, the effect of linear acceleration is to introduce extra terms into the governing equations. These *apparent acceleration* terms act to modify the body force terms such that g_{0i} now represents the net body force as a result of the vehicle acceleration and the acceleration due to gravity.

7.1.2 Spinning Nutating Coordinate System.

The rotation of the vehicle with respect to the inertial coordinate frame is considered here. Consider a coordinate system x_1 that is fixed on the vehicle, and thus,

its angular orientation with respect to coordinate system x_0 can change as a result of vehicle rotation. The instantaneous angular orientation of coordinate system x_1 , with respect to coordinate system x_0 , can be described by the superposition of three successive rotations. The three angles of rotation, ψ_i , $i = 1, 2, 3$, which define the angular orientation of the coordinate system, are known as the *Euler angles*. In a right-hand coordinate system, there are a total of twelve possible sequences of rotations that can be used to define a given angular orientation. The *zyx* convention used here defines the following sequence, which is also illustrated graphically in Figure 7.2. The x_0 coordinate system is rotated counterclockwise by an angle ψ_3 about the x_{03} axis. The resulting intermediate coordinate system \bar{x}_1 is then rotated counterclockwise by an angle ψ_2 about the \bar{x}_{12} axis to yield the coordinate system labelled \bar{x}_1 . A third counterclockwise rotation by an angle ψ_1 about the \bar{x}_{11} axis yields the desired x_1 system.

The coordinates of any point in x_1 can then be related to its respective coordinates in x_0 by,

$$x_{1i} = \alpha_{ji} x_{0j} \quad \text{and} \quad t_1 = t_0 = t \quad (7.5a)$$

where α_{ij} represents the transformation tensor containing the metrics and is given in the Appendix C. The metrics are obtained from the geometry of Figure 7.2, and are generally products of simple trigonometric functions in terms of the Euler angles ψ_i .

Introducing a new contravariant velocity relative to the rotated coordinate system x_1 ,

$$u_{1i} = \alpha_{ji} u_{0j} + \dot{\alpha}_{ji} \alpha_{jk} x_{1k} \quad (7.5b)$$

into the governing equations (7.3) yields,

$$\begin{aligned} \frac{\partial u_{1n}}{\partial t} + u_{1i} \frac{\partial u_{1n}}{\partial x_{1i}} - 2\beta_{rni} u_{1i} - \beta_{tni} x_{1i} - \beta_{fni} x_{1i} = \\ - \frac{1}{\rho} \frac{\partial p}{\partial x_{1n}} - g_{1n} + \nu \delta_{ij} \frac{\partial^2 u_{1n}}{\partial x_{1i} \partial x_{1j}} \end{aligned} \quad (7.6a)$$

$$\frac{\partial u_{1i}}{\partial x_{1i}} = 0 \quad (7.6b)$$

where $\beta_{r ij} = \dot{\alpha}_{ki} \alpha_{kj}$,

$$\beta_{t ij} = \ddot{\alpha}_{ki} \alpha_{kj},$$

$$\beta_{f ij} = \dot{\alpha}_{ki} \dot{\alpha}_{kj} - \dot{\alpha}_{ki} \dot{\alpha}_{nm} \alpha_{km} \alpha_{nj},$$

and $g_{1i} = \alpha_{ij} g_{0j}$.

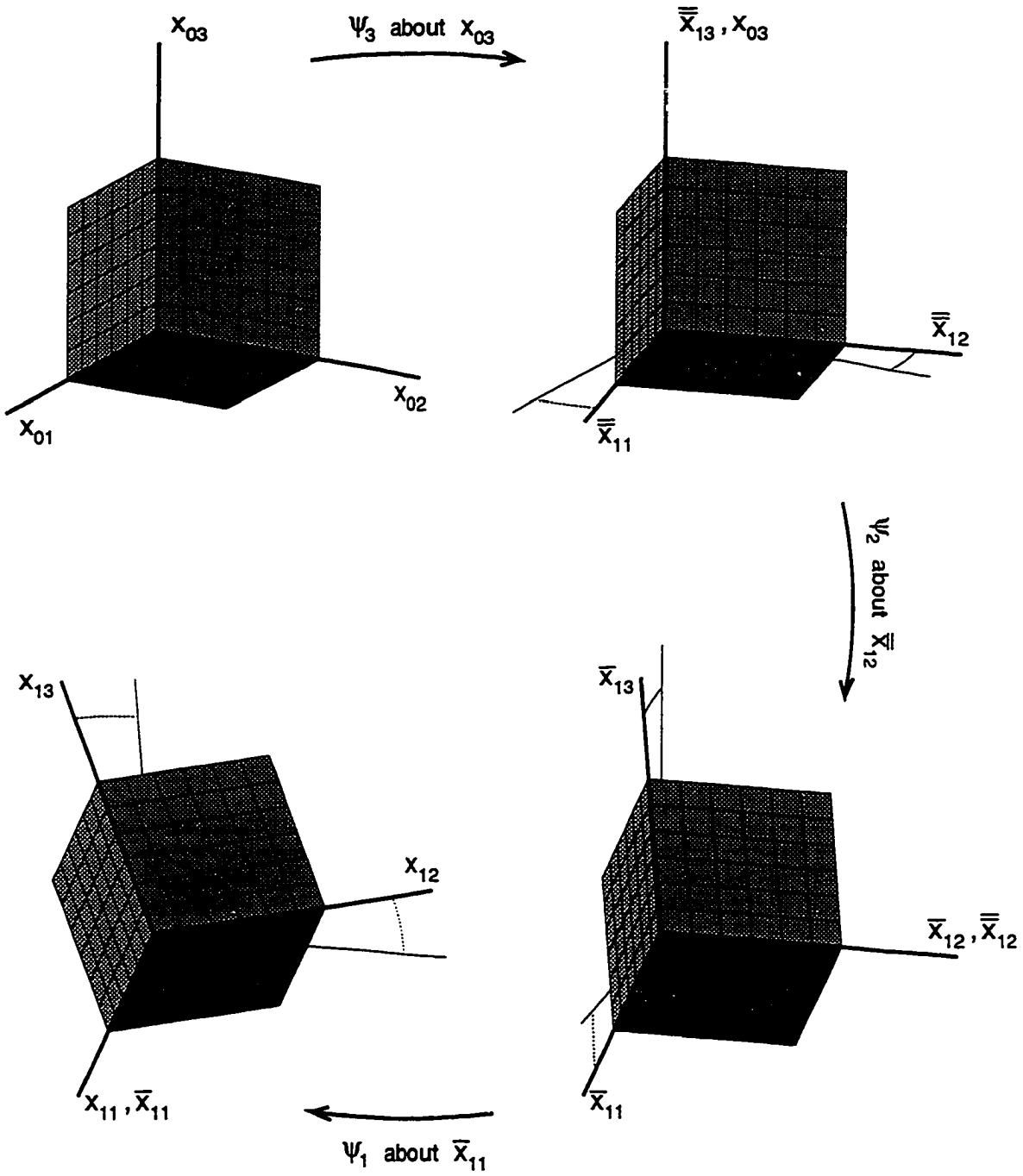


Figure 7.2: Spinning Nutating Coordinate System, x_1

Consequently, the rotation of the coordinate system x_1 with respect to x_0 results in the appearance of three new types of terms in the governing equations. The term $\beta_{r_{ni}}u_{1i}$ represents the Coriolis acceleration effects experienced by fluid particles as a result of the rotation of the axis. The term $\beta_{f_{ni}}x_{1i}$ represents centrifugal acceleration effects induced by the axial rotation. The term $\beta_{t_{ni}}x_{1i}$ can be separated into tangential acceleration terms and additional centrifugal acceleration terms.

The transformation introduced here is particularly useful in capturing the effects due to spin stabilization and the possible nutation of a flight vehicle such as a satellite. The Euler angles, ψ_i , can be directly related to gyroscopic telemetry data in terms of the roll, pitch, and yaw angles of the vehicle. However, where it may be an advantage to describe the motion of the vehicle in terms of its Euler angles for complex cases involving unpredictable rotations, it becomes a disadvantage for cases involving a simple, constant angular velocity, rotation of the vehicle. Since the metrics of the transformation, α_{ij} , depend on the position rather than the angular velocity of the vehicle, they must be re-evaluated whenever the angular position of the vehicle changes.

7.1.3 Body Centered Coordinate System

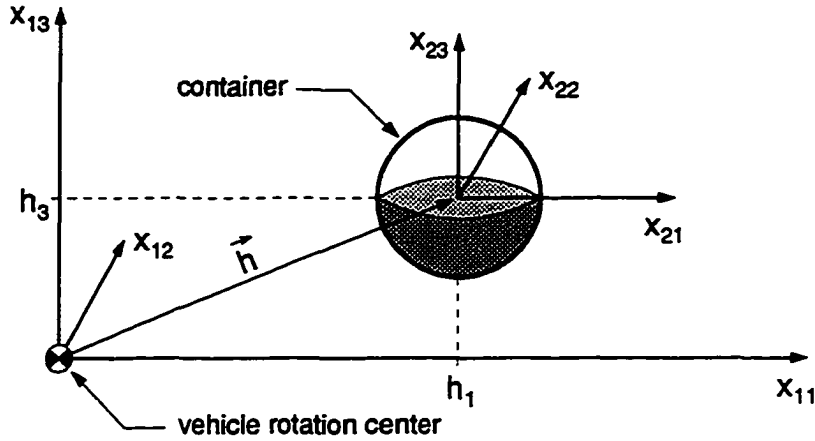
The first two coordinate transformations, $x \rightarrow x_0 \rightarrow x_1$, dealt with the motion of the vehicle itself relative to the inertial coordinate frame, x . The next two transformations relate the position of the container enclosing the liquid, relative to the center of rotation of the vehicle, which is represented by the origin of coordinate system x_1 .

The container is assumed to be an integral part of the solid structure of the vehicle. Let h_i denote the position of a coordinate system x_2 , with respect to the rotating coordinate system x_1 . The origin of the x_2 coordinate system coincides with the center of the container as depicted in Figure 7.3. As a result of possible elastic deformations of the vehicle frame, this position will in general be time dependent. The governing equations in the body centered coordinate system x_2 , which is free to undergo pure translation with respect to system x_1 , are obtained by replacing x_1 and u_1 by,

$$x_{2i} = x_{1i} - h_i \quad \text{and} \quad t_2 = t_1 = t \quad (7.7a)$$

and,

$$u_{2i} = u_{1i} - \dot{h}_i \quad (7.7b)$$

Figure 7.3: Body Centered Coordinate System, x_2

in equations (7.6) to yield,

$$\begin{aligned} \frac{\partial u_{2n}}{\partial t} + u_{2i} \frac{\partial u_{2n}}{\partial x_{2i}} - 2\beta_{rni} u_{2i} - \beta_{t ni} (x_{2i} + h_i) \\ - \beta_{f ni} (x_{2i} + h_i) = -\frac{1}{\rho} \frac{\partial p}{\partial x_{2n}} + g_{2n} + \nu \delta_{ij} \frac{\partial^2 u_{2n}}{\partial x_{2i} \partial x_{2j}} \end{aligned} \quad (7.8a)$$

$$\frac{\partial u_{2i}}{\partial x_{2i}} = 0 \quad (7.8b)$$

where $g_{2i} = g_{1i} - \ddot{h}_i$.

As a result of this transformation, the body force term g_{2i} is modified to reflect the linear acceleration experienced by a fluid particle within the container as a result of the motion induced by the elastic vehicle frame.

7.1.4 Body Fixed Coordinate System

The flexible frame of the vehicle will experience bending, torsional, and elongational deformations in response to forces exerted on its members as a result of the time dependent motion. Consequently, a coordinate system fixed on the container will undergo rotational as well as linear motion with respect to the nutating coordinate system x_1 . The effects of the linear component of the motion caused by the elastic deformation have been already captured by the transformation to the body centered coordinate system, x_2 . To capture the effects of rotation caused by deformation, coordinate system x_3 is introduced which is fixed on the container and thus experiences rotation with respect to x_2 . The orientation of the body fixed coordinate system x_3

with respect to coordinate system x_2 is described by the three Euler angles ϑ_i defined based on the same zyx convention as in section 7.1.2. The coordinates of any point in x_3 can then be related to its respective coordinates in x_2 by,

$$x_{3i} = \alpha_{ji}^* x_{2j} \quad \text{and} \quad t_3 = t_2 = t \quad (7.9a)$$

where α_{ij}^* represents the transformation tensor containing the metrics and is given in the Appendix C. Introducing a new contravariant velocity relative to the body fixed coordinate system x_3 ,

$$u_{3i} = \alpha_{ji}^* u_{2j} + \dot{\alpha}_{ji}^* \alpha_{jk}^* x_{3k} \quad (7.9b)$$

into the governing equations (7.8) yields,

$$\begin{aligned} \frac{\partial u_{3n}}{\partial t} + u_{3i} \frac{\partial u_{3n}}{\partial x_{3i}} - 2\Lambda_{rni} u_{3i} - (\Lambda_{tni} + \Lambda_{fni}) x_{3i} \\ - (R_{tni} + R_{fni}) h_i = -\frac{1}{\rho} \frac{\partial p}{\partial x_{3n}} + g_{3n} + \nu \delta_{ij} \frac{\partial^2 u_{3n}}{\partial x_{3i} \partial x_{3j}} \end{aligned} \quad (7.10a)$$

$$\frac{\partial u_{3i}}{\partial x_{3i}} = 0 \quad (7.10b)$$

where $\Lambda_{rij} = \beta_{rij}^* + \alpha_{ni}^* \alpha_{mj}^* \beta_{rnm}$,

$$\Lambda_{tij} = \beta_{tij}^* + \alpha_{ni}^* \alpha_{mj}^* \beta_{tnm},$$

$$\Lambda_{fij} = \beta_{fij}^* + \alpha_{ni}^* \alpha_{mj}^* \beta_{f nm} + 2\alpha_{ki}^* \alpha_{nm}^* \beta_{r mj}^* \beta_{r kn},$$

$$R_{tij} = \alpha_{ki}^* \beta_{tkj},$$

$$R_{fij} = \alpha_{ki}^* \beta_{fkj},$$

$$g_{3i} = \alpha_{ij}^* g_{2j},$$

with $\beta_{rij}^* = \dot{\alpha}_{ki}^* \alpha_{kj}^*$,

$$\beta_{tij}^* = \ddot{\alpha}_{ki}^* \alpha_{kj}^*,$$

$$\beta_{fij}^* = \dot{\alpha}_{ki}^* \alpha_{kj}^* - \dot{\alpha}_{ki}^* \dot{\alpha}_{nm}^* \alpha_{km}^* \alpha_{nj}^*.$$

Consequently, the rotation of the coordinate frame x_3 with respect to x_2 due to the elastic deformation of the vehicle frame results in the appearance of additional Coriolis, centrifugal, and tangential acceleration terms in the governing equations.

7.1.5 Self Adjusting Body Fixed Coordinates

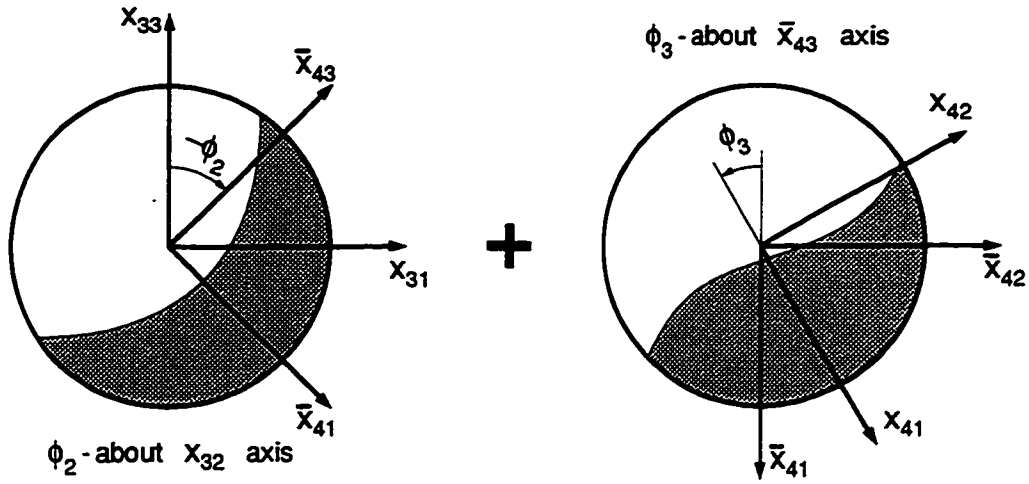
All the physical principles needed to describe the motion of a fluid particle within the container are embodied in equations (7.10). However, the presence of a free liquid surface introduces a nonlinearity into the model since it represents a boundary of unknown shape and position that has to be determined as part of the solution. In order to describe the motion of the free surface by a kinematic condition, its position F needs to be expressed as a function of time, t , as well as two of the three independent spatial coordinates x_{3i} . The choice of such a pair of spatial coordinates must be carefully considered to ensure that F remains single valued everywhere.

Since the initial value of Euler angle ψ_3 is arbitrary, the initial value of h_2 can be taken to be equal to zero without any loss in generality. This would imply that the center of the container lies initially in the $x_{11} - x_{13}$ plane. For a container that is rotating about the x_{13} axis, and with generally small deformation angles ϑ_i , the direction of the motion of the bulk of the liquid will be along the $x_{31} - x_{33}$ plane due to centrifugal acceleration effects. However, if the angular velocity of the container is sufficiently large, then neither of the two likely choices, $F(t, x_{31}, x_{32})$ or $F(t, x_{32}, x_{33})$, can ensure that F will remain single valued. Furthermore, if the rotation of the container is started abruptly, then significant flow may be induced in the $x_{32} - x_{33}$ plane as a result of tangential acceleration effects.

To help ensure that the free surface remains single valued, and thus extend the range of the model, a self adjusting body fixed coordinate system, x_4 , is introduced. The coordinate system x_4 is defined by a rotation by an angle ϕ_2 about the x_{32} axis, followed by a rotation by an angle ϕ_3 about the intermediate x_{43} axis. The self adjusting body fixed coordinates are illustrated graphically in Figure 7.4. With the position of the free surface described by $F(t, x_{42}, x_{43})$, the values of ϕ_2 and ϕ_3 can be adjusted to ensure that if possible F remains single valued. Furthermore, with the plane $x_{42} - x_{43}$ rotated as to follow the free surface of the liquid, the geometry of the domain of the problem becomes more simple in terms of the x_4 coordinate system. As a result, a more nearly orthogonal computational grid can be generated with less effort, thus improving both the speed and accuracy of the model.

The coordinates of a point with respect to the self adjusting frame x_4 can be determined from its coordinates with respect to frame x_3 from,

$$x_{4i} = s_{ji}x_{3j} \quad (7.11a)$$

Figure 7.4: Surface Tracking Coordinates, x_4

where s_{ij} is the transformation tensor given in Appendix C.

Replacing x_3 in the governing equations and introducing a new velocity,

$$u_{4i} = s_{ji}u_{3j} \quad (7.11b)$$

yields the following set of governing equations in the self adjusting frame,

$$\begin{aligned} \frac{\partial u_{4n}}{\partial t} + (u_{4i} + f_{ik}x_{4k}) \frac{\partial u_{4n}}{\partial x_{4i}} - (2\lambda_{rni} + f_{ni})u_{4i} - \lambda_{1ni}x_{4i} \\ - \lambda_{2ni}h_i = -\frac{1}{\rho} \frac{\partial p}{\partial x_{4n}} + g_{4n} + \nu \delta_{ij} \frac{\partial^2 u_{4n}}{\partial x_{4i} \partial x_{4j}} \end{aligned} \quad (7.12a)$$

$$\frac{\partial u_{4i}}{\partial x_{4i}} = 0 \quad (7.12b)$$

where $f_{ij} = \dot{s}_{ni}s_{nj}$,

$$\lambda_{rij} = \Lambda_{rnm}s_{ni}s_{mj},$$

$$\lambda_{1ij} = (\Lambda_{f nm} + \Lambda_{t nm})s_{ni}s_{mj},$$

$$\lambda_{2ij} = (R_{f nj} + R_{t nj})s_{ni},$$

and $g_{4i} = s_{ji}g_{3j}$.

The new terms appearing in the governing equations are due to the rotation of the axis. The x_4 coordinate system is rotating with respect to the x_3 system but the velocity u_4 is still measured with respect to x_3 . Thus, the Coriolis and the convection terms are modified to reflect this.

7.1.6 Poisson Equation for Pressure

The pressure distribution within the fluid can be determined by the solution of a Poisson equation which is derived from the momentum equations. Differentiating equation (7.12a) with respect to x_{4n} and contracting on n yields,

$$\begin{aligned} \frac{1}{\rho} \delta_{ij} \frac{\partial^2 p}{\partial x_{4i} \partial x_{4j}} = & \left[2\lambda_{rni} \frac{\partial u_{3i}}{\partial x_{4n}} + \delta_{ni} \lambda_{1ni} \right] \\ & + 2 [J_{12}(u_{41}, u_{42}) + J_{13}(u_{41}, u_{43}) + J_{23}(u_{42}, u_{43})] \\ & - \left[\frac{\partial D}{\partial t} + D^2 + (u_{4i} + f_{ik}x_{4k}) \frac{\partial D}{\partial x_{4i}} - \nu \delta_{ij} \frac{\partial^2 D}{\partial x_{4i} \partial x_{4j}} \right] \end{aligned} \quad (7.13)$$

where D represents the dilatation and is defined by

$$D = \frac{\partial u_{4i}}{\partial x_{4i}} \quad (7.14)$$

and the two dimensional Jacobians $J_{ij}(A, B)$ are defined by

$$J_{ij}(A, B) = \left(\frac{\partial A}{\partial x_{4i}} \frac{\partial B}{\partial x_{4j}} - \frac{\partial B}{\partial x_{4i}} \frac{\partial A}{\partial x_{4j}} \right)$$

The dilatation terms in equation (7.13), which are ideally zero for an incompressible fluid, are retained in the above derivation because they are subsequently used by the numerical method in obtaining a pressure solution which satisfies the divergence free condition.

7.1.7 Free Surface Kinematic Condition

The motion of the free surface is determined by the kinematic condition, which requires that $DF/Dt = 0$. This condition is based on the assumption that fluid particles that lie on the free surface must remain there [4]. For the geometry of the present problem the position of the free surface $F(t, x_{42}, x_{43})$ can be calculated from,

$$\frac{\partial F}{\partial t} = U_{41} + U_{42} \frac{\partial F}{\partial x_{42}} + U_{43} \frac{\partial F}{\partial x_{43}} \quad (7.15)$$

where $U_{ij} = u_{ij} + f_{jk}x_{ik}$.

The kinematic condition as formulated above is inappropriate in the viscous region adjacent to the container walls. Fluid particles on the free surface where it adjoins the walls can not simultaneously stay on the free surface and satisfy the no-slip constraint.

Thus, along the container wall the motion of the free surface is determined by requiring that the slope of the surface be equal to zero. This leads to a more robust boundary condition for F , and alleviates the type of the numerical problems which have been previously discussed (see section 4.4.4).

7.1.8 Boundary Conditions

The dynamic conditions at the free surface are obtained by requiring that the normal and tangential stress components be continuous across the liquid-vapor interface. The viscous stress components in the vapor (or gas) phase are very small. Consequently, these remaining liquid terms are set equal to zero, and the resulting dynamic conditions at the free surface are expressed in terms of a local curvilinear coordinate system as,

normal stress:

$$p - p_o = 2\mu \frac{\partial \mathcal{U}_n}{\partial n} + (\kappa_2 + \kappa_3)\mathcal{Y} \quad (7.16a)$$

tangential stresses:

$$\frac{\partial \mathcal{U}_n}{\partial \tau_2} + \frac{\partial \mathcal{U}_{\tau_2}}{\partial n} - \kappa_2 \mathcal{U}_{\tau_2} = 0 \quad (7.16b)$$

$$\frac{\partial \mathcal{U}_n}{\partial \tau_3} + \frac{\partial \mathcal{U}_{\tau_3}}{\partial n} - \kappa_3 \mathcal{U}_{\tau_3} = 0 \quad (7.16c)$$

where \mathcal{U}_n denotes the velocity component normal to the free surface and \mathcal{U}_{τ_2} and \mathcal{U}_{τ_3} the two velocity components tangent to the surface. The coefficient of surface tension is denoted by \mathcal{Y} , while p_o denotes the pressure of the vapor phase. The normal, n , and tangential coordinates, τ_2 and τ_3 along the free surface are based on the following set of unit vectors, which are defined in terms of the unit vectors of the x_{4i} coordinate system, \bar{e}_i , as,

$$\bar{n} \equiv \frac{-\bar{e}_{31} + F_2 \bar{e}_{32} + F_3 \bar{e}_{33}}{\sqrt{1 + F_2^2 + F_3^2}} = n_i \bar{e}_i \quad (7.17a)$$

$$\bar{\tau}_2 \equiv \frac{F_2 \bar{e}_{31} + \bar{e}_{32}}{\sqrt{1 + F_2^2}} = \tau_{2i} \bar{e}_i \quad (7.17b)$$

$$\bar{\tau}_3 \equiv \frac{F_3 \bar{e}_{31} - F_2 F_3 \bar{e}_{32} + (1 + F_2^2) \bar{e}_{33}}{\sqrt{1 + F_2^2 + F_3^2} \sqrt{1 + F_2^2}} = \tau_{3i} \bar{e}_i \quad (7.17c)$$

The κ_i represent the local curvatures of the free surface which are defined by

$$\kappa_i = \frac{F_{ii}}{(1 + F_i^2)^{3/2}} \quad (7.18)$$

with,

$$F_i = \frac{\partial F}{\partial x_{4i}} \quad \text{and} \quad F_{ii} = \frac{\partial^2 F}{\partial x_{4i}^2}$$

The dynamic free surface conditions and the continuity equation are used to provide boundary conditions for the pressure and the three velocity components along the free surface.

One of the advantages of the body fixed coordinate system is that the appropriate boundary conditions can be easily determined. Because the contravariant velocity, u_4 , is been used the no-slip condition for a viscous fluid along a wall retains its familiar form,

$$u_{4i} = 0 \quad (\text{along the container wall}) \quad (7.19)$$

The pressure boundary conditions along the container wall are obtained by forming an expression for the normal gradient along the wall from the momentum equations (see equation 7.31a).

7.1.9 Initial Conditions

The forcing experienced by the liquid is determined by the motion of the vehicle relative to the inertial coordinate system, x . The liquid is assumed to be in a state of static equilibrium for $t < 0$. At $t = 0$, the static equilibrium of the liquid is disturbed by a sudden change in the motion of the vehicle. If the vehicle experiences a step change in at least one of either its rectilinear acceleration components, $\ddot{\ell}_i$, or its angular acceleration components, $\ddot{\psi}_i$, then the pressure field instantaneously adjusts to the corresponding apparent accelerations experienced by the liquid. However, the liquid remains motionless at $t = 0^+$. The pressure distribution can be determined from a simplified form of the governing equations, which is obtained by setting $u_{4i} = 0$ in equations (7.12, 7.13).

Thus, for a step change in an acceleration component of the vehicle, the initial conditions at $t = 0^+$ are given by,

$$u_{4i} = 0 \quad (7.20a)$$

$$\frac{1}{\rho} \delta_{ij} \frac{\partial^2 p}{\partial x_{4i} \partial x_{4j}} = \delta_{ij} \lambda_{1ij} \quad (7.20b)$$

subject to the following boundary conditions along the container walls,

$$\frac{1}{\rho} \frac{\partial p}{\partial x_{4n}} = -g_{3n} + \lambda_{1ni} x_{4i} + \lambda_{2ni} h_i \quad (7.20c)$$

and a pressure distribution along the free surface given by,

$$p - p_o = (\kappa_2 + \kappa_3) \mathcal{V} \quad (7.20d)$$

If the vehicle experiences a step change in at least one of its velocity components, either the rectilinear velocities $\dot{\ell}_i$ or the angular velocities $\dot{\psi}_i$, then in order to determine the correct set of initial conditions the governing equations must be rescaled in terms of the *pressure impulse*, Π . Here, the rescaling of the equations is carried out following the procedure which has been previously presented in Chapter 3. Please refer to equation (3.22h) for the definition of Π , and to the accompanying discussion for the details. For a step change in the velocity of the vehicle, and assuming that the deformation angles $\vartheta_i = 0$, the resulting set of equations for the initial conditions of the problem is given by,

$$u_{4i} = -s_{ji} \alpha_{mj} \dot{\ell}_m + s_{ji} \dot{\alpha}_{mj} \alpha_{mn} (x_{4n} + h_n) - \frac{1}{\rho} \frac{\partial \Pi}{\partial x_{4i}} \quad (7.21a)$$

$$\frac{1}{\rho} \delta_{ij} \frac{\partial^2 \Pi}{\partial x_{4i} \partial x_{4j}} = 0 \quad (7.21b)$$

where equation (7.21a) is used to determine u_{4i} in the interior of the flowfield, and also serves as a boundary condition at the wall, with u_{4i} set equal to zero. Along the free surface, $\Pi = 0$. With the above set of equations providing a solution for a divergence free velocity field within the container at $t = 0^+$, the pressure distribution, p , at time $t = 0^+$, can be determined from the solution of the pressure Poisson equation, by setting the dilatation terms equal to zero in equation (7.13).

A case which involves an impulsively started rotation of a half filled spherical container will be presented in the next chapter. For this particular case, the container is spun about the x_{13} axis at a constant angular velocity, $\dot{\psi}_3$, with its center located at a distance h_1 from the axis of rotation. With the exception of h_1 , ψ_3 , and $\dot{\psi}_3$, the remaining parameters which control the forcing of the liquid are set equal to zero throughout the calculation. For $t < 0$, the liquid is assumed to be in a state of

hydrostatic equilibrium, with its free surface lying in a horizontal position. The initial angles for the self adjusting coordinates are set equal to $\phi_2 = -\pi/2$, and $\phi_3 = 0$. For this specific case, equation (7.21a) simplifies to the following component from,

$$u_{41} = -\frac{1}{\rho} \frac{\partial \Pi}{\partial x_{41}} \quad (7.22a)$$

$$u_{42} = -\dot{\psi}_3(x_{43} + h_1) - \frac{1}{\rho} \frac{\partial \Pi}{\partial x_{42}} \quad (7.22b)$$

$$u_{43} = \dot{\psi}_3 x_{22} - \frac{1}{\rho} \frac{\partial \Pi}{\partial x_{43}} \quad (7.22c)$$

The above simplified form of the momentum equations are used in conjunction with equation (7.21b) to obtain the initial velocity distribution at $t = 0^+$. With a known velocity field, the pressure at $t = 0^+$ is determined from the solution of equation (7.13).

7.1.10 Nondimensionalization

The liquid density, ρ , a characteristic length of the container, L , and a characteristic acceleration experienced by the liquid due to external body forces or the motion of the container, \mathbf{g} , are used to define the following primary Mass-Length-Time scales:

- mass $M \sim \rho L^3$
- length L
- time $\tau \sim \sqrt{L/g}$

Derived from these are the following characteristic scales used in nondimensionalizing the dependent variables:

- velocity $\mathcal{U} \sim \sqrt{Lg}$
- pressure $\mathcal{P} \sim \rho Lg$

The characteristic velocity scale, \mathcal{U} , is equivalent to the wave speed determined from shallow water wave theory, while τ represents the time interval for a wave disturbance to travel across the container and \mathcal{P} an Euler pressure scale based on \mathcal{U} .

The motion of the fluid is determined by a number of similarity parameters that emerge from the nondimensionalization. These parameters are separated into two distinct groups. The first group contains the parameters,

$$\frac{h_i}{L}, \frac{g_i}{\mathbf{g}}, \frac{\ddot{h}_i}{\mathbf{g}}, \frac{\ddot{\ell}_i}{\mathbf{g}}, \psi_i, \dot{\psi}_i\tau = \Omega_i, \ddot{\psi}_i\tau^2 = \dot{\Omega}_i,$$

$$\vartheta_i, \dot{\vartheta}_i\tau = \omega_i, \ddot{\vartheta}_i\tau^2 = \dot{\omega}_i$$

which pertain information on the motion of the container relative to the inertial coordinate frame. These parameters determine the net acceleration experienced by the fluid as a result of this motion.

The second group contains two similarity parameters related to the physical properties of the fluid. These are the Galileo number, Ga , and the Bond number, Bo , defined as,

$$Ga \equiv \frac{L^3 \mathbf{g}}{\nu^2} \quad \text{and} \quad Bo \equiv \frac{\rho \mathbf{g} L^2}{\gamma}$$

The Galileo number represents a ratio of body to viscous forces. The dimensionless Galileo number can also be viewed as being analogous to the square of a Reynolds number based on the characteristic velocity scale, \mathcal{U} . The Bond number represents a ratio of body to surface tension forces. It can also be expressed as the ratio of Weber to Froude numbers, the two dimensionless groups commonly associated with free surface flows. However, with the characteristic velocity and time scales used here, the Froude number does not emerge as an independent similarity parameter.

One of the advantages of the present model is that the equations of motion are derived based on the position of the container with respect to the inertial frame rather than on its relative motion. Consequently, the use of scales based on linear accelerations or angular velocities was avoided since under some sloshing conditions these can be zero or variable. Instead, the acceleration scale used here, \mathbf{g} , is treated as a constant whose value can be suitably chosen to match the magnitude of the prevailing acceleration experienced by the liquid under a *given* forcing condition.

7.2 Numerical Method

The three dimensional equations of motion developed in the previous section are solved using a numerical method to determine the motion of the liquid within the

container. A body fitted grid is used that conforms to the irregular, time dependent shape of the liquid region. The governing equations are expressed in terms of the generalized grid coordinates and solved using a second order accurate finite difference method. An outline of the numerical method used for the discretization and solution of the governing equations is given.

7.2.1 Generalized Grid Coordinates

The accuracy of a numerical solution is strongly dependent on the selection of the computational grid. This is particularly critical for moving boundary problems where the shape and position of the free boundary are generally unknown and are determined as part of the solution.

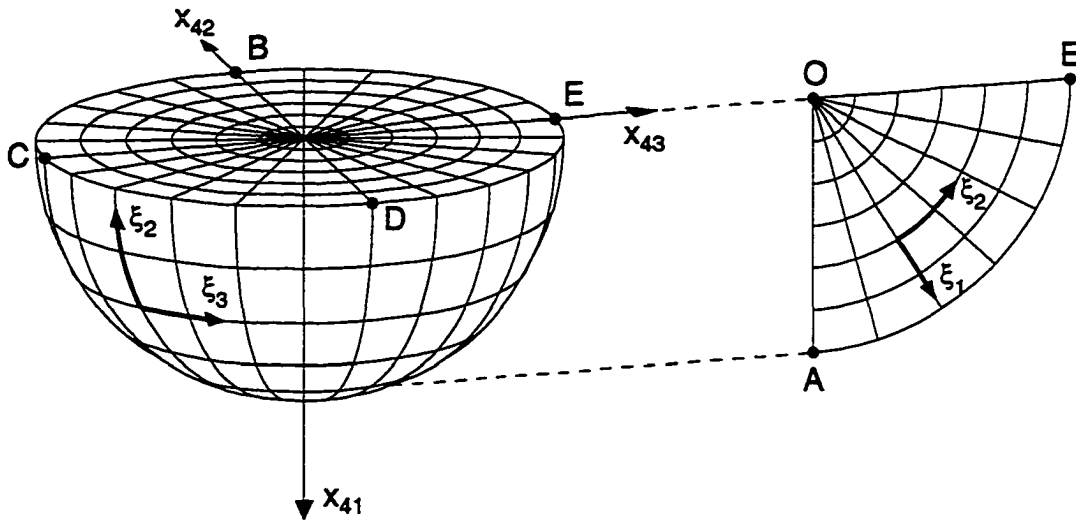
A body fitted grid, in terms of generalized grid coordinates ξ , is used for the solution of the governing equations. The mapping of the physical region of the problem onto the computational domain is depicted in Figure 7.5. In terms of the x_4 coordinate system, the physical domain of the problem is defined by the position of the free surface, $F(t, x_{42}, x_{43})$, and the geometry of the spherical container. The geometry of the physical region in Figure 7.5(a) is represented as a simple hemisphere. This is done to simplify the presentation of the mapping. In general, the shape of the free surface will be more irregular for $t > 0$.

The liquid region is mapped onto a cuboid, the dimensions of which, $\xi_{1\max}$, $\xi_{2\max}$, and $\xi_{3\max}$, are selected so that the distance between any two adjacent grid points in the computational domain is equal to unity. This is done to simplify the finite difference representations.

The point defined by the intersection of the x_{41} axis with the free surface is mapped onto the face of the cuboid defined by the $\xi_1 = 0$ plane. The boundary along the container wall is mapped onto the opposite face of the cuboid at $\xi_1 = \xi_{1\max}$. The x_{41} axis is mapped onto the $\xi_2 = 0$ plane while the free surface onto the $\xi_2 = \xi_{2\max}$ plane. Finally, a cut is taken along the plane defined by the x_{41} and the positive x_{42} axis and this section is mapped onto the $\xi_3 = 0$ and the $\xi_3 = \xi_{3\max}$ faces of the cuboid. The preceding transformation places the ξ_1 coordinate predominantly in the radial direction, while the ξ_2 and ξ_3 coordinates run predominantly along the azimuthal and circumferential directions of the liquid region.

The grid point distribution is determined by a combination of elliptic and algebraic schemes. The elliptic system of equations used here is similar in form to that proposed

(a) x_4 - space: Physical Domain



(b) ξ - space: Computational Domain

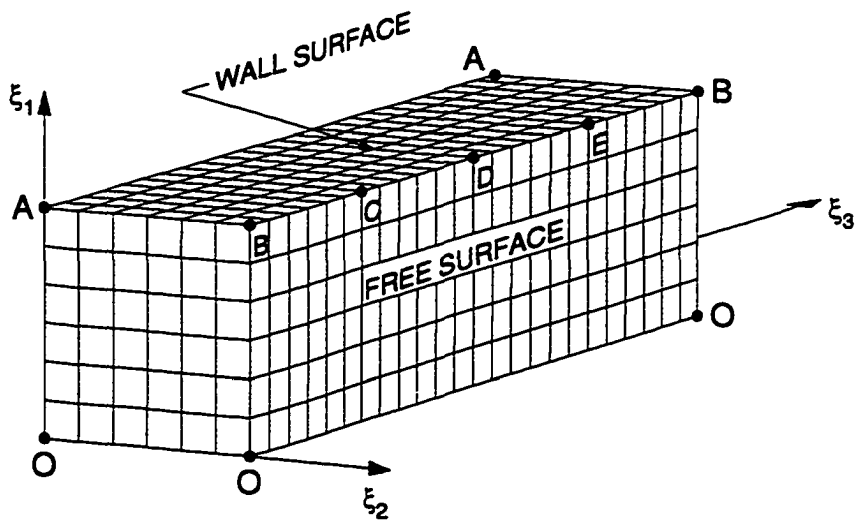


Figure 7.5: Generalized Grid Coordinates, ξ

in [72] and [73],

$$\nabla^2 \xi_i = Q_i(\xi_1, \xi_2, \xi_3) |\nabla \xi_i|^2 \quad \text{for } i=1,2,3 \quad (7.23)$$

where the control functions Q_i are adjusted to obtain the desired grid point distribution.

The procedure followed in solving these equations is similar to the one described in [73]. Equations (7.23) are transformed into the computational domain by interchanging the role of dependent and independent coordinates and solved using a finite difference method. The only significant deviation from the procedure described in [73] is that an algebraic equation is first used to approximate the grid to the desired degree of orthogonality along the boundaries. The control functions Q_i are then determined explicitly from the approximated grid values. This is done to save computational effort by taking advantage of the known geometrical features of the physical region. The grid generation procedure used in this study will be discussed in more detail in the sections that follow.

7.2.2 Metric Term Evaluation and Singularities

The evaluation of the metric terms which appear in the governing equations as a result of the transformation to the ξ coordinate space is carried out using the same differencing scheme as that used for the governing equations. Since the non-conservative form of the governing equations is used here, no special geometry differencing requirements *must* be satisfied. Nevertheless, the benefits of utilizing a consistent difference scheme have been clearly demonstrated in [74].

The finite differencing of the grid transformation metric terms, which are given by,

$$\dot{\eta}_i \equiv \frac{\partial \xi_i}{\partial t}, \quad \eta_{i,j} \equiv \frac{\partial \xi_i}{\partial x_{4j}}, \quad \text{and} \quad \eta_{k,ij} \equiv \frac{\partial^2 \xi_k}{\partial x_{4i} \partial x_{4j}} \quad (7.24)$$

is carried out using the difference representations defined in equations (7.32). Centered differences are used for all first and second order spatial derivatives in evaluating the metric terms $\eta_{i,j}$ and $\eta_{i,jk}$ in the interior of the computational domain. Along the container wall and the free surface normal derivatives are evaluated using three point one sided differences. The grid speed terms, $\dot{\eta}_i$, are evaluated using second order accurate backward time differences.

The Jacobian of the generalized grid transformation vanishes along the x_{41} axis. This corresponds to singularities in the governing equations and it requires the special treatment of the equations along the x_{41} axis. These singularities are caused by the collapse of the $\xi_2 = 0$ plane onto the x_{41} axis, and by the collapse of the $\xi_1 = 0$ plane onto a single point defined by the intersection of the x_{41} axis with the free surface. Two different procedures have been considered for obtaining the values of the depended variables along the x_{41} axis. These involve the use of a locally defined system of coordinates, or matching. The matching procedure is more simple to implement than the use of local coordinates. It is based on the requirement that a variable and its first derivative remain continuous across the x_{41} axis. This can be accomplished by the use of the following pseudo-boundary conditions,

$$A_{i,1,k}^{n+1,m+1} = A_{i,1,k_e}^{n+1,m} \quad \text{for } 0 \leq \theta < \pi \quad (7.25a)$$

$$\left. \frac{\partial A}{\partial \xi_2} \right|_{i,1,k}^{n+1,m+1} = \left. \frac{\partial A}{\partial \xi_2} \right|_{i,1,k_e}^{n+1,m} \quad \text{for } \pi < \theta \leq 2\pi \quad (7.25b)$$

where A denotes any of the dependent variables, u_{41} , u_{42} , u_{43} , p , or F . The subscripts (i, j, k) denote the grid position along the (ξ_1, ξ_2, ξ_3) coordinates respectively. The circumferential angle corresponding to the grid section identified by k , along which ξ_3 is constant, is denoted by θ . Note that k_e is used to denote the grid section which is displaced by 180° in the circumferential direction from the section denoted by k .

The matching procedure has been successfully used in the solution of several flows. However, despite an increase in complexity, the use of a local rectangular coordinate system appears to be a better suited choice for obtaining the values of the dependent variables along the x_{41} axis. The calculation of the dependent variables directly from first principles appears to have a noticeable impact on the solution of the problem, especially at lower grid resolutions. Furthermore, the use of a local coordinate system leads to the faster convergence of the pressure correction scheme that is used for the solution of the flow equations.

Two different local coordinates systems are necessary for the treatment of the singularities along the x_{41} axis. The coordinate system used for the solution of the dynamic free surface conditions involves an 11-point molecule which is shown in Figure 7.6(a). The ξ_1 coordinate line remains along the x_{41} axis. The redefined ξ_2 coordinate line is located along the $x_{42} = 0$ plane, while the ξ_3 line is located along the $x_{43} = 0$ plane. The four additional grid points needed for the evaluation of cross derivatives in terms of the (ξ_2, ξ_3) coordinates at the free surface are shown in the figure.

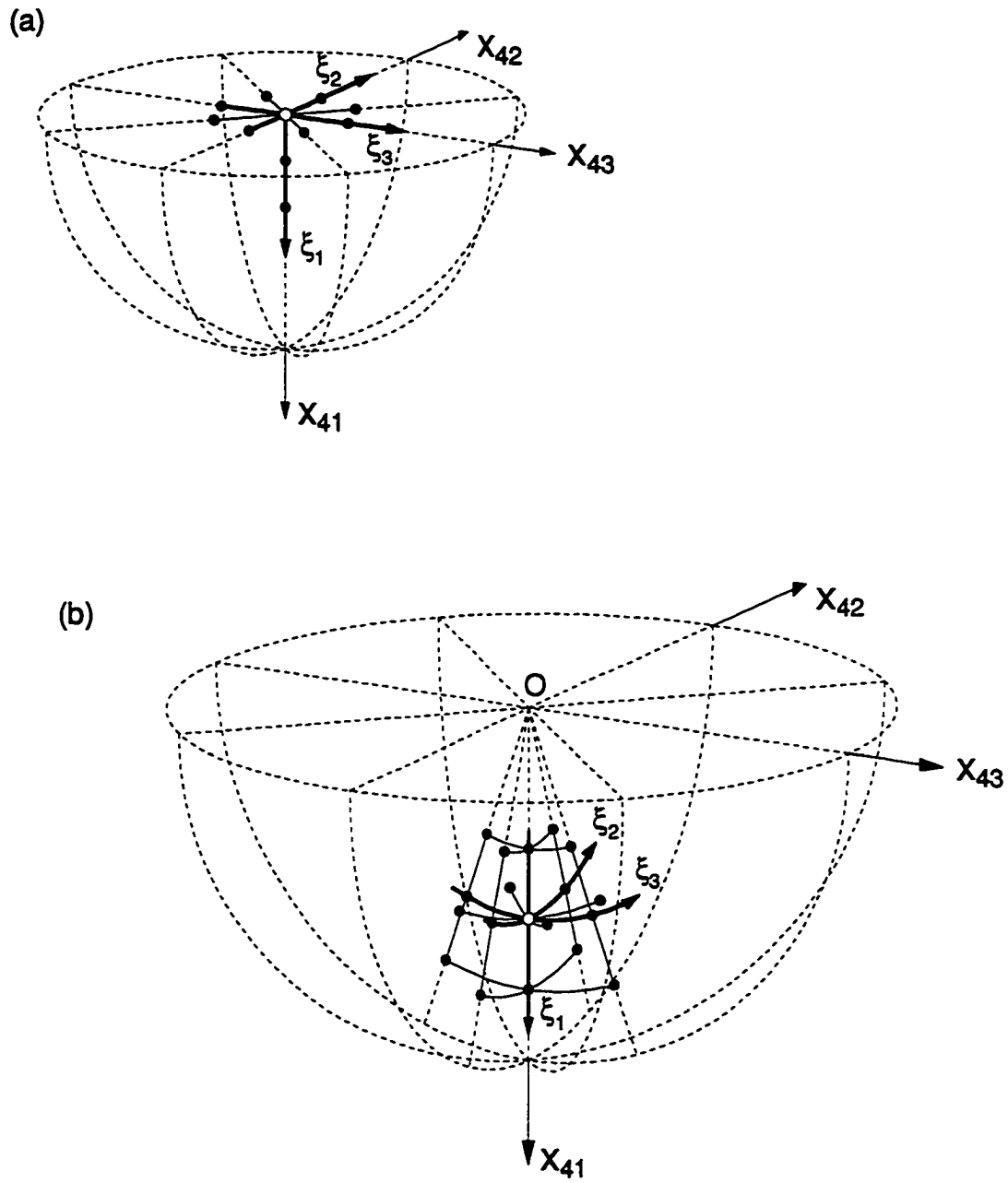


Figure 7.6: Local Grid Molecules on the x_{41} Axis

In the interior of the x_{41} axis, the 19-point grid molecule shown in Figure 7.6(b) is used for the solution of the equations. The ξ_1 coordinate is directed in the radial direction along the x_{41} axis. The locally redefined ξ_2 coordinate runs in the azimuthal direction along the $x_{43} = 0$ plane, and the locally redefined ξ_3 coordinate runs in the azimuthal direction along the $x_{42} = 0$ plane. With the exception of the three grid points located on the x_{41} axis, the remaining grid points are located on the surface of the conical grid section which is formed by grid points with a constant $\xi_2 = 1$ coordinate value.

With the metric terms, η_i , $\eta_{i,j}$, and $\eta_{i,j,k}$, evaluated along the x_{41} axis based on these locally redefined grid coordinates, the final form governing equations remains the same everywhere within the liquid region.

7.2.3 Governing Equations

The governing equations (7.12) are transformed in terms of the generalized coordinates ξ_i to take the following form:

momentum equations:

$$\begin{aligned} \frac{\partial u_{4n}}{\partial t} + (\eta_i + \eta_{i,j} u_{4j} + \eta_{i,j} f_{j,k} x_{4k}) \frac{\partial u_{4n}}{\partial \xi_i} \\ - (2\lambda_{r ni} + f_{ni}) u_{4i} - \lambda_{1 ni} x_{4i} - \lambda_{2 ni} h_i = \\ - \eta_{i,n} \frac{\partial p}{\partial \xi_i} + g_{4n} + \frac{1}{\sqrt{Ga}} \left(\gamma_{ij} \frac{\partial^2 u_{4n}}{\partial \xi_i \partial \xi_j} + \Gamma_i \frac{\partial u_{4n}}{\partial \xi_i} \right) \end{aligned} \quad (7.26a)$$

continuity:

$$\eta_{j,i} \frac{\partial u_{4i}}{\partial \xi_j} = 0 \quad (7.26b)$$

pressure equation:

$$\begin{aligned} \eta_{k,i} \eta_{n,j} \delta_{ij} \frac{\partial^2 p}{\partial \xi_k \partial \xi_n} + \eta_{n,i,j} \delta_{ij} \frac{\partial p}{\partial \xi_n} = 2\eta_{n,1} \eta_{m,2} \hat{J}_{nm}(u_{41}, u_{42}) \\ + 2\eta_{n,1} \eta_{m,3} \hat{J}_{nm}(u_{41}, u_{43}) + 2\eta_{n,2} \eta_{m,3} \hat{J}_{nm}(u_{42}, u_{43}) \\ + \left(2\eta_{j,n} \lambda_{r ni} \frac{\partial u_{4i}}{\partial \xi_j} + \lambda_{1 ij} \delta_{ij} \right) - S_p \end{aligned} \quad (7.26c)$$

where,

$$\gamma_{ij} = \delta_{nm} \eta_{i,n} \eta_{j,m} \quad , \quad \Gamma_i = \delta_{nm} \eta_{i,nm} \quad ,$$

and the pressure equation dilatation source term, S_p , is given by,

$$S_p = \frac{\partial D}{\partial t} + D^2 + (\dot{\eta}_i + \eta_{i,j}u_{4j} + \eta_{i,j}f_{jk}x_{4k}) \frac{\partial D}{\partial \xi_i} - \frac{1}{\sqrt{Ga}} \left(\gamma_{ij} \frac{\partial^2 D}{\partial \xi_i \partial \xi_j} + \Gamma_i \frac{\partial D}{\partial \xi_i} \right) \quad (7.27)$$

with the dilatation, D , given by,

$$D = \eta_{j,i} \frac{\partial u_{4i}}{\partial \xi_j} \quad (7.28)$$

the two dimensional Jacobians in terms of ξ_i defined by,

$$\hat{J}_{ij}(A, B) = \left(\frac{\partial A}{\partial \xi_i} \frac{\partial B}{\partial \xi_j} - \frac{\partial B}{\partial \xi_i} \frac{\partial A}{\partial \xi_j} \right)$$

The kinematic condition (7.15) at the free surface, $\xi_2 = \xi_{2max}$, can be written in terms of the generalized coordinates as,

$$\frac{\partial F}{\partial t} = U_{41} - [\dot{\eta}_1 + \eta_{1,2}U_{42} + \eta_{1,3}U_{43}] \frac{\partial F}{\partial \xi_1} - [\dot{\eta}_3 + \eta_{3,2}U_{42} + \eta_{3,3}U_{43}] \frac{\partial F}{\partial \xi_3} \quad (7.29)$$

7.2.4 Boundary Conditions

The three dynamic stress conditions at the free surface were defined by equations (7.16) in terms of a local curvilinear coordinate system, (n, τ_2, τ_3) . Before these equations can be numerically implemented they must be first expressed in terms of the dependent and independent variables of the x_4 coordinate system and then transformed in terms of the generalized coordinates, ξ . The normal and tangential velocities along the free surface can be decomposed in terms of the u_{4i} velocity components based on the following relations,

$$u_n = \vec{V} \cdot \vec{n} = n_i u_{4i}$$

$$u_{\tau_2} = \vec{V} \cdot \vec{\tau}_2 = \tau_{2i} u_{4i}$$

$$u_{\tau_3} = \vec{V} \cdot \vec{\tau}_3 = \tau_{3i} u_{4i}$$

while the normal and tangential derivatives along the free surface can be expressed in terms of,

$$\frac{\partial}{\partial n} = \nabla \cdot \vec{n} = n_j \frac{\partial}{\partial x_{4j}}$$

$$\frac{\partial}{\partial \tau_2} = \nabla \cdot \vec{\tau}_2 = \tau_{2i} \frac{\partial}{\partial x_{4i}}$$

$$\frac{\partial}{\partial \tau_3} = \nabla \cdot \vec{\tau}_3 = \tau_{3i} \frac{\partial}{\partial x_{4i}}$$

The above relations are substituted into equations (7.16), which are transformed in terms of the ξ coordinates to take the following form,

normal stress at $\xi_2 = \xi_{2max}$:

$$p = \frac{2}{\sqrt{Ga}} \left[n_i n_j \eta_{1k} \frac{\partial u_{4j}}{\partial \xi_k} + (n_2 \eta_{2k} + n_3 \eta_{3k}) \frac{\partial n_j}{\partial \xi_k} u_{4j} \right] + \frac{1}{Bo} (\kappa_2 + \kappa_3) \quad (7.30a)$$

tangential stresses at $\xi_2 = \xi_{2max}$:

$$\begin{aligned} & (\tau_{\ell i} n_j + \tau_{\ell j} n_i) \eta_{ik} \frac{\partial u_{4i}}{\partial \xi_k} + \\ & \left[(\tau_{\ell 2} \eta_{2k} + \tau_{\ell 3} \eta_{3k}) \frac{\partial n_j}{\partial \xi_k} + (n_2 \eta_{2k} + n_3 \eta_{3k}) \frac{\partial \tau_{\ell j}}{\partial \xi_k} \right] u_{4i} - \kappa_\ell \tau_{\ell i} u_{4i} = 0 \end{aligned} \quad (7.30b)$$

Equation (7.30b) represents both of the tangential stress conditions which may be obtained by setting the free index, ℓ , equal to either $\ell=2$ or $\ell=3$. The normal stress condition provides a boundary condition for the pressure along the liquid surface. The two tangential stress conditions are solved for the ξ_2 derivatives of the u_{42} and u_{43} velocity components. The ξ_2 derivative of the u_{41} velocity at the free surface is obtained from continuity, equation (7.26b).

Along the container wall, $\xi_1 = \xi_{1max}$, the pressure boundary condition is obtained by using the chain-rule to form an expression for the ξ_1 -gradient from the momentum equations. Thus,

at $\xi_1 = \xi_{1max}$:

$$\begin{aligned} \frac{\partial p}{\partial \xi_1} = & \left[\lambda_{1ni} x_{4i} + \lambda_{2ni} h_i + g_{4n} - f_{ik} x_{4k} \eta_{1,i} \frac{\partial u_{4n}}{\partial \xi_1} \right] \frac{\partial x_{4n}}{\partial \xi_1} + \\ & \frac{1}{\sqrt{Ga}} \left[\gamma_{11} \frac{\partial^2 u_{4n}}{\partial \xi_1^2} + 2\gamma_{12} \frac{\partial^2 u_{4n}}{\partial \xi_1 \partial \xi_2} + 2\gamma_{13} \frac{\partial^2 u_{4n}}{\partial \xi_1 \partial \xi_3} \right] \frac{\partial x_{4n}}{\partial \xi_1} + \end{aligned}$$

$$\frac{1}{\sqrt{Ga}} \left[\Gamma_1 \frac{\partial u_{4n}}{\partial \xi_1} \right] \frac{\partial x_{4n}}{\partial \xi_1} \quad (7.31a)$$

The velocities along the wall are set equal to zero in accordance with the no-slip boundary condition. Thus,

$$u_{4i} = 0 \quad \text{at} \quad \xi_1 = \xi_{1max} \quad (7.31b)$$

7.2.5 Finite Difference Method

The governing equations are approximated using an implicit second order accurate finite difference scheme. Sample difference approximations are given below for some of the terms in the governing equations. The time level is denoted by superscript n while superscript m is used to denote the iteration level. Subscripts i, j , and k , are used to denote the position of a grid point in the ξ_1, ξ_2 , and ξ_3 directions respectively, with I, J , and K , denoting the total number grid points in each of these directions.

In the interior of the liquid region, all of the spatial terms are finite differenced using traditional centered differences of the form:

$$\left. \frac{\partial u}{\partial \xi_3} \right|_{i,j,k} = \frac{1}{2} (u_{i,j,k+1} - u_{i,j,k-1}) \quad (7.32a)$$

$$\left. \frac{\partial^2 u}{\partial \xi_3^2} \right|_{i,j,k} = u_{i,j,k+1} - 2u_{i,j,k} + u_{i,j,k-1} \quad (7.32b)$$

The unsteady terms are approximated by second order backward time differences of the form:

$$\left. \frac{\partial u}{\partial t} \right|^{n+1} = \frac{1}{2\Delta t} (3u^{n+1} - 4u^n + u^{n-1}) \quad (7.32c)$$

To enhance the stability of the method by improving the diagonal dominance of the coefficient matrix, the convective terms are differenced according to equation (4.7). They are split into a first order upwind difference term, evaluated using information from the current iteration level $m+1$, plus a second order correction term which is evaluated at the previous iteration level, m .

Second order, three point backward differences are used to approximate the ξ_1 -gradients along the container wall, and the ξ_2 -gradients along the free surface. Thus, the ξ_1 pressure gradient at the wall, $\xi_1 = \xi_{1max}$, is differenced according to,

$$\left. \frac{\partial p}{\partial \xi_1} \right|_{I,j,k} = \frac{1}{2} (3p_{I,j,k} - 4p_{I-1,j,k} + p_{I-2,j,k}) \quad (7.32d)$$

where $z = I$ denotes the ξ_1 position of grid points located on the wall. The convective terms of the form,

$$U \frac{\partial F}{\partial \xi}$$

which appear in the kinematic equation (7.29), are upwind differenced using one-sided second order differences, following the same procedure that was previously outlined in section 4.2.4.

7.3 Computational Procedure

The resulting set of finite difference equations is solved iteratively using the Gauss-Siedel procedure. With the solution converged at time t , identified as time level n , the following sequence of steps is taken to advance the solution to the next time level, $n+1$, where $t^{n+1} = t^n + \Delta t$:

1. **Update of the free surface position:** Using the converged solution at time level n , the kinematic condition equation (7.29) is solved explicitly to obtain the new free surface position, F^{n+1} .
2. **Adjustment of forcing parameters:** The values of the various dimensionless parameters describing the position of the container, ℓ_i , ψ_i , ϑ_i , and h_i , are updated. Coefficients β_r , β_t , β_f , β_r^* , β_t^* , β_f^* , Λ_r , Λ_t , Λ_f , R_t , R_f , and g_3 , are then also updated.
3. **Adjustment of the surface tracking angles:** Based on the new position of the free surface, F^{n+1} , the values of the two surface tracking angles, ϕ_2 and ϕ_3 , are adjusted such that the coordinate system x_4 rotates to follow the center of gravity of the liquid. Coefficients f , λ_r , λ_1 , λ_2 , and g_4 that depend on ϕ_i are updated.
4. **Calculation of a new grid:** A new computational grid that conforms to the shape of the liquid region defined F^{n+1} is determined. The generalized coordinate metrics, η , are updated.
5. **Solution of the flow equations:** The three momentum equations (7.26a) and the pressure Poisson equation (7.26c) are solved using an iterative pressure correction scheme to obtain a divergence free velocity field u_{4i}^{n+1} , and p^{n+1} .

The above procedure, in terms of these five basic steps, is used to march the solution of the governing equations from $t = 0$ toward some steady state condition as $t \rightarrow \infty$. More detailed information on the procedures used for adjusting the surface tracking angles, generating the computational grid, and solving the flow equations is given in the following sections.

7.3.1 Adjustment of Surface Tracking Angles

The surface tracking angles, ϕ_2 and ϕ_3 , are adjusted at each time step so that the x_4 coordinate system rotates to follow the bulk of the liquid motion. The initial values of ϕ_i are selected such that the x_{41} axis passes through the center of gravity of the liquid. Thus, if the free surface is initially horizontal, then $\phi_2(0) = -\pi/2$ and $\phi_3(0) = 0$. The position of the center of gravity of the liquid with respect to the rotating coordinate system, x_4 , is denoted by \hat{X}_{4i} . These coordinates, \hat{X}_{4i} , can be evaluated from the following expressions,

$$\hat{X}_{4i} = \frac{3}{4\pi\mathcal{V}} \int_{\xi_1=0}^{\xi_1 \max} \int_{\xi_2=0}^{\xi_2 \max} \int_{\xi_3=0}^{\xi_3 \max} \hat{J}_{123}(x_{41}, x_{42}, x_{43}) x_{4i} d\xi_1 d\xi_2 d\xi_3 \quad (7.33)$$

where $\hat{J}_{123}(x_{41}, x_{42}, x_{43})$ denotes the Jacobian associated with the transformation to generalized grid coordinates, ξ . The dimensionless liquid volume is denoted by \mathcal{V} , and can be determined from,

$$\mathcal{V} = \frac{3}{4\pi} \int_{\xi_1=0}^{\xi_1 \max} \int_{\xi_2=0}^{\xi_2 \max} \int_{\xi_3=0}^{\xi_3 \max} \hat{J}_{123}(x_{41}, x_{42}, x_{43}) d\xi_1 d\xi_2 d\xi_3 \quad (7.34)$$

Note that, the numerical value for \mathcal{V} , as calculated by equation (7.34), is normalized by the total dimensionless volume of the spherical container, $4\pi/3$. Since theoretically \mathcal{V} should remain constant, equation (7.34) can also be used in monitoring the truncation error of the numerical solution.

The coordinates of the center of gravity of the liquid, \hat{X}_{4i} , can be used to calculate the incremental changes needed in adjusting the angles ϕ_2 and ϕ_3 such that the x_4 coordinates will keep up with the rotation of the center of gravity. These are given by,

$$\Delta\phi_2^{n+1} = \arctan\left(\frac{\hat{X}_{43}^{n+1}}{\hat{X}_{41}^{n+1}}\right) \quad \text{and,} \quad \Delta\phi_3^{n+1} = \arctan\left(\frac{\hat{X}_{42}^{n+1}}{\hat{X}_{41}^{n+1}}\right) \quad (7.35)$$

However, if the center of gravity is followed by the x_4 coordinate system too closely, then any variations which occur in its motion will be fed back into the governing equations through the transformation metrics, s_{ij} . Small changes in the shape of the free

surface, which occur from one time step to the next, can lead to very small amplitude but high frequency oscillations superimposed on the otherwise smooth motion exhibited by the center of gravity. The introduction of these oscillations into the governing equations can be effectively eliminated by adjusting the two angles, ϕ_2 and ϕ_3 , based on a time averaged rates of rotation.

The surface tracking angles are adjusted according to the following relations,

$$\phi_2^{n+1} = \phi_2^n + \Delta t \bar{\Phi}_2 \quad \text{and,} \quad \phi_3^{n+1} = \phi_3^n + \Delta t \bar{\Phi}_1 \quad (7.36)$$

where $\bar{\Phi}_2$ and $\bar{\Phi}_1$ represent time averaged angular velocities describing the rotation of the center of gravity relative to the non-rotating, body-fixed coordinate system x_3 . The position of the center of gravity relative to coordinate system x_3 can be determined from.

$$\hat{X}_{3i} = s_{ij} \hat{X}_{4j}$$

and its rotation can be described in terms of the two angles,

$$\Phi_1 = \arctan \left(\frac{\hat{X}_{33}}{\hat{X}_{32}} \right) \quad \text{and,} \quad \Phi_2 = \arctan \left(\frac{\hat{X}_{33}}{\hat{X}_{31}} \right) \quad (7.37)$$

where Φ_1 represents the angle defined by the projection of the center of gravity onto the $x_{32}-x_{33}$ plane and the x_{32} axis, and Φ_2 the angle defined by the projection onto the $x_{31}-x_{33}$ plane and the x_{31} axis.

7.3.2 Grid Generation Procedure

The physical domain of the problem is defined as the region bounded by the free surface, $F(t, x_{42}, x_{43})$ and the container wall surface. In advancing the solution of the problem from time level n to level $n+1$, a new free surface position, F^{n+1} , is determined by the solution of the kinematic equation. As the physical region of the problem changes, a new grid which conforms to the shape of F^{n+1} must be recalculated.

A three part procedure is followed in generating the computational grid for cases which involve flows within spherical containers. First, the positions of grid points along the free surface are adjusted based on the solution for F^{n+1} . Second, an algebraic equation is used to generate a provisional grid at each two-dimensional k -section of the grid, where each k -section is defined by a constant ξ_3 coordinate value. Finally, in the third step, the analytically generated grid is used to initialize the source functions, Q_i , used in the solution of the elliptic grid equations (7.23).

The function used in describing the position of the free surface, $F(t, x_{42}, x_{43})$, is expressed in terms of rectilinear coordinates, with F representing the height of the free surface with respect to the $x_{41} = 0$ plane. Consequently, values for F^{n+1} determined by the solution of the kinematic equation could force surface grid points along the contact line, defined by the intersection of the free surface with the container wall, to move either inside or outside the computational domain at time level $n+1$. This necessitates the adjustment of grid points along the free surface to ensure that the physical x_4 coordinates corresponding to grid point (I, J, k) are located on the container wall.

The procedure used in adjusting the grid along the free surface is outlined in Figure 7.7. Using calculated values for F_{ik}^{n+1} from the three grid points located closest to the wall, at $i = I, I-1$, and $I-2$, the free surface profile is curve fitted in terms of a second order polynomial of the form,

$$\hat{F}(r) = C_0 + C_1 r + C_2 r^2$$

where r represents the radial position in terms of the x_4 coordinate system at the given k grid section. The secant method is then used to solve the following constraint equation,

$$\hat{F}^2(r) + r^2 = 1$$

which represents the necessary condition for \hat{F}_{Ijk}^{n+1} to be located on the container wall. The solution yields r_{max}^{n+1} , which can be used to determine the x_4 coordinates of the grid point at the wall according to,

$$x_{41} = \hat{F}(r_{max}) \quad , \quad x_{42} = r_{max} \cos(\Theta_k) \quad , \quad \text{and} \quad x_{43} = r_{max} \sin(\Theta_k)$$

where Θ_k denotes the circumferential angle corresponding to the given k grid section. Once the position of the grid point at the wall has been determined, second order interpolation based on the F^{n+1} values is used to readjust the interior grid points along the free surface, for $i = 2, I-1$. The spacing of the grid points along the free surface, as well as along the x_{41} axis and the container wall, is determined by functions similar to that given in equation (4.1). The position of grid points along the x_{41} axis must also be adjusted due to changes in the value of F_{1jk}^{n+1} .

With the grid adjusted along the free surface and the x_{41} axis to account for changes in the position of the free surface, the following algebraic expression is used to generate the ξ_2 grid lines:

$$R(\Phi) = R_1 \left[1 + \frac{\Phi}{\Phi_2} \left(\frac{R_2}{R_1} - 1 \right) \sin \left(\frac{\pi \Phi}{2\Phi_2} \right) \right] \left[1 + C \left(\frac{\Phi}{\Phi_2} \right)^\zeta \sin \left(\frac{\pi \Phi}{\Phi_2} \right) \right] \quad (7.38)$$

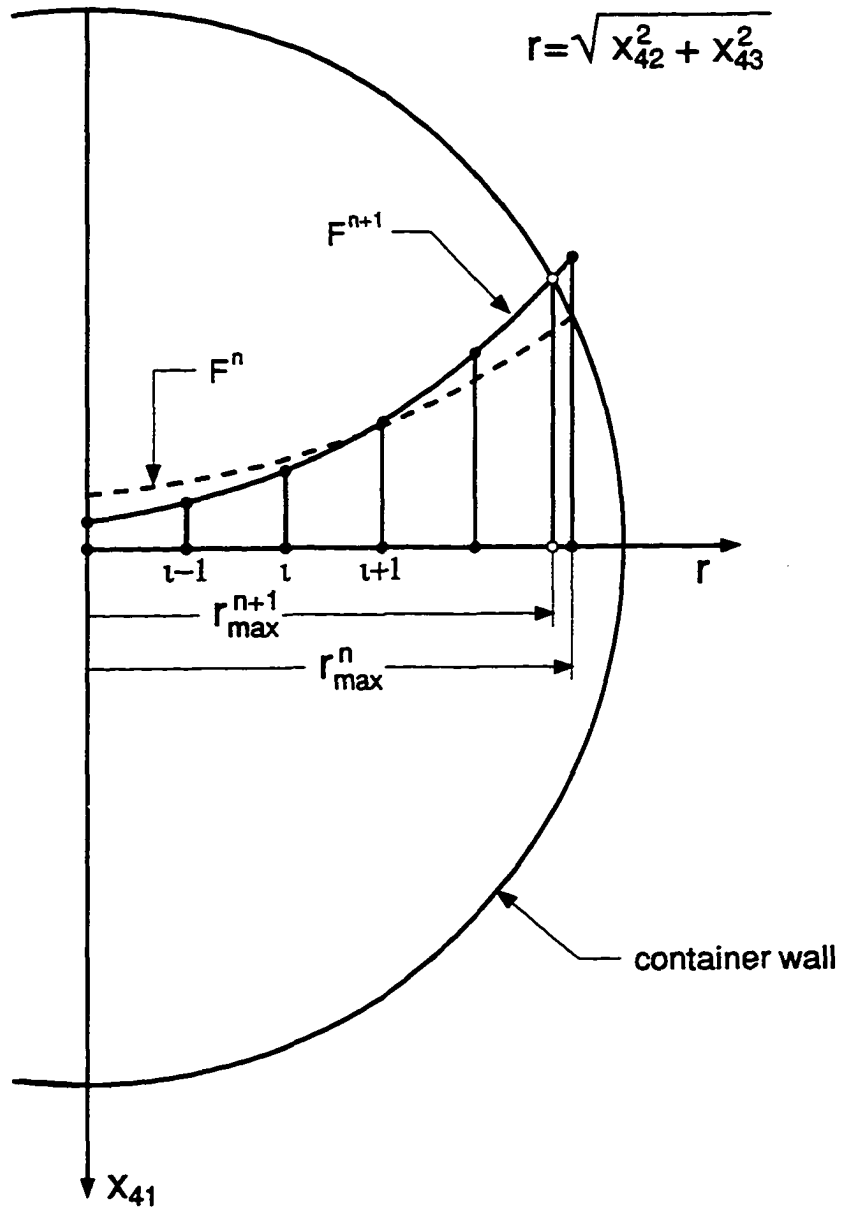


Figure 7.7: Adjustment of the Grid at the Free Surface

The notation used in equation (7.38) is illustrated in Figure 7.8(a). The position of the ξ_2 grid line is described in terms of polar coordinates (R, Φ) with respect to point- O , which is defined by the intersection of the x_{41} with the free surface. Here, $R(\Phi)$, represents the radial distance of the ξ_2 coordinate as a function of the azimuthal angle Φ , measured counterclockwise from the x_{41} axis. Using this equation, a ξ_2 grid line can be constructed between point P_1 , located on the x_{41} axis with $R=R_1$ and $\Phi=0$, and point P_2 , located on the free surface with $R=R_2$ and $\Phi=\Phi_2$.

The first bracketed term on the right hand side of equation (7.38) provides for the smooth transition in the value of R , from R_1 at the x_{41} axis to R_2 at the free surface. The second bracketed term is used to control the orthogonality of the grid lines at the free surface. The two unknown parameters, C and ζ , which appear in this term are given by,

$$C = \frac{1}{\pi R_2} \left(R_2 - R_1 - \Phi_2 \left. \frac{\partial R}{\partial \Phi} \right|_{\Phi_2} \right) \quad (7.39a)$$

and

$$\zeta = \xi_1 + 10|C| \quad (7.39b)$$

The parameter C is determined by requiring that the ξ_2 lines to be orthogonal with the ξ_1 grid lines that coincide with the free surface. The remaining parameter, ζ , controls the depth to which the correction for orthogonality extends. It is a *free* parameter which can be set to any value $\zeta \geq 1$. The value listed for ζ in equation (7.39b) was determined by numerical experimentation to work well for all the cases considered in this study.

The coordinates of grid points along each ξ_2 line is determined by using numerical integration to determine the length of the line, from $\Phi = 0$ to $\Phi = \Phi_2$, and then sectioning the line based on the desired pre-specified point distribution at the container wall. To improve the orthogonality of the resulting ξ_1 lines at the wall, the positions of the grid points along the three ξ_2 lines closest to the wall, $I, I-1, I-2$, are iteratively adjusted within some bounds specified in terms of a maximum allowable adjustment angles $\Delta\phi$. A sample grid generated using this procedure is shown in Figure 7.8(b).

Equation (7.38) is used to generate a provisional grid at each two dimensional k grid section, for $0 \leq \Theta \leq 2\pi$. The provisional grid coordinates are then used to initialize the Q_i source function for equation (7.23), and the elliptic equations are solved. The computational effort required in solving these equations is minimal once

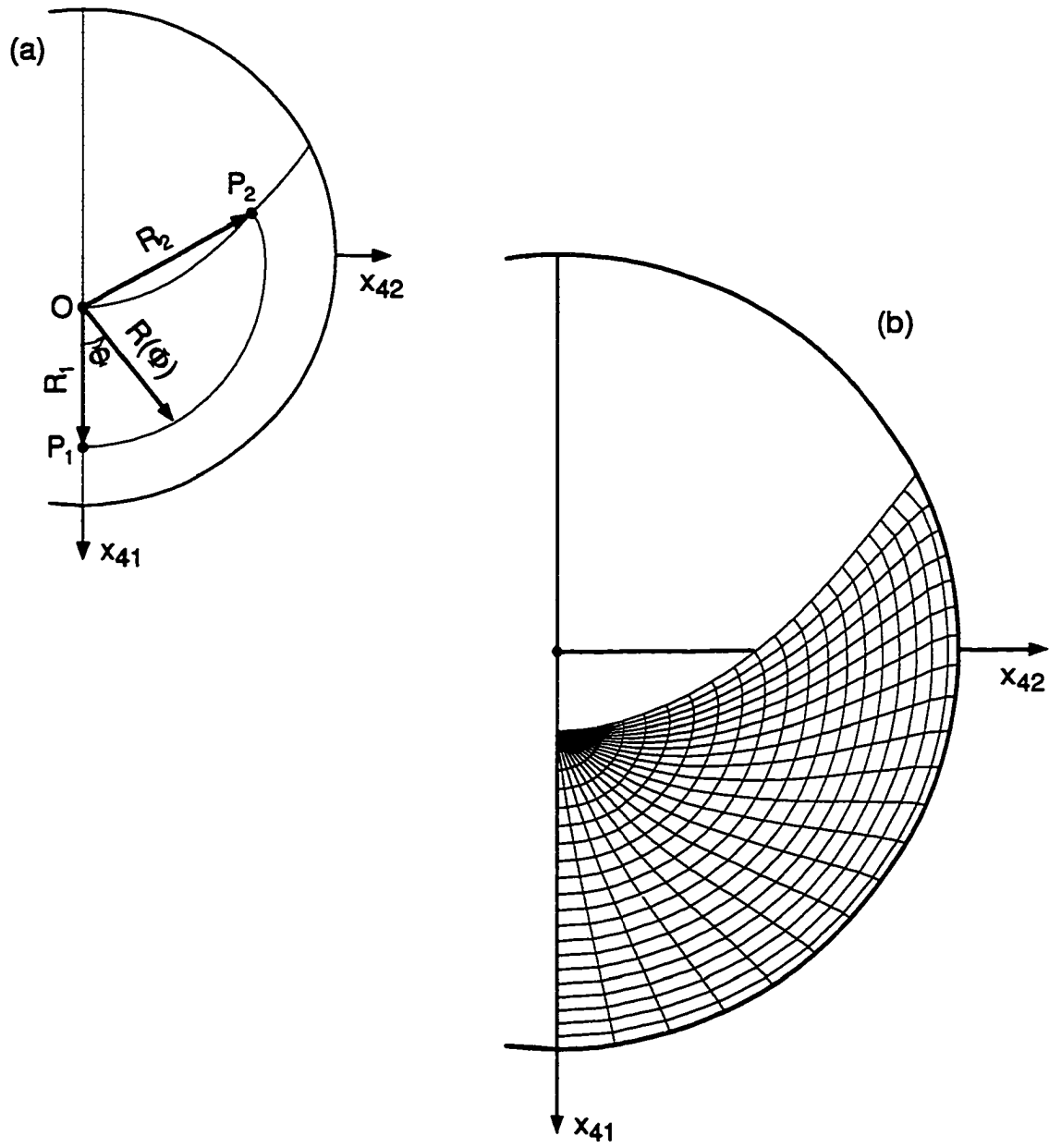


Figure 7.8: Algebraic Grid Generation Scheme

the function Q_i have been set. Overall, the grid generation procedure accounts for only 6–8% of the total computational time requirements.

7.3.3 Pressure Solution Algorithm

The solution of the momentum and pressure equations is carried out using a pressure correction scheme that is fundamentally the same with that used for the two dimensional model. The pressure correction scheme for the two dimensional model has been presented in considerable detail starting in section 4.2.2. The momentum and pressure equations are solved in separate steps, with the pressure field corrected at each step in order to obtain a solution that satisfies the divergence free condition. The pressure correction scheme is briefly summarized below based on the following notation. In addition to the superscript n , which is used to denote the time level in the integration of the equations, superscript m is used to denote the iteration level for the Gauss-Siedel iterations, and superscript ℓ is used to denote the pressure correction, or pressure update, level.

The momentum equations (7.26a) are solved by the Gauss-Siedel procedure subject to the no-slip condition (7.31b) at the wall. Along the free surface, the two tangential stress conditions (7.30b) are used to set the values of the u_{42} and u_{43} velocity components, while the continuity equation (7.26b) is used to set the value of the u_{41} component. The pressure gradients are evaluated using the most current, or updated pressure field, $p^{n+1,\ell}$. The following criterion is used in assuming the convergence of the Gauss-Siedel iterations for $u_{4i}^{n+1,\ell}$,

$$\left| \frac{A_{i,j,k}^{m+1} - A_{i,j,k}^m}{\max(A_{i,j,k}^{m+1})} \right| < \epsilon_1 \quad \text{for} \quad A = \{u_{4i}, p, F\} \quad (7.40)$$

where $\epsilon_1 = 10^{-7}$ represents a typical value used during the computations. The same convergence condition has also been used in the solution of the pressure equation and the free surface kinematic condition.

The calculated velocity field, $u_{4i}^{n+1,\ell}$, is then checked to ascertain if it satisfies the divergence free condition. Values for the dilatation, obtained by equation (7.28), are used to calculate a *normalized dilatation*, \mathcal{D} , according to,

$$\mathcal{D}_{i,j,k} \equiv \left| \sqrt[3]{\hat{J}_{123}(x_{41}, x_{42}, x_{43})} \sqrt{\frac{D^2}{u_{41}^2 + u_{42}^2 + u_{43}^2}} \right|_{i,j,k} \quad (7.41)$$

where $\hat{J}_{123}(x_{41}, x_{42}, x_{43})$ is the Jacobian of the $x_4 \rightarrow \xi$ transformation. The normalized dilatation, \mathcal{D} , represents the fraction by which the local speed must be altered to

enforce mass conservation. The convergence of the solution to a divergence free state is based on the condition,

$$\max(\mathcal{D}_{i,j,k}) < \epsilon_2 \quad (7.42)$$

where $\epsilon_2 = 10^{-4}$ was a typical value used during the computations.

If the solution, $(u_4^{n+1,\ell}, p^{n+1,\ell})$, does not meet the divergence free criterion in terms of \mathcal{D} , then the pressure field is updated to $p^{n+1,\ell+1}$ and the momentum equations are solved again for $u_4^{n+1,\ell+1}$. The pressure field is updated by adjusting the pressure dilatation source term, S_p , according to the following relation,

$$S_p^{\ell+1} = S_p^\ell - \frac{1}{\Delta t} [\omega D^\ell + (1 - \omega) D^{\ell-1}] \quad (7.43)$$

where ω represents a relaxation parameter, typically set equal to a value within the range $0.6 \leq \omega \leq 0.8$. The pressure dilatation source at the previous update level, S_p^ℓ , is given by:

$$\begin{aligned} S_p^{n+1,\ell} = & - \left(\eta_{k,i} \eta_{n,j} \delta_{ij} \frac{\partial^2 p}{\partial \xi_k \partial \xi_n} + \eta_{n,ij} \delta_{ij} \frac{\partial p}{\partial \xi_n} \right)^{n+1,\ell} \\ & + \left[2\eta_{n,1} \eta_{m,2} \hat{J}_{nm}(u_{41}, u_{42}) + 2\eta_{n,1} \eta_{m,3} \hat{J}_{nm}(u_{41}, u_{43}) \right]^{n+1,\ell} \\ & + \left[2\eta_{n,2} \eta_{m,3} \hat{J}_{nm}(u_{42}, u_{43}) \right]^{n+1,\ell} + \left(2\eta_{j,n} \lambda_{rni} \frac{\partial u_{4i}}{\partial \xi_j} + \lambda_{1ij} \delta_{ij} \right)^{n+1,\ell} \end{aligned} \quad (7.44)$$

The pressure Poisson equation (7.26c) is then solved by the SOR method for $p^{n+1,\ell+1}$, subject to the normal stress condition (7.30a) at the free surface. Pressure values along the container wall are set according to boundary condition (7.31a).

8. RESULTS AND DISCUSSION

The three dimensional model which has been developed in the previous chapter was used to generate solutions for several cases. These cases involved flows in containers of rectangular, cylindrical, and spherical geometry. Sample results from three of these computations are presented in the remainder of this chapter. Two additional cases of spinup in spherical containers are given in [71].

Section 8.1 deals with liquid flows in translating containers of rectangular geometry. These calculations represent a straight forward extension of the type of cases considered in the first part of this study. The flowfield and free surface position are examined for a case which involves a sudden step change in the velocity of the container. Furthermore, the effects due to a *finite* container depth on the period of oscillation and the rate of viscous dissipation are investigated.

The axisymmetric spin-up of a viscous liquid within a cylindrical container is examined in section 8.2. Here, the container is impulsively rotated about its vertical axis of symmetry. Viscous shear at the walls initiates the motion of the liquid, with the ensuing flow being two dimensional. In addition to the interesting physical features of this flow, this calculation allows for the comparison of the numerical solution with experimental data.

A three dimensional liquid flow within a spherical container is considered in section 8.3. The container is impulsively rotated about a vertical axis which is located some distance h_1 away from its center. Information on the flowfield and the free surface position are given.

8.1 Liquid Flows in Translating Rectangular Containers

Several cases involving the rectilinear motion of a rectangular container with respect to the inertial coordinate system, x , were considered. These calculations served a dual purpose. First, they were examined to ensure that the three dimensional model yields solutions which are consistent with the analytical and numerical results of Chap-

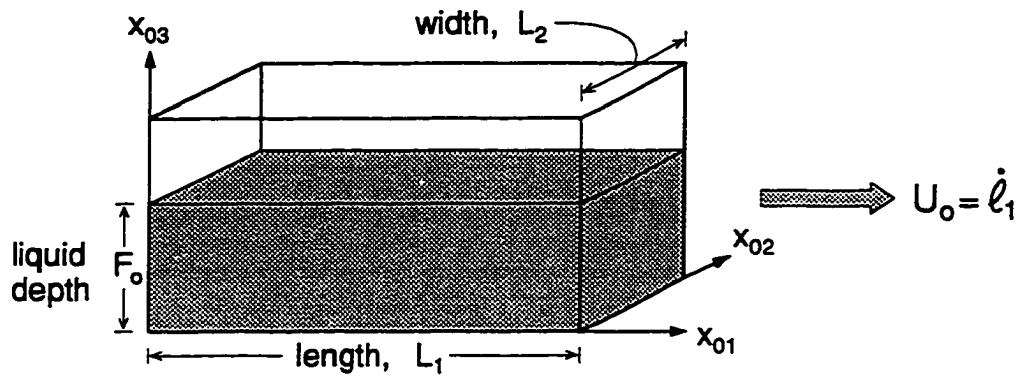


Figure 8.1: Problem Geometry for 3D Rectangular Containers

ter 5. And second, to ascertain the effects due to a finite container width on the period of oscillation and the rate of viscous dissipation for the liquid flow.

8.1.1 Use of the Numerical Model for Rectangular Geometries

The effects due to the rectilinear component of the vehicle acceleration on the liquid within the container are captured by the coordinate transformation, $x \rightarrow x_0$. This transformation was given in equation (7.2). The coordinate system x_0 moves along with the container. Its motion with respect to the inertial coordinate system, x , is described in terms of the position vector ℓ_i . For the cases considered here, the motion of the container is restricted along the x_1 coordinate axis, such that $\ell_2(t) = 0$, and $\ell_3(t) = 0$. The forcing experienced by the liquid as a result of the container motion, was also restricted to cases which involved either a step change in the velocity, $\dot{\ell}_1$, or the acceleration, $\ddot{\ell}_1$, of the vehicle at time $t = 0$. These conditions are analogous to forcing conditions used for the two dimensional model, where:

$$Q = \ddot{\ell}_1 \quad \text{and} \quad U_o = \dot{\ell}_1 \quad (8.1)$$

The liquid is initially assumed to be in a state of hydrostatic equilibrium with its free surface lying in the horizontal position. A schematic of the initial geometry of the liquid region is shown in Figure 8.1. The liquid region is described by the container length, \bar{L}_1 , along the x_{01} direction, the container width, \bar{L}_2 , along the x_{02} direction, and the initial height of the liquid, \bar{F}_o , along the x_{03} direction. To remain consistent with the 2D model of chapter 3, the container length is used as the characteristic

container dimension, $L = \bar{L}_1$, and used to define the dimensionless container depth, Λ , and the initial liquid depth, F_o , according to:

$$\Lambda \equiv \frac{\bar{L}_2}{\bar{L}_1} \quad \text{and} \quad F_o \equiv \frac{\bar{F}_o}{\bar{L}_1} \quad (8.2)$$

The solution of the governing equations is carried out based on the procedure outlined in the Chapter 7. With the forcing here determined either by a $\dot{\ell}_1 \neq 0$ or a $\ddot{\ell}_1 \neq 0$ condition, the remaining parameters used in describing the motion of the container with respect to the inertial coordinate frame are all set equal to zero. Thus,

$$\{\ell_2(t), \ell_3(t), \psi_i(t), h_i(t), \vartheta_i(t)\} = 0 \quad (8.3)$$

To minimize the modifications needed in the numerical model, the two tracking angles, ψ_2 and ψ_3 , are set equal to,

$$\psi_2(t) = -\frac{\pi}{2} \quad \text{and} \quad \psi_3(t) = 0 \quad (8.4)$$

and a body fitted computational grid is generated in terms of generalized grid coordinates ξ_i , with the ξ_1 coordinate lines extending along the x_{43} axis, the ξ_2 lines along the x_{41} axis, and the ξ_3 lines along the x_{42} axis. The distribution of the grids points in each direction is determined using the elementary stretching functions defined in equation (4.1). The transformation metrics η_i , $\eta_{i,j}$, and $\eta_{i,jk}$ are evaluated numerically.

8.1.2 Liquid Flow in an Impulsively Started Container

The flow of a viscous liquid in a rectangular container of dimensionless width $\Lambda = 0.5$ is considered here. The container is filled with liquid to an initial depth of $F_o = 0.3$. The physical properties of the liquid are described by $Ga = 10^6$ and $Bo = 10^5$. For a characteristic container dimension of $L \sim 0.1$ m these values are representative of a liquid such as SAE 10W oil.

At time $t = 0$, the container experiences a step change in its velocity, from a zero value for $t < 0$ to a value of $U_o = \dot{\ell}_1 = 0.1$ for $t > 0$. The sudden change in the velocity of the container at $t = 0$ sets the liquid in motion, which begins to oscillate about the equilibrium horizontal free surface position. Viscous dissipation brings the liquid back to a state of hydrostatic equilibrium as $t \rightarrow \infty$.

The velocity field for this case is shown in Figure 8.2. Each horizontal strip, consisting of three plots, depicts the velocity field for the same time level which is shown in the center plot. The velocity field, $(\bar{u}_{01}, \bar{u}_{03})$, along the container mid-plane

at $x_{02} = 0.25$ is shown in the center plot. Note that $x_{01} = 1.0$ represents the leading side of the container, while $x_{01} = 0$ the trailing side of the container. The left and right plots depict the velocity field, $(\bar{u}_{02}, \bar{u}_{03})$, at the cross sections defined by $x_{01} = 0.12$ and $x_{01} = 0.88$, near the trailing and leading ends of the container respectively.

In the absence of liquid viscosity, the forcing experienced by the liquid for this case will lead to a two-dimensional flowfield with $u_{02} = 0$. This is reflected by the inviscid initial condition at $t = 0$, which is shown in Figure 8.2(a). This initial flowfield is calculated based on the procedure outlined in section 7.1.9 by rescaling the governing equations in terms of the pressure impulse function, Π .

For $t > 0$, viscous effects cause the flowfield to become three dimensional. As the free surface moves away from its initial horizontal position, viscous drag along the two containers walls, at $x_{02} = 0$ and $x_{02} = \Lambda$, retards its motion. As a result, the free surface becomes curved, thus leading to non-zero pressure gradients in x_{02} direction. This sets up a secondary flow pattern in the $x_{02} - x_{03}$ plane for which $u_{02} \neq 0$. This secondary flow pattern can be seen in Figures 8.2(b-l) which cover the evolution of the flowfield for the first cycle of sloshing. If the free surface rises in the interior of the container to a somewhat higher elevation than it does near the walls, then the secondary flow in along the $x_{02} - x_{03}$ plane is directed toward the walls. If the free surface falls to a lower elevation in the interior than it does near the walls, then the secondary flow is directed away from the walls and toward the center of the container. The flow remains symmetric with respect to the container mid plane at $x_{02} = 0.25$. This was reflected by the calculated values for the dependent variables of the problem which generally agreed to five significant figures.

The effects of viscous dissipation on the flowfield are demonstrated by the sequence of Figures 8.2(p-s). Each of these figures depicts the flowfield as the liquid passes through the equilibrium horizontal position. In this position most of the available energy of the flow is in the form of kinetic energy. After the completion of approximately three full cycles of sloshing, the flowfield shown in Figure 8.2(s) possesses only about 9.2% of the initial energy of the flow.

The free surface position for this case, $F(t, x_{02}, x_{03})$, is shown at selected time intervals in Figure 8.3. Lines of constant pressure are also shown on the two container walls which are visible in the figure, at $x_{02} = 0$ and $x_{01} = 1$. The spacing between adjacent isobars is equal to $\Delta p = 0.02$. The free surface remains predominantly two dimensional. The effect of the secondary flow induced by viscous shear at the walls,

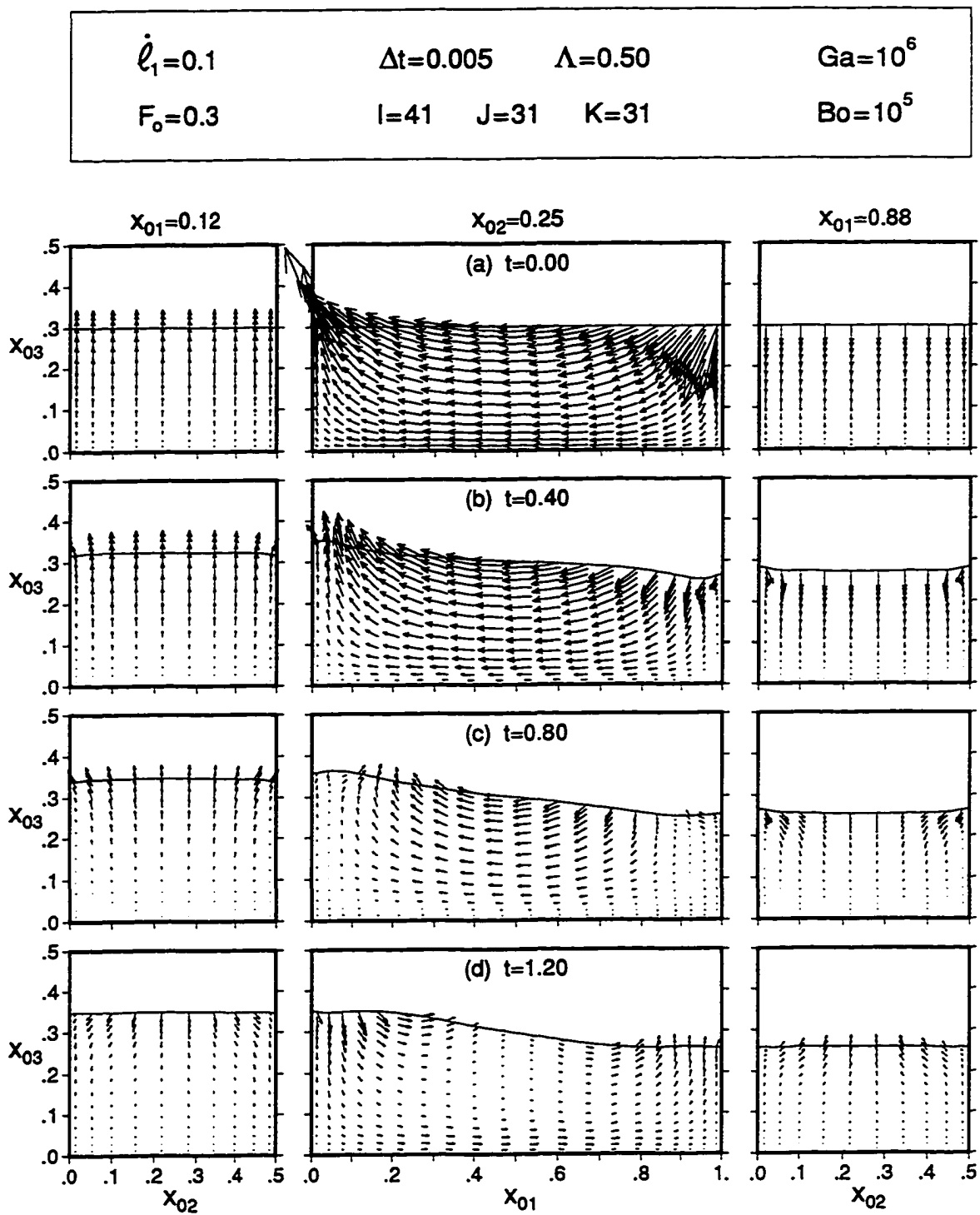


Figure 8.2: Velocity Field for an Impulsively Translated Rectangular Container

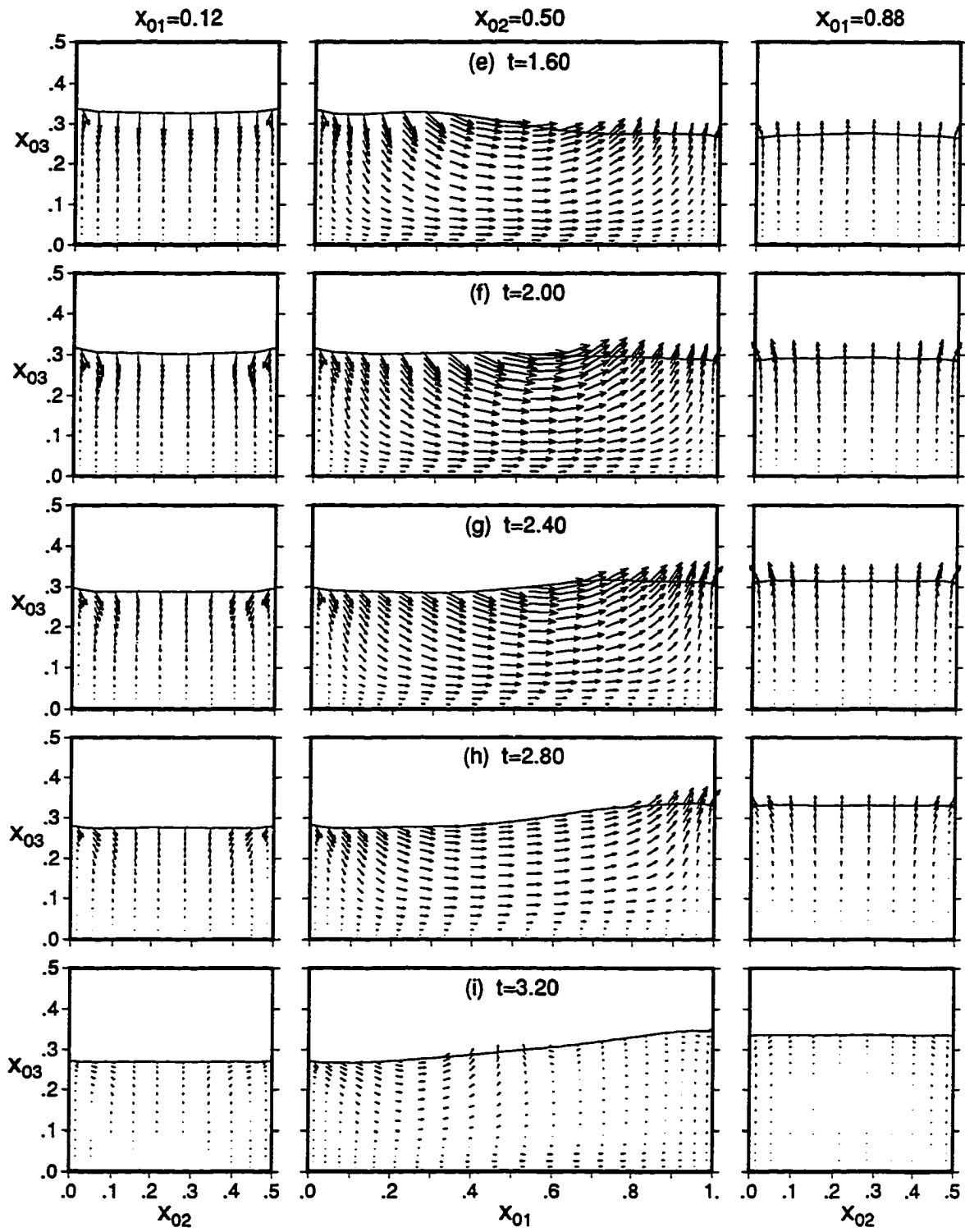


Figure 8.2 (Continued)

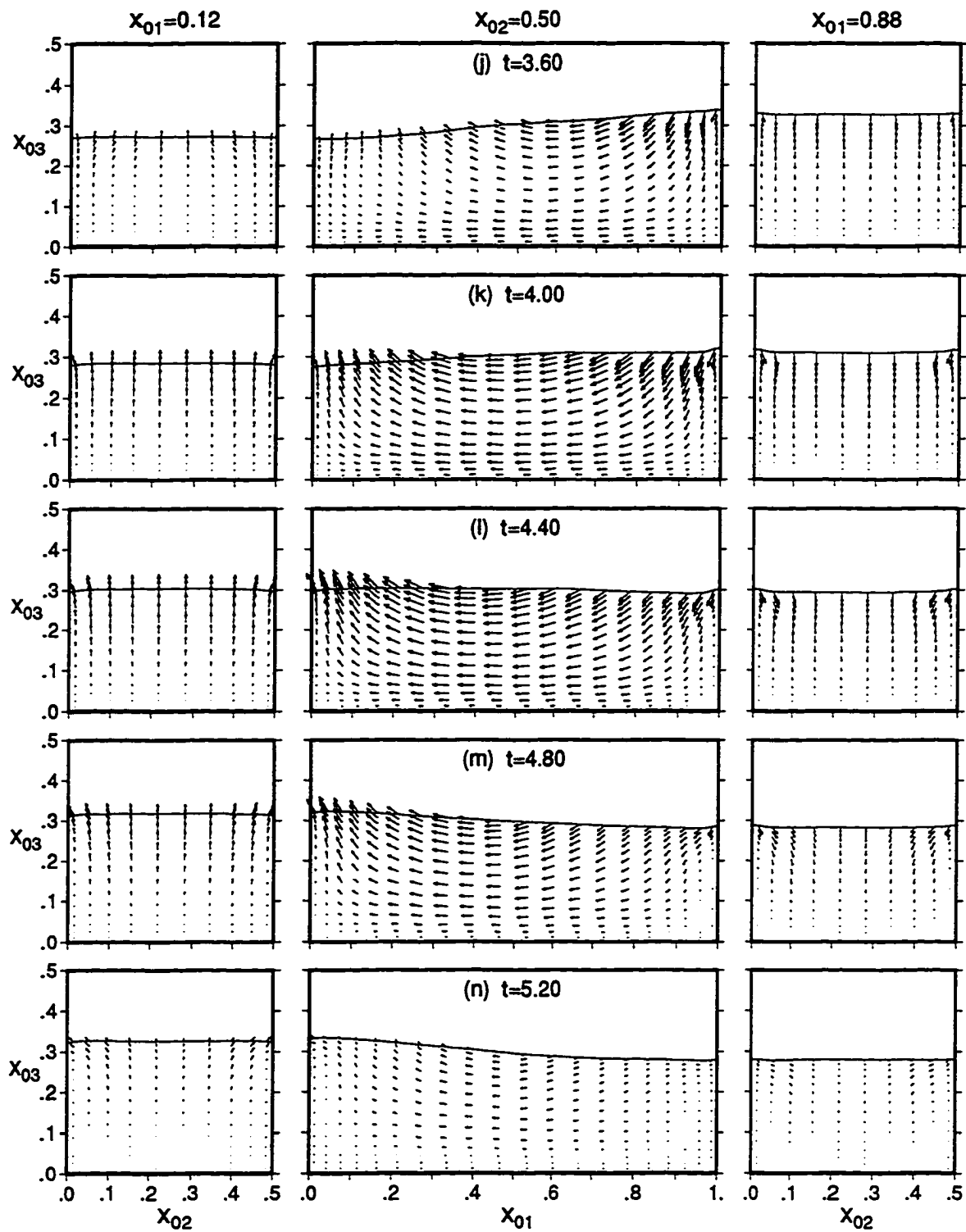


Figure 8.2 (Continued)

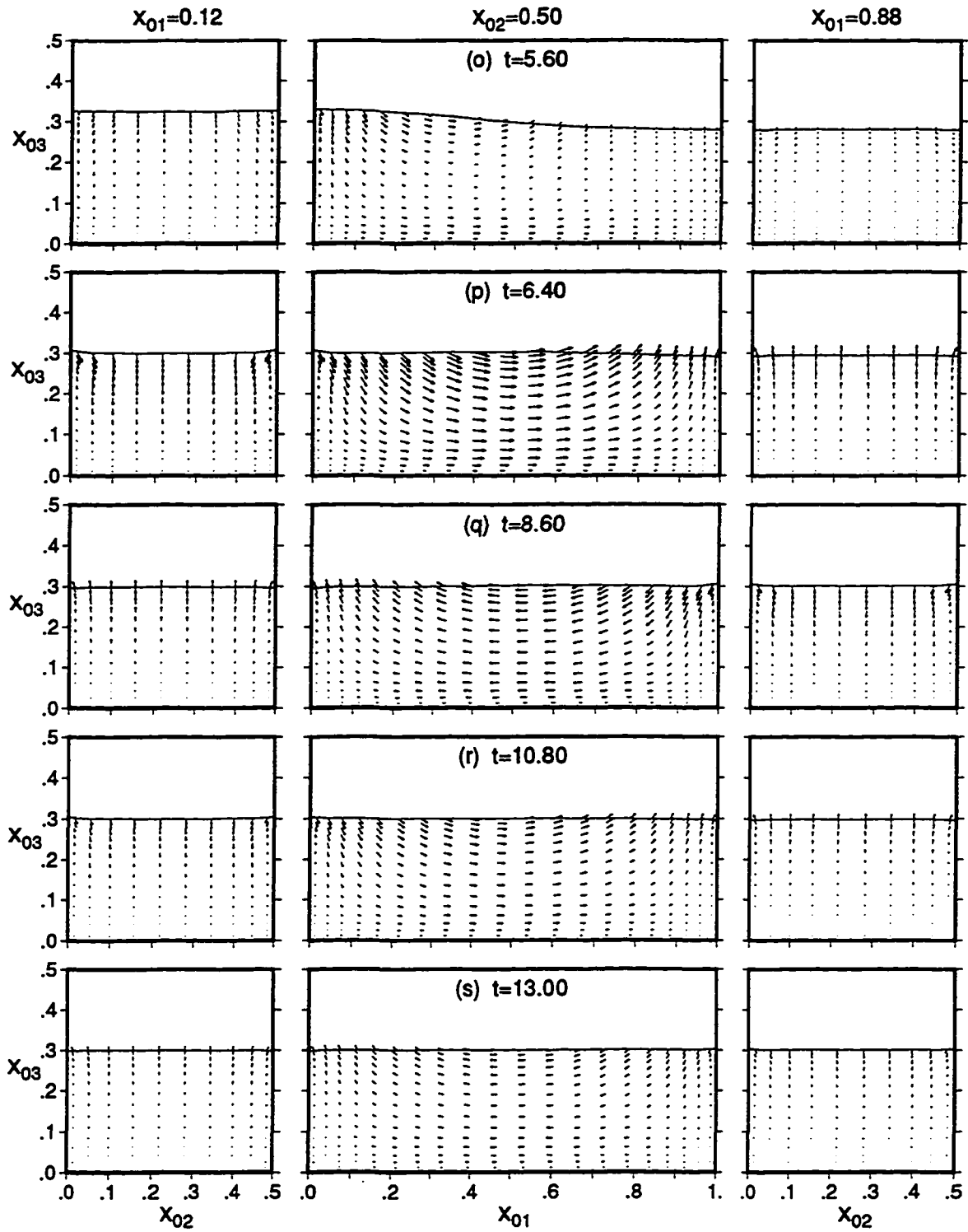


Figure 8.2 (Continued)

Table 8.1: Effect of Container Depth^a, Λ , on the Period of Oscillation, T , and the Modulus of Decay, τ

Container Depth Λ	Period of Oscillation		Modulus of Decay	
	T	$T(\Lambda)/T(\infty)$	τ	$\tau(\Lambda)/\tau(\infty)$
0.50	3.9209	1.035	0.0789	1.435
1.00	3.8470	1.015	0.0689	1.253
2.00	3.8169	1.007	0.0620	1.127
5.00	3.8061	1.004	0.0582	1.057
∞	3.7912	1.000	0.0550	1.000

^aFor cases with $F_o = 0.5$, $Q = 0.2$, $Ga = 10^6$, and $Bo = \infty$.

is to further flatten the shape of the free surface in the x_{02} direction. Note that the limited curvature of the free surface which exists at $t = 0.50$, Figure 8.3(b), decreases as the liquid approaches a position of maximum elevation on the trailing side of the container at $t \approx 1.00$, Figure 8.3(c).

The reduction in the amplitude of sloshing as a result of viscous dissipation is evident from Figures 8.3(c, g, and h). In each of these three figures the free surface is depicted near a position of maximum elevation at the trailing side of the container, during the first, second, and fourth cycles of sloshing. Where the liquid reaches a maximum elevation of $F_{max} = 0.3581$ during the first cycle, the maximum elevation reached during the second cycle drops to $F_{max} = 0.3339$, and to $F_{max} = 0.3083$ during the fourth cycle.

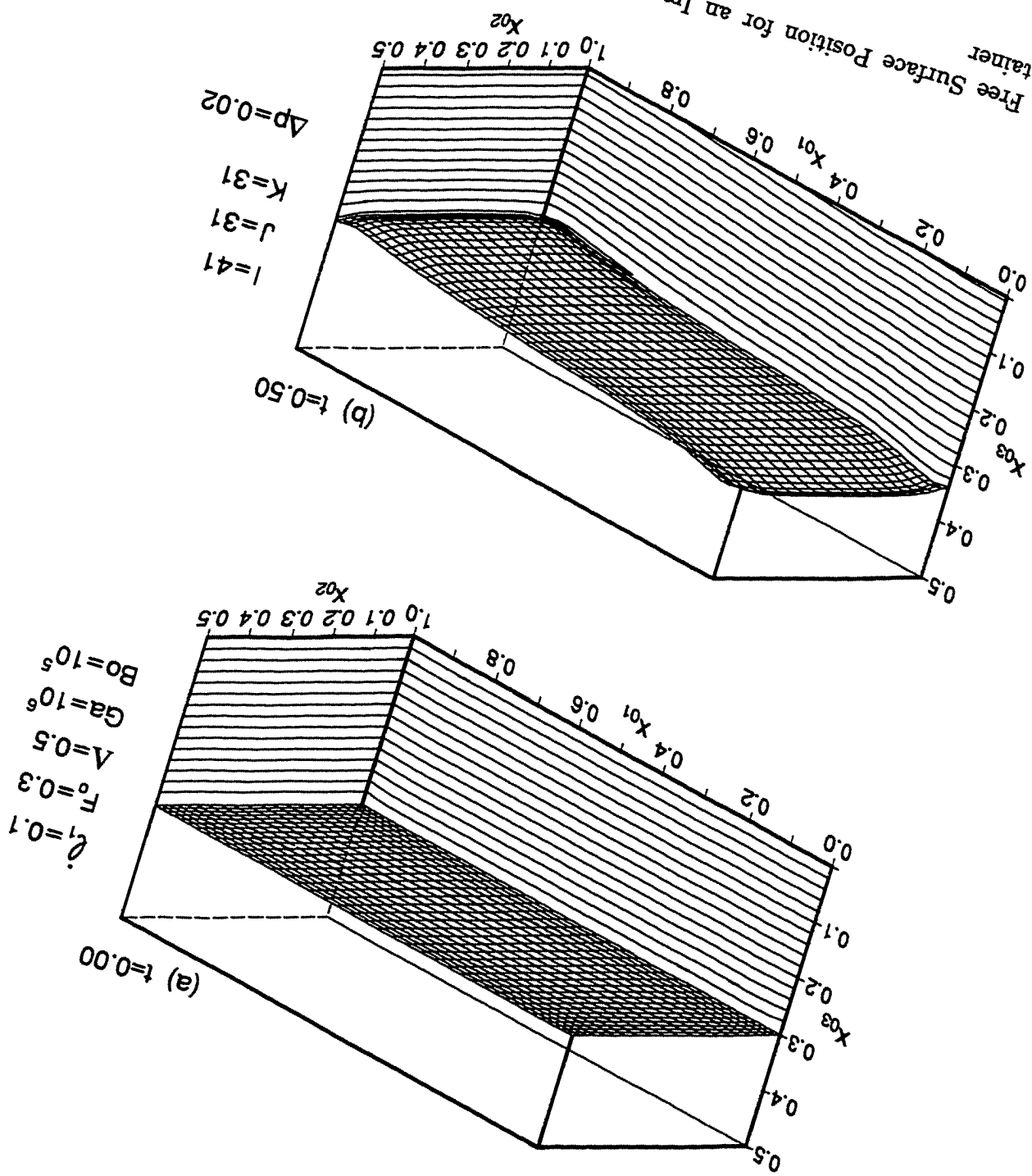
8.1.3 Parametric Effects of the Container Depth

The effects due to a finite container depth, Λ , on the period of oscillation, T , and the rate of viscous dissipation, τ , are summarized in Table 8.1. These results are derived from the solution of a set of cases calculated with $F_o = 0.5$, $Q = \ddot{\ell}_1 = 0.2$, $Ga = 10^6$, and $Bo = \infty$. A $41 \times 41 \times 41$ computational grid and a time step of $\Delta t = 0.002$ were used for the solution of these cases.

Numerical values for the period of oscillation, T , and the modulus of decay, τ , are listed in Table 8.1 as a function of the dimensionless container depth, Λ . These results are also compared with to a two dimensional result which corresponds to $\Lambda = \infty$.

Viscous drag along the container walls slows down the oscillations of the liquid mass. The period of oscillation becomes longer as the width of the container decreases.

Figure 8.3: Free Surface Position for an Impulsively Translated Rectangular Con-
tainer



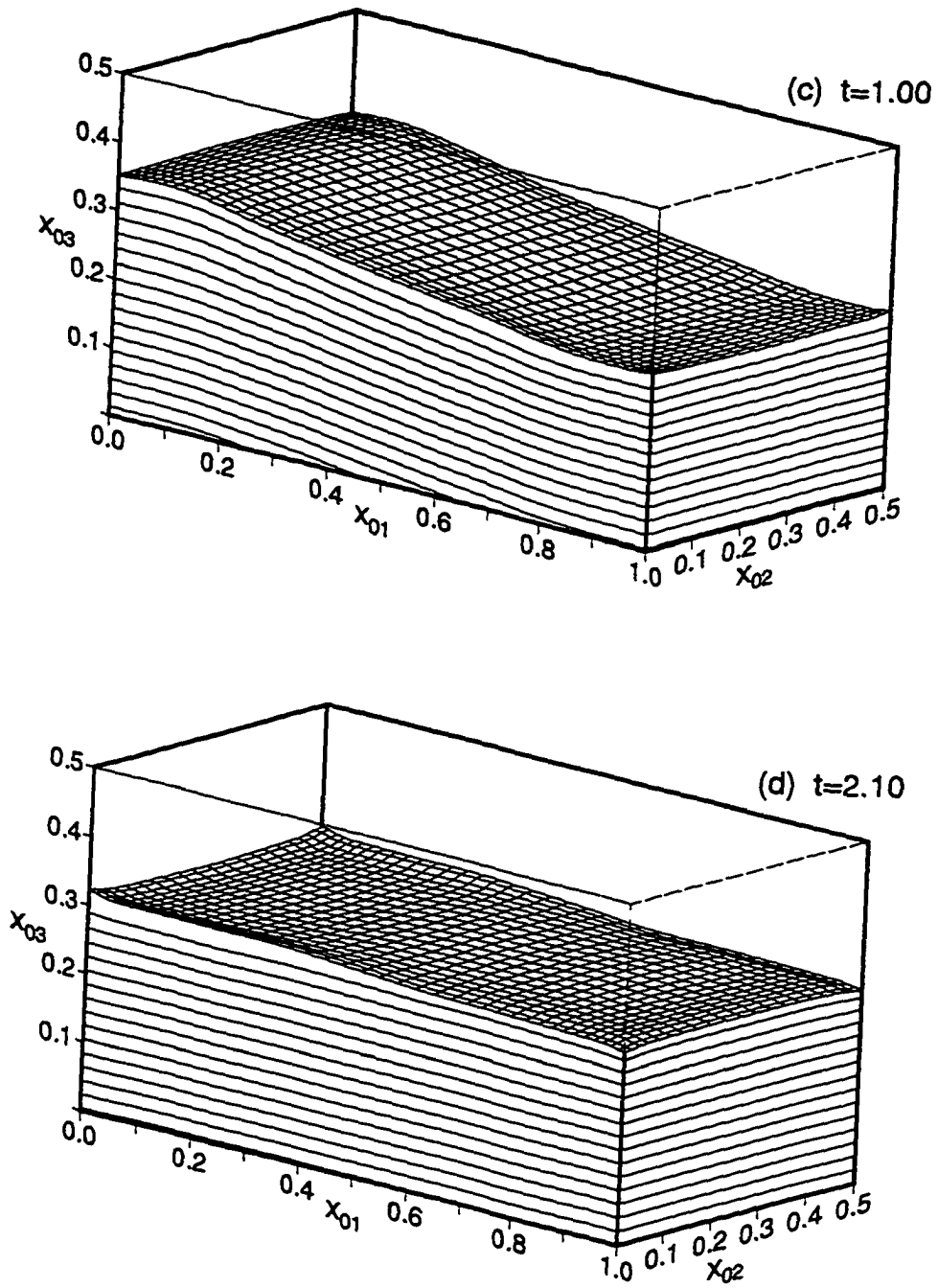


Figure 8.3 (Continued)

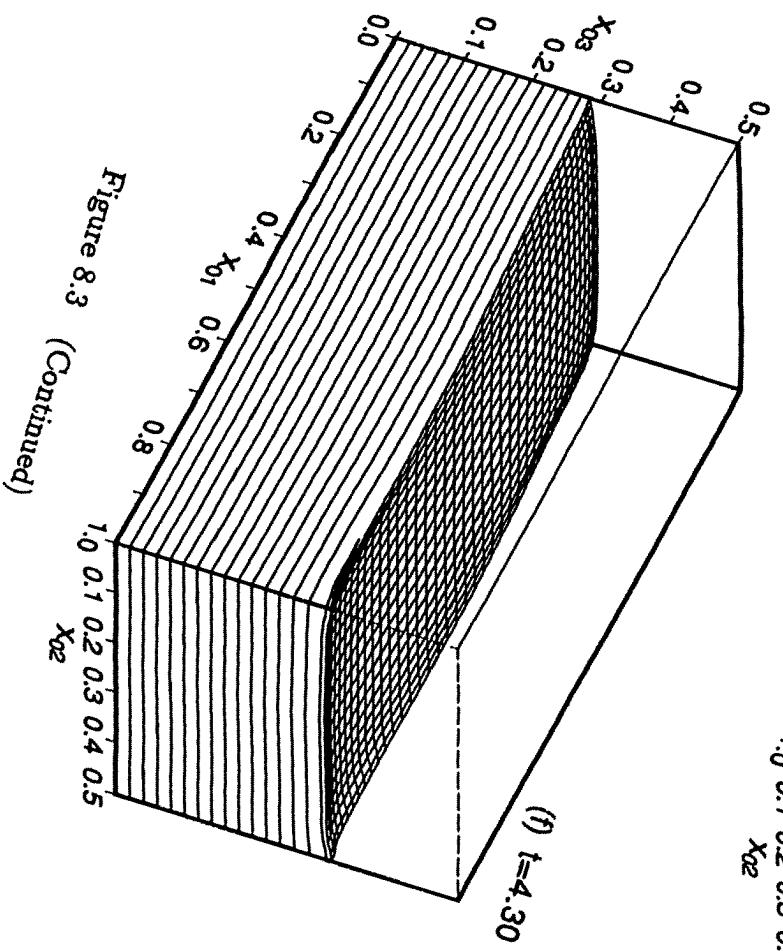
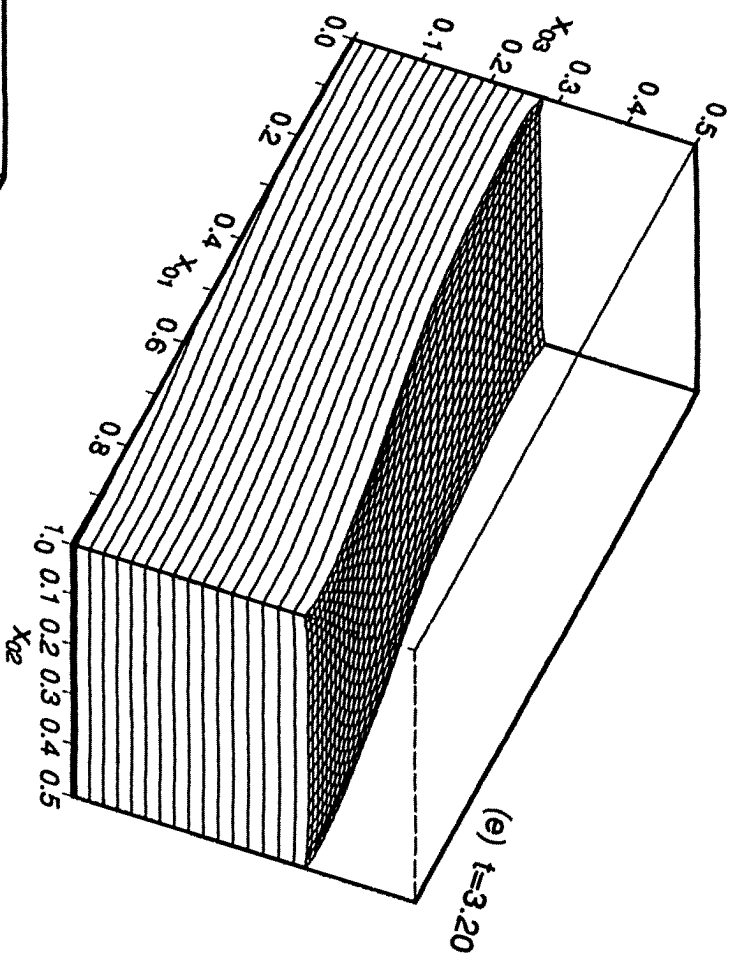


Figure 8.3 (Continued)

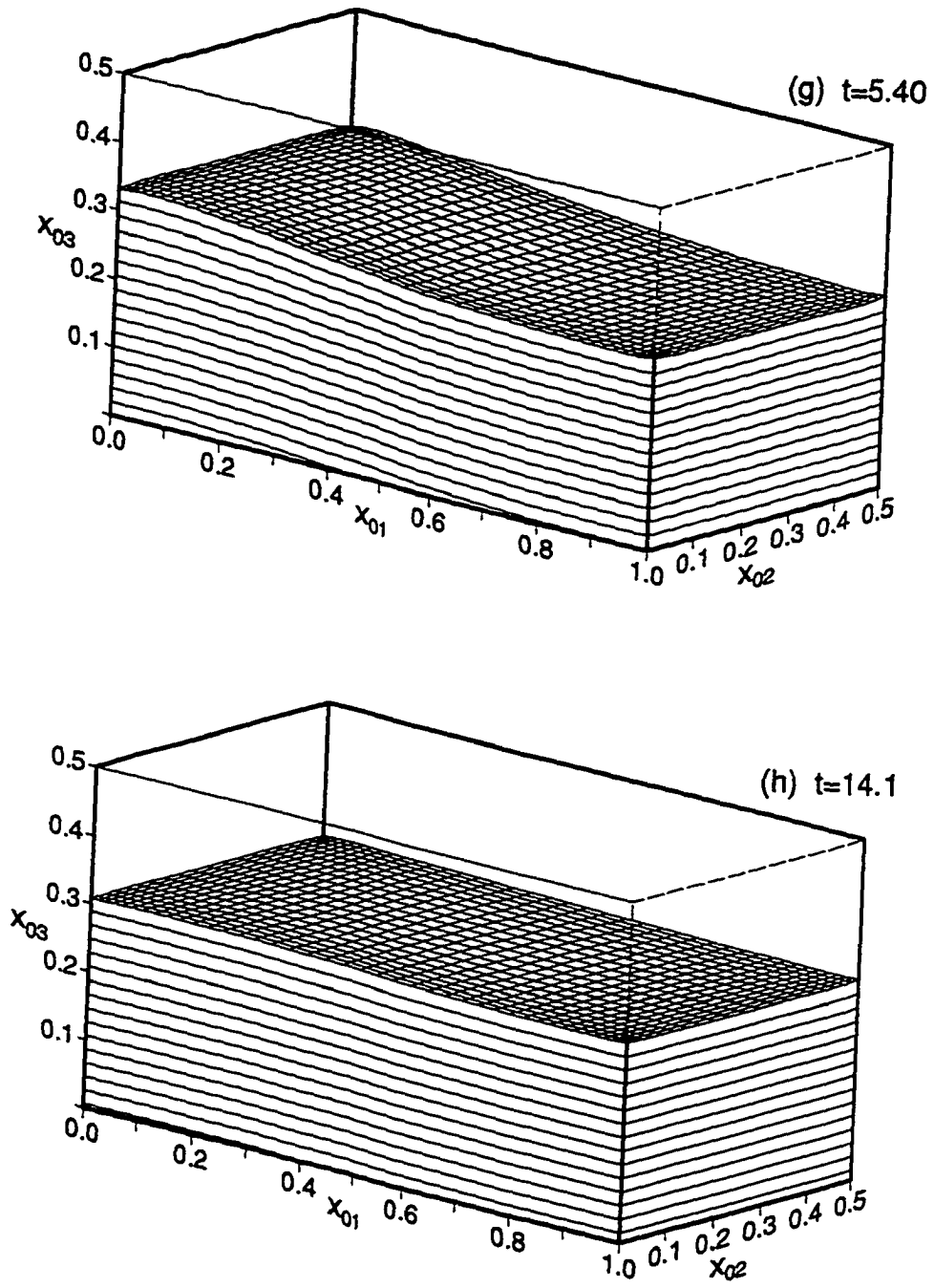


Figure 8.3 (Continued)

Where for $\Lambda = 5.0$ the period, T , is only about 0.4% longer than the two dimensional result, at $\Lambda = 0.5$ the increase in the value of T is about 3.5%. The increase in the rate of viscous dissipation is more profound. Even at $\Lambda = 5.0$ the modulus of decay, τ , is nearly 6% larger than the two dimensional result. At $\Lambda = 0.5$, the increased dissipation from the two container side walls causes τ to increase by more than 40% compared to the two dimensional result.

8.2 Axisymmetric Spin-up in a Cylinder

The spin-up of a viscous liquid within a partially filled cylindrical container is considered here. Initially, for $t < 0$, the cylinder is stationary and the liquid is in a state of hydrostatic equilibrium. The container experiences a step change in its angular velocity at $t = 0$, as it impulsively begins to rotate about its vertical axis of symmetry. The motion of the liquid is initiated by viscous shear along the container walls, with the resulting liquid flow being axisymmetric.

The specific details pertaining to the application of the numerical model to axisymmetric flows in containers of cylindrical geometry will be discussed. The numerical simulation of a specific case, which allows for a comparison between the numerical solution and the experimental results of [62], will be presented in detail. This case involves the spinup of a liquid with kinematic viscosity $\nu = 1.16 \times 10^{-5} \text{ m}^2/\text{sec}$, within a container of radius $R = 0.120 \text{ m}$, filled to an initial height of $\bar{F}_o = 0.508 \text{ m}$, and rotated at an angular speed of 118.93 rpm.

8.2.1 Use of the Numerical Model for the Cylindrical Spinup

The effects due to the rotational component of the vehicle acceleration on the liquid within the container are captured by the coordinate transformation, $x_0 \rightarrow x_1$. This transformation was defined in equation (7.5). The coordinate system x_1 is rotating along with the container. Its angular orientation with respect to the inertial coordinate system, x , is described in terms of the three Euler angles ψ_i . The rotation of the container about its vertical axis of symmetry can be fully described in terms of ψ_3 alone.

The governing equations for this case are nondimensionalized based on the scales defined for the dependent and independent variables in section 7.1.10. The character-

istic length, L , and acceleration, g , used in deriving these scales are given by,

$$L = R \quad \text{and} \quad g = R\bar{\Omega}^2 \quad (8.5)$$

where R is the container radius and $\bar{\Omega}$ is the dimensional angular velocity of the container. In this case, the use of the centrifugal acceleration as the characteristic acceleration, g , leads to a more physically meaningful velocity scale, $U \sim \sqrt{Lg} \sim R\bar{\Omega}$. Based on this choice for g , the dimensionless rotational Froude Number, Fr , defined by,

$$Fr \equiv \frac{R\bar{\Omega}^2}{g} \quad \text{Froude Number} \quad (8.6)$$

appears in the governing equations. The body force terms in the momentum equations (7.26a) are nondimensionalized according to g_i/g . Thus, in dimensionless form, the acceleration due to gravity becomes equal to the inverse of the rotational Froude number,

$$\frac{g}{\mathbf{g}} \rightarrow \frac{1}{Fr}$$

The forcing of the liquid for the this case is determined solely by the rotation of the Euler angle, ψ_3 . The angular position of the container can be simply described by,

$$\psi_3(t) = t \quad (8.7)$$

The remaining parameters used in describing the motion of the container with respect to the inertial coordinate frame are all set equal to zero. Thus:

$$\{\ell_i(t), \psi_1(t), \psi_2(t), h_i(t), \vartheta_i(t)\} = 0 \quad (8.8)$$

Based on the formulation of the model, the position of the free surface must be described by a function of the form $F(t, x_{42}, x_{42})$. To satisfy this requirement the x_{41} axis is placed in the vertical direction by setting the two tracking angles, ϕ_2 and ϕ_3 , equal to,

$$\phi_2(t) = \frac{\pi}{2} \quad \text{and} \quad \phi_3(t) = 0 \quad (8.9)$$

In order to reduce the computational effort required for the solution of this case the circumferential symmetry of the flow was explicitly enforced. The three dimensional equations were solved on a computational grid consisting of 61 nodes in the radial direction, 201 nodes in the axial direction, and only 3 nodes in the circumferential

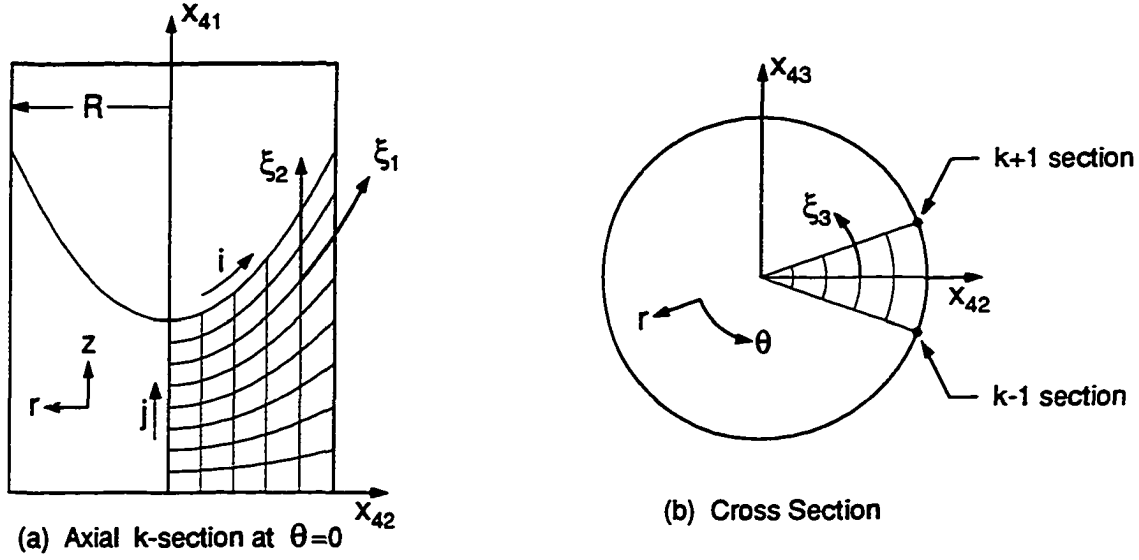


Figure 8.4: Computational Domain for Cylindrical Spin-up

direction. A schematic of the simplified computational domain used for the solution of this case is shown in Figure 8.4. A two dimensional grid section, denoted as k -section in the figure, was generated in the $x_{43} = 0$ plane in terms of generalized grid coordinates ξ_1 and ξ_2 . The grid was fitted to the shape of the liquid region. The distribution of the grid points along the ξ_1 and ξ_2 coordinate directions was determined by stretching functions of the form given in equation (4.1). Values for the dependent and independent variables of the problem at grid sections $k+1$ and $k-1$, which are needed for the evaluation of derivatives in terms of the ξ_3 coordinate, can be obtained from the circumferential symmetry of the problem. The solution of the problem in grid section k , in terms of the Cartesian coordinate system x_4 , can be related to the natural cylindrical coordinates (r, θ, z) according to,

$$[r, \theta, z] = [x_{42}, x_{43}, x_{41}]_{i,j,k} \quad \text{and} \quad [u_r, u_\theta, u_z] = [u_{42}, u_{43}, u_{41}]_{i,j,k} \quad (8.40)$$

provided that $\theta = 0$ (k -section only). The following symmetry relations can then be used to project the solution onto the $k-1$ and $k+1$ grid sections,

$$[x_{41}, u_{41}, p, F]_{i,j,k\pm 1} = [x_{41}, u_{41}, p, F]_{i,j,k} \quad (8.41a)$$

$$[x_{42}]_{i,j,k\pm 1} = [x_{42}]_{i,j,k} \cos(\theta_{k\pm 1}) \quad \text{and} \quad [x_{43}]_{i,j,k\pm 1} = [x_{42}]_{i,j,k} \sin(\theta_{k\pm 1}) \quad (8.41b)$$

$$[u_{42}]_{i,j,k\pm 1} = [u_{42}]_{i,j,k} \cos(\theta_{k\pm 1}) - [u_{43}]_{i,j,k} \sin(\theta_{k\pm 1}) \quad (8.41c)$$

$$[u_{43}]_{i,j,k\pm 1} = [u_{42}]_{i,j,k} \sin(\theta_{k\pm 1}) + [u_{43}]_{i,j,k} \cos(\theta_{k\pm 1}) \quad (8.41d)$$

where θ_{k+1} and θ_{k-1} denote the circumferential position of grid sections $k+1$ and $k-1$ with respect to grid section k . These two angles were set equal to ± 0.02 radians during the computations.

The flowfield in an axial cross section of the container, in terms of velocity components (u_r, u_z) can also be described in terms of the streamfunction, f . Here, the streamfunction is defined such that:

$$u_r = \frac{1}{r} \frac{\partial f}{\partial z} \quad \text{and} \quad u_z = -\frac{1}{r} \frac{\partial f}{\partial r} \quad (8.42)$$

For this case, the streamfunction appears to be a better choice for the description of the flowfield. It provides a more detailed and less cluttered picture of the flowfield than the velocity vector.

8.2.2 Development of the Flowfield

The liquid within the cylindrical container is initially assumed to be in a state of hydrostatic equilibrium. At $t = 0$, the container begins to rotate about its vertical axis of symmetry. Viscous diffusion at the container walls initiates the motion of the liquid by imparting angular momentum to the liquid adjacent to the walls. The subsequent spinup of the liquid can be described in terms of three distinct phases. A *boundary layer phase* of very short duration, during which viscous diffusion plays an important role in establishing the boundary layer flow along the container walls. It is followed by the *spinup phase*, where radial advection of angular momentum from the boundary layer region into the core of the flowfield brings the liquid near a state of solid body rotation. The characteristic time scale associated with the spinup phase was identified in [43]. For a completely filled cylinder experiencing an impulsive but small change in its rotation rate, the convective time scale associated with the spinup phase is of order $\bar{T}_c \sim \bar{D} / \sqrt{\nu \bar{\Omega}}$. Here, ν is the liquid viscosity, while \bar{D} represents the liquid depth between the two container endwalls. Viscous decay of residual oscillations occurs during the *final phase* of the spinup process where the liquid attains a state of solid body rotation. The equilibrium position reached by the free surface of the liquid at solid body rotation, $t \rightarrow \infty$, is given by,

$$F(\infty, r) = F_o + \frac{1}{2} F r \left(r^2 - \frac{1}{2} \right) \quad (8.43)$$

where r represents the dimensionless radial position ($0 \leq r \leq 1$).

The convective time scale given in [43], \bar{T}_c , can provide an approximate time scale for the spinup of partially filled cylindrical containers. Note that this result has been derived for cases of completely filled cylinders, where a boundary layer along the top wall contributes equally with the boundary layer along the bottom wall to the spinup of the liquid. To use this result for partially filled cylinders an effective liquid depth of $\bar{D} = 2\bar{F}_o$ must be used. Based on the parameters used in this study, T_c is given in dimensionless form by,

$$T_c \sim 2F_o Ga^{\frac{1}{4}} \quad (8.44)$$

The numerical solution for a case which was considered experimentally by Goller and Ranov, [62], is presented next. This case can be described in terms of the following set of dimensionless parameters:

Initial Liquid Depth:	$F_o = 4.233$
Galileo Number:	$Ga = 2.3979 \times 10^8$
Froude Number:	$Fr = 1.898$
Bond Number:	$Bo = \infty$

The transient development of the flowfield within the cylinder is depicted in Figure 8.5. In each of these plots the flowfield is shown at an axial cross section of the cylinder. The inward propagation of the boundary layer along the container sidewall is depicted on the left half side of this cross section by a set of lines that correspond to constant values of the circumferential velocity component, u_θ . Note that u_θ is measured with respect to an inertial, non rotating frame of reference. The secondary circulation driven by the boundary layer at the bottom wall is illustrated on the right half of the cross section in terms of lines defined by constant values of the streamfunction, f .

Immediately following the onset of rotation at $t=0$, the liquid is set into motion by viscous shear along the container walls. During these early stages of the spinup, the inward propagation of the boundary layer from the container sidewall is dominated by viscous diffusion. Along the bottom wall, as the liquid adjacent to wall gains angular momentum, centrifugal forces cause it to move outwards. The radial flow that develops leads to the formation of a boundary layer along the bottom wall. This occurs within the first full revolution of the container, $t < 2\pi$. Note that based on the scales used for the nondimensionalization of the equations, a dimensionless time interval of $\Delta t = 2\pi$ corresponds to one full revolution of the container. The number of completed revolutions by the container is denoted by N_r and is given in Figure 8.5. The radial

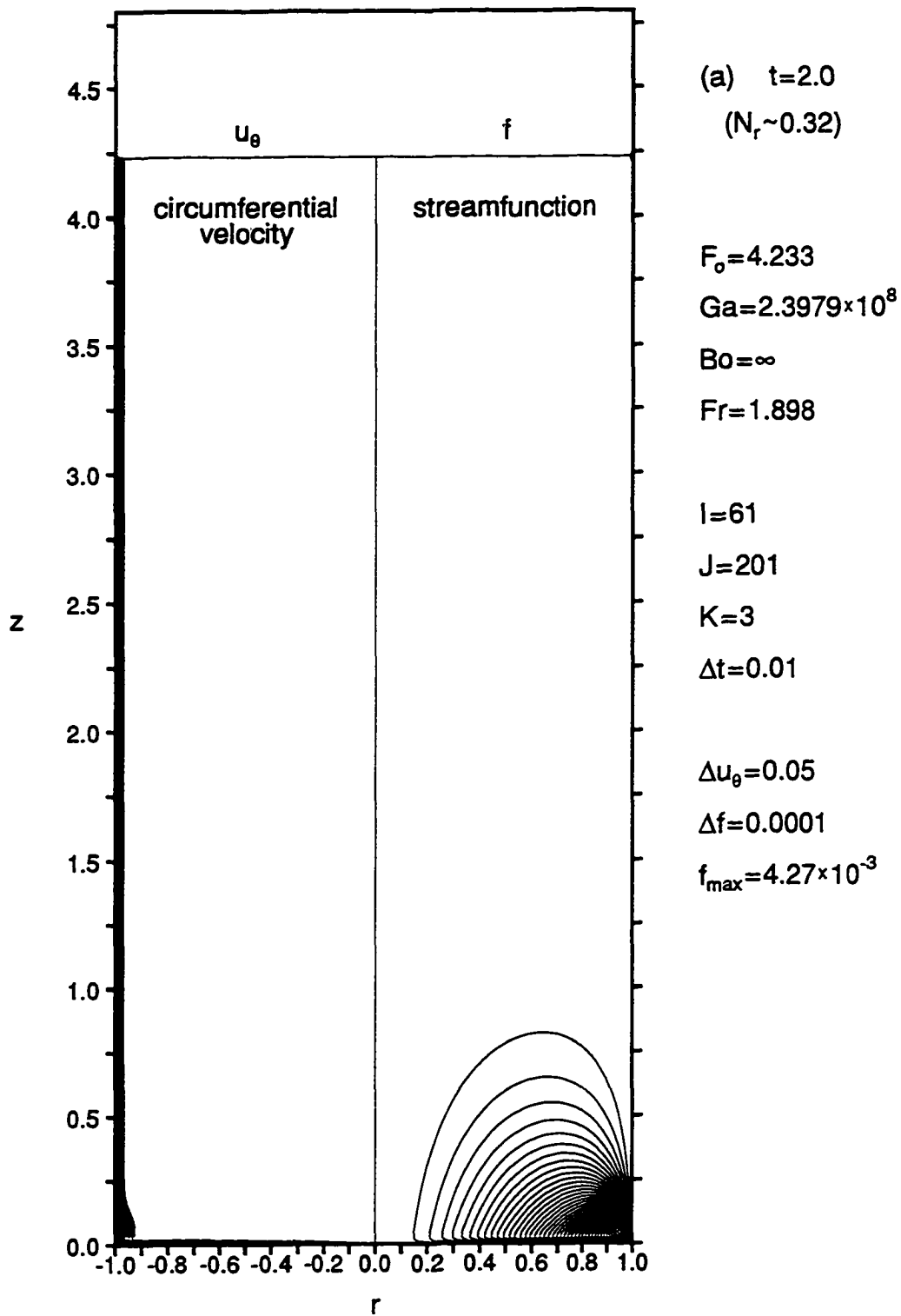


Figure 8.5: Developing Flowfield in a Spinning Cylinder

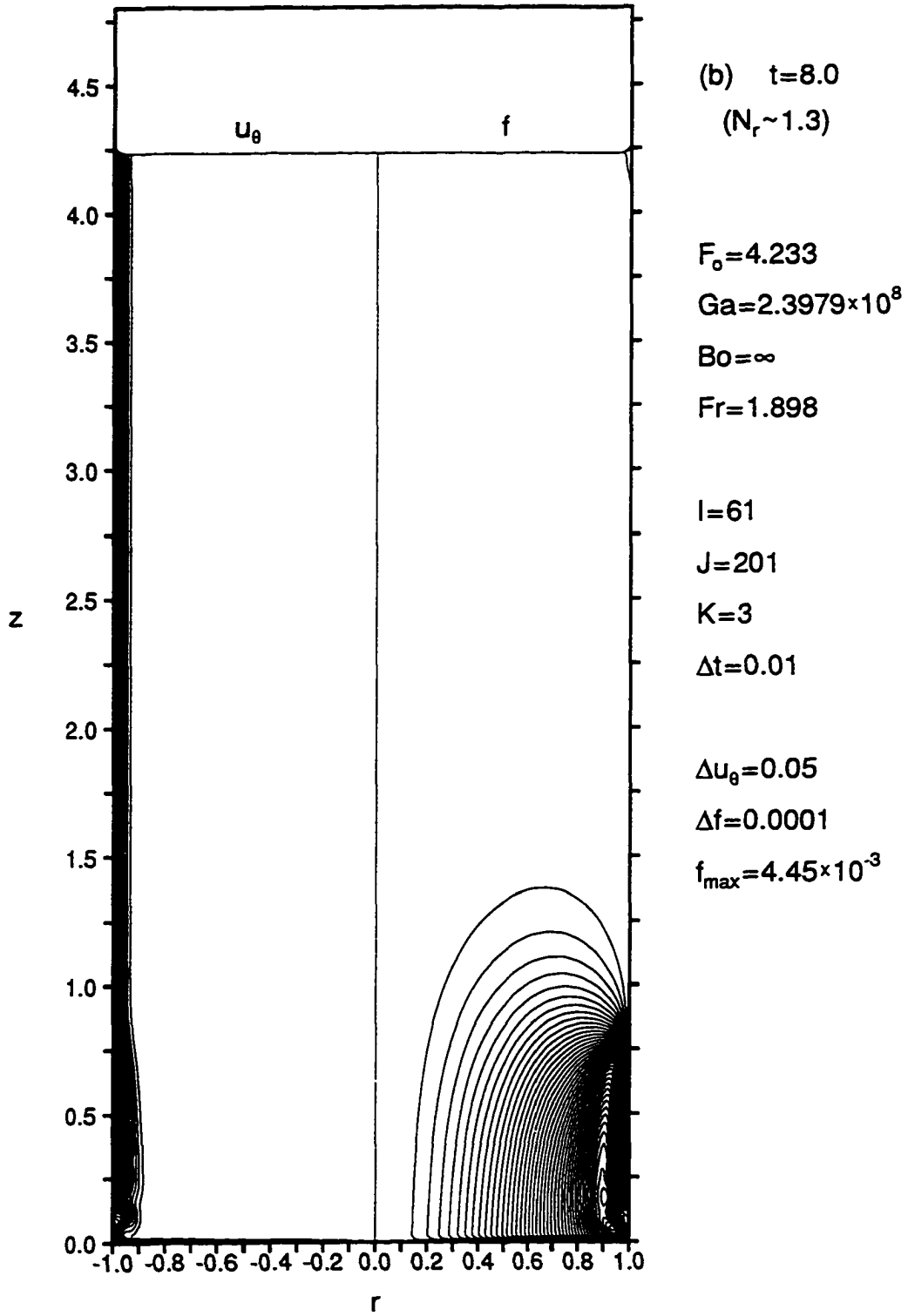


Figure 8.5 (Continued)

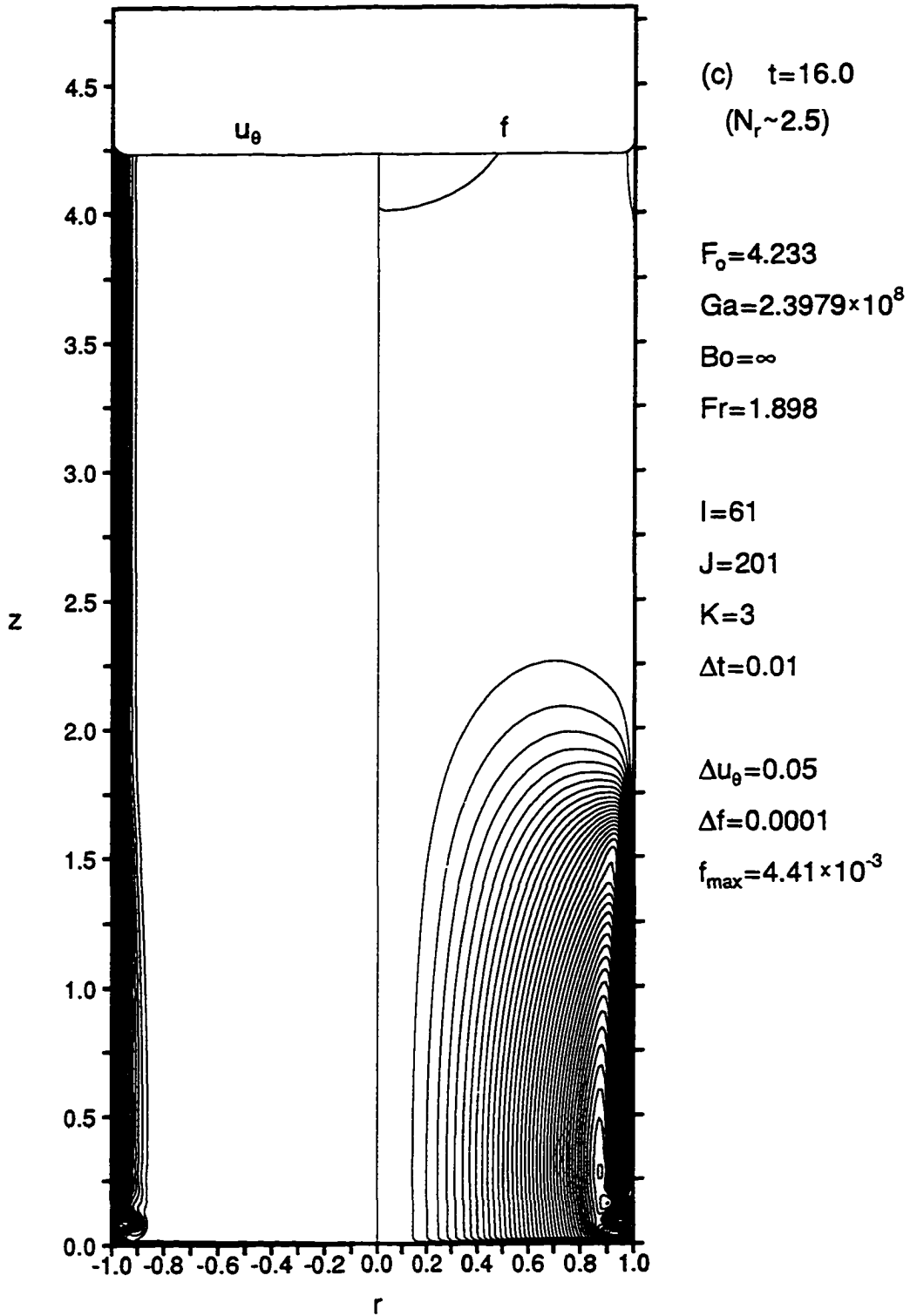


Figure 8.5 (Continued)

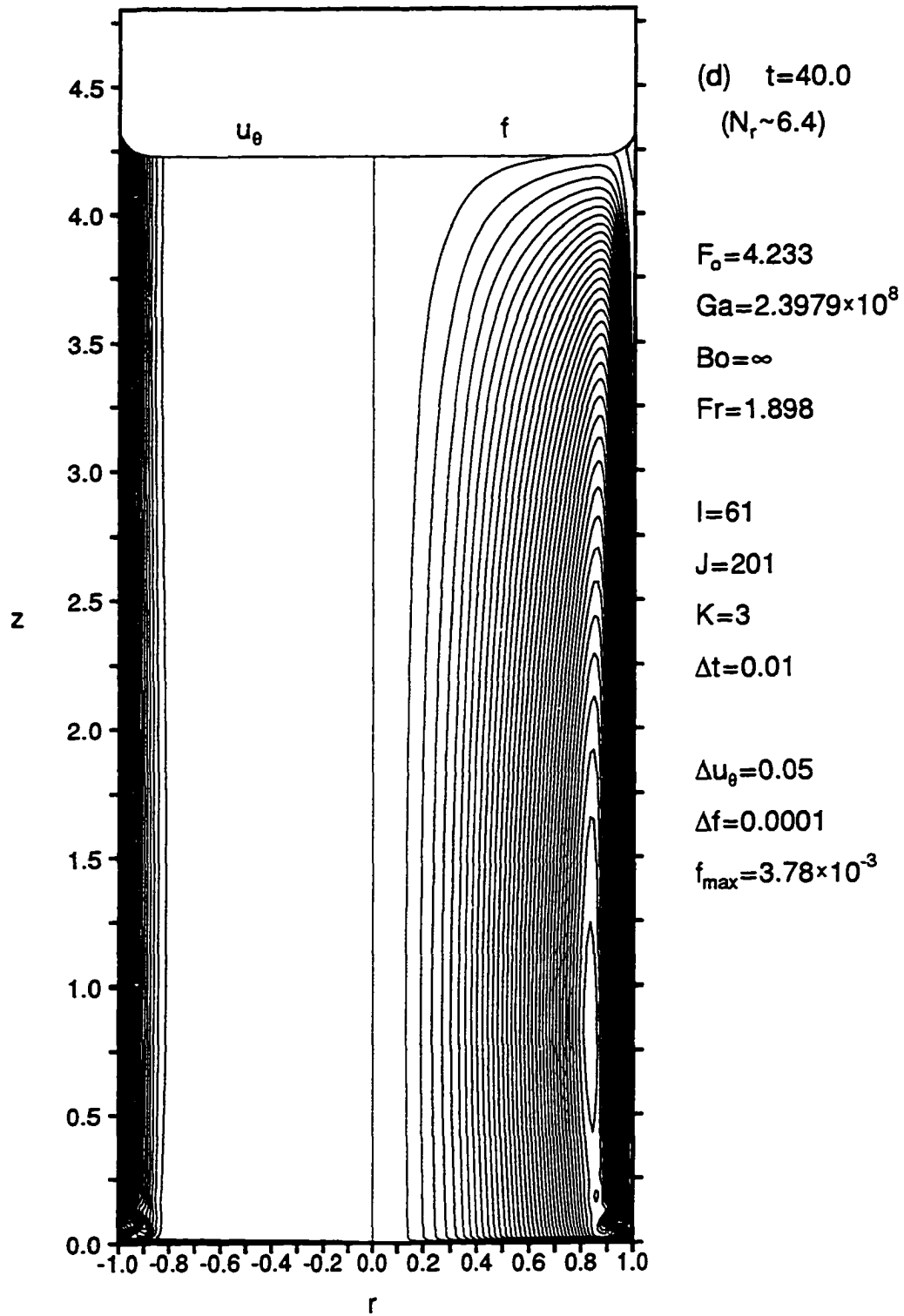


Figure 8.5 (Continued)

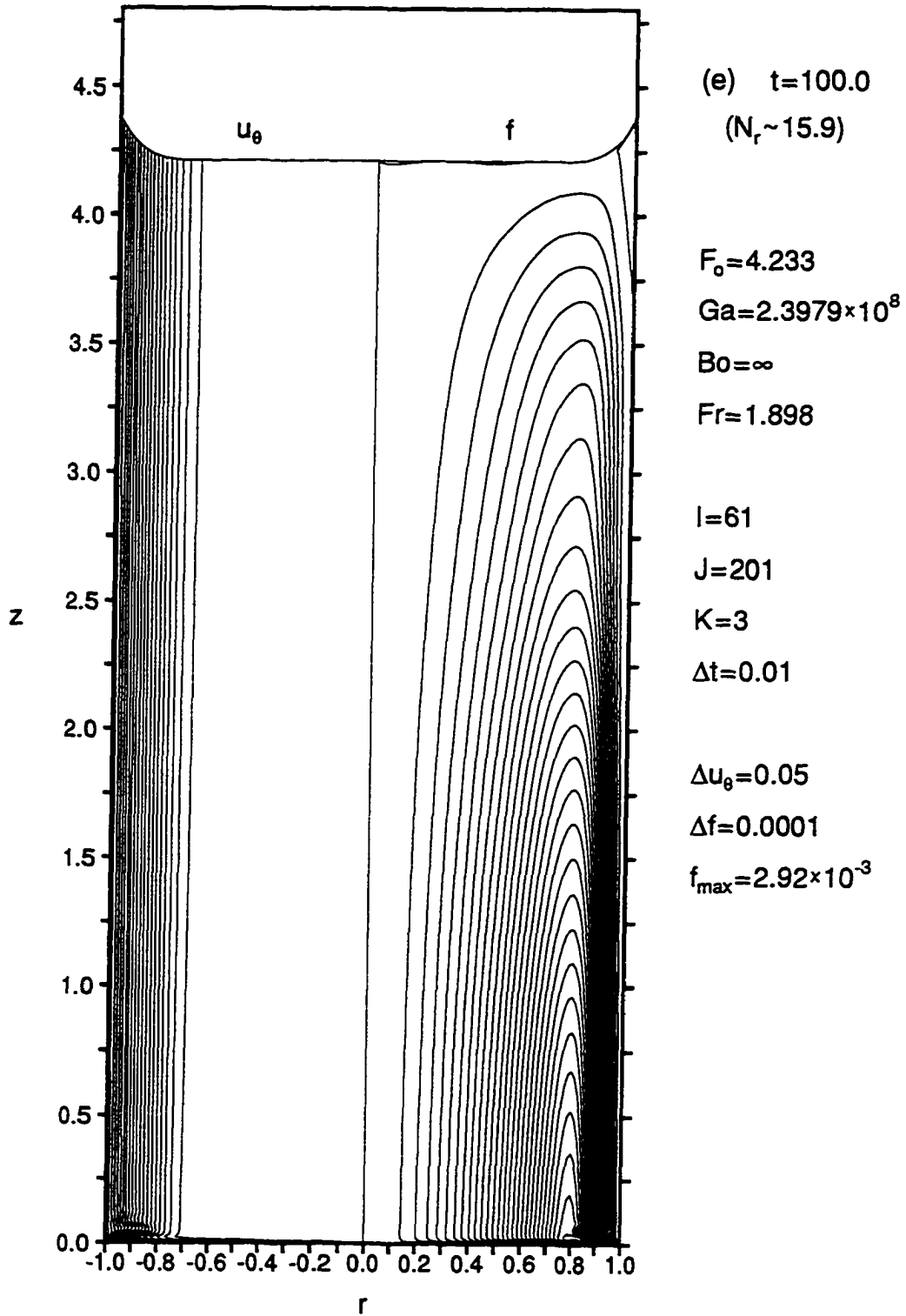


Figure 8.5 (Continued)

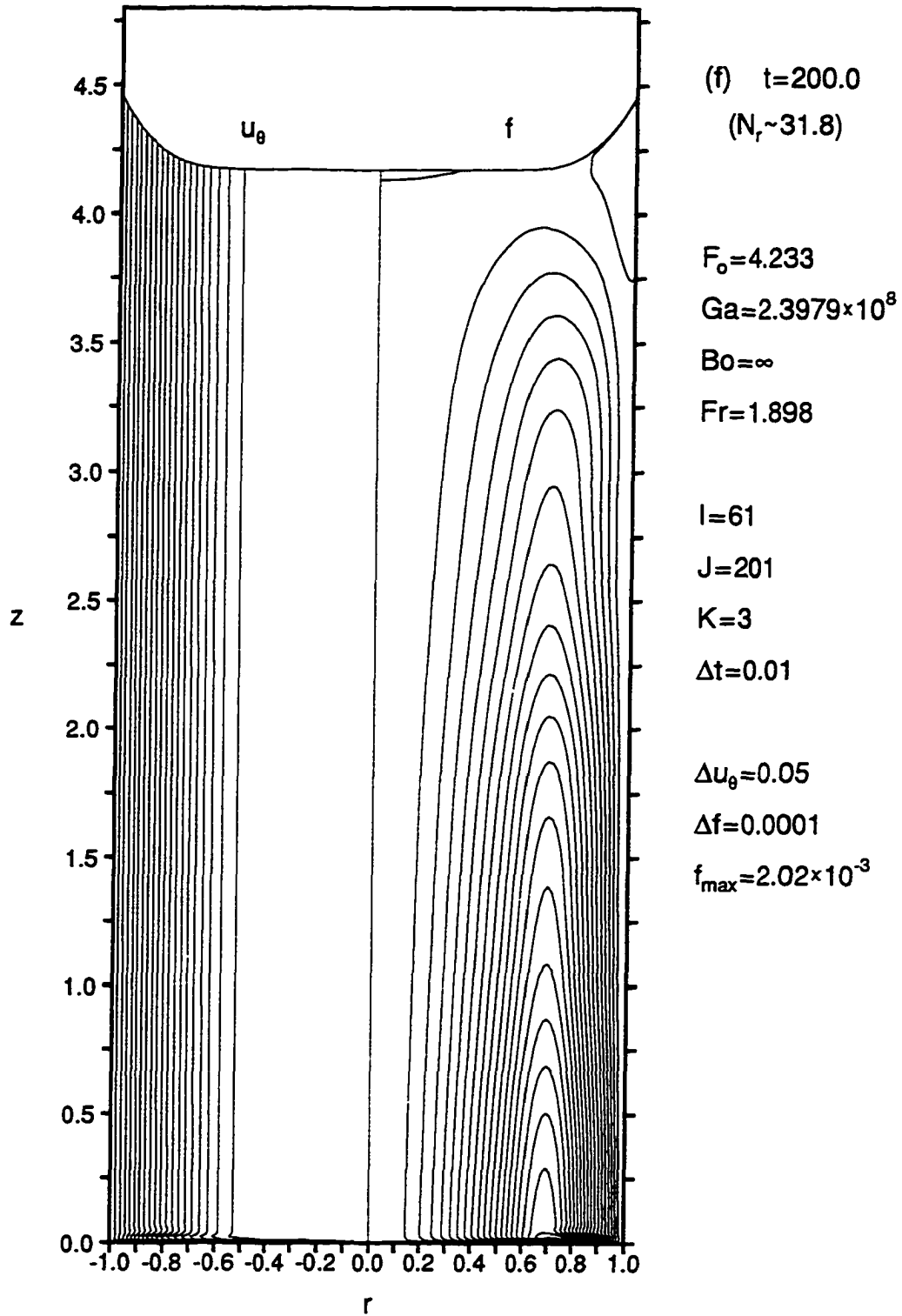


Figure 8.5 (Continued)

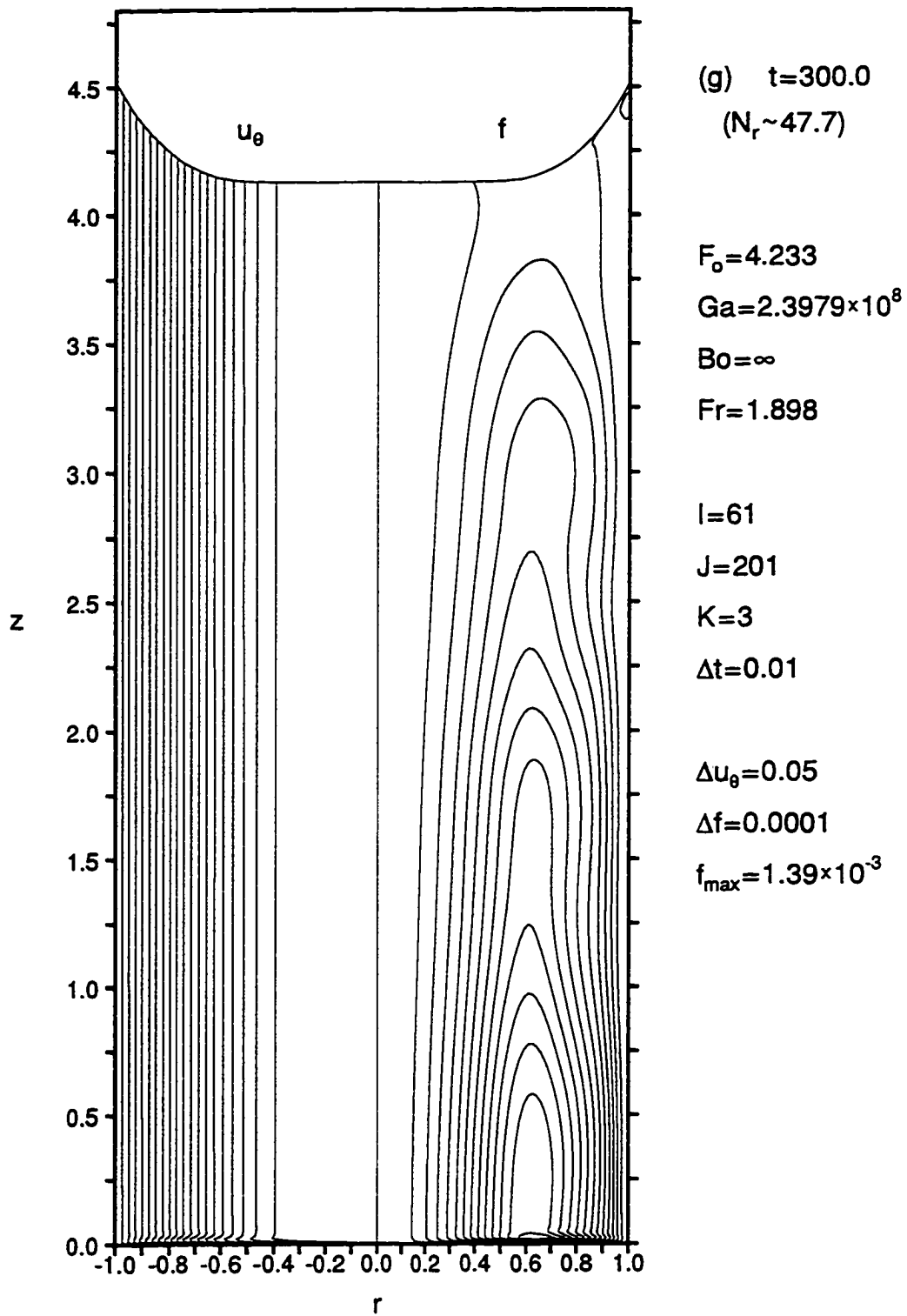


Figure 8.5 (Continued)

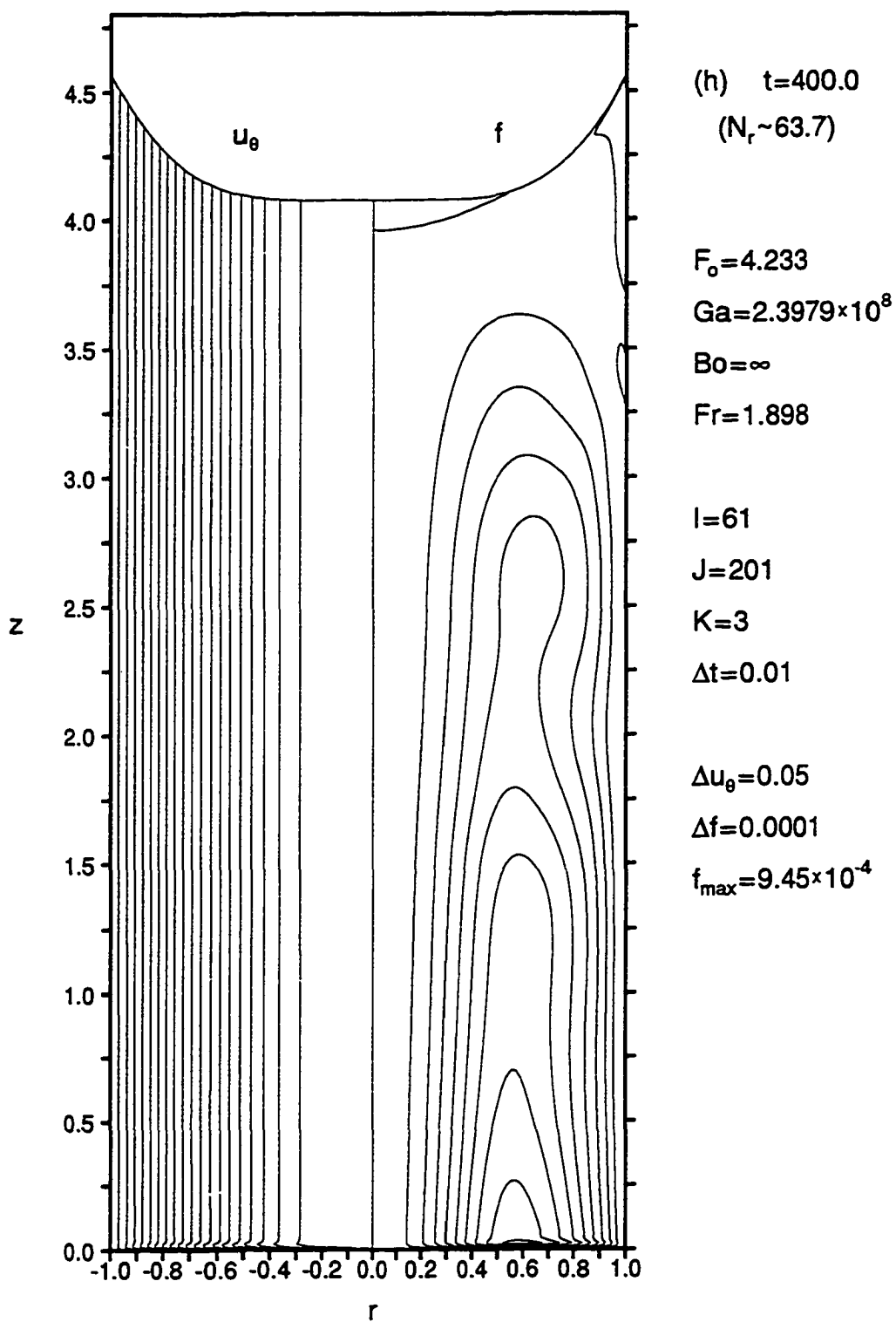


Figure 8.5 (Continued)

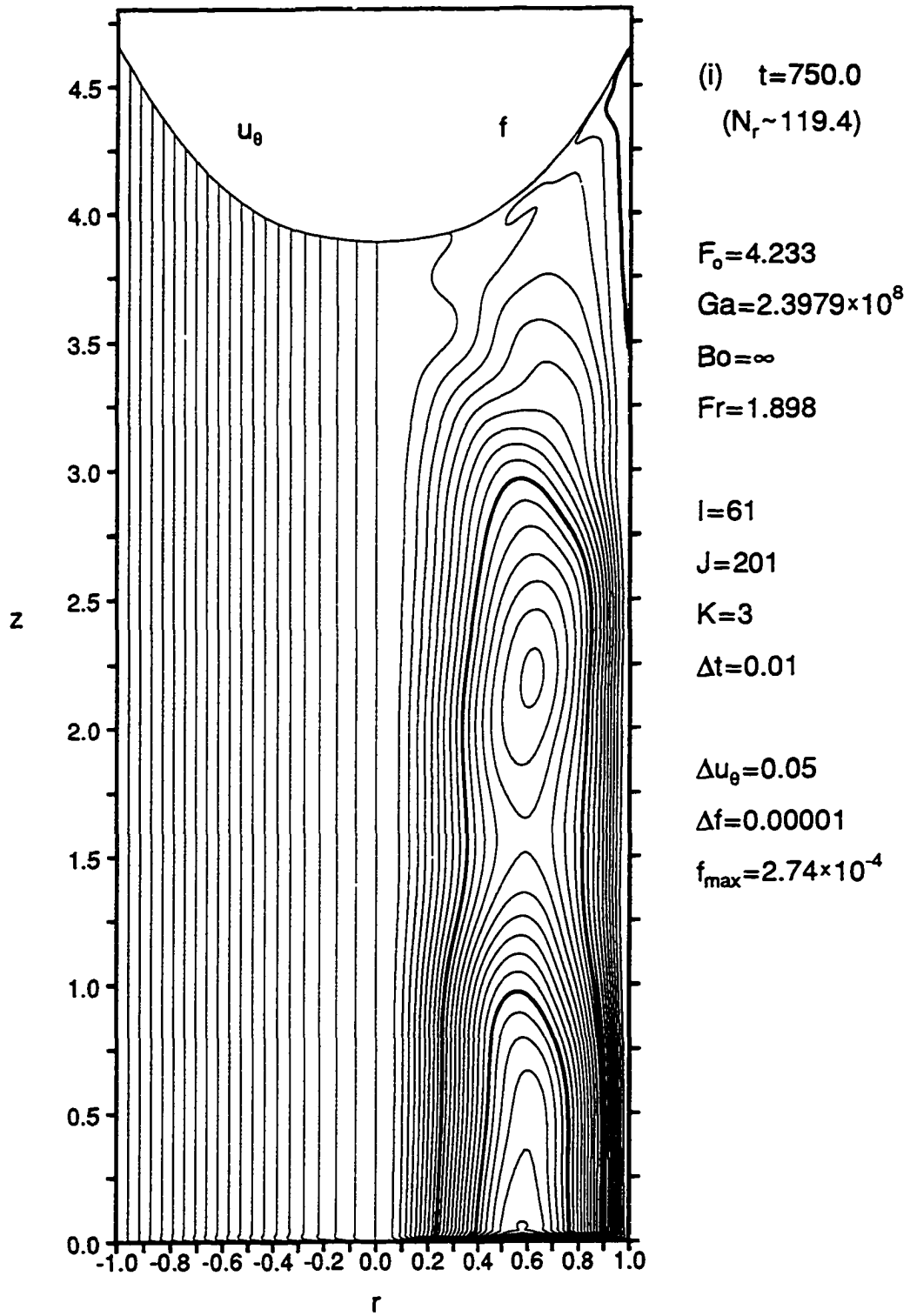


Figure 8.5 (Continued)

velocity component, u_r , reaches a maximum value of 0.208 at $t \approx 4.7$, $N_r \approx 3/4$, and subsequently decreases at a slow rate for the duration of the spinup process. The streamfunction reaches a maximum value of $f_{max} \approx 0.00456$ at $t \approx 4.5$ and it also decreases for the remainder of the flow. The angular velocity of the liquid next to the bottom wall increases at a very slow rate. The diffusion of angular momentum from the wall is balanced by radial advection and Coriolis forces. This keeps the thickness of the boundary layer approximately constant for a large portion of the spinup.

The effect of the secondary circulation on the inward propagation of the boundary layer along the container sidewall is very nicely depicted in Figure 8.5. Note the local increase in the speed of propagation as the secondary flow pattern grows in size and extends to higher and higher elevations. At $t = 2.0$, the thickness of the boundary layer is uniform with the exception of a small region in the lower corner of the container. The growth of the boundary layer at this time is still determined by diffusion. By $t = 8.0$, the inward convection of angular momentum by the secondary flow leads to an increased boundary layer growth the lower quarter section of the liquid region. Convective effects reach a height of $z \approx 2.5$ by $t = 16.0$, and by $t = 40.0$ ($N_r \approx 6.4$) they reach the free surface of the liquid. The boundary layer thickness becomes once again uniform with the u_θ lines being nearly vertical away from the bottom boundary. The boundary layer thickness remains uniform for the remainder of the spinup process. This is the result of a dynamic interaction between the convective, centrifugal, and Coriolis forces. This interaction also served as the leading mechanism in extending the secondary circulation upwards toward the free surface of the liquid. In Figure 8.5(b) for example, at $t = 8.0$, the strongest inward radial flow occurs at $z \approx 0.8$. Convection and Coriolis effects cause an increase in the thickness of the boundary layer at that location. However, as u_θ increases locally, the resistance offered by a stronger centrifugal force causes some of the radial flow to be redirected upwards, thus, extending the secondary circulation to a higher elevation.

During the initial stages of the spinup the flowfield near the lower corner of the container exhibits a strong transient behavior. The radial *jet like* flow along the bottom wall has sufficient kinetic energy to penetrate into the adverse pressure gradient of the stagnation region which exists in the corner of the container. As the flow approaches the container sidewall it is first turned inwards, at an angle of about 45° with respect to the container walls, as a result of the high pressure in the stagnation region. The flow is turned again outwards at a somewhat higher elevation as the local centrifugal

force increases by the inward convection of angular momentum and overcomes the local pressure gradient. This flow pattern is evident in Figure 8.5 by the "S" like bending exhibited by both the streamlines and the constant angular velocity lines near the corner of the container for $t \leq 100$. A close-up view of the corner region, at $t = 16.0$, is also shown in Figure 8.6. Here, lines of constant angular velocity are plotted in part (a) of the figure. The velocity vector, (\bar{u}_r, \bar{u}_z) , is drawn in part (b). The shape of the u_θ -lines in the corner region indicates that the angular momentum of the liquid does not increase monotonically with radial position. This represents an unstable stratification of angular momentum, leading to oscillations in the value of the angular velocity component, u_θ , at the forward edge of the boundary layer. An example of this behavior will be given shortly in the discussion that accompanies Figure 8.7.

The oscillations in the value u_θ predicted by the numerical solution here are consistent with previous numerical and experimental observations for liquid spinup in completely filled cylinders. The present result for the flow pattern in the corner region is qualitatively similar, both in form and duration, to numerical results given in [60]. The presence of these oscillations has also been verified experimentally by Warn-Varnas et al., [75]. Their conclusions, which are based on laser doppler measurements (LDM) of the velocity field, indicate that these oscillations are excited by the sudden increase in the rotation rate of the cylinder. For cases of spinup from an initial state of solid body rotation they detected inertial oscillations extending ahead of the boundary layer. For cases of spinup from rest these oscillations remained confined in the corner region since they are not supported by the irrotational liquid outside of the boundary layer.

The deformation of the free surface occurs at a very slow rate. The portion of the free surface that lies within the boundary layer rises monotonically. As the thickness of the boundary layer along the sidewall increases, and the viscous flow penetrates further into the interior of the flowfield, small amplitude disturbances are generated at the edge of the boundary layer. These disturbances appear to travel inward along the irrotational portion of the liquid surface. As a result, the fall of the free surface ahead in the interior core of the cylinder does not occur monotonically. Note for example in Figures 8.5(c, e, f, and h) the existence of small regions of positive streamfunction values on the portion of the free surface that lies outside the boundary layer. The free surface is actually in the process of rising in at least some part of these regions. To an observer focusing on the portion of the free surface that lies outside the boundary

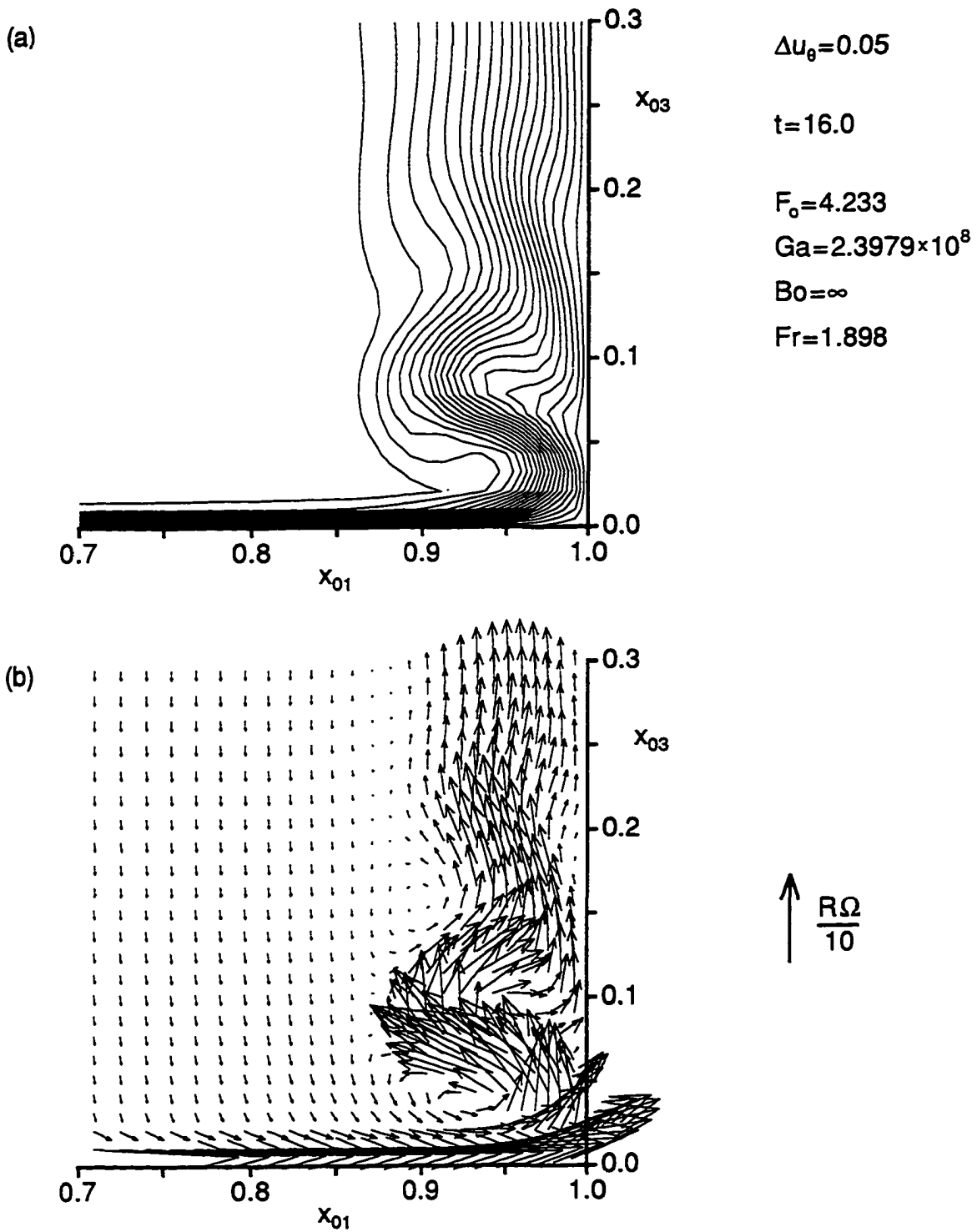


Figure 8.6: Flowfield in the Corner Region of the Cylinder

layer, it would appear as if the surface vibrates as it falls.

The flow induced by the deformation of the free surface is very weak. For a large part of the spinup process it does not affect the flowfield except in the immediate vicinity of the free surface. However, as the spinup progresses and the strength of the secondary circulation decreases, free surface effects extend somewhat deeper into the flowfield. The influence of these effects is limited to altering the structure of the secondary circulation in the top portion of the liquid region, with no apparent effect on the circumferential velocity profile. This can be seen in Figure 8.5(i). Note that the spacing between adjacent streamlines in part (i) of the figure has been decreased by a factor of ten compared to that used in parts (a-h). To gain a feeling for the reduction in the relative strength of the flowfield at $t = 750.0$ ($N_\tau \approx 120$), streamlines that correspond to the standard spacing of $\Delta f = 0.0001$ are drawn using thicker lines.

The rate at which the liquid attains its angular momentum is depicted in Figure 8.7. The angular momentum of a differential liquid element of mass, dm , about the spinning axis is given by, $d\bar{H} = u_\theta r dm$. The total angular momentum of the liquid \bar{H} , can be evaluated by integration over the entire liquid region. In dimensionless form, $H(t)$, is given by the following expression,

$$H(t) = \frac{\bar{H}}{\rho R^5 \Omega} = 2\pi \int_0^1 \int_0^F u_\theta r^2 dz dr \quad (8.45)$$

where ρ represents the density of the liquid. As the liquid reaches the state of solid body rotation, its angular velocity $u_\theta \rightarrow r$, while the position of the free surface, $F(\infty, r)$, is given by the parabolic profile of equation (8.43). The angular momentum of the liquid at steady state is given by:

$$H(\infty) = \lim_{t \rightarrow \infty} H(t) = 2\pi \left(\frac{F_o}{4} + \frac{Fr}{48} \right) \quad (8.46)$$

In Figure 8.7(a) the ratio of, $H(t)/H(\infty)$, is plotted as a function of time. The angular momentum of the liquid increases asymptotically with time. By $t \approx 133.0$ ($N_\tau \approx 21$), the liquid has already acquired half of its final angular momentum. The numerical solution was computed to a dimensionless time value of $t = 750.0$ ($N_\tau \approx 120$). At this time, the momentum of the liquid is within 6% of its final value.

The variation in the angular momentum of the liquid with respect to time can be approximated by the following expression in terms of the error function,

$$\frac{H(t)}{H(\infty)} = \text{erf} \left(\frac{5}{3} \left[\frac{t}{T_c} \right]^{\frac{2}{3}} \right) \quad (8.47)$$

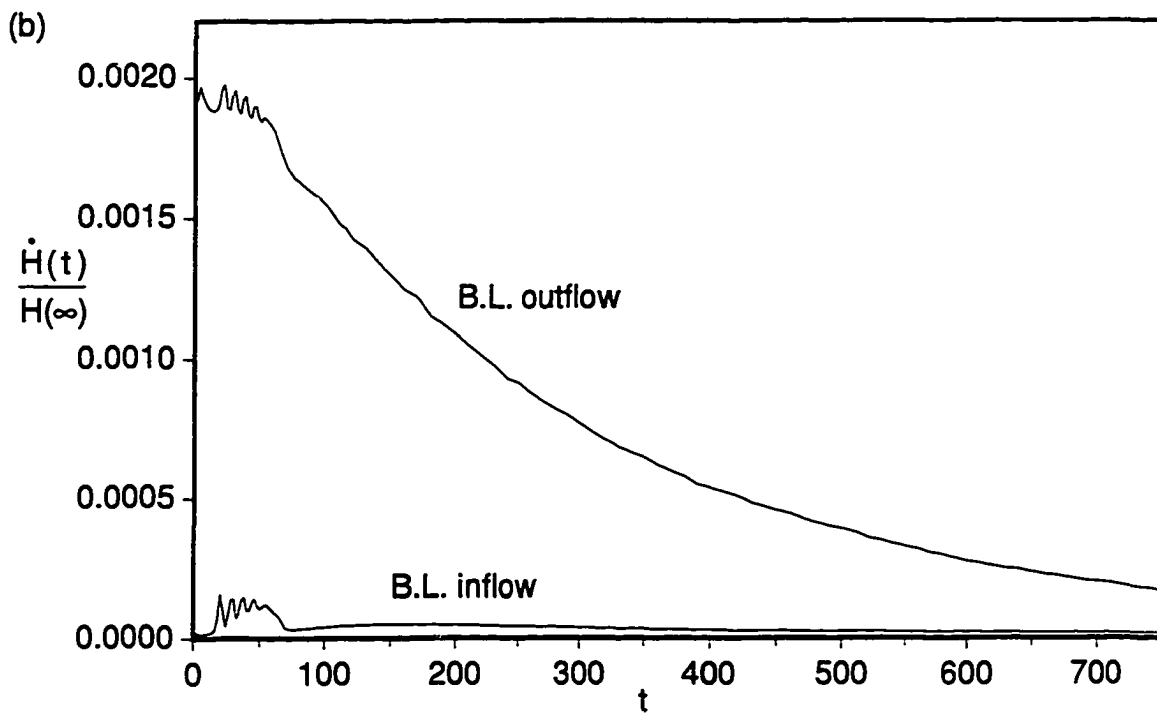
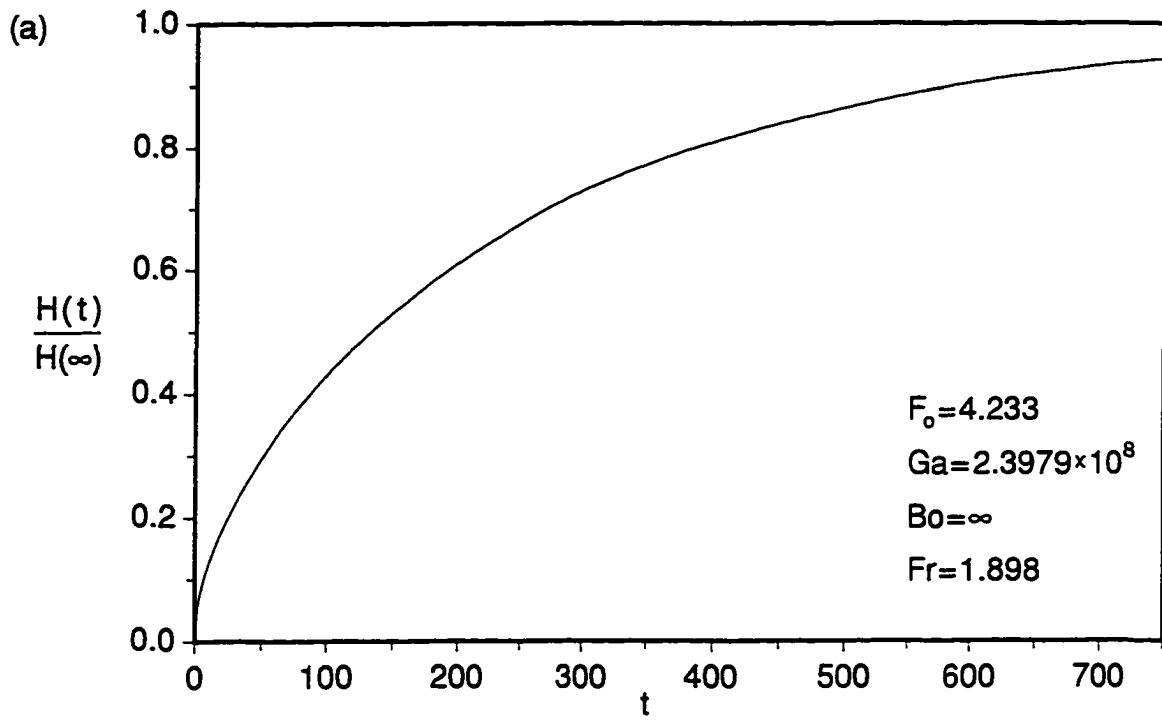


Figure 8.7: Angular Momentum of Liquid in a Spinning Cylinder

where T_c represents the convective time scale as given in equation (8.44). Based on the values of Ga and F_o which apply to this case, the convective time scale is equal to, $T_c = 1053.5$. For $t > 30.0$, equation (8.47) can be used to approximate the value of $H(t)$ to within one percent of the numerical result. However, during the initial boundary layer phase of the flow, $t < 30$, the angular momentum of the liquid increases as $H \sim \sqrt{t}$. As a result, the error of the approximation based on equation (8.47) increases as $t \rightarrow 0$.

The significance of the secondary circulation, which is driven by the boundary layer along the bottom container wall, is illustrated in Figure 8.7(b). Here, the flowrate of angular momentum into the boundary layer, \dot{H}_i , and the flowrate of angular momentum out of the boundary layer, \dot{H}_o , are shown as functions of time. The inflow and outflow of angular momentum from the boundary layer are determined from the following expressions,

$$\dot{H}_i(t) = 2\pi \int_0^1 \frac{1}{2} (|u_z| - u_z) u_\theta r^2 dr \quad (\text{Inflow}) \quad (8.48a)$$

$$\dot{H}_o(t) = 2\pi \int_0^1 \frac{1}{2} (|u_z| + u_z) u_\theta r^2 dr \quad (\text{Outflow}) \quad (8.48b)$$

with the integration being carried out at a constant value of the axial coordinate, equal to $z = 0.02$, which lies outside the boundary layer of the duration of the flow.

The inviscid core of the liquid, which lies outside the boundary layer, remains irrotational. Liquid of low angular momentum from the core enters the boundary layer along the bottom wall. It travels along a spiral path outwards, and exits the boundary layer along the bottom wall with its angular momentum having been significantly increased. By $t = 750.0$, the net outflow of angular momentum from the bottom wall boundary layer reaches about 57% of the steady state value, $H(\infty)$.

The effect of the oscillations which become excited in the corner region of the flow-field by the impulsive start of the container rotation are also visible in Figure 8.7(b). These oscillations last for approximately the first twelve revolutions of the cylinder, $0 \leq t \leq 75.0$. The dimensionless frequency associated with these oscillations is approximately equal to 0.120. The oscillations in the values of \dot{H}_i and \dot{H}_o appear to be out of phase by 180° .

8.2.3 Comparison with Experimental Results

The numerical result for the free surface position is compared with the experimental measurements of Goller and Ranov [62]. This comparison is shown in Figure 8.8.

The change in the position of the free surface from its initial value, $F(t, r) - F_0$, is compared after 30 and 60 second time intervals have elapsed from the onset of rotation. These time intervals correspond to dimensionless time values of $t = 373.63$ ($N_\tau \approx 55$) and $t = 747.26$ ($N_\tau \approx 110$).

The numerical result for the position of the free surface position at times, $t = 373.63$ and $t = 747.26$, are drawn in Figure 8.8 as solid lines. The experimental data are represented by the rectangular symbols. They have been reproduced here by scanning and digitizing results which appeared in the original publication. The error associated with the reproduction of these data is believed to be less than 0.05%. No quantitative information on the error associated with the experimental procedure was given in [62].

The two experimental free surface profiles overestimate the total volume of liquid within the cylinder. The height of the rectangular symbols represents a correction to the experimental data for this lack of mass conservation. The top side of each of these symbols coincides with the position of the free surface as determined by the reproduction procedure. The bottom side defines the position to which the free surface must be moved, by a uniform increment ΔF , such that the total liquid volume equals its initial value. The experimental profiles were shifted downward by an increment of $\Delta F = 0.0115$ at $t = 373.63$, and by $\Delta F = 0.0154$ at $t = 747.26$. These two increments are approximately equal to 2.5% and 2.0% of the maximum change in elevation across the free surface at times $t = 363.63$ and $t = 747.26$ respectively. By contrast, the corresponding error in terms of mass conservation for the numerical result is only 0.14% at $t = 373.63$ and 0.22% at $t = 747.26$.

The experimental procedure that was used in recording the free surface elevation involved the sweeping of the surface along the radial direction by a wire probe. As reported in [62], the process of completing a single sweep of the free surface by the probe required a time interval of nearly three seconds. However, during the transient phase of the spinup process, the position of the free surface changes significantly over a three second time interval. For example, at $t = 373.63$, the numerical solution predicts that the position of the free surface at the center of the container will change by an amount $\Delta F \approx 0.010$ over a three second interval. Given that the experimental profiles overestimate the total liquid volume, it is likely that the sweep of the surface by the wire probe was carried out starting from the center and moving toward the sidewall of the cylinder. Thus, it is also likely that the experimental free surface profiles overestimate the free surface elevation in the center region of the container. Since an estimate of the

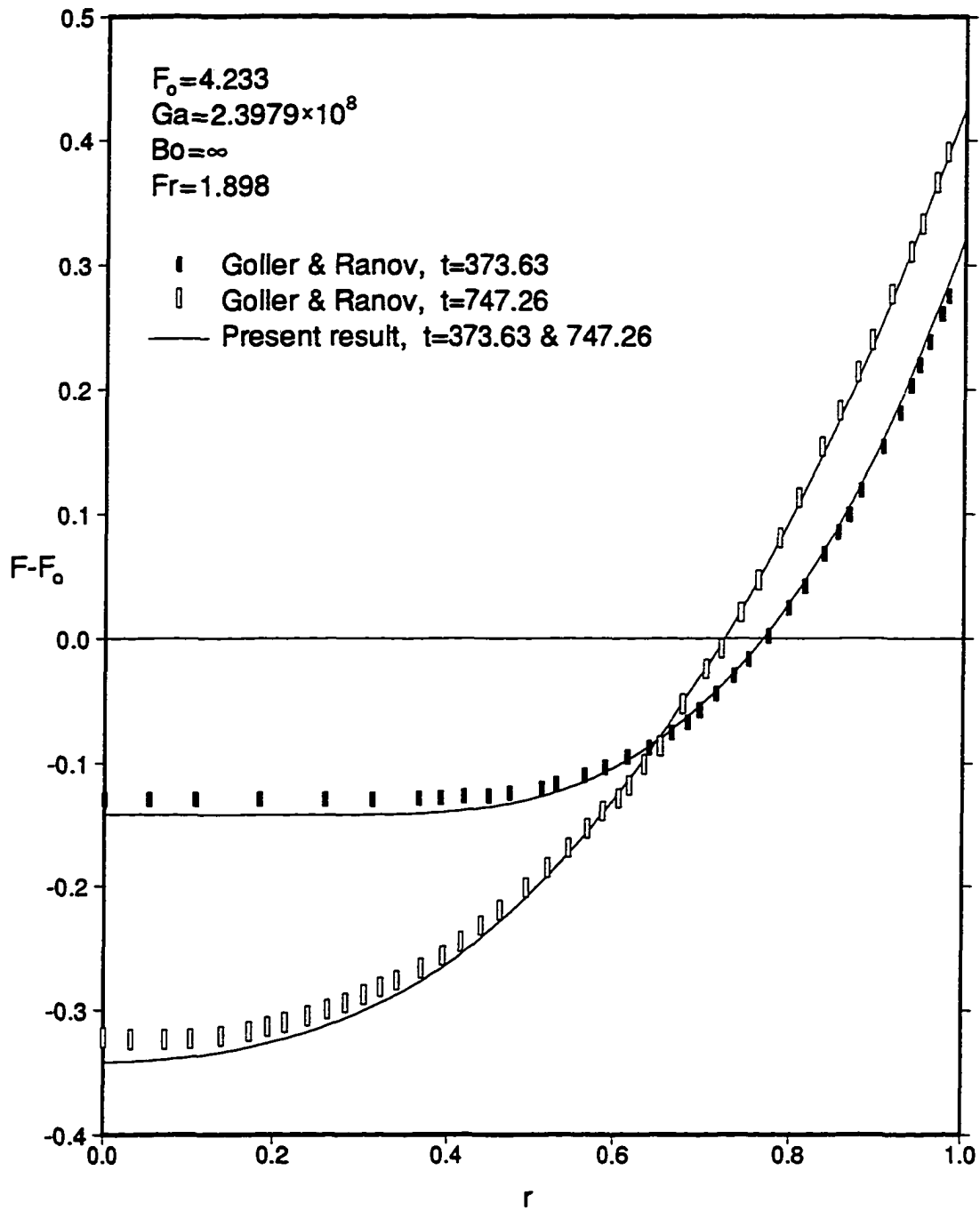


Figure 8.8: Comparison of Numerical and Experimental Free Surface Position

overall error associated with the experimental procedure is not provided, and further, the error in terms of mass conservation alone for the experimental data is nearly of the same order of magnitude as the difference between the numerical and experimental results, the agreement between the numerical and experimental free surface profiles is excellent.

8.3 Three Dimensional Flow in a Rotating Spherical Container

The three dimensional liquid flow which develops within an impulsively rotated spherical container is considered here. A schematic diagram illustrating the geometry of this case is shown in Figure 8.9. This numerical simulation involves a spherical container of radius $R = 0.1$ m, half-filled with SAE-10W oil, and impulsively rotated at 20 rpm about a vertical axis located at a distance $\bar{h}_1 = 0.2$ m away from its center. This case can be represented in terms of the following set of dimensionless parameters,

Initial Surface Position:	$F_o = 0.0$
Rotation Arm:	$h_1 = 2.0$
Angular Velocity:	$\Omega_3 = \dot{\psi}_3 = 0.21146$
Galileo Number:	$Ga = 1.240 \times 10^6$
Bond Number:	$Bo = 2434$

These parameters have been derived based on the scales defined for the dependent and independent variables of the problem in section 7.1.10. The container radius is used as the characteristic dimension, $L = R$, while the characteristic acceleration scale is based on gravity, $\mathbf{g} = g$. Based on these scales, the dimensionless angular velocity of the container is equal to the square root of the Froude number, $\Omega_3 = \sqrt{Fr}$. The initial free surface position, F_o , is measured with respect to the container horizontal mid-plane at $x_{33} = 0$. A computational grid consisting of thirteen nodes in the radial ($I = 13$) and azimuthal ($J = 13$) directions, and forty-one nodes in the circumferential ($K = 41$) direction was used for the solution of the problem. The solution was marched using a dimensionless time step of $\Delta t = 0.001$. The position of the container with respect to the inertial coordinate frame, x_0 , can be fully described in terms of the Euler angle ψ_3 , and the rotation arm, h_1 . The remaining parameters that relate the position of the container to the inertial coordinate frame are all set equal to zero,

$$\{\ell_i(t), \psi_1(t), \psi_2(t), h_2(t), h_3(t), \vartheta_i(t)\} = 0 \quad (8.49)$$

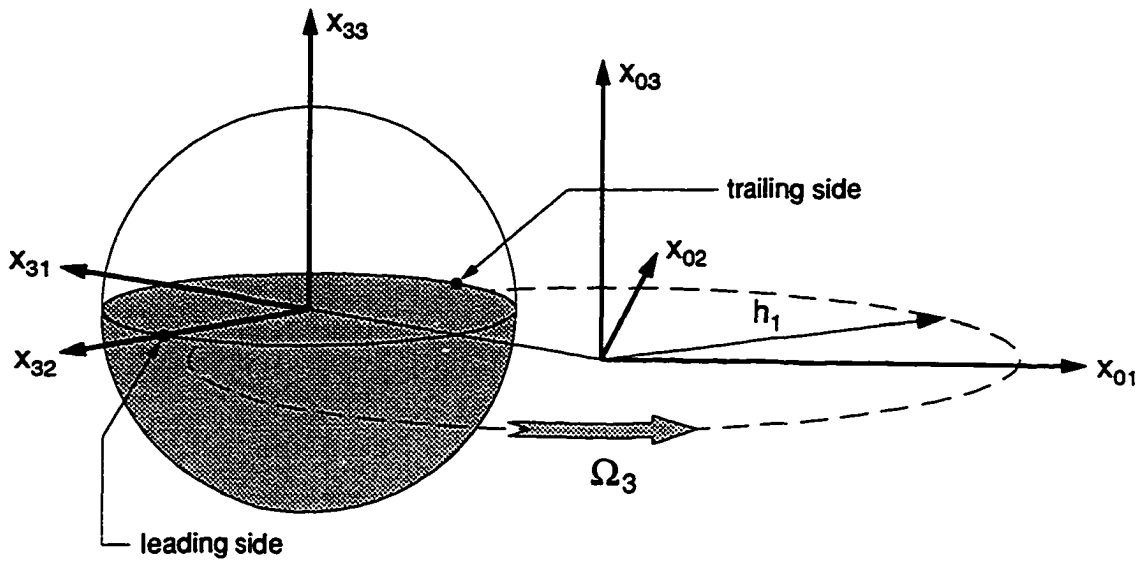


Figure 8.9: Simplified Geometry for Asymmetric Spherical Spinup.

The two surface tracking angles are initialized to $\phi_2(0) = -\pi/2$ and $\phi_3(0) = 0$, and for $t > 0$, they are adjusted according to the procedure described in section 7.3.1.

Initially, for $t < 0$, the container is stationary and the liquid within it is in a state of hydrostatic equilibrium. A step change in the angular velocity of the container at $t = 0$, sets the liquid in motion. The flowfield within the container at time $t = 0^+$, immediately following the onset of the impulsive rotation, is determined from the solution of the initial condition equations. These equations are rescaled in terms of the pressure impulse function, Π , and solved based on the procedure outlined in section 7.1.9.

The solution for the initial conditions of the problem is depicted in the following two figures. The pressure impulse function, Π , is shown in Figure 8.10. The actual pressure within the liquid at the onset of the sudden rotation, $t = 0$, behaves like $\sim \Pi/t$. Figure 8.10(a) shows the pressure impulse field along the container wall surface. Here, the hemispherical shape of the wetted container wall surface has been stretched into a circle. The position of a given point on the container wall surface is described in terms of two surface coordinates (angles), θ and φ . The angle θ describes the circumferential position measured relative to the positive x_{31} axis. The leading side of the container corresponds to $\theta = 90^\circ$, while the side of the container closest to the spin axis corresponds to $\theta = 180^\circ$. The angle φ , describes the azimuthal position of a point on the container wall surface. It is measured relative to the bottom container *pole*,

located at $x_{33} = -1$. Based on this convention, the position defined by the intersection of the initial free surface and the container wall, the *equator* of the sphere, is located at $\varphi = 90^\circ$. Note that the azimuthal angle φ as shown in the figure increases radially outwards. In Figure 8.10(b) the pressure impulse function, Π , is shown along a cross section defined by the $x_{31} = 0$ plane. In Figure 8.11(a), the velocity vector \vec{u}_3 is projected onto the plane defined by the initial position of the free surface ($x_{33} = 0$). The projection of the velocity vector onto the $x_{31} = 0$ plane is shown in Figure 8.11(b). The direction of the container motion and the location of the spin axis are indicated by the arrows in each of these figures.

The sudden onset of motion results in a velocity, U_0 , relative to the inertial, non-rotating, coordinate frame, x_0 :

$$\begin{aligned}\vec{U}_0 &= (\vec{h}_1 + \vec{r}) \times \vec{\Omega}_3 \\ &= \vec{h}_1 \times \vec{\Omega}_3 + \vec{r} \times \vec{\Omega}_3\end{aligned}\quad (8.50)$$

where, \vec{h}_1 , represents the position vector in terms of the *rotation arm* which relates the position of the center of the container relative to the spin axis, x_{03} . The position vector, \vec{r} , relates the coordinates of a given point relative to container center. The initial motion of the container can be represented by the superposition of a linear translation of the container along the x_{32} direction with a velocity $U_{32} = h_1 \Omega_3$, and a rotation about the x_{33} axis with an angular velocity equal to Ω_3 .

The singularity in the pressure field is the result of the sudden *linear push* experienced by the liquid due to motion of the container wall. The rotational component of the container velocity does not affect the initial flowfield. In fact, the initial motion of the liquid, viewed in terms of an inertial frame of reference is identical to that which would have resulted from a simple translation of the container in terms of $U_{32} = h_1 \Omega_3$. This is reflected by the solution of the initial conditions. The impulse function, Π , shown in Figure 8.10 is symmetric about the $x_{31} = 0$ plane. The velocity field shown in Figure 8.11 has a rotational component superimposed on it because it is measured relative to the rotating coordinate system, x_3 . At $t = 0^+$, the flowfield has not yet experienced any *rotational* effects.

The subsequent motion of the liquid within the spinning spherical container can be visualized with the aid of Figure 8.12. This figure represents a series of plots, depicting the geometry of the liquid region as would have been seen by an observer whose position remains *fixed* relative to the moving container. This hypothetical observer is located far away from the container, 135° counterclockwise from the x_{31} axis, and, 10° above the

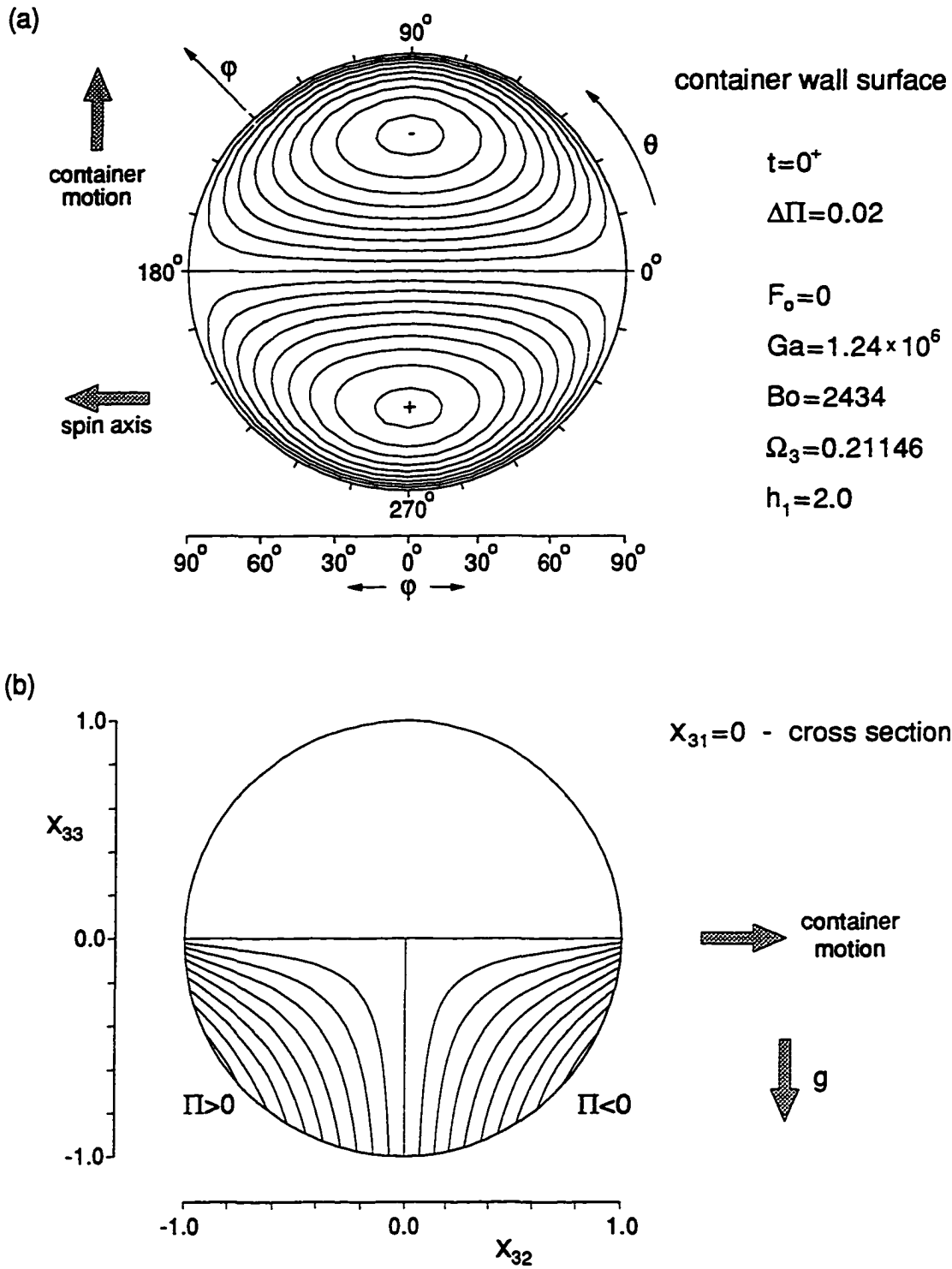


Figure 8.10: Initial Pressure Impulse, Π , in a Rotating Sphere.

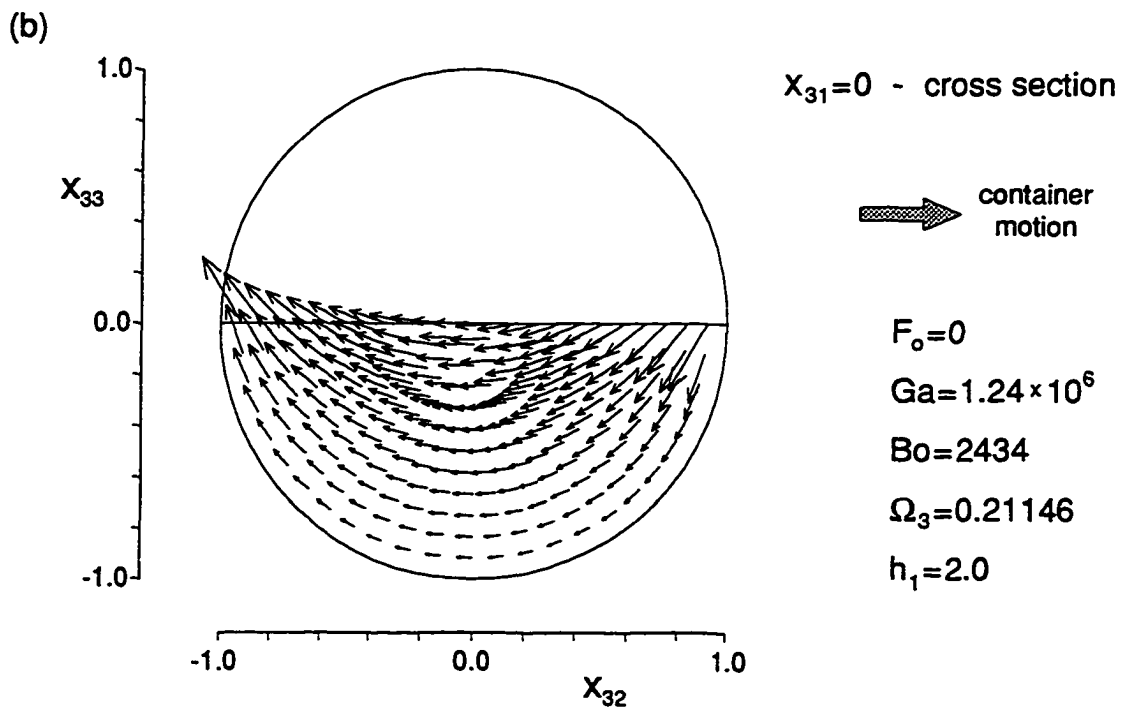
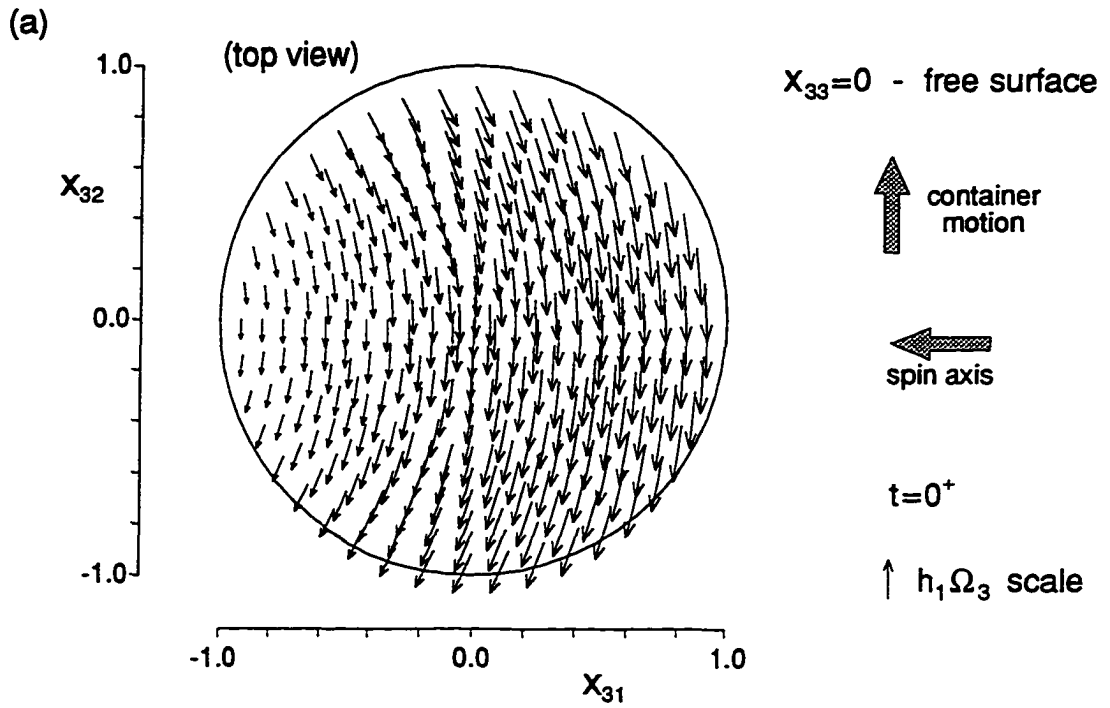


Figure 8.11: Initial Velocity Field, u_3^+ , in a Rotating Sphere.

horizontal container mid-plane with $x_{33} = 0$. Note that the direction of observation in this figure leads to a perspective which is identical to that of Figure 8.9. The direction of the container motion and the location of the spin axis are also indicated in each of these plots. The number of completed revolutions about the spin axis, denoted by N_r , is also given in the figure.

The initial velocity imparted to the liquid by the sudden onset of the container rotation causes the liquid mass to undergo in part a *lateral* sloshing motion. The liquid initially rushes back toward the trailing side of the container. It reaches a position of maximum wall elevation on that side of the container, and then it begins to move in the opposite direction, toward a position of maximum elevation on the leading side of the container. The liquid is also undergoing a simultaneous clockwise rotation. This rotation is initially about the x_{33} axis, but for $t \geq 0^+$ centrifugal acceleration effects cause a gradual shift in the orientation of the rotation axis. The combination of these two types of motion make the liquid appear to be sloshing back and forth while undergoing a clockwise rotation, with the bulk of the liquid slowly moving away from the spin axis.

The shape of the liquid region, as defined by the position of the free surface, is shown at constant time intervals equal to 0.60 dimensionless time units in Figures 8.12(a-p). The initial position of the liquid is shown in part (a) of the figure. Part (c) depicts the liquid near the first position of maximum elevation. The rotational component of the motion causes this maximum elevation position to occur more than 6° clockwise past the negative x_{32} axis, at a circumferential position of $\theta = -96.3^\circ$. The second position of maximum elevation is reached at $t \approx 3.96$ and it corresponds to an angle, $\theta \approx 34.5^\circ$, while the third occurs at $t \approx 6.46$ and $\theta \approx -152.8^\circ$.

The remaining plots, Figures 8.12(q-x), are intended to give a the reader a feeling about the long term effects of viscous damping. The lateral sloshing component of the liquid motion, with the liquid moving back and forth between position of maximum wall elevation, makes the flow to appear to be quasi-periodic. In parts (q-t) of the figure the liquid is shown near such positions of maximum elevation during the third, fourth, fifth, and sixth, sloshing cycles. The positions of maximum elevation shown in parts (u-x) correspond to two-cycle intervals starting from the eighth cycle.

The motion of the liquid within the rotating container is also illustrated in terms of Figure 8.13. This figure provides information on the motion of the center of gravity of the liquid. The coordinates of the center of gravity are calculated according to

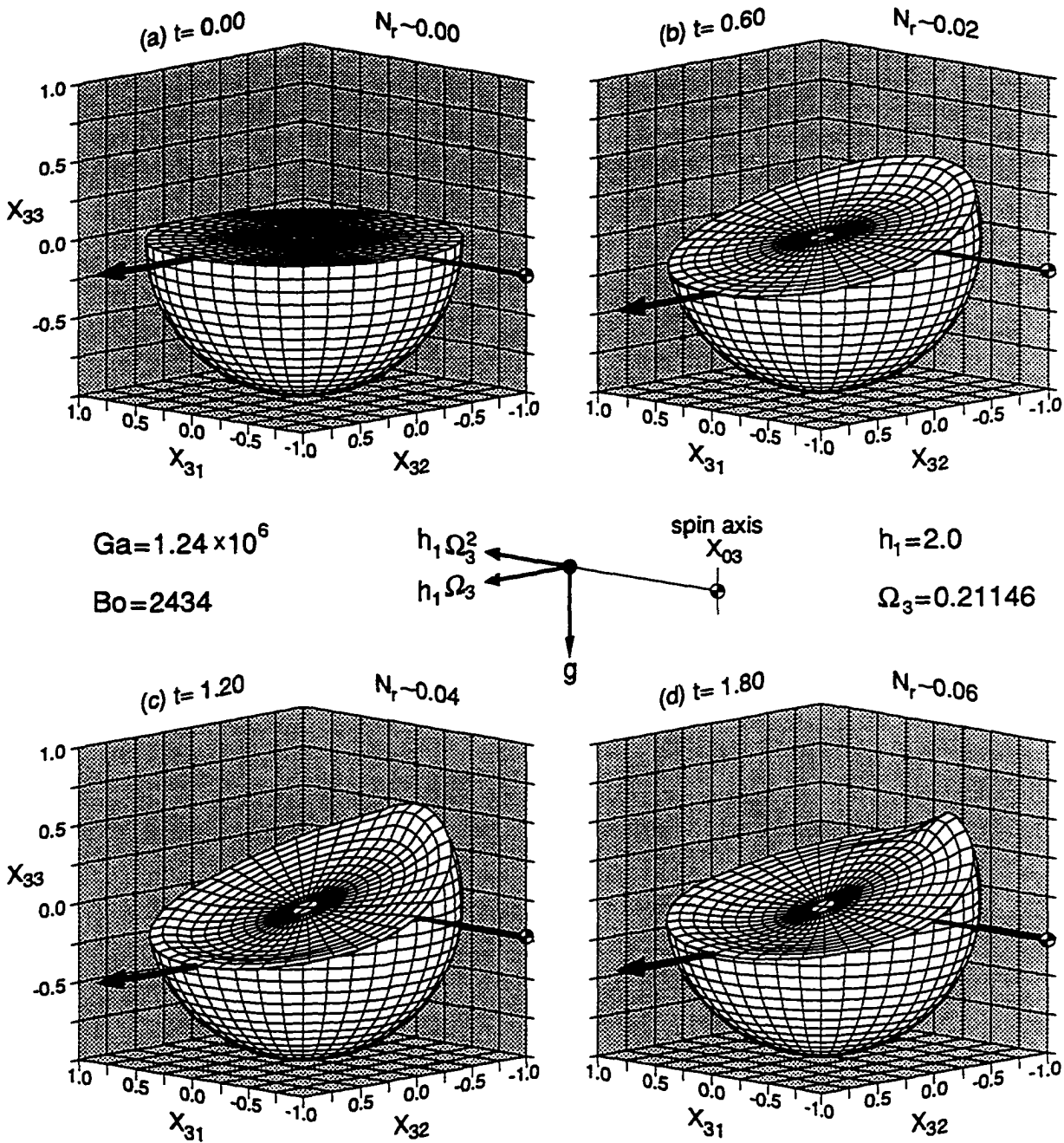


Figure 8.12: Liquid Motion in a Rotating Spherical Container.

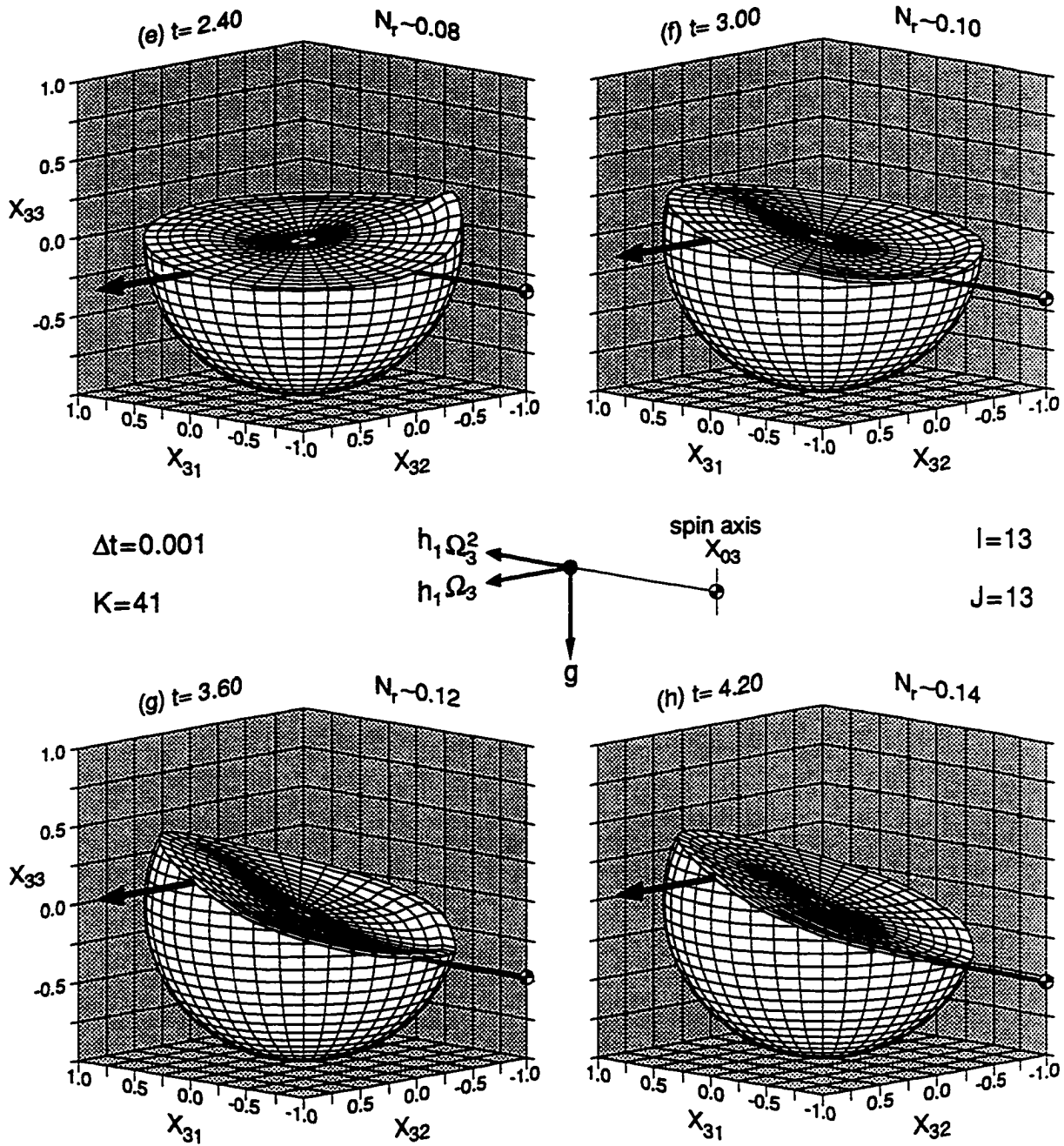


Figure 8.12 (Continued)

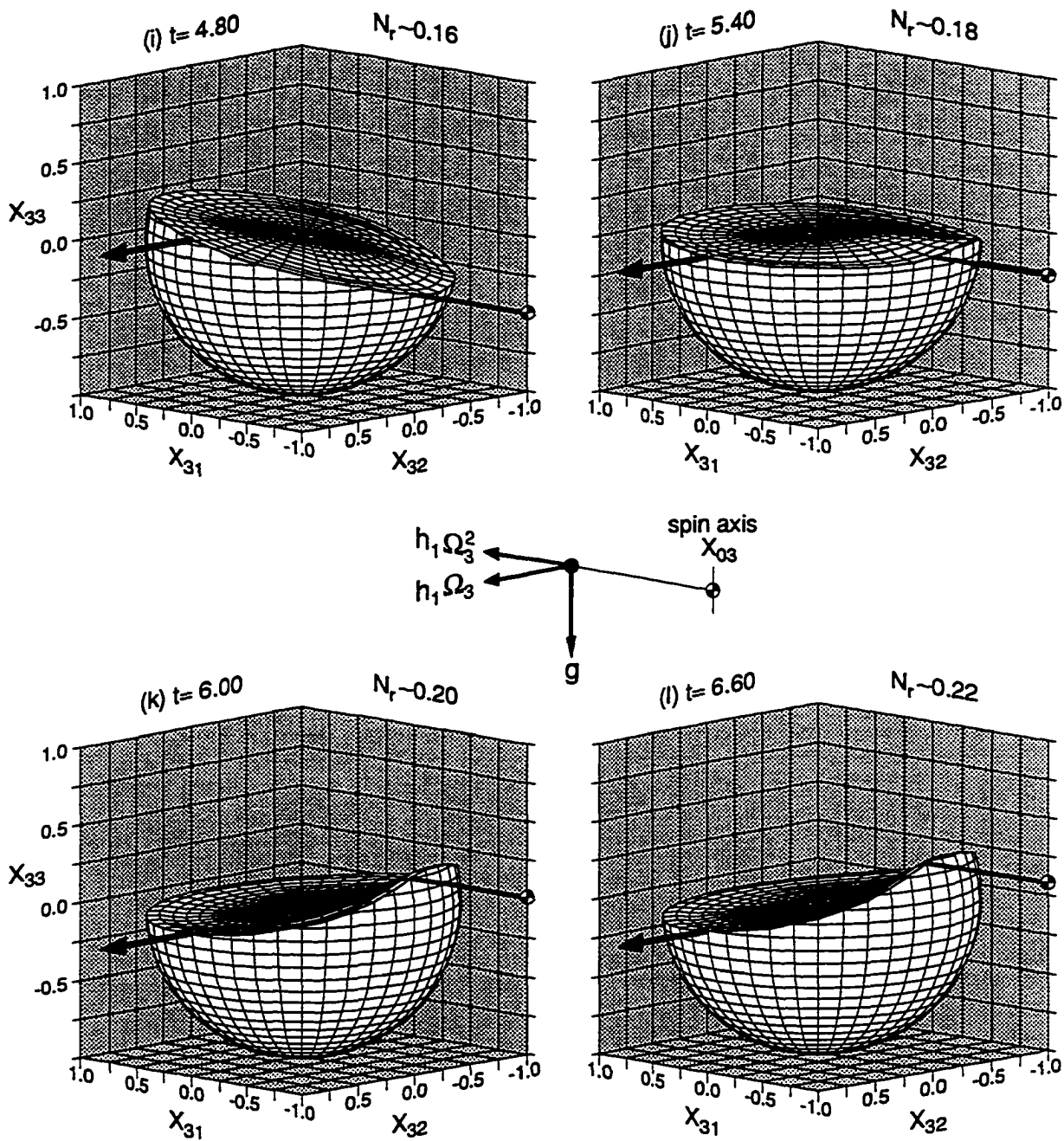


Figure 8.12 (Continued)

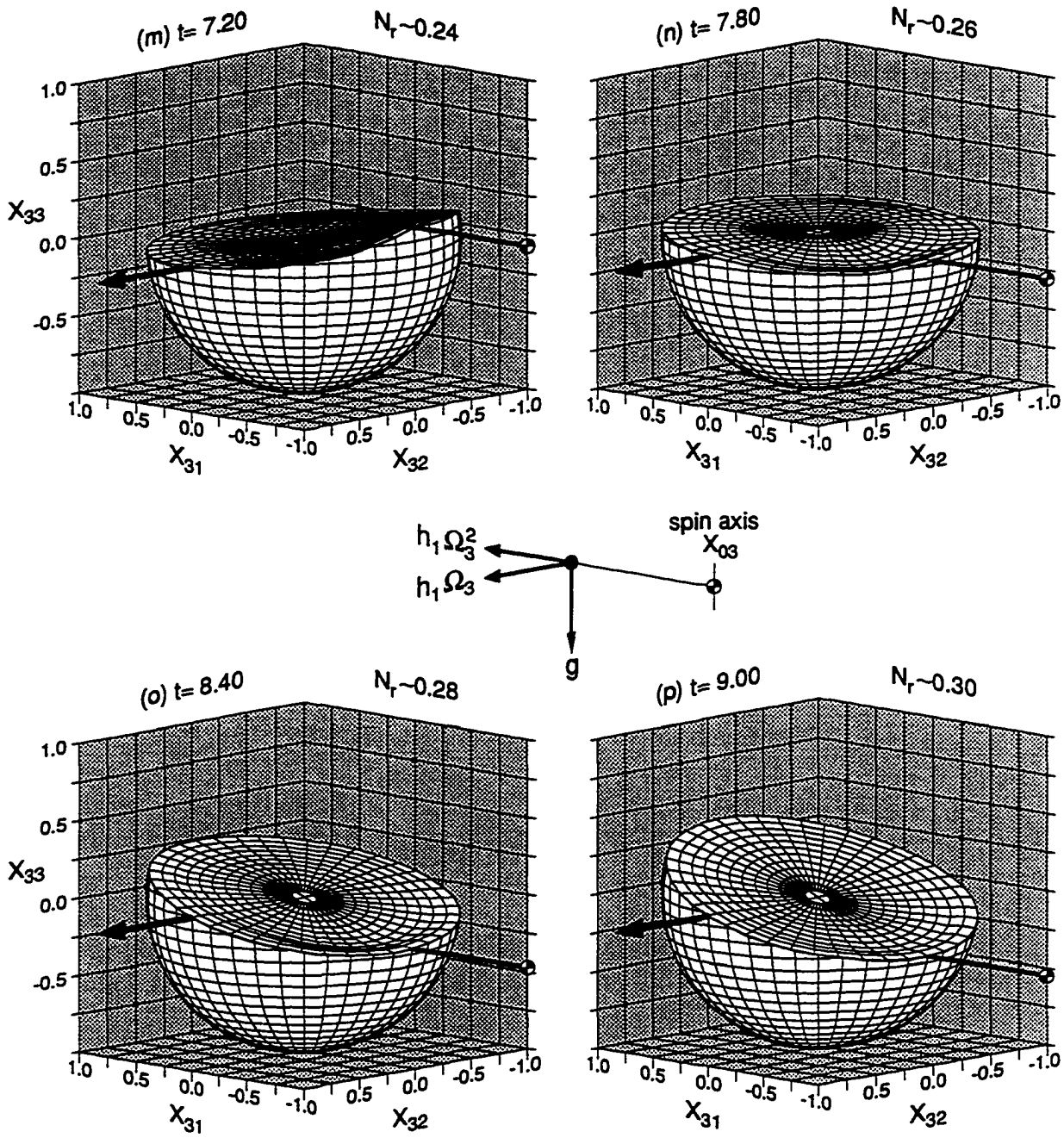


Figure 8.12 (Continued)

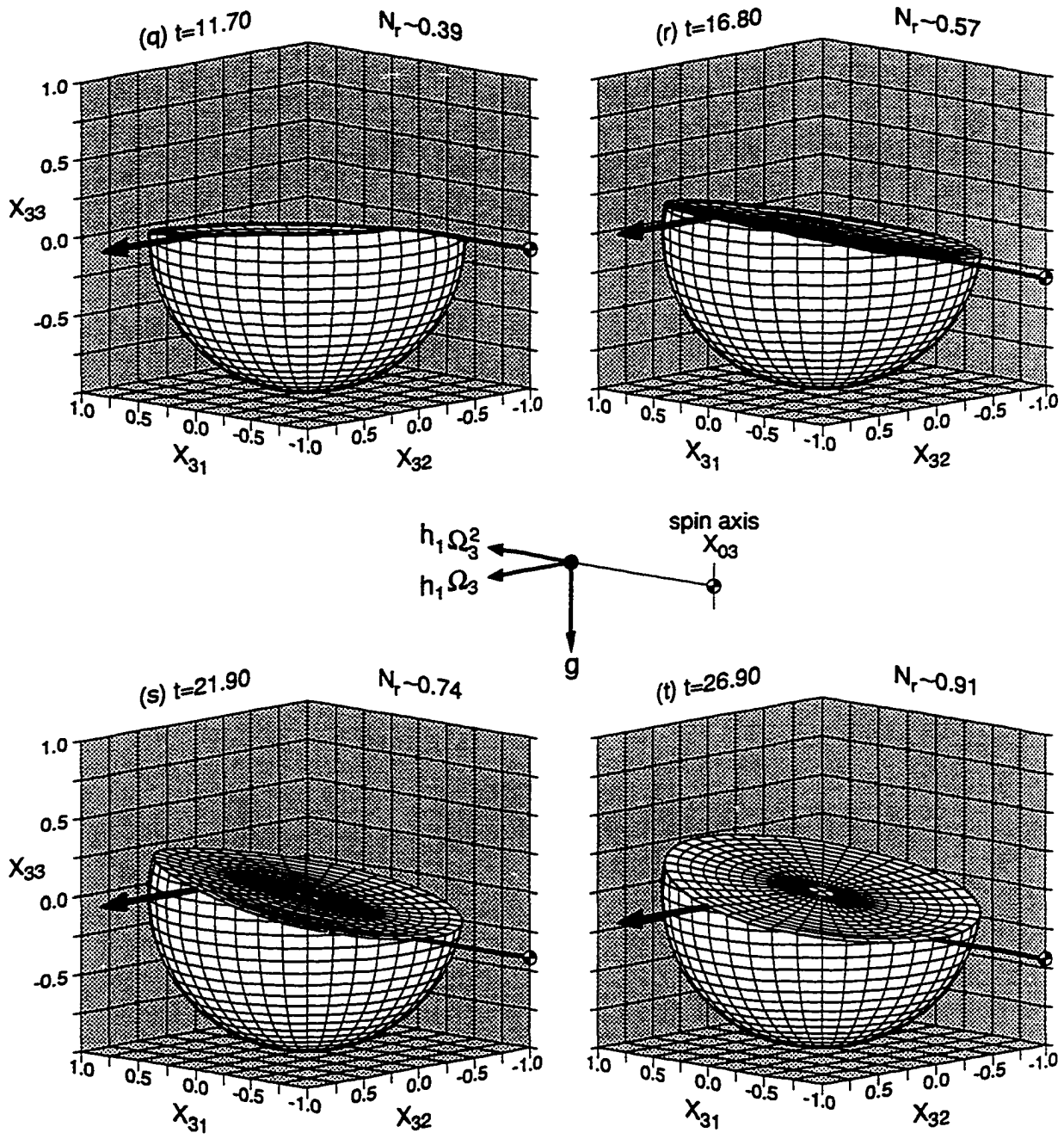


Figure 8.12 (Continued)

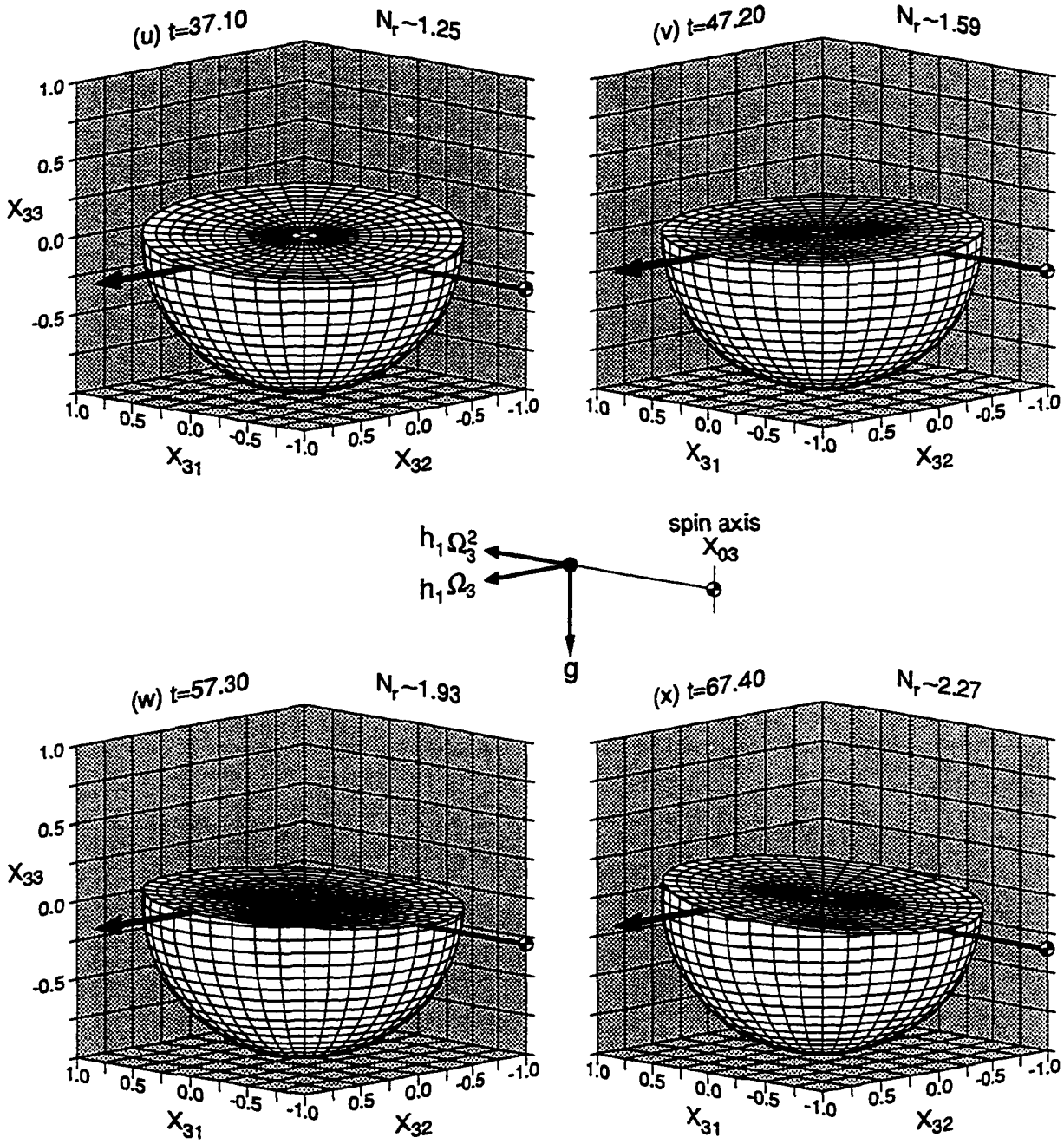


Figure 8.12 (Continued)

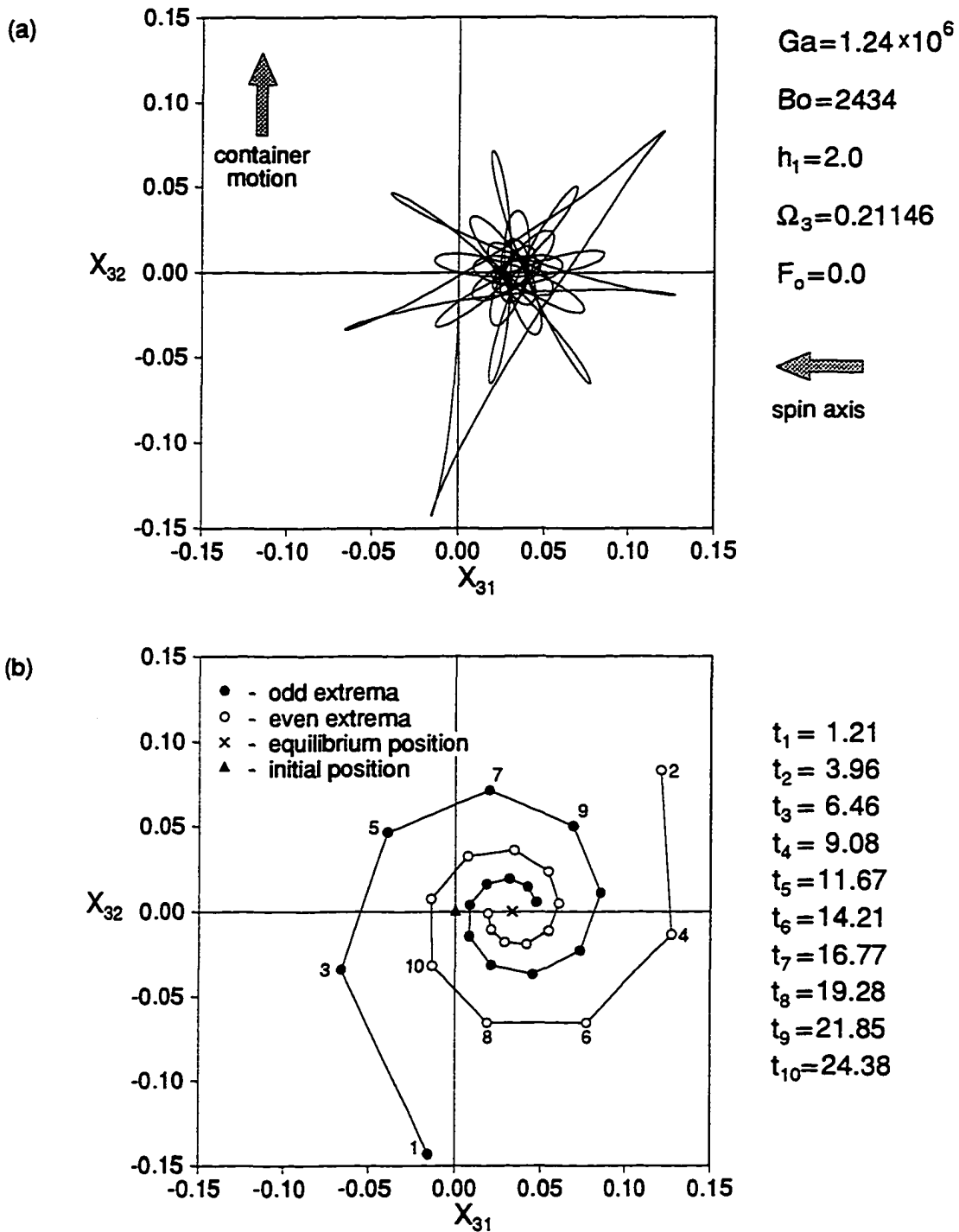


Figure 8.13: Trajectory of the Liquid Center of Gravity for Spherical Spinup.

equation (7.33). The complete trajectory traced by the center of gravity during the flow is projected onto a constant x_{33} plane in Figure 8.13(a). Positions that correspond to a maximum departure from the equilibrium position of the center of gravity are shown in Figure 8.13(b). These positions are consecutively numbered, and the corresponding time values at which they are reached are indicated in the figure. Based on this numbering, they are also labelled as odd and even extremes, since the elapsed time interval between any two consecutive odd (or even) extrema can be used in defining a period, T , for the lateral sloshing component of the liquid motion.

Figure 8.13(b) provides a very nice picture of the slow decay of the liquid flow toward the position of static equilibrium with respect to both gravity and the centrifugal force. The equilibrium position of the center of gravity is indicated in the figure. It is determined from the final parabolic position reached by the free surface as $t \rightarrow \infty$. The final position of the free surface is given by,

$$F(\infty, x_{31}, x_{32}) = C_o + \frac{1}{2}\Omega_3^2 (x_{31}^2 + x_{32}^2) + \Omega_3^2 h_1 x_{31} \quad (8.51)$$

where C_o represents a constant that is determined from a global mass balance. For a given rotation rate, Ω , it is a function of the amount liquid volume within the container. Based on the values of F_o and Ω_3 used for this case, $C_o = -0.01125$. It should also be noted that the equilibrium position of the free surface, as given in equation (8.51), is only approximately correct because it ignores surface tension effects.

The *spiral* like motion of the center of gravity toward its equilibrium position is also depicted in Figure 8.14. The rate at which the rotational component of the liquid motion decays as a result of viscous dissipation is shown in Figure 8.14(a). Here, ω denotes the angular velocity of the center of gravity of the liquid about its equilibrium position. Plotted in the figure is the ratio of ω/Ω_3 , with the values of ω having been averaged over a full cycle time interval. Note that the damping of the rotational component occurs rather slowly. After more than 14 full cycles, the liquid is still rotating at an angular speed which is about 60% of the initial rate.

The numerical result for damping of the lateral sloshing component of the liquid flow is depicted in Figure 8.14(b) in terms of the open circle symbols. Here, S represents the distance of the projected position of the center of gravity from its equilibrium position. It is calculated from the following relation, equation,

$$S(t) = \sqrt{\left(\hat{X}_{31}(t) - \hat{X}_{31}(\infty)\right)^2 + \left(\hat{X}_{32}(t) - \hat{X}_{32}(\infty)\right)^2} \quad (8.52)$$

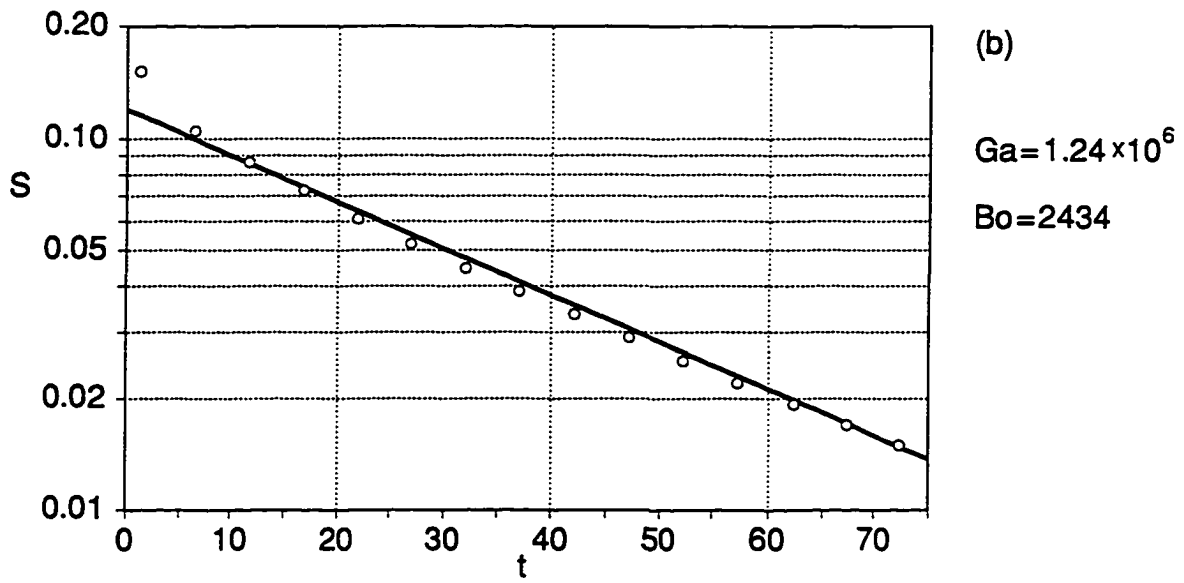
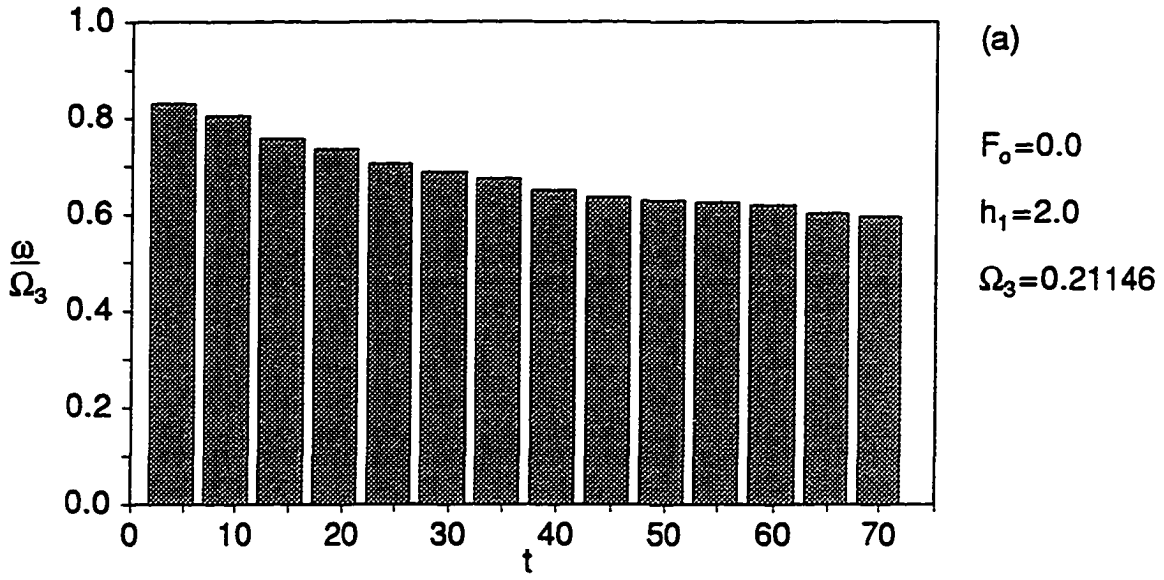


Figure 8.14: Viscous Decay for Spherical Spinup.

where, \hat{X}_{3i} represents the coordinates of the center of gravity of the liquid. The solid line in Figure 8.14(b) is a representation of previous experimental measurements of the damping rate associated with first mode lateral sloshing in spherical containers. A correlation for a *logarithmic form* of the damping rate, δ_R , is given in [1] as equation (4.11b). This correlation, which predicts the value of δ_R as a function of the Galileo number, Ga , is based on several experimental works. The logarithmic damping rate is defined in [1] as,

$$\delta_R \equiv \ln \frac{F_{\max}^n}{F_{\max}^{n+1}} \quad (8.53)$$

where F_{\max} represents the maximum elevation reached by the liquid during a given cycle, and n denotes the cycle number. Assuming that the maximum elevation of the free surface is proportional to maximum departure of the center of gravity from its equilibrium position,

$$\frac{F_{\max}^n}{F_{\max}^{n+1}} \sim \frac{S_{\max}^n}{S_{\max}^{n+1}}$$

then, the result given in [1] can be expressed in terms of a *modulus of decay*, τ , the parameter used in this study for describing the rate of dissipation. Let the exponential variation in $S(t)$ be denoted by,

$$S(t) = S_o e^{-\tau t} \quad (8.54)$$

where S_o denotes its initial value, and τ is the modulus of decay. Substituting in equation (8.53) leads to,

$$\delta_R = \ln \frac{S_o e^{-\tau t}}{S_o e^{-\tau(t+T)}} = \tau T \quad (8.55)$$

where, T denotes the period of oscillation. Thus the value of $\delta_r = 0.14884$ given in [1] is divided by the period, $T_e = 5.15$ (experimental result), to yield $\tau = 0.0289$. This value for τ is used to determine the slope of the solid line in Figure 8.14(b) with the value of S_o chosen for a best fit of the numerical data. Note that with exception of the first numerical data point, the comparison of the present result with the experimental data is excellent.

An excellent agreement was also obtained by comparing the present numerical result for the period of oscillation, T , with previous experimental measurements given in [1] (see Table 2.3). The solution of the spherical spinup case was calculated for somewhat over fourteen cycles. The numerical result for the period of oscillation

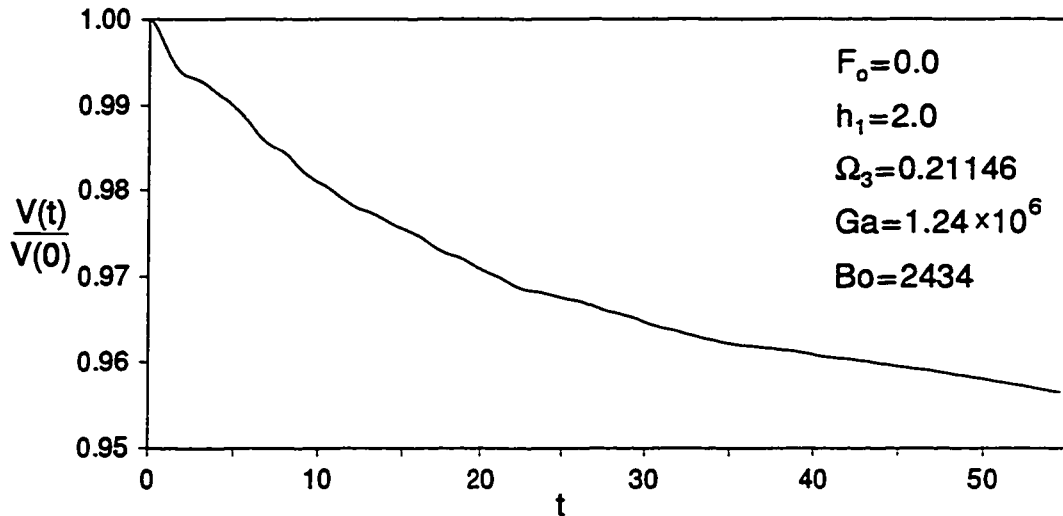


Figure 8.15: Liquid Volume Error for Spherical Spinup.

displayed some variation, generally decreasing with time. A value of $T = 5.25$ was obtained for the first cycle, and a value of $T = 5.04$ for the fourteenth cycle. The average period over these fourteen cycles was equal to $\bar{T} = 5.09$. Experimental measurements for the period associated with first mode sloshing in spherical containers indicate a value of $T_e = 5.15$, which is only 1.15% larger than the numerical result for the average period, \bar{T} .

The truncation error of the solution is not precisely known since no grid resolution studies were conducted. This is in part due to the fairly extensive computational requirements of this case. One measure of the truncation error is provided by the behavior of the calculated dimensionless liquid volume, V . The calculation of V is based on equation (7.34). The variation in $V(t)/V(0)$ is shown in Figure 8.15. The calculated value for V decreased throughout the calculation. This error reached approximately 4.37% after the first ten cycles of sloshing.

The solution for this case was computed to a dimensionless time of $t = 75.0$, using a marching time step of $\Delta t = 0.001$. It required a total of approximately 190 hours of CPU time on an *HP* 700 series machine, with a computational speed of ~ 30 Mflops.

9. CONCLUDING REMARKS

The numerical simulation of liquid sloshing in moving containers has been considered. Numerical models have been developed and applied to both two and three dimensional flows. These models are based on the Navier-Stokes equations, recast in a non-inertial coordinate frame which follows the motion of the container. Singularities produced by the onset of sudden motions have been removed from the formulation using an asymptotic analysis to renormalize the governing equations. A primitive variable formulation is used, and the pressure solution is based on a Poisson equation. The position of the free surface is determined from a kinematic condition. The governing equations are approximated by finite differences which are second order accurate both in time and space. An iterative SOR method is used for the solution of the problem.

Results for several cases involving sloshing in simply translating two and three dimensional rectangular containers have been presented. These include forcing conditions based on sudden changes in the container acceleration, and in the container velocity. The effect of the forcing conditions and the physical properties of the liquid on the sloshing problem have been examined in terms of a parametric study. A forcing condition based on a constant driving external force was also considered. The solution of an axisymmetric spinup problem in a cylindrical container was given. A full three dimensional spinup problem of spherical geometry was also presented.

A brief summary that highlights some of the contributions and conclusions drawn from the study follows.

9.1 Formulation Summary

Sloshing liquid flow is induced as a result of the container motion. A sudden change in the acceleration of the container causes a discontinuous jump in the pressure field. A sudden change in the velocity of the container leads to a discontinuous jump in the velocity field and a momentary singular pressure field. The formulation has been regularized based on an extensive investigation of the asymptotic behavior of the

liquid following these abrupt changes in the motion of the container. The correct set of initial conditions has been determined for both simply translating and rotational sloshing problems. For cases involving a rectangular geometry analytical solutions for the initial conditions were given.

The small but finite interfacial region existing between a liquid and a gas is approximated by a material surface, the *free surface* of the liquid. The requirement that the stress vector be continuous across the interface leads to a zero tangential stress condition, and a normal stress condition which accounts for the pressure difference across the interface. This modeling approximation has the following implications: The free surface of a viscous fluid can not undergo a change in shape without generating vorticity. Since it is also a material surface, viscous diffusion becomes the sole mechanism through which free surface vorticity can enter the interior flow. In the limit of vanishing liquid viscosity, vorticity generated at the free surface remains on the free surface. First law analysis of the interfacial region suggests that the deformation of the free surface is accompanied by a change in its free Helmholtz energy due to surface tension. Furthermore, the displacement of the free surface leads to an increase in the internal energy of the interfacial region due to viscous dissipation. Numerical calculations suggest that the loss of available energy from the system due to dissipation at the free surface of the liquid represents nearly one tenth of the total dissipation loss.

The foundations for a method that simplifies the coupling of the dynamics of the liquid with those of the moving vehicle have been laid out. This method, which is applicable to rigid (non-breathing) containers, utilizes the concept of an *apparent mass* for the liquid, which is formulated in a manner that measures the resistance offered by the liquid to sudden changes in the acceleration experienced by the vehicle. It enables the solution of the solid and liquid equations based on a simple explicit coupling scheme, which offers significant savings over the implicit coupling of the equations. Results obtained by this method indicate that the fundamental frequency of sloshing increases with an increasing liquid payload.

For three dimensional flows in spherical containers an adaptive transformation technique has been developed and implemented which improves the accuracy and extends the range of the model. A transformation is utilized prior to grid generation, which allows for the continuous and interactive transformation of the governing equations to a coordinate system that is best suited for their solution. By following the bulk of the moving liquid, a more nearly orthogonal grid can be generated with less

effort, using a combination of algebraic and elliptic schemes. This either alleviates or eases the one-to-one limitation imposed on the shape of the free surface by the use of a kinematic condition.

9.2 Numerical Method Summary

The following conclusions are drawn from specific experience gained through experimentation with the two dimensional model that was presented in the first part of this study. This experience has been limited to iterative solution methods, and liquid flows that are in essence quasi-periodic in nature. Thus, the extent to which the following conclusions can be generalized to other types of flows or methods of solution is uncertain.

A primitive variable formulation of the incompressible equations requires the use of some form of a pressure correction scheme due to the lack of a specific equation for the pressure variable. The two most popular methods for accomplishing this task, the Artificial Compressibility Method (ACM), and the Pressure Poisson Method (PPM), have been examined in this study (see section 4.4.5). Solutions based on the PPM method satisfied globally the divergence free condition of the flowfield better. The magnitude of the average dilatation for a PPM solution tended to be an order of magnitude smaller than the corresponding value based on an ACM solution. Algorithms based on the ACM method, which solved the momentum and pressure equations simultaneously, tended to be slower than PPM algorithms which solved these equations separately.

Compared to first order, second order time differencing was found to greatly improve the long term accuracy of the numerical solution. For the quasi-periodic type of flows considered in this study, where long term accuracy is desirable, the use of first order time differencing is not recommended.

The explicit integration of the free surface kinematic condition was also found to have a negative impact on the long term accuracy of the solution. If the available computational resources prohibit the use of an implicit integration scheme, then it is worth while considering alternatives to the straight forward explicit integration of the kinematic equation. For example, rather than basing the integration on calculated velocity values from the previous time level, using extrapolated velocity values at the current time level was found to significantly improve the accuracy of the explicit method.

9.3 Summary of Results

Detailed information on the free surface position, the velocity field, and the pressure field has been given for several representative cases. Information on the fundamental sloshing frequency and the rate of viscous dissipation was also provided. The numerical result demonstrated excellent agreement with analytical and experimental results, when such comparisons were possible.

The flow of the sloshing liquid is intricate and complex. Noteworthy is that while the forcing of the liquid results in the excitation of a wide spectrum of frequencies, the flow appears for the most part to be almost periodic because the amplitude of oscillations associated with the fundamental frequency tends to dominant over other frequencies. The fundamental frequency is affected by several factors. Its magnitude increases with increasing liquid depth and decreases with increasing liquid viscosity or amplitude of forcing. It also increases with increasing surface tension effects. The rate of viscous dissipation increases with increasing liquid viscosity (decreasing Ga), and also with increasing surface tension effects (decreasing Bo). It also increases with decreasing liquid depth, but appears to be insensitive to the type of forcing.

In a regime dominated by surface tension effects, the amplitude of the liquid oscillations is small, while their frequency is high. The liquid oscillations appear to be more like free surface vibrations. The static equilibrium position of the liquid may also be undeterminable in advance, if the net body force acting on the liquid is not normal to the initial position of the free surface. In a regime where surface tension forces are of comparable strength to inertial, body, and surface forces, the forcing of the liquid may lead to its sub-harmonic excitation, thus making the liquid oscillations to appear to be more non-periodic.

APPENDIX A: FREE SURFACE DYNAMIC CONDITIONS

The dynamic free surface conditions have been defined in Chapter (3) in terms of local curvilinear coordinates by the following equations,

$$\frac{\partial \bar{u}_\tau}{\partial n} - \kappa \bar{u}_\tau + \frac{\partial \bar{u}_n}{\partial \tau} = 0 \quad (\text{tangential stress}) \quad (\text{A.1a})$$

$$\bar{p} - \bar{p}_o = 2\mu \frac{\partial \bar{u}_n}{\partial n} + \kappa \mathcal{Y} \quad (\text{normal stress}) \quad (\text{A.1b})$$

where the normal, \bar{e}_n , and tangential, \bar{e}_τ , unit vectors at the free surface (see Figure 3.2) are defined by:

$$\bar{e}_n = \frac{-\bar{F}_x \bar{i} + \bar{j}}{\sqrt{1 + \bar{F}_x^2}} \quad \text{and} \quad \bar{e}_\tau = \frac{\bar{i} + \bar{F}_x \bar{j}}{\sqrt{1 + \bar{F}_x^2}} \quad (\text{A.2})$$

with,

$$\bar{F}_x = \frac{\partial \bar{F}}{\partial \bar{x}}, \quad \bar{F}_{xx} = \frac{\partial^2 \bar{F}}{\partial \bar{x}^2}, \quad \text{and} \quad \kappa = -\frac{\bar{F}_{xx}}{(1 + \bar{F}_x^2)^{\frac{3}{2}}}$$

The normal, \mathcal{U}_n , and tangential, \mathcal{U}_τ , velocity components along the free surface are given by,

$$\mathcal{U}_n \equiv \vec{V} \cdot \bar{n} = \frac{-\bar{F}_x \bar{u} + \bar{v}}{\sqrt{1 + \bar{F}_x^2}} \quad \text{and} \quad \mathcal{U}_\tau \equiv \vec{V} \cdot \bar{\tau} = \frac{\bar{u} + \bar{F}_x \bar{v}}{\sqrt{1 + \bar{F}_x^2}} \quad (\text{A.3})$$

The derivatives in terms of the curvilinear coordinates (n, τ) which appear in equations (A.1) can be decomposed into rectilinear derivatives in terms of the (\bar{x}, \bar{y}) coordinate system according to the following relations:

$$\frac{\partial}{\partial n} \equiv \vec{\nabla} \cdot \bar{e}_n = \frac{1}{\sqrt{1 + \bar{F}_x^2}} \left(-\bar{F}_x \frac{\partial}{\partial \bar{x}} + \frac{\partial}{\partial \bar{y}} \right) \quad (\text{A.4a})$$

$$\frac{\partial}{\partial \tau} \equiv \vec{\nabla} \cdot \bar{e}_\tau = \frac{1}{\sqrt{1 + \bar{F}_x^2}} \left(\frac{\partial}{\partial \bar{x}} + \bar{F}_x \frac{\partial}{\partial \bar{y}} \right) \quad (\text{A.4b})$$

Using equations (A.3, and A.4), the dynamic free surface conditions as given by equations (A.1) can be transformed into the following forms,

$$(1 - \bar{F}_x^2) \left(\frac{\partial \bar{u}}{\partial \bar{y}} + \frac{\partial \bar{v}}{\partial \bar{x}} \right) - 2 \bar{F}_x \left(\frac{\partial \bar{u}}{\partial \bar{x}} - \frac{\partial \bar{v}}{\partial \bar{y}} \right) = 0 \quad (\text{A.5a})$$

$$\bar{p} - \bar{p}_o = \frac{\mu}{1 + \bar{F}_x^2} \left[\left(\frac{\partial \bar{v}}{\partial \bar{y}} - \bar{F}_x \frac{\partial \bar{v}}{\partial \bar{x}} \right) - \bar{F}_x \left(\frac{\partial \bar{u}}{\partial \bar{y}} - \bar{F}_x \frac{\partial \bar{u}}{\partial \bar{x}} \right) \right] + \kappa \mathcal{Y} \quad (\text{A.5b})$$

which were given as equations (3.13) in Chapter (3).

APPENDIX B: BOUNDARY LAYER SOLUTION

An asymptotic analysis of the governing equations at $\bar{t} = 0$ was presented in section 3.2.1. For cases that involve a sudden change in the velocity of the container the pressure at $\bar{t} = 0$ is singular. Based on the scales identified in equation (3.18), the governing equations were reduced into a simplified form, and solve to obtain the analytical solution given in terms of equations (3.32). This solution is valid in the core of the liquid, away from the immediate vicinity of the container walls and the free surface. Here, similarity solutions will be developed by reconsidering the balance of terms in the governing equations within thin boundary layers along each of these boundaries. Since the form of the resulting equation for the boundary layers along each of the container walls is identical, the focus of the analysis will be on the boundary layer along the bottom wall, and similarity solutions for the two side walls will be simply given. The boundary layer along the free surface will be considered separately.

The characteristic scales of equation (3.18) suggest that within a small region of thickness $\bar{\delta} \sim \sqrt{\nu \Delta \bar{t}}$, next to the bottom boundary at $\bar{y} = 0$, the viscous term becomes of order, $\sim \mathcal{O}(U_o/\Delta \bar{t})$, the same order as the remaining dominant terms in the equation (3.18). Within this region, continuity suggests that $\Delta \bar{v} \sim \bar{\delta} \Delta \bar{v}/L$. The balance of terms in the vertical component of the momentum equation indicates that the change in pressure across the boundary layer is of order, $\Delta \bar{p} \sim \rho \Delta \bar{u} \bar{\delta}^2/\Delta \bar{t}$. The dependent and independent variables of the problem are nondimensionalized according to scales appropriate for the boundary layer, according to:

$$t_* = \frac{\bar{t}}{\sqrt{L/g}}, \quad x_* = \frac{\bar{x}}{L} \quad \text{and} \quad y_* = \frac{\bar{y}}{\sqrt{\nu \bar{t}}} \quad (\text{B.1a})$$

$$u_*^+ = \frac{\bar{u}}{\sqrt{Lg}}, \quad v_*^+ = \bar{v} \sqrt{\frac{L}{g\nu \bar{t}}} \quad \text{and} \quad p_*^+ = \frac{\bar{p}}{\rho g L} \quad (\text{B.1b})$$

Using the above expressions, the governing equations are nondimensionalized and integrated in a small neighborhood of $t=0$ to obtain the following set of initial condition

equations for the bottom wall boundary layer:

$$\frac{\partial^2 u_*^+}{\partial y_*^2} + \frac{1}{2} y_* \frac{\partial u_*^+}{\partial x_*} - u_*^+ = U_o + \frac{\partial \Pi_*}{\partial x_*} \quad (\text{B.2a})$$

$$\frac{\partial \Pi_*}{\partial y_*} = 0 \quad (\text{B.2b})$$

$$\frac{\partial v_*^+}{\partial y_*} = -\frac{\partial u_*^+}{\partial x_*} \quad (\text{B.2c})$$

The solution of the above set of equations can be obtained as follows: Based on equation (B.2b), Π_* remains constant across the boundary layer and can be matched to Π for the core flow, evaluated at the edge of the boundary layer,

$$\Pi_*(x_*, y_*)|_{y_*=\infty} = \Pi(x, y)|_{y=0} \quad (\text{B.3})$$

Since Π_* is independent of y_* , the right hand side of equation (B.2a) also becomes independent of y_* , and according to equation (3.30b) is in fact equal to the core value of u^+ , evaluated at $y = 0$. Thus, the right hand side of equation (B.2a) can be replaced by the negative of u_∞^+ , which is defined as follows:

$$u_\infty^+ \equiv u^+(x, y)|_{y=0} = -U_o - \frac{\partial \Pi}{\partial x}|_{y=0} \quad (\text{B.4})$$

Equation (B.2a) can be rearranged into a form that facilitates its analytical solution by redefining new variables,

$$W \equiv u_*^+ - u_\infty^+ \quad \text{and} \quad z \equiv \frac{y_*}{2} \quad (\text{B.5})$$

which when introduced into equation (B.2a) lead to the following form:

$$\frac{\partial^2 W}{\partial z^2} + 2z \frac{\partial W}{\partial z} - 4W = 0 \quad (\text{B.6})$$

This equation can be solved subject to boundary conditions that require u_*^+ to vanish at the wall, and to match the core velocity as $y_* \rightarrow \infty$. Based on these conditions, the corresponding boundary condition in terms of z and W are given by,

$$W = -u_\infty^+ \quad \text{at} \quad z = 0 \quad (u_*^+ = 0 \quad \text{at} \quad y_* = 0) \quad (\text{B.7a})$$

$$\lim_{z \rightarrow \infty} W = 0 \quad \left(\lim_{y_* \rightarrow \infty} u_*^+ = u_\infty^+ \right) \quad (\text{B.7b})$$

An analytical solution for equation (B.6) can be determined in terms of the *error function*, $\text{erf}(x)$. A definition for the error function and further information on the solution of this equation can be found in [76]. The resulting velocity profile for the horizontal velocity component with the bottom boundary layer is given by,

$$u_{\star}^{+}(y_{\star}) = u_{\infty}^{+} \mathcal{G}(y_{\star}) \quad (\text{B.8a})$$

where \mathcal{G} is defined by,

$$\mathcal{G}(x) \equiv \left(1 + \frac{x}{2}\right) \text{erf}\left(\frac{x}{2}\right) - \frac{x^2}{2} + \frac{x}{\sqrt{\pi}} e^{-x^2/4} \quad (\text{B.8b})$$

An analytical expression for the vertical velocity component within the boundary layer, v_{\star}^{+} , can be found by integration of equation (B.2c) based on the above profile for u_{\star}^{+} . The result is,

$$v_{\star}^{+} = \left(\frac{\partial u_{\infty}^{+}}{\partial x} \Big|_{y=0} \right) \mathcal{F}(y_{\star}) \quad (\text{B.9a})$$

where \mathcal{F} is defined by,

$$\mathcal{F}(x) \equiv \left(\frac{4}{3\sqrt{\pi}} + x \right) + \left(x + \frac{x^3}{6} \right) \left[1 - \text{erf}\left(\frac{x}{2}\right) \right] - \frac{4}{3\sqrt{\pi}} \left(1 + \frac{x}{2} \right) e^{-x^2/4} \quad (\text{B.9b})$$

The boundary layer flow along the bottom wall has been defined by a similarity solution in terms of equations (B.3), (B.8), and (B.9). The same velocity profiles exist within boundary layer along the container side walls. The flow within these layers can be described by the following similarity solutions:

Left wall at $x = 0$:

$$v_{\star}^{+}(x_{\star}) = v_{\infty}^{+} \mathcal{G}(x_{\star}) \quad (\text{B.10a})$$

$$u_{\star}^{+}(x_{\star}) = \left(\frac{1}{F_o} \frac{\partial v_{\infty}^{+}}{\partial y} \Big|_{x=0} \right) \mathcal{F}(x_{\star}) \quad (\text{B.10b})$$

$$\Pi_{\star}(x_{\star}, y_{\star})|_{x_{\star}=\infty} = \Pi(x, y)|_{x=0} \quad (\text{B.10c})$$

where,

$$x_{\star} = \frac{\bar{x}}{\sqrt{\nu \bar{t}}}, \quad y_{\star} = \frac{\bar{y}}{LF_o}, \quad u_{\star}^{+} = \bar{u} \sqrt{\frac{L}{g\nu \bar{t}}}, \quad v_{\star}^{+} = \frac{\bar{v}}{\sqrt{Lg}} \quad (\text{B.10d})$$

Right wall at $x = 1$:

$$v_{\star}^{+}(x_{\star}) = v_{\infty}^{+} \mathcal{G}(x_{\star}) \quad (\text{B.11a})$$

$$u_*^+(x_*) = \left(\frac{1}{F_o} \frac{\partial v_\infty^+}{\partial y} \Big|_{x=1} \right) \mathcal{F}(x_*) \quad (\text{B.11b})$$

$$\Pi_*(x_*, y_*)|_{x_*=\infty} = \Pi(x, y)|_{x=1} \quad (\text{B.11c})$$

where,

$$x_* = \frac{L - \bar{x}}{\sqrt{\nu \bar{t}}}, \quad y_* = \frac{\bar{y}}{LF_o}, \quad u_*^+ = \bar{u} \sqrt{\frac{L}{g\nu \bar{t}}}, \quad v_*^+ = \frac{\bar{v}}{\sqrt{Lg}} \quad (\text{B.11d})$$

and v_∞^+ represents the matching value of the vertical velocity component of the core flow,

$$v_\infty^+ = v^+(x, y)|_{x=0} \quad (\text{Left B.L.}) \quad \text{or} \quad v_\infty^+ = v^+(x, y)|_{x=1} \quad (\text{Right B.L.})$$

The inviscid solution for the core flow at $t = 0^+$, given by equations (3.32), fails to satisfy the tangential stress condition (3.10) at the free surface. An asymptotic analysis of the governing equations in a small region next to the free surface, where the inviscid solution suggests that $u \approx U_o$, and $\Pi \approx 0$, indicates that the dependent and independent variables must be rescaled within a boundary layer of thickness $\bar{\delta} \sim \sqrt{\nu \Delta \bar{t}}$ according to:

$$t_* = \frac{\bar{t}}{\sqrt{L/g}}, \quad x_* = \frac{\bar{x}}{L} \quad \text{and} \quad y_* = \frac{\bar{F}_o - \bar{y}}{\sqrt{\nu \bar{t}}} \quad (\text{B.12a})$$

$$\bar{u}^+ = \sqrt{Lg} \left(\frac{\sqrt{\nu \bar{t}}}{L} u_*^+ - U_o \right), \quad \bar{v}^+ = \sqrt{Lg} \left(\frac{\nu \bar{t}}{L^2} v_*^+ + v_\infty^+ \right) \quad (\text{B.12b})$$

$$\bar{p}^+ = (\rho g L) p_*^+ \quad (\text{B.12c})$$

where v_∞^+ represents the value of the normal velocity component of the core flow,

$$v_\infty^+(x_*) \equiv v^+(x, y)|_{y=1}$$

Note that u_*^+ and v_*^+ represent corrections to the inviscid solution, and that for within an order $\sim \mathcal{O}(\sqrt{Lg})$ they are both negligible.

The liquid flow within a boundary layer along the free surface at time $t = 0^+$ is given by the solution of the following set of equations,

$$\frac{\partial^2 u_*^+}{\partial y_*^2} + \frac{1}{2} y_* \frac{\partial u_*^+}{\partial y_*} - \frac{1}{2} u_*^+ = 0 \quad (\text{B.13a})$$

$$\frac{\partial v_*^+}{\partial y_*} = \frac{\partial u_*^+}{\partial x} \quad (\text{B.13b})$$

$$\frac{\partial p_*^+}{\partial y_*} = 0 \quad (\text{B.13c})$$

subject to boundary conditions,

$$\lim_{y_* \rightarrow \infty} u_*^+ = 0, \quad \lim_{y_* \rightarrow \infty} v_*^+ = 0, \quad \text{and} \quad \lim_{y_* \rightarrow \infty} p_*^+ = 0 \quad (\text{B.13d})$$

and along the free surface, at $y_* = 0$, the tangential stress condition,

$$\left. \frac{\partial u_*^+}{\partial y_*} \right|_{y_* = 0} = \frac{\partial v_\infty^+}{\partial x} \quad (\text{B.13e})$$

The analytical solution of equations (B.13) is given in terms of the following expressions,

$$u_*^+ = \frac{\partial v_\infty^+}{\partial x} \left(\frac{2}{\sqrt{\pi}} e^{-x_*^2/4} - \frac{x_*}{2} \left[1 - \operatorname{erf} \left(\frac{x_*}{2} \right) \right] \right) \quad (\text{B.14a})$$

$$v_*^+ = \frac{\partial^2 v_\infty^+}{\partial x^2} \left(\left[1 + \frac{y_*^2}{2} \right] \left[1 - \operatorname{erf} \left(\frac{y_*}{2} \right) \right] - \frac{y_*}{\sqrt{\pi}} e^{-y_*^2/4} \right) \quad (\text{B.14b})$$

$$p_*^+ = 0 \quad (\text{B.14c})$$

The flowfield within the free surface boundary layer is then determined by the superposition of the inviscid core solution and these viscous corrections according to,

$$u^+ = u_*^+ - U_o, \quad \text{and} \quad v^+ = v_*^+ + v_\infty^+ \quad (\text{B.15})$$

APPENDIX C: TRANSFORMATION METRICS

The position of a given point in the nutating coordinate system x_{1i} can be related to its respective coordinates in the x_{0i} coordinate system by,

$$x_{1i} = \alpha_{ji} x_{0j}$$

where the metrics of the transformation in terms of the three Euler angles ψ_i are given by,

$$\alpha_{ij} = \begin{pmatrix} C_3 C_2 & C_3 S_2 S_1 - S_3 C_1 & C_3 S_2 C_1 + S_3 S_1 \\ S_3 C_2 & S_3 S_2 S_1 + C_3 C_1 & S_3 S_2 C_1 - C_3 S_1 \\ -S_2 & C_2 S_1 & C_2 C_1 \end{pmatrix} \quad (\text{C.1})$$

where for equation (C.1), $S_i = \sin(\psi_i)$ and $C_i = \cos(\psi_i)$.

The transformation from body centered to the body fixed coordinate system is given by,

$$x_{3i} = \alpha_{ij}^* x_{2j}$$

where the transformation metrics in terms of the deformation angles, ϑ_i , are given by,

$$\alpha_{ij}^* = \begin{pmatrix} C_3 C_2 & C_3 S_2 S_1 - S_3 C_1 & C_3 S_2 C_1 + S_3 S_1 \\ S_3 C_2 & S_3 S_2 S_1 + C_3 C_1 & S_3 S_2 C_1 - C_3 S_1 \\ -S_2 & C_2 S_1 & C_2 C_1 \end{pmatrix} \quad (\text{C.2})$$

where for equation (C.2), $S_i = \sin(\vartheta_i)$ and $C_i = \cos(\vartheta_i)$.

The transformation from the x_3 to the x_4 coordinate system is described by,

$$x_{4i} = s_{ji} x_{3j}$$

where the metrics s_{ij} are defined in terms of the surface tracking angles, ϕ_2 and ϕ_3 by,

$$s_{ij} = \begin{pmatrix} \cos(\phi_2) \cos(\phi_3) & -\cos(\phi_2) \sin(\phi_3) & -\sin(\phi_2) \\ \sin(\phi_3) & \cos(\phi_3) & 0 \\ \sin(\phi_2) \cos(\phi_3) & -\sin(\phi_2) \sin(\phi_3) & \cos(\phi_2) \end{pmatrix} \quad (\text{C.3})$$

BIBLIOGRAPHY

- [1] Abramson, H. N., "The Dynamic Behavior of Liquids in Moving Containers." NASA Report No. NASA SP-106, National Aeronautics and Space Administration, Washington, D.C., 1966.
- [2] Peterson, L. D., Crawley, E. F., and Hansman, R. J. "Nolinear Fluid Slosh Coupled to the Dynamics of a Spacecraft." *AIAA Journal*, 27, No. 9, 1230-1240, 1989.
- [3] Kana, D. D. "Validated Spherical Pendulum Model for Rotary Liquid Slosh.", *Journal of Spacecraft and Rockets*, 26, No. 3, 188-195, 1989.
- [4] Lamb, H. *Hydrodynamics*. Cambridge University Press/Dover Publications Inc., New York, 1945.
- [5] Zedd, M. F., and Dodge, F. T., "Energy Dissipation of Liquids in Nutating Spherical Tanks Measured by a Forced Motion-Spin Table." NRL Report No. 8932, Naval Research Laboratory, Washington, D.C., 1985.
- [6] Chen, W., Haroun, M. A., and Liu, F. "Large Amplitude Liquid Sloshing in Seismically Excited Tanks", *Earthquake, Engineering, and Structural Dynamics Journal*, Vol. 25, 653-69, 1996.
- [7] Ye, Z., and Birk, A. M. "Fluid Pressures in Partially Liquid-Filled Horizontal Cylindrical Vessels Undergoing Impact Acceleration", *Journal of Pressure and Vessel Technology*, Vol. 116, 449-58, 1994.
- [8] Sun, L. M., Fujino, Y., and Chaiseri, P. "The Properties of Tuned Liquid Dampers Using a TMD Analogy", *Earthquake, Engineering, and Structural Dynamics Journal*, Vol. 24, 967-77, 1995.
- [9] Sun, L. M., Fujino, Y., and Koga, K. "A Model of Tuned Liquid Damper for Suppressing Pitching Motions of Structures", *Earthquake, Engineering, and Structural Dynamics Journal*, Vol. 24, 625-636, 1995.
- [10] Fujino, Y., Sun, L., and Pacheco, B. M. "Tuned Liquid Damper (TLD) for Suppressing Horizontal Motion of Structures", *Journal of Engineering Mechanics*, Vol. 118, 2017-30, 1992.

- [11] Greenspan, H. P. *The Theory of Rotating Fluids*. Cambridge University Press, Cambridge, 1969.
- [12] Feng, Z. C., and Sethna, P. R. "Symmetry-Breaking Bifurcations in Resonant Surface Waves". *Journal of Fluid Mechanics*, 199, 495-518, 1989.
- [13] Simonelli, F., and Gollub, J. P. "Surface Wave Mode Interactions: Effects of Symmetry and Degeneracy." *Journal of Fluid Mechanics*, 199, 471-494, 1989.
- [14] Stoodt, T. J., and Slatery, J. C. "Effect of the Interfacial Viscosities upon Displacement.", *AIChE Journal*, 30, 564-568, 1984.
- [15] Scriven, L. E. "Dynamics of a Fluid Interface: Equation of Motion for Newtonian Surface Fluids." *Chemical Engineering Science Journal*, 12, 98-108, 1960.
- [16] Aris, R. *Vectors, Tensors, and the Basic Equations of Fluid Mechanics*. Prentice-Hall Inc., Englewood Cliffs, N.J., 1962.
- [17] Slattery, J. C. "General Balance Equation for a Phase Interface.", *I&EC Fundamentals*, 6, 108-115, 1967.
- [18] Wei, L. Y., Schmidt, W., and Slattery, J. C. "Measurement of the Surface Dilational Viscosity." *Journal of Colloid Interface Science*, 48, 1-13, 1974.
- [19] Gupta, L., and Wassan, D. T. "Surface Shear Viscosity and Related Properties of Adsorbed Surfactant Films." *I&EC Fundamentals*, 13, 26-33, 1974.
- [20] Jiang, T. S., Chen, J. D., and Slattery, J. C. "Nonlinear Interfacial Stress-Deformation Behavior Measured with Several Interfacial Viscometers." *Journal of Colloid and Interface Science*, 96, 8-19, 1983.
- [21] Wassan, D. T., Gupta, L., and Vora, M. K. "Interfacial Shear Viscosity at Fluid Interfaces.", *AIChE Journal*, 17, 1287-1295, 1971.
- [22] Huh, C., and Mason, S. G., "The Steady Movement of a Liquid Meniscus in a Capillary Tube." *Journal of Fluid Mechanics*, 81, 401-409, 1977.
- [23] Goldstein, S., *Modern Developments in Fluid Mechanics*, Dover Publications, New York, 1965.
- [24] Dussan V., E. B., and Davis, S. H., "On the Motion of a Fluid-Fluid Interface Along a Solid Surface". *Journal of Fluid Mechanics*, 65, 71-95, 1974.
- [25] Dussan V., E. B. "The Moving Contact Line: The Slip Boundary Condition". *Journal of Fluid Mechanics*, 77, 665-684, 1976.
- [26] Stokes, G. G., "On the Theory of Oscillatory Waves." *Transactions of the Cambridge Philosophical Society*, 8, 441-455, 1847.

- [27] Boussinesq, J., "Théorie de l'Intumescence Liquide Appelée onde Solitaire ou de Translation se Propageant dans un Canal Rectangulaire". *Comptes Rendus*, 72, 755-759, 1871.
- [28] Rayleigh, Lord, "On Waves." *Philosophical Mag.*, 5, 257-279, 1876.
- [29] McIver, P., "Sloshing Frequencies for Cylindrical and Spherical Containers Filled to an Arbitrary Depth." *Journal of Fluid Mechanics*, 201, 243-257, 1989.
- [30] McIver, P., and McIver, M., "Sloshing Frequencies of Longitudinal Modes for a Liquid Contained in a Trough." *Journal of Fluid Mechanics*, 252, 525-541, 1993.
- [31] Penney, W. G., and Price, A. T., "Some Gravity Wave Problems in the Motion of Perfect Liquids". *Philosophical Transactions of the Royal Society of London*, A244, 254-284, 1952.
- [32] Hogan, S. J., "Some Effects of Surface Tension on Steep Water Waves, Part 2", *Journal of Fluid Mechanics*, 96, 417-445, 1980.
- [33] Batchelor, G. K., *An Introduction to Fluid Dynamics*, Cambridge University Press, Cambridge, 1967.
- [34] Proudman, J., "On the Motions of Solids in a Liquid Possessing Vorticity". *Proceedings of the Royal Society of London*, A92, 408-24, 1916.
- [35] Taylor, G. I., "Experiments with Rotating Fluids". *Proceedings of the Royal Society of London*, A100, 114-21, 1921.
- [36] Pedlosky, J., *Geophysical Fluid Dynamics*. Springer-Verlag Publishers, New York, 1987.
- [37] White, F. M., *Viscous Fluid Flow*, McGraw-Hill Book Company, New York, 1974.
- [38] Kelvin, Lord, "Vibrations of a Columnar Vortex". *Mathematical and Physical Papers, iv, Hydrodynamics and General Dynamics*, Cambridge, England, 152-165, 1880.
- [39] Fultz, D., "A Survey of Certain Thermally and Mechanically Driven Systems of Meteorological Interest". *Proceedings of the First Symposium on the Use of Models in Geophysical Fluid Dynamics*, Johns Hopkins University, Baltimore, 27-63, 1953.
- [40] Aldridge, K. D., and Toomre, A., "Axisymmetric Inertial Oscillations of a Fluid in a Rotating Cylinder". *Journal of Fluid Mechanics*, 37, 307-323, 1969.
- [41] Chandrasekhar, S., *Hydrodynamic and Hydromagnetic Stability*. Dover Publications, New York, 1981.

- [42] Taylor, G. I., "Stability of a Viscous Liquid Contained Between Two Rotating Cylinders". *Philosophical Transactions of the Royal Society of London*, A233, 289-343, 1923.
- [43] Greenspan, H. P., and Howard, L. N., "On a Time-Dependent Motion of a Rotating Fluid". *Journal of Fluid Mechanics*, 17, 385-404, 1963.
- [44] Wedemeyer, E. H., "The Unsteady Flow Within a Spinning Cylinder". *Journal of Fluid Mechanics*, 20, 383-399, 1964.
- [45] Weidman, P. D., "On the Spin-Up and Spin-Down of a Rotating Fluid. Part 1. Extending the Wedemeyer Model". *Journal of Fluid Mechanics*, 77, 685-708, 1976.
- [46] Venezian, G., "Nonlinear Spin-Up". *Topics in Ocean Engineering*, 2, 87-101, 1970.
- [47] Maas, L. R., "Nonlinear and Free-Surface Effects on the Spin-Down of Axisymmetric Vortices." *Journal of Fluid Mechanics*, 246, 117-141, 1993.
- [48] Floryan, J. M., and Rasmussen, H. "Numerical Methods for Viscous Flows with Moving Boundaries." *Applied Mechanics Reviews*, 42, No. 12, 323-341, 1989.
- [49] Patankar, S. V., and Spalding, D. B., "A Calculation Procedure for Heat, Mass and Momentum Transfer in Three-Dimensional Parabolic Flows." *International Journal of Heat and Mass Transfer*, 15, 1787-1806, 1972.
- [50] Chorin, A. J., "A Numerical Method for Solving Incompressible Viscous Flow Problems." *Journal of Computational Physics*, 2, 12-26, 1967.
- [51] Stone, H. L., "Iterative Solution of Implicit Approximations of Multi-dimensional Partial Differential Equations." *SIAM Journal of Numerical Analysis*, 5, No.3, 1968.
- [52] Schneider, G. E., and Zedan, M. "A Modified Strongly Implicit Procedure for the Numerical Solution of Field Problems." *Numerical Heat Transfer*, 4, 1-19, 1981.
- [53] McCormick, S. F., *Multigrid Methods: Theory, Applications, and Supercomputing*. Marcel Dekker Publications, New York, 1988.
- [54] Amsden, A. A. "The Particle-In-Cell Method for the Calculation of Compressible Liquids." *Los Alamos Scientific Laboratory Report*, LA-3466, 1966.
- [55] Welch, J. E., Harlow, F. H., Shannon, J. P., and Daly, B. J., "The MAC Method." *Los Alamos Scientific Laboratory Report*, LA-3425, 1966.
- [56] Nichols, B. D., and Hirt, C. W., "Improved Free Surface Boundary Conditions for Numerical Incompressible-Flow Calculations." *Journal of Computational Physics*, 8, 434-448, 1971.

- [57] Hirt, C. W., Nichols, B. D., and Romero, N. C., "SOLA - A Numerical Solution Algorithm for Transient Fluid Flows." *Los Alamos Scientific Laboratory Report*, LA-5852, 1975.
- [58] Hirt, C. W., and Nichols, B. D., "Volume of Fluid (VOF) Method for the Dynamics of Free Boundaries." *Journal of Computational Physics*, 39, 201-225, 1981.
- [59] Partom, I. S., "Application of the VOF Method to the Sloshing of a Fluid in a Partially Filled Cylindrical Container." *International Journal for Numerical Methods*, 7, 535-550, 1987.
- [60] Kitchens, C. W., "Navier-Stokes Equations for Spin-Up in a Filled Cylinder." *AIAA Journal*, 18, 929-934, 1980.
- [61] Hyun, J. M., Leslie, F., Fowles, W. W., and Warn-Varnas, A., "Numerical Solutions for Spin-Up From Rest in a Cylinder." *Journal of Fluid Mechanics*, 127, 263-281, 1983.
- [62] Goller, H., and Ranov, T., "Unsteady Rotating Flow in a Cylinder With a Free Surface." *ASME Journal of Basic Engineering*, 90, 445-454, 1968.
- [63] Homicz, G. F., and Gerber, N., "Numerical Model for Fluid Spin-Up From Rest in a Partially Filled Cylinder." *ASME Journal of Fluids Engineering*, 109, 194-197, 1987.
- [64] Choi, S., Kim, J. W., and Hyun, J. M., "Transient Free Surface Shape in an Arbitrarily-Rotating, Partially-Filled Cylinder." *ASME Journal of Fluids Engineering*, 111, 439-442, 1989.
- [65] Dommermuth, D. G., "The Laminar Interaction of a Pair of Vortex Tubes with a Free Surface". *Journal of Fluid Dynamics*, 246, 91-115, 1993.
- [66] Kassinos, A. C. *Melting in Rectangular Geometries in the Presence of Subcooling and Density Change*. M.S. Thesis. Iowa State University, Ames, Iowa, 1986.
- [67] Anderson, D. A., Tannehill, J. C., and Pletcher, R. H. *Computational Fluid Mechanics and Heat Transfer*. McGraw-Hill Book Co., New York, 1984.
- [68] Roache, P. J. *Computational Fluid Dynamics*. Hermosa Publishers, Albuquerque, New Mexico, 1972.
- [69] Welch, J. E., Harlow, F. H., Shannon, J. P., and Daly, B. J. "The MAC Method.", LASL Report No. LA-3425, Los Alamos Scientific Laboratory, Los Alamos, New Mexico, 1966.
- [70] Harlow, F. H. and Welch, J. E. "Numerical Calculation of Time-Dependent Incompressible Flow of Fluid with Free Surface." *The Physics of Fluids*, 8, No. 12, 2182-2189, 1965.

- [71] Kassinos, A. C., and Prusa, J. M. "A Numerical Model for 3-D Sloshing in Moving Containers", *Recent Advances and Applications in Computational Fluid Dynamics*, ASME Special Publications, FED Vol. 103, 75-86, 1990.
- [72] Shanks, S. P., and Thompson, J. F. "Numerical Solution of the Navier-Stokes Equations for 2D Hydrofoils in or Below a Free Surface", *Proceedings of 2nd Numerical Ship Hydrodynamics*, University of California, Extension Publ. 1987.
- [73] Thomas, P. D., and Middlecoff, J. F. "Direct Control of Grid Point Distribution in Meshes Generated by Elliptic Equations", *AIAA Journal*, Vol. 18, 650-666, 1980.
- [74] Hindman, R. G. "Geometrically Induced Errors and Their Relationship to the Form of the Governing Equations and the Treatment of Generalized Mappings", *AIAA Journal*, Paper 81-1008, Palo Alto, California, 1981.
- [75] Warn-Varnas, A., Fowles, W. W., Piasek, S., and Lee, S. M., "Numerical Solutions and Laser Doppler Measurements of Spin-Up", *Journal of Fluid Mechanics*, 85, 609-639, 1978.
- [76] Abramowitz, M., and Stegun, I. A., *Handbook of Mathematical Functions*. Dover Publications, New York, 1972.